How to improve major bone defect reconstruction?

From the periosteum to a bio-engineered osteogenic membrane

A tissue-based approach

Julie Manon

Août 2024

Thèse présentée en vue de l'obtention du grade de docteur en sciencies biomédicales et pharmaceutiques

Secteur des sciences de la santé

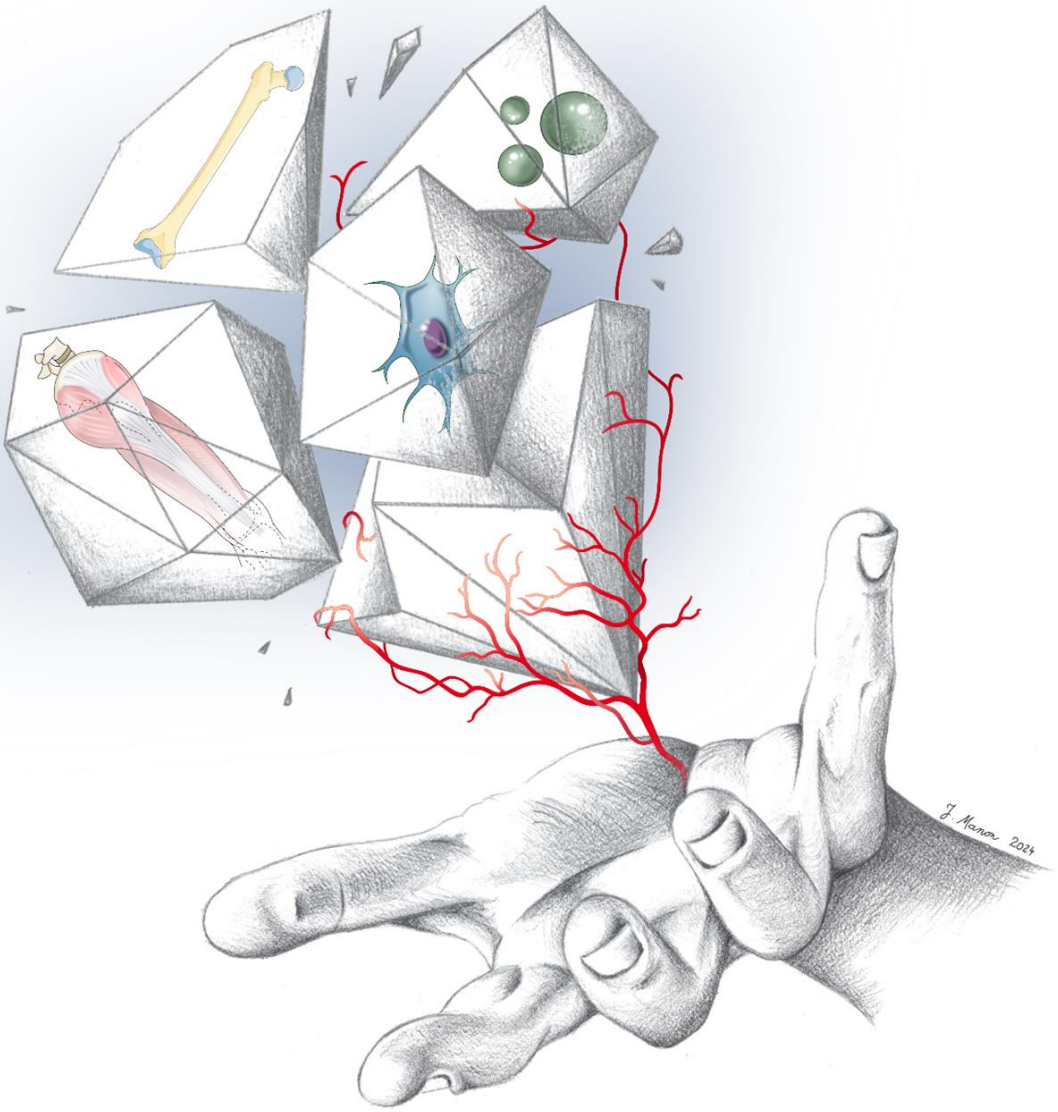

Cover illustration:

This illustration encapsulates the essence of my research through the « Diamond » concept, symbolizing the intricate interplay of body tissues, cells, signalling molecules, and blood vessels. The hand represents the delicate balance and precision needed to unify these elements. This visual metaphor evokes the harmony and complexity of life, inviting contemplation on the interconnectedness of the biological systems that sustain us. It sets the tone for the exploration and discoveries detailed within this thesis.

Université catholique de Louvain
Faculté de médecine
Institut de Recherche Expérimentale et Clinique
Neuromusculoskeletal Laboratory – Pole of Morphology
Service de Chirurgie Orthopédique et traumatologique

How to improve major bone defect reconstruction?

From the periosteum to a bio-engineered osteogenic membrane

A tissue-based approach

Julie Manon, PT, MD

Promotor: Pr. Olivier Cornu, MD, PhD
Co-Promotor: Pr. Catherine Behets, MD, PhD

Thesis submitted in fulfilment of the requirements for the PhD degree in Biomedical and Pharmaceutical Sciences

August 2024

Cliniques universitaires SAINT-LUC UCLouvain BRUXELLES | BANQUE DE TISSUS ET CELLULES DE L'APPAREIL LOCOMOTEUR

À mon Papa et mon Papy, dont les Forces et les Faiblesses m'ont construite

À Yvan, qui m'a appris que les Forces surpassaient les Faiblesses

À ma Maman, cet exemple, en laquelle je n'ai jamais vu de Faiblesses

À Berny, qui m'apprend que c'est une Force de montrer aussi mes Faiblesses

À ces patients qui pensent venir en consultation avec leurs Faiblesses mais dont la Force donne du sens à notre investissement

Jury

President of the jury	**Prof. Luc Bertrand** *Université Catholique de Louvain*
Promotor	**Prof. Olivier Cornu** *Université Catholique de Louvain*
Co-promotor	**Prof. Catherine Behets** *Université Catholique de Louvain*
Jury members	**Prof. Benoît Lengelé** *Université Catholique de Louvain*
	Prof. Greet Kerckhofs *Université Catholique de Louvain*
	Prof. Thomas Schubert *Université Catholique de Louvain*
	Prof. Pascale Saussoy *Université Catholique de Louvain*
Invited external jury members	**Prof. Alain-Charles Masquelet** *Université Paris – Sorbonne* *Académies Nationales de médecine et de chirurgie*
	Dr. Sophie Verrier *AO Research Institute Davos*

Author

Julie Manon
Université Catholique de Louvain – Service de Chirurgie Orthopédique et traumatologique
Avenue Hippocrate, 10 – B-1200, Brussels, Belgium
ORCID number : 0000-0002-2558-8723
julie.manon@uclouvain.be – ju-manon@hotmail.com - +32 495/61.15.64

Remerciements

Pourquoi laisse-t-on toujours l'écriture de ce paragraphe pour « la fin » alors qu'il se trouve toujours dans les premières pages, en avant-plan d'un manuscrit ? Est-ce la difficulté d'exprimer ou de révéler nos émotions, la crainte de se tromper dans les mots employés, de savoir si le message sera perçu avec la même intensité que son écriture ou le souci de parvenir à transmettre l'importance de cette section ?

Dans ce parcours effréné de fin de thèse, je voudrais m'arrêter, me poser et prendre le temps pour tenter d'exprimer les mots trop souvent tus… Au fil de ce manuscrit, vous trouverez çà et là quelques citations parsemées. Ne regardez pas la couleur, la grandeur, l'appartenance ou l'influence politique que pourrait avoir chaque auteur mais laissez-vous simplement inspirer par les mots. Chacune de ces citations est appelée dans cette section de remerciements. Une citation qui vous est associée, un message ou une inspiration qui relie le chapitre et votre personne, qui fait référence à notre rencontre, notre histoire, votre influence ou votre impact, une citation qui vient de vous, une citation pour vous, une autre manière de vous dire merci.

Comment penser au mot « Merci » sans commencer par mon promoteur, le **Professeur Olivier Cornu** *(pg. 285)*. C'est lui qui m'a littéralement ouvert l'esprit au monde scientifique, depuis mon mémoire en médecine jusqu'à cette thèse doctorale. C'est lui qui m'a interpellée, motivée, poussée, épaulée, et encouragée tout au long de ce parcours du combattant. Son imagination et sa créativité scientifique sont inégalables. Les petites réunions de 5 minutes se transformaient plus que fréquemment en échanges et débats de plusieurs heures parfois, plus intéressants et captivants les uns que les autres. J'entrais dans son bureau avec une question et ressortait avec plus de 10 idées nouvelles tel un feu d'artifice faisant exploser son inventivité. Je ne pourrai jamais affirmer que je serais arrivée au bout de tous ces projets sans son soutien inconditionnel, et pour cela, un simple merci ne sera jamais suffisant. Son humanisme mis au service des étudiants, des assistants, de ses doctorants mais aussi et surtout de ses patients nous offre les plus beaux aspects de la chirurgie qui n'est pas un métier comme les autres et qui restera, pour moi, une image dont je voudrais m'inspirer pour ma future carrière.

Ma co-promotrice, le **Professeur Catherine Behets** *(pg. 5)* est la seule personne qui a tracé et suivi tout mon cheminement éducatif depuis le début, depuis mes premiers pas à l'université. En effet, Professeur d'anatomie et d'histologie en kinésithérapie, elle avait

déjà marqué mon parcours par sa connaissance incroyable dans l'organisation tissulaire et le lien entre le micro- et le macroscopique. Elle m'a fait redécouvrir l'importance de la filiation des travaux et je ne la remercierai jamais assez pour ses corrections attentives, soignées, précises et en profondeur ainsi que pour ses qualités de modératrice.

La complémentarité de mes promoteurs restera pour moi, une des plus grandes qualités de leur encadrement. Je leur suis profondément reconnaissante également de m'avoir fait confiance et de m'avoir permis de m'investir dans le projet « M.A.R.S. » en parallèle de cette thèse.

Je remercie tous les membres du jury dont le président, le **Professeur Luc Bertrand**, pour ses questions et conseils lors des comités d'encadrement, le **Professeur Greet Kerckhofs** pour son intérêt, sa vision d'ingénieur et son apport considérable en sciences fondamentales, ainsi que le **Professeur Pascale Saussoy** pour sa gentillesse, son soutien et ses encouragements réconfortants. Il ne faut pas oublier **Sandrine Wollanders** qui orchestre d'une main de maître tout le côté administratif des comités et du chemin doctoral.

Figure emblématique et Maître d'anatomie par excellence, le **Professeur Benoît Lengelé** *(pg. 43)* a pris une très grande place dans mon parcours éducatif et doctoral. Depuis les bancs de l'école, j'écoutais attentivement avec les yeux émerveillés d'une enfant, le récit du théâtre anatomique se déroulant à la craie sur le tableau noir. Je ne pourrai jamais exprimer mieux que lui la rigueur, la précision, la justesse et l'intensité de ces enseignements, digne d'une œuvre d'art et je vous invite donc chaleureusement à lire la remarquable transmission « l'anatomie au chevet de l'Histoire » (B. Lengelé, 2023[1]). J'en suis et en resterai la première conteuse pour tenter de transmettre l'importance, l'impact et le retentissement de ces dessins, de ces mots, et de cet investissement qui sont les siens. Plus tard, il m'a démontré l'importance de la recherche et de la transition entre le fondamental et la clinique, notamment par la touchante histoire de Samuel. Mettant un point d'honneur aux soins de ses patients, la problématique pathologique demande une réponse réfléchie et approfondie sur base de preuves irréfutables via l'étude précise et rigoureuse des structures anatomiques et leur ultrastructure microscopique. Il m'a donc appris les fondements de l'« evidence-based medicine ». Il a fait bien plus que me transmettre son enseignement et ses valeurs, il m'a poussée dans mes retranchements, il m'a mise face à mes erreurs et mes responsabilités et m'a appris à réfléchir sur moi-même. Je n'oublierai jamais cet enseignement marquant.

Doté d'un esprit curieux, critique et pragmatique, le **Professeur Thomas Schubert** *(pg. 21)* m'a guidée par sa manière d'appréhender les problèmes. La narration de ses échecs et succès de thèse nous aura déjà valu quelques fous rires, mais surtout tellement de bons

conseils et astuces qui m'ont permis de ne pas réinventer la roue. Merci pour ce transfert et partage d'expérience précieux. En plus de ses gestes et de son aisance chirurgicale que j'aimerais parvenir à imiter un jour, je retiendrai également son abnégation sans faille envers ses patients.

L'honneur est immense d'avoir pu discuter de mes travaux avec le **Professeur Alain-Charles Masquelet** *(pg. 355)*. Alors que j'apprenais la technique de la membrane induite en tant qu'élève attentive, pensant naïvement apprendre une chirurgie transmise depuis "plusieurs générations", quel ne fut pas mon enthousiasme à l'idée d'apprendre qu'il était possible de rencontrer son fondateur ! Notre première rencontre remonte à novembre 2021 dans le décours des 1ères Rencontres Internationales de Chirurgie Française (RICF) à l'Académie Nationale de Chirurgie, suivies du congrès de la SOFCOT à Paris. Mes attentes ont rapidement été surpassées par ses nombreuses qualités de chirurgien, de chercheur, d'enseignant, de philosophe, mais aussi et surtout par son humilité qui force l'admiration. Son récit sur la découverte de cette membrane induite et la sérendipité me fascine. Il m'explique qu'il ne s'agit pas d'une invention mais d'une découverte fortuite alors qu'il se disait, je le cite, « fainéant » de ne pas vouloir débrider la néomembrane, pour éviter également un saignement excessif. Quelle modestie alors qu'il obtient le prestigieux Prix Meyer cette année 2024, récompensant les plus grandes découvertes ou innovations mondiales en orthopédie. Cet exemple de Grand Homme inspire et oriente nos chemins, merci pour ce modèle !

Ma rencontre avec le **Docteur Sophie Verrier** *(pg. 361)* n'est pas matérielle mais idéologique. Sa détermination, ses ambitions et convictions ainsi que son jusqu'au-boutisme qu'elle laisse transparaître à travers son écrit dans « Voices for change » (*https://www.aofoundation.org/who-we-are/about-ao/news/2023/ao-voices-for-change-sophie-verrier*) résonnent avec les miens. Je suis enchantée et la remercie grandement d'avoir accepté de faire partie de mon jury.

Ce travail n'est pas le fruit d'une imagination soudaine née un beau matin au milieu de nulle part, il découle directement d'une filiation institutionnelle qui m'a touchée. En effet, cette idée n'aurait jamais pu émerger sans les bases solides construites par le **Professeur Christian Delloye** *(pg. 37)*, précédent chef de service d'orthopédie aux Cliniques universitaires Saint-Luc et fondateur de la Banque des tissus. De son vivant, il a fait naître et évoluer ce projet pour « redonner de la vie aux greffes osseuses ». Dans ses pas, je m'efforce de ne pas décevoir l'exemple et le message qu'il nous a laissés, celui d'un Homme

passionné, brillant, inspirant et dévoué. Le **Fonds Christian Delloye** nous a apporté un soutien incommensurable et a littéralement porté ce projet qui n'aurait jamais pu voir le jour autrement. Que son épouse, **Christiane Van Zuylen,** ainsi que ses frères et toute la **Famille Delloye**, reçoivent ici l'expression de ma plus chaleureuse reconnaissance et de mon dévouement infini.

Un travail de thèse n'est pas non plus le reflet d'une personne, mais d'une équipe. Une équipe sans qui la mise en œuvre et la réalisation des objectifs seraient impensables. Je suis consciente de la chance énorme que j'ai eue d'avoir pu travailler avec cette équipe riche en couleur, expérience, motivation, et partage.

La première personne de cette équipe que je souhaite remercier du fond du cœur, et qui en est la pièce maitresse, n'est autre que **Lies Fievé** *(pg. 133)*. Sa rigueur, sa précision, son organisation, son souci de comprendre son travail et son intelligence de comportement ont ensoleillé mon quotidien et en font une technicienne en or. Je souhaite à tous les doctorants de pouvoir un jour être accompagnés par une perle aussi rare car ce soutien et cette confiance sont inestimables.

L'équipe ne serait rien sans l'assemblage d'une belle brochette de doctorants *(pg. 191)* avec qui j'ai partagé tant de choses mémorables. **Robin Evrard**, mon compagnon de galères par excellence, grâce à qui et avec qui j'ai pu affronter et vivre les pires comme les meilleurs moments de cette thèse, et dont la qualité m'a toujours poussée vers le haut. **Louis Maistriaux**, mon voisin de bureau pendant mes 2 premières années, qui aura changé à tout jamais ma vision de la chanson « Petite Marie » et de « Monsieur Ouille ». **Alexandre Englebert,** qui a préféré faire médecine parce qu'il savait qu'il pouvait faire ingénieur tout seul : sa capacité d'auto-apprentissage et son aide toujours généreuse m'étonneront toujours. **Randy Buzisa,** avec qui j'ai déjà pu discuter des heures durant de nos perspectives et aspirations. **Clotilde de Dorlodot,** ma nouvelle voisine de bureau dont le sourire et la bonne humeur me reboostent toujours. **Guillaume Glaudot,** fervent supporter de Tchalou. **Grégoire André**, le camarade de course à pied. **Antoine Chrétien,** qui ajoute une petite touche de couleur française au labo. **Gaspary Fodjeu**, qui a toujours la pêche. **Cédric Dongmo**, mon « filleul ». Et aussi **Loïc Fonkoué**, **Hervé Poilvache, Matias Ramirez,** et tous les doctorants de **NMSK** qui m'ont toujours accueillie les bras ouverts.

Plusieurs étudiants ont également mis la main à la pâte et méritent ma sincère reconnaissance *(pg. 67)*, notamment les étudiants en médecine (**Lucien Van den Broeck**, **Mathieu Jacob** et **Lukas Dohmen**), en kinésithérapie (**Laurie Gallant**, **Paul Gérard** et **Frédéric Delandmeter**), en sciences biomédicales (**Julia Vettese**), en polytechnique

(**Laurine Bonaventure** et **Eléonore Gillerot**) et de la Haute Ecole Léonard de Vinci (**Nawal Azghay** et **Philippine Vanham**). Ainsi que les autres étudiants qui m'ont rejointe sur d'autres projets annexes mais qui m'ont permis de ne jamais me reposer sur mes lauriers, incluant également des étudiants en médecine (**Julien Meert**, **Antoine Hachez** et **Maurine Pireau**) et de l'ECAM (**Seynabou Cissé** et **Wassil Hodaibi**). Leur diversité était une réelle source d'inspiration pour évoluer en pédagogie. Merci à eux tous pour leur investissement.

Je souhaite remercier particulièrement **Julia Vettese** *(pg. 177)*, qui a débuté à nos côtés il y a maintenant 3 ans lors de son stage de Master 1 puis Master 2, qui progresse de manière exponentielle et qui a entrepris un nouveau chemin doctoral cette année, reprenant la suite de ma thèse. Je ne connaissais pas avant ce bonheur de pouvoir transmettre à quelqu'un de super motivée et de confiance. Je suis très fière de son parcours et certaine que sa persévérance et sa détermination la mèneront loin. Comme promis, je serai toujours là pour t'épauler si tu en ressens le besoin et serai la plus ravie de suivre ton évolution.

Gestionnaire des commandes et de nos budgets, **Murielle Callier** *(pg. 63)* fait partie de cette équipe et aura été la plus belle rencontre virtuelle de ma vie ! Bien que je sois pour les échanges réels et n'étant pas spécialement adepte des rencontres à distance, une complicité est née au travers des innombrables emails échangés… Comme quoi, le « courant » peut bien passer par « ordinateur » et je lui dois une aide administrative considérable. Merci Mumu !

Ce travail étant relativement multidisciplinaire, j'ai eu le grand privilège de pouvoir collaborer et évoluer dans plusieurs laboratoires et environnements de travail, ce qui était d'une richesse fantastique.

Au sein de l'Institut de Recherche Expérimentale et Clinique (**IREC**), le laboratoire du système neuromusculosquelettique (**NMSK)**, auquel je suis affiliée, m'a accueillie en début de parcours doctoral avec une épaule sereine et rassurante. Le **Professeur Christine Detrembleur** m'a donné confiance en moi et m'a transféré sa passion pour les statistiques, science redoutée de chacun, mais qu'elle a su rendre fascinante pour moi.

Le laboratoire de morphologie (**MORF)** a été en quelque sorte ma maison durant ces 4 années. Il m'a donné tant et plus de ressources pratiques et intellectuelles pour le bon déroulement de cette thèse. Parmi ses membres, je voudrais citer **Michelle Cougnon**, cette oreille attentive et empathique, **Walter Hudders**, l'homme de toute situation, le **Professeur Marie-Christine Many**, dont la mémoire et la bienveillance sont épatantes, et bien évidemment, **Christine de Ville de Goyet**, la reine de l'histologie, **Bernard Caelen** et **Nicolas Charles-Pirlot**.

Je ne peux écrire ces remerciements sans avoir une pensée pour le **don de corps**, les défunts et leurs familles, pour qui le don devient le cadeau le plus cher.

Le laboratoire de chirurgie expérimentale et transplantation (**CHEX**), singulièrement spécifique, où se réunissent salle d'opération, microchirurgie et animalerie, reçoit également ma sincère reconnaissance. Les **Professeurs Pierre Gianello** et **Eliano Bonaccorsi Riani** m'ont tous deux permis de réaliser les expérimentations animales dans les meilleures conditions. À ce titre, le **Professeur Jean-Paul Dehoux**, notre maître vétérinaire, **Daela Xhema**, la force vive du laboratoire, **Gwen Beaurin**, le chasseur légendaire au discours sans détour, **Tom Darius**, qui m'a initié à la chirurgie porcine, **Pavel Babczenko**, **Pascale Segers**, **Martial Vergauwen**, **Nizar Mourad**, **Adèle Fleurus** et **Antoine Buemi**, ont tous été des acteurs primordiaux partageant soit leur expérience, leur savoir ou leur enthousiasme. Vivement merci !

La contribution de la **Banque de tissus** a été d'un réel renfort, service et soutien dans ce travail. **Xavier Merny**, **Olivier Goffin**, **Laurence Lekeux**, **Dimitri Roman**, **Andreia Teixeira da Cunha**, **Shalaw Fawzi**, **Angélique Arts**, **Anthony Marais**, **Dimitri Pinto**, **Paulo Ferreira Gomes Duarte**, **Bernard Godts** et tous les membres de cette entité ont été des atouts généreux pour qui j'atteste toute ma gratitude.

Faisant un boulot remarquable et accessible à tout l'institut, la **plateforme d'imagerie 2IP** n'a jamais hésité à apporter et partager ses compétences avec envie, sourire et passion. Je dois ce support technique considérable au **Docteur Caroline Bouzin**, à **Aurélie Daumerie**, **Michele de Beukelaer** et **Marc de Bournonville** que je remercie infiniment.

La partie microCT n'aurait pu voir le jour sans le développement et la présence de l'équipe **ContrasT Team**, dirigée par le **Professeur Greet Kerckhofs**, avec notamment **Grzegorz Pyka**, **Pierre Schneidewind**, **Delia Hoffmann** et **Walid El Aazmani**.

Les échanges « externes » à l'IREC ont aussi permis d'apporter une richesse à cette équipe, fruit d'une collaboration avec les Cliniques Universitaires Saint-Luc (**Professeur Pierre-Louis Docquier**, qui répond présent à chaque demande d'aide, **Dr. Audrey Lentini**, qui m'a appris toutes les bases et détails du lambeau ALT, **Xavier de Spiegeleire** et **Quentin Lostrie**, techniciens hors pairs en radiologie, **Sandrine Frédéric**, cheffe de la stérilisation, **Dominique Dutrieux**, alias « Domi », technicienne en microbio), avec l' « Institute of Condensed Matter and Nanosciences » à Louvain-la-Neuve (IMCN, **Delphine Magnin**) et l'Ecole Nationale Supérieure de Techniques Avancées (ENSTA) à Paris (**Ugo Heller**, ainsi que les **Professeurs Jean Boisson** et **Natacha Kadlub**).

Je souhaite également adresser un remerciement véritable au service de **chirurgie orthopédique et traumatologique de Saint-Luc** ainsi que tous ses membres pour leur accueil et leur encadrement dans ma formation chirurgicale.

Plus personnellement, il y a des personnes sans qui je ne serais jamais arrivée ici. Impossible pour moi d'oublier d'où je viens quand je pense à ceux qui m'ont fait grandir.

Yvan Keuwez *(pg. 289)*, mon entraîneur de volley, aura laissé une trace indélébile dans ma construction en tant qu'adolescente. Je devais « allumer mes neurones », « arrêter de me comporter comme une enfant », « ne pas rester dans le pot commun », « avoir la haine de la défaite », « viser le haut du pavé », avoir un « fighting spirit », et j'en passe… Je sais aujourd'hui, grâce à lui, ce que veut dire le mot « transmission », c'est l'éternité !

Je ne trouverai jamais les mots adéquats pour qualifier l'intensité de mes sentiments et de ma reconnaissance envers ma **Maman**, preuve irréfutable de courage et de ténacité, et sans qui ce parcours académique tiré en longueur aurait tout simplement été impossible, ma petite sœur **Hélène**, mon exemple de stabilité et de force tranquille, et **Louis**, le petit frère le plus fidèle et attachant et avec qui j'aime refaire le monde. Au-delà de ma façade rocailleuse, je m'efforce d'être/devenir l'épaule sur laquelle ils pourront toujours compter, avec beaucoup de sensibilité inexprimée *(pg. 7)*. Une pensée également pour **Nounou**, dont la gentillesse et la bienveillance nous accompagnent depuis tant d'années.

Un chemin de thèse doctorale est jalonné de joies, de peines, de victoires, de défaites, de reconnaissances et de tourments. Il m'est difficile d'exprimer ô combien la présence d'êtres chers comme la famille et les amis est primordiale dans ces émotions diamétralement opposées.

Merci aux valeureux Clermontois *(pg. 235)* qui ont mis tellement de cœur à rendre ce travail plus simple et léger comme par exemple, le **Rapide**, le créateur de la table chirurgicale pour cochons, **Ruddy Coulon**, qui a sauvé mon cochon, **Yvonic Tevel**, qui m'a permis de faire des trous borgnes grâce à ses tarauds sophistiqués ou **Philippe Thibaut**, qui a joué les bricoleurs en pleine période d'écriture. Que ces derniers mais également tous ceux qui m'ont soutenue de près ou de loin soient remerciés chaleureusement.

Mes sentiments les plus chers vont à **Berny** *(pg. 357)*, qui m'a tant soutenue et encouragée à chaque instant et qui continue à m'apprendre bien plus chaque jour que ce que je ne pourrai jamais trouver dans les livres !

À **Jean**, **Julien** et **Louise**, puisque je ne suis finalement pas « décédée » après avoir « autant travaillé » … Par ce travail, j'espère vous transmettre l'envie de vous donner les moyens de vos ambitions *(pg. 357)*. Ne vous arrêtez jamais de penser que vous êtes capables de vos rêves !

Merci enfin à tous ceux qui, de manière consciente ou non, m'ont toujours portée vers le haut et ont cru en moi.

Le temps de s'arrêter, regarder en arrière le chemin parcouru et se rendre compte que sans toutes ces personnes, le chemin n'aurait pas eu la même saveur, le même sens, ou n'aurait peut-être même tout simplement jamais existé !

Merci !



Paris, 2021

Table of contents

Foreword 1

General introduction 5

Bone union & non-union 7

A. Bone structure 7

B. Bone union & fracture healing 9

B. 1. Physiological healing 9

B. 2. Clinical healing 14

C. Bone non-union & major bone defect 16

C. 1. Fracture non-union – Pseudarthrosis 16

C. 2. Major or critical-size bone defect 19

Bone regeneration concepts: Periosteum, Diamond concept & Induced Membrane 21

A. Periosteum 21

A. 1. Tissular structure 21

A. 2. Function 24

B. Diamond concept 26

C. Induced membrane 29

C. 1. The discovery 29

C. 2. Surgical technique 30

C. 3. A biological chamber 32

C. 4. Up-to-date clinical knowledge 34

Current treatments & limitations 37

A. Current treatments 37

B. Current limitations 38

B. 1. Integration and unification of bone regeneration concepts 38

B. 2. Massive bone allografts 38

Hypothesis: Tissue engineering contribution 43

A. Tissue engineering concept 43

B. Scaffolding: Biomaterial & technique 44

C. Decellularization 47

C. 1. Techniques and agents 47

C. 2. Validation criteria 50

D. Sterilization & storage 51

E. Recellularization 52

E.1. Cell potency and phenotype 52

E.2. Mesenchymal stem cells 53

E.3. Periosteal mesenchymal stem cells 56

E.4. Transplant donors 58

F. Application: Fascia lata based scaffold 59

F.1. Fascia lata & iliotibial tract 59

F.2. Clinical use 61

F.3. Tissue bank protocol – NaOH-based decellularization 61

Objectives 63

CHAPTER I. Native tissue comparison 67

Research questions emerging from the Diamond 67

Paper 1 – Periosteum and fascia lata: Are they so different? 69

Abstract & graphical abstract 71

Full-length article 75

– TAKEAWAYS – 99

Paper 2 – 2D and 3D microstructural analysis of the iliotibial tract 101

Abstract 103

Full-length article 105

– TAKEAWAYS – 127

Back to the Diamond 129

CHAPTER II. Decellularization 133

Research questions emerging from the Diamond 133

Paper 3 – HLA Awareness in Tissue Decellularization: A Paradigm Shift for Enhanced Biocompatibility, studied on the Model of the Human Fascia Lata Graft 135

Abstract & graphical abstract 137

Full-length article 141

– TAKEAWAYS – 175

Collagen fibres & cross-links 177

A. Collagen fibres 177

B. Collagen cross-links 178

B. 1. Enzymatic cross-links 179

B. 2. Non-enzymatic cross-links 179

B. 3. GAG interfibrillar bridges 179

Paper 4 – Collagen molecular organization preservation in human fascia lata and periosteum after tissue engineering 181

Abstract 183

– TAKEAWAYS – 185

Back to the Diamond 187

CHAPTER III. New osteogenic membrane 191

Research questions emerging from the Diamond 191

Paper 5 – A New Osteogenic Membrane to Enhance Bone Healing: At the Crossroads between the Periosteum, the Induced Membrane, and the Diamond Concept 193

Abstract & graphical abstract 195

Full-length article 199

– TAKEAWAYS – 227

Back to the Diamond 229

CHAPTER IV. *In vivo* transposition – Critical-size bone defect repair 233

Research questions emerging from the Diamond 233

Technical considerations 235

A. Model of critical-size bone defect in the porcine femur 235

B. Mechanical stability & osteosynthesis 235

B. 1. Mechanical stability, a facet of the Diamond 235

B. 2. Intramedullary nailing creation 237

C. Surgical table 238

Paper 6 – FixThePig: a custom 3D-printed femoral intramedullary nailing for preclinical research applications 241

Abstract 243

– TAKEAWAYS – 245

Paper 7 – An osteogenic membrane to enhance massive bone allograft integration: *In vivo* pilot study in a minipig model 247

Abstract 249

Full-length article 251

– TAKEAWAYS – 279

Back to the Diamond 281

CHAPTER V. Vascularization 285

Relationship between angiogenesis & osteogenesis 285

A. Angiogenesis & bone growth/repair 285

B. Ischemic threshold 287

Osteogenic membrane revascularization 289

A. New vascular network creation by tissue engineering 289

A. 1. In vitro pre-vascularization strategies 289

A. 2. In vivo pre-vascularization strategies 290

B. Native vascular network use 292

Research questions emerging from the Diamond 293

Paper 8 – A single Angiofil-latex injection for both radiological and anatomical assessment of arterial territories in the limbs 295

Abstract & graphical abstract 297

– TAKEAWAYS – 301

Paper 9 – Beneath the Perforators: Unravelling Fascia Lata Intrinsic Vascular Architecture 303

Abstract 305

Full-length article 307

– TAKEAWAYS – 323

Paper 10 – Revisiting the variants of the Anterolateral Thigh Flap based on 3D Microscopic Vascular Investigations 325

Abstract 327

Full-length article 329

– TAKEAWAYS – 349

Back to the Diamond **351**

General discussion & conclusion 355

Main achievements **355**

Limitations **357**

Future directions & perspectives **361**

Appendices 367

Paper 4 – Collagen molecular organization preservation in human fascia lata and periosteum after tissue engineering **369**

Abstract 371

Full-length article 373

Paper 6 – FixThePig: a custom 3D-printed femoral intramedullary nailing for preclinical research applications **391**

Abstract 393

Full-length article 395

Paper 8 – A single Angiofil-latex injection for both radiological and anatomical assessment of arterial territories in the limbs **413**

Abstract & graphical abstract 415

Full-length article 419

List of abbreviations 445

Definitions of useful terms 455

References 457

Grants & awards related to this thesis 491

Thesis annexe 497

Tharsis mission – A Martian Simulation 497

Summary 499

Foreword

« Je m'appelle Marjorie. J'ai 44 ans. J'ai 3 enfants et je suis institutrice maternelle. Un peu banal me direz-vous. Pas pour moi. A 8 ans, j'ai failli perdre ma jambe. A 10 ans, j'aurais pu perdre mon pied. Si je suis aujourd'hui sur mes 2 pieds et capable de vivre cette vie banale, c'est grâce aux allogreffes, aux progrès de la science et au génie des chirurgiens que j'ai rencontrés sur ma route.

Mai 1989, j'ai mal au genou, je boîte. Je ne suis pas du genre à me plaindre, mes parents m'emmènent chez un orthopédiste. Le verdict tombe : ostéosarcome du fémur. La chimio démarre mais l'orthopédiste qui s'occupe de moi ne pense pas pouvoir sauver ma jambe. Mes parents rencontrent alors son assistant : Le Dr Delloye. Lui veut sauver ma jambe. Il veut tenter de me mettre une prothèse sur une allogreffe, une première en Belgique. Mes parents acceptent et il le fait. Je me souviens encore de la joie dans le couloir du service orthopédie quand j'ai bougé mes orteils.

J'ai 8 ans, je ne me rends pas compte du miracle qui vient de se réaliser. Je reprends ma vie là où je l'avais laissée : je cours, je danse, je fais du ski, du patin à roulettes. Bref, je vis.

Pendant ce temps, à l'intérieur de mon corps, un miracle se produit, l'allogreffe prend bien et devient mon os.

1990. J'ai mal à la cheville. Je ne suis toujours pas du genre à me plaindre. Les médecins n'hésitent pas, ils me font des radios. Nouveau verdict : ostéosarcome de la malléole. De nouveau, réticence de l'orthopédiste qui a gardé mon suivi : il peut peut-être sauver mon pied mais il va devoir l'immobiliser à 90°. Nouvelle intervention du Dr Delloye : il va sauver et mon pied et la mobilité de mon articulation. Après une reconstruction et un peu de patience, ma cheville est mobile. Encore une belle réussite.

J'ai 10 ans et je ne me rends toujours pas compte du nouveau miracle. Je vis toujours aussi normalement. Peut-être même plus intensément que les autres d'ailleurs.

1998. J'ai quelques douleurs. La radio montre une usure de la prothèse. Il faut changer un matériel qui a vécu avec moi. L'opération est un succès.

2008 : Je suis institutrice maternelle et j'ai eu 2 enfants. Ma vie n'en a été que plus intense. Il faut de nouveau changer la prothèse et faire une nouvelle greffe. L'opération se passe bien mais la greffe ne prend pas à fond. Cela ne m'empêche pas de continuer à fonctionner normalement.

2015 : Aie, ma vie est peut-être trop intense, je casse un morceau de fémur greffé. Nouvelle opération de sauvetage, nouvelle reconstruction.

2020 : Descellement de la prothèse. Nouveau chirurgien, le Dr Schubert reprend le flambeau. Je suis en confiance. Nouvelle reconstruction, nouveau succès. Je suis très vite sur pied.

11 octobre 2023 : C'est le drame : j'ai cassé des vis qui faisaient fonctionner l'articulation de ma hanche correctement. 3 longs mois à attendre l'implant. 3 mois de béquilles pour essayer de sauver ce qui n'est pas abîmé. Ma vie n'est pas en danger mais ma santé mentale en prend un coup.

16 janvier 2024 : Le jour tant attendu est enfin arrivé. Le Dr Schubert et le Dr Cornu ont du boulot. La reconstruction et la pose de l'implant sont un succès.

21 mars 2024 : Je reprends le travail. Je marche bien. Ma mobilité est meilleure qu'avant. J'ai retrouvé ma vie.

Ce témoignage est sûrement plein d'erreurs. Je ne suis pas médecin et surtout, j'ai décidé de ne garder que le positif. Oui, j'ai souffert. Oui, j'ai douté. Mais j'ai toujours été soignée afin que ma vie reste belle.

Le Dr Schubert m'a dit cette phrase avant la dernière opération : « Quand vous aviez 8 ans, on a sauvé votre jambe et donné une qualité de vie. Il est maintenant de notre responsabilité de la maintenir ».

Alors merci. Merci aux médecins qui se battent pour que nous puissions vivre notre meilleure vie. Merci aux chercheurs. Et merci à ceux qui les financent. »

Marjorie,
Lundi 25 mars 2024



Courtesy of Romain Joly, https://romainjolyillustration.com/

General introduction

« The art of reading is the art of thinking with a little help. »

Translated from Emile Faguet, 1898

Marjorie's history is singular for you… But not for her… And not for them!
Marjorie's journey with treatment on massive allografts offers a poignant glimpse into the challenges faced by many patients grappling with bone defects. Her story, though unique, resonates with countless others who are also in need of effective medical solutions.

Osteosarcoma is a primitive osseous malignant tumor causing bone and soft tissue invasion that requires massive resections for treatment. However, this tumor is far less frequent than metastases, infections, or fractures. In Belgium, 75,000 cancers are diagnosed per year, with predominance of prostate and breast cancers in men and women respectively[2–4]. Breast, prostate, kidney, thyroid, and lung cancers are recognized to preferentially metastasize to bone[3]. Sepsis can occur as a nosocomial complication such as after a prosthetic joint replacement (prosthetic joint infection, PJI), which has progressively increased over the years[5], or consequently to a fracture. Bone fractures are the most prevalent form of traumatic injuries in human beings[6].

As we delve deeper into the possible aetiologies requiring treatment similar to Marjorie's, it becomes evident that she is not alone in her quest for healing. The number of bone lesions necessitating treatment increased twofold from 2012 to 2020[7]. Since this phenomenon can be attributed to factors such as aging, traumas, lifestyle, congenital conditions, and obesity, the prevalence can be expected to be in constant increase. Therefore, the demand for bone replacement, tailored approaches, and innovative treatments has risen significantly on a global scale, presenting a major scientific, socio-economic, and clinical challenge.

Upon leaving school, we learned from books, repeating, and memorizing with the ambition of Pavlov's dog to receive a reward, good points on the school report. Despite several years of learning, we still find ourselves at the very bottom of the ladder, sometimes at a loss when faced with a real patient with concrete pathologies. The ability to draw on our theoretical knowledge and put it into practice is not as intuitive as it sounds. Moreover, practice is often hampered by a lack of knowledge or scientific evidence to apply evidence-based medicine.

These patients, like Marjorie, place their hopes in the advancements of modern evidence-based medicine and the dedication of healthcare professionals. They look to us, the medical community, with anticipation and trust, hoping that our collective efforts can pave the way for improved outcomes and enhanced quality of life. Marjorie's experience serves as a reminder of the broader landscape of patients awaiting solutions, urging us to delve deeper into research, explore new technologies, and push the boundaries of medical knowledge.

This thesis is designed to engage readers at various levels. It begins by exploring foundational theoretical concepts, creating a solid framework for comprehending subsequent research. Each chapter then delves into specific topics, supplemented by relevant scientific papers linked to the subject matter. Every paper is introduced with its abstract and, when available, graphical abstract, followed by the full-length original article. Key contributions of each paper are succinctly summarized in « takeaways » for quick recall, in alignment with the common thread of the thesis. Methodological papers are included in appendices. Each chapter starts with the research question emerging from the Diamond concept and concludes with a « back to the Diamond » section, answering those questions. This structure allows readers to either explore topics in-depth or opt for a more concise understanding, tailored to their preferences and needs. Visual elements throughout the thesis, including schemas and figures, are either custom-designed or adapted from cited sources, providing visual anchors to the concepts presented.

In this way, we aim to cater to the diverse expectations of our readers, with the hope that they will find enjoyment and enlightenment in exploring this work, much as we did in its creation.

Bone union & non-union

« There's always something of childhood left, always… »

Translated from Marguerite Duras, 1946

A. Bone structure

Bones are complex skeletal structure providing structural support and protection to the body. These living organs serve multiple functions, including haematopoiesis within the bone marrow, mineral homeostasis by storing calcium and phosphorus, and facilitating movement thanks to joints and muscles. Three main parts compose a long bone (Fig. 1).

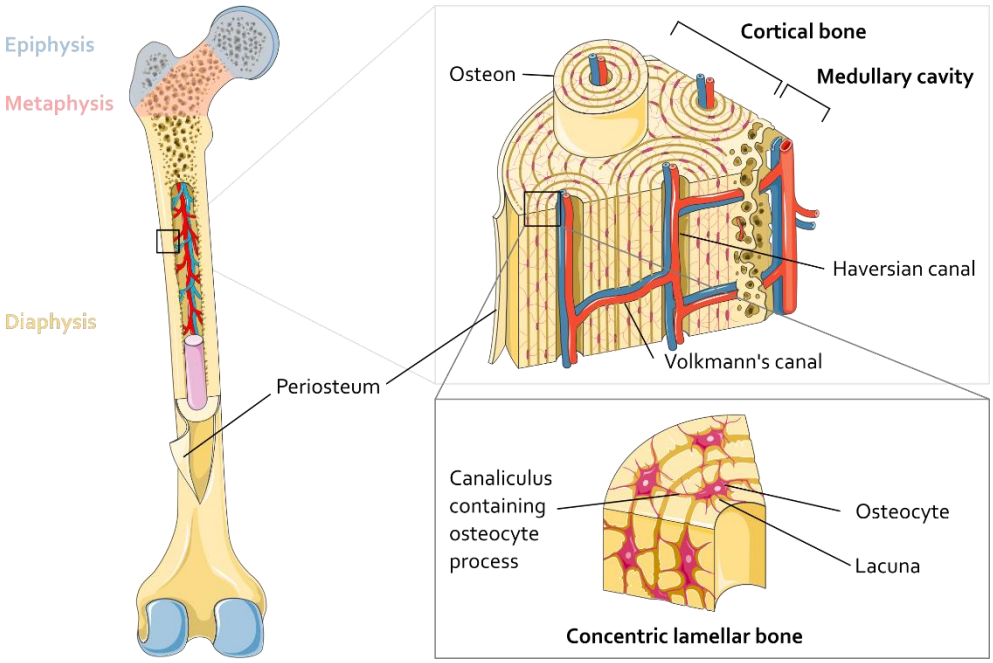

Figure 1. Bone structure at different levels, from a macroscopic to a microscopic view.

The diaphysis is the main tubular part, composed of a central medullary cavity, surrounded by compact cortical bone and enveloped into an external collagenic soft membrane, the periosteum[8]. The epiphyses, partly covered with articular cartilage, are the bone extremities and join the diaphysis through metaphyses, both consisting of a 3D network of cancellous or trabecular bone. The cortical bone is mainly composed of circumferential lamellar bone which can be organized concentrically around a Haversian vascular canal forming an osteon subunit parallel to the main bone axis[9,10]. Haversian systems are connected through transversal Volkmann's canals[10].

Bone tissue is composed of a variety of cells (osteoblasts, osteoclasts, osteocytes) and a composite extracellular matrix (ECM) consisting of organic matrix that is reinforced by inorganic minerals (calcium and phosphate combined in hydroxyapatite: $Ca_{10}(PO_4)_6(OH)_2$)[11]. The organic bone matrix is made up of type I collagen (Col-1) fibres (up to 95%[12]), and non-collagenous proteins (*e.g.* proteoglycans, bone morphogenetic protein (BMP), osteocalcin (OC) and alkaline phosphatase (ALP))[11].

This dynamic tissue undergoes constant remodelling, balancing processes of bone resorption by osteoclasts and bone formation by osteoblasts[12]. The remodelling is a coordinated sequence of cellular activities that follow the order of quiescence, activation, osteoclastic resorption, inversion, osteoblastic apposition, and back to quiescence[10,13]. Osteocytes are osteoblasts enclosed into the new bone matrix (Fig. 2)[12].

Remodelling is a perpetual process that continually replaces old bone with new secondary bone, giving bone its vitality and turn-over, striving to preserve the maximal bone stock and mechanical integrity throughout life[10,12].

These characteristics also confer on bone the incredible advantage of *ad integrum* restitution when healing conditions are appropriate[11,14], such as mechanical stability, adequate blood supply, and early or safe mobilization according to AO Trauma principles of fracture management[15]. However, the extent of restoration can vary depending on a large amount of factors such as the demographics and health of the individual, the fracture type, and the treatment effectiveness[16,17].

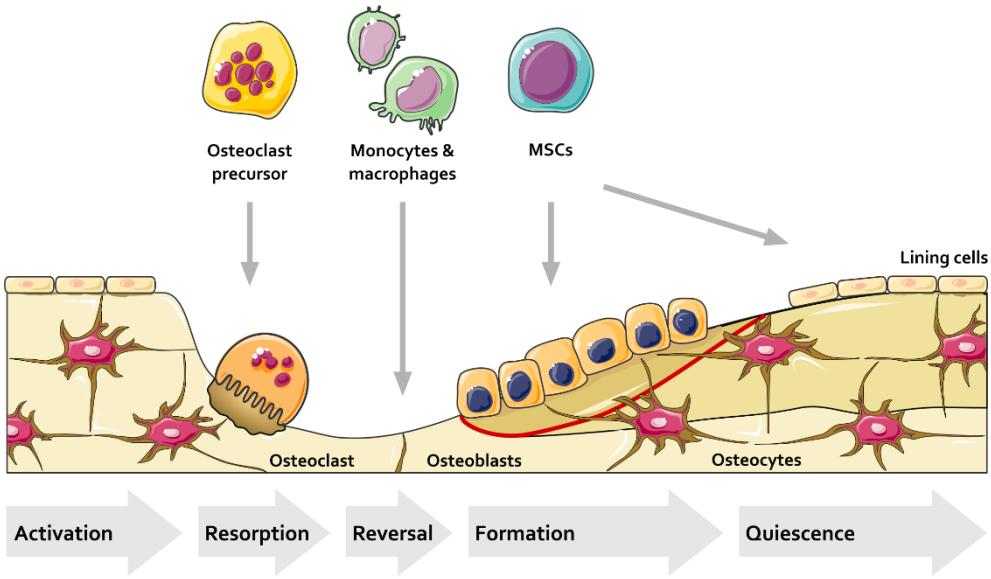

Figure 2. Coordinated sequence of bone remodelling. Activation initiates the transformation of osteoclast precursors into active osteoclasts, and the retraction of lining cells to expose the bone surface for resorption. Osteoclasts attach to the bone matrix via podocytes, forming Howship's lacuna, where they secrete protons (H+) and lytic enzymes to degrade the bone matrix. Inversion follows, marked by osteoclast apoptosis and replacement by macrophages and monocytes to clear the resorption site. Formation ensues as osteoblasts deposit new osteoid matrix, which subsequently mineralizes to complete the remodelling cycle. MSCs: mesenchymal stem cells. Lightest beige: old bone, medium beige: new mineralized bone, darker beige: osteoid seam or pre-osseous zone. Red line: zone of demarcation, or ossification front between osteoid and mineralized bone[12].

B. Bone union & fracture healing

The most frequent type of bone union or regeneration occurs through fracture healing, where processes of normal fetal bone development are replayed[18]. Fracture healing is the restoration of bone continuity, intending to recover the original function of the bone, both structurally and functionally.

B. 1. Physiological healing

Bone can heal by two physiologically distinct ossification processes[15,19]. Both types of healing are effective ways to repair fractures, but the choice often depends on

the nature of the fracture, the bone type (flat versus long bone), the degree of stability needed, and the treatment approach employed by orthopaedic surgeons.

Direct bone healing involves internal remodelling through the existing haversian system and the cutting cones which directly bridges the fracture site[20] (Fig. 3).

The cutting cone is the osteon remodelling unit with a cone-shaped head of osteoclasts that tunnelled the bone resorption, and a following queue of osteoblasts deposing new bone matrix around a central growing blood vessel. Following Perren's strain theory[20], the repair process requires absolute stability between compressed bone ends in close contact (< 0.15mm[19]), without any significant movement (< 2% strain[21,22]), and is usually achieved through surgical fixation after anatomical reduction[20,22]. This type of healing bypasses the formation of a visible callus.

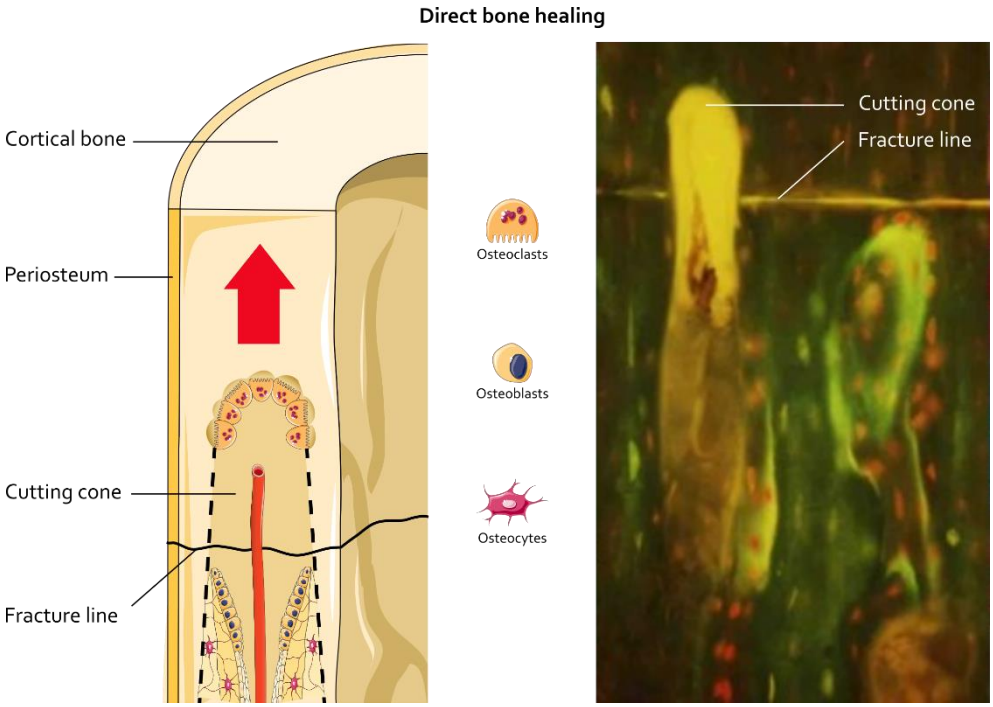

Figure 3. Direct bone healing involving bone remodelling: schematic cutting cone crossing the fracture line. The arrow shows the ossification direction. Fluorescent picture from Coutelier, 1969[23].

Indirect bone healing occurs in case of relative stability[20,24] or controlled microscopic movements at the fracture site (2-10% strain[21,22]). The initial response involves a visible callus formation and the transformation of cartilaginous tissue into bone to bridge the gap and stabilize bone ends. The process can occur with or without surgical intervention, depending on the degree of stability required, but paradoxically usually lasts less time than direct healing[22].

Indirect healing is the most frequent form of bone repair[25] and is divided into four overlapping steps (Fig. 4), each involving specific cellular and molecular components[15,26]. However, the transition from one phase to another is seamless.

Inflammatory phase (± 1 – 7 days) = A bone fracture creates a concomitant disruption of adjacent soft tissues and blood vessels from the periosteum, the Haversian system, and the medullary cavity leading to the formation of a haematoma[8] (Fig. 4 – b). The platelet (PLT) aggregation and coagulation cascade are activated. This is the best breeding ground for inflammatory cells such as neutrophils and macrophages to clean up the fracture site[27]. Haematoma contains a high calcium level from the clearing osteolysis of bone ends and the breakdown of bone debris[23].

Soft callus phase (± 1 – 4 weeks) = Cytokine production by the haematoma components induces angiogenesis[28]. The soft callus is a granulation tissue progressively replaced by cartilage at the fracture site[8]. Simultaneously, periosteal reaction generates a subperiosteal peripheral callus encircling the diaphysis (Fig. 4 – c), initiating primary intramembranous ossification[8,23] where the oxygen level is high by induced hyperaemia[23]. Meanwhile, chondroblasts start to proliferate, hypertrophy and produce ECM at the fracture site, in the hypoxic zone (Fig. 4 – e), giving rise to endochondral ossification[23]. Chondrogenesis progressively invades the haematoma, bridging bone ends and providing temporary stability for healing.

Hard callus phase (± 1 – 4 months) = As a continuum of the previous one, this bone-forming phase implies osteogenic cells, derived from mesenchymal stem cells (MSCs) in the periosteum and medullary cavity. Differentiation into osteoblasts yields woven bone, or primary bone, in the subperiosteal area. Concurrently, endochondral ossification continues to progress and initiates mineralization through calcium hydroxyapatite deposition, gradually reinforcing the fracture site and enhancing stability beyond the soft callus stage.

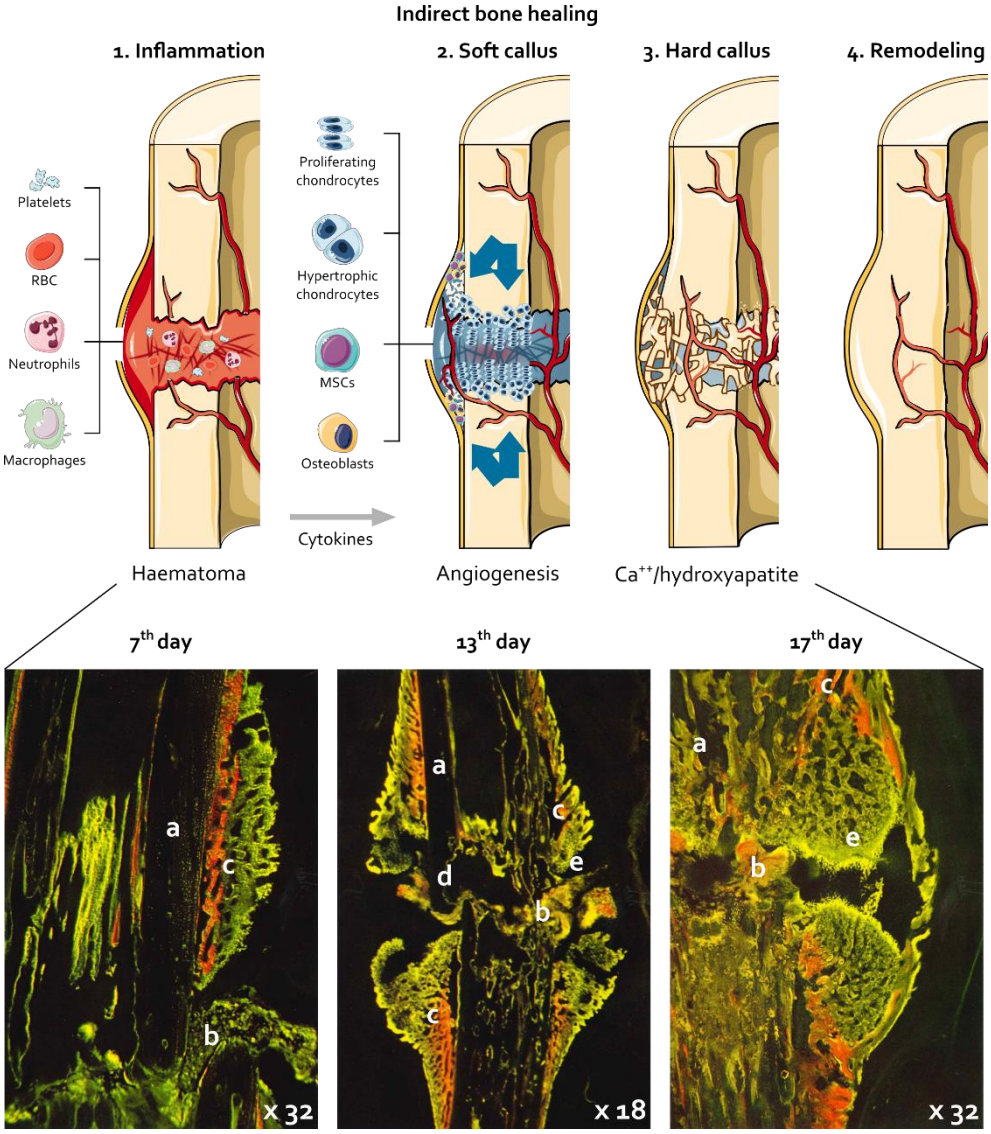

Figure 4. Normal bone healing process into four main phases: inflammation, soft callus, hard callus, and remodelling. The arrows show the ossification direction. RBC: red blood cells, MSCs: mesenchymal stem cells., Ca^{++}: calcium. Fluorescence pictures illustrate the overlapping steps of the healing of a fractured rabbit rib at 7, 13 and 17 days post-fracture. Red marking with hematoporphyrin at mid-term and yellow marking with tetracycline at the end of follow-up, before euthanising the animal. a: bone fragment, b: haematoma, c: subperiosteal osteogenesis with intramembranous ossification, d: cortical resorption, e: endochondral ossification. Fluorescent pictures from Coutelier, 1969[23].

Remodelling phase (± 4 – 24 months) = As previously explained, this balanced step is made possible by the coordinated action of osteoclasts and osteoblasts. Hard callus tissue is resorbed by osteoclasts, while osteoblasts deposit new, mature lamellar bone in its place[8]. The final architecture is adapted to withstand normal mechanical stress since the modelling is driven by Wolff's law[29–31].

This bone healing process is tightly regulated by various cytokines, growth factors (GFs), and signalling molecules that orchestrate the activity of different cell types involved in the repair process (Table 1).

Table 1. Signalling molecules involved in fracture repair process, at each healing phase.

Signalling molecule	Inflammation	Soft callus	Hard callus	Remodelling
Cytokines				
IL	+			
IFN-γ	+	+	+	
TNF-α	+			
RANKL	+		+	
PDGF	+		+	
OPG	+	+		
MCSF	+	+		
Morphogens				
TGF-β	+	+	+	
BMP	+	+	+	
IGF		+	+	
GDF	+	+	+	
VEGF	+	+	+	+
Angiogenin		+	+	+
ALP			+	+
FGF		+	+	+
MMP		+	+	+

IL: interleukin, IFN-γ: interferon gamma, TNF: tumor necrosis factor, RANKL: receptor activator of nuclear factor kappa-B ligand, PDGF: platelet-derived growth factor, OPG: osteoprotegerin, MCSF: macrophage colony-stimulating factor, TGF-β: transforming growth factor beta, BMP: bone morphogenetic protein, IGF: insulin-like growth factor, GDF: growth differentiation factor, VEGF: vascular endothelial growth factor, ALP: alkaline phosphatase, FGF: fibroblast growth factor, MMP: matrix metalloproteinase. Based on studies written by Meyer and Wiesmann (2006) and Perrin et al. (2022)[11,32].

Among them, BMPs, mostly being part of the transforming growth factor-beta (TGF-β) superfamily, are numerous and can play specific relevant roles and functions in bone formation, homeostasis and healing (Table 2)[33]. BMP-2 and BMP-7 have the most important impact on bone regeneration[32,34].

Table 2. Description of Bone Morphogenetic Proteins

Signalling molecule *(name and synonym)*		Function
BMP-1	*mTLD*	MMP cleaving the C-propeptide in collagen maturation, osteogenesis
BMP-2	*BMP-2a*	Osteogenesis, chondrogenesis, osteoinduction, fracture healing initiation, osteoblast differentiation, endochondral ossification, apoptosis
BMP-3	*Osteogenin*	Negative regulator of bone morphogenesis
BMP-3b	*GDF-10*	Negative regulator of bone morphogenesis
BMP-4	*BMP-2b*	Osteogenesis, chondrogenesis, finger patterning
BMP-5	-	Limb development, osteogenesis, chondrogenesis
BMP-6	*Vgr-1, DVR-6*	Osteoblast differentiation, chondrogenesis
BMP-7	*OP-1*	Osteogenesis, chondrogenesis, osteoblast differentiation, PMSCs activation
BMP-8	*OP-2*	Osteogenesis, chondrogenesis
BMP-9	*GDF-2*	Osteogenesis
BMP-11	*GDF-11*	Axial skeleton patterning
BMP-12	*CDMP-3, GDF-7*	Structural bone integrity, negative regulator of chondrogenesis, ligament and tendon development
BMP-13	*CDMP-2, GDF-6*	Cartilage development and hypertrophy, ligament and tendon development
BMP-14	*CDMP-1, GDF-5*	Chondrogenesis, angiogenesis, finger patterning, ligament and tendon development

BMP: bone morphogenetic protein, mTLD: mammalian tolloid, MMP: matrix metalloproteinase, GDF: growth differentiation factor, DVR: decapentaplegic Vg-related protein, OP: osteogenic protein, PMSCs: periosteal mesenchymal stem cells, CDMP: cartilage-derived morphogenetic protein. Adapted from Wang et al. (2014)[33].

B. 2. Clinical healing

Physical examination remains the elementary approach to assess fracture evolution. Clinically, healing manifestations include release of pain, swelling,

tenderness, haematoma at the site of injury, as well as return to full range of motion, stability and weightbearing or manual skills.

Biologically, serological biomarkers can help to inform on healing kinetics and osteoblast activity. Osteoblast-derived serum markers include, among others, ALP and OC. Bone specific ALP serum level initially increases during fracture repair and is correlated with radiological healing score, before returning to a baseline level within 2 months post-fracture[35]. However, these concentrations may remain unchanged or may persist at a high level for a prolonged period, which is a relative predictor of healing problem[35]. High OC values are present in normal fracture healing. A delay in OC increase might also predict delayed healing[35]. Matrix also involves markers such as N-terminal propeptides of type I collagen (PINP), and osteoclast-derived C-terminal telopeptides of type I collagen (CTX)[36]. PINP and CTX are fragments taking part in the maturation of the type I collagen molecule (*cfr. CHAPTER II. Decellularization – Collagen fibres and cross-links).* While PINP is an anabolic marker, CTX informs on collagen catabolism[36]. However, all biomarkers are not ideal in terms of sensitivity, specificity, predictability, robustness, and invasiveness and have therefore limited routine use[35].

Radiologically, different imaging techniques are available to assess fracture healing including radiography (X-rays), computed tomography (CT scan), ultrasonography (US), and nuclear medicine[37,38]. However, X-rays and CT scan remain the most currently used in clinical practice. In the case of indirect healing, the hard callus is usually visible on X-rays from 4 to 6 weeks, once the soft callus has acquired mineral substance. Bone consolidation is defined by at least three mineralized bridges joining both fracture ends in two different incidences (anteroposterior and lateral views). Scoring systems were developed to increase intra- and interobserver agreement (ICC ≥ 0.8)[39–43]. After a historical evolution, the modified radiographic union score (mRUS[43]) and the tomographic union score (TUS[41]) now standardize long bone union on both imaging modalities[44]. These scoring systems attribute a score from 1 to 4 at each cortical segment visible on anteroposterior and lateral views for X-rays, and on two paramedian coronal and two paramedian sagittal reformats for CT scans (2 fractured cortices for each plane). Individual cortical scores were summed up into a total score per fracture for mRUS and TUS, and further divided by two for the TUS (Table 3).

Table 3. Radiological scoring systems to evaluate bone healing on X-rays and CT

Score	1	2	3	4	Total
Scoring systems					
mRUS	No callus	Non-bridging callus	Bridging immature callus	Remodelled mature callus	**4 → 16**
TUS					**4 → 32 / 2**

mRUS: modified radiographic union score, TUS: tomographic union score.

These scoring values significantly increase with time from fracture and could detect delayed union at 3 months post-fracture[44] (Fig. 5).

C. Bone non-union & major bone defect

C. 1. Fracture non-union – Pseudarthrosis

Non-union, or pseudarthrosis, is defined by the American Food and Drug Administration (FDA) as a persistence of a fracture line 9 months post-injury, with at least 3 months without radiologic signs of progressive healing[15,19,45] either on X-rays or CT, and is associated with pain, deformity, instability and poor function. This condition requires additional intervention such as surgical procedures to promote bone healing and union[46]. Worldwide, 2 to 15% of bone fractures fail to heal[18,26,35,37,47,48]. The cost discrepancy between healing fracture and non-union is double[49], including revision surgeries, rehospitalization, pain medication, outpatient physiotherapy, as well as economic impact[50].

The aetiology of non-union can be multifactorial. Risk factors include patient-dependent criteria (*e.g.* age, sex, BMI, comorbidities), fracture-related criteria (*e.g.* fracture complexity, high energy trauma, biological environment), and treatment or surgery-related criteria (*e.g.* time, antibioprophylaxis, adequate stability, soft tissue interposition, infection)[16,17,37,46,19,51,52]. Classically, septic non-union and aseptic non-union are considered two independent entities because aetiology, physiopathology, and treatment strategies differ.

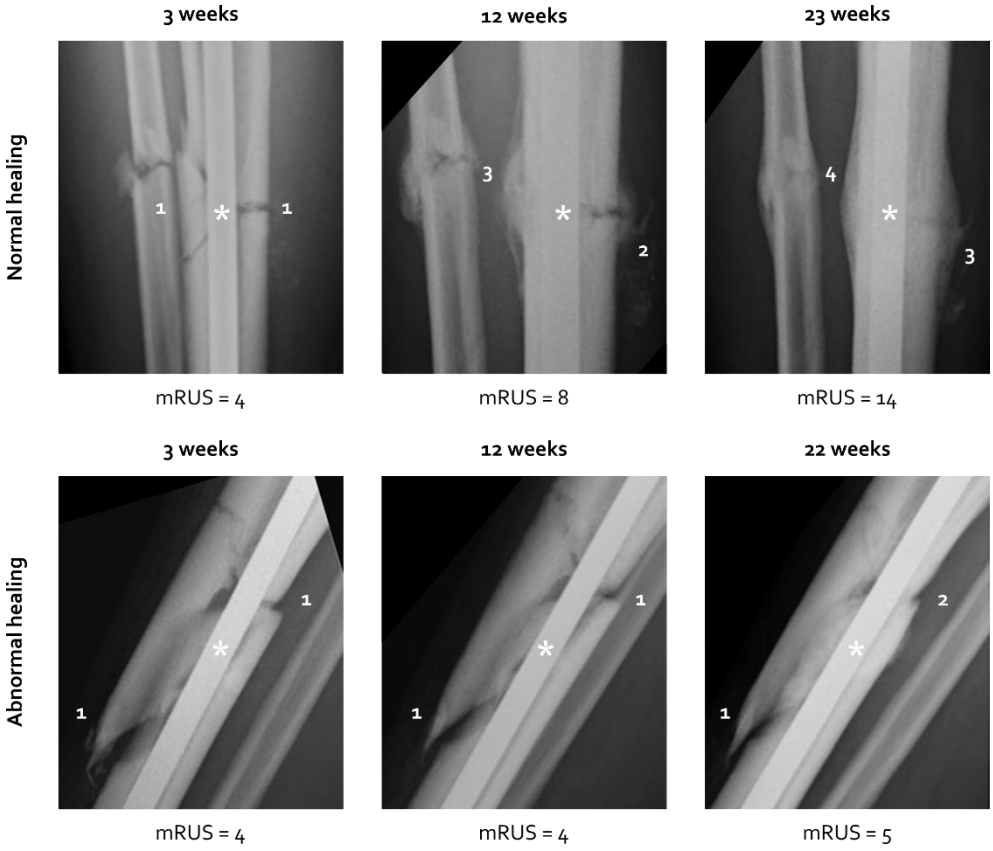

Figure 5. Evolution of the modified radiographic union score (mRUS) after tibial (± fibular) shaft fractures treated by intramedullary nailing (*). White numbers on the X-rays indicate the single score attributed to each cortical segment visible on anteroposterior views (lateral views not shown). These individual cortical scores were summed up into a total score per fracture. For example, a mRUS=4 is the sum of four individual cortical scores of 1 (two scores 1 on anteroposterior views as shown, and two scores 1 on lateral views, not shown). The total mRUS, calculated for each X-rays, shows a positive increase of the score during normal healing and almost an absence of score evolution during abnormal healing. Radiographs courtesy of Dr. Vasiliki Perlepe[44].

Septic non-union results from an infected fracture site, where bacteria impair the body's normal healing process, causing inflammation and bone tissue necrosis. Treatment typically involves antibiotics and surgical debridement to clear the infection before attempting to promote fracture healing[53].

In aseptic non-union, the callus morphology can help to understand the underlying physiopathology and to guide treatment, according to Weber's classification[15,54]. Two main physiological opposing mechanisms concern either a lack of mechanical stability (immediate connection to Wolff's law[29,30]) with a preserved biology, or a lack of sufficient biological supply (Fig. 6).

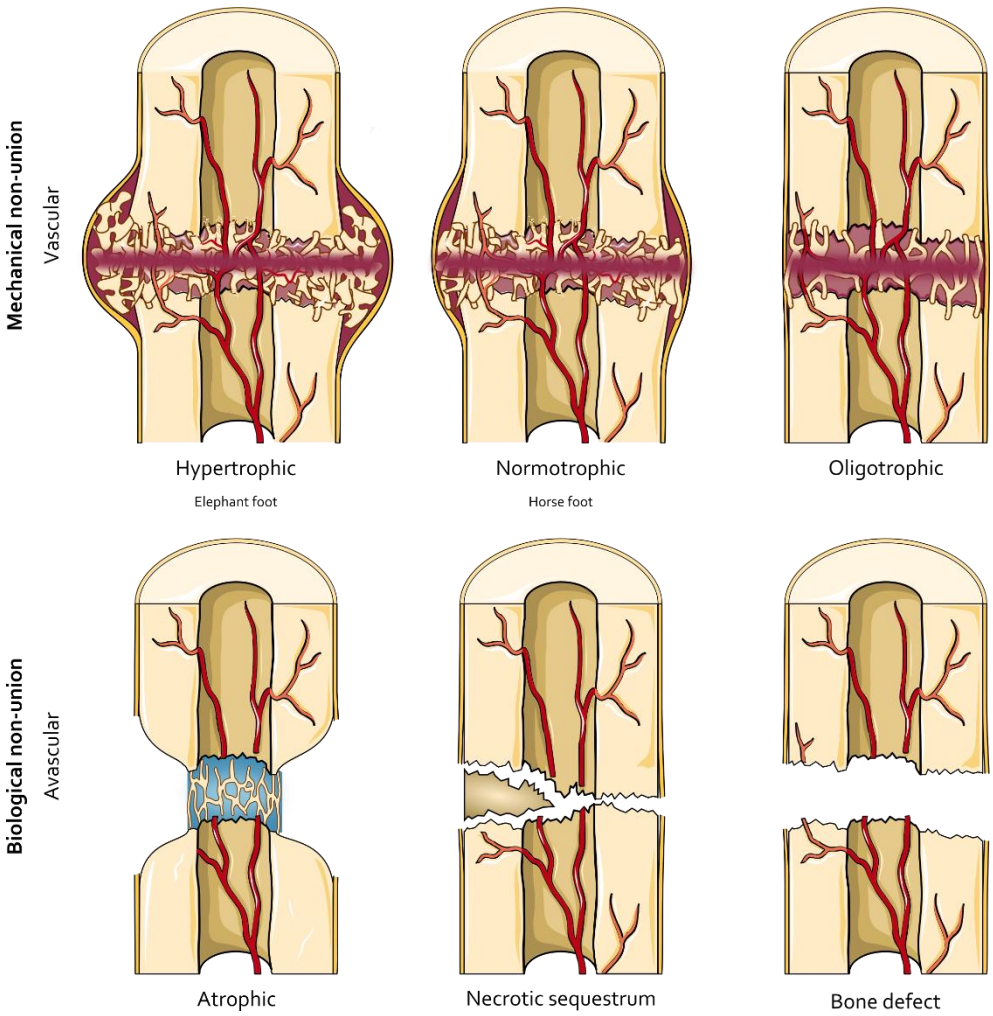

Figure 6. Non-union types based on callus visualization, according to Weber's classification[54].

Mechanical non-union – Vascular non-union

- *Hypertrophic callus* = Excess of bone formation without continuous bridging callus, as an elephant foot shape.
- *Normotrophic callus* = Normal response, as a horse foot.
- *Oligotrophic callus* = Minimal callus formation.

Biological non-union – Avascular non-union

- *Atrophic callus* = No bone formation with resorption of fracture ends. This is the most frequent type of non-union (80%[26]) and can result either from a lack of biology, from a non-osteogenic tissue interposition or an excessive instability (> 10% strain)[46,55].
- *Necrotic bone sequestrum* = Avascular dead bone wedge.
- *Bone defect* = Residual gap exceeding the normal healing capacity, requiring specialized therapeutic management.

C. 2. Major or critical-size bone defect

In major bone defect or critical-size bone defect (CSBD), the spontaneous bone healing capacity is exceeded despite adequate stabilization and initial treatment. The defect size is beyond the capacity of the body's natural healing processes to bridge or fill such a gap without external intervention or additional treatment[14]. Even if no single definition of the critical size exists, the literature agreed on a defect length over 2.5cm or more than 50% loss of bone circumferential contact[56,57] to talk about critical size defect, and over 5cm to talk about segmental defect[14]. This term can also be defined as a segmental bone defect 2–2.5 times longer than the diameter of the affected bone[58,59]. In addition, the critical size can vary depending on the bone, the defect location, the patient's comorbidities or the surrounding soft-tissue and biological environment[50,60].

Like non-union, the risk of CSBD is multifactorial. However, CSBD differs from non-union by an inability to regenerate substantial bone loss in spite of adequate biology and stability.

The CSBD may occur after a high-energy trauma, an osteolytic infection or a massive bone resection for sepsis, tumor or congenital malformations (Fig. 7).

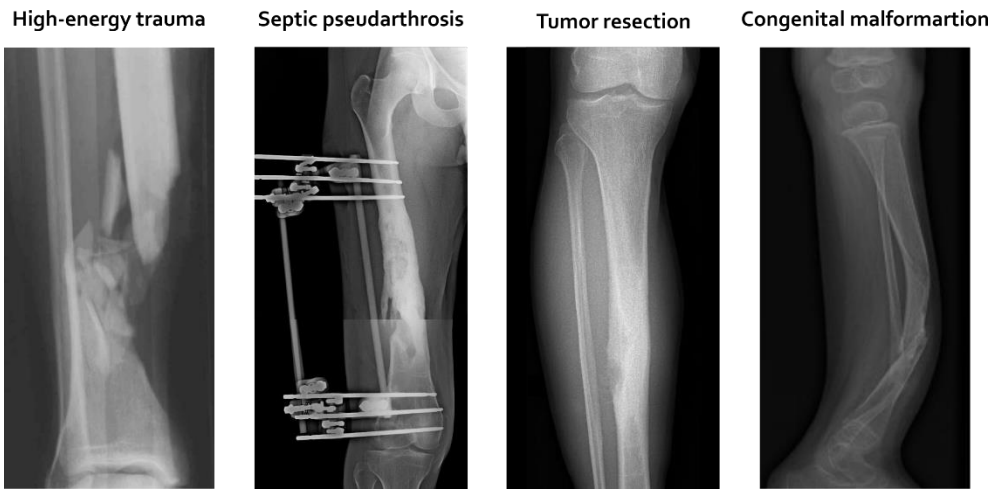

Figure 7. Critical-size bone defects of different aetiologies including high-energy trauma (highly comminuted fracture), femoral septic pseudarthrosis, tibial shaft tumor, and congenital malformation (tibial congenital pseudarthrosis), which all will require debridement or resection and surgical treatment.

Bone regeneration concepts: Periosteum, Diamond concept & Induced Membrane

« The beginning of all science is wonder at the things. »

Aristote, 350 BC

The bone regeneration process involves not only bone components but also intricate interactions between cells and proteins from the newly formed tissue, external soft tissues around the bone defect, and the biological and physical environment. To ensure healing or treatment success, some regeneration concepts have to be taken into account such as the periosteum, the diamond concept and the potential of Masquelet's induced membrane.

A. Periosteum

Periosteum, derived from the perichondrium[14], is a dense connective tissue, richly vascularized, with anabolic properties. It covers the external surface of a bone to which it is attached by Sharpey's fibres[61], from one epiphysis to the other, except articular surfaces[62].

A. 1. Tissular structure

Periosteum is composed of two distinct superimposed layers[25,61] (Fig. 8).

Fibrous layer = This outer layer gives the periosteum its structural integrity. Less cellular than the cambial layer, it is made up of dense connective tissue, providing strength and protection to the bone. The superficial part is a compact type I collagen matrix, relatively inelastic, with sparse fibroblasts, but rich unmyelinated neural arborescence[25,61]. It is the most abundantly vascularized part of the periosteum thickness[61]. The deep part is fibroelastic with many elastic fibres interlaced in collagen fibres, but less nerves and vessels[25,61].

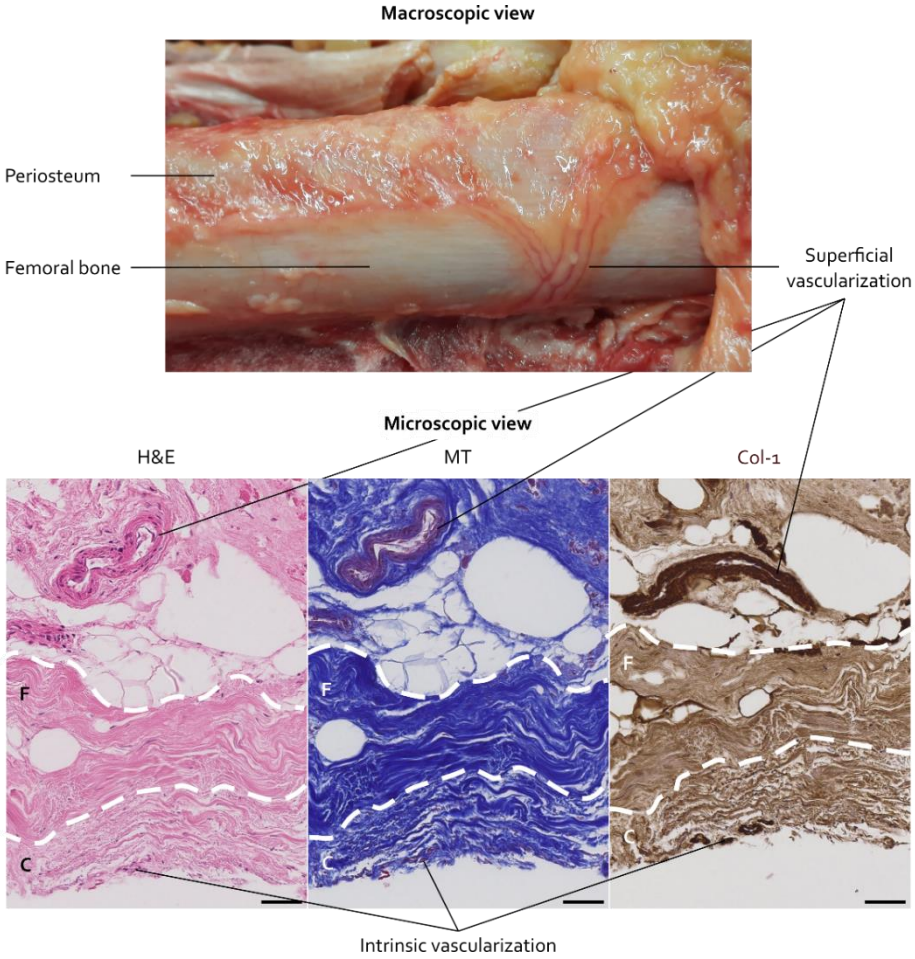

Figure 8. Macroscopic and microscopic structure of the periosteum (femur of an 88-year-old man). The histological (H&E: haematoxylin and eosin, MT: Masson's trichrome) and immunohistochemical (Col-1: type I collagen) sections illustrate the composition in two distinct layers (F: fibrous layer, C: cambial layer). Scale bar: 50µm.

Cambial layer = Making a comparison with trees, where the cambium is in charge of appositional growth, Duhamel du Monceau first referred to the inner layer of the periosteum as the cambium in 1742[25,62] (Fig. 9).

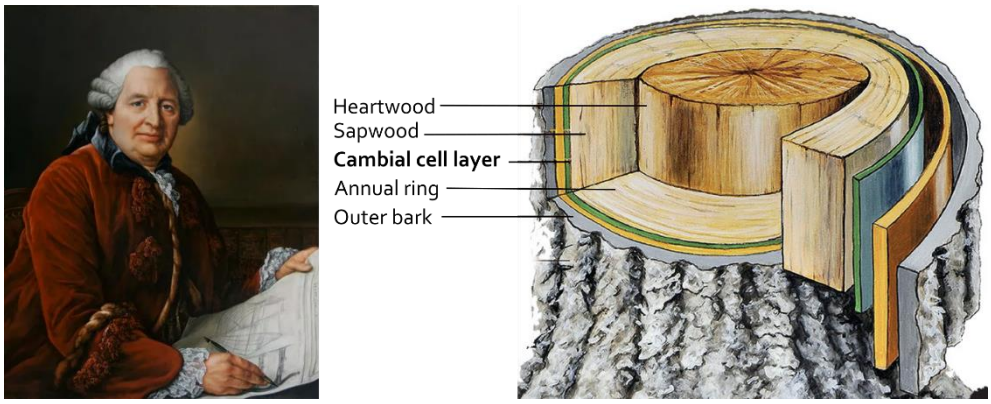

Figure 9. Henri-Louis Duhamel du Monceau and its reference to the tree structure. Henri-Louis Duhamel du Monceau (1700-1782) was a notorious French scientist at the Age of Enlightenment, who made significant contributions across physics, agronomy, chemistry, botany, and naval architecture. Notably, in 1728, he discovered and effectively treated the saffron bulb disease, earning acclaim from the Académie des Sciences. His diverse body of work, including influential writings on agriculture such as « Traité de l'agriculture », solidified his legacy as a pioneering figure in modern agronomy and forestry. Adapted from Loiret archives[63,64] and Anatomy of a tree[65].

This osteogenic layer contains a heterogenous cell population[66] and is the main niche of periosteal mesenchymal stem cells (PMSCs), osteochondral progenitors that will further differentiate into osteoblasts or chondroblasts for bone formation[11,14,32,66,67], as well as fibroblasts. The pool of PMSCs is continuously restored by periostin protein[67]. This layer is vascularized, innerved[61], and very thick and elastic in children, explaining greenstick fractures[68] (Fig. 10).

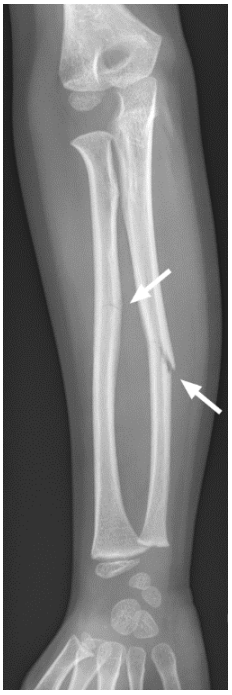

Figure 10. Greenstick fracture of both forearm bones in a 4-year-old girl.

However, it atrophies with age[25,68,69]. The notable difference lies in the reduction in the density and cellular quantity of this layer[70] (Fig. 11).

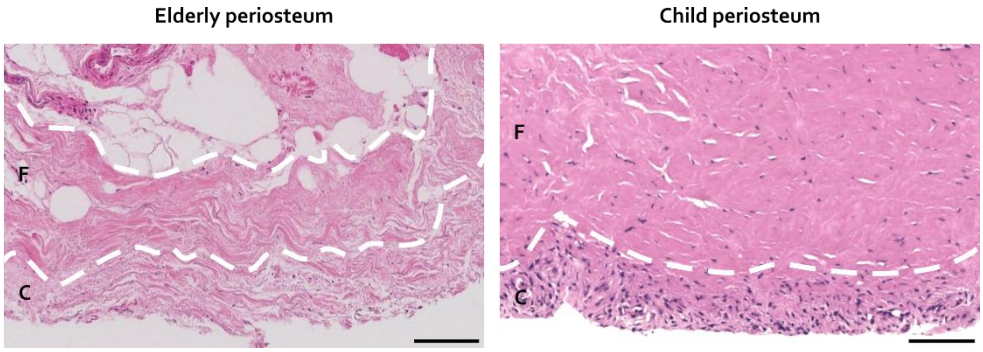

Figure 11. Histological sections through the periosteum of an 88-year-old man and a 14-year-old girl (H&E staining). F: fibrous layer, C: cambial layer. The periosteum was stripped off the bone, which is not visible anymore on the sections but would be at the bottom side. Scale bar: 100µm.

A. 2. Function

Periosteum is involved in multiple functions of the musculoskeletal system, particularly in both *endochondral* and *intramembranous* ossifications[25].

Bone growth = First of all, the periosteum plays a crucial role in bone development and growth, during organogenesis and childhood[25]. Initially, mesenchyme condenses into a cartilaginous anlage model. In the middle of this model, chondrocytes hypertrophy, die, and calcify, creating the primary ossification centre. The ossification front progresses centrifugally towards each bone extremity, thereby constituting the physeal zone, responsible for the bone length growth. At the periphery of the anlage, the perichondrium densifies and turns into a periosteum with the arrival of blood vessels, initiating *appositional membranous ossification*. This new bone encloses the cartilaginous model as a bark and contributes to the bone width growth. Bone enlargement will confer mechanical strength since the relationship between bone diameter and torsion or bending resistance is exponential[62,69]. At the level of the physis, this periosteal bark is called the perichondral ring of Lacroix[9] (Fig. 12). During growth, the periosteum actively contributes to bone modelling, shaping the bone to accommodate specific biomechanical forces[71].



Figure 12. Pierre Lacroix (1910 – 1971) was a Belgian orthopaedic surgeon and an ordinary Professor at UCLouvain where he taught anatomy. He held the first chair of orthopaedic surgery in Belgium. The remarkable quality of his research work, particularly on bone organization, osteogenesis and fracture repair, has earned him a wide international reputation[9].

Fracture repair = Periosteum is a central mediator of bone repair through both *intramembranous* and *endochondral* ossifications[23,62]. Lacroix demonstrated this bipotentiality of cambial PMSCs by grafting periosteum around a hyaline cartilage rod under the kidney capsule[9]. During fracture healing, new bone is formed at the periphery of the fracture site[25,32]. On the contrary, in the core of fracture line, periosteum can produce up to 90% of the cartilaginous tissue further mineralized and ossified[25,32,62]. Several signalling pathways can influence the activation, the proliferation and the differentiation of PMSCs, such as BMP, Wingless-related integration site proteins (Wnt), fibroblast growth factor (FGF), platelet-derived growth factor (PDGF), and TGF-β signals[32,62]. BMP signalling pathway activates PMSCs in response to bone injury within the first three days[32,66]. Radiologically, the periosteal reaction can be seen as a fine edging upon its mineralization (3 weeks after fracture event) (Fig. 13), particularly in younger individuals[68,72]. *A contrario*, its predominant role is illustrated by delayed union in case of important periosteum stripping or damage[25].

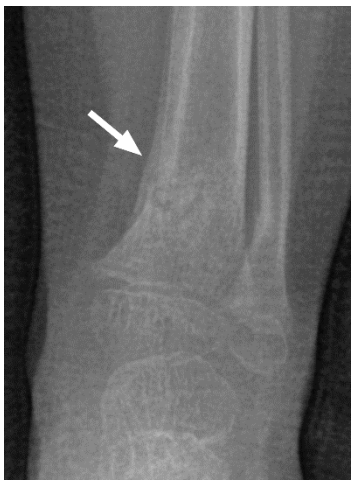

Figure 13. Periosteal reaction after metaphyseal-shaft fracture of both bones of the left leg in a 2-year-old boy.

Sensory function = The periosteum contains mechanoreceptors and nociceptors. In stress-free conditions, elastic fibres apply a pre-tension state[61]. Excessive tension, pressure, and damage can be detected and transformed into a cellular response. Sensorial inputs activate repair function and bone regeneration[69]. For example, the haematoma at the early stage of fracture healing distends the fibrous layer of the periosteum which responds by activating quiescent osteogenic cells of the cambial layer. Moreover, recent research highlighted the mechanosensitivity of periosteal osteochondroprogenitor cells and their activation and proliferation in response to compression load[73,74]. Other authors described a third intermediate and undifferentiated layer that could act as a "shock absorber" transmitting overpressure and tension to the cambial layer[61].

Vascularization – Nutrient supply = Periosteum has abundant microvessels[61] coming from four distinct sources including intrinsic periosteal network, musculoperiosteal and fascioperiosteal systems, and periosteocortical anastomoses[61,68]. Periosteal vasculature provides 70-80% of the cortical blood supply[62,75]. The exchange of oxygen, nutrients, and waste products is carried out by vascular channels in cortical bone[14]. Up to 30% of the cortical volume is occupied by vascular channels[76], which interconnect nutrient arteries, periosteal vessels, and epiphyseal vessels. The network of transcortical vessels is a primary contributor to blood circulation in cortical bone, providing a direct link between the marrow, endocortical, and periosteal circulations[77–79].

Enthesis = Tendons and ligaments attach to the periosteum in the deep part of its fibrous layer[61], anchoring muscles to the bone. This allows movement and stability of the skeletal system.

The periosteum is proven to be essential and indispensable in osteogenesis through different pathways and PMSCs definitely stand as a keystone of bone regeneration.

B. Diamond concept

The complexity of CSBD and non-union integrates multiple factors which were simplified in a comprehensive framework designed by Giannoudis et al. (2007),

called the Diamond concept[80] (Fig. 14). The Diamond concept emerged from the consideration of six essential facets, each representing a crucial element required for successful bone regeneration.

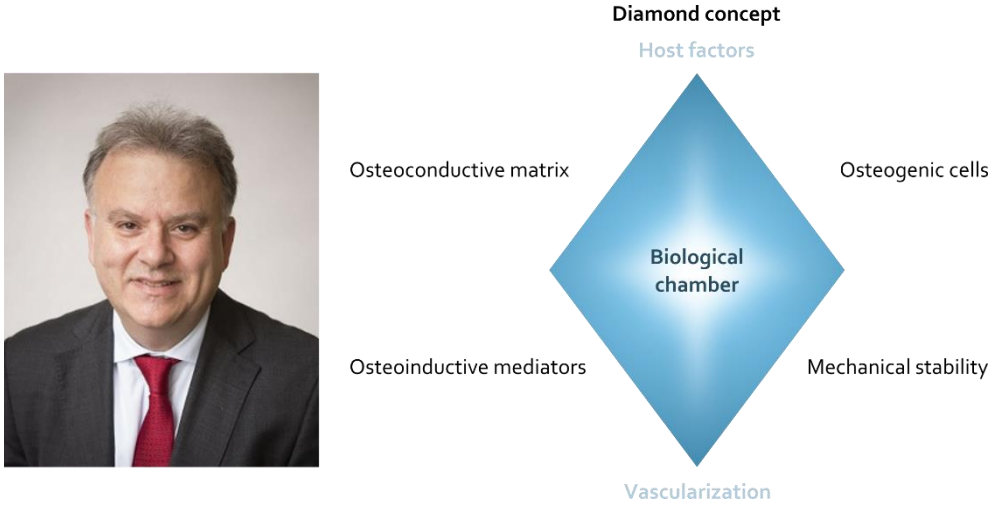

Figure 14. Peter Giannoudis is a British orthopaedic surgeon and researcher in the field of trauma surgery. He is particularly renowned for his contributions to the management of CSBD, non-union, and fractures, especially the inflammatory or immune post-trauma response, MSC biology, and notably the development of the Diamond concept[80]. He is Professor at the University of Leeds (UK), Honorary Consultant and head of the department at Leeds General Infirmary (a major trauma unit). He has been president of multiple associations and still fellow of the Royal College of Surgeons of England[81,82].

Osteoconductive matrix = Passive scaffold allowing *osteoconduction* (cell migration and ingrowth of new bone formation)[83–86]. The matrix should promote the migration and adhesion of osteoinductive mediators and osteogenic cells[19]. The microstructure of the scaffold is therefore relevant.

Osteoinductive mediators = GFs coming from the inflammatory phase of fracture healing and playing the role of *osteoinduction* (active recruitment, stimulation and differentiation of MSCs into bone-forming cells or osteoprogenitors)[83–86]. The predominant mediators activating mitogenesis and osteoblastic differentiation are PDGF, FGF, insulin-like growth factor (IGF), and TGF-β including BMPs[19,66].

Osteogenic cells = Cell types capable of *osteogenesis* (active direct bone formation)[83–86], including PMSCs, bone-marrow mesenchymal stem cells (BMSCs),

adipose mesenchymal stem cells (AMSCs), other source MSCs[35] and endothelial progenitor cells[19]. These osteogenic cells are also able to secrete other specific GFs to enhance the response cascade[19], and to boost the phase of hard callus mineralization.

All these three factors constituted the traditional triangular concept but the Diamond concept was born from the addition of following factors that were overlooked before[80].

Mechanical Stability = Adequate mechanical stability is crucial to ensure proper alignment of bone fragments and to prevent excessive or insufficient movement during the healing process, extensively explored by Perren's works[87,20,88,89]. This facet exclusively depends on the surgeon and has considerable impact on the healing process[90,91]. In the early phases, axial micromovements tend to stimulate the healing while the effect reverses during the callus hardening[92]. Cells can sense their mechanical environment through electrochemical signals generated by fluid shift inside osteocyte canaliculi or through membrane mechanoreceptors[19,93]. Mechanical stimulation can also influence cell phenotype. In case of suitable GFs, fibroblasts thrive in tensional environments, chondroblasts in shear environments, and osteoblasts in environments combining compression and distraction[92].

Vascularization = Good vascular bed is a prerequisite to deliver the osteoinductive mediators and osteogenic cells on site[90,91]. CSBD must be supplied in oxygen, nutrients, signalling molecules and MSCs. In addition, surgeons know that an open reduction and internal fixation (ORIF) leads to evacuation of the haematoma, associated with a reduced chance of healing[94]. By the way, angiogenesis *per se* is vital for the transformation of avascular cartilage into vascular bone tissue during endochondral ossification[91].

Host factors = As previously mentioned, patient comorbidities or genetic predispositions are host-dependent risk factors for union problem[51,91].

The goal of this concept is to confine any biological improvement into the non-union bed for optimal impact, converting it in a controlled ***biological chamber*** that promotes all the essential physiological influx of healing[90]. The human body serves as an *in vivo* and *in situ* bioreactor for enhanced healing[19], akin to the central or pivotal element in the Diamond configuration[90].

The first five factors, namely the *regeneration pentagone*[91], can be influenced by the surgical procedure, with a primary focus on these aspects. If only one factor is considered at a time, as monotherapy, the healing success does not surpass 50% to 89%[19,95]. However, when all facets are rigorously considered together in polytherapy, healing succeeds in 84% to 100% of cases[19,46].

By considering and optimizing these five factors, the Diamond concept aims to create an optimal environment for bone healing and regeneration, and has become a widely recognized approach in the field[19]. It guides surgeons and researchers in the selection of appropriate biomaterials, surgical techniques, and treatment strategies for CSBD and non-union, leading to improved clinical outcomes.

C. Induced membrane

C. 1. The discovery

The development of the induced membrane technique, also known as the Masquelet's technique, was born out of the observations of Masquelet et al. in 1986[96] (Fig. 15), while treating posttraumatic septic critical-size non-unions. He noticed that, when a cement spacer was placed into a bone defect, the formation of a thick (1-2mm) vascularized membrane was induced all around, able to create a favourable environment for bone regeneration.



Figure 15. Alain-Charles Masquelet is a French orthopaedic surgeon, Professor and member of the "Académie nationale de chirurgie", who significantly contributed to the field of orthopaedic surgery, particularly in the management of bone defects. Apart from his work on the induced membrane technique, he published numerous scientific articles and books on topics related to bone healing, bone grafting, limb reconstruction, and orthopaedic trauma. Professor Masquelet's innovative techniques and dedication to enhancing patient's outcomes earned him international recognition. He has received several awards and honours, notably the most prestigious and highest international Honor in Orthopaedics, the Meyer Award this year (2024)[97].

Professor Masquelet and his team further investigated this biological model and developed the two-stage induced membrane technique based on their findings in the 1990s[96]. His fundamental studies and clinical experience have demonstrated the effectiveness of this surgical technique which is now used worldwide thanks to its simplicity, efficacy, reliability and reproducibility[60,98–100].

C. 2. Surgical technique

The technique involves two main stages[96] (Fig. 16).

Stage 1 = Induced membrane formation

An external fixator can be placed in the early first step to maintain limb length and rotation before being lost by aggressive debridement[101]. Once the limb is stabilized, the surgeon proceeds with a radical debridement of infected or necrotic bone and a soft-tissue reconstruction if needed[96]. The level of debridement can be determined with preoperative magnetic resonance imaging (MRI) or with the peroperative paprika sign (active punctuate bleeding holes in the cortex)[101]. To prevent bone margin burn-necrosis, the osteotomy is performed using a drill bit and an osteotome[101].

The defect space is filled with a temporary polymethyl methacrylate (PMMA) monobloc cement spacer, and the limb is stabilized by an external fixator. The cement spacer needs to mimic exactly the structure of the missing bone in terms of diameter and length to overlap the native bone ends[86]. A simple tip to facilitate its hand-fashioning is the use of a syringe with the same diameter than the bone and 1-3cm longer than the space of CSBD[60,98,100]. The syringe is longitudinally cut, wrapped around the defect and filled with PMMA. Soft tissues need to be protected from exothermic solidification of the cement thanks to saline irrigation or a piece of glove[100,101]. The presence of the cement spacer during 4-8 weeks induces the formation of a biological nonadherent membrane around it[96].

Stage 2 = Bone grafting

After 4-8 weeks during which the soft tissues heal, the infection is controlled and the induced membrane matures and becomes vascularized[102,103], the second surgery includes a careful longitudinal incision of the membrane, without excision, and the removal of the cement spacer. The medullary cavity is curetted at both

extremities[100] and the cortical ends are decorticated[98,100]. The bone defect is filled with a morselized (1mm pieces[100]) cancellous bone autograft from the iliac crest[100] or the reamer/irrigator/aspirator technique (RIA technique), tightly disposed to mould the void[100]. The membrane is self-stitched over the graft, resulting in a closed chamber. The induced membrane, now rich in blood vessels and osteogenic factors, acts as a biological chamber that enhances the incorporation and integration of the bony graft.

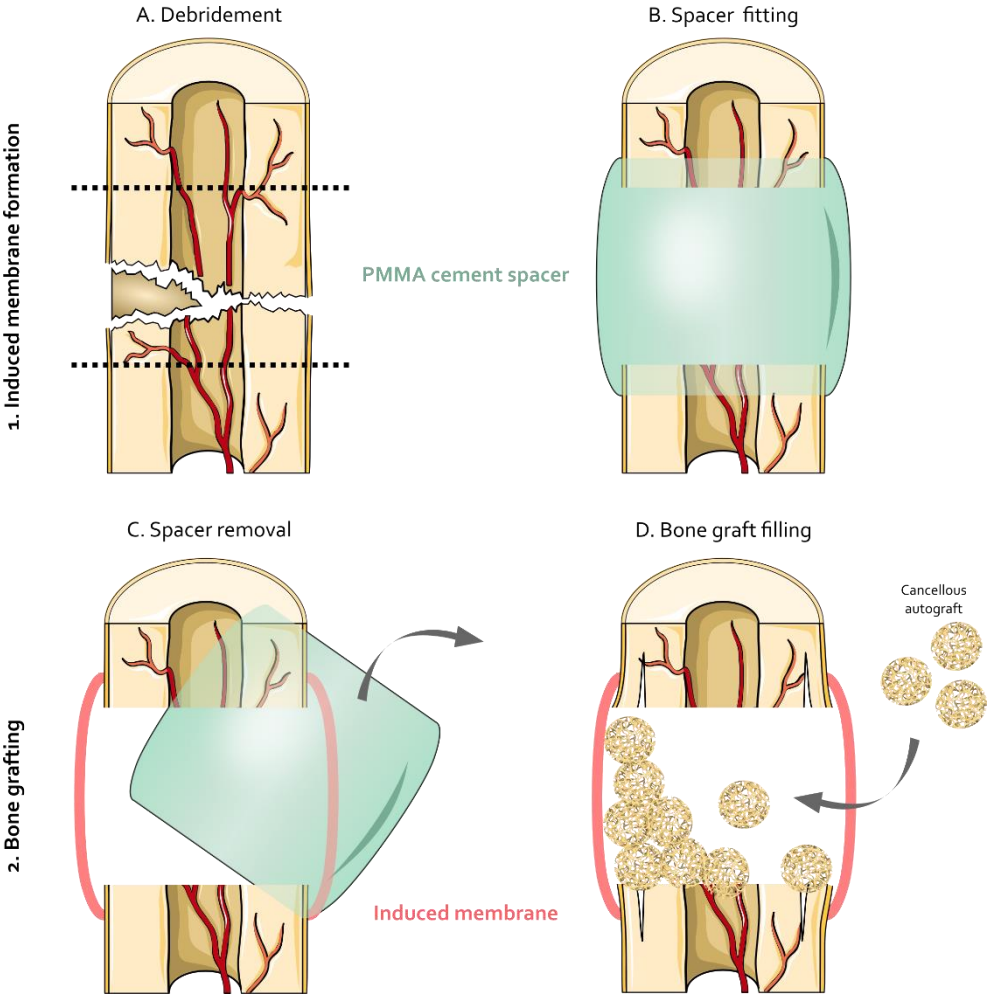

Figure 16. Surgical technique of the Masquelet's induced membrane including two main steps corresponding to two-stage surgical times. The first surgical time consists of debridement of sick/dead zone and spacer fitting inside the defect. The second surgical time consists of spacer removal and bone graft filling. PMMA: polymethyl methacrylate.

This surgical technique could allow weightbearing after 5-6 months under external fixation protection and after 7-8 months without any protection[96,104]. The healing time is independent of the size length since the majority of the cases consolidate after 4-12 months[96,99,100,104,105].

C. 3. A biological chamber

Successive studies and further research explored and validated the biological impact of the induced membrane over the years.

The cement spacer behaves as a foreign body *in situ*[106]. The immune system responds through a five-step process including[60,96,99,106,107] :

- The adsorption of plasmatic proteins on the foreign body surface
- An acute inflammatory phase with neutrophil recruitment
- A chronic inflammatory phase involving lymphocytes, monocytes, and fibroblasts
- An accumulation of macrophages forming giant cells, all secreting cytokine
- The formation of a fibrous capsule around the foreign body, isolating it from the surrounding tissue to mitigate its impact

The micro-rugosity of the PMMA is important since it produces the best appropriate irritation reaction, not too much, not too low[108,109]. When being impregnated by antibiotics (most frequently gentamicin), the cement could also play an antibacterial role with little systemic resorption[107]. In septic non-unions, the benefit of time between the two stages for local antibiotic treatment through PMMA spacer (and/or systemic if needed) gives also a synergic effect[60]. However, the thickness and elasticity of the membrane can be influenced by the presence and type of antibiotics[60,108,110], why the pioneers do not recommend to use antibiotic-loaded spacer[100].

Histologically, the induced membrane is a type I collagen matrix[107] structured in two layers. The internal layer is a synovial-like tissue and the external layer is a highly vascularized oriented fibrocollagenic tissue (mostly type I and III collagen[99]) hosting fibroblasts and myoblasts[96,107]. The morphologic analogy was made with periosteum although the induced membrane is significantly thicker than periosteum[99,111]. The periosteum is elastic and anisotropic with a pre-tension

strength unlike the isotropic induced membrane[99]. The membrane cellular density is another difference compared to periosteum, with more numerous viable cells, including lymphocytes and pericytes, known to participate in vessel maturation and share some proliferative and differentiation properties with MSCs, but the same amount of endothelial cells[111]. Blood vessels are observed within the membrane as early as 2 weeks after cement implantation, peaking at 4 weeks, and are oriented perpendicular to the cement[109].

By creating a biological chamber, this induced membrane can create and control its own local environment and serves several purposes.

Natural barrier = The membrane acts as a barrier, preventing soft tissue interposition into the defect[14,60,99], which is a predictor of non-union. It also avoids graft resorption[96,99] and prevents ectopic ossification[107]. This semipermeable membrane enables to block negative mediators but concentrates pro-regenerative signals inside the chamber[99].

Graft revascularization = The microvascular network is rich and close enough to the graft to allow its invasion[108]. The graft revascularization provides oxygen, cells, and nutrients and removes waste, which is mandatory for its integration and bone regeneration[99]. Noteworthy, graft revascularization is conditional on guaranteed stability depending on the osteosynthesis[108].

Anabolic and catabolic signals = Secretion of GFs and cytokines promotes bone regeneration and angiogenesis[14,60,99,112,113]. After 2 weeks of PMMA implantation, the concentrations of vascular endothelial growth factor (VEGF) and TGF-β are highly increased and BMP-2 peaks after 4 weeks[96,99,114], influencing the time of spacer retention[99]. VEGF and BMP amount were similar to those of the periosteum[99,111].

The development of osteoclasts inside the membrane is still debated but early markers of osteoclast differentiation (*e.g.* calcitonin receptor and receptor activator of nuclear factor kappa-B (RANK)) and osteoclast-related genes (*e.g. Trap* and *Rankl*) were detected and could clearly support their presence and/or their proliferation[99,109,113]. This could be in line with a bone remodelling capacity, mimicking the creeping substitution[113].

MSC recruitment = This collagenic sheet participates in the recruitment and proliferation of MSCs, with characteristic trilineage differentiation potential (osteogenesis, chondrogenesis and adipogenesis)[96,99,111]. When the membrane matures, it can also bring trophic membrane-derived cells, maybe derived from residual PMSCs[99]. Even if the bone regeneration originates from native bone cuts[14,99], the membrane can stimulate the entire process of bone formation.

C. 4. Up-to-date clinical knowledge

Through few decades of clinical experience, complications are not rare. Morelli et al. (2016) performed the first meta-analysis including 427 patients, and described a rate of 18% of infection or non-union persistence or recurrence[115]. This incidence can range from 8% to 50%, depending on the cohorts[60,105]. The second meta-analysis was conducted by the team of Giannoudis (2020) involving 677 patients, with < 1% of re-fractures and implant failure, 3% of malalignment and amputation, and limited leg length discrepancy[104,105]. In 2021, another one led by Masquelet gathered and compared both ouctomes[98]. Time to union was similar but the anatomical location of CSBD (tibia) was highlighted as a risk factor for post-procedural complications[98,104]. Other recent meta-analyses (2020 and 2023) focused on the treatment of tibial and femoral defects using the induced membrane to identify risk factors for complications[116,117]. Post-operative tibial infection was statistically related to initial septic non-union and defect length (≥ 7cm)[117]. Even if the femoral complication rate was lower than for the tibia[98], final femoral non-union status or infection was significantly more frequent in older patients (> 65 years) and in case of external fixation, respectively[116]. However, the use of an antibiotic-impregnated spacer[116,117], a pure autologous bone graft[116], and an intramedullary nailing (IMN) for osteosynthesis[98,104,116,118] was significantly associated with a higher union rate and shorter union time.

In general, the distinction between the recurrence/persistence of a pre-existing problem (*e.g.* infection) and the appearance of a neo-complication (*e.g.* implant failure, malunion, leg length discrepancy) is unclear. To the best of that knowledge, very few studies to date have highlighted novel complications intimately linked to the technique rather than to the course of the underlying pathology. To this end, Mathieu et al. (2021) proposed a systematic classification discriminating preventable (inaccurate analysis of the clinical situation or

inappropriate surgical tactic) and nonpreventable (altered biological properties of the membrane) failure[98]. The non-responders in creating an induced membrane, in particular, exhibited a modified membrane composition with fewer fibroblast-like cells, an absence of MSCs, and an alteration of ECM remodelling[119]. Most of the time, failures are related to the pathology recurrence which could be avoided by a meticulous procedural observance of the technique, including a correct radical debridement in the first as well as the second phase[98,104,105], an adequate antibiotic medication and soft tissue management[98,104], and a stable enough osteosynthesis for graft revascularization[98,108].

Overall, the induced membrane technique provides a niche of MSCs in a biological and richly vascularized environment, conducive to bone regenerative capacity almost similar to that of the periosteum. Its continuously increasing interest lies in the biological enigma, yet to be fully unravelled[108,112]. Despite open-field fundamental research is still ongoing, this two-stage surgery usually achieves a success of critical-size bone union from 82% to 100%[60,96,98,105,115]. Very long-term functional outcomes (≥ 10 years follow-up) are also encouraging with, among others, unrestricted walking distance[104]. All of these observations defined this technique as a groundbreaking discovery or disruptive innovative advancement[97].

Current treatments & limitations

« Only passions and great passions can lift the soul to great things. »

Translated from Denis Diderot, 1762

A. Current treatments

Non-union treatment can take many different forms. Depending on the type of aseptic non-union, correcting the mechanical stability and adding the necessary biology resolves the problem in a single surgery in 75-100% of cases[15,120], provided the underlying pathophysiological process has been properly studied and understood. These surgical treatments have evolved over time and usually include bone autograft, which is still the gold standard[46,84,85,120–123], and, among others, dynamization[124], Judet's decortication[125,126], and many bone substitutes[45,84,121] (*e.g.* demineralized bone matrix (DBM)[83,127], GFs (rhBMP-2[123,128,129] or BMP-7[46,129,130]), platelet-rich plasma (PRP)[131,132]). Development of bone substitutes knew an exponential growth last decades to such an extent that listing all of them would be impossible. A novel classification of all bone substitute materials was established to guide surgeon selection[84].

Some non surgical or adjuvant treatments can also be helpful such as electrical stimulation[18,21] or pulsed electromagnetic field[133,134], and low-intensity pulsed ultrasound (LIPUS)[135–137].

On the contrary, the treatment of CSBD is *always* surgical and *always* a challenge. Since non-unions still have a plethora of available treatments, CSBD treatment only relies on autograft (cancellous or cortical[85,121], iliac crest[46,138,139] or RIA technique[18,46,50,86]) if the defect is limited (< 5cm[96]), on processed corticocancellous allograft (delipidation, decellularization, virus and prion inactivation, and sterilization)[83] or more frequently on massive structural bone allografts[121,122], distraction osteogenesis or bone transport[14,50,140,141], Masquelet's induced membrane[96,99,108], free vascularized bone transfer[14,85,142,143], megaprosthesis[144] or

other regenerative techniques[46,121] including synthetic bone scaffold[84,85,121,145] (*e.g.* ceramic or bioactive glass) and bone adhesives (*e.g.* specific cement or glue)[84,146].

The choice of treatment refers to a complex analysis of the physiopathology and is usually not evident. To help surgeons in decision-making, the non-union scoring system (NUSS) indicates recommended treatment measures according to the total score[45,147,148]. Treatment solutions can vary from improvement of mechanical stability by changing for a different osteosynthesis method (score from 0 to 25), to arthrodesis, mega-implant or limb amputation (score from 76 to 100). Other similar scores are known to help surgeon's decision such as the Mangled Extremity Severity, Limb Salvage Index, Predictive Salvage Index, Nerve injury – Ischemia – Soft tissue injury – Skeletal injury – Shock – Age of patient (NISSSA) score, and Hannover Fracture Scale-97[58].

B. Current limitations

B. 1. Integration and unification of bone regeneration concepts

CSBDs continue to pose substantial challenges in healthcare[149]. The pathology usually implies multiple surgeries, long-term immobilization, rehospitalization, social costs, which represents a significant burden for patients[150]. Precisely defining CSBD and establishing clear guidelines for its management remain areas lacking sufficient high-level evidence. Currently, therapeutic strategies must be tailored to each individual patient, following the principles outlined above, and with a thorough understanding of the available options.

Most of CSBD treatments do not consider all the bone regeneration concepts together and usually focus on some separate advantages combined (Table 4).

B. 2. Massive bone allografts

Due to the restricted availability and donor-site comorbidities of autografts[151], as well as the development of bone and tissue banks since the 1980s[152,153], bone allografts have emerged as one of treatment options for CSBD[121]. Human bone allografts were among the first tissues in high demand during the 1990s[83,154] and the growing field of tissue engineering has further underscored this need for access

to human tissues[154]. Nowadays, bone grafting stands at the second place of the most prevalent tissue transplantation in the world[155].

Table 4. Critical-size bone defect treatment and properties, according to the Diamond concept.

Quality	Osteogenic	Osteoconductive	Osteoinductive	Structural strength	Vascularization	Availability	One-stage surgery
Treatment							
Autograft	+	+	+	-	-	-	+
Cancellous	+	+	+	-	-	-	+
Cortical	+	+	+	+/-	-	-	+
Allograft	-	+	-	+/-	-	+	+
Processed corticocancellous	-	+	-	+/-	-	+	+
Massive or structural	-	+	-	+	-	+	+
Bone transport	+	-	+	-	+	+	-
Induced membrane	+/-	+	+	-	+	+	-
Free vascularized bone transfer	+	+	-	+	+/-	-	+
Synthetic bone scaffolds	-	+	-	+/-	-	+	+
Megaprosthesis	-	-	-	+	-	+	+

+: present, -: absent, +/-: variable

Massive bone allografts (MBAs) (at least 5cm in length in human[83,156]) are sterilely harvested, fresh-frozen, and stored at -80°C in tissue banks[34,83]. Their primary advantage lies in providing immediate structural stability and anatomical reconstruction[83,141], fixed with classical osteosynthesis (plate or IMN). Another benefit is the preservation of soft tissues (*e.g.* tendons, ligaments, joint capsule) attached on the allograft that can be further sutured or reinserted on host tissues to restore function. These allografts are commonly categorized into structural

patterns: osteochondral, intercalary, allograft prosthesis composite (APC), arthrodesis, and inlay cortical allograft[83] (Fig. 17).

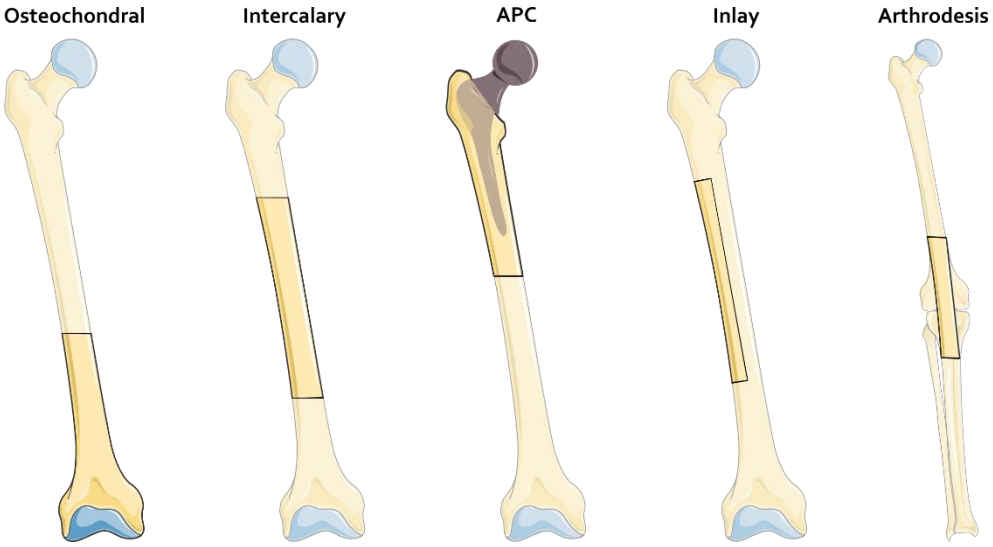

Figure 17. Massive bone allograft according to structural different patterns. APC: allograft prosthesis composite.

This thesis will focus on intercalary massive allografts to reconstruct diaphyseal CSBDs.

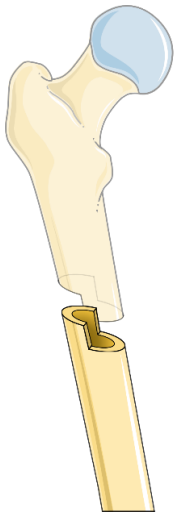

Figure 18. Step cut technique

The creeping substitution defines allograft incorporation by a remodelling-like process involving osteoclastic resorption of dead bone from the allograft and its replacement by new living bone formed by hosting osteoblasts[83,141,157]. The main limitation of using MBA is the absence of osteogenicity and the poor vascularization, leading to a restricted creeping substitution at the graft extremities and substantial complications[6,157]. Diaphyseal junction between the graft and host bone takes longer time to consolidate (9 to 12 months[123,158]). A step cup technique (Fig. 18) can enhance rotational stability and surface of bone contact to improve bone union but pseudarthrosis (> 18 months[156]) still occurs in 10% to 40% of cases[83,156,158–160], with a significant predominance for intercalary allograft[141,156,160].

Fracture is not uncommon with a prevalence of 15-30% after an average of two years post-transplantation[83,141,156,160], especially for long allograft (> 10-20cm[156,160]). Repetitive usage of an implanted massive allograft can provoke micro-cracks, namely a fatigue or stress fracture[86] because it is devoid of remodelling process. The restricted intrinsic osteogenic and angiogenic properties do not enable the fracture healing, and revision surgery is mandatory.

Local sepsis (5-18%[83,141,156,160]) and allograft resorption[14,161,162] are both other complications of massive allografts, despite an adequate soft tissue coverage and antibioprophylaxis. Potential risk of disease transmission is also a concern[163].

In our institution, a recent review of 246 massive allografts of the limbs between 1970 and 2009 showed one third of allograft retrieval (35%) due to complications (Table 5) (data not published).

Table 5. Complications and associated risk factors for a cohort of 246 massive limbs allografts.

	Prevalence	Risk factors	p-value
Complications			
Non-union	30%	Young patients	0.019
		Intercalary graft	<0.001
Fracture	24%	Young patients	<0.001
		IMN	0.030
		Allograft length	0.013
Infection	15%	Prior infection	<0.001
Resorption	8%	Young patients	0.003

IMN: intramedullary nailing.

These complications significantly worsened the survival curve (p<0.001) of the grafts, which still have a median survival of 27.8 years. In this case, surgical revision is performed to remove the allograft (15-35%), increasing the time of follow-up and altering long-term outcomes. All these observations were confirmed by the literature[50,123,156,160,164]. Most complications occurred within the first three or four years after initial surgery[141,160,164]. However, if early complications can be avoided, MBAs can last more than 20 years[141,165] (Fig. 19).

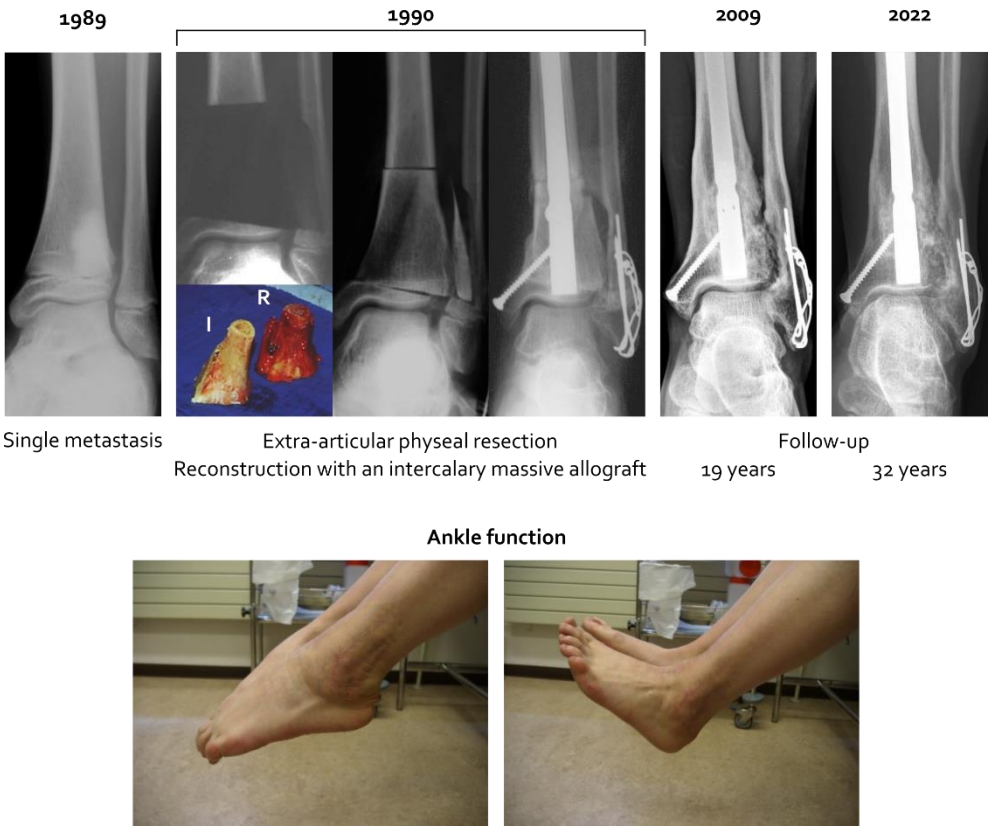

Figure 19. Survival and functional outcomes of a massive bone allograft. 1989: 10-year-old patient in orthopaedic consultation for left ankle pain diagnosed as a single metastasis after an osteosarcoma of the proximal end of the right femur. 1990: Extra-articular tibia and fibula physeal resection including the syndesmosis, and reconstruction with an intercalary massive bone allograft. R: resected tumoral bone, I: implanted allograft. 2009 and 2022: Follow-up after 19 and 32 years respectively. The ankle function was very good, similar to the contralateral side with a maximal plantar flexion (50°) and dorsiflexion (5°).

The osteogenicity and the vascularization need to be improved in order to minimize complication occurrence and maximize graft survival and function.

Actually, the best treatment would respect all the criteria of the Diamond concept while being available off-the-shelf in one-stage surgery.

Hypothesis: Tissue engineering contribution

« I touch the future. I teach. »

Christa McAuliffe, 1986

Since regenerative and personalized medicine show exponential interest, the tissue engineering concept and associated scientific literature follow similar ascension. A quick overview of PubMed database with the keywords « bone tissue engineering » shows 60,268 studies indexed since 1948 (Fig. 20). The inflexion point of the curve occurs from the 2000s onwards, with approximatively one-third of all publications (22,804 papers) being very recent (≥ 2020).

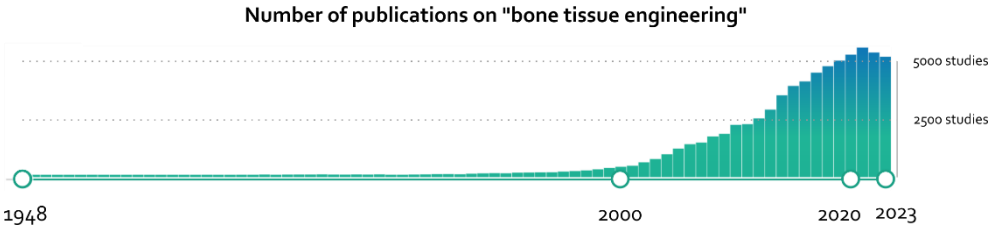

Figure 20. Overview of scientific research on "bone tissue engineering" from the PubMed database over the years (consulted on 24 March 2024).

A. Tissue engineering concept

Tissue engineering is a multidisciplinary field combining principles from medicine, biology, engineering, and material science to develop biological substitutes that could restore or replace a damaged organ, tissue or function[11,18,166,167]. This characteristic is referred to as biomimicry. The European Commission (Scientific Committee on Medical Products and Medical Devices, SCMPMD) gave the following definition: « Tissue engineering is the regeneration of biological tissue through the use of cells, with the aid of supporting structures and/or biomolecules »[11] (Fig. 21).

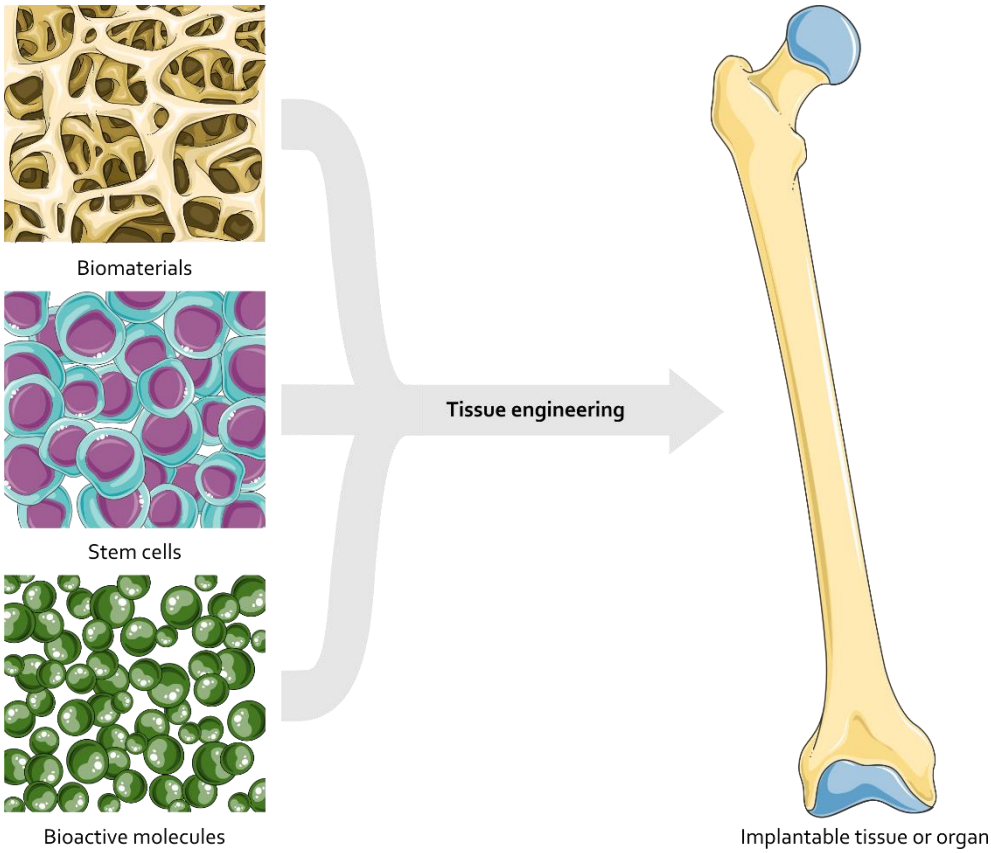

Figure 21. Classical triad of tissue engineering concept combining a supporting structure (biomaterials), cells (stem cells), and bioactive molecules (growth factors) to create a new biological tissue which can further be implanted. Inspired by Rustard et al.[168].

Tissue engineering has evolved in various forms, using a diverse range of scaffolds including biological and synthetic materials[169], a wide array of cell sources, and an extensive selection of GFs. This diversity in research poses challenges for systematic synthesis and comparison.

B. Scaffolding: Biomaterial & technique

In tissue engineering, scaffolds serve as templates to guide tissue regeneration and undeniably support cell adhesion, proliferation, migration and differentiation[168,170,171]. They can be elaborated with different material types

(biological or synthetic materials), and different morphologies or properties (*e.g.* mechanical, structural, functional). However, they all need to be biocompatible.

Natural, or biological materials (based on proteins (*e.g.* collagen and gelatin) or polysaccharides (*e.g.* alginate and chitosan)), and synthetic materials (based on polymers (*e.g.* polylactic acid (PLA) and polyglycolic acid (PGA)) or ceramics (*e.g.* tricalcium phosphate (TCP) and hydroxyapatite) are the two main types of biomaterials used for scaffolding[169,171–173]. Both can be biodegradable, reducing the need for subsequent surgeries to remove the material.

While synthetic materials can be precisely engineered (*e.g.* by 3D-printing, electrospinning and so many others[171,173]) to meet specific mechanical and structural requirements, biological materials can offer a natural ECM environment and 3D microarchitecture by decellularization process of a native biological matrix. This specific tissue engineering approach typically follows three main steps. First, the native tissue is harvested and decellularized, secondly, sterilized and finally recellularized to restore physiology (Fig. 22).

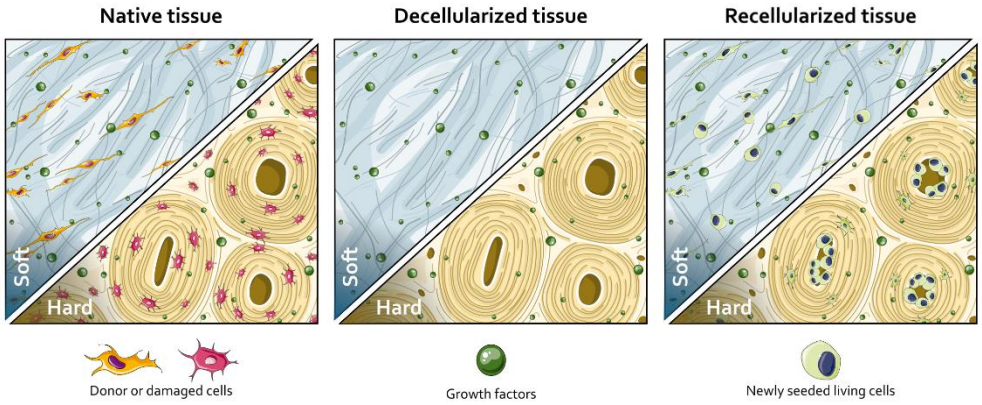

Figure 22. Tissue engineering procedure based on decellularization-recellularization technique of a native matrix for soft tissue (with fibroblastic cells, yellow) or hard cortical bone tissue (with osteocyte cells, pink). The goal is to replace donor or damaged cells with newly seeded living cells, keeping the extracellular matrix intact.

The decellularization process removes donor cells in the case of allo- or xenotransplantation, or damaged cells in the case of autotransplantation, while endeavouring to preserve the ECM components and GFs. This process seeks to create a non-cytotoxic 3D matrix that avoids triggering an immunogenic response

from antigenic epitopes, such as complement cascade activation, or activation of the adaptive immune system, and chronic inflammation[174,175]. The engineered graft should also possess the ability to thrive, remodel, and self-repair *in vivo*. Subsequently, recellularization takes place within a sterile ECM, allowing the seeding of new living cells for either autologous or allogenic transplantation.

Pros and cons of both scaffolding techniques are summarized in Table 6.

Table 6. Comparison between biological and synthetic scaffolds.

	Advantages	Disadvantages
Scaffold origin		
Biological decellularized tissue	Natural biocompatibility Removed immunogenicity Inherent bioactivity 3D complex microarchitecture Tissue integration Native vascular architecture Simplified clinical transposition	Different regenerative capacity Limited quantity/availability Quality variation Risk of disease transmission Limited long-term storage Undefined *in vivo* degradation rate
Synthetic engineered scaffold	Controlled structural and mechanical properties Standardized quality control Large quantity/availability Reproducibility Long-term storage	3D complex microarchitecture No natural biocompatibility or bioactivity No vascular architecture Foreign body reaction (infection, rejection, encapsulation) Potential toxic by-products Harder clinical transposition (// medication, FDA-approval)

FDA: American Food and Drug Administration. Inspired from multiple studies[170–172].

The choice between both techniques could depend on the requirements of the specific application and the desired balance between structural properties (size, shape, surface, morphology)[176,177], mechanical properties (strength and stiffness)[170,171], biocompatibility, and the ability to support cellular adhesion, migration, and functions[172].

Although the development of recent techniques has been exponential[171], a major drawback of synthetic scaffolds is their difficulty in recreating the complexity of human-sized and clinically effective tissues and organs[168]. The inherent 3D microarchitecture and biological signals present in natural ECM are challenging to

replicate, potentially resulting in suboptimal cellular responses. Therefore, biological decellularized tissue received our preference for its natural ECM benefiting from a combination of structural and functional proteins, an ultrastructural 3D organization that facilitates interface and interaction with cells[172].

C. Decellularization

The best decellularization technique consists in good balance between removing all cellular components and antigens, and preserving ECM 3D ultrastructure[174,175]. Not only do cells play an active role, but the ECM also exerts influence on cell mitogenesis, differentiation, and remodelling[175,178,179] due to its specific components (*e.g.* collagen fibres, glycosaminoglycans (GAGs), elastin), architecture, and mechanical properties[175]. Additionally, its osteoconductivity and osteoinductivity characteristics, the latter attributed to sequestered GF and cytokines, contribute to these effects[174,179]. The ECM serves as a substrate for cellular functions to respond to mechanical stimulation, regulate the availability and activity of soluble factors (*e.g.* BMPs), and activate intracellular signalling pathways through cell adhesion molecules[179].

C. 1. Techniques and agents

Four techniques are distinctively employed based on the tissue morphology, two of which are most frequently used (Table 7). Diffusion decellularization by agitation in successive agent baths is carried out for simple tissues, typically no thicker than a few millimetres, while perfusion decellularization is performed for entire thick organs.

A wide range of decellularization agents have been developed to optimize this objective. Decellularization agents are traditionally divided into three categories: physical, chemical and biologic agents (Table 7).

Table 7. Techniques and agents for decellularizing tissues or organs.

Technique	Mode of action	Risk on ECM
Technique of decellularization		
Agitation	Chemical exposure Cell lysis Removal of cellular material	If aggressive → ECM disruption
Perfusion	Chemical exposure Removal of cellular material	If aggressive → ECM disruption
Pressure gradient	Chemical exposure Removal of cellular material	If aggressive → ECM disruption
Supercritical fluid	Chemical exposure Cell burst Removal of cellular material	If aggressive → ECM disruption
Agent	**Mode of action**	**Risk on ECM**
Physical and miscellaneous agents		
Temperature		
Freezing and thawing	Cell membrane disruption by intracellular ice crystals	If aggressive → ECM disruption or fracture
Direct force	Cell burst Removal cell remnants	Direct ECM damage
Pressure	Cell burst Removal cell remnants	If aggressive → ECM disruption
Electroporation		
Pulsed electrical field	Cell membrane disruption	If aggressive → ECM disruption
Gamma-irradiation	Cell death	No evacuation of cell remnants ECM disruption
Chemical agents		
Acids and bases	Cytoplasmic components solubilization Nucleic acid disruption Protein denaturation	Collagen (cross-links), GAG and GF damage
Hypo-/Hypertonic solutions	Cell lysis by osmotic shock Disruption of DNA-protein interactions	No evacuation of cell remnants
Non-ionic detergents	Disruption of DNA-protein interactions Disruption of lipid-lipid and lipid-protein interactions Disruption of protein-protein interactions	
Triton X-100		Efficacy dependent on tissue More effective cell removal on thin tissue Less effective < SDS GAG removal Ultrastructure disruption
Ionic detergents	Cell solubilization Nucleic membrane solubilization Protein denaturation	

SDS	Nuclear remnant removal Cytoplasmic protein removal	Ultrastructure disruption GAG removal GF removal Collagen damage
Sodium deoxycholate		Efficacy dependent on tissue thickness Ultrastructure disruption GAG removal
Triton X-200	Cell removal in thin tissue	Ultrastructure disruption +++
Zwitterionic detergents	// ionic and non-ionic detergents	
CHAPS		Ultrastructure disruption of thin tissue
Sulfobetaine-10 and -16		Ultrastructure disruption of thin tissue
Solvents		
Alcohols	Cell lysis by dehydration Lipid solubilization and removal Pyrogen inactivation	Protein (collagen) cross-link and precipitation
Acetone	Cell lysis by dehydration Lipids solubilization and removal	Protein (collagen) cross-link and precipitation
Tributyl phosphate	Stable complex with metals Disruption of protein-protein interactions	Efficacy dependent on tissue Collagen loss Minimal impact on mechanical properties
Biologic agents		
Enzymes		
Nucleases	Ribonucleotide hydrolysis Deoxyribonucleotide chain hydrolysis	Difficult rinse
Trypsin	Peptide bond cleavage on the C-terminal chain of Arg and Lys	If prolonged → ECM disruption Collagen, laminin, fibronectin, elastin, GAG removal Less GAG removal< detergents
Dispase	Specific peptide cleavage (mainly fibronectin and collagen IV)	If prolonged → ECM disruption Fibronectin and collagen IV removal
Chelating agents (EDTA, EGTA)	Metallic ion binding → Cell-ECM adhesion disruption	Ineffective alone Typically used with enzymes

Black: major action, grey: secondary action. ECM: extracellular matrix, GAGs: glycosaminoglycans, GFs: growth factors, DNA: deoxyribonucleic acid, SDS: sodium dodecyl sulfate, Arg: arginine, Lys: lysine, EDTA: ethylenediaminetetraacetic acid, EGTA: ethyleneglycoldiaminetetraacetic acid. Adapted from Crapo et al.[178] and Keane et al.[174]

Each method or agent used to remove cells has its advantages but will inevitably modify the ECM composition and lead to some level of ultrastructure disruption[174]. The goal of decellularization is to minimize these effects rather than completely avoid them[178].

Techniques and agents can be combined depending on the tissue/organ to achieve the best balance possible. Regardless of the agent used, the abundant rinse eliminates immunogenic cell remnants[180] as well as cytotoxic decellularization agents[174,178].

C. 2. Validation criteria

The presence of residual cellular material within the ECM can lead to *in vitro* cytocompatibility issues and potentially elicit adverse host responses *in vivo*[178], by the activation of acquired and innate immune systems[174,180].

The effectiveness of a decellularization process is conditioned by the avoidance of these two undesirable events, and defined qualitatively and quantitatively by[178] :

- Lack of visible nuclear material in tissue sections stained with 4',6-diamidino-2-phenylindole (DAPI) or haematoxylin and eosin (H&E)
- < 50ng double-stranded DNA (dsDNA) per mg ECM dry weight
- < 200 base pairs deoxyribonucleic acid (DNA) fragment length

After confirming the successful removal of cellular components, understanding the impact of decellularization on mechanical and material properties of the ECM scaffold is of interest. For this purpose, collagen, GAGs, elastin and GF can be quantified alongside mechanical tests, although standardized validation criteria are currently lacking.

Ultimately, the decellularized scaffolds should be devoid of cytotoxic substances. *In vitro* cytotoxicity assessments (cell viability and proliferation) can be conducted prior to *in vivo* biocompatibility (matrix implantation) (Fig. 23).

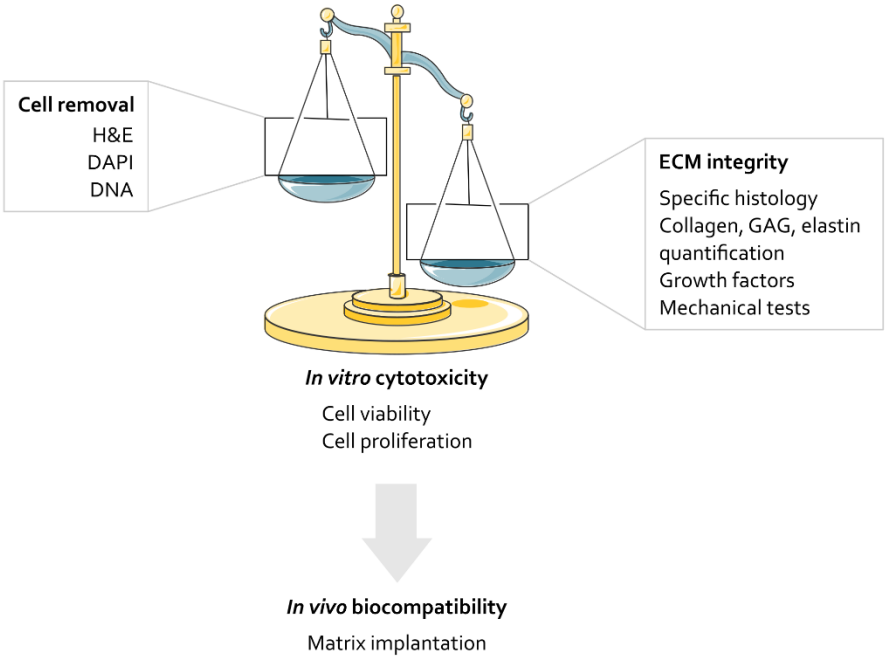

Figure 23. Balance of validation criteria between cell removal and ECM integrity leading to in vitro cytotoxicity and in vivo biocompatibility assessments, and their respective method of evaluation. H&E: haematoxylin and eosin staining, DAPI: 4',6-diamidino-2-phenylindole staining, DNA: deoxyribonucleic acid, GAGs: glycosaminoglycans.

D. Sterilization & storage

A sterile scaffold is essential for *in vitro* cell seeding to prevent bacterial overgrowth, which could jeopardize the desired cell growth. Sterilization also includes depyrogenation to eliminate viral and bacterial DNA, as well as Gram-negative bacterial endotoxins[178]. Ethanol, peracetic acid, ethylene oxide, and ultraviolet light are multiple methods of sterilization reported in the literature. Since only the ionizing radiation (gamma-irradiation) is currently validated for clinical use by the American National Standards Institute (ISO 11137-3, 2023[181] and ISO TIR22456, 2022[182]), this manuscript will essentially focus on this sterilization mode. The legal minimal dose of gamma rays of 25kGy is appropriate for bacteria[183] and hepatitis C virus (HCV)[184,185] but not effective enough for human immunodeficiency virus (HIV)[186] and prions[187]. Another drawback of gamma-

irradiation is the risk of mechanical alteration[175,188–190]. Low doses (< 15kGy) enhance the strength and ECM modulus, but mechanical properties decrease in a dose-dependent manner at doses exceeding 15kGy[190], which is partially explained by breakage of collagen cross-links[188]. However, frozen irradiated bones (standard dose of 25kGy) retain their compression strength[191]. Non-defatted fresh-frozen bones still contain a significant amount of lipids in the medullary cavity, which can become peroxidized and cytotoxic following gamma-irradiation[192]. This sterilization method is therefore not recommended for non-processed fresh-frozen bones, but it is suitable for tissue-engineered scaffolds.

Freeze-drying and cryopreservation are common methods for long-term storage of scaffolds, but freeze-drying tends to have a greater negative impact on mechanical properties than cryopreservation[189]. While fresh-frozen bones are typically stored at -80°C to preserve their mechanical strength, tissue-engineered scaffolds can be stored using both methods to extend their longevity.

E. Recellularization

Recellularization is the process of reintroducing new viable cells into the decellularized scaffold. The goal is to repopulate the scaffold with functional cells that can regenerate or mimic biological and mechanical properties of native tissue. The newly seeded cells are expected to adhere to the ECM, proliferate, differentiate, to allow tissue remodelling, and self-repair within the living organism. Several techniques are used for recellularization including static seeding, perfusion, injection, and 3D bioprinting. Each of these methods has its advantages and limitations, and the choice of technique often depends on the specific tissue type, desired cell distribution, and intended application of the recellularized tissue. Among them, static seeding is the simplest and used for thin tissue recellularization. Cells are directly seeded onto the surface of the scaffold and allowed to adhere and proliferate.

E.1. Cell potency and phenotype

Stem cells are by far the most widely used cells in tissue engineering[7,193]. This unique type of cell has the remarkable ability to develop into any different cell

types in the body. These undifferentiated cells are able to proliferate indefinitely, to self-renew, and to differentiate into specialized cell phenotypes with related precise functions[7,167]. This ability makes them crucial for development, tissue repair, and regeneration[193].

There are several types of stem cells, each with different advantages and drawbacks[7,167,168].

Embryonic stem cells = *Pluripotent* stem cells derived from embryos, which enable the fetus development[167] and include every types of cell phenotype in a human body. They have great potential for regenerative medicine but raise ethical considerations due to their origin, and risk of teratoma formation[7,168].

Adult stem cells = *Multipotent* stem cells (also known as somatic or tissue-specific stem cells) found in various fully-differentiated tissues throughout the body (*e.g.* bone marrow, blood, adipose tissue, and periosteum)[167,194]. They provide homeostasis and regeneration of damaged specific tissue in the body[7]. In spite of their limited lifespan *in vitro,* they have immune-privileged properties and less controversial ethical issues for tissue engineering[7,168].

Induced pluripotent stem cells = *Pluripotent* stem cells artificially generated by reprogramming adult somatic cells (*e.g.*, skin cells)[195,196]. They bypass ethical issues associated with the use of embryonic stem cells[168], but the risk of tumorigenicity and the safety about retroviral transfection are concerned[7].

E.2. Mesenchymal stem cells

As previously briefly introduced, MSCs, discovered by Friedenstein et al. (1966)[197] and later named by Caplan et al. (1991)[198], are non-hematopoietic undifferentiated adult stem cells essential for bone regeneration[7,194]. Once osseous injury releases cytokines from the haematoma, MSCs are mobilized by chemotaxis from their niche[194], transmigrate through the endothelium of local vasculature, proliferate and differentiate *in situ*[58]. Their descendants follow specific pathways to become mature cells responsible for building unique tissue type, such as bone[198]. Their interest in tissue engineering was tremendous because of their multipotency, their ease of isolation and expansion in culture[194], and their absence of teratogenicity or ethical issues[199]. MSCs are defined by three minimal criteria from the

Mesenchymal and Tissue Stem Cell Committee of the International Society for Cellular Therapy[200] (Fig. 24).

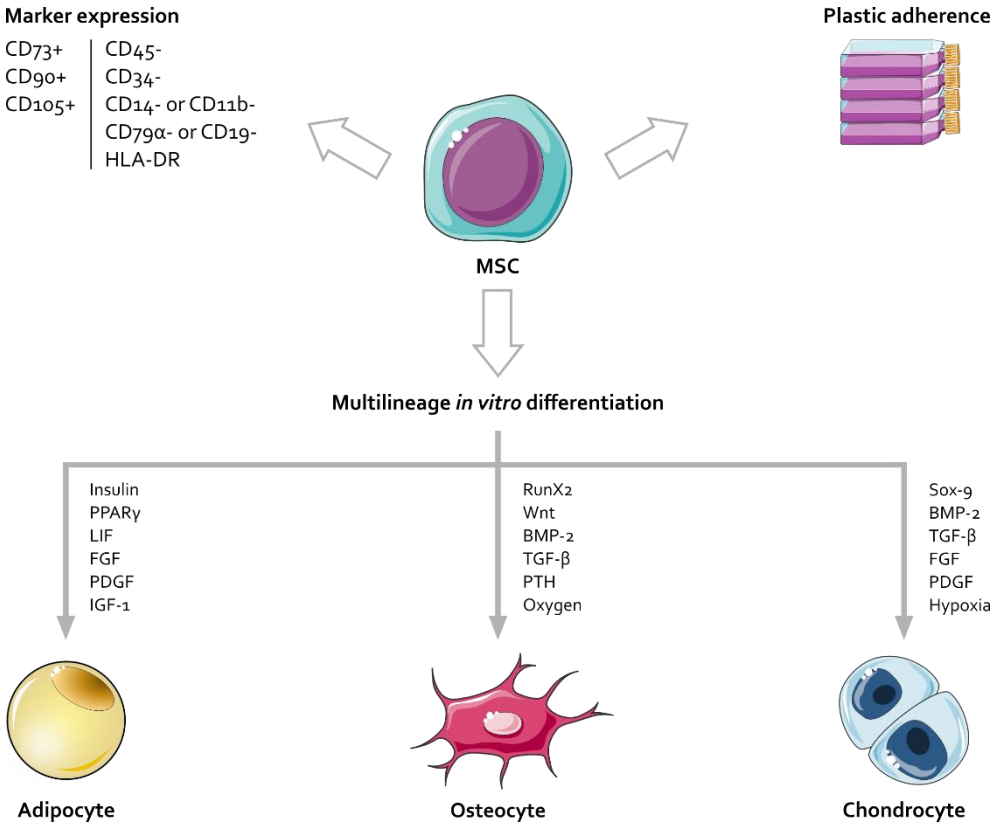

Figure 24. Minimal criteria defining mesenchymal stem cells according to the Mesenchymal and Tissue Stem Cell Committee of the International Society for Cellular Therapy. Signalling molecules for each of the trilineage differentiation are given as non exhaustive list. CD: cluster of differentiation, HLA: human leucocyte antigen, MSC: mesenchymal stem cell, PPAR-γ: peroxisome proliferator-activated receptor gamma, LIF: leukaemia inhibitory factor, FGF: fibroblast growth factor, PDGF: platelet-derived growth factor, IGF: insulin-like growth factor, RunX2: runt-related transcription factor 2, Wnt: Wingless-related integration site proteins, BMP: bone morphogenetic protein, TGF-β: transforming growth factor beta, PTH: parathyroid hormone. Adapted from multiple studies[32,58,200–204].

Plastic adherence = MSCs can be cultured in plastic flasks, similarly to fibroblasts.

Surface marker expression = MSCs typically express specific cell surface markers (CD73, CD90, and CD105)[32] (≥ 95% of cells), while lacking expression (≤ 2% of cells)

of hematopoietic markers or other surface molecules (CD45, CD34, CD14, CD11b, CD79α, CD19, and HLA-DR).

Multipotency = MSCs have the capacity of trilineage mesenchymal differentiation. Thus, they can differentiate *in vitro* into cells of mesodermal origin, namely to tissues such as bone (osteogenic phenotype), cartilage (chondrogenic phenotype), and fat (adipogenic phenotype).

The osteogenic lineage progression induces the step-by-step transformation from MSC to osteocyte[7]. At each step of cell development, inherent genetic capacity of the cells (intrinsic factors) and local boost (extrinsic factors) are signalling pathways that interact to regulate the pace and specific characteristics of cell phenotype, that can be recognized by cell markers[7,198] (Fig. 25).

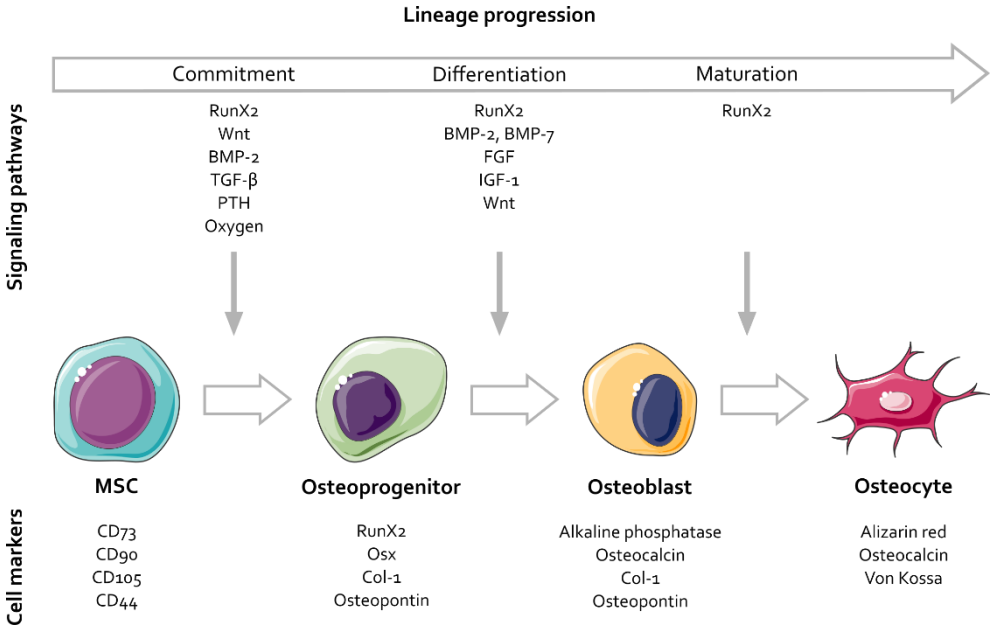

Figure 25. Lineage step of cell differentiation from the mesenchymal stem cell (MSC) to the osteocyte with their corresponding signalling pathways and cell markers (non exhaustive lists). RunX2: runt-related transcription factor 2, Wnt: Wingless-related integration site proteins, BMP: bone morphogenetic protein, TGF-β: transforming growth factor beta, PTH: parathyroid hormone, FGF: fibroblast growth factor, IGF: insulin-like growth factor, CD: cluster of differentiation, Osx: osterix, Col-1: type I collagen. Adapted from multiple studies[201,205–207].

Osteoprogenitors are committed cells towards the osteogenic lineage and are therefore more specific than MSCs. Their major action is to substitute differentiated cells lost by the normal turnover or an unexpected injury. Differentiation increases as potency decreases, ultimately leading to the formation of differentiated osteoblasts and mature osteocytes.

Later on, some other outstanding characteristics of MSCs were recognized and studied, including their immunomodulatory role and their resistance to oxidative or hypoxic stress.

Immunomodulation = MSCs have the ability to modulate the immune host's response, which makes them hypoimmunogenic[167,208–211]. Some authors described MSCs as immunosuppressive due to the lack of HLA-DR (major histocompatibility complex (MHC) class II antigens) marker[7,210,212] and costimulatory molecules expression[208,210]. This property led to their use in the treatment of graft-versus-host diseases[6,210,212].

Resistance = MSCs possess the ability to withstand oxidative or hypoxic stress, and produce GF[211]. Oxygen levels also influence cell differentiation, with hypoxia preferentially leading to chondrogenesis whereas normoxia favours commitment to osteogenic lineage[61]. During a fracture, local hypoxia simultaneously triggers chondrogenic differentiation and induces the release of VEGF angiogenic factors, promoting neoangiogenesis and oxygen supply to stimulate subsequent osteogenic differentiation[6,32].

E.3. Periosteal mesenchymal stem cells

MSCs can be obtained from various sources[6,7], with bone marrow (BMSCs), adipose tissue (AMSCs or adipose-derived stem cells, ASCs[7]), and periosteum (PMSCs) being recognized for their abundance compared to other niches[194,211]. Their provenance is related to the efficiency of their handling or function[7,211] (Table 8).

Table 8. Comparison of three different MSC niches according to their handling or function.

Handling / Function	Harvest amount	Ease of harvest	*In vitro* proliferation	Osteogenic differentiation	Chondrogenic differentiation
Cell type					
BMSCs	++	+	++	++	+
AMSCs	+++	+++	++	++	+
PMSCs	+	+	++	+++	+++

+, ++, +++ gives an indication of the intensity level. Adapted from Ho-Shui-Ling et al. (2018)[6].

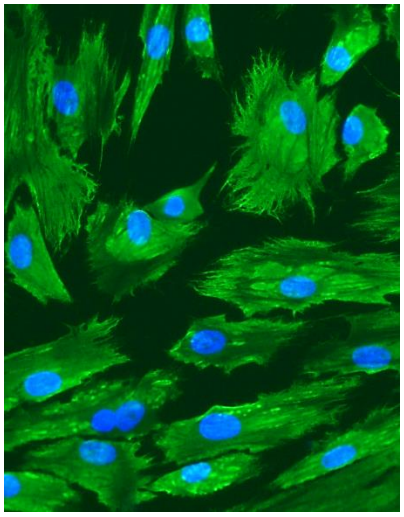

Figure 26. In vitro cultured periosteal mesenchymal stem cells highlighted by immunofluorescence of vimentin (green) and Hoechst (blue).

PMSCs, also known as periosteal-derived stem cells (PDSCs)[213] (Fig. 26), are naturally injury-responsive and activated during the inflammatory phase of fracture healing[32,66,67,214]. Their function is therefore innately predestined for bone regeneration[67,214,215], on the contrary of AMSCs. However, BMSCs can also locally participate in bone regeneration from the medullary cavity[216]. The difference stands in that the periosteum provides more chondrocytes for endochondral ossification, alongside with osteoblasts for intramembranous ossification[6,32,66,67,204,216], confirmed by donor-matched comparison[215]. However, PMSCs express lower adipogenic potential, supporting their preferential commitment to osteochondral

lineage, needed for fracture repair[215]. On the opposite, AMSCs have been described as inhibitor of chondrocyte proliferation and stimulators of chondrocyte apoptosis[217]. Besides, periosteum contains the highest density of MSCs[62,215,218], up to 1500 fold-higher than AMSC density[215], and the harvest is more homogeneous[67,215]. PMSCs display higher clonogenicity, activation, proliferation, and differentiation into chondrogenic and osteogenic lineages than other cell sources[32,62,67]. Their *in vitro* osteogenic potential is higher than other MSCs[7,67,219], especially from load-bearing bones such as the tibia[220].

In contrast to other MSCs, PMSCs from elderly donors exhibit similar performance to those isolated from teenagers[7]. This may be explained by the absence of telomerase, resulting in longer telomeres and sustained stability of these cells[62,204,221]. Despite periosteal atrophy with age, elderly people still exhibit the ability for bone healing, possibly elucidated by this phenomenon.

All these positive aspects of PMSCs compensate the small number of harvested cells and make them the MSCs of choice for osteogenic purpose[67,216].

E.4. Transplant donors

Various factors related to the cell handling have to be taken into account to maximize outcomes[7]:

- The availability and harvesting procedure of the desired tissue
- The potential morbidity at the donor-site
- The efficiency of cell isolation methods and final yield
- The osteogenic and angiogenic capacities of the cells
- The cell proliferation rate
- The uniformity of isolated cells
- The stability of cell phenotype and safety post-implantation
- The risk of immunogenicity
- The establishment of quality control protocols for cell and graft production.

While some of these factors have been approached in previous paragraphs, many of them can be addressed by the unique choice between autologous and allogenic sources of PMSCs, which should be balanced according to this intended use (Table 9).

Table 9. Comparison between autologous or allogenic sources of PMSCs.

	Advantages	Disadvantages
Transplant donor source		
AUTO-graft	No immunogenic reaction Perfect host integration Easy clinical transposition	Limited quantity Uncontrolled quality Interpersonal variation Intrapersonal lifespan variation Two-stage surgery Delay between 1st and 2nd surgeries Potential donor-site morbidity
ALLO-graft	Storage in tissue banks Standardized quality control Available off-the-shelf One-stage surgery Large quantity No donor-site morbidity	Potential immunogenic reaction Lower host integration HLA-typing? Harder clinical transposition (// medication, FDA-approval)

HLA: human leucocyte antigen, FDA: American Food and Drug Administration. Inspired from multiple studies[6,7].

F. Application: Fascia lata based scaffold

F.1. Fascia lata & iliotibial tract

Fasciae of the human body are now recognized as important structural tissues in the body and are classified into four functional categories: linking, fascicular, compression, and separating fasciae. The human fascia lata (HFL) is the deep fascia of the thigh, a dense and fibrous connective tissue that encases the muscles, separating and supporting them. Its lateral thickening called the iliotibial tract (ITT) or Maissiat's iliotibial band, connects and links the iliac crest to Gerdy's tubercle on the lateral condyle of the tibia[222–227], between the gluteal fascia and the fascia lata[228] (Fig. 27).

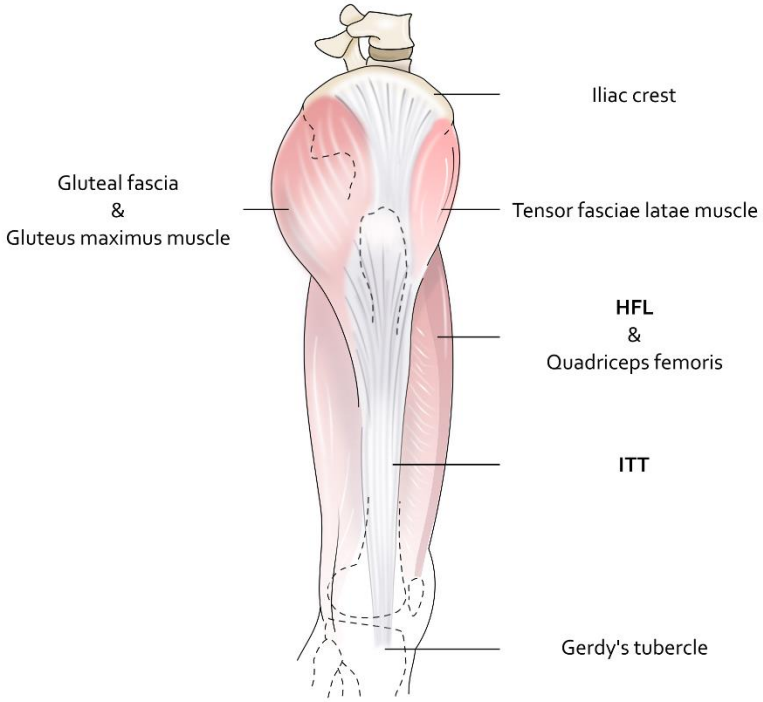

Figure 27. Schematic representation of the human fascia lata (HFL), the deep fascia of the thigh, and the iliotibial tract (ITT), the lateral thickening of the HFL.

No fewer than five distal insertions of the ITT were described, namely the most important insertion being Gerdy's tubercle, followed by the lateral condyle of the femur, the fibular head through the lateral collateral ligament, the linea aspera via the lateral intermuscular septum of the thigh, and the retinaculum of the patella[229,230]. The ITT is a dense connective tissue whose collagen fibres[223,231] can form different layers with a specific orientation. The proximal part of the ITT is separated into three layers[224]. The superficial and intermediate ones surround the tensor fasciae latae muscle; the deepest one fuses more distally, coming from the supra-acetabular groove[224,229]. The ITT plays a major role in hip and knee stabilization when walking by playing a tendon role for the tensor fasciae latae and gluteus maximus muscles[223,225,232].

F.2. Clinical use

The HFL and ITT are already extensively used in reconstructive surgery in various indications other than CSBDs. They serve as covering flaps for duraplasty[233], abdominal wall reconstruction[234], lung breaches sealing[235], colpopexy[236], soft tissue defects on limbs[237], and the reconstruction of structures like the acetabular labrum[238], rotator cuff[239], patellar ligament[240], and anterior cruciate ligament[241], among others. Additionally, they can also be used as interposed material in congenital tarsal coalition resection in adolescents[242].

For these applications, harvested avascular tissues from cadavers undergo several processing steps validated for clinical uses before being stored in a tissue bank until needed for use.

F.3. Tissue bank protocol – NaOH-based decellularization

The bone and tendon tissue bank of the *Cliniques Universitaires Saint-Luc* developed treatments to improve the biocompatibility of allografts several years ago. A protocol was specifically developed for the fascia lata[243] based on different successive solvent baths of acetone, ether, ethanol (70°), sodium hydroxide (NaOH, 1N), and hydrogen peroxide (H_2O_2).

Among them, the principal decellularization agent NaOH (1N) offers the supplementary property to be an inactivator for conventional (virus/bacteria) and non-conventional (prion) pathogens. The H_2O_2 also ensures bacterial inactivation. These two components therefore make the graft secure, which is a major advantage over detergent treatment. It also makes it possible to eradicate allogenic transmission of HIV, HCV and prions, which gamma-irradiation could not do. Frozen decellularized HFL scaffolds are then gamma-irradiated (min 25kGy) and cryopreserved for long-term storage.

Objectives

« A very important principle of the organization is that vital activity requires an envelope, which protects from the external elements. This envelope may be bark, skin, or shell, all that is living should be wrapped up. »

Johann Wolfang von Goethe,
The Metamorphosis of Plants, 1790.

Massive bone allograft is a major player of the therapeutic arsenal in the fight to cure CSBDs. It can save and/or reconstruct quality of life. However, substantial complications are still burden because of the limited creeping substitution, and the absence of life in the heart of the graft. The central concern of the present thesis is to improve graft vitality by providing the osteogenicity and the vascularization needed for its long-lasting functionality. The best therapy would respect all the criteria of the Diamond concept while being available in one-stage surgery.

The tissue engineering field tends to be fundamentally driven, often leading researchers to focus narrowly on specific components while sometimes overlooking the broader clinical and surgical integration beyond. This thesis aims to leverage each individual technique or piece of knowledge to develop a comprehensive model that optimally achieves effective and efficient preclinical applications, transposed into an *in vivo* porcine femoral CSBD.

Building upon Masquelet's theory, the concept of guided-bone regeneration[111] was meticulously refined. This project proposes the development of a bespoke bioactive membrane derived from decellularized HFL recellularized with porcine allogenic PMSCs. This innovative osteogenic membrane (OM) would envelop the porcine MBA, replacing the PMMA cement used in the Masquelet's technique. Using MBA offers a mechanically stable framework for healing, available off-the-shelf in one-stage surgery, and enabling immediate full weightbearing. Serving as a protective shield for the CSBD, the membrane would create a biological chamber conducive to optimal bone regeneration. Functioning as a guide, the membrane

would facilitate the controlled growth of new bone tissue integrating the MBA, effectively transforming the body into an *in vivo* bioreactor (Fig. 28).

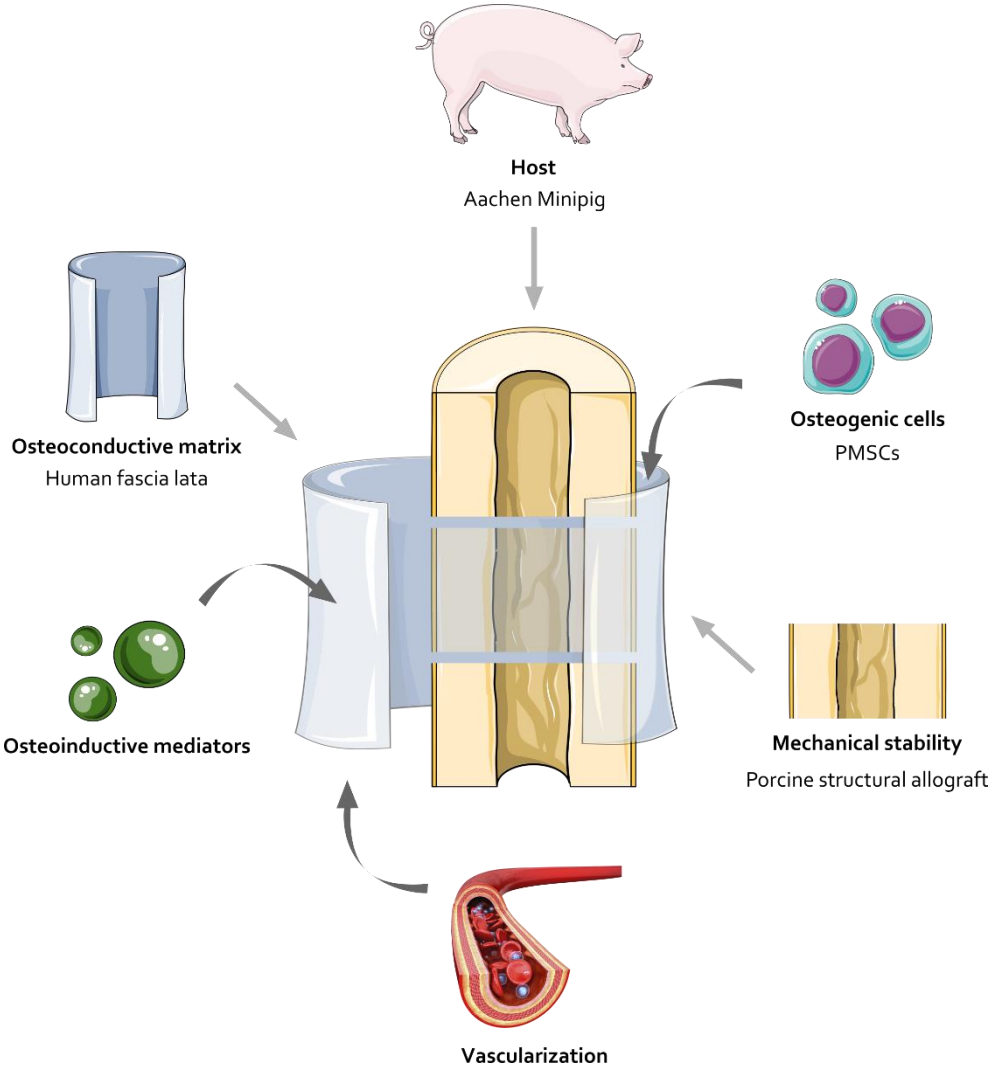

Figure 28. Design of the experiment including all criteria of the Diamond concept to repair a critical-size bone defect and improve bone massive allograft integration.

Defining requirements based on the Diamond is crucial for establishing the desired characteristics of a bio-engineered OM. This process aims to clarify objectives, structure the scientific approach, set achievement benchmarks, and facilitate a feedback discussion and improvement throughout the thesis.

– REQUIREMENT SPECIFICATIONS –

Requirement	Specification	Validation
Osteoconductive matrix		
Composition	- Col-1 membrane	
Morphology	- 2 layers - Thickness (1 thin + 1 thick layers) - Large size - Shapeable	
Biocompatibility	- No immunogenicity - Carrier for cells - No cytotoxicity	
Osteoinductive mediators		
Bioactivity	- Osteogenic GF - Osteogenic differentiation - Chondrogenic differentiation	
Osteogenic cells		
Osteogenicity	- Cell adhesion, proliferation, replication - Osseous ECM production	
Mechanical stability		
Membrane properties	- Sheet malleable support - Resistance to handling - Isotropy or anisotropy?	
	AND	
In vivo model	- Stitchable - Mechanical stability	
Vascularization		
Vascular supply	- Angiogenic properties - Neoangiogenesis **OR** - Intrinsic vascular architecture - Functional vascular network	
In vivo transposition		
Clinical needs	- Off-the-shelf availability - One-stage surgery	

CHAPTER I. Native tissue comparison

« Waking up means seeking out the world. »

Translated from Alain (Emile-Auguste Chartier), 1928

Research questions emerging from the Diamond

Since biological scaffolds are valued for their singular properties, the study of native tissues is beneficial to better understand the tissue of interest before considering any tissue-engineered transformations.

In the first paper, the HFL is thus compared to the periosteum, which serves as the benchmark for native osteogenic tissue. Various characteristics are examined including cellular compartment, ECM composition, mechanical properties, as well as osteogenic potential. Identifying the differences and similarities is a step in aligning HFL characteristics with the requirements of an OM.

More precisely in the second paper, the ITT is investigated in terms of tissular microstructural organization. This study delves into microstructure regional variations in total thickness, layer count and thickness, and fibre characteristics via 2D histology and 3D analyses of cryogenic contrast-enhanced microcomputed tomography (cryo-CECT). Understanding this tissue organization enables to select the optimal harvest site for the membrane based on the specifications required.

This chapter aims to answer the following questions:

- **Is the HFL a suitable scaffold to replace the HP for guided-bone regeneration?**
- **Based on its microstructural analysis, where should the HFL membrane be harvested to meet the specific requirements of an OM and maximize reproducibility?**

Paper 1 – Periosteum and fascia lata: Are they so different?

Julie Manon, Robin Evrard, Louis Maistriaux, Lies Fievé, Ugo Heller, Delphine Magnin, Jean Boisson, Natacha Kadlub, Thomas Schubert, Benoît Lengelé, Catherine Behets, Olivier Cornu

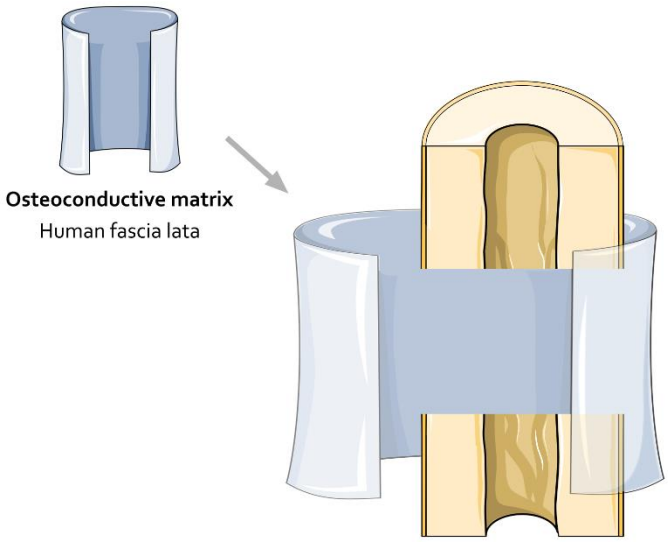

Published in

Front. Bioeng. Biotechnol. 10:944828. (IF=6.064)

doi: 10.3389/fbioe.2022.944828

Abstract

Introduction: The HFL is used widely in reconstructive surgery in indications other than fracture repair. The goal of this study was to compare microscopic, molecular, and mechanical properties of HFL and human periosteum (HP) from a bone tissue engineering perspective.

Material and Methods: Cadaveric HP and HFL (N=4 each) microscopic morphology was characterized using histology and immunohistochemistry (IHC), and the ECM ultrastructure assessed by means of scanning electron microscopy (SEM). DNA, collagen, elastin, GAGs, MHC class I (MHC-1), and BMP contents were quantified. HP (N=6) and HFL (N=11) were submitted to stretch tests.

Results: Histology and IHC highlighted similarities (Type I collagen fibres and two-layer organization) but also differences (fibre thickness and compaction and cell type) between both tissues, as confirmed using SEM. The collagen content was statistically higher in HFL than HP (735 vs. 160.2µg/mg dry weight, respectively, $p<0.0001$). On the contrary, DNA content was lower in HFL than HP (404.75 vs. 1,102.2µg/mg dry weight, respectively, $p=0.0032$), as was the immunogenic potential ($p=0.0033$). BMP-2 and BMP-7 contents did not differ between both tissues ($p=0.132$ and $p=0.699$, respectively). HFL supported a significantly higher tension stress than HP.

Conclusion: HP and HFL display morphological differences, despite their similar molecular ECM components. The stronger stretching resistance of HFL can specifically be explained by its higher collagen content. However, HFL contains many fewer cells and is less immunogenic than HP, as the latter is rich in PMSCs. In conclusion, HFL is likely suitable to replace HP architecture to confer a guide for bone consolidation, with an absence of osteogenicity. This study could pave the way to a bio-engineered periosteum built from HFL.

Graphical abstract

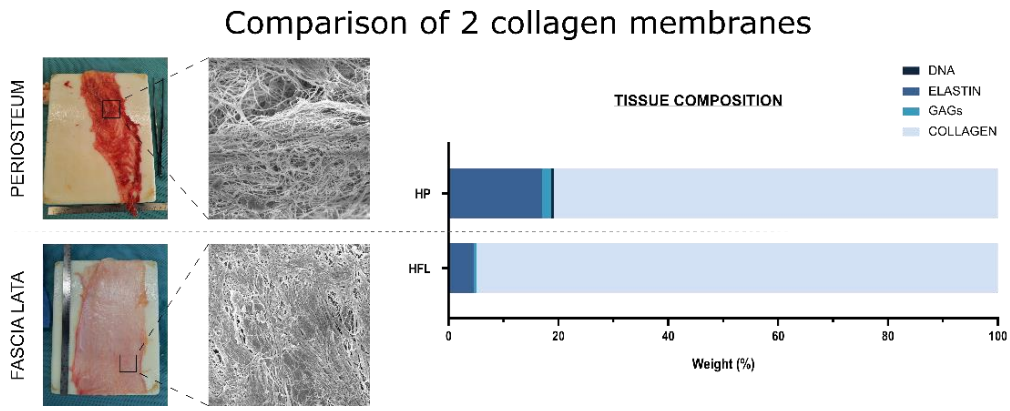

A. Introduction

Periosteum plays a major role in long bone fracture healing and transverse bone growth[25,69,244]. This richly vascularized membrane surrounding bone is made up of two layers. The outer one, the fibrous or sterile layer, is mainly composed of dense connective tissue, *i.e.*, Type I collagen fibres and fibroblasts. The inner layer, the cambial or fertile layer, is in close contact with the cortical bone, and it participates in bone modelling, as well as initiating the fracture callus, owing to the primordial attendance of PMSCs[25,69,245].

However, in the challenging treatment of a CSBD following trauma, tumor resection, infection, or congenital defect, the periosteum can be missing and thus no longer able to contribute to bone healing. This research field has grown rapidly since the 2000s, with multiple new therapeutic options made available, such as bone allograft, vascular autograft, surgical bone transport technique, synthetic implants, and new engineered periosteum scaffold, leading to some improvements but often being burdened by complications nevertheless[14,156,244,246–248]. Among previous approaches, Masquelet's induced membrane[108] reaches nearly all (4/5) of the diamond concept conditions (osteoconductive matrix, osteogenic cells, osteoinductive mediators, mechanical stability, and vascularization), leading to an 89% consolidation rate[19]. However, it requires a two-stage surgery aimed to debride and insert a cemented spacer prior to delicately open the newly formed membrane and replace the spacer with a bone autograft. This induced membrane plays the role of a well-vascularized periosteum-like tissue, without exactly mimicking it, due to the lack of MSCs and the specific periosteal microarchitecture. This tubing sheet also plays a role in guided-bone regeneration and barrier membrane. This concept has times been reported in the literature as being designed to conduct and promote bone healing, as well as preventing soft tissue invasion[249]. The development of an off-the-shelf induced membrane that could play the same role but in a one-stage surgery may emerge as a solution that could reduce the time and costs involved in this challenging surgical treatment.

Most authors who seek to develop a new scaffold based on tissue engineering techniques usually go straight to their target, while bypassing fundamental tissue knowledge. The ITT, which constitutes a thickening of the fascia lata of human

thigh, is a biological sheet that is already used in other reconstructive surgeries, such as duraplasty[233], colpopexy[236], and abdominal wall reconstruction[234] instead of an artificial mesh, or for head and neck reconstruction as vascularized flap[250]. In orthopaedics, the HFL has already been employed to repair rotator cuff tear[239], in the "anchovy" interpositional arthroplasty of the hallux metatarsophalangeal joint[251], to reconstruct patellar ligament[240] or after anterior cruciate ligament rupture[241]; nevertheless, it has never been considered for CSBD treatment. The fascia lata has already been used to enhance the stability and support strength of other soft tissues, such as the periosteum[249], although the HFL has never been directly compared to the HP from a tissue engineering point of view. The goal of this study was to compare the HFL microscopic, molecular, and mechanical characteristics/properties with those of HP in order to explore its potential use as a periosteal-like scaffold in the treatment of CSBDs.

B. Materials & methods

B. 1. Human tissue harvesting

Femoral HP and HFL were obtained from cadaveric donors (one woman and four men; average age: 91.3 ± 1.8 years) who were received at the Human Anatomy Department of UCLouvain (IRB00008535, Brussels, Belgium), following local ethics committee authorization (Ref 2021-30AOU-356 approved on 13 September 2021). For the mechanical tests, independent tissues were collected from other donors (11 HFL from three women and three men, average age: 88.8 ± 3.2 years; six HP from two women and three men, average age: 86.4 ± 6.0 years). These bodies were provided by the Ecole de Chirurgie de Paris (Agence Générale des Equipements et Produits de Santé [AGEPS], Assistance Publique Hôpitaux de Paris [APHP]). Permission to perform the study using cadaveric specimens was obtained from the institutional review board (Ecole de Chirurgie, AGEPS, APHP, IRB00011591, Paris, France). All cadaveric subjects had previously provided their consent for their body being employed for medical research.

All the samples were harvested from the thigh using a longitudinal incision from the anterosuperior iliac spine to the upper border of the patella. The HFL was first cautiously dissected and sectioned from the median line to the lateral lip of linea

aspera. Then, the quadriceps femoris was carefully elevated, and the HP was harvested using a rugin following a circumferential incision above the femoral condyles and below the lesser trochanter. Both tissues were divided into several samples that were differently processed in the following analyses.

B. 2. Histological analysis

Micromorphological analyses were explored using classical histology. In each tissue from four donors, three 1cm² samples were fixed in formaldehyde 4% (VWR, 9713.9010), embedded in paraffin, and sectioned in 5µm thick transverse or longitudinal slices, which were stained using H&E, Masson's trichrome (MT), Sirius red (SR), and Alcian blue (AB), following the manufacturers' protocols. In order to examine DNA, sections were also stained with 2'-(4-ethoxyphenyl)-5-(4-methyl-1-piperazinyl)-2,5'-bi-1H-benzimidazole trihydrochloride (Hoechst, 1:5,000; Life Technologies, H3570). All sections were captured with a slide scanner (SCN400, Leica Microsystems, Wetzlar, Germany) or visualized using a fluorescence microscope (AxioImager Z1, Zeiss, Oberkochen, Germany) at a 40-fold magnification. The images were then annotated with ImageScope software (Aperio ImageScope, v12.4.3.5008, Leica Biosystems). This latter software was also used to measure the tissue thickness of the MT-stained sections. The HP cambial layer and HFL transverse layer were both the thinnest layers, termed Layer 1 (L1). The HP fibrous layer and HFL longitudinal layer were both the thickest layers, termed Layer 2 (L2). The percentage of the thinnest layer, which is useful to bear MSCs, was calculated for each sample, as follows:

$$Layer\ percentage\ (\%) = \frac{L1\ thickness}{Total\ thickness}\ x\ 100$$

B. 3. Immunohistochemistry analysis

Paraffin-embedded slices were handled for IHC detection of collagen I, MHC-1, and elastin. Endogenous peroxidase was inactivated with 3% H_2O_2 in methanol. Antigen retrieval was achieved by a combination of tris-ethylenediaminetetraacetic acid (EDTA) buffer (Tris, Merck, 1.08387.250; EDTA, Sigma, E5134) for 5min and then proteinase K (1:1,000, Roche, 03115828001) for 20min, both at 37°C in the incubator. Unspecific antigens were blocked at room temperature (RT) by a solution of 5% bovine serum albumin (BSA, Merck, 12659-500 GM) in 0.05% tris-buffered saline (TBS)/Triton (Tris, Merck, 1.08387.250;

Triton, VWR, M143) over 1h. The sections were incubated with rabbit primary antibodies, namely anti-collagen I (1:1,000, Abcam, ab34710), anti-MHC-1 (1:150, Abcam, ab134189), and anti-elastin (1:100, Novus biotechne, NB100-2076) at 4°C overnight, followed by peroxidase conjugated antirabbit secondary antibody (Envision, Dako, K4003) at 4°C for 1h. The detection was achieved with 3,3'-diaminobenzidine (DAB) peroxidase substrate (Dako, K3468) at RT for 5min. Haematoxylin was used as counterstaining. After mounting, the slices were scanned using the Leica slide scanner. The MHC-1 was quantified by QuPath Software (v0.3.0., University of Edinburgh)[252].

Fluorescent multiplex IHC (indirect immunofluorescence horseradish peroxidase (HRP)-conjugated secondary antibody) with tyramide amplification signal was performed on paraffin-embedded slices in order to detect CD73, CD90, and CD105, which are three specific surface markers of MSCs, according to the International Society for Cellular Therapy[200,253]. The same initial steps as conventional IHC were executed and then followed by antigen retrieval, realized by citrate buffer (citric acid, Merck 1.00244.0500; Na3 citrate, Alfa Aesar A12274-500 gr) at pH 5.7 in the microwave. Unspecific antigens were blocked by a solution of 5% BSA (Karl Roth, 3854.3, Albumin fraction V) in TBS/Tween 20 (VWR, 663684B) at RT during 30min. The slices were incubated with first mouse primary monoclonal antibody for CD105/Endoglin (1:200, Cell Signaling, #14606) at 4°C overnight. Sections were then washed using TBS/Tween three times for 3min. The peroxidase conjugated anti-mouse secondary antibody (Envision, Dako, K4001) was then incubated at RT for 45min. Signal was amplified by AlexaFluor Tyramide 647 (1:200, InvitroGen, B40958) at RT for 10min in borate solution (boric acid, Sigma B6768-500gr; sodium chloride (NaCl), VWR, 27810.295-1kg; H_2O_2 0.003%). After three new washes, the steps from antigen retrieval were repeated using successively rabbit primary monoclonal antibodies for NT5E/CD73 (1:300, Cell Signaling, #13160) and for Thy1/CD90 (1:100, Cell Signaling, #13801) and tyramides as amplifiers (AlexFluor Tyramide 555 (1:200, InvitroGen, B40955) and 488 (1:200, InvitroGen, B40953), respectively). Hoechst was used for counterstaining (1:1,000, Sigma, 14533-100mg). After mounting, the slices were scanned using the fluorescent slide scanner Axioscan. A negative control, without the primary antibody, was always included to check for absent detection for both standard IHC and multiplex IHC.

B. 4. Scanning electron microscopy

The ultrastructure of the ECM was assessed superficially by means of SEM. One sample from each of four donors and for each tissue was cut into 5mm² pieces and mounted on synthetic corks. These samples were fixed by immersion in 3% glutaraldehyde buffered with 0.1M phosphate buffer at RT for 4h. They were then rinsed three times using 0.1M phosphate buffer during 10min. For the first dehydration process, the specimens were dehydrated in a series of graded ethanol dilutions (30%, 50%, 70%, 80%, 90%, 95%, and 3 × 100%) and then dried in specimen bottles on a slow shaking plate with an equilibration step of 15min each. After the first dehydration process, the samples were dried using Critical Point Dryer technique (CPD) (Balzers, CPD020). The samples were then mounted on stubs and coated with a 10nm gold layer (Cressington sputter, 208 HR) to create a thin conductive layer allowing for minimizing degradation and drifting due to thermal expansion. At least 12 pictures of SEM images for each tissue and donor were produced using a field emission SEM (JSM-7600F, Jeol Ltd. Akishima, Tokyo, Japan) and then analysed.

B. 5. Cellular & extracellular matrix components quantification

DNA, collagen, elastin, and GAG contents were quantified to compare both tissue compositions. For each dosage, three random biopsies of each tissue from each donor (N=4) were performed, resulting in 24 analysed biopsies of 25, 20, 25, and 10mg for DNA, collagen, GAGs, and elastin quantification. All biopsies were freeze-dried and dry-weighted. DNA was extracted using the DNeasy® Blood & Tissue kit (Qiagen, Italy), which included an overnight tissue lysis by proteinase K in a water-bath at 56°C and successive passages through DNeasy columns with different buffers, and was dosed using the Quant-iT PicoGreen DNA assay kit (ThermoFisher Scientific). After adding the Quant-iT PicoGreen reagent to the sample and following incubation for 5min, the fluorescence was read using the SpectraMax (SofMax Pro 6 software) (excitation: 480nm/emission: 520nm). The collagen content was extracted and measured by means of the Quickzyme Total Collagen Assay (Quickzyme, Leiden, Netherlands). The extraction consisted of an overnight tissue lysis by hydrochloric acid (HCl) 6M in a water-bath at 95°C, while the dosage ended by an absorbance reading at 570nm of wavelength. The Blyscan Sulfated-GAG assay kit (Biocolor LTD., Carrickfergus, Northern Ireland) was used

to quantify the GAG content of ECM, and it also consisted of an extraction and dosage step using dye and dissociation reagents, while the final absorbance was read at 630nm of wavelength. The elastin dosage was achieved by means of the Fast Elastin assay kit (Biocolor LTD., Carrickfergus, Northern Ireland). This quantification was based on two extraction repetition, which was followed by the dosage phase with successive additions and incubations of precipitating, dye and dye dissociation reagents (absorbance wavelength: 510nm). All kits were employed in line with each detailed manufacturer's protocol. Plates were filled in duplicates and read three times. Taking mean of the three readings was followed by taking the mean of the duplicates before performing the final average quantification of the three biopsies so as to increase the precision. The final DNA concentration was expressed in ng/mg of dry weight, while ECM proteins concentration was expressed in µg/mg of dry weight.

B. 6. Immunoblot

BMPs are GFs that likely exert a relevant osteogenic function; they were evaluated using immunoblot in order to evaluate intrinsic osteogenic potential of both tissues. For this purpose, a 50mg biopsy of each tissue (N=3) was chopped, lysed with a radioimmunoprecipitation assay (RIPA) buffer containing protease inhibitor cocktail and Pho-Stop before being melded using the Precellys Homogenizer (Bertin Technologies SAS, France) by consecutive cycles at 7200rpm (8114xg). The supernatant was collected, and its protein concentration was determined using the PierceTM BCA Protein assay kit (ThermoFisher, 23227) following the manufacturer's protocol. Thereafter, the RayBio C-Series – Human BMP related array 2 (RayBiotech, AAH-BMP-2–8) quantified BMP-11, -2, -4, -5, -6, -7, -8, and -9. To this end, 100µg of proteins were incubated in pre-blocked membrane (Blocking Buffer for 30min at RT) on a shaker plate at RT for 2.5h, followed by a succession of washes and incubations of biotinylated antibody cocktail, as well as diluted HRP-Streptavidin according to the manufacturer's protocol. Different baths of detection buffers preceded the revelation on chromatographic films by chemiluminescence. Using Fiji software (ImageJ-win64) and based on previously described methods[254], each BMP densitometry spot was subtracted from the background density and normalized to positive control and to the ratio of the total amount of proteins to the weight of each respective sample (expressed in µg of

proteins/mg of tissue). Final data were expressed as the mean density of two detection spots for each BMP followed by the mean of all donors.

B. 7. Mechanical tests

Tensile tests were applied to underscore differences in mechanical properties. HFL (N=11) were cut into five strips of 2cm width and 5cm length (total of analysed samples=55), while HP (N=6) were cut into one strip of 1cm width and 5cm length (total of analysed samples=6). Specimens were stored frozen and then thawed at RT 2h before testing. To carry out uniaxial tensile tests, samples were placed between two custom-made jaws in order to prevent slipping. The specimen length was measured between the jaws, with its width and thickness measured in its centre using a calliper.

Traction tests were performed with two different uniaxial elongation machines, consisting of a 34SC-5 single column (Instron Corp., Illinois Tool Works Inc., Glenview, IL, United States) with a 5kN load cell (2519-5kN series, Instron Corp., Illinois Tool Works Inc., Glenview, IL, United States) for HFL and a 3342 single column (Instron Corp., Illinois Tool Works Inc., Glenview, IL, United States) with a 100N load cell (2519-100N series, Instron Corp., Illinois Tool Works Inc., Glenview, IL, United States) for HP. Four successive tests were conducted. Before testing, a preconditioning process consisting of 10 consecutive cycles at a speed of 0.25mm/s to a final deformation of 7% was applied. Immediately thereafter, two tensile tests were conducted at two different speeds (S1=0.25mm/s and S2=0.5mm/s) up a strain of 10%. A final traction procedure was completed at 0.25mm/s until complete rupture of the sample, which was defined as the drop of at least 40% of the force. The force and displacement data were collected during these tests and transformed into stress and strain values according to the following formulas:

$$Stress \equiv \sigma = \frac{F}{S}$$

where σ is the axial stress in Pascal (Pa), F the force in Newton (N) registered by the force cell, and S the section of the specimen (m^2).

$$Strain \equiv \varepsilon = \frac{\Delta l}{l}$$

where ε is the strain (%), Δl the distance variation measured during the tensile test, and l the initial distance between the two jaws.

The stress-strain curves are divided into two regions, of which one displayed a low slope at a small deformation ($\varepsilon \lesssim 0.5$) and the other one a large slope at high deformation. The slope of the curve's steep linear part was considered the apparent elastic modulus of the sample. These moduli were extracted from each stress-strain curve for each speed. The rupture stress corresponded to the maximum value observed during the last traction test (rupture test).

B. 8. Statistical analysis

Statistical comparison between both tissues was carried out using GraphPad Prism 8.0.1 (GraphPad Software, San Diego, CA, United States) and SPSS software (V.27, IBM SPSS, Inc., Chicago, IL, United States). The normality of continuous variables was checked using a Shapiro-Wilk test and QQ plots. All variables following a Gaussian distribution were compared by means of a parametric unpaired T-test for the thickness, which was also applied for proteins or DNA comparisons. In other cases, non-parametric tests (Mann-Whitney) were used to compare BMP factors between HP and HFL. All tests were two-tailed. The difference was always considered statistically significant at a p-value of 0.05. The data shown in the graphics are presented as the mean and standard error of the mean (SEM).

C. Results

C. 1. Macro- & micro-structure

At first glance, the macrostructure of HP and HFL (Fig. 29 – A) appeared to be quite different. Indeed, HP harvesting was more difficult and left holes in the tissular sheet, or it required preservation of muscle insertion, while HFL was taken in a single wide and long sheet with fewer holes created by the perforator vessels. However, the microstructure displayed some similarities under SEM analysis (Fig. 29 – B). Both tissues were made of aligned fibres with a main orientation along the femoral axis. At a higher magnification, the density and organization of HFL fibres were more relevant. Density was characterized by a numerously higher

compaction of fibres in a same area, while organization is about the higher fibres' parallelism.

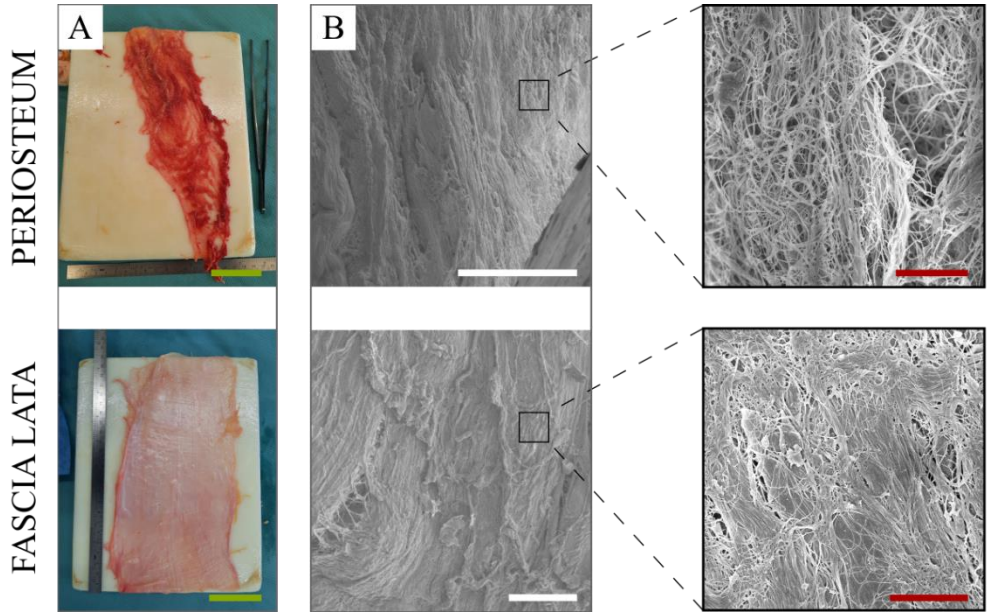

Figure 29. Macrostructure (A) and microstructure (B) of the periosteum (top) and fascia lata (bottom) (including zoom in), visualized under electron microscopy. Green scale bars: 5cm. White scale bars: 100µm. Red scale bars: 5µm.

Histological analysis highlighted the fibrous composition of both tissues, along with their bi-layered structure (Fig. 30). Both tissues were built by two successive and well-defined layers. A dense connective tissue was present in the fibrous periosteal layer, with a loose connective tissue in the cambial one. HP was significantly thinner (258 ± 27µm) than HFL (1,124 ± 108µm). Similarly, HP cambial (85 ± 7µm) and fibrous layers (173 ± 23µm) were significantly thinner than HFL transverse (255 ± 29µm) and longitudinal layers (869 ± 86µm), respectively. However, the ratio of the thickness of the cambial layer to HP (34 ± 2%) was significantly greater than the ratio of the thickness of the transverse layer to the HFL (23 ± 2%).

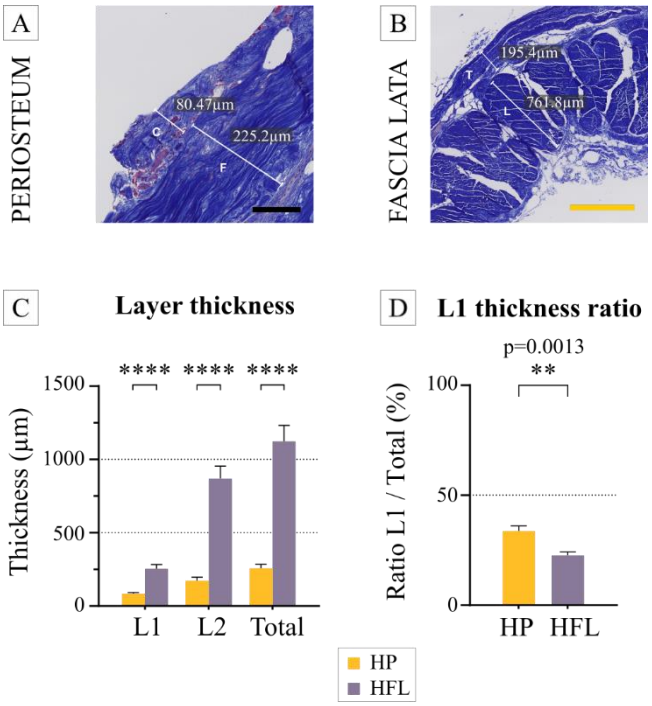

*Figure 30. Example of a thickness measurement of the periosteum (A) and fascia lata (B). The mean thickness of both tissues (N=4 donors) was compared, along with their respective layers (C), as well as the ratio of the thinnest layer to total thickness (N=4 donors) (D). C: cambial layer, F: fibrous layer, L: longitudinal layer, T: transverse layer, HP: human periosteum, HFL: human fascia lata, L1: cambial or transverse layer, L2: fibrous or longitudinal layer. Black scale bar: 100µm. Yellow scale bar: 500µm. ** p ≤ 0.01, **** p ≤ 0.0001.*

C. 2. Extracellular matrix compartment

The molecular components of ECM were identical for both tissues, containing Type I collagen fibres, GAGs, and elastin.

Collagen content

MT staining (Fig. 31 – A) revealed that wavy collagen fibres were well organized parallel to the bone surface for HP, and in oriented fascicles along the limb long axis for HFL. In addition, HFL contained a second layer made of transverse fibres, perpendicular to the main femoral axis, as seen on several slide orientations (transverse sections on Figure 31 – A–C showing a transverse cut into longitudinal

fibres; the longitudinal section is shown in Figure 32 – A, with a parallel view of longitudinal fibres).

MT staining discriminated connective fibres from muscle while SR (Fig. 31 – B) stained unspecific collagen fibres in red. IHC highlighted specifically Type I collagen fibres, which were very abundant in both tissues (Fig. 31 – C). In SEM (Fig. 31 – D) at a higher magnification, HFL fibres appeared more compact and straighter than HP ones. In a complementary way, collagen quantification revealed a significantly higher amount of collagen in HFL than HP matrix (Fig. 31 – E).

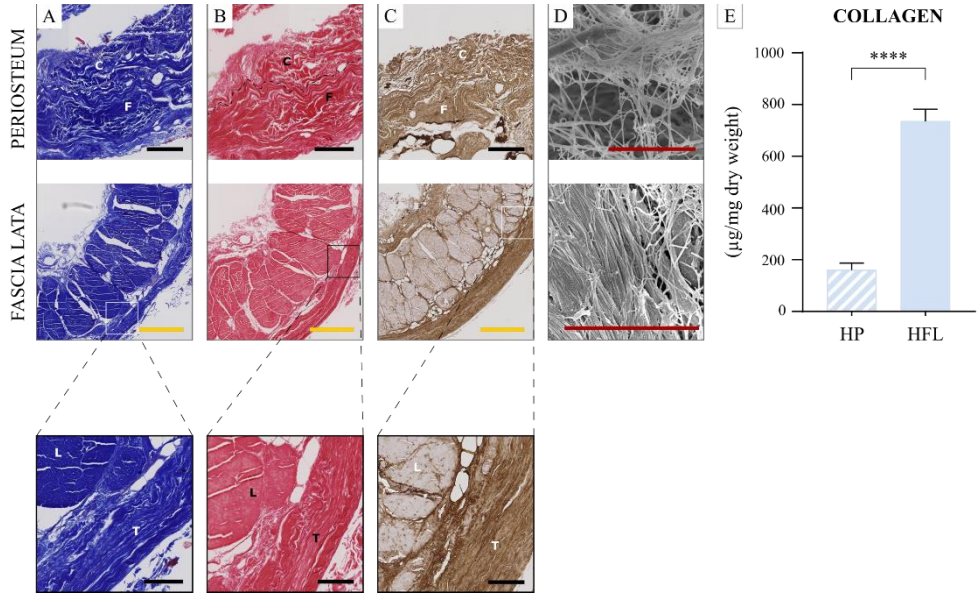

*Figure 31. Comparison of HP (top) and HFL (bottom including zoom in) by Masson's trichrome staining (A), Sirius red staining (B), immunohistochemistry for Type I collagen (C), electron microscopy (D) and collagen quantification (N=4 donors × three samples from each donor leading to n=12 specimens analysed for each tissue) (E). C: cambial layer, F: fibrous layer, L: longitudinal layer, T: transverse layer, HP: human periosteum, HFL: human fascia lata. Black scale bars: 100µm. Yellow scale bars: 500µm. Red scale bars: 5µm. **** p<0.0001.*

Glycosaminoglycan content

GAGs, stained in blue with AB, was similarly present in both tissue ECM (Fig. 32).

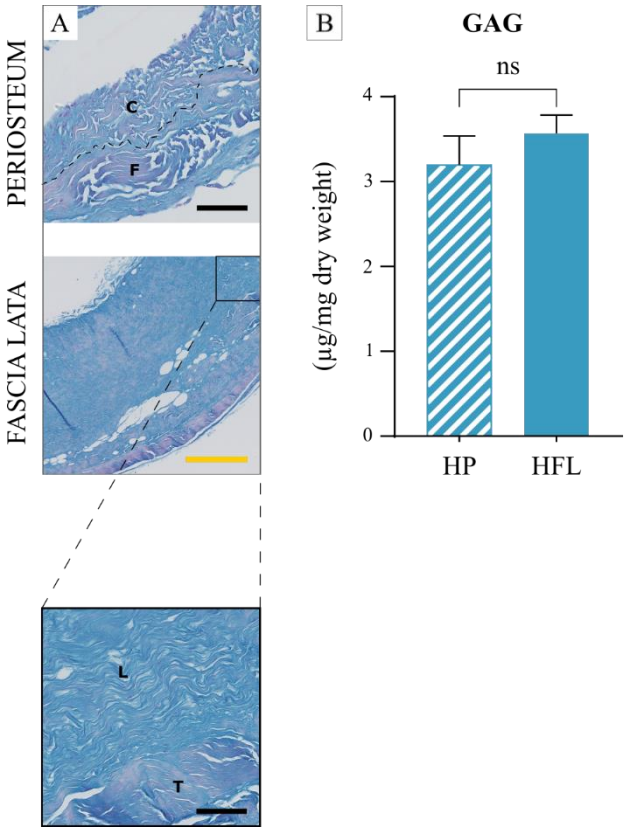

Figure 32. Comparison of HP and HFL (including zoom in) with alcian blue staining (A) and glycosaminoglycan (GAG) quantification (N=4 donors x three samples from each donor leading to n=12 specimens analysed for each tissue) (B). C: cambial layer, F: fibrous layer, L: longitudinal layer, T: transverse layer, HP: human periosteum, HFL: human fascia lata. Black scale bars: 100µm. Yellow scale bar: 500µm, ns: non-significant.

Elastin content

IHC highlighted the presence of elastin in both tissues (Fig. 33 – A). No statistical difference was recorded between the tissues in either qualitative or quantitative absolute analyses (Fig. 33 – B). Nevertheless, the elastic potential of HP was higher than that of the tendon sheet or fascia, due to its relative higher content (Fig. 37).

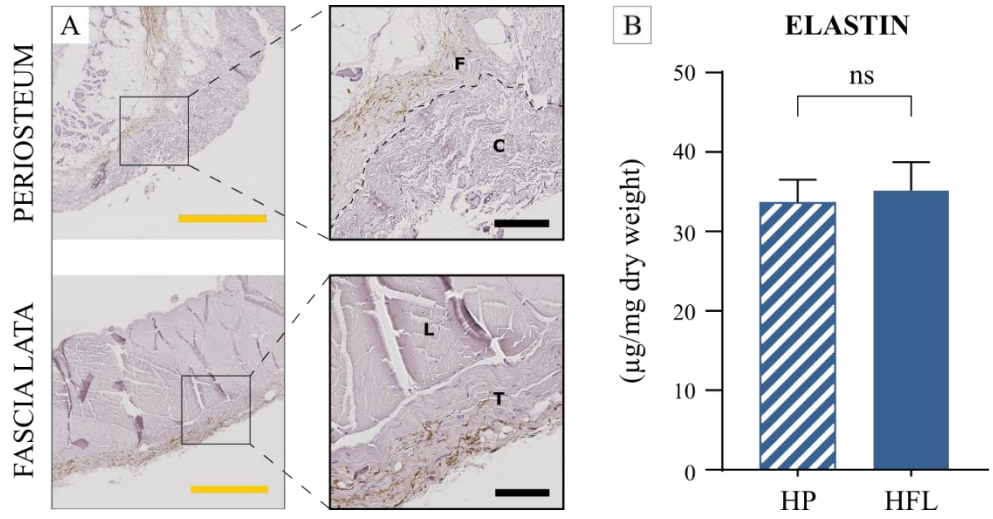

Figure 33. Comparison of the HP and HFL by immunohistochemistry for elastin (A) (including zoom in) and elastin quantification (N=4 donors x three samples from each donor leading to n=12 specimens analysed for each tissue) (B). C: cambial layer, F: fibrous layer, L: longitudinal layer, T: transverse layer, HP: human periosteum, HFL: human fascia lata. Black scale bars: 100µm. Yellow scale bars: 500µm, ns: non-significant.

C. 3. Cellular compartment

The cellular compartment was analysed in three ways, *i.e.*, by assessing DNA content, which approximated the number of nuclei; by multiplex IHC for CD73, CD90, and CD105, which highlighted MSCs; and by MHC-1 content in the cytoplasmic membrane, which largely reflected tissue immunogenicity.

DNA content & mesenchymal stem cells

Under H&E staining (Fig. 34 – A), the HP cambial layer likely contained more numerous cells than the fibrous layer, while HFL fibroblasts were more homogeneously spread over the entire tissue, interspersed into the undulated collagen fibres. Hoechst staining (Fig. 34 – B) highlighted cell nuclei that were fairly distributed in HFL, although they were slightly more numerous in the transverse layer than in HP, which contained a much more condensed cellular layer of large cells. Indeed, cambial periosteal cells appeared larger than fibroblasts in SEM analysis (Fig. 34 – C). The DNA content was significantly higher in HP than HFL (Fig. 34 – D).

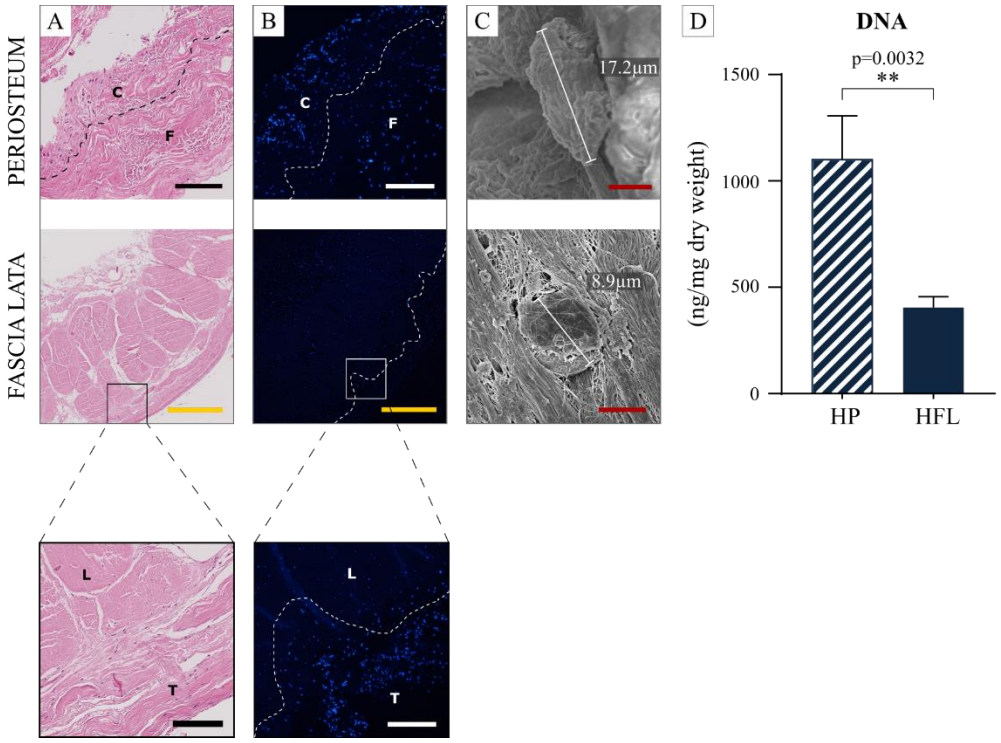

*Figure 34. Comparison of the HP and HFL by haematoxylin and eosin staining (A), by fluorescent cytochemistry (Hoechst) (B) (including zoom in), by electron microscopy (C) as well as DNA quantification (N=4 donors x three samples from each donor leading to n=12 specimens analysed for each tissue) (D). C: cambial layer, F: fibrous layer, L: longitudinal layer, T: transverse layer, HP: human periosteum, HFL: human fascia lata. White/black scale bars: 100µm. Yellow scale bars: 500µm. Red scale bars: 5µm. ** p ≤ 0.01.*

Multiplex IHC with tyramide amplification signal showed that only the cambial layer of HP revealed areas of concomitant CD73, CD90, and CD105 signal (Fig. 35). The fibrous layer as well as both HFL layers never exhibited an association of all three signals. Only one or a maximum of two simultaneous signals were found.

Immunological comparison

Similar to DNA analysis, the specific IHC for MHC-1 (Fig. 36 – A), which constitutes an immune cell surface antigen, revealed that the HP cambial layer is the most immunogenic tissue. The quantification also attested that HP displayed a statistically higher immunogenic potential than HFL (Figure 36 – B).

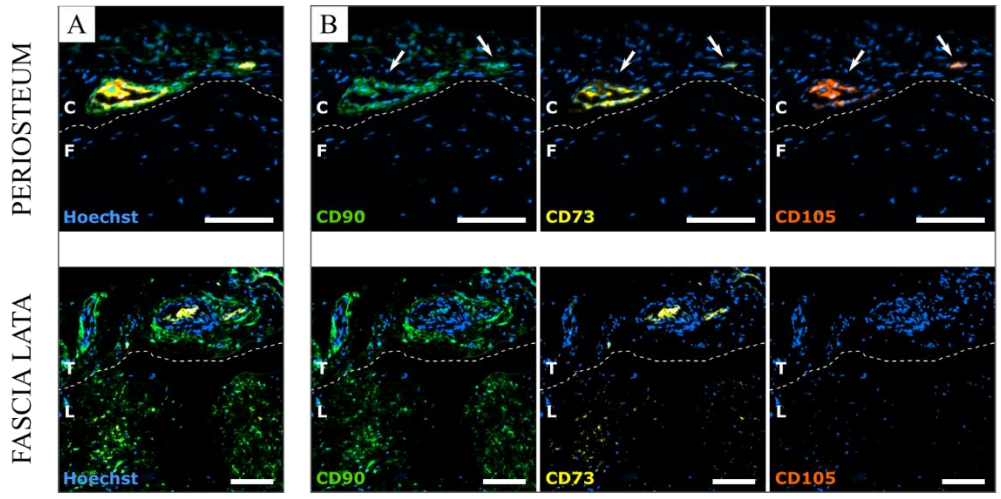

Figure 35. Comparison of the HP and HFL by multiplex immunohistochemistry with tyramide signal amplification for CD90, CD73 and CD105 with merged signals (A) or separate signals (B). Blue: Hoechst, Green: CD90, Yellow: CD73, Red: CD105. White arrows show the simultaneous presence of the three signals on the same location. C: cambial layer, F: fibrous layer, L: longitudinal layer, T: transverse layer. White scale bars: 100µm.

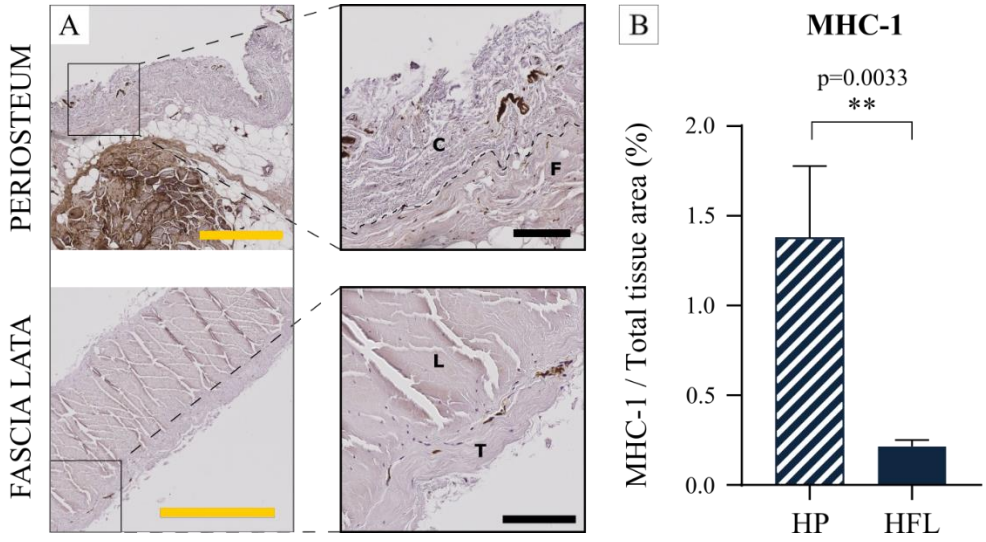

*Figure 36. Comparison of the HP (top) and HFL (bottom) by immunohistochemistry for MHC-1 (A) (including zoom in) and MHC-1 quantification (N=4 donors x three samples from each donor leading to n=12 specimens analysed for each tissue) (B). C: cambial layer, F: fibrous layer, L: longitudinal layer, T: transverse layer, HP: human periosteum, HFL: human fascia lata. Black scale bars: 100µm. Yellow scale bars: 500µm. ** $p \leq 0.01$.*

C. 4. Total tissue composition

Both membranes were mainly composed of Type I collagen fibres and, to a lesser extent, of elastin (Fig. 37). The amounts of GAGs and DNA were very low in both tissues. The relevance of the components differed relative to the point of view. Indeed, if absolute weight is considered, HP and HFL seem to be different only in their collagen content, but if the relative weight is analysed, the relative importance of each compartment revealed a higher elastin proportion at the expense of collagen for the HP.

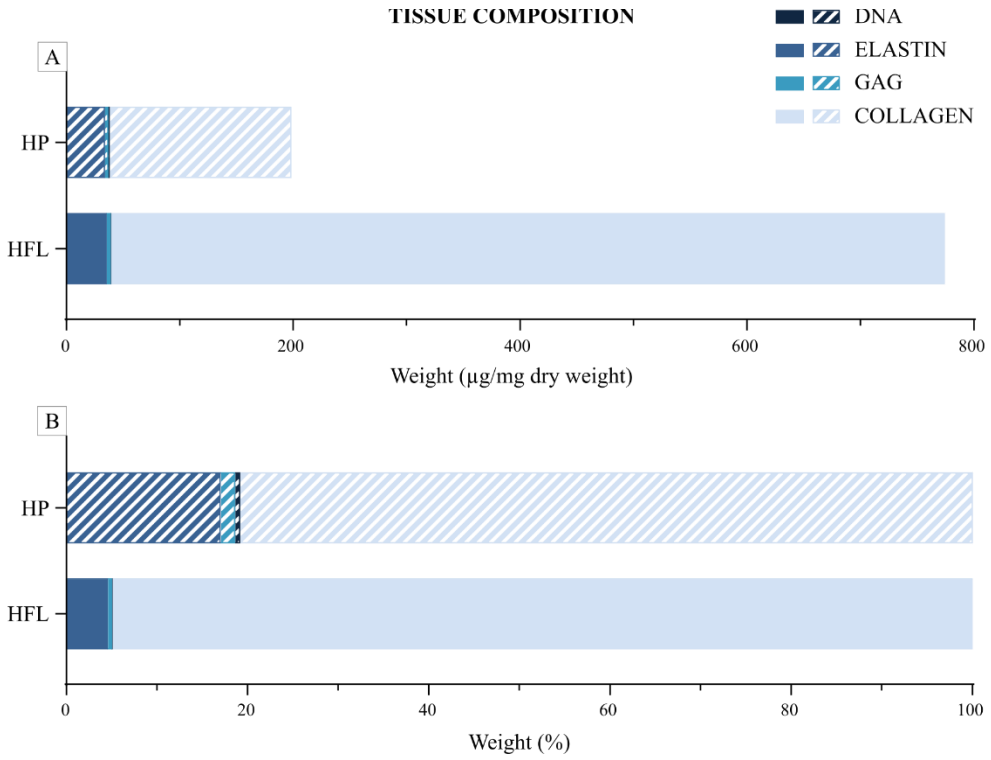

Figure 37. Tissue composition of periosteum and fascia lata regarding collagen, elastin, GAG and DNA depending on absolute average weight (µg/mg dry weight) (A) or relative average weight (%) (B). HP: human periosteum, HFL: human fascia lata, GAG: glycosaminoglycan.

The main specific quantification data are presented in Table 10 for the ECM compartment as well as for the cellular compartment.

Table 10. Comparison of main quantification data between both tissues (N=4 donors x three samples from each donor leading to n=12 specimens analysed for each quantification and each tissue).

	ECM compartment			Cellular compartment	
	Collagen *(µg/mg dry weight)*	***GAGs*** *(µg/mg dry weight)*	***Elastin*** *(µg/mg dry weight)*	***DNA*** *(ng/mg dry weight)*	***MHC-1*** *(%)*
HP					
Mean (± SEM)	160.2 (± 27.1)	3.2 (± 0.3)	33.7 (± 2.9)	1102.2 (± 204.7)	2.2 (± 0.5)
HFL					
Mean (± SEM)	735 (± 47.1)	3.6 (± 0.2)	35.1 (± 3.6)	404.8 (± 50.5)	0.2 (± 0.03)
Comparison between tissues					
p-value	< 0.0001	0.365	0.745	0.0032	0.0006

HP: Human periosteum, HFL: Human fascia lata, SEM: Standard error of the mean, MHC-1: Major histocompatibility complex of type 1, GAGs: Glycosaminoglycans.

C. 5. Intrinsic osteogenic properties

Both tissues contained different BMP quantities, with BMP-2 and -7 being the most abundant, and BMP-8 and -9 the least abundant (Fig. 38). Comparison of HP with HFL showed a significantly lower content of BMP-11 (p=0.002), BMP-4 (p=0.009), BMP-6 (p=0.002), BMP-8 (p=0.026), and BMP-9 (p=0.002), with no significant difference demonstrated for BMP-5 (p=0.052). The amounts of BMP-2 and -7, both being primarily implicated in bone osteogenesis and bone repair, did not significantly differ between HFL and HP (p=0.132, p=0.699, respectively). The average BMP-2 content in HFL was about 78% of that observed in HP, with BMP-7 content in HFL reaching 95% of that registered in HP.

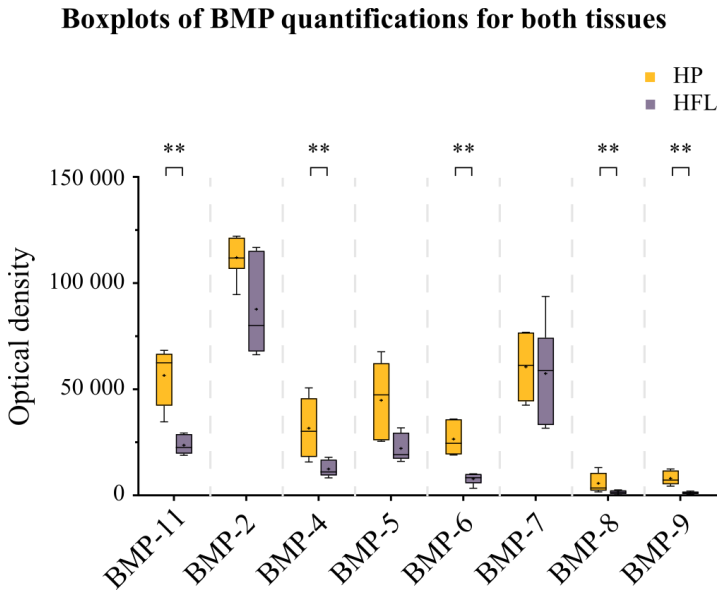

*Figure 38. Intrinsic osteogenic properties of both tissues (HP and HFL) illustrating by Boxplots of BMP quantifications (N=3 donors x two detecting plots per donor leading to n=6 optical densities analysed for each tissue). HP: human periosteum, HFL: human fascia lata, BMP: bone morphogenetic protein. +: mean, ** p<0.01.*

C. 6. Mechanical properties

HFL and HP exhibit similar mechanical behaviours, as is the case for all soft tissues. Mechanically, HFL supports a significantly higher tension than HP, as reflected by their two distinct mean stress/strain curves, shown in graphs with very different scales on the y-axis in Figure 39.

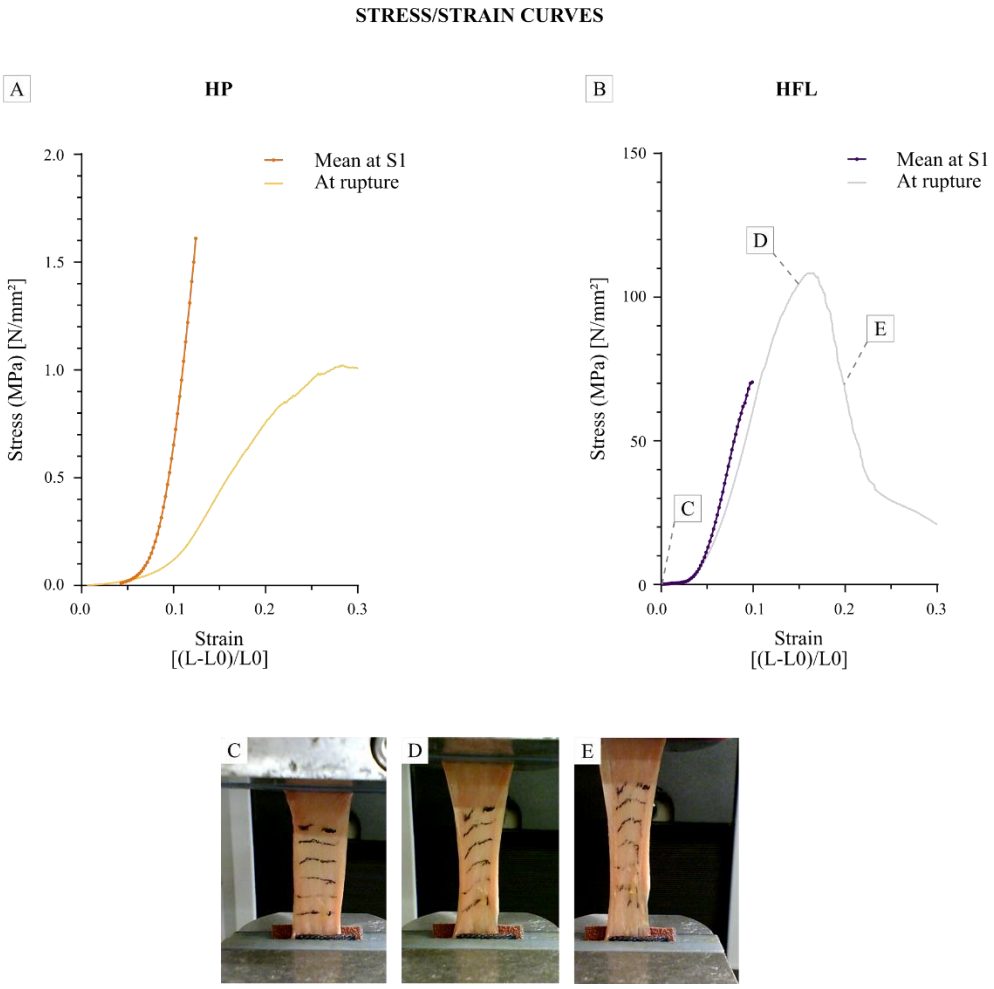

Figure 39. Stress/strain curves for periosteum (N=6 donors x one strip from each donor leading to n=6 specimens analysed for each speed) (A) compared to the fascia lata ones (N=11 donors x five strips from each donor leading to n=55 specimens analysed for each speed) (B). Graphs illustrate each average curve at S1 of all donors and provide an example of stress/strain curve of one donor for each tissue until the rupture. HP: human periosteum, HFL: human fascia lata, L: final length, L0: initial length. Fascia lata deformation during a tensile test from the beginning (C), at 15% of deformation (D), and until the rupture (E), which is also registered on the fascia lata stress/strain curve.

The mean rupture stress was much lower for HP (9.8MPa) than HFL (96.8MPa). This difference was also observed in the apparent elastic modulus, *i.e.*, with this modulus being at S1 was 97.8MPa for HP versus 1,533.6MPa for HFL. The results of mechanical analyses are presented in Table 11.

Table 11. Mechanical outcomes after tensile tests.

	Apparent elastic modulus		Rupture stress
	S1 (MPa)	*S2* (MPa)	(MPa)
HP			
Mean (± SEM)	97.8 (± 25.4)	99.5 (± 27.0)	9.8 (± 1.6)
HFL			
Mean (± SEM)	1533.6 (± 50.4)	1545 (± 55.0)	96.8 (± 3.2)

S1: Speed 1 (0.25mm/s), S2: Speed 2 (0.5mm/s), HFL: Human fascia lata (N=11 donors x five strips from each donor leading to n=55 specimens analysed for each speed), HP: Human periosteum (N=6 donors x 1 strip from each donor leading to n=6 specimens analysed for each speed), SEM: Standard error of the mean.

D. Discussion

Both HP and HFL are fibrous bi-layered membranes, mainly composed of Type I collagen fibres, as previously described in the literature. The originality of this paper lies in the comparison of the membranes, with the prospect to replace one for another. Based on this comparison, we have highlighted that stronger HFL mechanical properties were associated with a higher collagen content, and that the immunogenic HP properties were aligned with a higher number of cells and MHC-1 content.

Periosteum from different sources, *i.e.*, the tibia, femur, rib, and calvarium, were previously compared to produce decellularized scaffolds, demonstrating somewhat different functional properties and architecture[25,255,256]. By comparison, Masquelet's induced membrane was shown to organize itself into an inner epithelial-like layer close to the cement and an outer layer of parallel collagen fibres with fibroblasts and inflammatory cells (giant cells and macrophages)[14,99,107]. While this is very helpful for CSBD treatment, this induced membrane differed from HP in terms of its composition, thickness, and mechanical isotropy[99].

From Badylak's review concerning several biological ECM properties[175] pertaining to the variability in periosteal properties and functions, the relative efficacy of quite lowly approaches, and the approximative knowledge of engineered scaffold effectiveness, encouraged us, along with authors like Dalisson et al. (2021), to

question the legitimacy of the requirement to reproduce a biomaterial mimicking a composition or structure identically[14,245]. These authors challenged the utility of a sophisticated construct, given the ability of the body itself to heal bone defects with only a few exogenous factors[14]. Indeed, cost effectiveness is currently considered by our healthcare systems to be a real actual point of interest. This has to be kept in mind. For this purpose, HFL could represent a new means to replace HP, which is still poorly available and displays a huge interpersonal variability and immunogenicity, while being burdened with a high donor-site morbidity in relation to its extensive, cautious, and time-consuming surgical approach.

HP and HFL were shown to exhibit morphological and structural differences despite their identical ECM components, with some advantages that deserve to be discussed.

While the difference in thickness between the tissues was expected, it can now be further discussed. Indeed, HP thickness has been shown to decrease with age, with a thicker cambial layer during childhood supporting bone growth by supplying a considerable amount of MSCs[25]. In our study, cadaveric donors were aged more than 85 years, and their periosteum could thus be considered to be atrophic, while HFL thickness was deemed to be quite more stable along the life course. Comparing HFL and HP thickness of younger subjects could highlight their possible similarity with those of children. In the current analyses, the lateral part of HFL, called the iliotibial tract (ITT), was harvested, being the thickest part of the whole tight fascia lata. Pirri et al. (2021) measured the thickness of ITT at average 1,112 ± 237.9µm, quite similar to the measurement of 1,124 ± 108µm obtained in our study. These authors also proved that its thickness was likely dependent on the harvested HFL localization. For example, the thickness was found higher on proximal or distal sides. Also, HFL sometimes presents an additional 3rd layer, which is either longitudinal or transverse[227,257]. In this study, only two main layers were considered given that the 3rd one was too random. Nevertheless, a more precise histo-anatomical study could still provide us with more new information depending on the harvesting location, as well as on the antero/posterior part or medial/lateral side, especially concerning the ITT. Moreover, its organization in a bi-layered structure of collagen fascicles oriented along two main axes appeared to be attractive, given that the longitudinal thick layer could offer some architecture and manoeuvrability to the scaffold, while the transverse thin one

could accommodate a cell seeding and be applied in close contact with a bone structural replacement material. The presence of a membrane around a new bone component (massive allograft, cancellous or morselized bone graft, or other approaches) appeared to be likely relevant so as to contain and guide osteogenesis, as well as to prevent ectopic ossification and soft tissue interposition[107,249].

From this last point of view, HFL did not contain the same cellular number of HP, being rich in PMSCs, with these latter confined in its cambial layer. MSCs enabling the creation of a bone healing therapeutic solution were found to be absent from HFL. However, a recent study showed that some fibroblasts lying on ITT exhibited a weak yet present osteogenic differentiation capacity[258], suggesting that this matrix might preserve the differentiation capacity of stem or progenitor cells.

Regarding GFs, HFL was shown to contain similar amount of BMP-2 and -7. Although most other BMPs were found to be significantly less present in HFL than HP, these two last ones were known to be the most important factors for osteoinduction[33,259,260]. Non-recombinant or recombinant BMP-2 and -7, which were both approved by the FDA for some human uses, such as in spinal fusion and tibial pseudarthrosis, are currently employed in off-label uses, including CSBDs[260–262]. They both play a key role in osteoblast differentiation and initiating facture healing[33,259]. The natural presence of those BMPs in HFL, along with their natural biological density, could make this membrane a good niche to welcome MSCs and initiate their osteo-differentiation, while avoiding complications of external BMPs[260,263]. Nevertheless, this observation has been deemed unable to make HFL an osteogenic membrane *per se*. The osteogenic capacity of HP still needs to be explored in an attempt to transfer it to the new scaffold.

The immunological response associated with cell or tissue transplantation has also attracted great interest over the last decade, with numerous authors considering periosteum and decellularization process as means to prevent rejection[246,247]. The MHC-1 content was found to be significantly lower in HFL than HP, thereby conferring it a lower risk of rejection after being allotransplanted. It must, however, be noted that there are still minor histocompatibility complexes, as well. Nevertheless, decreased immunogenicity was shown to impact the inflammatory

and rejection response, while this influence on fracture and bone defect healing is still being investigated in tissue engineering[150,264,265].

Considering the mechanical behaviour of both tissues, notable differences were found. These outcomes were consistent with those reported in the literature[266–269], despite relevant disparities in results across several studies[257,270,271]. These were mainly accounted for by methodological differences in measuring the mechanical response. Given that the protocol applied was the same for HFL and HP, we were able to compare apparent elastic moduli and rupture stresses. They were both more than 10 times higher for HFL than for HP. The stronger stretching resistance and stiffness of HFL could be specifically explained by its significantly higher quantity of collagen fibres. Both membranes were stretch-tested longitudinally, *i.e.*, parallel to the main fibre direction, following the long bone axis. This choice was made because most constraints were exerted in this orientation and in the direction of bone growth in length. In the literature, the anisotropic properties of both membranes have been well described[257,272]. Nevertheless, in fracture healing, bone formation has been shown to mainly progress longitudinally from the fractured ends, leading to stronger constraints in the long bone axis. Their anisotropy was explained as based on collagen fibre orientation, thus conferring the tissue stiffness[257,273]. The elasticity of a tissue could also influence its anisotropy, and it has recently been revealed that deep HFL does not contain many elastic fibres[274]. In our study as well, differences in relative elastin content could also be a clue for different anisotropy between HFL and HP. These mechanical data could be consolidated by increasing the number of HP samples (6), which were lower than that of HFL samples (55). This discrepancy was due to the specific difficulty inherent to harvesting HP.

This study performed a cross-sectional analysis through fundamental histology, macro-/microstructure, and mechanical properties of a native tissue like HP, with the aim to explore its potential replacement by another like HFL. In the perspective of tissue engineering, the decellularization process could avoid immunological rejection after allotransplantation, yet it might decrease the acute inflammatory response that is required to initiate the consolidation. Native HFL were shown to contain fewer immunological components than HP, which raises the question of the decellularization stage requirement. The five Diamond concept angles should ideally be present. Indeed, the seeding of MSCs would be a crucial step to render

the membrane osteogenic. The vascularization, which is a critical point well-highlighted by the Masquelet's membrane, must now be further explored, given the huge limitations of tissue engineering concepts.

E. Conclusion

In conclusion, while HFL actually differed from HP in that its large surface tendinous sheet was mainly composed of Type I collagen, it was easy to harvest and be shapeable on demand in favour of a personalized medicine, having already been collected and processed by tissue banks with a broad range of validated clinical applications. Nevertheless, it remains unexplored as a substitute for bone reconstruction.

HFL could be suitable to replace the HP architecture on account of its strong mechanical properties that confer a stable guide for bone consolidation with potential osteoinduction properties needing to be further explored. Nevertheless, osteogenicity was likely to be absent from HFL owing to the lack of MSCs. This study could pave the way towards a cheaper and effective CSBD treatment by means of a bio-engineered periosteum built from HFL.

– TAKEAWAYS –

Paper 1 – Periosteum and fascia lata: Are they so different?

- *<u>Similarities</u> = Molecular composition*
  Organized in two layers
  BMP-2 and BMP-7 content

- *<u>Differences</u> = Fibre organization*

  Cellular content — *HP > HFL*

  ↳ *Immunogenicity* — *HP > HFL*

  Absence of MSCs in HFL

  Col-1 — *HP < HFL*

  ↳ *Mechanical resistance* — *HP < HFL*

⇨ *<u>HFL</u> = Suitable scaffold to replace HP for guided-bone regeneration*
Osteoinductive potential to be explored

BUT lack of osteogenicity

Paper 2 – 2D and 3D microstructural analysis of the iliotibial tract

Julie Manon, Laurie Gallant, Paul Gérard, Lies Fievé, Pierre Schneidewind, Grzegorz Pyka, Greet Kerckhofs, Benoît Lengelé, Olivier Cornu, Catherine Behets

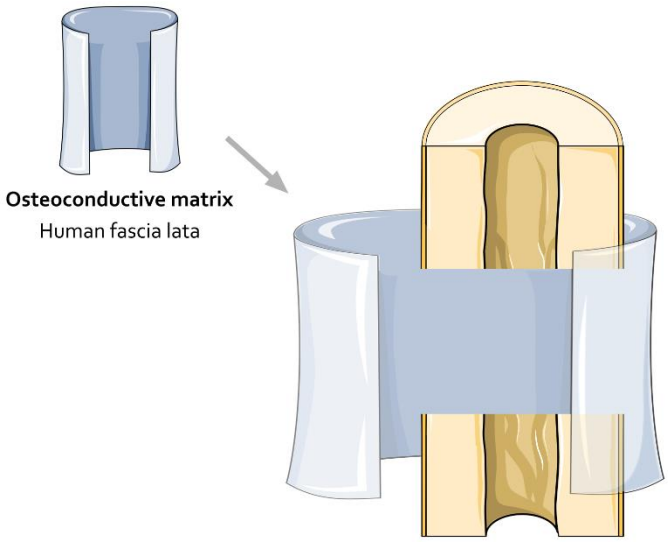

Published in

Journal of Anatomy (IF=2.921)

doi: 10.1111/joa.14125

Abstract

The fascial system has gained recognition for its integral role in connecting skin, superficial and deep fasciae, and underlying muscles. However, consensus on its microstructure depending on its topography remains elusive as well as its implications in clinical practices, such as reconstructive surgery and physiotherapy techniques. This study focuses on the ITT implicated in the iliotibial band syndrome. The goal is to describe microstructural characteristics using classical 2D histology and cryo-CECT such as the total thickness, number of layers, layer thickness, fibre orientation and tortuosity, according to the specific topography.

The total thickness of the ITT varied across topographic regions, with the superior part being on average thicker but non-significantly different compared to the other regions. The inferior part showed heterogeneity, with the anterior region (AI) being the thinnest and the posterior one (PI) the thickest. The ITT exhibited 1 to 3 layers, with no significant differences among regions. Most commonly, it consisted of two layers, except for the antero-superior (AS) and antero-middle (AM) regions, which sometimes had only one layer. The posterior regions frequently had 2 or 3 layers, with the PI region having the highest mean (2.7 layers). The intermediate layer was the thickest one, varying from the AI region (0.368mm ± 0.114) to the PI region (0.640mm ± 0.305). The superficial layer showed regional variability, with the AS region being the thinnest. The deep layer appeared thinner than the superficial one. Fibre orientation analysis indicated that the intermediate layer mainly consisted of oblique longitudinal fibres, orientated downward and forward, while the superficial and deep layers had transversal or oblique transversal fibres. Cryo-CECT 3D observations confirmed these findings, revealing distinct orientations for different layers. Fibre tortuosity exhibited differences based on orientation. Transversal fibres (> 65°) were significantly less tortuous than longitudinal fibres (< 25°) and oblique intermediate fibres (25°-65°), aligning with 3D plot observations.

This quantitative study highlights various microstructural characteristics of the ITT, offering insights into its regional variations. The analysis accuracy is increased due to the novel technology of cryo-CECT which emerges as a valuable tool for precise assessment of 3D fibre orientation and tortuosity. These findings contribute to a deeper understanding of the ITT structure, useful in clinical

practices, such as reconstructive surgery and physiotherapy, and future research endeavours.

A. Introduction

Whereas the fascial system was not considered by clinicians a few decades ago[223,226,231,275], healthcare givers now recognise the importance of fascial tissues as a system connecting the skin, the superficial and deep fasciae, and the underlying muscles[223,275,276].

The ITT or Maissiat's iliotibial band is considered a linking fascia between the gluteal fascia and the fascia lata, below the level of the tensor fasciae latae muscle[228]. This lateral thickening of the fascia lata connects the iliac crest to Gerdy's tubercle on the lateral condyle of the tibia[222–227]. It is a major insertion for the gluteus maximus muscle[277]. No fewer than five distal insertions of the ITT were described, namely the most important insertion being Gerdy's tubercle, followed by the lateral condyle of the femur, the fibular head through the lateral collateral ligament, the linea aspera via the lateral intermuscular septum of the thigh, and the retinaculum of the patella[229,230]. The ITT is a dense connective tissue whose collagen fibres[223,231] can form different layers with a specific orientation. The proximal part of the ITT is separated into three layers[224]. The superficial and intermediate ones surround the tensor fasciae latae muscle; the deepest one fuses more distally, coming from the supra-acetabular groove[224,229]. The ITT takes a major part in the hip and knee stabilization when walking by playing a tendon role for the tensor fasciae latae and gluteus maximus muscles[223,225,232].

Like all fasciae, different measurements were reported depending on the region analysed[275]. However, standardized norms are missing, especially for the ITT itself[227]. The limited but growing number of studies demonstrates that the measurement of microstructural parameters or the establishment of fascia standards are an emerging research area[226]. Indeed, the necessity of digging deeper into the comprehension of the fascial microstructure is multiple.

First, the iliotibial band syndrome can cause pain on the iliac tubercle[229,278], on the greater trochanter[279], or on the lateral condyle of the femur[222,223,225,226,229,280] in case of irritation or inflammation. This pathology is easily diagnosed but hardly treated. Some physiotherapy techniques use a deep transverse massage which involves deep, cross-fibre friction applied to the affected area, aiming to break down scar tissue, improve blood flow, and promote healing[231,281]. To be effective, the precise

orientation of the fibres should then be known by the therapist. Exploring the ITT structure more in detail might also permit to better understand its mechanical role on the lower limb when walking or its associated pathologies[225,231].

Next, the ITT is largely used in the field of reconstructive surgery. It can be used as a covering flap for duraplasty[233], soft tissue defect on the limb[237], sealing lung breaches[235], for colpopexy[236], as well as for reconstruction of acetabular labrum[238], rotator cuff[239], patellar ligament[240], as interposed material in congenital tarsal coalition resection in adolescents[242] or even the anterior cruciate ligament[241]. However, the needs for all those reconstructive surgeries are not exactly the same. Sometimes the surgeon might need a thinner flap for tibial coverage or a thicker one to fill a gap. Depending on the number of layers or the fibre orientation, the mechanical characteristics might also be different[227] and could influence the surgical decision on where to harvest the best sample[282].

Since several imaging techniques, like US or MRI, previously tried to evaluate the microstructure of fasciae with mitigated quality[226,227,280], new technologies emerged such as the contrast-enhanced microcomputed tomography (CECT). This technique allows 3D microstructure analysis of biological tissues with limited destruction of the tissue[283,284]. Since tendons and ligaments have low X-ray attenuation, contrast-enhancing staining agents (CESAs) were developed to enhance discrimination of such tissues[283–287] but the individual fascicle or fibre visualisation and analysis were still challenging. The newly described cryo-CECT could allow these microstructural investigations[288].

The goal of this paper is to establish quantitative microstructural parameters, specifically for the ITT, using classical 2D histology and cryo-CECT, and to map them according to harvesting regions. Since the physiology relies on the close relationship between structure and function[275,289], this study could allow the deeper understanding of the ITT anatomy, structure, organization and related function in order to help both the clinical and the research fields. Clinically, this can open the reflexion about the efficacy of physical and manual therapies impacting the fascia, about various deep surgical procedures that require cutting and suturing fascia, and about the harvesting of fascio-cutaneous flaps for reconstructive surgeries.

B. Methods

B. 1. Tissue harvesting & sampling

Human ITTs were harvested from deceased donors (N=5, four men and one woman; average age=79 ± 17 years [50 – 93 years]), received at the Morphology lab of UCLouvain (IRB00008535, Brussels, Belgium). The local ethics committee (Ref 2021-30AOU-356 approved on September 13, 2021) authorized all the experiments.

For classical 2D histology, the ITT was harvested below the level of the tensor fasciae latae muscle extending up to the lateral femoral condyle insertion, following a previously described technique[290,291] and then divided into nine regions in order to map and analyse them separately (Fig. 40). A specific nomenclature was attributed to each region (PS: postero-superior, MS: medio-superior, AS: antero-superior, PM: postero-middle, MM: medio-middle, AM: antero-middle, PI: postero-inferior, MI: medio-inferior, AI: antero-inferior). Per region, two samples (1x2cm) were cut (n=18 per individual) to permit to conduct a systematic analysis. The orientation of the tissue is of uppermost importance to assess the fibre organization. Into each region, the most superior sample was cut transversally to the main axis of the ITT and the inferior one, longitudinally.

The nine regions allowed to locate and orientate the samples into two different directions, the sagittal (postero-, medio-, antero-) and the longitudinal one (superior, middle, and inferior), but the transversal one was also investigated in order to identify the superficial or the deep side of the ITT. To do so, an ectopic distinct muscle patch was harvested at the same time to be further embedded with each sample to mark the tissue orientation correctly.

For cryo-CECT, random 2cm² samples were harvested from other human ITT (N=3 donors, one sample per donor, two men and one woman; average age= 80.6 ± 3.3 years [77 – 83 years]). A thread served as a landmark to orientate the tissue.

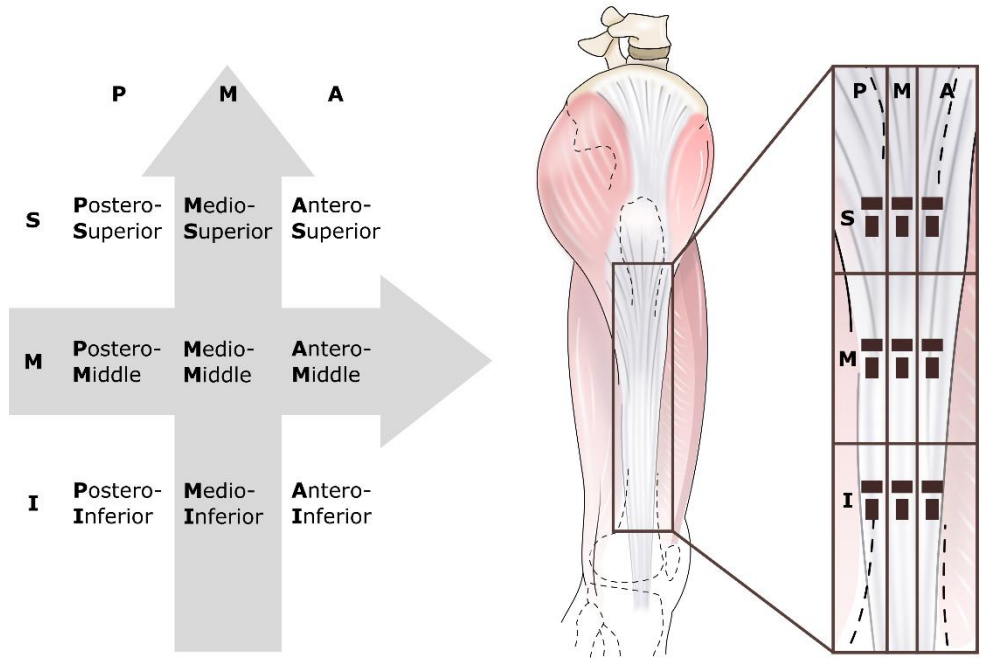

Figure 40. Sample harvesting and mapping into nine regions. Each region is called by two capital letters corresponding to the topography in sagittal direction (postero-, medio-, antero-) and longitudinal direction (superior, middle, and inferior). They all contain one sample of 1x2cm cut transversally and one longitudinally (dark rectangles on the right picture). PS: postero-superior, MS: medio-superior, AS: antero-superior, PM: postero-middle, MM: medio-middle, AM: antero-middle, PI: postero-inferior, MI: medio-inferior, AI: antero-inferior.

B. 2. Classical 2D histology protocol

A precise protocol was established to keep track of the tissue orientation (Fig. 41). The samples were put into cassettes with the muscle patch guide to orientate the tissue in the three planes (Fig. 41 – a). The muscle patch was always positioned on the superior and anterior side of each sample and the superficial side was always facing the operator. All the samples were fixed within their cassettes in formaldehyde 4% (VWR, 9713.9010) for 48 hours thereafter, processing for paraffin embedding. The paraffin embedding respected the correct orientation of the samples into their respective moulds (Fig. 41 – b). As previously, the guide was always positioned on the superficial face and the anterior border for transversal samples and on the superficial face and the superior border for longitudinal

samples. The anterior part for longitudinal samples as well as the superior part for transversal samples were always facing the cassettes during the embedding phase.

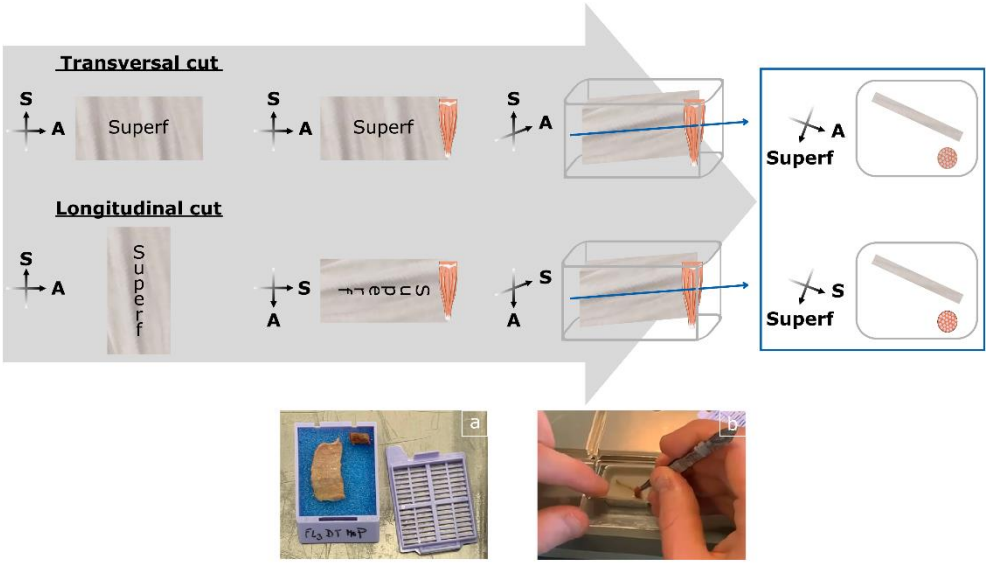

Figure 41. Procedure to respect the tissue 3D orientation, according to transversal or longitudinal cuts of samples. A muscle guide was associated with each sample to keep the good orientation during all the procedure. (a) Correct positioning of the sample and the muscle guide within the cassette. (b) Embedding step respecting the relative position between the sample and the muscle guide. The grey boxes represent the cassettes, in which the samples were cut following blue arrows to obtain transversal views through the cassettes shown in the blue rectangle at the right. S: superior, A: anterior, Superf: superficial.

The paraffin embedded blocks were then sliced into in 5µm thick sections. These latter were stained with H&E and MT before being digitised with a slide scanner (SCN400, Leica Microsystems, Wetzlar, Germany) at a 40-fold magnification, and annotated with SlideViewer software (v2.5.0., Budapest, Hungary).

B. 3. Classical 2D histological analyses

A layer is described by all the fibres that have the same orientation. Four different qualitative orientations were defined: pure longitudinal, pure transversal, oblique longitudinal and oblique transversal. The distinction of layers and their associated fibre orientation were qualitatively assessed on stained sections by two independent examiners. The fibre orientation was indicated for each transversal

and longitudinal sections as well as each region and was finally defined by the largest headcount in one region.

The quantitative analyses included the total ITT thickness, the number of layers, and the layer thicknesses in each region. They were quantified using the SlideViewer software. In order to establish the total ITT thickness, three measures were taken on one section for each sample. For transversal/longitudinal sections, one measure was taken respectively at 0.5mm from the antero-/superior extremity, one in the medio-/middle of the samples and one at 0.5mm from the postero-/inferior extremity. The mean of the three measures was also averaged by the longitudinal and the transversal sections, and the mean of the five donors to best determine the total average ITT thickness. The number of layers and their respective thickness were assessed by the mean data in longitudinal and transversal sections for each region, followed by the average of the five donors. All quantitative data were expressed as the mean and standard deviations (SDs). Heatmaps were used in order to illustrate quantitative outcomes related to the appropriate region and to compare regions to each other.

B. 4. Cryogenic contrast-enhanced computed tomography & microstructural analysis

All the 2cm² samples were stained with 1:2 hafnium(IV)-substituted Wells-Dawson polyoxometalate (Hf-WD POM, 3.5% (3.5mg Hf-WD POM/mL of phosphate buffered saline (PBS) solution, 25:1 solution to sample volume ratio) on a shaker plate for 15 days, following previously described protocol[288]. The samples were then packed in small plastic bags and snap-frozen by immersion in cold isopentane (-78°C, VWR, 24872.323) during 2 minutes, and stored at -80°C. Specimens were imaged using a Phoenix NanoTom M (GE Measurement and Control Solutions, Germany) inside an in-situ cryo-stage at -40°C[288] (parameters in Table 12).

3D fibre analyses were performed using Avizo software (2022.1, ThermoFisher Scientific, France). Successive processing modules were applied following the *XFiber protocol* previously described[292] (Fig. 42).

Table 12. Cryo-CECT acquisition and module parameters

Acquisition parameters		Cylinder correlation parameters		Trace correlation Lines parameters	
Voxel size (µm)	3	*Cylinder length (µm)*	200	*Minimum Seed Correlation*	40
Source voltage (kV)	110	*Angular Sampling*	5	*Minimum Continuation Quality*	30
Tube current (µA)	114	*Mask Cylinder Radius (µm)*	15	*Direction Coefficient*	0.3
Exposure time (ms)	500	*Outer Cylinder Radius (µm)*	14	*Minimum Distance (µm)*	28
Number of images	5200	*Inner Cylinder Radius (µm)*	0	*Minimum Length (µm)*	200
*Average**	6			*Search cone Length (µm)*	200
*Skip**	1			*Search cone Angle*	37
Scan time (min)	317			*Minimum step size (µm)*	10

** Information about those parameters were previously given in the literature[288].*

First, *Extract Subvolume* module permitted to analyse exactly the same volume (0.9 x 0.9 x 1.8mm) in each sample, centred on a random ITT area. The main axis was orientated following the main limb axis. The fibres were segmented and extracted using *semi-manual segmentation* tools (*magic wand, brush, …*) and the *Filter Sandbox* module thanks to their grey values. The fibre analysis included *Cylinder correlation* module, *Mask* module, and *Trace Correlation Lines* module. All the detailed acquisitions and module parameters are resumed in Table 12.

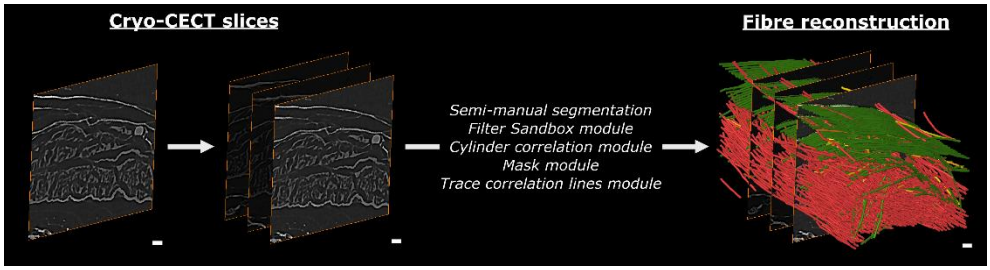

Figure 42. Cryogenic contrast-enhanced computed tomography (cryo-CECT) of iliotibial tract from slices to fibre reconstruction using different modules from Avizo software (2022.1, ThermoFisher Scientific, France). Scale bars: 100µm.

A *Spatial Graph View* module allowed to reconstruct the 3D organization of the fibres following the theta orientation (θ angle formed with the Z-axis, aligned with the main limb axis, and ranging from 0° (longitudinal fibres) to 90°(transversal fibres)). A *Plot 3D orientation* module plotted and schematized the density of different fibre orientations.

The *Spatial Graph Statistics* module quantified the tortuosity of the reconstructed fibres. Tortuosity is independent of fibre orientation angles, pertains to the microscopic intrinsic waviness of an individual fibre, and is defined by the ratio of curved length on the chord length of a fibre (ratio starting from 1 = no tortuosity at all, and increasing progressively with the tortuosity).

B. 5. Statistical analysis

All statistics were made using GraphPad Prism software (v.8.0.1, San Diego, CA, United States). Independent quantitative values were first analysed by descriptive analyses, boxplots, and histograms to evaluate their distribution. Regarding orientation data highlighting two main almost orthogonal orientations, the fibres were divided into three groups according to the θ angle (Group 1: < 25°, group 2: between 25°-65°, group 3: > 65°) in order to discriminate the tortuosity.

The normal distribution of all quantitative data was evaluated by QQ plots and Shapiro-Wilk tests. Since no distribution was normal, only nonparametric Kruskal-Wallis tests were used, with a Dunn's correction for multiple comparisons. Data are expressed as the mean ± SD. The threshold for significance is set at 0.05.

C. Results

C. 1. Iliotibial tract thickness

The total ITT thickness varied from one region to another (Fig. 43). The superior part of the ITT was thicker (PS=0.653mm ± 0.173, MS=0.654mm ± 0.160, AS=0.690mm ± 0.245) than others (MP=0.597mm ± 0.158, MM=0.560mm ± 0.173, AM=0.590mm ± 0.247, MI=0.638mm ± 0.227) although not significantly, and its thickness was the most uniform.

On the contrary, the inferior part was the most heterogeneous with the thinnest anterior region (AI=0.527mm ± 0.182) and the thickest posterior one (PI=0.693mm ± 0.206), which were statistically different (p=0.016).

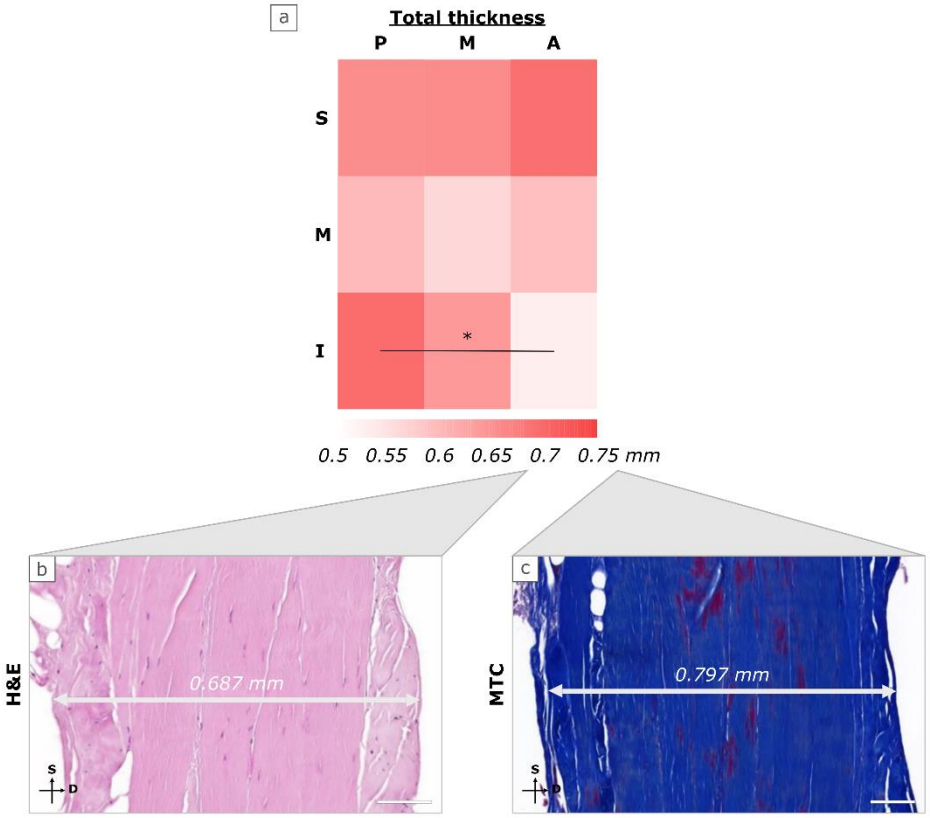

*Figure 43. Total thickness depending on the regions. (a) Heatmap of iliotibial tract total thickness (mm). Data represent multiple consecutive averages of three measurements, two section orientations, and five donors. Horizontal= P: postero-, M: medio-, A: antero-, Vertical= S: superior, M: middle, I: inferior. *: p<0.05. (b) Longitudinal cut of a sample from the PS region stained with H&E. (c) Longitudinal cut of a sample from the MS region stained with MT. H&E: haematoxylin and eosin, MT: Masson's trichrome. S: superior, D: deep. White scale bar: 100µm.*

C. 2. Number of layers

The heatmap illustrated the average number of layers per region (Fig. 44 – a) and the bubble chart displayed their prevalence (Fig. 44 – b). The number of layers varied from one to maximum three, but was never significantly different among regions. In most cases, the ITT was composed of two layers (Fig. 44 – c and e). The AS (1.9 layers ± 1.0) and the AM (1.8 layers ± 0.7) regions were the only ones that sometimes contain only one layer. The posterior parts of the ITT are more frequently composed of two or three layers (Fig. 44 – d and f) with the maximum mean for the PI region (2.7 layers ± 0.5). However, the most constant region was the PM one with two constant layers in 80% of cases.

C. 3. Layer thickness

After being measured on histological sections (Fig. 45 – a and b), the different heatmaps showed the thickness depending on each layer and each region (Fig. 45 – c).

The predominant layer is obviously the intermediate one with thicknesses ranging from 0.368mm ± 0.114 in the AI region to 0.640mm ± 0.305 in the PI one. Regarding the superficial layer, it was the thinnest in the AS region (0.053mm ± 0.034) while the intermediate layer was one of the thickest in this same region (0.606mm ± 0.319). The rest of the superficial layer was homogeneous varying from 0.110mm ± 0.029 in the AI region to 0.154mm ± 0.103 in the PS one. The deep layer looked thinner than the superficial one with thicknesses comprised between 0.058mm ± 0.048 for the MM region and 0.201mm ± 0.124 for the MS region.

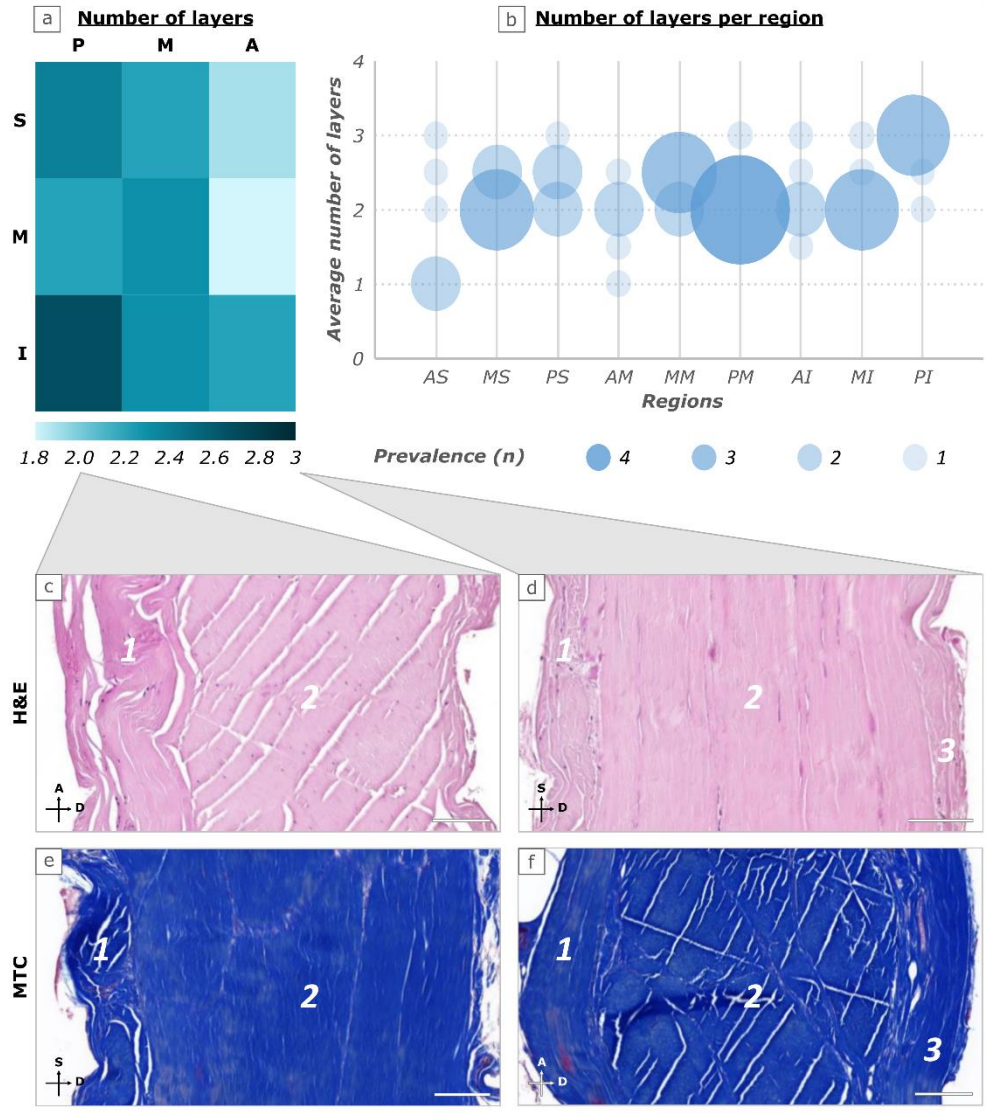

Figure 44. Number of layers according to the region, illustrated by (a) the heatmap of iliotibial tract, (b) the bubble chart, and (c to f) histology. Horizontal= P: postero-, M: medio-, A: antero-, Vertical= S: superior, M: middle, I: inferior. The bubble chart allows to identify the number of layers per region associated with their respective prevalence illustrated by the width of the bubble. (c) Transversal cut of a sample from the AI region stained with H&E. (d) Longitudinal cut of a sample from the MI region stained with H&E. (e) Longitudinal cut of a sample from the AI region stained with MT. (f) Transversal cut of a sample from the PI region stained with MT. H&E: haematoxylin and eosin, MT: Masson's trichrome. A: anterior, S: superior, D: deep. White scale bar: 100µm.

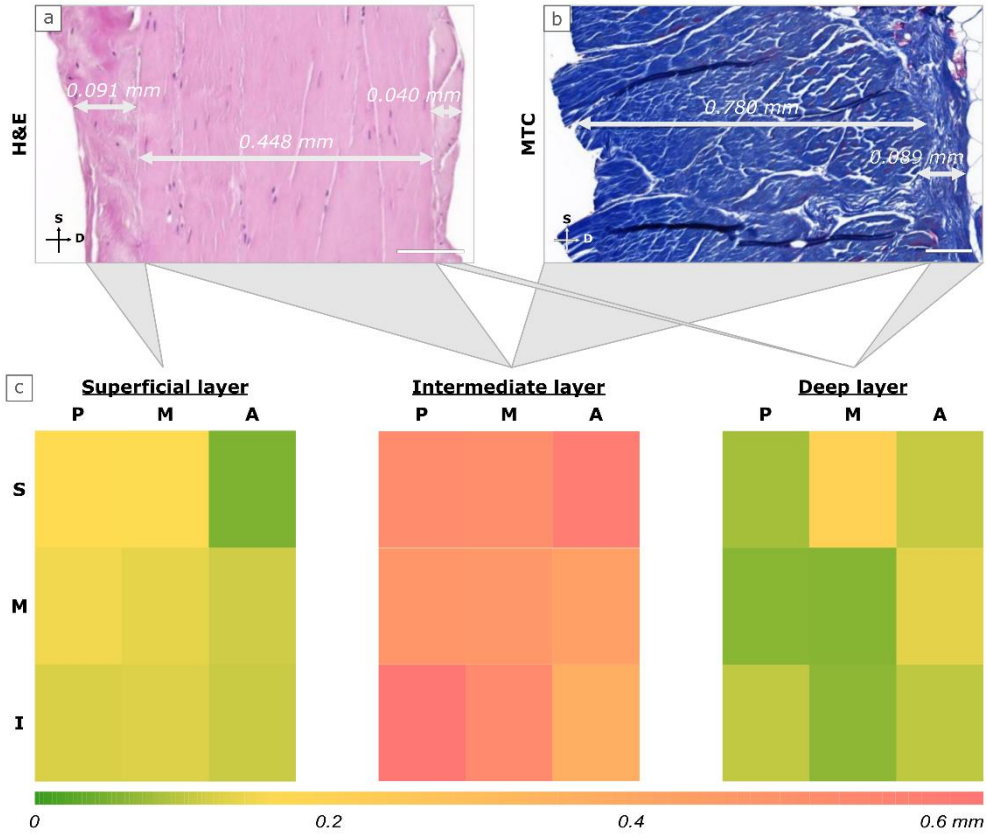

Figure 45. Layer thickness depending on the regions. (a) Longitudinal cut of a sample from the PS region stained with H&E. (b) Longitudinal cut of a sample from the PI region stained with MT. H&E: haematoxylin and eosin, MT: Masson's trichrome. S: superior, D: deep. White scale bar: 100µm. (c) Heatmap of each layer thickness according to the nine regions. Data represent multiple consecutive averages of three measurements, two section orientations, and five donors. Horizontal= P: postero-, M: medio-, A: antero-, Vertical= S: superior, M: middle, I: inferior.

The boxplots indicated the data dispersion and homogeneity depending on the region (Fig. 46). In the superior regions, the intermediate layer is the most variable while the superficial one is the most constant. The middle regions had the most predictable uniform thickness, whether for superficial, intermediate, or deep layer values (no significant differences, $p>0.05$). The most variable region in the ITT is the inferior part with a high fluctuation in the intermediate layer thickness. The maximal thickness found among the whole ITT is in the PI region (1.2mm).

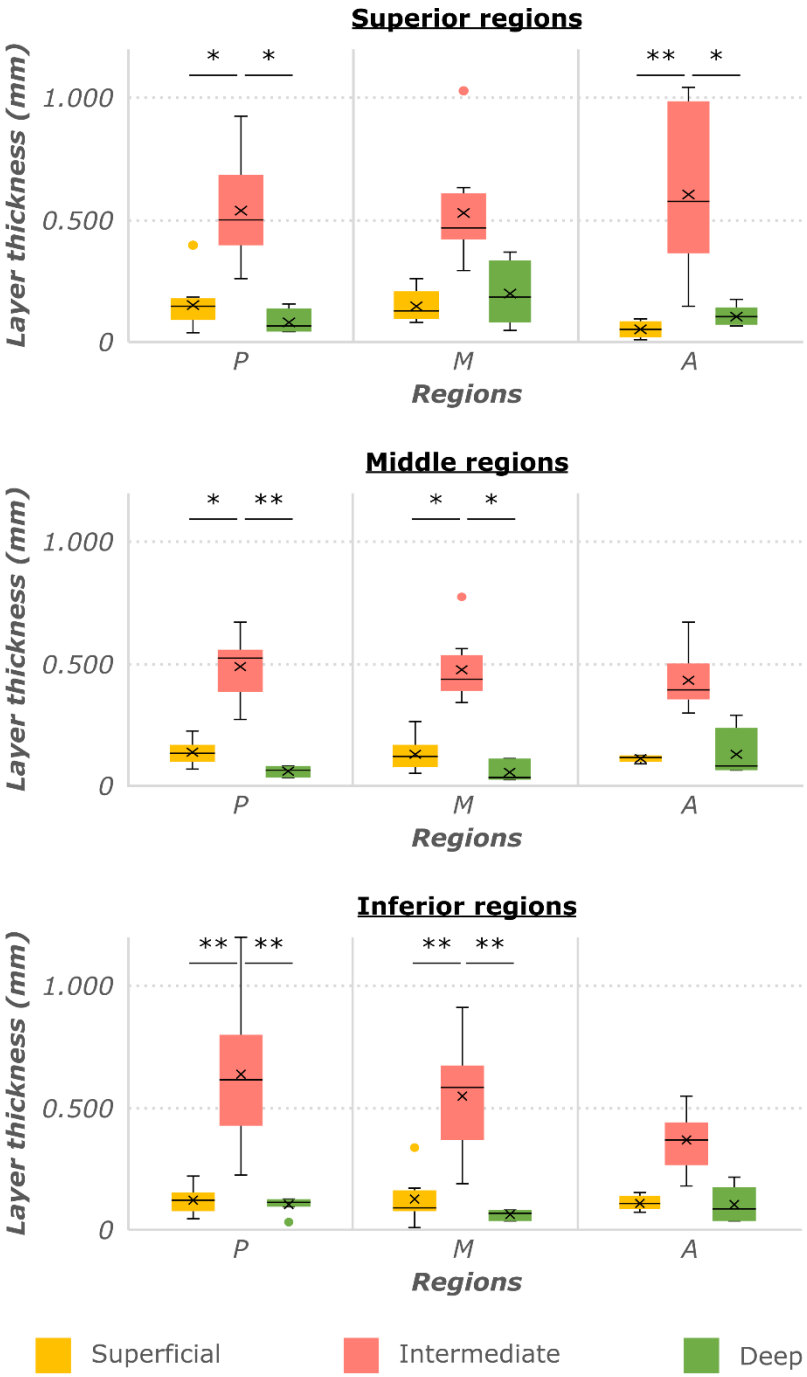

*Figure 46. Boxplots of the layer thickness depending on respective regions and each layer. P: postero-, M: medio-, A: antero-, x: mean. *: p<0.05, **: p<0.01.*

C. 4. Fibre orientation

The main fibre orientation is represented for each layer of each region in the figure 47 – a. The intermediate layer is mostly composed of oblique longitudinal fibres (Fig. 47 – e and i) while the superficial and the deep layers are mostly composed of transversal (Fig. 47 – b and f) or oblique transversal fibres (Fig. 47 – d and h). The deep layer is made of more strict transversal fibres than the superficial one.

Cryo-CECT also allowed to examine the fibre orientation in full 3D (Fig. 48). Among the three subvolumes analysed, one has only one layer (ITT 3), one has two main layers (ITT 1), and the last one has three layers (ITT 2). This 3D representation also shows that the main thick intermediate layer is composed of longitudinal fibres (red) while the thin superficial and deep layers are mainly composed of transversal fibres (green). The 3D plots schematise the θ angle in between the fibres. When a minimal of two layers are present, two main orientations emerge, both in a sagittal plane, and with an interlayer angle from 80.11° to 84.78°. The height of the bars shows that green transversal fibres are more numerous for one same single orientation. This means that they are more parallel to each other than the red longitudinal fibres that are more spread around an axis almost perpendicular to the latter.

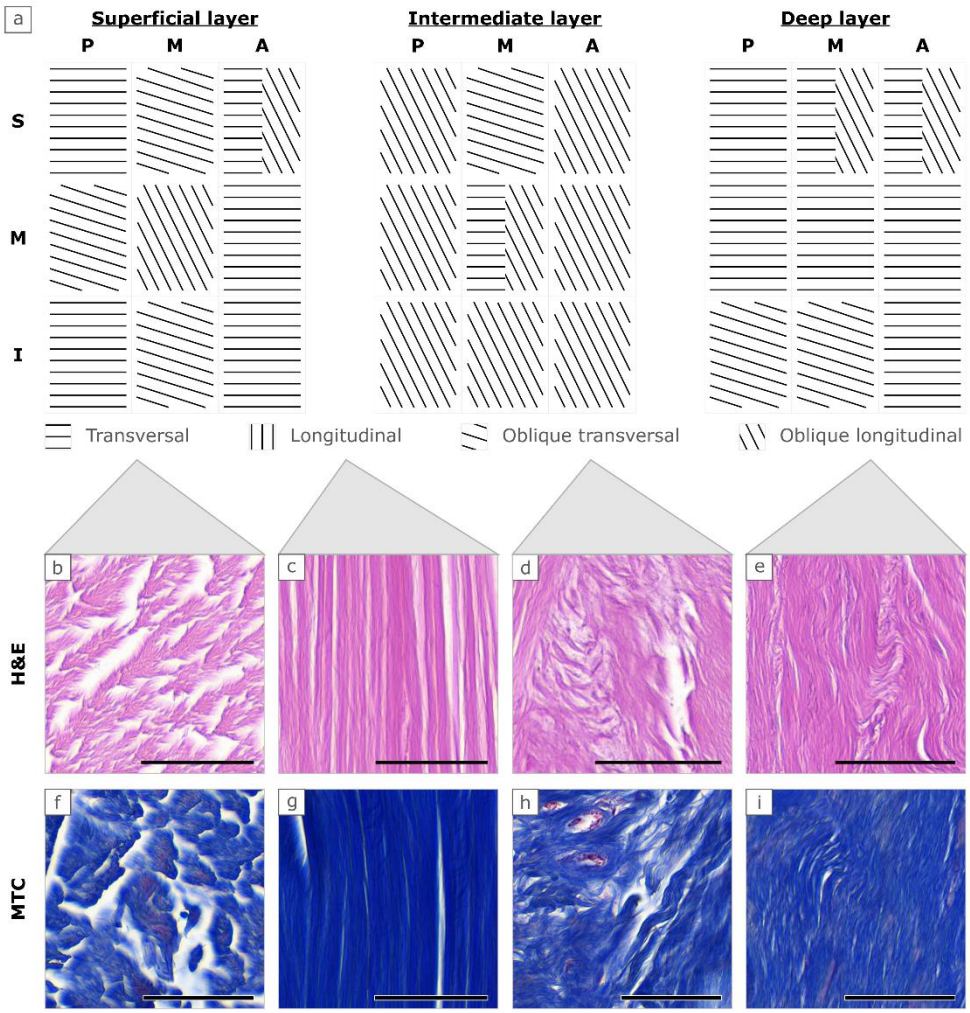

Figure 47. Fibre orientation analyses using histology. (a) Fibre orientation map according to each region from each layer in the ITT samples analysed with classical histology. Horizontal= P: postero-, M: medio-, A: antero-, Vertical= S: superior, M: middle, I: inferior. (b) Transversal cut of a sample from the PI region stained with H&E. (c) Longitudinal cut of a sample from the PI region stained with H&E. (d) Longitudinal cut of a sample from the PI region stained with H&E. (e) Longitudinal cut of a sample from the AI region stained with H&E. (f) Longitudinal cut of a sample from the PI region stained with MT. (g) Longitudinal cut of a sample from the MM region stained with MT. (h) Longitudinal cut of a sample from the PI region stained with MT. (i) Longitudinal cut of a sample from the PM region stained with MT. H&E: haematoxylin and eosin, MT: Masson's trichrome. Black scale bar: 50µm.

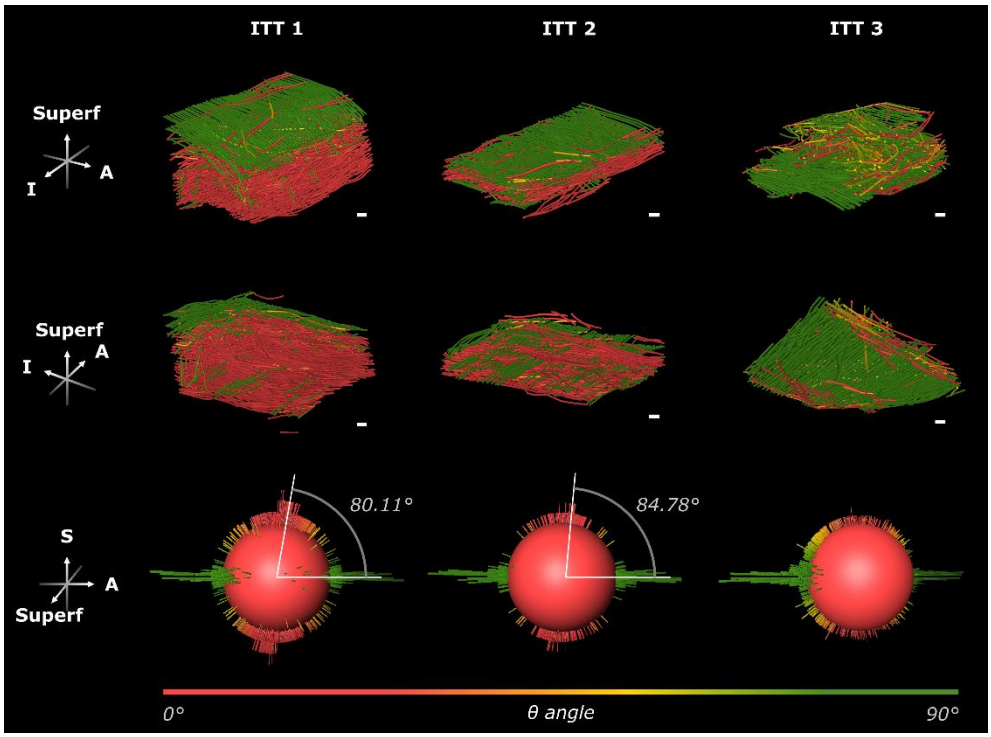

Figure 48. Fibre orientation analyses using the cryo-CECT. 3D fibre reconstruction of ITT subvolumes coming from three different donors (ITT 1, ITT 2, ITT 3), and 3D plots schematising the ϑ orientation of fibres. The fibre colour is associated with the ϑ angle (red 0° = longitudinal fibres – green 90° = transversal fibres). The height of the bars expresses the fibre count. White scale bar: 100µm. Colormap scale bar: ϑ angle (orientation) of the fibres. ITT: iliotibial tract, ϑ: theta angle. Superf: superficial, A: anterior, S: superior, I: inferior.

C. 5. Fibre tortuosity

While the distribution of θ orientation values follows a U-shape with highest prevalences at the extreme values (data not shown), the fibre tortuosity does not follow the same distribution. These data follow a decreasing exponential prevalence starting from the ratio of 1, meaning no tortuosity at all, with the curved length equal to the chord length. The transversal fibres (> 65°) were significantly less tortuous (1.019 ± 0.047) than longitudinal fibres (< 25°) (1.024 ± 0.027) and oblique intermediate fibres (25°-65°) (1.039 ± 0.070) ($p<0.0001$). These observations are in line with the 3D fibre reconstructions.

D. Discussion

This study demonstrated specific differences in fibre organization between anatomical regions of the ITT, *i.e.* a higher thickness of the intermediate layer, especially in the superior and the postero-inferior regions, a higher number of layers of the PI region, and an almost perpendicular orientation of two consecutive layers.

Total thickness

The superior part of the ITT is the thickest and the most homogeneous part, where the different layers of fascia converge after enveloping the tensor fasciae latae muscle. Its posterior region is reinforced by tendinous fibres coming from the gluteal aponeurosis covering the gluteus maximus[224], confirmed by our outcomes. As previously mentioned[231,293,227], the fascial thickness tends to decrease in the middle region and to increase again distally around the knee. In our study, the thickest region is the PI one, which corresponds to the gathering of fibres before insertion on Gerdy's tubercle. However, the comparison with the literature is not easy, since different anatomical regions into the whole fascia lata were screened[226,227] but never specific regions into the ITT itself, nor the different layers insofar as this is possible. The thickness is also often evaluated precisely at the level of the lateral condyle *in vivo*[280,294–296], which is one of the thickest zones where fibres gather towards Gerdy's tubercle.

While the average total thickness of a fascia is around 1mm[275], different tools permit to measure it. Using the US, the ITT thickness was measured from 1.1mm ± 0.2 to 1.95mm ± 0.3[294,297,295,296,227], which is almost double our data. *Ex vivo* tissue processing for classical 2D histology is known to induce some fibre shrinkage and therefore to diminish the data compared to *in vivo* US[227] or MRI measurements[280]. Those authors were not able to highlight the relationship between the thickness and the age, sex, weight, or side dominance[295]. Their population was also younger (18-68 years) than our old one (50-93 years). Additionally, the MRI is not so accessible, and US is operator dependent. The intra- and inter-operator reliability can vary substantially[226]. The probe position may influence the outcomes because of tissue anisotropy and dynamic variation of the measures. In living patients, the interstitial space between fascial layers can vary and may affect the measured

thickness. Factors such as hydration status, tissue health, and even the dynamic nature of tissues during movement might influence the appearance and measurements obtained via imaging techniques like US. As a general example, the deep fascia sometimes seems adherent to the superficial one, thus leading to wrong measurements of both fasciae[226]. The US and MRI are very useful to participate in the diagnosis and the treatment follow-up as non-invasive techniques[226,280] but consequently, not the best tools to establish thickness measurements. In addition, measurements taken from different sources lead to inaccurate and non comparable data[227]. For classical 2D histology, another point to consider is the impact of the cutting orientation on histological slices. If the sample is not strictly perpendicular to the cutting plane, the thickness might be falsely increased. Anatomical dissection remains the ancestral reference, but classical 2D histology can still help to discern microscopic structures such as layer and fibre orientation. Knowing that, our results closely approximate the anatomically measured ITT thickness (0.8 to 0.9mm) obtained using callipers on cadaveric specimens[225,298].

Number of layers & layer thickness

All these observations bring more details and knowledge compared to the single mean layer thickness of about 115 to 277µm described in the literature[275,299].

The ITT is a fusion of three collagen tissue layers including superficial, intermediate and deep layers[224], each one separated by a light stratum of loose connective tissue[231,226,227]. This organization is essential for the inter-layer and tissue sliding[231,275]. However, no study to our knowledge linked the number of layers with the specific regions of the ITT. Our results showed that the mean number of layers is above 2 in most of the regions, excluding the AS and the AM ones. If only the longitudinal orientation is considered, the inferior level is the only one that always contains an average of 2 layers, regardless of the region in the sagittal plane. This could reflect a more complex organization of the distal ITT. This difference could be related to the complexity of the ligamentous and tendinous network around the knee and the Gerdy's tubercle[293,227]. The PI region is the area with the highest average number of layers, the most frequent three layers, as well as the largest total thickness. On the contrary, the AS region is also a thick region but generally counts only one layer. This observation can corroborate the fusion of the thin

superficial and deep layers with the intermediate one. The high thickness of these two regions is mostly explained by the thickness of the mean intermediate layer. Indeed, when AS region contains seldom one superficial layer, the latter is the thinnest one. In addition, the AI region with the thinnest intermediate layer corresponds to the thinnest total thickness, and the PI region with the thickest intermediate layer corresponds to the thickest total thickness. The high thickness fluctuation of the inferior part of the ITT also matches the fluctuation of the intermediate layer thickness. In all the regions, this intermediate layer was always the thickest, and in the middle when three layers existed. When only two layers existed, this thick layer was more often found on the deep side than on the superficial side. Contrariwise, when three layers existed, the deep one was usually thinner than the superficial one. Actually, the fascia has the ability to adapt to changes in muscular volume in a horizontal direction, which could explain the thinner thickness in the middle of the deep layer[282].

Fibre orientation

The variability of fibre orientation was previously established, depending on the harvested site of the fascia lata[231,225]. However, the different regions in the ITT itself were not discriminated. While linking fasciae are described as dense unidirectional collagen tissue[228], our study demonstrated that different layers of a single linking fascia such as the ITT can be composed of parallel ordered collagen fibres with several different orientations. The majority of fibres of superficial and deep layers are transversal or oblique transversal while they are oblique longitudinal for the intermediate layer. The interlayer angle approached an orthogonal plane, described in the literature from 75 to 80°[298,299].

The transversal deep layer surrounds the thigh muscles and can be confounded with the epimysial fascia[231]. The superficial layer contains the superficial fibres of the gluteus maximus that are oblique transversal in the superior region, converging downward and forward. Concerning the inferior region, fibrous expansions coming from the ITT form an arc covering the patella, especially for the lateral retinaculum[300,301,229]. This could explain the predominance of arciform or transversal fibre orientation in the superficial and deep layers respectively in this region[301].

Structure is associated with function[302,223,225]. The transversal layers could be involved in muscle containment such as an exoskeleton protecting underlying tissues and organs, and in proprioception[231,275,223]. This description was proposed for compression fasciae that play a role in compartment pressure, its venous return, and muscular force distribution[223,275,282,228]. Otherwise, this specification is well known to be harmful during excessive pressure in compartment syndrome of lower limbs[282]. Interestingly, the transversal stiffness and Young's modulus were statistically the lowest for the ITT compared to the rest of the fascia lata[225]. Fasciae are known as anisotropic[225,298]. While the majority of fibres are orientated oblique longitudinally in the intermediate layer, the stiffness and tensile forces are higher in an oblique vertical direction[282,225,290,298]. In surgical application, this is potentially important, as a graft required to withstand stresses over an extended length must be cut along this longitudinal axis obliquely downwards and forwards, rather than strictly longitudinally, to prevent shear forces that could cause graft rupture. This layer is implicated into the main function of the ITT, namely the forces transmission through the lower limb and walk stability[302,231,275,282,225]. In this study, histological measurements were taken without tension, thus not replicating weight-bearing force transmission conditions. Tension might potentially influence fibre tortuosity and layer thickness, while *rigor mortis* could also slightly affect fibre organization. Further studies are thus warranted to investigate the precise relationship between tissue structure and organization under tension transmission conditions. A structure modification, such as an adhesion point or cicatricial scars in a fascia after trauma or surgery, can alter the function, *i.e.* tensile force lines leading to changes in muscle glide[275]. The presence and function of fasciacytes in between the layers could also influence fascia gliding and might cause subsequent myofascial pain[303]. A stiffer ITT could also increase mechanical loading to the knee leading to osteoarthritis[304]. Moreover some surgical techniques involve a structure change to improve the function, such as an ITT release in ITT syndrome[223,305]. In the opposite, the function can also drive the structure. For example, the stiffness and the thickness of the ITT can be modified according to postural positions or repeated dynamic friction, sometimes leading to ITT syndrome[306]. The thickness of the ITT is then related to the pain in conditions such as patellofemoral pain[307], lateral knee pain[280], or greater trochanteric pain syndrome[279]. Donor characteristics such as weight, height, or femur length could also be considered in relation to the structure and function of the ITT.

New techniques

For less-destructive evaluation of the microstructure of the ITT, clinical CT scan is not the imaging of choice for soft tissue, and US and MRI have too low spatial resolution[226,308]. Both imaging techniques are not efficient enough to discriminate each single fibres and analyse their characteristics. For research purposes or to establish precise norms, cryo-CECT could be a good compromise to associate spatial resolution and fibre visualisation[288]. Its precision is sufficient to characterize fascicules and individual fibres, without shrinking the tissue. Freezing can create microcrystals of ice that can spread the fibres slightly apart, which must be considered when analysing the microstructure, even if snap-freezing reduces this phenomenon. Even if this technique cannot be applied *in vivo*, it allows more quantitative measurements than possible with previous techniques. For example, the 3D fibre orientation and the tortuosity can be quantified. Even if all ratios were very close to 1 (no tortuosity), this study showed that the longitudinal fibres, mainly localized in the intermediate layer, and oblique fibres are significantly more tortuous than transversal fibres of the deep/superficial layers. This newly developed technology is doubtless to be considered for further assessment on more numerous samples.

E. Conclusion

Given the interdependence of function and structure, establishing precise standards is imperative for a comprehensive understanding of tissue dynamics. Advanced techniques for assessing the morphological characteristics of the fascia not only reveal its functional significance but also hold promise for refining therapeutic strategies. This understanding could pave the way for the creation or adaptation of more effective therapeutic interventions such in the treatment of ITT syndrome, to enhance the coordination of fascial function and contractions of underlying muscles, and to harvest tissue where the structure and the function are the most adapted to the surgical transplant site.

While our study offers valuable insights, it is important to note that further studies on larger sample size and with younger persons are needed to determine strict norms. Looking ahead, future research could explore the implications of our

findings for conditions like ITT syndrome and optimize the judicious use of an ITT graft in reconstructive procedures.

– TAKEAWAYS –

Paper 2 – 2D and 3D microstructural analysis of the iliotibial tract

- *Structure* ⇔ *Function*
- *Total thickness = Depends on the intermediate layer thickness*

Thickness HP < HFL < Induced membrane[111]

Intermediate layer	*Superficial layer*
Thick +	*Thin –*
Longitudinal fibres	*Transversal fibres*

Interlayer angle ≈ 90°

→ *Mechanical properties*

→ *Containment properties*

⇨ *What do we need to create an OM?*

The membrane should be harvested in regions with 2 layers: one thick intermediate providing support and a thin superficial layer for cell seeding. This approach offers the flexibility of using the layers in a reversed configuration, with the thinnest layer in contact with the bone, similarly to the periosteum or induced membrane structures.

Back to the Diamond

- **Is the HFL a suitable scaffold to replace the HP for guided-bone regeneration?**

HP and HFL are both fibrous membranes predominantly composed of type I collagen fibres. Unlike HP, which is not suitable or large enough for wrapping CSBDs, HFL is easily harvestable with minimal donor-site morbidity and can cover larger surface areas. This adaptability allows HFL to be tailored for various CSBDs, providing a single, continuous piece for effective wrapping.

The higher collagen content of HFL imparts stronger mechanical properties, which can be an advantage for its malleability, handling resistance, and relative stability in enclosing the bone consolidation chamber around a CSBD. Although reproducing HP anisotropy remains an open question, the isotropic nature of the Masquelet's induced membrane, which functions effectively as an OM, suggests that mechanical requirements for an OM involve a broad discussion. This also includes mechanotransduction and cellular responses to mechanical stimuli[309–311]. By the way, the mechanical stability encountered in the Diamond concept for bone healing will be further addressed by incorporating an MBA, suitable osteosynthesis, and the ability to stitch the membrane around the entire construct.

Regarding osteoinduction, both HP and HFL exhibit comparable levels of BMP-2 and BMP-7. However, HFL lacks the high cellular content of HP, particularly PMSCs, which are abundant in HP cambial layer but absent in HFL. Despite HFL apparent lack of intrinsic osteogenicity, its osteoinductive potential warrants further exploration.

Though HFL has never been considered for CSBD treatment, it presents a viable biological opportunity for guided-bone regeneration, replacing HP which displays poor availability and quantity, high inter- and intrapersonal variability and high donor-site morbidity. Further investigation is needed to fully understand and enhance HFL osteoinductive potential, to validate tissue engineering steps, to secure the biological scaffold and to bring osteogenicity.

- **Based on its microstructural analysis, where should the HFL membrane be harvested to meet the specific requirements of an OM and maximize reproducibility?**

First considering the thickness, HFL is intermediate between HP and the induced membrane, regardless of the harvest location. Like HP and the Masquelet's induced membrane, HFL usually consists of two layers, *i.e.* a thin superficial layer and a thick deep layer with almost orthogonal fibres. All three membranes feature a longitudinal thick layer with dense collagen fibres aligned along the long axis of the limb, providing structural integrity and scaffold manoeuvrability. The thin transverse layer functions as a containment barrier, potentially suitable for cell seeding. Unlike HP and the induced membrane, which have their thin layer inward, HFL can be harvested and reversed to place its thin external layer in close contact with the bone, while the deep longitudinal layer remains outward.

Among all ITT regions, the middle ones are the least variable in layer number and thickness, ensuring reproducibility in microstructural characteristics. Harvesting a large sample from the middle height of the ITT (Fig. 49), cut along fibre long axis obliquely downwards and forwards, allows to obtain a reproducible, resistant, one-piece sample that meets the OM requirements, sufficiently large for wrapping a CSBD.

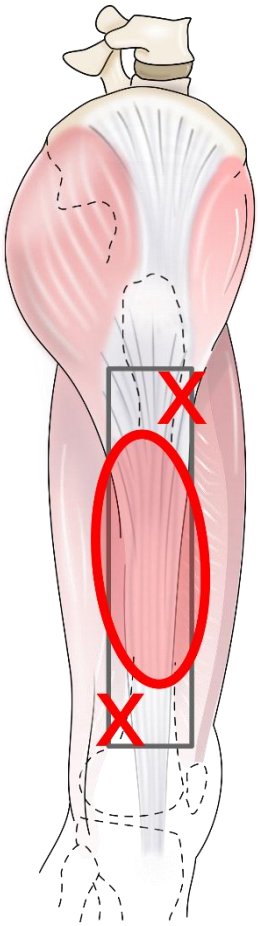

Figure 49. Representation of the best harvest zone for iliotibial tract scaffold. Red crosses: most variable zones, red circle: most reproducible zone, where the scaffold should be harvested.

– REQUIREMENT SPECIFICATIONS –

Requirement	Specification	Validation
Osteoconductive matrix		
Composition	- Col-1 membrane	V
Morphology	- 2 layers - Thickness (1 thin + 1 thick layers) - Large size - Shapeable	V V V
Biocompatibility	- No immunogenicity - Carrier for cells - No cytotoxicity	≈
Osteoinductive mediators		
Bioactivity	- Osteogenic GF - Osteogenic differentiation - Chondrogenic differentiation	≈
Osteogenic cells		
Osteogenicity	- Cell adhesion, proliferation, replication - Osseous ECM production	X
Mechanical stability		
Membrane properties	- Sheet malleable support - Resistance to handling - Isotropy or anisotropy?	V V ≈
In vivo model	**AND** - Stitchable - Mechanical stability	
Vascularization		
Vascular supply	- Angiogenic properties - Neoangiogenesis **OR** - Intrinsic vascular architecture - Functional vascular network	
In vivo transposition		
Clinical needs	- Off-the-shelf availability - One-stage surgery	

CHAPTER II. Decellularization

« If you want to achieve something you've never had, you have to try something you've never done. »

Translated from Pericles, 5th century BC

Research questions emerging from the Diamond

The first step toward the creation of the OM based on tissue engineering techniques is to decellularize the native fascia lata. Based on the wide panel of decellularization agents described earlier, the choice must be guided by respect for an appropriate balance between cell removal and ECM preservation. In our current practice, the most used decellularization agents are:

- Ionic detergent = Sodium dodecyl sulfate (SDS)
- Non-ionic detergent = Triton X-100
- Enzymes = Deoxyribonuclease (DNAse)
- Solvent = Acetone, ethanol

One method to process the most efficient decellularization is to combine agents and physical means[178]. The combination of the first three agents forms the protocol basically used in our laboratory, while the last ones take part of the protocol employed in our tissue bank, described earlier.

One of the goals of the next papers is to compare laboratory-based protocol to tissue bank one in terms of efficacy, balance cell removal/ECM preservation, cytotoxicity, biocompatibility, neovascularization and immunization.

This chapter aims to answer the following questions:

- **What is the best protocol for achieving decellularization?**
- **What is the best protocol for preserving ECM?**
- **Which protocol should be considered for further investigations?**

Paper 3 – HLA Awareness in Tissue Decellularization: A Paradigm Shift for Enhanced Biocompatibility, studied on the Model of the Human Fascia Lata Graft

Julie Manon, Robin Evrard, Louis Maistriaux, Lies Fievé, Daela Xhema, Ugo Heller, Lucien Van den Broeck, Julia Vettese, Jean Boisson, Thomas Schubert, Benoît Lengelé, Catherine Behets, Olivier Cornu

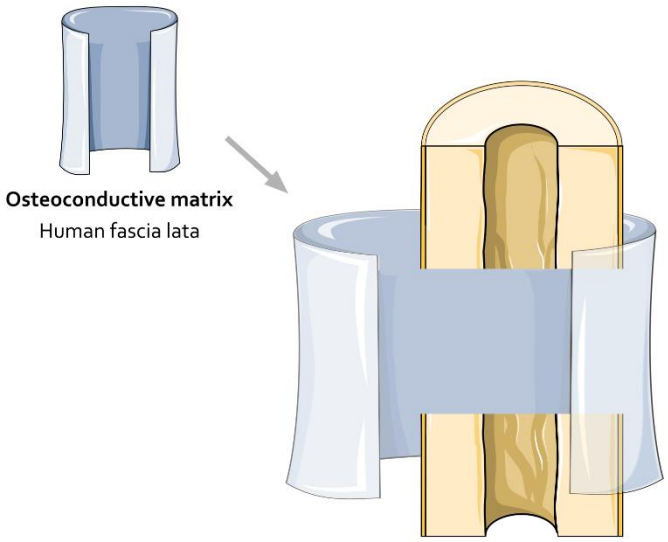

Published in

Biomaterials (IF=15.304)

doi: 10.1016/j.biomaterials.2024.122741

Abstract

Last twenties, tissue engineering has rapidly advanced to address the shortage of organ donors. Decellularization techniques have been developed to mitigate immune rejection and alloresponse in transplantation. However, a clear definition of effective decellularization remains elusive. This study compares various decellularization protocols using the HFL model. Morphological, structural and cytotoxicity/viability analyses, indicated that all the five tested protocols were equivalent and met Crapo's criteria for successful decellularization. Interestingly, only the *in vivo* immunization test on rats revealed differences. Only one protocol exhibited Human Leucocyte Antigen (HLA) content below 1% residual threshold, the only criterion preventing rat immunization with an absence of rat anti-human immunoglobulin G (IgG) switch after one month (N=4 donors for each of the 7 groups, added by negative and positive controls, n=28). By respecting a refined set of criteria, *i.e.* lack of visible nuclear material, < 50ng DNA/mg dry weight of ECM, and < 1% residual HLA content, the potential for adverse host reactions can be drastically reduced. In conclusion, this study emphasizes the importance of considering not only nuclear components but also MHC in decellularization protocols and proposes new guidelines to promote safer clinical development and use of bioengineered scaffolds.

Graphical abstract

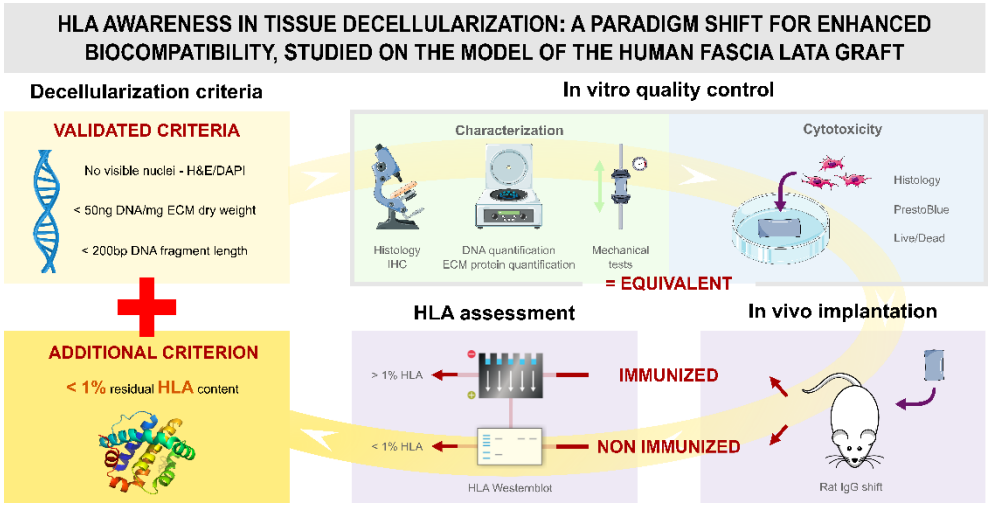

A. Introduction

Since several years, the field of tissue engineering has experienced exponential growth in terms of technique development, pathologic indications and clinical applications. One of the uppermost goal of tissue engineering processes is to counteract the drastic shortage of available organ and tissue donors[312]. A major challenge in transplantation surgery is the control of immune rejection including allorecognition, alloresponse[313–315] and immunosuppressive medication, all reasons why the decellularization was primarily elaborated[312,316]. A decade earlier, a high-level overview was written by Crapo et al. (2011) about tissue and whole organ decellularization[178]. Similar to subsequent authors, they described all the different acceptable methods to remove the cells while preserving the complex 3D ultrastructure of the ECM of a tissue. However, an accurate definition of effective decellularization has never been established. Does it mean no cell viability, removal of all cells or fragments or complete washout of immunogenic antigens? Some authors defined decellularization as the absence of positive staining for intact nuclei, while others considered a "significant" reduction in dsDNA amount compared to native samples[174,178,317–322]. One of Crapo's main goals was to establish quantitative metrics on a decellularization standard that has been proven to prevent negative host reactions upon implantation and to promote beneficial regenerative responses[178]. This standard requires:

- lack of visible nuclear material on routine histology (DAPI or H&E staining)
- < 50ng DNA/mg dry weight of ECM
- < 200bp DNA fragment length

Crapo's team and some other authors already mentioned the need to respect those criteria and to wash out all the cellular remnants[174,175,180,323–327]. Keane et al. explained that failure to follow these guidelines resulted in a less favourable host reaction, a swelling and seroma formation[174,324]. In order to minimize or prevent adverse immunologic response induced by allogenic or xenogenic scaffolds, it is essential to effectively remove antigenic epitopes linked to intracellular components but also to cell membranes[175,316,326–329]. However, the precise cellular components responsible for adverse host responses and the extent of their involvement are not fully understood[174,178,326,327]. Additionally, very little attention was paid to the host immune response after a bioengineered scaffold

transplantation in the past[326]. Since their definition took only nuclear components into account, these authors agreed that in the event of an association between cytosolic or membrane constituents and adverse host reaction, those criteria should be amended or upgraded[178,324].

After ABO blood group antigens, a major risk of human allograft hyperacute rejection is the HLA mismatch[313–315,325,326,330,331]. The HLA Class I, also known as the MHC-1, is a cell surface protein that is almost ubiquitous in the body. It enables the recognition of foreign molecules from our own[313–315,330]. This is a keystone of the cell immunity. Its genotypic match is usually mandatory for kidney and pancreas transplants and highly required for heart and lung ones[314]. As an example, prior to a renal transplant, a comprehensive immunologic assessment, including ABO blood group determination, HLA typing, screening for antibodies to other phenotypes, and cross-matching, are necessary to prevent antibody-mediated rejection[330,332]. The impact of an HLA mismatch can not only lead to acute or hyperacute rejection but also affect functional outcomes, remodelling, and the long-term viability of the graft[174,330,331,333,334].

If HLA and/or MHC-1 are so investigated in case of clinical allotransplantation, the same can not be said for decellularization and bioengineered scaffolds, studied in the literature. The first few links between *in vivo* clinical immune concepts and *in vitro* decellularization concepts were established through heart valve surgeries due to the higher immunogenicity resulting from the ABO and HLA mismatches, which are associated with graft failure in children[335]. Cryopreserved native heart valve allografts exhibit a massive immunogenicity with high levels of HLA class I and II antibodies already one month after the surgery, unlike decellularized ones[336–338]. Unfortunately, none of these studies correlated their results with decellularization criteria. Very recently (2023), the quality control of cell-free commercialized heart valves was reviewed to confirm that the DNA was below 10ng/mg dry weight for 90% of the vessel walls, with very good clinical outcomes[334], but still without association with a potential HLA threshold or immunogenicity. In another field, residual amounts of MHC-1 were found in commercialized bone blocks even after decellularization[339]. Fretwurst et al. suggested that these molecular remnants can trigger an immune response and lead to a graft failure, but they did not study the interaction with the *in vivo* immunogenicity. All other studies to our knowledge neither took HLA into account at all, for the most part, nor explored it only

qualitatively[340–344]. Studies and data correlation are lacking. The exact antigen threshold at which an immunization switch occurs is not yet defined, and no link exists to account for *in vivo* immunogenicity, the respect of decellularization criteria and antigen threshold, all together.

This study compares different decellularization protocols based on associations of chemical (non-ionic or ionic detergents and solvents), biologic (DNAse), and physical agents (agitation and freezing). All components are well known to combine membrane lysis, protein coagulation, defatting, and removal of cellular material in a duration depending on the tissue thickness and density[178]. The first goal was to investigate the most suitable decellularization protocol for HFL grafts, with the aim of creating a new bioengineered membrane to enhance bone and tissue healing. To achieve this goal, the effectiveness of cellular washout while preserving the ECM architecture was evaluated for all the protocols. Cytotoxicity testing was performed to ensure the absence of toxicity in the residual products of decellularization, thus providing a conducive environment for viable cells. The comparison of the decellularization protocols was finalized through *in vivo* implantation, evaluating aspects such as biocompatibility, revascularization, and immune response.

Nevertheless, the real intrigue of this paper extends beyond a simple comparison of protocols. It lies within the unanticipated findings that prompted a more profound exploration, aiming to unravel the underlying causes. This endeavour ultimately aimed to address a compelling question: "*Why does a thoroughly decellularized matrix retain immunogenicity after transplantation?*". This study explores a groundbreaking path in tissue engineering, focusing on the overlooked HLA and proposes to strengthen the definition of decellularization success according to the outcomes.

B. Materials & methods

Figure 50 summarizes the methodological plan. Precise subsections are described just after.

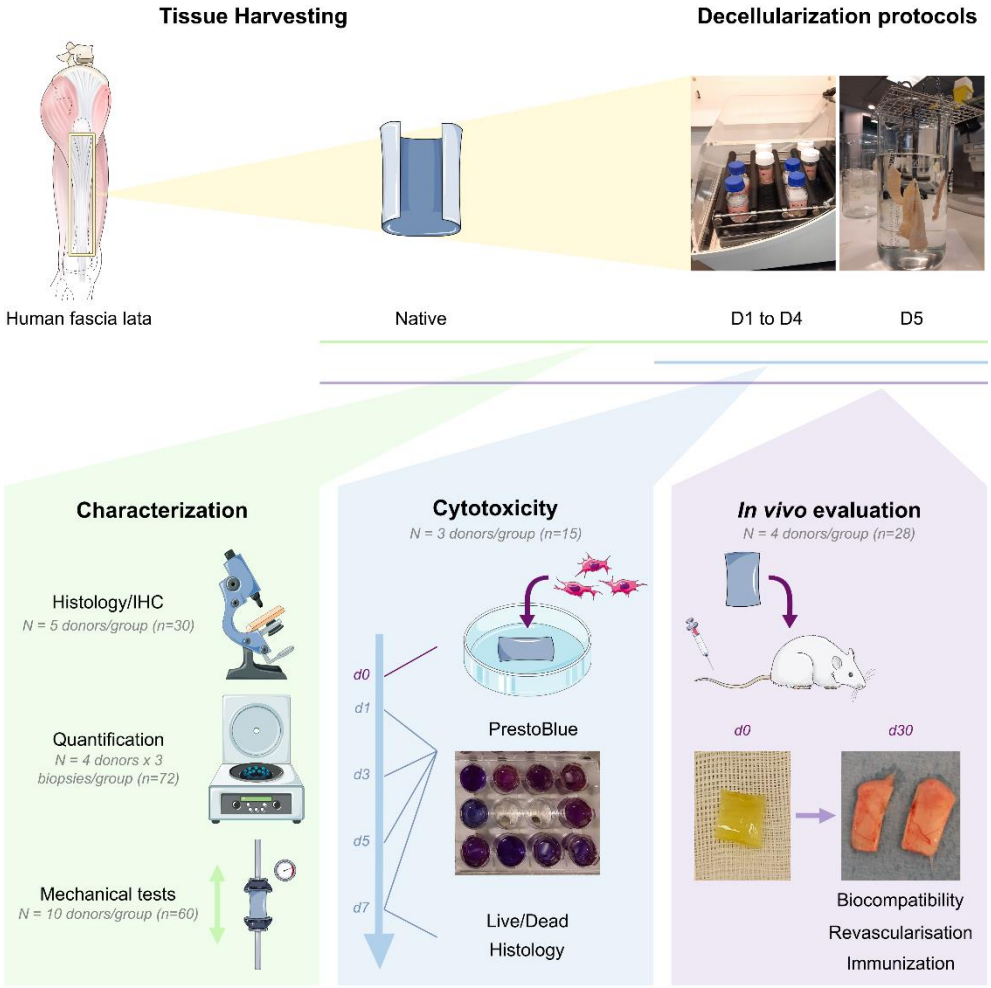

Figure 50. Flow chart illustrating the methodological plan. The yellow section outlines the different sample statuses analysed (native and decellularized). The study is then divided into three main sections: characterization of the samples, cytotoxicity assessment of decellularized tissues, and in vivo evaluation of biocompatibility, revascularization, and immunization following tissue implantation. Coloured horizontal bars indicate which samples are considered for each section of the study. D1 to D5: the five different decellularization protocols, do to d30: day number, N: number of donors, n: total number of samples.

B. 1. Human tissue harvesting

For most analyses, HFLs were obtained from cadaveric donors (N=5, four men and one woman; average age: 91.3 ± 1.8 years) that were received at the Human Anatomy Department of UCLouvain (IRB00008535, Brussels, Belgium), following

local ethics committee authorization (Ref 2021-30AOU-356 approved on September 13, 2021). Mechanical tests were conducted using an independent cohort of harvested tissues (N=10). Those HFL came from three men and three women (average age of 88.8 ± 3.2 years) sourced from the *Ecole de Chirurgie de Paris (Agence Générale des Equipements et Produits de Santé [AGEPS], Assistance Publique Hôpitaux de Paris [APHP])*. The study was conducted with the approval of the institutional review board (*Ecole de Chirurgie, AGEPS, APHP*, IRB00011591, Paris, France). All deceased donors had previously provided informed consent for their bodies to be used in medical research. The dissection technique was proceeded as previously described[290,291].

B. 2. Decellularization protocols

Five different decellularization protocols (D1 to D5) were compared in this study (Table 13).

Table 13. Decellularization protocols (D), from D1 to D5.

	Decellularization steps
Protocol number	
D1	SDS (12h) – Triton X-100 (4h) – DNAse (12h)
D2	Triton X-100 (12h) – SDS (4h) –DNAse (12h)
D3	SDS (24h) – Triton X-100 (4h) – DNAse (12h)
D4	Triton X-100 (24h) – SDS (4h) –DNAse (12h)
D5	Acetone – Ether – Ethanol – NaCl / NaOH – H_2O_2

SDS: sodium dodecyl sulfate, DNAse: deoxyribonuclease, NaCl: sodium chloride, NaOH: sodium hydroxide.

Four of the five protocols (D1 to D4) were based on immersion in SDS (1%, VWR, 27926.295), Triton X-100 (1%, VWR, M143) and type I bovine DNAse (25mg/L, 37°C, Roche, Sigma-Aldrich, 11284932001) under continuous agitation as usually described in *in vitro* experimentations[291]. The only difference was the sequence and immersion duration (Table 13). All the protocols included rinse with demineralized water (min 12h).

The fifth protocol (D5) was the one employed in our institutional tissue bank outlined beforehand[243,341,345]. Succinctly, it involved several steps performed under continuous agitation, separated by rinses of continuous flow of demineralized

water. The process began by successive baths of acetone and ether, followed by ethanol (70°), NaOH (1N) and hypertonic NaCl (7%) solution, and H_2O_2 baths. The properties of this solvent-based protocol ensured the removal of fat, digestion of cellular membranes, coagulation of proteins, precipitation of nucleic acids, and deactivation of prions, bacteria, and viruses (such as HIV, hepatitis C virus (HBV), and HCV). Each decellularized sample underwent a quality control assessment to check for any residual chemical reagents (acetone and H2O2), and the pH was adjusted to fall within the range of 7.0 to 7.85.

If storage was needed, samples (D1 to D5) were frozen and stored at -80°C. To ensure sterility for cytotoxic and *in vivo* tests, the final step of every protocol involved gamma-irradiation at a minimum guaranteed dose of 25kGy (IBA Mediris, Fleurus, Belgium). This protocol has been validated for representative bacteria, virus, and prion inactivation and has been used in clinical practice for more than 30 years [346–348].

B. 3. Characterization of decellularized tissues

Histology

Conventional histology allowed to analyse the micromorphology of the tissues. Fresh samples of 1cm² (N=5 donors for each group, *i.e.* the native and each of the decellularization protocols) were fixed in formaldehyde 4% (VWR, 9713.9010). After embedding in paraffin and sectioning in 5µm thick slices, standard staining protocols, including H&E, MT, Picrosirius Red (PSR), and AB were used. In addition, the sections were stained with 2'-(4-ethoxyphenyl)-5-(4-methyl-1-piperazinyl)-2,5'-bi-1H-benzimidazole trihydrochloride (Hoechst, 1:5000; Life Technologies, H3570) at a concentration of 2µg/mL to visualize DNA. All stained slices were visualized under a fluorescence microscope (40-fold magnification, AxioImager Z1, Zeiss, Oberkochen, Germany) for Hoechst stained ones and/or captured with slide scanners (Leica Microsystems, SCN400, Wetzlar, Germany or Panoramic ScanII slide scanner, 3DHistech, Budapest, Hungary) with a 20-fold Plan-Apochromat objective, for other staining. For annotation, the open-source Cytomine software (v.3.1.0., www.cytomine.org[349]) or SlideViewer software (v2.5.0., Budapest, Hungary) was used, respectively for each slide scanner.

Immunohistochemistry analyses

IHC analyses were performed on paraffin-embedded slices to detect MHC-1 and elastin, as previously described[290,291]. To start, endogenous peroxidase activity was deactivated using 3% H_2O_2 in methanol. The antigen retrieval process involved treating the sections with a combination of tris-EDTA buffer (Tris, Merck, 1.08387.250; EDTA, Sigma, E5134) and proteinase K (1:1000, Roche, 03115828001) at 37°C in the incubator for 5 and 20 minutes, respectively. Unspecific antigens were blocked with a solution of 5% BSA (Merck, 12659-500GM) in 0.05% TBS/Triton (Tris, Merck, 1.08387.250; Triton, VWR, M143) at RT for 1h. Depending on the chosen analysis, slices were then incubated with rabbit primary antibodies against MHC-1 (1:150, Abcam, ab134189) or mouse primary antibodies against elastin (1:100, Novus biotechne, NB100-2076) at 4°C overnight. Next, the incubation with peroxidase-conjugated anti-rabbit secondary antibodies (Envision, Dako, K4003) or anti-mouse secondary antibodies (Envision, Dako, K4001) at 4°C took an additional hour. The detection of the target proteins was achieved using DAB peroxidase substrate (Dako, K3468) at RT for 5 minutes, counterstained by haematoxylin. The mounted slices were then scanned with the same Leica slide scanner.

Cellular & extracellular matrix composition

Both intracellular component (DNA) and ECM contents (collagen, GAGs, and elastin) were quantified in exactly the same way as previously described[290,291]. The decellularized samples of each protocol were compared to each other as well as to native tissues. As brief reminder, three random biopsies were collected from four donors for each decellularization protocol and native tissues (n=3 biopsies x 4 donors x 6 tissue preparations = 72 biopsies analysed in total, 12 in each comparative group). Those biopsies (20, 25, 10, and 25mg for collagen, GAGs, elastin, and DNA quantification, respectively) were all freeze-dried and weighted dry. DNA was extracted using the DNeasy® Blood & Tissue kit (Qiagen, Hilden, Germany) and its concentration was measured using the Quant-iT PicoGreen DNA assay kit (ThermoFisher, Waltham, MA, USA). Collagen content in the ECM was quantified using the Quickzyme Total Collagen Assay (Quickzyme, Leiden, Netherlands). GAGs were extracted and their content was measured using the Blyscan Sulfated-GAG assay kit (Biocolor LTD., Carrickfergus, Northern Ireland),

while elastin quantification was conducted using the Fast Elastin assay kit (Biocolor LTD., Carrickfergus, Northern Ireland). To ensure accuracy, duplicates were prepared by filling the plates, which were then read three times. The average value from the three readings and duplicates was followed by the mean of the three biopsies which was taken as the final quantification for each group. The final DNA content was expressed as ng/mg of dry weight, while the ECM protein ones were as µg/mg of dry weight.

Mechanical evaluation

Each harvested HFL (N=10) was cut into six 2cm-wide and 5cm-long strips, one for each decellularization protocol and a native comparative (n=60). Prior to testing, the frozen specimens were thawed at RT for 2h. Uniaxial tensile tests were performed using custom-made jaws to prevent slipping. The length of the sample between the jaws and its width and thickness at the centre were measured with a calliper. A uniaxial elongation machine (34SC-5 single column, Instron Corp., Illinois Tool Works Inc., Glenview, IL, USA) instrumented with a 5kN load cell (2519 series, Instron Corp., Illinois Tool Works Inc.) was used. The tests included a preconditioning process with 10 consecutive cycles (speed=0.25mm/s, final strain=7%), two tensile tests at two different speeds (S1=0.25mm/s and S2=0.5mm/s, final strain=10%), and a final traction procedure until complete rupture (defined as at least a 40% drop in force, speed=0.25mm/s). Data related to force and displacement were collected and converted into stress and strain values using the appropriate formulas[290]. For each speed, the apparent elastic modulus was determined as the slope of the steepest linear part of the slope. The rupture stress was defined as the maximum load observed during the final traction test. All the values are expressed in MPa ± SEM.

B. 4. Cytotoxicity of decellularized matrices

The cytocompatibility and the absence of cytotoxicity of the decellularized products were verified using human fibroblast seeding for 7 days.

Fibroblast seeding

After decellularization and sterilization processes, HFL (N=3 donors for each decellularization protocol, n=15), cut into 1cm² patches, were rehydrated with

sterile PBS solution (Sigma-Aldrich, 59321C-1000ml) within sterile Cell-Crown™ inserts (12-well plate inserts, Sigma-Aldrich, Z742383-6EA) at 37°C for 1h. They were then incubated overnight at 37°C using proliferation medium (PM), namely the Dulbecco's Modified Eagle Medium (DMEM, Westburg, BE12-604F) supplemented with fetal bovine serum (FBS, 10%, Gibco, 10270-106), penicillin-streptomycin (1%, Gibco, 15140-122), and amphotericin B (1%, Gibco, 15290-026). The following day, designated as day zero (d0), 5×10^5 primary cultured human fibroblasts were seeded onto each patch, dry incubated at 37°C and 5% CO_2 for 2h to enhance cell adhesion. The PM was then added and changed every two days just after the Prestoblue analysis. After one week, cell occupation was assessed by H&E staining, and cell viability by Live/Dead test. Positive controls (C+, cells seeded into four wells without scaffold) and a negative control (C-, one scaffold in a well without seeded cells) were included to corroborate comparative evaluation.

Growth kinetics – PrestoBlue

Cell growth kinetics was evaluated using the PrestoBlue Assay (PrestoBlue™ Cell Viability Reagent, ThermoFisher, Invitrogen, A13261) every two days starting from the first day post-seeding (d1, d3, d5 and d7). At each timepoint, the PM was replaced with 2.5mL of preheated PrestoBlue solution (10%) and incubated at 37°C for 2h. Then, 100µl of the solution were transferred into a 96-well opaque plate. Fluorescence was measured three times using a microplate reader (SpectraMax i3x, Molecular Devices; Sunnyvale, CA, USA) at Ex:560/Em:590nm. The mean of the three readings was followed by the average of the three donors. The fluorescence ratio between d7 and d1 also highlighted the growth rate at the end of the culture.

Viability – Live/Dead

At d7, the cell viability on each entire patch was assessed using Live/Dead staining (LIVE/DEAD™ Viability/Cytotoxicity Kit, ThermoFisher, Invitrogen, L3224) following the manufacturer's protocol. After three slow delicate rinses with sterile PBS, all the wells were immersed in 2mL of the working solution. Plates were kept away from light for 40 minutes. Following two additional washes, the patches were mounted onto glass slides with Dako fluorescent mounting medium. They were then observed using the AxioImager Z1 microscope and analysed with the AxioVision software (v.4.8.2.0., Zeiss, Oberkochen, Germany). A total of five

pictures were captured: one at the centre and four at the corners, all at 2.5-fold magnification, to ensure an average representation of the whole sample area. Fiji software (ImageJ-win64), an open-access software available at *https://imagej.nih.gov/ij/index.html*, allowed us to determine the cell viability by averaging the ratio of living cells (green dots) to the total number of cells (living-green + dead-red cells) from the five pictures of each seeded scaffold and C+.

B. 5. In vivo evaluation of biocompatibility, neovascularization & immunization

Subcutaneous implantation in rat allowed to investigate the biocompatibility (classical histology) of HFL after the different decellularization protocols, their revascularization potential (IHC for CD31), as well as their immunotolerance or immunogenicity (IHC for CD3 and CD68, flow cytometry for IgG, and western blot for HLA). The entire experiment was approved by the local ethics committee (Ref 2021/UCL/MD/067, approved on November 15, 2021).

Surgical procedure

HFL patches (1cm²) from four different human donors were implanted subcutaneously on the back of adult female immunocompetent Wistar rats (N=4 donors for each of the 7 groups = 28 rats in total). Groups comprised all the decellularization protocols (from D1 to D5), native patches as positive controls (N) and negative controls (agarose, A). Under general anaesthesia with continuous isoflurane ventilation (3%), a median incision was made along the spine of the rat. A pocket under the skin was created and one patch was inserted per rat. The wound was closed by Donati sutures using 3/0 Vicryl thread. All the rats were euthanised on postoperative day 30 (d30). The patches were explanted with a thin layer of surrounding connective tissues and directly fixed in the formaldehyde for further histology.

Immunohistochemistry & Tyramide signal amplification

The vascularization of the implants was evaluated by CD31 IHC staining of endothelial cells. IHC also permitted to explore the lymphocytes (CD3) and the macrophages (CD68) of the inflammatory reaction. The protocol was quite similar as in section B.3, subsection « Immunohistochemistry analyses ». Only the steps

that changed are described here. The antigen retrieval was done with tris-EDTA buffer for IHC against CD31, and with citrate buffer (pH=5.7, citric acid, Merck 1.00244.0500; Na3 citrate, Alfa Aesar A12274-500 gr) for IHC against CD3 and CD68, all in the microwave (900W, 4min10 – 90W, 15min – 900W, 1min30 – Back to RT, 15min). Primary antibodies were rabbit anti-CD31 (1:2000, Abcam, ab182981), anti-CD3 (1:100, Abcam, ab828), and mouse anti-CD68 (1:600, Abcam, ab31630), followed by peroxidase conjugated anti-rabbit (Envision, Dako, K4003) and anti-mouse antibodies (Jackson ImmunoResearch, 715-035-151), respectively, at RT for 45min. Each IHC was separately quantified using QuPath Software (v0.3.0., University of Edinburgh)[252]. Two slices were analysed per patch and their mean DAB amount was averaged with the four donors for each group. For IHC against CD31, outcomes were expressed as the mean percentage (%) of DAB positive surface out the whole tissue area. However, for IHC against CD3 and CD68, the artificial intelligence of the software was trained to recognize positive cells (DAB-stained) or negative ones (haematoxylin). These outcomes were presented as the average percentage (%) of cells that exhibited staining for CD3 or CD68, out of the total number of cells stained with haematoxylin. The results were also expressed as the number of positive cells on the total tissue surface (cells/mm²).

To illustrate all the three proteins together, immunofluorescence using tyramide amplification signal, a multiplex technique, was conducted on paraffin-embedded slices. All the specific steps just described for IHC against CD68, CD31 and CD3 were performed in this respective order. The only difference was that each entire sequence was separated by a signal amplification of each respective secondary antibody. After three washes, the amplification was performed with AlexaFluor (AF) Tyramide 555 (1:200, InvitroGen, B40955) for CD31, AF Tyramide 647 (1:200, InvitroGen, B40958) for CD68, and AlexFluor Tyramide 488 (1:200, InvitroGen, B40953) for CD3, each time in borate solution (boric acid, Sigma B6768-500gr; NaCl, VWR, 27810.295-1kg; H_2O_2 0.003%) at RT for 10 minutes. Hoechst (1:1000, Sigma, 14533-100mg) was used for counterstaining. Finally, the slices were scanned with the fluorescent slide scanner Axioscan.z1 (Zeiss, Oberkochen, Germany). To ensure accuracy, a negative control, without the primary antibody, was included for both standard IHC and multiplex IHC.

Flow cytometry

Immunization was investigated by assessing rat anti-human IgG after 30 days of implantation. Both the day of implantation (do) and the day of removal (d30), a volume of 500µL of blood was obtained through a tail puncture. The extracted blood samples were centrifuged at 3000rpm (1811xg) for 15 minutes, and the resulting serum was stored at -80°C until the flow cytometry. Freshly isolated human peripheral blood mononuclear cells (PBMCs) were exposed to recipient serum at RT for a duration of 30 minutes in the dark, which was heat-treated at 56°C for 35 minutes to inactivate complement proteins. The cells were then washed twice with fluorescence-activated cell sorting buffer (PBS containing 3.6% FBS (Lonza, DE14-802F) and 1% sodium azide (Sigma-Aldrich, S2002)). Subsequently, a saturating amount of AF 488 goat anti-rat IgG (H+L) Cross-Adsorbed Secondary Antibody AF 488 (ThermoFisher, A-11006) was added and incubated at RT for another 30 minutes in the dark, followed by two rounds of washing. To account for nonspecific reactions, each analysis involved the appropriate AF 488-conjugated antibody with PBMCs only. The cells were analysed using the BD g Calibur (BD Bioscience Benelux NV, Belgium) driven by CellQuest Pro software (BD Bioscience Benelux NV, Belgium). A shift of more than 10 channels in average fluorescence intensity was considered a positive reaction when comparing donor PBMCs tested with post-transplantation serum (d30) to pre-transplantation one (do). The percentage (%) of PBMCs in this positive area (shift zone) at do, d30, and the difference between d30 and do permitted to quantitatively compare the immunization potential of each decellularization protocol.

Western blot

A random biopsy of each tissue (N=3) weighing from 20 to 50mg was chopped, lysed and homogenized with a RIPA buffer containing protease inhibitor cocktail (Sigma-Aldrich, P8340) and Pho-Stop (Roche, Basel, Switzerland, 04906837001) before being melded using the Precellys Homogenizer (Bertin Technologies SAS, France) by consecutive cycles at 7200rpm (8114xg). The supernatant was collected. Its protein concentration was determined using the Pierce™ BCA Protein assay kit (ThermoFisher, 23227) and was normalized depending on the biopsy weight. A protein quantity of 10µg was loaded per well on 12% SDS-PAGE gel and migration

buffer (Biorad, 161-0772) permitted the migration under 140 V for 60 minutes. The proteins were transferred by electrophoresis onto nitrocellulose blotting membranes (Hybond ECL-Amersham, 10600003) using a constant voltage of 100 V for 90 minutes in transfer buffer (Tris-base, Merck, 1.08387.2500; Glycine, Millipore, 1.04169.1000; SDS, VWR, 2.7926.295; methanol, VWR, 20903.368). TBS with 0.1% Tween and 5% BSA was used to block the membranes at RT for 1h. Primary anti-MHC class I antibodies (1/1000, Abcam, ab134189) were incubated at 4°C overnight. Membranes were then washed in TBS-Tween and incubated with the HRP-conjugated anti-rabbit secondary antibody (1/5000, ThermoFisher, 31460) at RT for 1h. Subsequently, CL-X Posure® films (ThermoFisher, Waltham, MA, USA) were used to develop the membranes with ECLTM Western Blotting Detection Reagents (GE Healthcare, Chicago, IL, USA). After the stripping of first antibodies (Stripping buffer, ThermoFisher, 21059), same steps were repeated using primary antibody against beta-actin (1/10000, Sigma, Burlington, MA, USA, A5441) and anti-mouse secondary antibody (1/5000, ThermoFisher, 31430). As beta-actin is a cytosolic protein, released and washed by decellularization processes, HLA level was normalized to its own positive control (native corresponding sample, N-HLA). The films were scanned and subjected to densitometry using Fiji software (ImageJ-win64).

B. 6. Statistical analyses

The data of all processed and native tissues were statistically compared with SPSS software (V.28.0.1.1 (15), IBM SPSS, Inc., Chicago, IL, USA) and GraphPad Prism (v.8.0.1, GraphPad Software, San Diego, CA, United States). Shapiro-Wilk tests and QQ plots were conducted to verify the normality of continuous variables. As they did not all follow a normal distribution, the differences between all the six groups (or seven in case of negative control) were analysed using Kruskal-Wallis tests, followed by Dunn's multiple comparisons tests. For data from HLA assessment, which all followed a Gaussian distribution, a one-way ANOVA was performed to compare all the groups, followed by Bonferroni's multiple comparison tests. All the tests were conducted as two-tailed analyses. A statistically significant difference was consistently determined with a p-value set at 0.05. Data are presented as means ± SEM or 95% confidence interval of the mean (95% CI).

C. Results

C. 1. Characterization of decellularized tissues

Decellularization

As previously shown[291], the macroscopic aspect of native and decellularized HFL was the same for all the five protocols and did not enable to differentiate them (data not shown). At histological analysis with H&E and Hoechst staining, no more cells were visible in both superficial and deep layers of D1 to D5 decellularized samples as compared to native HFL (Fig. 51 – a). Microscopically, MHC-1 also appeared absent in the majority of decellularized cases, with only a very few slices showing scattered faint DAB spots. The Crapo's criteria[178], used to define the success of the decellularization, were met with a DNA content always significantly below the critical threshold of 50ng/mg of dry weight (Fig. 51 – b and Supplementary data – Table 16). None of the decellularization protocol was significantly different from each other for DNA content ($p>0.05$).

Extracellular matrix components

At histological analysis, the collagen did not appear drastically altered by all the decellularized protocols neither qualitatively nor quantitatively (Fig. 52 – a, MT and PSR). The deep layer seemed sometimes less dense, and fibres seemed sometimes wavier (as illustrated for D3 and D5 tissues) but without any impact on the content (Fig. 52 – b). Assessment of GAGs and elastin with AB staining (Fig. 52 – a, AB) and IHC (Fig. 52 – a, Elastin), respectively, was not conclusive and required specific quantitative assays which highlighted their significant loss (Fig. 52 – c and d, and Supplementary data – Table 16).

None of the decellularization protocol was significantly different from each other, whether for collagen, GAG or elastin content ($p>0.05$).

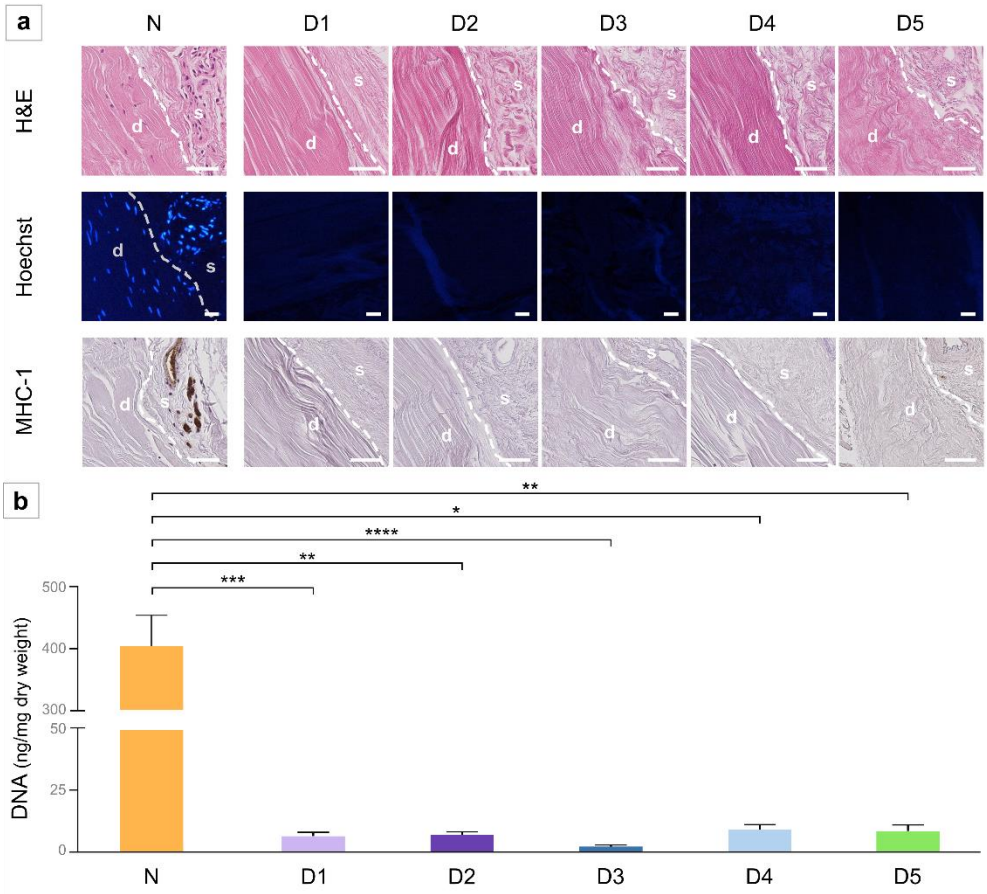

*Figure 51. Assessment of cellular components in native (N) and decellularized (D1 to D5) human fascia lata samples. (a) Qualitative analysis with histology (H&E: haematoxylin and eosin staining), fluorescence microscopy (Hoechst staining) and immunohistochemistry (MHC-1: major histocompatibility complex class 1). (b) Quantification of deoxyribonucleic acid (DNA). s: superficial layer, d: deep layer. White scale bars: 50µm. Error bars: SEM. *: p<0.05, **: p<0.01, ***: p<0.001, ****: p<0.0001.*

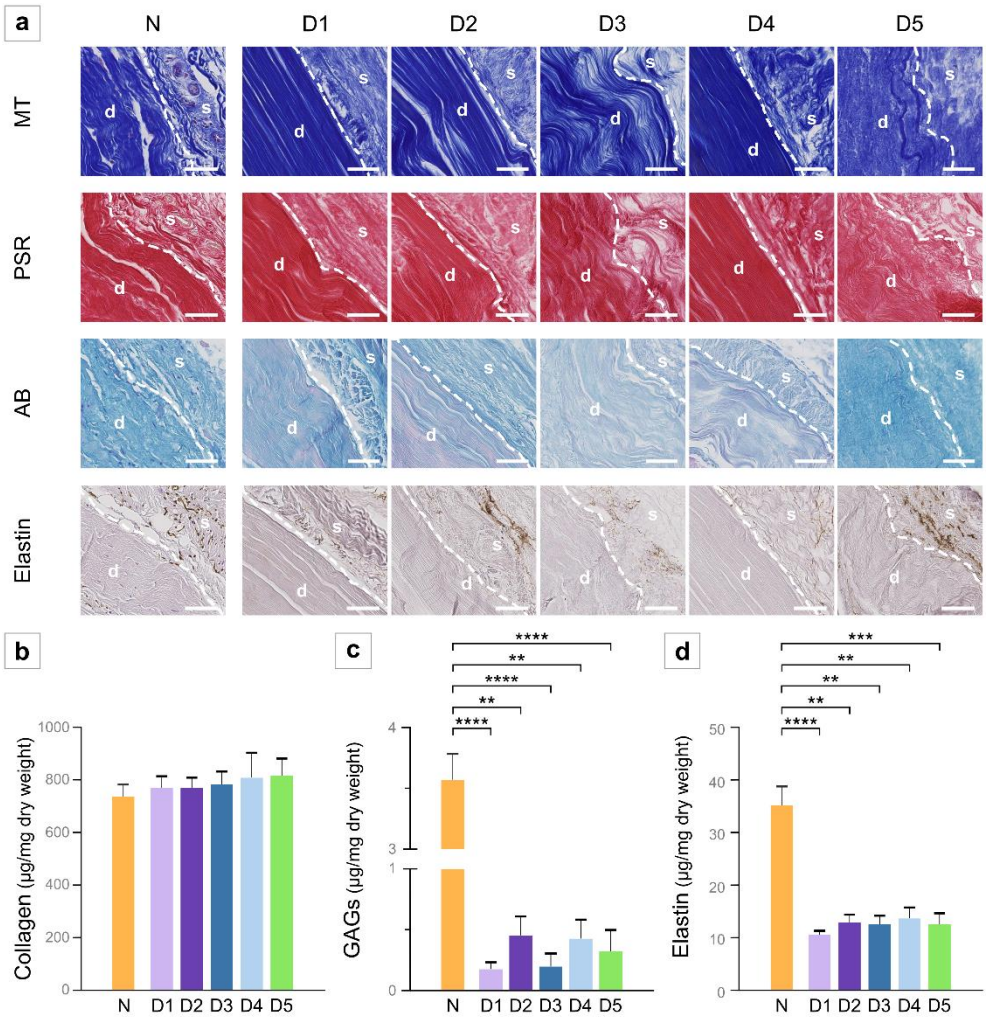

*Figure 52. Assessment of extracellular matrix for native (N) and decellularized (D1 to D5) samples of human fascia lata. (a) Qualitative histological analysis of collagen fibres (MT, Masson's trichrome and PSR, picrosirius red staining), and glycosaminoglycans (GAGs) (AB, Alcian blue staining), as well as elastin immunohistochemistry. (b) Quantification of collagen content. (c) Quantification of GAGs. (d) Quantification of elastin content. s: superficial layer, d: deep layer. White scale bars: 50µm. Error bars: SEM. **: p<0.01, ***: p<0.001, ****: p<0.0001.*

Mechanical characteristics

The stress-strain curve of all the native and decellularized tissues followed the same ascending shape corresponding to the classic J-shape of connective tissues (Fig. 53). The different decellularization protocols did not alter the high stiffness

region, which occurs at large strain values (L/L0-1>0.04). On the contrary, the low stress region extends to lower strain values for the decellularized tissues compared to native ones. This means that for a given stress, the decellularized tissue curves show a smaller strain.

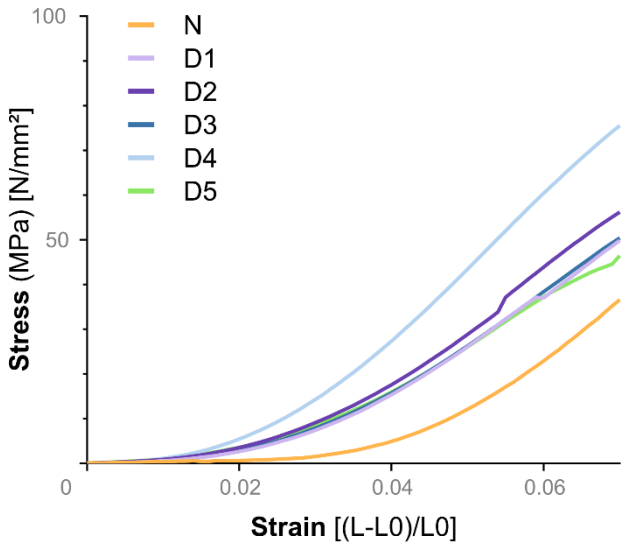

Figure 53. Stress-strain average curve of native (N) and decellularized (D1 to D5) samples. MPa: megapascal, N: newton, L: length, L0: initial length.

Regarding the mean values, the apparent elastic moduli of high strain region were similar but the stress at rupture was lower for D5 (Table 14).

Table 14. Apparent elastic modulus and rupture stress outcomes after tensile tests applied to native and decellularized (D1 to D5) human fascia lata. S1: speed 1 (0.25mm/s), S2: speed 2 (0.5mm/s). Data are expressed as mean ± standard error of the mean (SEM).

	Apparent elastic modulus		Rupture stress
Tissue status	S1 *(MPa)*	S2 *(MPa)*	*(MPa)*
Native	1533.6 (± 50.4)	1545 (± 55.0)	96.8 (± 3.2)
D1	1471.5 (± 131.5)	1547.98 (± 108.5)	106.8 (± 7.4)
D2	1519.6 (± 126.3)	1485.9 (± 154.9)	92.1 (± 7.7)
D3	1293.8 (± 84.5)	1422.1 (± 101.0)	92.0 (± 65.1)
D4	1661.7 (± 82.4)	1675.4 (± 85.8)	102.8 (± 6.9)
D5	1509.4 (± 127.8)	1442.98 (± 122.4)	83.2 (± 9.4)

C. 2. Cytotoxicity of decellularized matrices

After seven days of culture, human fibroblasts were well seeded and spread on the entire patch surface independently of the decellularization protocol (Fig. 54 – a, H&E). All these cells were qualitatively viable at the end of the culture and dead cells were quite absent suggesting a welcoming environment for cellular growth (Fig. 54 – a, Live/Dead).

Interestingly, although the initial cell growth on the decellularized patches was lower than that of the cells into positive control wells (C+), their average growth slope was higher, independently of the decellularization protocol, and led to similar and even higher values as soon as day 3 (Fig. 54 – b).

The difference was highlighted by the ratio of d7/d1 (Fig. 54 – c). While C+ expressed a slight growth over the 7 days (ratio=1.105), decellularized patches enhanced the cell proliferation (mean ratio=2.118).

Quantitatively, the viability at d7 was statistically non-different ($p>0.05$) between C+ (88.05 ± 2.73%) and decellularized patches (D1: 92.00 ± 2.20%, D2: 92.45 ± 1.98%, D3: 89.84 ± 1.81%, D4: 83.12 ± 3.81%, and D5: 93.91 ± 0.98%) (Fig. 54 – d).

All these observations confirmed the absence of cytotoxicity of the decellularized products and attested to a good cytocompatibility of the engineered patches.

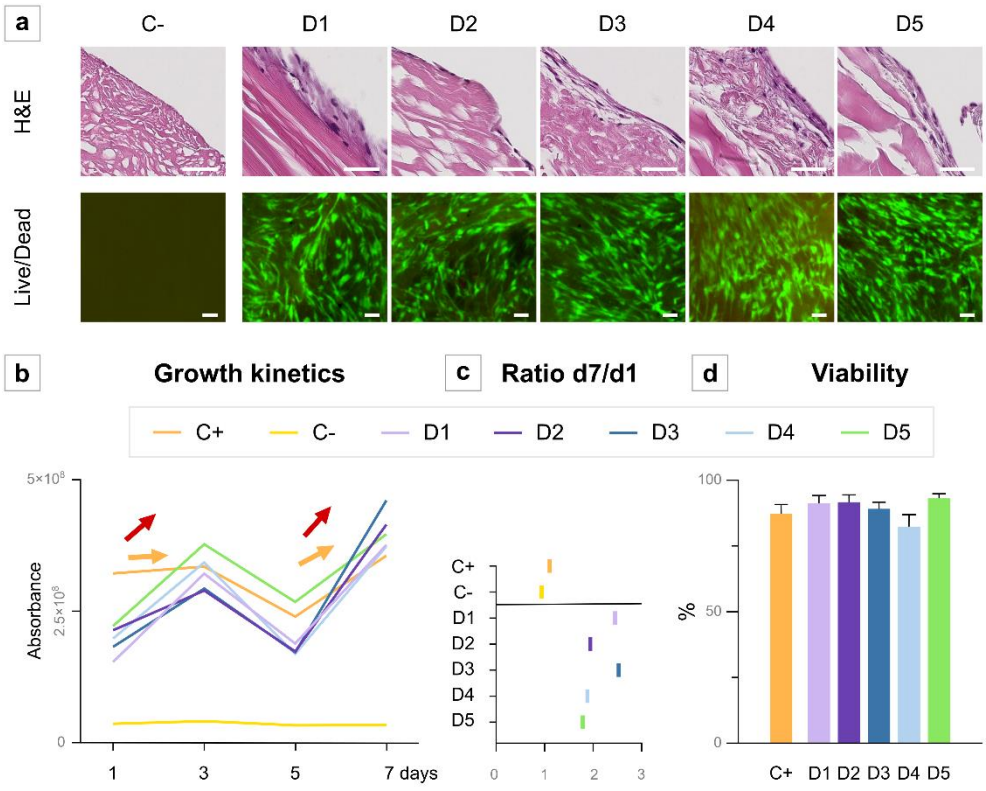

Figure 54. Assessment of cytocompatibility after human fibroblast seeding on decellularized human fascia lata (HFL). (a) Qualitative histological and Live/Dead analysis. (b) Quantitative analysis of cell growth kinetics (PrestoBlue Assay). (c) Ratio of cell growth between the end (d7) and the beginning (d1) of the experiment. (d) Quantitative analysis of viability (Live/Dead). C-: negative control (HFL without cells), C+: positive control (cells without HFL), D1 to D5: the five decellularization protocols, H&E: haematoxylin and eosin. Orange arrow: average growth of native samples, red arrow: average growth of decellularized samples. White scale bars: 50µm. Error bars: SEM.

C. 3. In vivo evaluation of biocompatibility, neovascularization & immunization

Biocompatibility

At explantation, all the implants showed macroscopic integration within the surrounding tissue except agarose. At d30, the native explants were surrounded by a thick layer of connective tissue with numerous inflammatory cells (Fig. 55 – a, between dotted and dashed lines), and the depth of the implant remained rather acellular (Fig. 55 – a, star zone). The decellularized tissues (D1 to D4) displayed a thickness spectrum of connective tissue external layer as well as a density spectrum of inflammatory cells surrounding the samples. For example, in figure 55 – a, the outer cellular shell was absent or difficult to delineate around D1, D2 and D4 implants, while it was somewhat thick around D3 implant. Some decellularized HFL samples were not fully encapsulated but completely invaded by many inflammatory cells (D2 and D4). Only the D5 samples displayed no real fibrous capsule, no thick inflammatory cells layer, no tissue digestion, and showed however a few cellular invasion close to a normal, low-inflammatory or low-immunogenic situation.

*Figure 55. Assessment of biocompatibility, revascularization and inflammatory response of native (N) and decellularized (D1 to D5) tissues at d30 after transplantation in Wistar rats. (a) Qualitative histological analysis (H&E: haematoxylin and eosin, MT: Masson's trichrome) and immunofluorescence detection of CD31, CD3 and CD68 (TSA: tyramide signal amplification). Quantitative analysis of proportion of cells positive for CD31 (b), CD3 (c) and CD68 (d). Violin plots show the median, the first and third quartiles, the maximum and minimum values, as well as the frequency represented by the width of the plots. (e) Circulating rat anti-human IgG at do and d30 after transplantation, depending on native or decellularized tissues. Arrows show the shift or the stay of IgG pattern. A: agarose (negative control), dotted lines on histology: between the neovascularized layer and the inflammatory cell layer, dashed lines on histology: between the inflammatory cell layer and the HFL depth, White *: inside the HFL sample, dotted lines into violin plots: 1st and 3rd quartiles, dashed lines into violin plots: medians, do: day of implantation, d30: day of explantation. Black scale bars: 1mm, red scale bars: 100µm. **: p<0.01.*

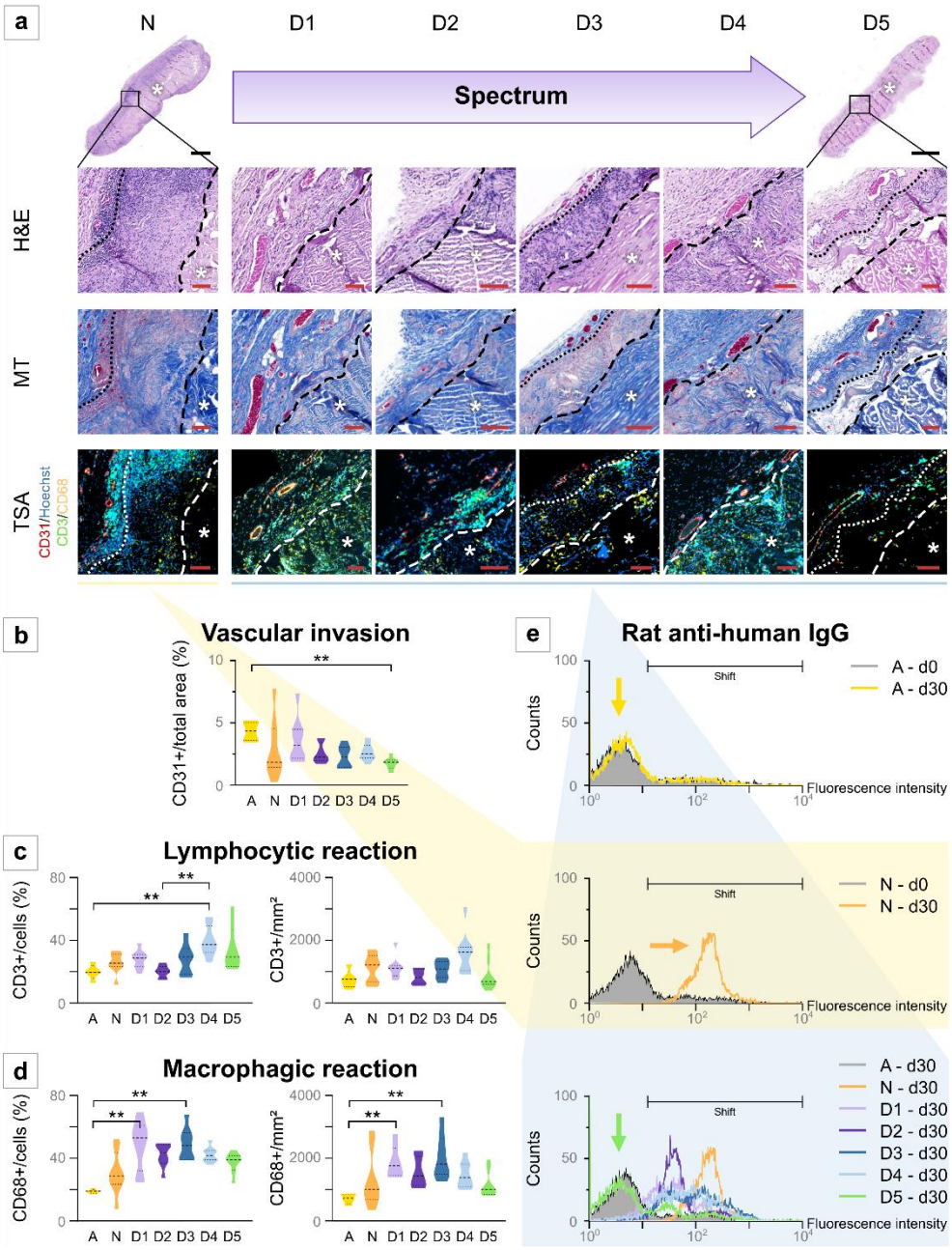
a
N
D1
D2
D3
D4
D5
Spectrum
H&E
MT
TSA
CD31/Hoechst
CD3/CD68
b
Vascular invasion
CD31+/total area (%)
A N D1 D2 D3 D4 D5
c
Lymphocytic reaction
CD3+/cells (%)
CD3+/mm²
d
Macrophagic reaction
CD68+/cells (%)
CD68+/mm²
e
Rat anti-human IgG
Counts
Shift
Fluorescence intensity
A - d0
A - d30
N - d0
N - d30
D1 - d30
D2 - d30
D3 - d30
D4 - d30
D5 - d30

Vascular invasion

Whereas native explants showed a vascular layer only outside the thick layer of inflammatory cells (Fig. 55 – a, left to the dotted lines), neo-vessels were present in the periphery of decellularized samples but were also able to penetrate the latter. Their proportion was almost statistically equivalent in all groups (Fig. 55 – b) but the vascularization of D5 (1.76 ± 0.17%) was lower than that of agarose (4.33 ± 0.33%) (p=0.0059). Even if the quantity of neo-vessels seemed to decrease in decellularized tissues, their localization was more spread and homogeneous.

Immunization

Despite the qualitative observation that D5 did not have a thick outer layer of inflammatory cells nor a massive invasion to resorb the tissue, the quantitative evaluation was not able to highlight a significant lower amount of inflammatory cells than in the other groups. D4 was the protocol with the most abundant lymphocytic reaction (39.44 ± 3.47% of CD3+ cells out of the total amount of cells), significantly more than D2 (20.10 ± 1.34%, p=0.0015) and agarose (19.74 ± 2.13%, p=0.0099) (Fig. 55 – c). However, when considering the number of cells on the tissue surface (cells/mm²), the groups were not statistically different from each other, suggesting that even if the total amount was higher, lymphocytes were more homogeneously distributed in decellularized tissues. Concerning the macrophages (Fig. 55 – d), D1 (49.03 ± 5.60%, p=0.0030; 1898 ± 175.6 cells/mm², p=0.0063) and D3 (49.31 ± 3.69%, p=0.0027; 2056 ± 252.2 cells/mm², p=0.0030) were statistically more reactive than the agarose (19.12 ± 0.64%; 730.4 ± 70.8 cells/mm²), in terms of CD68+ cells out of the total amount of cells, as well as on the surface area, respectively. The inflammatory cellular response of native tissues was not shown different by quantitative analyses compared to all the decellularization protocols.

However, some rats became immunized against human antigens after 30 days. While the agarose was completely inert and no immunogenic (Fig. 55 – e), rats receiving native tissues showed an IgG shift and became completely immunized at d30. Regarding the decellularization protocols, various shift intensities were seen for D1 to D4. Only the D5 never led to an IgG shift and was considered non immunogenic at all. The table 15 quantitatively summarizes those observations

and shows that only the agarose (14.73% shifted IgG at d30, -10.42% shifted IgG difference (d30-do)) and the D5 (24.83% shifted IgG at d30, -0.38% shifted IgG difference (d30-do)) permitted to preserve rats from immunization at d30.

Table 15. Quantification of rat anti-human IgG in all surgical groups. SEM: standard error of the mean, do: day of implantation, d30: day of explantation, A: agarose, N: native HFL, D1 to D5: the five decellularization protocols.

	Rat anti-human shifted IgG (%)		
Tissue status	do *mean (± SEM)*	d30 *mean (± SEM)*	Difference (d30 – do) *(%)*
A	25.15 (± 5.47)	14.73 (± 0.79)	-10.42
N	25.49 (± 4.96)	82.97 (± 15.72)	57.47
D1	26.69 (± 8.22)	45.24 (± 13.63)	18.55
D2	37.90 (± 19.60)	77.26 (± 17.22)	39.36
D3	37.38 (± 13.98)	59.06 (± 17.20)	21.68
D4	20.74 (± 4.94)	46.21 (± 16.38)	25.48
D5	25.20 (± 12.20)	24.83 (± 4.91)	-0.38

After these results, we went back to the H&E staining. Even if H&E stained slices seemed to be completely washed at a 20-fold magnification after decellularization (Fig. 56 – a), some residual cellular components can be viewed at a 40-fold magnification as illustrated by an example on D2 sample. These corresponded to membrane remnants containing HLA, illustrated by the IHC against MHC-1. The residual HLA was thus semi-quantified in each tissue by western blot. Even if the HLA content was significantly decreased after all decellularization protocols (Fig. 56 – b, $p<0.0001$), only upon zooming in on D1 to D5, it became evident that only D5 fell below 1% residual HLA threshold (Fig. 56 – c).

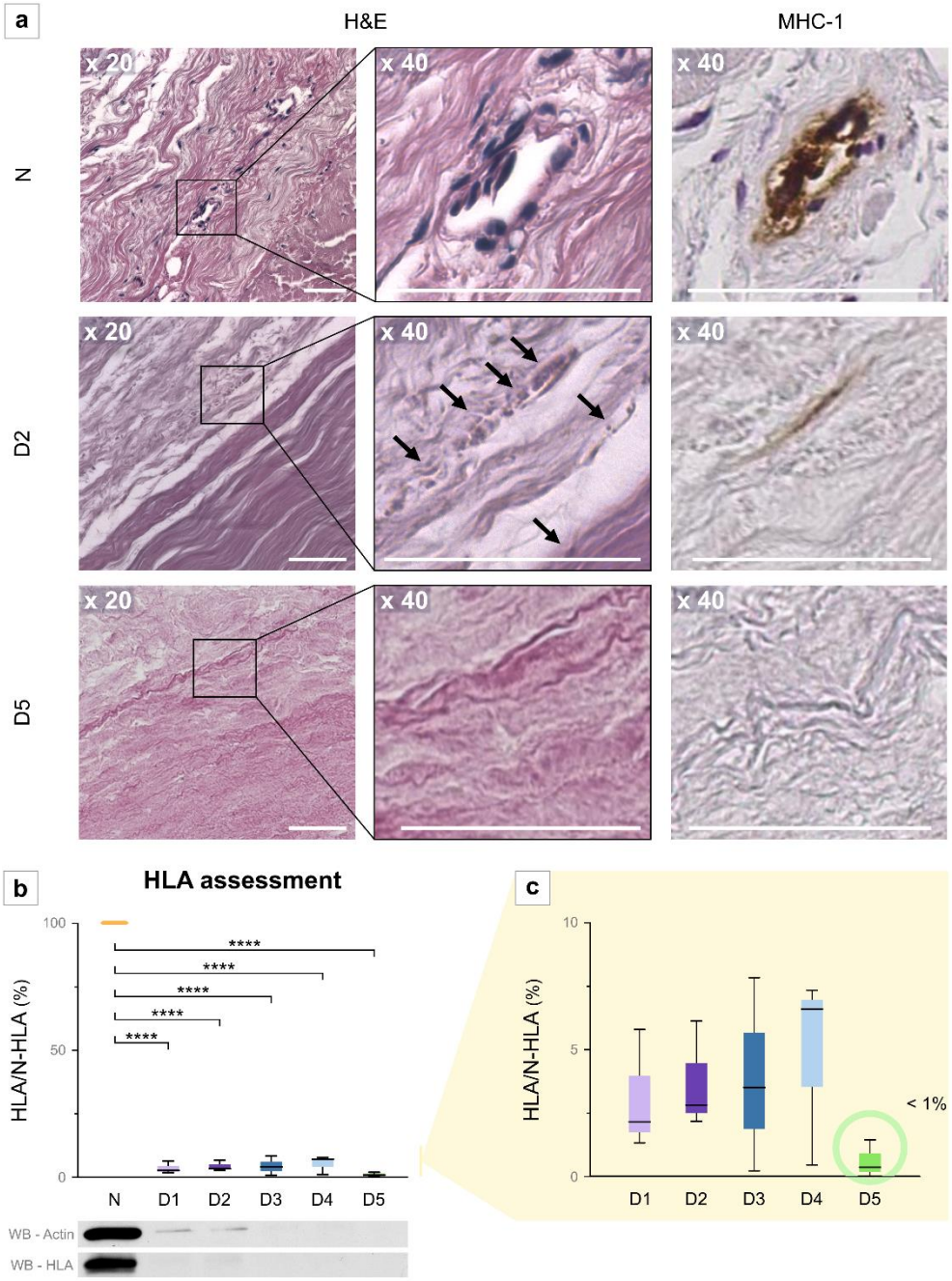
a
H&E
MHC-1
N
D2
D5
x 20
x 40
x 40
x 20
x 40
x 40
x 20
x 40
x 40
b
HLA assessment
HLA/N-HLA (%)
100
50
0
****
****
****
****
****
N
D1
D2
D3
D4
D5
WB - Actin
WB - HLA
c
HLA/N-HLA (%)
10
5
0
< 1%
D1
D2
D3
D4
D5

*Figure 56. Deeper investigation of rat immunization. (a) Qualitative review of haematoxylin and eosin (H&E) stained slices as well as major histocompatibility complex class 1 (MHC-1) immunohistochemistry, and comparison between native (N) and decellularized (D2 and D5) tissues. Black arrows show the potential membrane remnants. (b) Human Leucocyte Antigen (HLA) assessment with western blot and comparison between native and decellularized (D1 to D5) tissues. (c) Zoom in the western blot analysis of only decellularized tissues. N-HLA: HLA content of native tissues, WB: western blot. White scale bars: 50µm. ****: p<0.0001.*

D. Discussion

The five decellularization protocols tested in the present study met the Crapo's criteria, namely the absence of visible nuclei on H&E and Hoechst stained sections and the DNA content under the critical threshold of 50ng/mg of dry weight ($p<0.05$)[178]. None of the protocols gave different results from each other, suggesting that all succeeded to reach a full decellularization, following this definition. Quantitatively, all the decellularization processes altered the GAGs and elastin content as already known in the literature[174,291,350]. However, the collagen amount remained intact and was the most abundant component of our tissue of interest. The goal of reducing at most the undesirable effect of ECM alteration was then also achieved. Qualitative alteration of the collagen fibres by the decellularization in terms of waviness and curviness was recently explored through cross-link analysis, which showed no statistical difference between all these five protocols in terms of enzymatic and non-enzymatic cross-links[351]. However, gamma-irradiation seems to increase enzymatic cross-link alteration after decellularization. In addition, D5 led to significantly less decorin (DCN) content than other protocols. Even if D5 could still appear to be more disruptive to the fibrillar component of the ECM, this qualitative morphological alteration does not seem to have significant repercussions on the mechanical characteristics of the decellularized graft. The stress-strain curves also revealed changes in elastin and collagen fibres. In fact, elastin primarily contributes to the mechanical strength in the low-strain region, while the stiffness in the high-strain region primarily results from the stretching of collagen fibres[352]. Hence, the reduction in the low-strain region of decellularized tissues, along with the observed decrease in elastin content, implies that the decellularization processes likely affected elastin fibres, resulting in the stretching of collagen fibres at lower strain. To explore this

hypothesis further, microfocus computed tomography (microCT) imaging or cross-link difference analysis could be considered.

Regarding residual chemical agents, quality control measures for acetone, H_2O_2, and pH, as validated for clinical purposes, showed no residual decellularization products in our study, consistent with clinical practices. SDS was not specifically assessed in this study, as previous research demonstrated that with extended SDS exposure and reduced rinse duration, only 0.0026% residual SDS was detected, indicating effective washing of the reagent[353,354]. Triton X-100 is also known to aid in the effective removal of residual SDS[174]. Additionally, cytotoxic analysis with fibroblast seeding confirmed that all tissues were rinsed thoroughly, allowing for robust cellular growth and viability (Fig. 54). A decellularized patch was a more welcoming environment than a classic plastic culture well, probably because the 3D structure permitted to increase the space to proliferate and because of the allogenic human fibroblasts seeding. This suggests that these ECMs will be well tolerated for future human clinical implantation. Preliminary implantation tests, conducted as xenotransplantation in rats, aimed to provide better evidence of any potential immune reaction should it occur. This *in vivo* experiment showed that only the D5 protocol did not induce any immunogenic response.

As expected and according to previous evidence[316,325,341,342], the native tissues induced a reaction against foreign body after implantation, which was characterized by a fibrous encapsulation associated with numerous inflammatory cells (CD3+ lymphocytes and CD68+ macrophages), minimal tissue degradation, and a peripheral neovascularization (CD31+ endothelial cells). Despite no statistical difference with native tissues, only D5 implants did not give rise to a particular inflammatory or immune response. All other protocols showed a spectrum of reactions including outer cellular shell or invasion and resorption/remodelling of the tissue by inflammatory cells. The topographic arrangement of inflammatory cells was also different. Lymphocytes were more widespread in decellularized tissues than in native ones, where they were all concentrated in the outer shell. These features were very suggestive of a general immunogenic response against a cellular graft, which looks like an inflammatory reaction characterized by increased levels of tumor necrosis factor alpha (TNF-α), antibody production against the implant, massive infiltration of inflammatory

cells, macrophage activation, and substantial accumulation of immune components within the grafts[325].

Regarding the neovascularization, the difference between native implants and decellularized ones relied more on the organization than on the quantity. The neo-vessels penetrated deep into the decellularized patches in opposition to the native ones, where they proliferated in the peripheral capsular shell to provide immune and inflammatory cells, as previously described[325].

When shifted rat anti-human IgG reached a ratio of approximately 50% of the total amount of rat IgG or showed a positive difference from their initial rate, rats were considered immunized, as observed in native and D1-D4 implants. Only the D5 allowed a safe transplantation, biocompatible and without any immunization, whereas all the protocols led to a successful decellularization following Crapo's criteria. Our initial question thus requires clarification, elucidation and discussion: "*Why a so-called decellularized matrix can still exhibit immunogenicity after transplantation?*"

The potential for residual cellular material to trigger an unfavourable host reaction was only briefly addressed in the literature and no precision, guideline or threshold was initially defined. For example, many authors mentioned the need to rinse scaffolds thoroughly to remove all cellular remnants[174,178,180,323,327]. If cell residues are not removed, they can trigger the release of « damage-associated molecular patterns » (DAMPs), able to activate the innate immunity[174,355]. Most authors focused on nuclear components such as DNA. Only Crapo et al. laid the foundations for the recommendations of DNA threshold and decellularization quality control[178]. Unfortunately, several recent studies in various fields did not respect Crapo's criteria[317–322]. Even though Berger et al. mentioned various DNA grades to rate the success of decellularization[319], the aforementioned authors considered their tissues/organs to be « decellularized » with DNA content up to 629ng/mg dry weight[317–322,331] without evaluating the immune rejection or any association between even weak immune response and potential immunogenic remnants. Nevertheless, there were some successful studies but also failed ones in terms of preclinical or clinical results[316,324,326]. Some other molecules should play an important role to explain these controversies. In summary, the quality and the

precise threshold of residual immunogenic remnants, aside from DNA, have hardly been extensively explored so far.

Upon further quantitative investigation of the residual HLA, all the decellularized implants exhibited a significant reduction in HLA content when compared to the native ones ($p<0.0001$). However, a closer examination of D1 to D5 samples revealed that only D5 ones displayed HLA content below 1% residual threshold. The differences in decellularization agents could account for the varying outcomes. Ionic agents like SDS are known to solubilize nuclear membranes and remove cytoplasmic proteins[178] and can be effective alone[174]. In contrast, non-ionic agents like Triton X-100 disrupt DNA-protein, lipid-lipid, and lipid-protein interactions[178], but are ineffective alone[174]. Enzymatic DNAse hydrolyses nucleotides but does not affect cell membranes and membrane proteins like HLA. However, in the fifth protocol, more aggressive solvents may explain its superior HLA protein removal. While ether is mainly used to neutralize acetone, alcohols and acetone facilitate cell lysis through dehydration and lipid solubilization, leading to significant two-step defatting[178]. Subsequent steps with hypertonic NaCl (osmotic shock) and H_2O_2 further enhance and complete nucleic acid precipitation, protein coagulation, and cell membrane degradation[178,243,341]. These processes likely degrade cytoplasmic membranes and proteins more effectively, thereby eliminating HLA proteins more thoroughly. This observation might explain the xenotolerance and the absence of immunization after implantation of D5 samples. Even if the IHC for MHC-1 seemed to be modified, lowered and cleared in decellularized tissues, the quantitative analysis of HLA showed that the qualitative assessment was not enough to rely on. This latter can be heterogeneous depending on the level of slices and the analysed zone that do not always represent the whole sample. This study highlighted the need for respecting Crapo's criteria which focused on nuclear antigens but also for adding membrane antigens, *i.e.* HLA content assessment, when claiming the success of decellularization. Overall if the goal of tissue engineering is to move to patient transplantation. Therefore, we propose to optimise the definition of decellularization success for human allotransplantation by those three criteria:

- Lack of visible nuclear material on routine histology (DAPI or H&E staining)
- < 50ng DNA/mg dry weight of ECM
- < 1% of residual MHC-1 content within the ECM

Historically, DNA fragment length was considered a standalone criterion for decellularization, but this has been largely abandoned. Researchers found that DNA fragment length alone does not fully capture the immunogenic potential of residual cellular material and is more likely to be involved in the inflammatory response than in the direct immunogenic potential. Both DNA content and fragment length are altered simultaneously during decellularization. As even short DNA fragments can trigger an immune response, minimizing total DNA content is considered sufficient[174,324,326]. Recent literature focuses on DNA content as the primary criterion, along with H&E and DAPI staining, simplifying the evaluation process and ensuring comprehensive assessment. Therefore, consolidating DNA components into a single measure of DNA content is proposed as the most effective criterion for successful decellularization, from a nuclear point of view.

However, by adding the immunogenic membranous criterion and respecting all these criteria together, the variations in adverse host reactions will be drastically reduced or even eliminated. Doing that, only the beneficial host response could act towards reconstructive and remodelling outcomes with a site-specific insight following the well-known and natural phases of haemostasis, inflammation, proliferation and remodelling[326,356]. Seeded MSCs are also able to replace the initial HLA genotype of a decellularized ECM to impose their own[331]. This point emphasizes the importance of removing all DNA fragments as well as residual HLA epitopes to facilitate the replacement of HLA genotype by host cells.

The main outcomes of this study were not those initially intended. Therefore, the subcategories of immune cells or cell components were not fully considered but might be very interesting for future investigations. Only HLA-A and B, namely MHC-1, were quantified but repeating the experiment with other HLA groups would be interesting. Another study tried to quantify the HLA-I and II epitopes into DBM products but failed to demonstrate an association with a potential immunogenicity[328]. By evaluating immunogenicity at the level of HLA eplets (the surface regions of HLA molecules recognized by antibodies), the specificity of considerations could be improved[333]. Using a full quantitative analysis like enzyme-linked immunosorbent assay (ELISA) might also precise the exact threshold of HLA content.

They are also many other minor histocompatibility complexes that are well less understood[313,357]. Regarding adaptive immunity, some researchers also focused on T helper lymphocytes and showed that an acellular scaffold elicited wound-healing, anti-inflammatory and remodelling Th2 cytokines[358,359]. More recently, Badylak's team evaluated the innate response by the macrophage reaction after ineffective decellularization, more in favour of a pro-inflammatory M1 macrophage phenotype than anti-inflammatory M2 macrophages[324,327]. In contrast, macrophages in the remodelling phase (CD163+) were found to predominate than those in the inflammatory phase (CD80+) in an acellular scaffold[344,360]. Other possible remnants such as mitochondria or other cell-associated components deserve a specific attention in order to further evaluate their implication into a potential immune host response[174,327,355]. Londono et al. (2017) demonstrated that all the DNA, cell membrane as well as mitochondria remnants promoted M1 macrophages both *in vitro* and *in vivo*[327]. Further perspectives could also explore more in details the innate and acquired immune reaction and the potential correlation with specific immunogenic cells such as macrophages, lymphocytes, multinucleate giant cells, natural killers, etc.

This study focused on a single connective tissue type characterized by an abundant ECM with few native cells. As shown in Figure 56, MHC-1 clusters predominantly around blood vessels, likely because these are the most cellular structures in this paucicellular HFL tissue. However, MHC-1 is also present in other areas. At this scale, it can be challenging to differentiate isolated non-vascular cells from capillaries. Future research could investigate a correlation between MHC-1 marked areas and the endothelial cell marker CD31, which could help distinguish capillaries and provide a more specific assessment of whether the residues are primarily located in blood vessels.

Two donor cohorts were used as mechanical tests were not feasible on the same samples used for other analyses. The age does not significantly impact decellularization efficiency, which depends more on tissue quality, porosity, density, and the exposure and duration of decellularization agents. All donors were cadaveric, likely with already dead cells that may be easier to detach and wash than living cells. However, this is not a significant issue since most tissue engineering techniques aim to improve and increase organ transplants from deceased donors or facilitate xenotransplantation.

This model, of common clinical use in musculoskeletal system reconstruction, served as an excellent starting point to illustrate fundamental principles that need to be confirmed in multiple other, more cellular and more composite tissues. However, the host reaction might differ according to the source of the ECM, the anatomical site of implantation, and the immune function of the host[174,178]. Since the function of the transplanted organ or tissue can vary, the criteria for successful scaffold decellularization can also be modified accordingly. As only one example, residual phospholipids in decellularized heart valves were associated with calcification and, therefore, should be added as a 4th criterion for this special clinical application[361,362].

Patients can be immunized by previous organ transplantation, pregnancies and/or blood transfusions[313,330,336,339]. Since many patients with a need of bioengineered tissues or organs may have already undergone a previous surgery, usually had previous blood transfusion or will need it during the surgery or will need an implant replacement because of ageing, all surgeons should think about immunization. Otherwise, 1% of the population presents anti-MHC alloantibodies without obvious reason, similar to a self-immunization process[313]. In this context, the HLA should always be taken into account to avoid (hyper)acute rejection or massive adverse response to another allogenic contact[336], but also to enhance functional outcomes and survival of a first allograft[363,364].

The translation to xenotransplantation has also to be discussed. To determine whether the level of the α-Gal epitope (Galα1,3-Galβ1–4GlcNAc-R), a non-primate animal cell surface antigen[316,327], would also be reduced to 1% should be very interesting for all the animal-source scaffolds.

E. Conclusion

The exponential ascension of tissue engineering and decellularization applications is noteworthy. After relying on methods traditionally used in the literature and existing standardized Crapo's criteria, all our decellularization protocols seemed exactly as effective as each other. The need to look further afield was obvious. With only one protocol, the decellularized samples were completely accepted by rats without any immunization, with a residual HLA under 1%. As the clinical use of

ECM-based scaffolds continues to rise, the demand for well-defined decellularization guidelines is growing. Observing this newly proposed set of criteria could permit to give strict guidelines for commercial or clinical development and use[174]. Standardized accepted criteria should also permit to compare protocols and outcomes more accurately. The development and the promotion of clinical applications will certainly be emphasized thanks to the assurance that their new ECM product would be safer for patient care.

F. Supplementary data

Supplementary data – Table 16. Quantification of intra- and extracellular components. N: native HFL, D1 to D5: the five decellularization protocols, CI: confidence interval.

Tissue status	Mean	95% CI of mean	P-value (compared with native)
Intracellular components			
DNA *(ng/mg dry weight)*			
Native	404.8	293.6 – 515.9	-
D1	6.08	2.67 – 9.49	0.0003
D2	6.53	3.80 – 9.26	0.0037
D3	1.89	0.80 – 2.98	<0.0001
D4	8.76	4.36 – 13.16	0.0132
D5	8.14	2.55 – 13.72	0.0014
Extracellular components			
Collagen *(µg/mg dry weight)*			
Native	735.0	631.3 – 838.7	-
D1	769.9	674.6 – 865.2	>0.9999
D2	769.2	684.3 – 854.1	>0.9999
D3	782.9	677.0 – 888.8	>0.9999
D4	807.8	600.0 – 1015.5	>0.9999
D5	815.8	673.8 – 957.8	>0.9999
GAGs *(µg/mg dry weight)*			
Native	3.57	3.10 – 4.04	-
D1	0.18	0.05 – 0.30	<0.0001
D2	0.46	0.11 – 0.80	0.0050
D3	0.20	-0.03 – 0.43	<0.0001
D4	0.43	0.09 – 0.77	0.0035
D5	0.33	-0.05 – 0.70	<0.0001
Elastin *(µg/mg dry weight)*			
Native	35.16	27.30 – 43.03	-
D1	10.56	8.89 – 12.24	<0.0001
D2	12.95	9.80 – 16.11	0.0027
D3	12.60	9.11 – 16.08	0.0017
D4	13.70	9.22 – 18.18	0.0035
D5	12.61	8.11 – 17.12	0.0004

– TAKEAWAYS –

Paper 3 – HLA Awareness in Tissue Decellularization: A Paradigm Shift for Enhanced Biocompatibility, studied on the Model of the Human Fascia Lata Graft

- *New set of decellularization criteria* = *Absence of visible nuclei on H&E and DAPI stained sections*

  < 50ng DNA/mg dry weight of ECM

  < 1% of residual MHC-1 content within the ECM

- *ECM modification* =

Preserved	*Altered*
Col-1	*GAGs*
Mechanical properties	*Elastin*

⇨ *Tissue bank NaOH-based decellularization protocol*

This protocol stands out as the only one eliciting no immunogenic response, providing a non-cytotoxic, biocompatible, and secure transplant with the potential for neoangiogenesis.

Collagen fibres & cross-links

« The student is not a container you have to fill, but a torch you have to light. »

Translated from Albert Einstein, 1879 – 1955

The assessment of ECM alteration is governed not only by molecular quality or content but also by its 3D organization. Although the collagen content remains intact, qualitative modifications in collagen fibres were observed in conventional histological sections, expressed by an increased waviness and curviness. Investigating potential alterations in collagen cross-links is thus relevant in this context.

A. Collagen fibres

Type I collagen molecules, primarily secreted by fibroblasts, have a triple helical structure, meaning they consist of three polypeptide α-chains (two pro-α1 chains and one pro-α2 chain) (Fig. 57). Each chain is made up of a repeating sequence of amino acids, with the most common sequence being Glycine-X-Y, where X and Y are often proline and hydroxyproline[365,366]. After post-translational modifications (PTMs) (most of proline and lysine hydroxylation), this specific amino acid composition allows for hydrogen and disulfide bonds, which stabilize the triple helix structure and give rise to the procollagen molecule[367]. Once secreted into the extracellular compartment, the N- and C-terminal propeptides of the procollagen are cleaved resulting in the tropocollagen molecule, less soluble[366]. Collagen triple helices then associate with each other to form larger fibrils, which in turn organize into fibres. These fibres provide tissues their tensile strength[367].

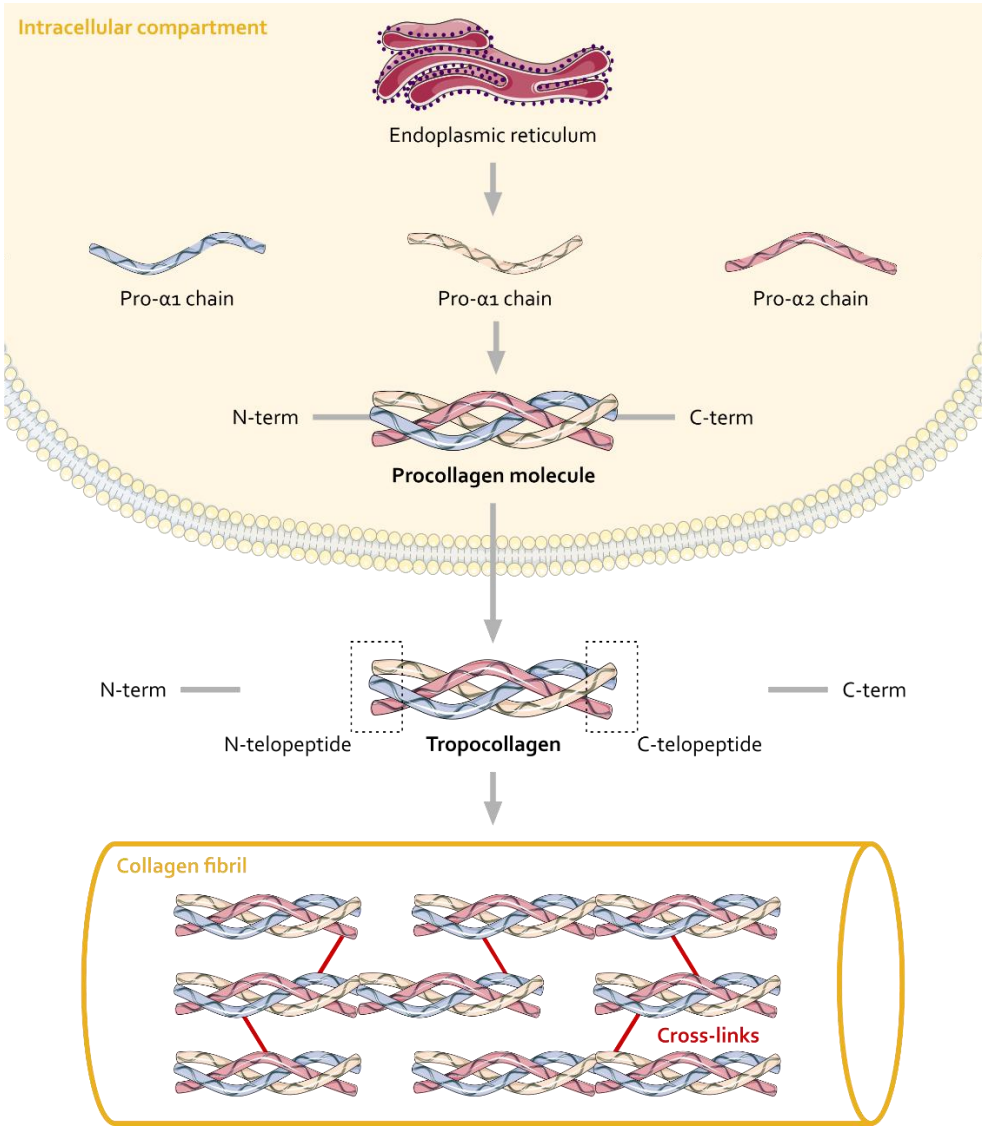

Figure 57. Type I collagen biosynthesis and post-translational modifications. Term: terminal propeptide. Adapted from Yamauchi et al. (2012)[366].

B. Collagen cross-links

Collagen cross-linking refers to the process by which chemical bonds form between collagen molecules. These bonds create a network of interconnected

collagen fibres, which enhances the strength, stability, and resilience of the collagen structure[367]. These cross-links play a crucial role in the integrity and function of various tissues and organs in the body, including bone, skin, tendons, and cartilage[366,368]. Cross-links are divided in three types: enzymatic, non-enzymatic (or advanced glycation end products) and GAG interfibrillar bridges (Fig. 58).

B. 1. Enzymatic cross-links

Enzymatic cross-links are formed through a controlled and complex PTM of lysine and hydroxylysine residues in the telopeptides, involving intra- and extracellular steps[366,369]. These cross-links are catalysed by the lysyl oxidase (LOX) enzyme and result in the formation of divalent immature enzymatic cross-links that mature into trivalent ones (*e.g.* pyridinoline and pyrrole)[366,369,370]. This process leads to the formation of intermolecular cross-links between adjacent collagen molecules[371], contributing to tissue mechanical properties[371].

B. 2. Non-enzymatic cross-links

Non-enzymatic cross-links, known as advanced glycation end products (AGEs), are formed through a glycation process involving the interaction of lysine residues with aldehydes[369,372,373]. These AGEs accumulate along the entire length of collagen molecules, leading to increased tissue rigidity and reduced remodelling capacity[372,374]. Pentosidine is a well-characterized AGE, often used as a marker for AGE accumulation[369,373]. The accumulation of AGEs has been suggested as a significant contributor to the bone fragility observed with aging[369,373].

B. 3. GAG interfibrillar bridges

Interfibrillar bridges are formed through the interaction of GAGs with DCN residues[375]. GAGs are negatively charged polysaccharide macromolecules. DCN, a proteoglycan essential for tissue regulation, is composed of a core protein and a GAG side-chain at the N-terminal extremity[375,376]. Horseshoe-shape DCN has a high affinity to bind collagen triple helix, hence its name: it "decorates" collagen[377,378], maintaining specific distances between fibrils[375,377]. In addition to its structural role, DCN also acts as a reservoir for GFs and cytokines and regulates their availability in the ECM[375,378].

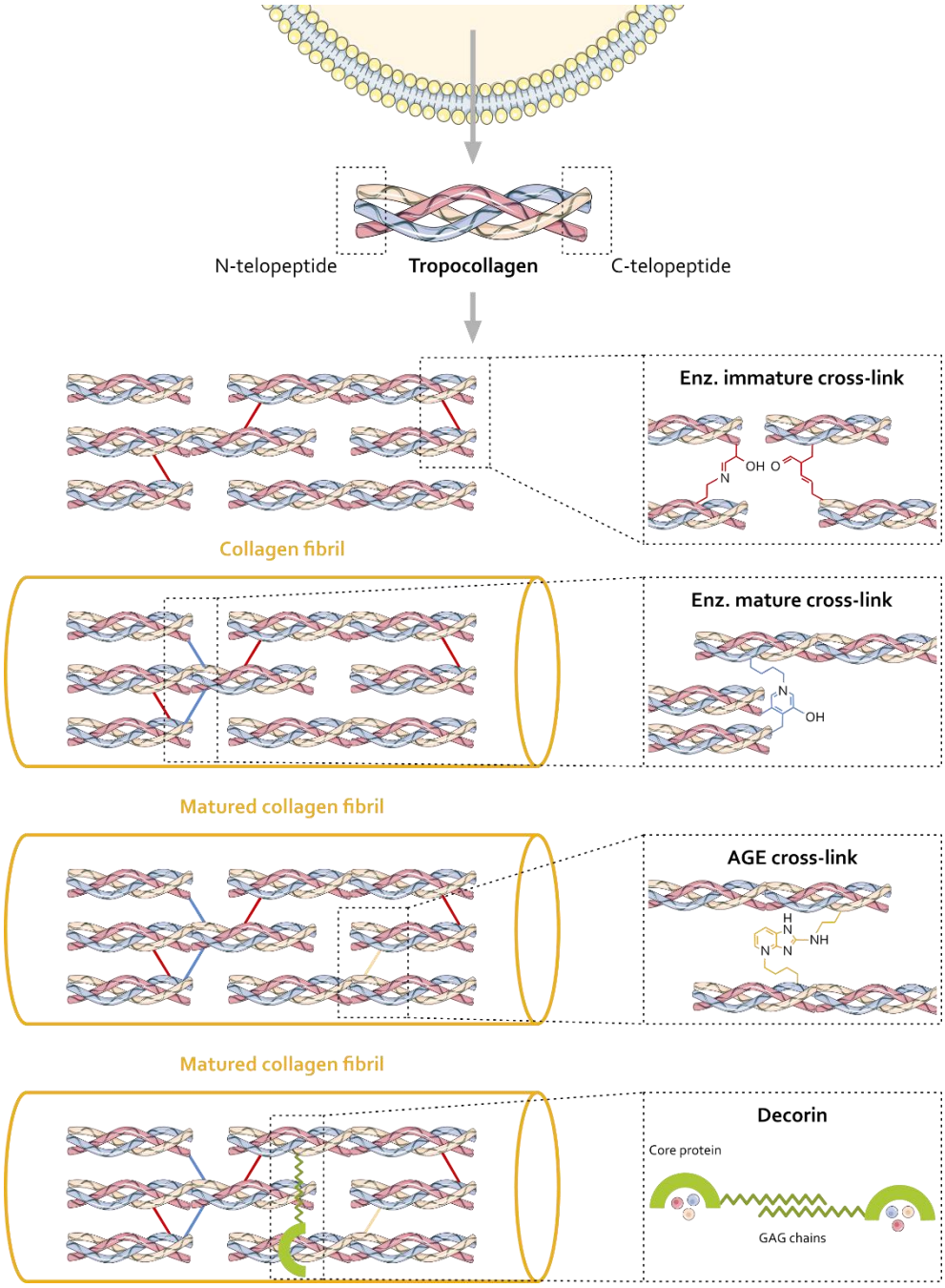

Figure 58. Cross-link types, formation and organization. Enz: enzymatic, AGE: advanced glycation end products, GAG: glycosaminoglycan. Inspired from multiple studies[366,370,377].

Paper 4 – Collagen molecular organization preservation in human fascia lata and periosteum after tissue engineering

Julia Vettese, Julie Manon*, Antoine Chretien, Robin Evrard, Lies Fievé, Thomas Schubert, Benoît Lengelé, Catherine Behets†, Olivier Cornu†*

** Share first authorship*
† Share last authorship

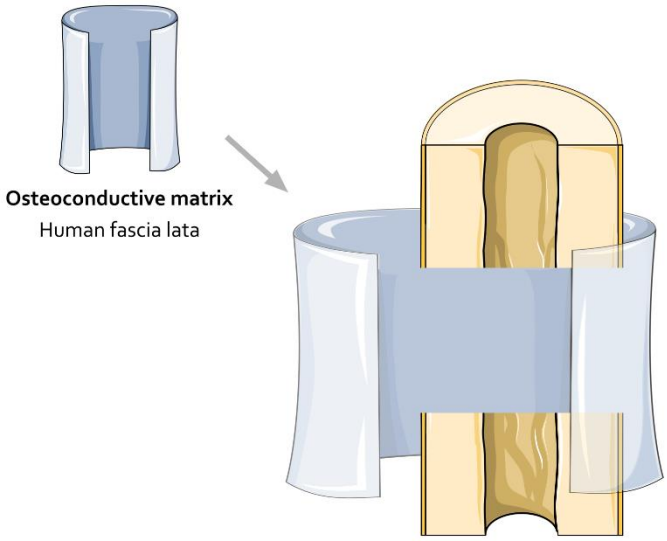

Published in

Front. Bioeng. Biotechnol. 12:1275709. (IF=6.064)

doi: 10.3389/fbioe.2024.1275709

Abstract

Large bone defect regeneration remains a major challenge for orthopaedic surgeons. Tissue engineering approaches are therefore emerging in order to overcome this limitation. However, these processes can alter some of essential native tissue properties such as intermolecular cross-links of collagen triple helices, which are known for their essential role in tissue structure and function.

We assessed the persistence of ECM properties in HFL and HP after tissue engineering processes such as decellularization and sterilization. Harvested from cadaveric donors (N=3), samples from each HFL and HP were decellularized following five different chemical protocols with and without detergents (D1-D4 and D5, respectively). D1 to D4 consisted of different combinations of Triton, SDS and DNAse, while D5 is routinely used in the institutional tissue bank. Decellularized HFL tissues were further gamma-irradiated (minimum 25kGy) in order to study the impact of sterilization on the ECM. Polarized light microscopy (PLM) was used to estimate the thickness and density of collagen fibres. Tissue hydration and content of hydroxyproline, enzymatic cross-links, and non-enzymatic cross-links (pentosidine) were semi-quantified with Raman spectroscopy. ELISA was also used to analyse the maintenance of the DCN, an important small leucine-rich proteoglycan (SLRP) for fibrillogenesis.

Among the decellularization protocols, detergent-free treatments tended to further disorganize HFL samples, as more thin fibres (+53.7%) and less thick ones (−32.6%) were recorded, as well as less collagen enzymatic cross-links (−25.2%, p=0.19) and a significant decrease of DCN (p=0.036). GAG content was significantly reduced in both tissue types after all decellularization protocols. On the other hand, HP samples were more sensitive to the D1 detergent-based treatments, with more disrupted collagen organization and greater, though not significant loss of enzymatic cross-links (−37.4%, p=0.137). Irradiation of D5 HFL samples led to a further and significant loss in the content of enzymatic cross-links (−29.4%, p=0.037) than what was observed with the decellularization process.

Overall, the results suggest that the decellularization processes did not significantly alter the matrix. However, the addition of gamma-irradiation is deleterious to the collagen structural integrity of the tissue.

Full-length article in Appendix.

– TAKEAWAYS –

Paper 4 – Collagen molecular organization preservation in human fascia lata and periosteum after tissue engineering

- *ECM Structure* ⇔ *ECM molecular composition*

- *HFL matrix modification after tissue bank NaOH-based decellularization*

Preserved	*Altered*
Enz. cross-links *Non-enz. cross-links*	*Slight disorganization* ↘ *DCN* ↘ *GAGs*

↳ *If gamma-irradiation (min > 25kGy) :* ↘ *Enz. cross-links*

⇨ *Relatively good preservation of the ECM after tissue bank NaOH-based decellularization protocol, without repercussion on the mechanical characteristics of the HFL.*

Back to the Diamond

- **What is the best protocol for achieving decellularization?**

All five protocols succeeded in decellularizing HFL tissues according to Crapo's criteria, showing no significant differences in cell and DNA removal, cytotoxicity, or biocompatibility. However, since the goal of decellularization is to produce a non immunogenic scaffold, immunogenicity, not covered by Crapo's criteria, was investigated. Surprisingly, only D5 protocol did not immunize rats due to the lower presence of HLA, which we identified as essential for decellularization. Thus, considering this additional criterion, only D5 achieved truly non-immunogenic decellularization.

- **What is the best protocol for preserving ECM?**

Initial histological analyses and ECM protein quantifications revealed no significant superiority among the protocols. All protocols reduced the quantity of GAGs and elastin but preserved collagen content and macroscopic organization. However microscopically, increased waviness in collagen fibres was observed. The study of collagen cross-links indicated that D5 preserved non-enzymatic cross-links but altered enzymatic cross-links after gamma-irradiation, causing slight ECM disorganization without significantly impacting mechanical properties.

- **Which protocol should be considered for further investigations?**

The optimal protocol should balance cell removal and ECM preservation as best as possible. Although collagen cross-links are altered after decellularization and sterilization, the resultant slight fibre disorganization more closely resembles the native HP collagen structure, which is less dense and looser. This perturbation is therefore acceptable but should be kept in mind in future investigations concerning cell seeding and response. Given these considerations and the fact that D5 is the only non immunogenic protocol already validated for clinical use, this protocol legitimately emerges as the preferred choice for the next stages of our research.

– REQUIREMENT SPECIFICATIONS –

Requirement	Specification	Validation
Osteoconductive matrix		
Composition	- Col-1 membrane	V
Morphology	- 2 layers - Thickness (1 thin + 1 thick layers) - Large size - Shapeable	V V V
Biocompatibility	- No immunogenicity - Carrier for cells - No cytotoxicity	V V V
Osteoinductive mediators		
Bioactivity	- Osteogenic GF - Osteogenic differentiation - Chondrogenic differentiation	≈
Osteogenic cells		
Osteogenicity	- Cell adhesion, proliferation, replication - Osseous ECM production	X
Mechanical stability		
Membrane properties	- Sheet malleable support - Resistance to handling - Isotropy or anisotropy?	V V ≈
In vivo model	**AND** - Stitchable - Mechanical stability	
Vascularization		
Vascular supply	- Angiogenic properties - Neoangiogenesis **OR** - Intrinsic vascular architecture - Functional vascular network	
In vivo transposition		
Clinical needs	- Off-the-shelf availability - One-stage surgery	

CHAPTER III. New osteogenic membrane

« I never lose, I either win or learn! »

Nelson Mandela, from the 1980s onwards

Research questions emerging from the Diamond

After comparing the fascia lata to the periosteum, extensive research was conducted on the decellularization process and its effects on ECM organization. While its non-cytotoxic, biocompatible, and safe properties for transplantation were well-documented, its osteogenicity and osteoinductivity aspects remain to be fully elucidated.

The necessity of living cells for an OM is clear. However, the question of whether to implant differentiated or undifferentiated cells remains unanswered[90,91].

Osteoinductivity, crucial for bone regeneration, relies on orthobiological concepts[18] and GFs that guide cell development and differentiation into specific tissues[168]. Various bone graft substitutes incorporating active biomolecules like recombinant GFs, ECM-derived peptides, or small molecules interacting with signalling pathways were already developed and commercialized[6]. Although inherent part of the Diamond concept, external GFs may not always be beneficial, as noted by Masquelet et al. regarding induced membrane[108]. Therefore, harnessing the potential intrinsic GFs could offer a natural and controlled advantage.

The synergistic effect of these components warrants further investigation to complete the Diamond concept. The upcoming paper delves into the cell-matrix interplay, exploring the presence of intrinsic osteogenic and angiogenic GFs. Three

key facets of the Diamond will be examined: the osteoconductivity, osteoinductivity, and osteogenicity of the proposed new OM.

This chapter aims to answer the following questions:

- **Is it possible/better to use PMSCs to provide osteogenicity to the osteoconductive HFL matrix?**
- **Is it possible/better to take advantage of intrinsic GFs?**
- **Is it possible/better to implant differentiated or undifferentiated cells?**

Paper 5 – A New Osteogenic Membrane to Enhance Bone Healing: At the Crossroads between the Periosteum, the Induced Membrane, and the Diamond Concept

Julie Manon, Robin Evrard, Lies Fievé, Caroline Bouzin, Delphine Magnin, Daela Xhema, Tom Darius, Eliano Bonaccorsi-Riani, Pierre Gianello, Pierre-Louis Docquier, Thomas Schubert, Benoît Lengelé, Catherine Behets, Olivier Cornu

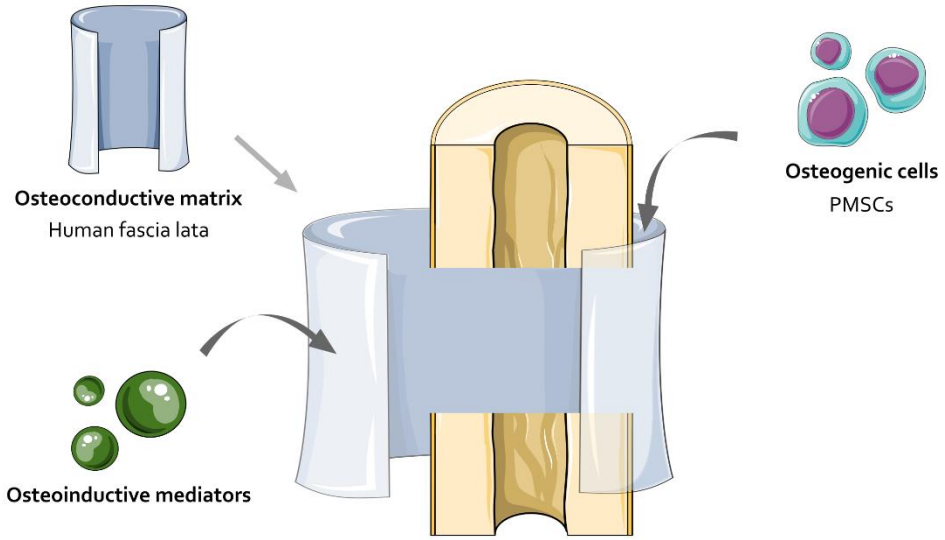

Published in

Bioengineering 2023, 10, 143. (IF=5.046)

doi: 10.3390/bioengineering10020143

Abstract

The lack of viability of MBAs for CSBD treatment remains a challenge in orthopaedic surgery. The literature has reviewed the advantages of a multicombined treatment with the synergy of an osteoconductive ECM, osteogenic stem cells, and GFs. Questions are still open about the need for ECM components, the influence of the decellularization process on the latter, the related potential loss of function, and the necessity of using pre-differentiated cells. In order to fill in this gap, a bone allograft surrounded by an OM made of a decellularized collagen matrix from HFL and seeded with PMSCs was analysed in terms of de-/recellularization, osteogenic properties, PMSC self-differentiation, and angiogenic potential. While the decellularization processes altered the ECM content differently, the main GF content was decreased in soft tissues but relatively increased in hard bone tissues. The spontaneous osteogenic differentiation was necessarily obtained through contact with a mineralized bone matrix. Trying to deepen the knowledge on the complex matrix–cell interplay could further propel these tissue engineering concepts and lead us to provide the biological elements that allow bone integration *in vivo*.

Graphical abstract

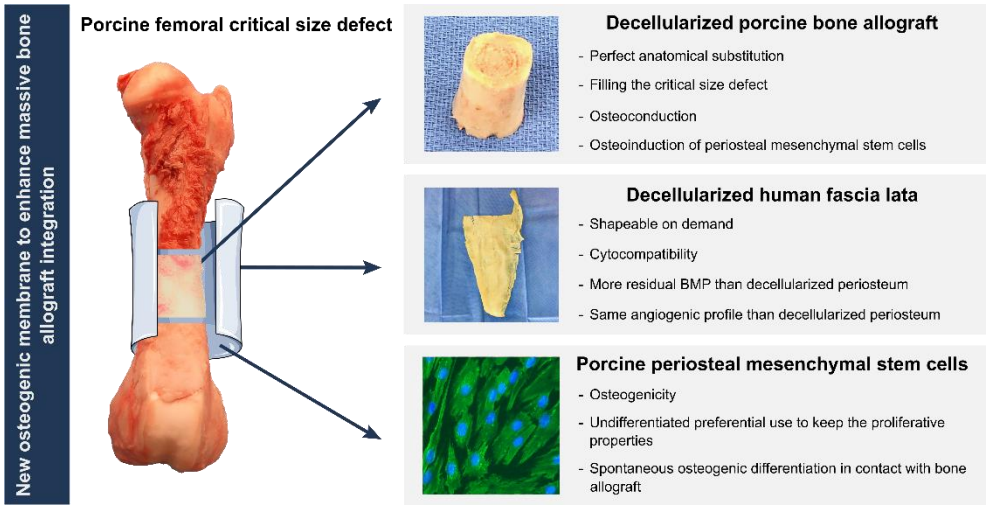

A. Introduction

CSBD has always been a major challenging issue in orthopaedic reconstructive surgery. After trauma, infection, oncologic resection, or congenital malformation, the bone architecture is destroyed, and the healing capacity is insufficient due to the defect size, the poor environment, and/or the concomitant damages to the periosteum and surrounding soft tissues. Many researchers have provided some answers for small defects but definite solutions still fail for larger bone gaps over time[14,18,138,156,247]. At present, none of the proposed therapeutic solutions can reach both the important architectural volume to replace and the viability to restore bone homeostasis. To fill in this scientific gap, this study aims to create a novel OM to enhance the integration of MBAs and to deepen the knowledge about the cell–matrix interplay.

In the goal to improve the efficiency of CSBD management, different concepts must be taken into consideration. In actuality, three main entities are known to participate in or massively improve bone consolidation. First, the periosteum is one essential tissue taking part in natural bone repair. This highly-vascularized bilayer collagen membrane covering the bone surface has an evident and unique osteogenic potential for bone healing through endochondral ossification[32,245,379,380]. Thanks to the presence of PMSCs, it contributes to transverse bone growth and bone remodelling, as well as initiating the fracture callus[25,69,245,379,380]. The MSCs differentiation towards the osteogenic pathway is regulated by multiple orchestrated signals coming from the surrounding microenvironment, one of the critical ones being the ECM–cell interaction[179]. Secondly, the Masquelet technique of the induced membrane also already solicits the biological natural resources of the human body, in the absence of a periosteum, to reproduce a well-vascularized membrane around a cement spacer[96,99,108]. Thirdly, the diamond concept was then described by Giannoudis et al. In order to summarize all the criteria needed to reach nearly 90% of bone regeneration, namely, an osteoconductive matrix, osteogenic cells, osteoinductive mediators, mechanical stability, and vascularization[19].

Based on these concepts, the combination of a bone allograft with a surrounding OM made of a decellularized collagen matrix and seeded with MSCs could provide the biological elements for improving bone integration. Previous studies already

approached this concept of a multicomponent treatment[211,244,246,248,249,273,341], but some questions still remain unsolved:

- Which best assembly of grafts should be used? Is there any combination required?
- How do tissue engineering processes influence the ECM outcomes from a GFs point of view? What happens to their angio- and/or osteoinductive potential?
- How the spontaneous differentiation of PMSCs towards the osteogenic lineage can be induced without any differentiation culture medium?

This study will attempt to answer these questions by focusing on the fascia lata, PMSCs, and bone allografts. The HFL, or, more specifically, the ITT, is a wide tendon sheet extending from the tensor fascia lata muscle to the Gerdy's tubercle and lying on the vastus lateralis of the quadriceps femoris. It is used for a large panel of therapeutic or reconstructive surgeries[233,234,236,239–241,250] and is therefore routinely harvested and processed by our tissue bank[243,341]. Nevertheless, to our knowledge, it has never yet been considered directly for CSBD treatment. This membrane was already compared with the HP and has proven to be a good candidate to be used as an off-the-shelf membrane scaffold thanks to its wide shapeable surface, its mechanical resistance, and its easy harvesting[290]. However, the absence of osteogenic cells in HFL is critical and needs to be implemented by MSCs. PMSCs are multipotent stem cells deeply confined in the periosteum and were recently shown to play a role in intramembranous ossification as well[204,381]. The superiority of PMSCs over bone marrow MSCs was also previously demonstrated[66,67,215,245,247], in line with their higher osteogenic potential when harvested on load-bearing sites[204].

The association of all these components was tested in this study by assessing the efficacy of de-/recellularization processes on HFL, the PMSC induced/spontaneous differentiation potential, and the presence of osteo-/angiogenic GFs (angio-GFs) in the construct to obtain a function as close as possible to the crossroads between the periosteum and the induced membrane for further *in vivo* implantation.

B. Materials & Methods

B. 1. Tissue harvesting & processing

Human fascia lata & human periosteum

HFL tissues were harvested from five deceased donors (four men and one woman; average age: 91.3 ± 1.8 years), in the Human Anatomy Department of UCLouvain (IRB00008535, Brussels, Belgium), respecting the local ethics committee authorization (ref. 2021-30AOU-356, approved on the 13th of September 2021).

After a full-length incision of each thigh, going from the anterosuperior iliac spine to the base of the patella, HFL sheets were carefully isolated and cut from the median line to the lateral lip of the linea aspera. Harvested tissues were split into several samples that were differently handled in the following analyses.

The decellularization protocol was the one that was routinely used in our institutional tissue bank, as previously described (D5) [243,341]. Briefly, it consists of washing in a NaCl solution and successive baths of pure acetone, ether, ethanol (70°), NaOH (1N), and H_2O_2. All of these steps were realized under continuous agitation and separated with a continuous flow of demineralized water. These consecutive solvents ensure sample defatting, cellular membrane digestion, protein coagulation, nuclear acid precipitation, and bacterial, prions, and virus deactivation (such as HIV, HBV, and HCV). Each decellularized ECM was passed through a quality control process for residual chemical reagents, and the pH was adjusted ($7.0 < pH < 7.85$). The decellularized HFL tissues were then frozen at –80°C to be stored. The final tissue engineering step was sterilization with gamma-irradiation at min 25kGy (IBA Mediris, Fleurus, Belgium).

As a comparison, HP tissues were also harvested from the whole femoral circumference, starting from one lip of the linea aspera to the other and between the proximal and distal metaphyses of the same donors. They were processed in exactly the same way as the HFL tissues.

Porcine periosteal mesenchymal stem cells & porcine bone allograft

Tibial periosteum tissues were harvested from Landrace pigs (n=10 tibial periostea from N=5 pigs, young adults of +/- 40 kg) and Aachen minipigs (n=4 tibial periostea from N=2, adults of +/- 40–50 kg). These animals were available after euthanasia from other studies in order to reduce the number of animals (3R concept). All these studies were authorized by the institutional ethics committees (ref. 2020/UCL/MD/027 and A1/UCL/2021-A1, approved on the 14th of September 2020 and the 6th of April 2021, respectively, and ref. 2021/UCL/MD/062, approved on the 5th of November 2021). After a sterile dissection of the lower limb, the periosteum was cautiously removed using a periosteal stripper following a circumferential limit above the distal tibial metaphysis and below the anterior tibial tuberosity. Samples were directly transferred from the operating room to the laminar-flow hood in sterile PBS (Sigma-Aldrich, 59321C-1000mL, Saint Louis, MO, USA) without calcium and magnesium ions. They were then cut into the smallest pieces possible (< 1–2mm), which were immersed in 50mL Falcons containing a filtered solution of Hanks' balanced salt solution (HBSS with calcium and magnesium, Gibco, 14025-050) and type I-A collagenase (0.2%, Sigma-Aldrich, C0130-1G, Saint Louis, MO, USA) and put in a stirring water bath at 37°C for 3h. This solution was changed twice an hour while storing the supernatant. The proteolysis was inactivated by adding a two-fold volume of a PM, namely, the Dulbecco's Modified Eagle Medium/Nutrient Mixture F-12 (DMEM/F-12, Thermofisher, 11320033, Waltham, MA, USA), and supplemented with FBS (10%, Gibco, 10270-106), penicillin-streptomycin (1%, Gibco, 15140-122), and amphotericin B (1%, Gibco, 15290-026). All harvested cells were washed twice via successive steps of centrifugation (1500rpm/377xg–5min) and resuspended in DMEM-F12. Cells were counted before seeding on a 6-well plate (an average of 461,735 cells (+/- 148,014) in each well) and incubated at 37°C and 5% CO_2, which was considered the initial passage (P0). The PM was changed every two days and cells were cultured until passage four (P4) in order to select the proliferative PMSCs. PMSCs in P4 were frozen at –80°C before being analysed or used.

Porcine forearm bones were harvested from the same previous Landrace pigs with a direct approach between the fasciae of the pectoralis and serratus anterior muscles. The vasculature was carefully isolated and dissected from the axillary vessel to the interosseous artery, until the nutrient artery foramen. The porcine

bone allografts (PBAs) were harvested with their interosseous pedicles after proximal and distal disarticulation.

B. 2. Histology

The efficiency of decellularization and recellularization was analysed using classical histology. For all donors, 1cm² specimens were embedded in paraffin after fixation in 4% formaldehyde (VWR International, 9713.9010, Radnor, AR, USA). They were then sectioned into 5µm thick slices and stained with H&E, MT, PSR, and AB, according to standard protocols. Sections were also stained with 2'-(4-ethoxyphenyl)-5-(4-methyl-1-piperazinyl)-2,5'-bi-1H-benzimidazole trihydrochloride (Hoechst, 2µg/mL, Life Technologies, H3570, Carlsbad, CA, USA) in order to examine DNA. All sections were digitalized using slide scanners (Leica Microsystems, SCN400, Wetzlar, Germany or a Panoramic ScanII slide scanner, 3DHistech, Budapest, Hungary) with a 20-fold Plan-Apochromat objective or viewed at a 40-fold magnification under a fluorescence microscope (AxioImager Z1, Zeiss, Oberkochen, Germany). The pictures were finally annotated with the open-source Cytomine software (v.3.1.0., www.cytomine.org, first access on the 16th of November 2020)[349] or with SlideViewer software (v2.5.0., Budapest, Hungary), respectively, depending on the slide scanner used.

B. 3. Immunohistochemistry

The same protocols as those previously described[290] were used in order to detect elastin (on tissues), type I collagen (col-1), OC, and runt-related transcription factor 2 (RunX2) (on cell aggregates) on paraffin-embedded slices. Briefly, after paraffin removal, endogenous peroxidase was inactivated with H_2O_2 (3%) in methanol. For elastin and col-1, antigen retrieval was achieved via proteinase K (18.7 µg/mL, Roche, 03115828001) incubation in a buffer of tris-EDTA (Tris, Merck, 1.08387.250, Darmstadt, Germany; EDTA, Sigma-Aldrich, E5134, Saint Louis, MO, USA) at 37°C for 20min. For OC and RunX2, heat-induced epitope retrieval was achieved in a citrate buffer (pH=5.7) using a microwave. Aspecific binding sites were blocked with 5% BSA (Merck, 12659-500 GM, Darmstadt, Germany) mixed with 0.05% TBS/Triton (Tris, Merck, 1.08387.250, Darmstadt, Germany; Triton, VWR, M143, Radnor, AR, USA) at RT over 1h. The slices were incubated with rabbit primary antibodies, *i.e.*, anti-elastin (1:100, Novus biotechne, NB100-2076), anti-collagen I (1:200, Abcam, ab34710), and anti-RunX2 (1:6000, Cell signaling, 12556S), or with

mouse primary antibodies, namely, anti-OC (1:200, Thermofisher, MA1-20786, Waltham, MA, USA), at 4°C overnight. An HRP-conjugated antirabbit secondary antibody (Envision, Dako Agilent, K4003, Santa Clara, CA, USA) or an anti-mouse secondary antibody (Envision, Dako Agilent, K4001, Santa Clara, CA, USA) were incubated, respectively, at 4°C for 1h. The detection was realized using a DAB peroxidase substrate (Dako Agilent, K3468, Santa Clara, CA, USA) at RT for 5min. The counterstaining was achieved using haematoxylin. After mounting with a rapid mounting medium (Entellan new, Sigma-Aldrich, 1.07961.0100, Saint Louis, MO, USA), the slices were also digitalized.

Multiplex immunofluorescence IHC (mIF-IHC) was performed on paraffin-embedded slices based on a published protocol[382]. The same first steps of conventional IHC were performed, including paraffin removal, epitope retrieval, and non-specific antigen blocking with a mix of 5% BSA (Carl Roth, 3854.3, Albumin fraction V, Karlsruhe, Germany) in TBS/Tween20 (0.1%, VWR, 663684B, Radnor, AR, USA) at RT for 30min. The sections were incubated with the primary antibodies at 4°C overnight (Table 17). They were washed in TBS/Tween three times. Thereafter, anti-peroxidase-conjugated secondary antibodies were incubated at RT for 45min and visualized using tyramide signal amplification (TSA) using AF-conjugated tyramides in a borate solution (boric acid, Sigma-Aldrich B6768-500gr, Saint Louis, MO, USA; NaCl, VWR, 27810.295-1 kg; H_2O_2 0.003%) at RT for 10min. After antibody stripping with a new citrate buffer incubation step (this step detached antibodies from tissue sections), the identical protocol was applied with the second primary antibodies, adequate secondary antibodies, and AF-conjugated tyramide amplification following the sequence in Table 17. After a washing step in PBS, nuclei were finally stained with Hoechst (10 µg/mL, Sigma, 14533–100mg).

After mounting with the Dako fluorescent mounting medium, the sections were digitalized with the fluorescent slide scanner Axioscan.z1 (Zeiss, Oberkochen, Germany), annotated with the AxioVision software (v.4.8.2.0., Zeiss, Oberkochen, Germany), and stored at −20°C. A negative control, without primary antibodies, was always included to check for absence of detection in both standard IHC and mIF-IHC.

Table 17. Combination of primary and secondary antibodies, and AlexaFluor-conjugated tyramides for multiplex immunofluorescence IHC.

#	Antigen	Primary antibody			Secondary antibody	AF-conjugated tyramide		
		Dilution	Company	Ref	Polymer HRP	Company	Ref	Fluorochrome
1	*Col-1*	1:500	Abcam	*ab34710*	Anti-rabbit	InvitroGen	*B40955*	AF555
1	*RunX2*	1:6000	Cell signalling	*12556S*	Anti-rabbit	InvitroGen	*B40955*	AF555
2	*OC*	1:200	Thermofisher	*MA1-20786*	Anti-mouse	InvitroGen	*B40958*	AF647

#: Sequence of use, Ref: Catalog number, and AF: AlexaFluor.

The mIF-IHC for RunX2/OC/Hoechst was quantified with the open-source image analysis QuPath software (v0.3.0., University of Edinburgh, Scotland)[252]. Blur areas, damaged tissue, and artefacts were manually excluded. Cells were then detected at a high resolution (0.8µm/pixel) with a nuclear-based cell classifier relying on the Hoechst staining. Following cell segmentation, cells were classified according to their expression of RunX2 and/or OC. The same parameters were kept constant for all slides. Data were expressed as a percentage of stained cells compared with the total amount of cells labelled via the Hoechst staining.

B. 4. Scanning electron microscopy

SEM was used to visualize the presence or removal of cells and the seeding of PMSCs on HFL patches. This technique was the same as previously described[290]. One native and one decellularized sample from each of the four donors were sectioned into 5mm² samples, fixed on synthetic corks, and immersed in 3% glutaraldehyde. Successive increasing grades of ethanol (30%, 50%, 70%, 80%, 90%, 95%, and 3 × 100%) permitted us to dehydrate the tissues, which were completely dried using the CPD technique (Balzers, CPD020). A coating of 10nm gold (Cressington sputter, 208 HR) created a thin conductive layer on the samples. At least 15 images for each decellularized tissue and donor and a minimum of 30 pictures for the recellularized ECM were generated using field-emission SEM (JSM-7600F, Jeol Ltd. Akishima, Tokyo, Japan) and then examined. The same analysis was performed exactly seven days after PMSCs seeding to highlight the superficial recolonization of the ECM.

B. 5. Extracellular matrix & cellular components quantification

Native (N) and decellularized (D) tissue compositions were compared using the dosages of DNA, collagen, GAGs, and elastin contents. For each quantification, three random biopsies were harvested from native and decellularized tissues of four donors, resulting in 24 analysed biopsies (12 native and 12 decellularized) of 20, 25, 10, and 25mg for collagen, GAGs, elastin, and DNA quantification, respectively. The next few steps were exactly reproduced as previously described[290], with the freeze-drying and dry-weighting of all biopsies, DNA extraction using the DNeasy® Blood & Tissue kit (Qiagen, Hilden, Germany), measuring using the Quant-iT PicoGreen DNA assay kit (ThermoFisher, Waltham, MA, USA), quantification of the collagen content in the ECM using the Quickzyme Total Collagen Assay (Quickzyme, Leiden, Netherlands), GAG content extraction and dosage by means of the Blyscan Sulfated-GAG assay kit (Biocolor LTD., Carrickfergus, Northern Ireland), and elastin quantification with the Fast Elastin assay kit (Biocolor LTD., Carrickfergus, Northern Ireland). To increase the precision, plates were filled in duplicate and read three times. After taking the mean of the three readings and the duplicates, the final average quantification of the three biopsies was performed. While the final DNA concentration was expressed in ng/mg of dry weight, ECM protein amounts were expressed in µg/mg of dry weight.

B. 6. Differentiation through specific differentiation media

PMSCs in P4 were used to evaluate their differentiation capacity into the three phenotypes (chondrogenic, adipogenic, and osteogenic) that characterize MSCs according to the International Society for Cellular Therapy[200,253]. For all three differentiations, 1×10^5 cells of each porcine donor were seeded in triplicate in 6-well plates and expanded first with a PM. Specific differentiation media (DM) replaced the PM when 80–90% confluence was reached. All the culture-wells were evaluated by specific colorations on days 7, 14, and 21. A triplicate of the negative control was always performed using PMSCs in classical PM.

<u>Chondrogenic differentiation — Alcian blue staining</u>

The chondrogenic differentiation was achieved by means of the StemPro™ Chondrogenesis Differentiation kit (Thermofisher, A1007101, Waltham, MA, USA).

On day 21, culture-wells were rinsed three times in PBS and fixed with 4% formaldehyde at RT for 20min. After three new washings, the AB staining (1%, Sigma-Aldrich, A3157-10G, Saint Louis, MO, USA) was added to the wells for 30min to stain proteoglycans. The last three washes were performed with HCl (0.1N, Sigma-Aldrich, 1.09057.1000, Saint Louis, MO, USA).

Adipogenic differentiation — Oil red O staining

The StemPro™ Adipogenesis Differentiation kit (Thermofisher, A1007001, Waltham, MA, USA) was used following the manufacturer's protocol. The well preparation with washing and fixation was the same as that for the chondrogenic differentiation assessment. Then, Oil red O (ORO) staining (0.5%, Sigma-Aldrich, O0625-25G, Saint Louis, MO, USA) was added at RT for 10min to highlight neutral lipids. The last three washes were performed with distilled water.

Osteogenic differentiation — Alizarin red staining

The osteogenic DM was a mix of classical PM with added dexamethasone (1µM, Sigma-Aldrich, D4902-25mg), sodium dihydrophosphate (35mg/mL, Merck, 1.06346.1000, Darmstadt, Germany), and sodium ascorbate (25µg/mL, Sigma-Aldrich, A4034-100G, Saint Louis, MO, USA), as already defined by other authors[211]. The Alizarin Red staining (AR, 2%, Sigma-Aldrich, A5533-25G, Saint Louis, MO, USA) followed the same steps of washing in distilled water before and after staining but, for this staining of the calcium deposit, the fixation was in ethanol (70%) at RT for 1h. AR was incubated at 37°C for 10min. After the washes, all wells (chondrogenic, adipogenic, and osteogenic differentiations) were visualized under distilled water with the AxiovertS100 microscope (Zeiss, Oberkochen, Germany) and annotated with the AxioVision software.

Cell aggregate creation

Massive cellular gathering spontaneously formed cell aggregates after 12–14 days in the chondrogenic DM and after 14–21 days in the osteogenic DM. Because the osteogenic potential was the primary goal of this study, only osteogenic cell aggregates were characterized through histology and IHC for OC, col-1, and RunX2, as described in Sections B.2 and B.3. Using the same steps as in the

standard histology, AR staining (2%, pH 4.2, at 37°C for 2min) was also used to highlight the calcium deposit.

B. 7. Recellularization

In order to evaluate the cytocompatibility of processed scaffolds, cryopreserved PMSCs were seeded for seven days.

Periosteal mesenchymal stem cells seeding

Decellularized and sterilized HFL patches (N=5) of 1cm² were placed in sterile Cell-Crown™ inserts (12-well plate inserts, Sigma-Aldrich, Z742383-6EA, Saint Louis, MO, USA) and incubated in classical PM overnight in order to rehydrate and preheat them. The day after, or day zero (d0), 5×10^5 PMSCs were seeded on each patch, and the PM was added after 2h of dry incubation at 37°C and 5% CO_2 to enhance cell adhesion. On day one (d1), the inserts with seeded patches were moved into a new blank 12-well plate to avoid the impact of cells attached to the well walls in future analyses. The PM was replaced every two days just after examining the cell growth (d1, d3, d5, and d7). The cell viability was assessed at the end of the 7th day. The final analyses after seven days also included H&E, MT staining, and mIF-IHC for Col-1/Hoechst, as described above. The whole procedure was performed in duplicate in order to perform a SEM analysis on the whole patches and to assess the cellular spread. All the experimentations included a positive control (cells seeded in wells without a scaffold) and a negative control (scaffold in wells without seeding cells).

Cell growth—PrestoBlue

The kinetics of cell expansion was assessed using the PrestoBlue Assay (PrestoBlue™ Cell Viability Reagent, ThermoFisher, Invitrogen, A13261, Waltham, MA, USA) on d1, d3, d5, and d7. For this purpose, the PM was replaced by 3mL of preheated PrestoBlue solution (1:10 reagent with PM) and incubated at 37°C. After 3h, 100µl of the solution was transferred into a 96-well opaque plate, in duplicate, and the fluorescence was measured with a microplate reader (SpectraMax i3x, Molecular Devices; Sunnyvale, CA, USA) at Ex:560/Em:590nm.

Cell viability—Live/Dead

After the last PrestoBlue test on d7, Live/Dead staining (LIVE/DEAD™ Viability/Cytotoxicity Kit, ThermoFisher, Invitrogen, L3224, Waltham, MA, USA) evaluated the percentage of cell viability on the whole patch. Wells containing seeded scaffolds were rinsed three times with sterile PBS before being submerged in 2mL of working solution and sheltered from the light for 40min. After two more washes, patches were transferred onto glass slides and were mounted with Dako fluorescent mounting medium and then visualized using the AxioImager Z1 microscope and processed with the AxioVision software. A total of five pictures of each seeded scaffold (at the four corners and one in the centre) were taken at 2.5-fold magnification to average the entire sample area. The cell viability was calculated via the ratio between living cells (green dots) and total cells (living/green + dead/red cells) on pictures using Fiji software (ImageJ-win64, an open-access software on *https://imagej.nih.gov/ij/index.html*).

B. 8. Differentiation through extracellular matrix

This part of the differentiation experiments aimed to determine if the ECM could initiate osteogenic differentiation on its own, without including the DM. For this purpose, the same seeding as for classical differentiation was performed but, when confluence was reached, instead of feeding the cells with the DM, the ECM was added to the wells, which were supplied only with the PM. AR staining was also performed on d7, d14, and d21. A negative control (only cells with the PM) and a positive one (only cells with the DM) were included and compared with the differentiation through ECM. After the 21st day, the ECM was removed from the culture wells. Residual cells were washed in PBS, scraped out, and centrifugated at 1500rpm (377xg) for 5min. The supernatant was discarded and a prewarmed agarose solution (3%, VWR, Cambrex Bio Science, 44366 5W-250 g) was poured on the pellet. After solidification in a fridge (15–20min), agarose blocks were carefully demoulded and fixed in 4% formaldehyde to allow mIF-IHC for RunX2/OC. For this last manipulation, a native porcine periosteum (N-PP) was added as an additional tissue control.

Extracellular matrix preparation

Native and processed PBAs (N-PBA and D-PBA, respectively), processed HFL (D-HFL), and HP (D-HP) (N=3 donors for each type of matrices) were used to compare their own osteoinductive potentials. The HFL and HP were processed with the same decellularization protocol as described above. D-PBA was decellularized based on an earlier described perfusion protocol[340,342,353] with successive solutions of SDS (1%, VWR, 27926.295, Radnor, AR, USA), Triton X-100 (1%, VWR, M143, Radnor, AR, USA), type-1 DNAse (Roche, Sigma-Aldrich, 11284932001, Saint Louis, MO, USA) at 37°C and PBS washes. All ECMs were sterilized via gamma-irradiation despite the N-PBA that had been sterilely harvested. All ECMs were rehydrated, and each of them was incubated in a 50mL Falcon containing the PM for 24h before being added into the culture wells. This permitted us to maximize the recovery of the respective GFs in case the ECM had already released them into the medium. These preloaded PMs were retrieved and used to change the mediums every two days in the respective culture wells.

B. 9. Growth factors — Immunoblot

Two main types of GFs were explored: the angiogenic and the osteogenic. Angio-GFs present and/or preserved after the tissue engineering process would considerably increase the potential *in vivo* revascularization after transplantation as well as cell survival or new cellular attraction. BMPs are GFs that exert a relevant osteogenic function. Immunoblots allowed us to appraise the intrinsic angiogenic/osteogenic potentials of all these GFs present in our different types of ECM. For these quantifications, native periosteum (N-HP) and fascia lata (N-HFL) tissues (N=3, also for both native tissues) were added to compare and evaluate the persistence of GFs after decellularization.

Protein extraction from extracellular matrix

The protein extraction differed between tissue types. Indeed, hard bone tissues could not be dissolved using soft tissue techniques. For soft tissues (N/D-HP and N/D-HFL), a 50mg biopsy was chopped and lysed with a RIPA buffer containing a protease inhibitor cocktail and Pho-Stop. A Precellys Homogenizer (Bertin Technologies SAS, Montigny-le-Bretonneux, France) melded the samples in four

consecutive cycles at 7200rpm (8114xg). The samples were centrifugated at 2000rpm (626xg) for 5min, and only the clear residual supernatant was collected.

For their part, hard bone tissues (N/D-PBA) were ground with an electric saw and pestle and mortar to obtain 500mg biopsies of bone powder. The protein extraction was then achieved with an extraction solution made of 100mL of guanidine HCl (8M, Sigma-Aldrich, G7294-100ML, Saint Louis, MO, USA), 10mL of N-ethylmaleimide (0.2M, Sigma-Aldrich, E3876-25G, Saint Louis, MO, USA), 5mL of benzamidine (0.2M, Sigma-Aldrich, B6506-25G, Saint Louis, MO, USA), 2mL of phenylmethylsulphonyl (0.2M, Sigma-Aldrich, P7626-1G), and 83mL of demineralized water under continuous agitation at 4°C for 24h. A Tris HCl buffer (50mM, Trizma® hydrochloride solution, Sigma-Aldrich, T2663-1L, Saint Louis, MO, USA) was added to the supernatant and incubated on a shaking plate at 4°C for 5h. The samples were centrifugated at 3000rpm (1509xg) for 10min and only the residual supernatant was collected.

For all extractions, the protein concentration in the homogenized supernatant was defined using the PierceTM BCA Protein assay kit (ThermoFisher, 23227, Waltham, MA, USA), following the manufacturer's protocol.

Angiogenic growth factor quantification

The RayBio® C-Series Human Angiogenesis Antibody (Tebu-Bio, 126AAH-ANG-1-8, Le Perray-en-Yvelines, France) quantified 20 different angio-GFs. For this purpose, membranes were blocked at RT for 30min and incubated with 100µg of proteins on a shaker plate at RT for 2.5h. Next, the steps exactly followed the manufacturer's protocol, with a few washes, incubations in a biotinylated antibody cocktail, and dilution in HRP Streptavidin, as well as baths of detection buffers preceding the chemiluminescent revelation on chromatographic films. Based on a published method[25] and using Fiji software, each densitometry spot was subtracted from the background density and normalized to the ratio of the positive control of an arbitrarily chosen reference tissue (N-HP) to the positive control of the analysis in question. The normalization was completed via the multiplication of the obtained value by the global quantity of proteins to the weight of each respective sample (expressed in µg of proteins/mg of tissue). Final outcomes were averaged on the mean density of two detection spots for each GF and the mean of all three donors.

Bone morphogenetic protein quantification

Exactly the same procedure was followed in order to quantify BMP-2, -4, -5, -6, -7, -8, -9, and -11 using the RayBio® C-Series Human BMP Related Array 2 (Tebu-Bio, 126AAH-BMP-2–8, Le Perray-en-Yvelines, France).

B. 10. Statistical analyses

Statistical analyses were realized using GraphPad Prism (v.8.0.1, GraphPad Software, San Diego, CA, United States) as well as SPSS software (v.27, IBM SPSS, Inc., Chicago, IL, United States). A Shapiro–Wilk test and QQ plots checked the normality of continuous variables. All data with a Gaussian distribution were compared using parametric unpaired T-tests for DNA and ECM components comparisons before/after decellularization, as well as for the Live/Dead. Levene's test was always used to check the equality of variances beforehand. A Welch's correction was applied if the latter was not assumed. Kruskal–Wallis tests were used to analyse angiogenic or osteogenic GF content, followed by post hoc multiple comparisons (Mann–Whitney) if justified and adjusted with a Bonferroni correction. All tests were two-tailed. The level of significance was always set at 0.05 in order to reject the null hypothesis. All outcomes displayed in the graphics are expressed as means ± SEMs.

C. Results

C. 1. Decellularization

Macro- and microscopic aspects illustrated the decellularization success on 1124µm (± 108µm) thick HFL samples since all of Crapo's criteria were met[178]. Both the H&E and Hoescht staining showed a no-man's-land concerning nuclei (Fig. 59 – a), and the DNA content fell below the critical threshold of 50ng/mg of dry weight (Fig. 59 – b, p=0.000008). The ECM was also preserved according to the qualitative and quantitative persistence of collagen (p=0.323), which is the main ECM component of the HFL[290]. GAGs and elastin were qualitatively preserved but quantitatively altered via the decellularization process (p<0.0001).

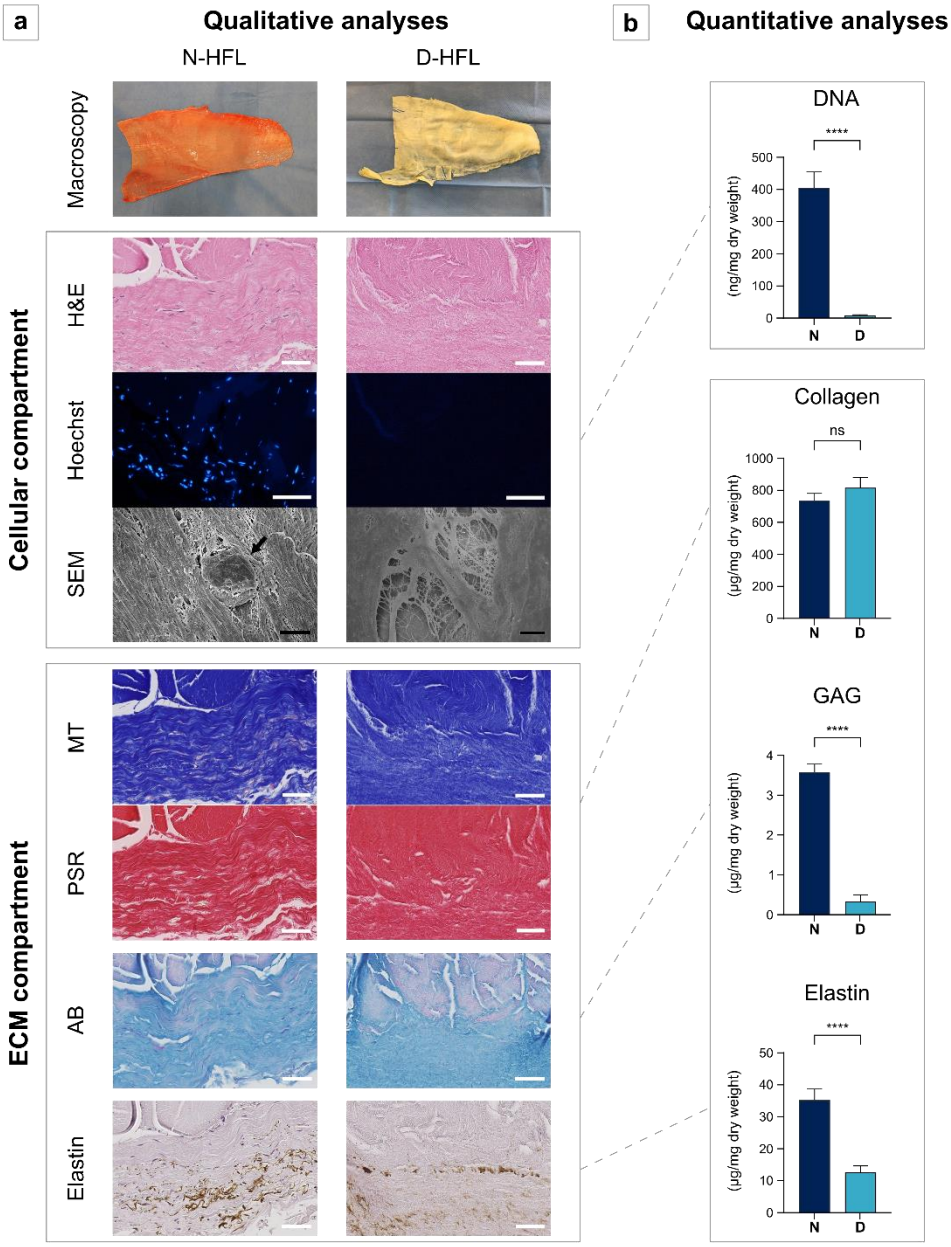

Figure 59. Qualitative (a) and quantitative (b) evaluation of the cellular and extracellular matrix compartments before/after decellularization. The DNA extraction was achieved with the DNeasy® Blood & Tissue kit (Qiagen, Italy) and measured using the Quant-iT PicoGreen DNA assay kit (ThermoFisher Scientific). The quantification of the collagen content was carried out using the Quickzyme Total Collagen Assay (Quickzyme, Leiden, Netherlands),

*the GAG content extraction and dosage by means of the Blyscan Sulfated-GAG assay kit (Biocolor LTD., Carrickfergus, Northern Ireland), and the elastin quantification with the Fast Elastin assay kit (Biocolor LTD., Carrickfergus, Northern Ireland). ECM: extracellular matrix, N-HFL: native human fascia lata, D-HFL: decellularized fascia lata, H&E: haematoxylin and eosin, SEM: scanning electron microscopy, MT: Masson's trichrome showing collagen fibres, PSR: Picrosirius Red showing collagen fibres, AB: Alcian blue showing proteoglycans, DNA: deoxyribonucleic acid, and GAG: glycosaminoglycan content. Black arrow shows a cell. White scale bars: 50µm. Black scale bars: 5µm. ****: p<0.0001; ns: non-significant.*

C. 2. PMSC differentiation & cell aggregates

PMSCs from landraces and minipigs behaved the same way and showed differentiation into three different phenotypes on day 21 (Fig. 60 – a). The PMSCs from only one Landrace failed to differentiate into the chondrogenic phenotype but were positive for the adipogenic and osteogenic ones. Among all wells (7 donors x triplicate = 21 wells for each phenotype), five osteogenic cell aggregates were spontaneously formed between the 14th and 21st days. Their characterization (Fig. 60 – b) showed an aggregation of cells of different shapes on the H&E-stained sections, expressing RunX2 and OC, and surrounded by a new ECM containing col-1 fibres. The calcium deposit was highlighted via the AR staining, attesting to the osteogenic phenotype of these cell aggregates.

C. 3. Recellularization & cytocompatibility

The cytocompatibility of D-HFL was confirmed. Indeed, after PMSCs seeding, all the histological stainings and the mIF-IHC showed cell recolonization on the surface with the onset of invasion deeper into the tissue (Fig. 61 – a). The col-1 fibres were organized to support the cell bed in recellularized tissue. The SEM supported that the scaffold was a welcoming environment for the PMSCs, as the latter were numerous and well spread out, which is a sign of well-being. The Live/Dead staining pointed in the same direction, with qualitatively very few red/dead cells visualized compared with the green/alive ones. Quantitatively, the PMSCs growth followed the same kinetic growth curve as the positive control wells, and both viabilities were close to 100% on the 7th day (p=0.190) (Fig. 61 – b).

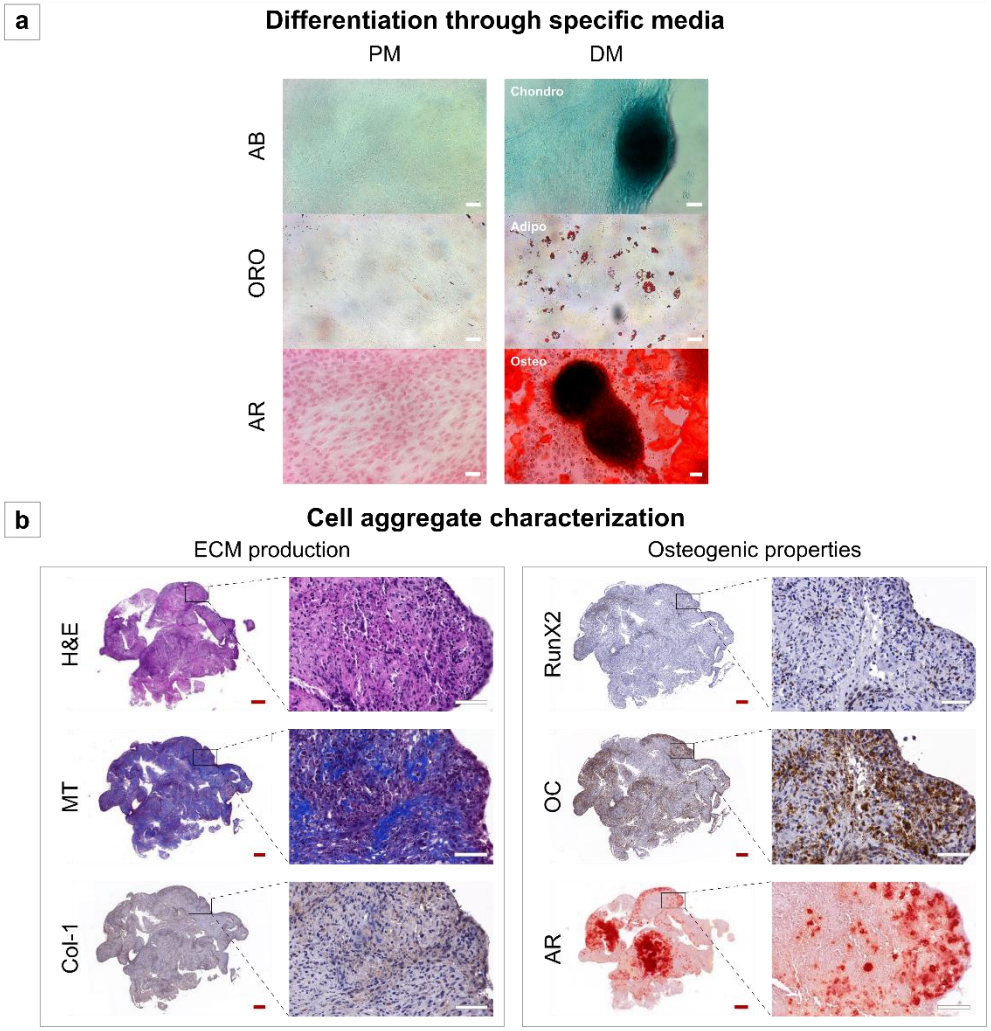

Figure 6o. Porcine periosteal mesenchymal stem cell differentiation through chondrogenic, adipogenic, and osteogenic differentiation media (a) and cell aggregate characterization after spontaneous formation between 14th and 21st days (b). All figures were taken on the 21st day. PM: proliferation medium, DM: differentiation medium, Chondro: chondrogenic differentiation medium, Adipo: adipogenic differentiation medium, Osteo: osteogenic differentiation medium, AB: Alcian blue staining, ORO: Oil red O staining, AR: Alizarin Red staining, H&E: haematoxylin and eosin staining, MT: Masson's trichrome staining, Col-1: type I collagen immunohistochemistry (IHC), and OC: osteocalcin IHC. White scale bars: 50µm. Red scale bars: 200µm.

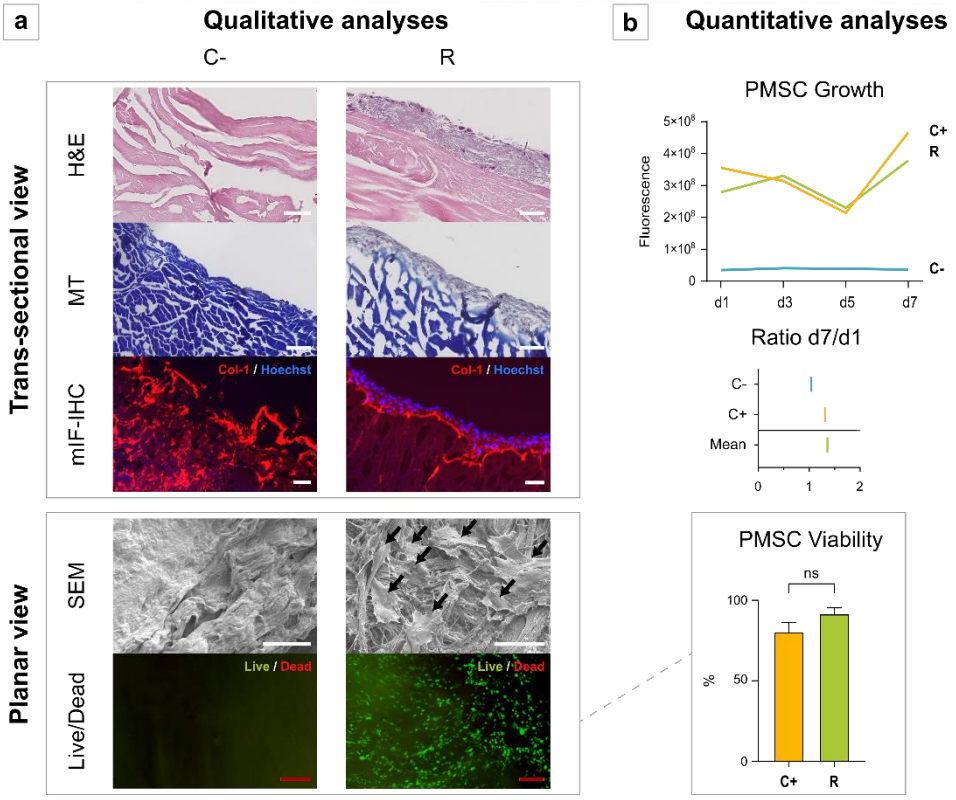

Figure 61. Qualitative (a) and quantitative (b) evaluation of D-HFL scaffold recellularization with PMSCs. The PMSCs growth was assessed using the PrestoBlue Assay (PrestoBlue™ Cell Viability Reagent, ThermoFisher, Invitrogen, A13261, Waltham, MA, USA) on days (d) 1, 3, 5, and 7. The ratio d7/d1 expresses the ratio of the number of cells on d7 to that on d1. The Live/Dead staining (LIVE/DEAD™ Viability/Cytotoxicity Kit, ThermoFisher, Invitrogen, L3224, Waltham, MA, USA) evaluated the cell viability by the ratio between the number of living cells and the total number of cells on the patch. C-: negative control (scaffold without cells), R: recellularized scaffold, C+: positive control (cells without scaffold), H&E: haematoxylin and eosin, MT: Masson's trichrome, mIF-IHC: multiplex immunofluorescence immunohistochemistry, Col-1: type I collagen, SEM: scanning electron microscopy, and dx: day number x. Black arrows show seeded PMSCs. White scale bars: 50µm. Red scale bars: 200µm. ns: non-significant.

C. 4. Angio-induction potentials of extracellular matrices

Angio-GFs were studied with the aim of measuring the angio-induction potentials of different ECMs after transplantation. First, our scaffold of interest (N/D-HFL) was compared with N/D-HP, which is richly vascularized in order to approximate the baseline for both soft tissues (Fig. 62 – a).

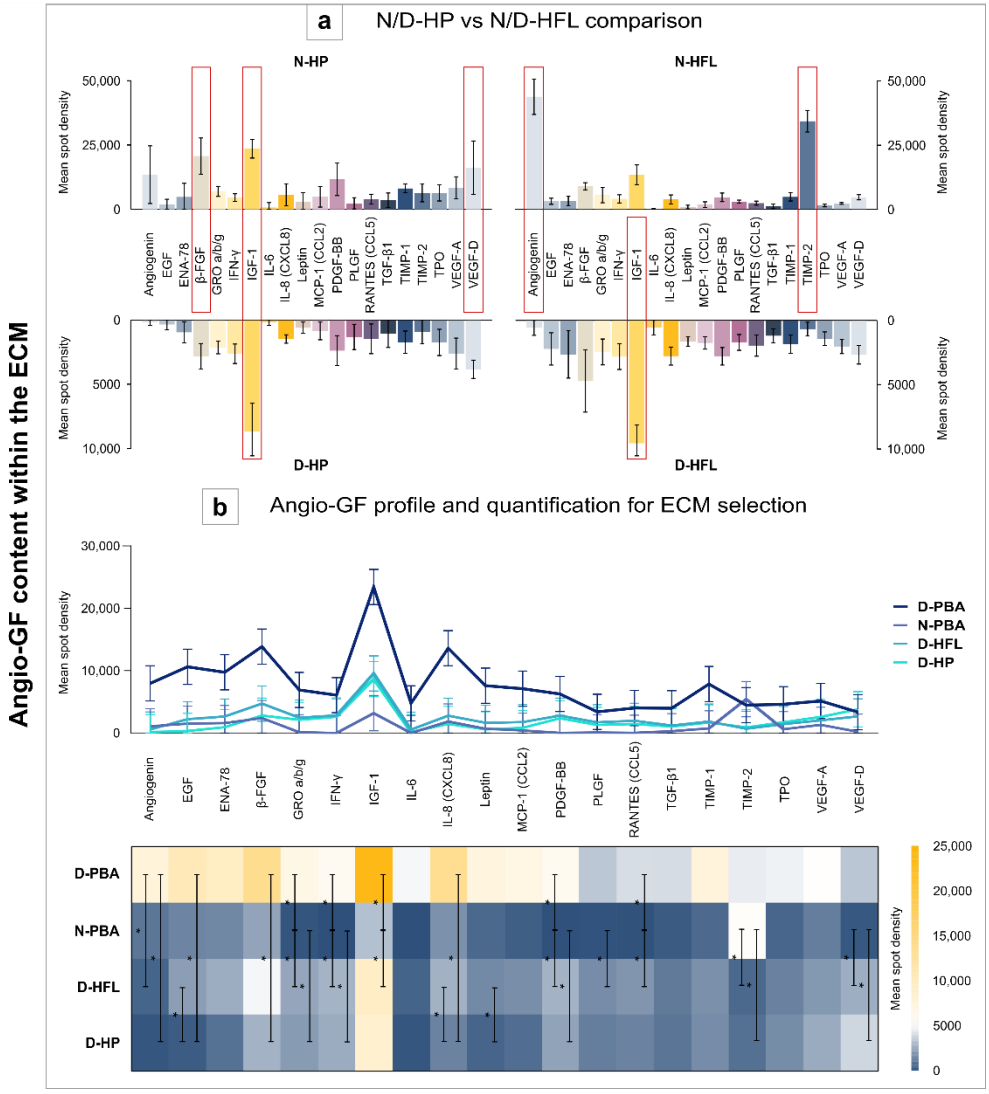

*Figure 62. Evaluation of angio-induction potentials of ECMs via the angiogenic GF content in each matrix. The RayBio® C-Series Human Angiogenesis Antibody (Tebu-Bio, 126AAH-ANG-1-8, Le Perray-en-Yvelines, France) was used for this quantification (a and b). First, the D-HFL membrane, which is our membrane of interest, was compared with the periosteum (a). Then, the angiogenic GF content was expressed according to each ECM with a profile graph and a heatmap (b). Angio-GF: angiogenic growth factor, N/D-HP: native or decellularized human periosteum, N/D-HFL: native or decellularized human fascia lata, D-PBA: decellularized porcine bone allograft, and N-PBA: native porcine bone allograft. Error bars: 95% confidence interval (CI); *: p<0.05.*

The main angio-GFs present in N-HP were β-FGF, IGF-1, and VEGF-D, whereas N-HFL contained more angiogenin and tissue inhibitors of metalloproteinase 2 (TIMP-2). However, after decellularization, both tissues lost a certain amount of all angio-GFs, but the best preserved one was IGF-1 in both tissues. In order to evaluate and/or to choose the right complex association of ECM, the profile graph and the heatmap (Fig. 62 – b) allow us to illustrate the relatively higher quantity of all angio-GFs for D-PBA. IGF-1 was always the most abundant, except for N-PBA. Each angio-GF was statistically compared between all the ECMs (Table 18).

Table 18. Comparison of angiogenic growth factors content between each different ECM.

	Kruskal-Wallis			Mann-Whitney post-hoc		
Dependent variable	df	H	p-value	Tissue 1	Tissue 2	p-value
Angiogenin	3	15.30	.002	D-PBA	D-HP	.012 [a]
					D-HFL	.024 [a]
EGF	3	16.78	.001	D-PBA	D-HP	.012 [a]
				D-HFL	D-HP	.012 [a]
ENA-78	3	10.36	.016			
ß-FGF	3	11.53	.009	D-PBA	D-HP	.024 [a]
GRO a/b/g	3	13.85	.003	N-PBA	D-HP	.012 [a]
					D-HFL	.012 [a]
					D-PBA	.012 [a]
IFN-γ	3	13.57	.004	N-PBA	D-HP	.012 [a]
					D-HFL	.012 [a]
					D-PBA	.012 [a]
IGF-1	3	16.29	.001	N-PBA	D-HFL	.012 [a]
					D-PBA	.012 [a]
IL-6	3	9.30	.026			
IL-8 (CXCL8)	3	13.10	.004	D-PBA	D-HP	.024 [a]
				D-HFL	D-HP	.012 [a]
Leptin	3	12.19	.007	D-HFL	D-HP	.012 [a]
MCP-1 (CCL2)	3	10.75	.013			
PDGF-BB	3	13.97	.003	N-PBA	D-HP	.012 [a]
					D-HFL	.012 [a]
					D-PBA	.012 [a]
PlGF	3	9.16	.027	N-PBA	D-HFL	.012 [a]
RANTES (CCL5)	3	11.82	.008	N-PBA	D-HFL	.012 [a]
					D-PBA	.012 [a]
TGF-ß1	3	6.53	.093			

TIMP-1	3	10.17	.017			
TIMP-2	3	8.65	.034	N-PBA	D-HP	.012 [a]
					D-HFL	.012 [a]
TPO	3	5.61	.132			
VEGF-A	3	4.13	.248			
VEGF-D	3	12.95	.005	N-PBA	D-HP	.012 [a]
					D-HFL	.012 [a]

[a]*With Bonferroni correction for multiple comparisons.*

Kruskal-Wallis tests were used in order to analyse angiogenic GF content and were followed by post-hoc multiple comparisons (Mann-Whitney) if justified, adjusted with a Bonferroni correction. All tests were two-tailed. EGF: Epidermal growth factor, ENA-78: epithelial neutrophil-activating peptide 78, β-FGF: Beta fibroblast growth factor, GRO a/b/g: Growth-regulated oncogene a/b/g, IFN-γ: Gamma interferon, IGF-1: Insulin-like growth factor 1, IL-6: Interleukin 6, IL-8 (CXCL8): Interleukin 8 (C-X-C motif ligand 8), MCP-1 (CCL2): Monocyte chemoattractant protein 1 (C-C motif ligand 2), PDGF-BB: Platelet-derived growth factor BB monomer, PlGF: Placental growth factor, RANTES (CCL5): Regulated upon activation normal T cell expressed and secreted (C-C chemokine ligand 5), TGF-β1: Transforming growth factor-β1, TIMP-1 & 2: Tissue inhibitors of metalloproteinase 1 & 2, TPO: Thrombopoietin, VEGF-A & D: Vascular endothelial growth factor A & B, N-PBA: Native porcine bone allograft, D-PBA: Decellularized porcine bone allograft, D-HP: Decellularized human periosteum, D-HFL: Decellularized human fascia lata, df: degrees of freedom, H: The test statistic of Kruskal-Wallis test. Grayed out boxes highlight angio-GF with a significant difference at Kruskal-Wallis test and for which a post-hoc multiple analysis was performed.

C. 5. Osteoinduction potential of extracellular matrices

<u>BMP content within the extracellular matrices</u>

When comparing D-HFL with the native one or N/D-HP, which is also the innate natural osteogenic membrane, we observed that N-HP contained much more BMPs than N-HFL (Fig. 63 – a). However, after decellularization, D-HFL kept more BMPs than D-HP. The heatmap and the profile graph (Fig. 63 – b) both indicate that BMP-2 and BMP-7 were the most abundantly expressed BMPs in all the ECMs. However, there were statistical differences between each ECM depending on the studied BMP (BMP-2, -5, -7, or -11) with a higher content found in D-PBA (Table 19).

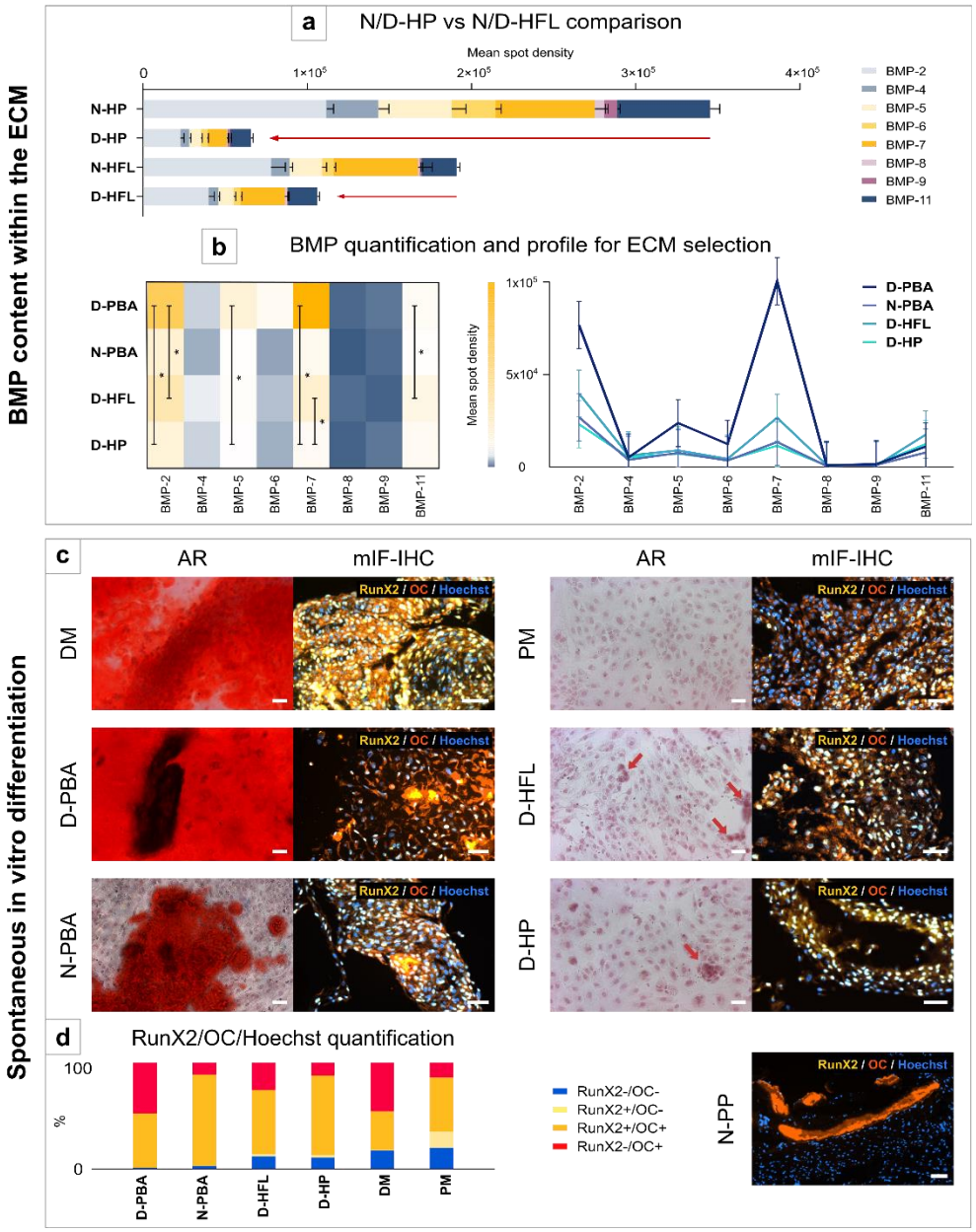
BMP content within the ECM
a
N/D-HP vs N/D-HFL comparison
Mean spot density
0
1×10⁵
2×10⁵
3×10⁵
4×10⁵
N-HP
D-HP
N-HFL
D-HFL
BMP-2
BMP-4
BMP-5
BMP-6
BMP-7
BMP-8
BMP-9
BMP-11
b
BMP quantification and profile for ECM selection
D-PBA
N-PBA
D-HFL
D-HP
Mean spot density
1x10⁵
5x10⁴
0
BMP-2
BMP-4
BMP-5
BMP-6
BMP-7
BMP-8
BMP-9
BMP-11
Spontaneous in vitro differentiation
c
AR
mIF-IHC
RunX2 / OC / Hoechst
DM
PM
D-PBA
D-HFL
N-PBA
D-HP
d
RunX2/OC/Hoechst quantification
100
%
0
D-PBA
N-PBA
D-HFL
D-HP
DM
PM
RunX2-/OC-
RunX2+/OC-
RunX2+/OC+
RunX2-/OC+
N-PP

*Figure 63. Evaluation of the osteoinduction potentials of ECMs via the BMP content in each matrix and spontaneous differentiation of PMSCs in vitro. The RayBio® C-Series Human BMP Related Array 2 (Tebu-Bio, 126AAH-BMP-2–8, Le Perray-en-Yvelines, France) was used for the BMP quantification (a, b). First, the D-HFL membrane was compared with the periosteum via a stacked bars diagram of all types of BMPs (a). Then, the BMP content was expressed according to each ECM with a heatmap and a profile graph (b). PMSC spontaneous differentiation was confirmed with AR staining and mIF-IHC for RunX2 and OC (c). This last experiment was quantified in order to increase the knowledge about the ECM impact on PMSC differentiation stage (d). This graph shows the relative content of cells labelled with RunX2 alone (RunX2+/OC-), RunX2 and OC (RunX2+/OC+), OC alone (RunX2-/OC+), or none of them (RunX2-/OC-). N/D-HP: native or decellularized human periosteum, N/D-HFL: native or decellularized human fascia lata, BMP: bone morphogenetic protein, D-PBA: decellularized porcine bone allograft, N-PBA: native porcine bone allograft, AR: Alizarin Red staining, mIF-IHC: multiplex immunofluorescence immunohistochemistry, OC: osteocalcin, DM: differentiation medium, PM: proliferation medium, and N-PP: native porcine periosteum. White scale bars: 50µm. T-bars: standard error of the mean (SEM), error bars: 95% confidence interval (CI), and *: p<0.05.*

Table 19. Comparison of BMP content between each different ECM.

	Kruskal-Wallis			Mann-Whitney post-hoc		
Dependent variable	df	H	p-value	Tissue 1	Tissue 2	p-value
BMP-2	3	13.25	.004	D-PBA	D-HFL	.012 [a]
					D-HP	.012 [a]
BMP-4	3	3.07	.381			
BMP-5	3	10.79	.013	D-PBA	D-HP	.012 [a]
BMP-6	3	3.33	.343			
BMP-7	3	14.37	.002	D-PBA	D-HP	.012 [a]
				D-HFL	D-HP	.012 [a]
BMP-8	3	4.51	.211			
BMP-9	3	5.78	.123			
BMP-11	3	11.97	.007	D-PBA	D-HFL	.012 [a]

[a]With Bonferroni correction for multiple comparisons.

Kruskal-Wallis tests were used in order to analyse angiogenic GF content and were followed by post-hoc multiple comparisons (Mann-Whitney) if justified, adjusted with a Bonferroni correction. All tests were two-tailed. BMP: Bone morphogenetic protein, N-PBA: Native porcine bone allo-graft, D-PBA: Decellularized porcine bone allograft, D-HP: Decellularized human periosteum, D-HFL: Decellularized human fascia lata, df: degrees of freedom, H: The test statistic of Krus-kal-Wallis test. Grayed out boxes highlight angio-GF with a significant difference at Kruskal-Wallis test and for which a post-hoc multiple analysis was performed.

Spontaneous *in vitro* differentiation

PMSCs clearly differentiated in contact with D-PBA and N-PBA in the same manner as with the DM (Fig. 63 – c). At a higher magnification (×20), some sparse PMSCs in the D-HFL wells could suggest the beginning of a calcium deposit even though no clear differentiation was visible. The same observation was made for the D-HP wells but to a lesser extent. After 21 days of culture, mIF-IHC showed some positive osteogenic markers in almost all wells but in different proportions. The control N-PP confirmed the OC staining of the remaining bone harvested together with the periosteum, but no periosteal cell expressed either OC or RunX2. According to the quantification, an interesting observation is that the ECMs producing a clear osteodifferentiation with calcium deposits in the AR staining have the highest proportions of RunX2-/OC+ and/or RunX2+/OC+ cells (Fig. 63 – d).

D. Discussion

The actual gold standard for hard tissue grafting is the bone autograft, which integrates most criteria of the diamond concept. Nevertheless, its quantitative availability is limited and only suitable for small defects[18,50]. The harvest site morbidity is also a point of consideration[383–386]. All these reasons usually direct CSBD treatment towards bone allografts, which were considered in this study. Because of their burden of complications due to the lack of viability[14,156], the need for a synergic association was evident in order to complete the diamond.

A new bone component (cancellous or morselized bone graft, massive allograft, or other approaches) wrapped by a membrane has already been described as relevant so as to prevent soft tissue interposition and ectopic ossification as well as to guide osteogenesis[107,249]. While the periosteum is the natural shell of the bone, the induced membrane could reproduce its main function of supplying the biological needs to promote bone regeneration. Even if very helpful for CSBD treatment by ensuring the function of a vascularized periosteum-like tissue, this induced membrane requires a two-stage surgery with the associated disadvantages and differs from HP in its composition, thickness, and mechanical isotropy[99]. In actuality, the induced membrane is thicker and contains more MSCs than HP[111]. The goal of this study was not to reproduce these tissues identically, but rather to

use the knowledge of these membranes to learn how to mimic their function. The creation of an off-the-shelf induced membrane that could ensure the function sought in a one stage surgery may emerge as a solution to reduce the time, costs, and drawbacks for society and patients involved in this challenging surgical treatment.

Although the HFL was already used for a huge panel of indications in the reconstruction surgery field, it was never used to repair CSBDs. In this study, this musculoskeletal tissue was, however, a very good cell carrier for PMSCs. A recent study also demonstrated that PMSC viability, survival, and migration were better when seeded on a collagen membrane than when in a synthetic bone[387]. The complex multicomponent association still seems mandatory, because even if PMSCs brought the osteogenicity, contact with a mineralized matrix was needed to provide the osteoinduction. All these outcomes allowed us to answer our previous questions, but some points deserve to be argued.

First, the chondrogenic and osteogenic potential of PMSCs alone *in vitro*, without any ECM interaction, was promising in itself. A recent study also showed the bipotentiality of PMSCs, which can help in endochondral and intramembranous ossification[32,66]. The spontaneous formation of cell aggregates expressing RunX2, producing a col-1-based matrix, and generating calcium deposits was very encouraging for the purpose of bone regeneration.

Furthermore, during the natural bone healing steps, the initial fracture bleeding gives rise to a haematoma, which provides a series of cytokines, GFs (VEGF, IGF, FGF, TGF-β, EGF, PDGF, CCL5, as well as BMP), and pro-inflammatory factors that promote initial healing[19,32,66]. All these molecules work in the mitogenesis process, osteoblastic differentiation, as well as neovascularization to restore the appropriate environment for soft/hard callus formation.

The tissue engineering processes have already been largely explored, and the decrease in GAGs and elastin in different connective tissues was previously described in the literature[178,179,340,342,388] but did not affect the goal of obtaining a malleable and consistent membrane, because the HFL is mostly composed of col-1 fibres[290]. However, the GAG depletion and/or dysfunction after decellularization were hypothesized to influence the GF linkage to the ECM[178,179,388].

For example, the remaining GAGs from decellularized tissues would not be able to fix FGF and TGF-β1[389] or have an effect on VEGF binding[390]. IL-8 (CXCL8) is also directly attached to sulfated GAG chains[390]. In addition to their vascular function, these angio-GFs also play a function in bone homeostasis and/or osseous regeneration, *i.e.*, IGF-1, FGF, and TGF-β activate osteoblastic proliferation, increase col-1 synthesis, and reduce osteoblast apoptosis[391–393]. An interesting observation in our study was that despite a distinct angio-GF profile in N-HP and N-HFL, the decellularization process modified the matrices to obtain a strictly similar profile between both tissues with the highest preservation for IGF-1, which intervenes at both the osteogenic and angiogenic levels[394]. The specific roles of IGF-1 include osteogenesis induction and the formation of endothelial cells both by the phosphoinositide-3-kinase (PI3-K)/Akt and the mitogen-activated protein kinase (MAPK) pathways as well as the control of bone homeostasis by regulating the RANK ligand (RANKL)[394,395]. Therefore, in terms of angiogenic potential, D-HP did not show superiority over D-HFL. Angio-GFs present and/or preserved after the tissue engineering process would increase the potential *in vivo* revascularization after transplantation as well as cell survival or new cellular attraction. While the angiogenic potentials of the different ECMs were explored in this study, the angiogenesis could further be evaluated using a coculture of PMSCs and endothelial cells.

From an osteogenic point of view, GAGs seemed to have a significant impact on the biological activities of BMPs and improve the expression of RunX2, a key pro-osteogenesis regulator gene, as well as the subsequent osteoblastic differentiation[390]. The tissue engineering processes did not affect the BMP content of our ECMs in the same way. Indeed, the total BMP amount was much more lowered in D-HP than in D-HFL. Since N-HP is much more cellular than N-HFL[290], GF proteins are produced and secreted in higher amounts, and the absolute GF content of the intracellular compartment probably explained the higher total quantity of BMPs in N-HP. On the contrary, the BMPs expressed in N-HFL are probably already fixed to the ECM because of its fewer cells and are then more resistant to cellular decimation. The relatively higher residual BMP content in D-HFL is in favour of using it as a cell carrier with an osteogenic purpose. This does not necessarily mean that D-HFL could start osteogenic differentiation. Nevertheless, some authors recently indicated that fibroblasts lying on the HFL displayed a weak yet real osteogenic differentiation capacity[258], suggesting that

this ECM might preserve a few osteoinduction potentials for MSCs. Even though a few cells showed some calcium metabolism, PMSCs started to express osteogenic markers as soon as they were placed into culture wells with the PM, as highlighted with the mIF-IHC. This fact is very encouraging because PMSCs are probably the MSCs pre-programmed to preferentially differentiate towards the osteogenic pathway. However, this cellular behaviour was clearly not enough to induce positive AR staining. The explanation may lie in the percentage of labelled cells and the degree of associated differentiation. Indeed, RunX2 is a very early nuclear gene marker in the osteogenic differentiation pathway (osteoprogenitor marker), while OC secretion labels occur at a later stage of differentiation (osteoblast marker)[204]. The very last stage of osteogenic differentiation still expresses OC but loses RunX2 expression. Only mineralized ECMs (N/D-PBA) were able to increase the percentage of advanced stages of differentiation, *i.e.*, RunX2+/OC+ and RunX2-/OC+ cells, as much as needed to allow spontaneous osteogenic differentiation. Previous authors showed that the demineralization of a scaffold plays a relevant role in reducing the *in vitro* osteogenic differentiation of bone marrow MSCs compared with a mineralized scaffold[396]. Interestingly, in complete opposition to the soft tissue, hard bone tissues benefited from a more important GF expression after decellularization. This difference may be related to the organization of the mineralized bone matrix that hides GFs in N-PBA and that may be unmasked via decellularization. D-PBA has been shown to contain significantly more BMP-2 and -7, which are some of the most relevant factors for osteoinduction[33,259,260]. They can initiate fracture healing and play a crucial role in osteoblast differentiation[33,259] as well as in mature bone homeostasis but sometimes lead to ectopic ossifications[19,33,383]. To avoid this side effect, taking advantage of the BMPs that are naturally active in D-PBA and/or containing them via a periosteal flap[397], for example, could orientate and contain their action. The induced increase in those BMPs' expressions in D-PBA could potentially compensate for the loss in D-HFL, send an osteogenic signal, and initiate PMSC differentiation while avoiding the complications of external BMPs[260,263].

This study aimed at characterizing the engineered D-HFL and its interaction with PMSCs, in comparison with the HP, so as to produce the best osteogenic complex to maximize the impact on *in vivo* models. The perfect multicomponent device to guarantee bone regeneration could then associate a D-HFL as a carrier of PMSCs seeded on its internal side, surrounding a D-PBA that could serve as an

osteoconductive matrix as well as an osteoinductive signal for PMSC differentiation after transplantation. Keeping this in mind, undifferentiated PMSCs could be used in order to maintain their proliferative and replicative potential while ensuring progressive osteogenic differentiation *in vivo* in contact with D-PBA. In contrast, if the decellularization could avoid the immune response after allotransplantation[175] and improve BMP expression in D-PBA, it might lead to a drop in the acute inflammatory response responsible for the initiation of bone healing. Moreover, surrounding the bone with a tubing sheet could create a hypoxic chamber that might contain the surgical haematoma and the inflammatory process initiating the healing procedure. This new question rising from this *in vitro* study could only be addressed using *in vivo* models. As has already been developed in our institution[398], a femoral non-union pig model will assess the new OM in stringent conditions of a CSBD typical of the clinical situation. This model will be representative of what orthopaedic surgeons face in patients and will allow, in the case of success, us to consider the first clinical trials of this innovative approach.

E. Conclusions

Our data allow us to consider the association between a bone allograft, which can fill in the missing volume (stability) while providing osteogenic GFs (osteoinduction), and a surrounding D-HFL membrane (osteoconduction), shapeable on demand, containing some angio-GFs (vascularization) and seeded with PMSCs (osteogenic cells). This complex *in vitro* model could provide the biological elements that allow bone regeneration *in vivo*.

– TAKEAWAYS –

Paper 5 – A New Osteogenic Membrane to Enhance Bone Healing: At the Crossroads between the Periosteum, the Induced Membrane, and the Diamond Concept

- *<u>Interplay</u>* *Cell* ⇔ *ECM*

- *<u>OSTEOCONDUCTION</u>* < *D-HFL + bone allograft*
  - → *Intrinsic osteo- and angio-GFs*
  - → *Niche for cell seeding*

- *<u>OSTEOGENICITY</u> (= Intramembranous ossification)* < *PMSCs*
  - *Col-1-based ECM production* ←
  - *Ca^{++} deposit* ←

- *<u>CHONDROGENICITY</u> (= Endochondral ossification)* < *PMSCs*

- *<u>OSTEOINDUCTION</u>* < *Contact with mineralized matrix*

⇨ *D-HFL provides an excellent matrix for hosting undifferentiated PMSCs, preserving their proliferation and replication abilities, while fostering their inherent potential for chondrogenic and osteogenic differentiation in conjunction with a bone allograft.*

Back to the Diamond

- **Is it possible/better to use PMSCs to bring osteogenicity in the osteoconductive HFL matrix?**

D-HFL serves as an excellent carrier and niche for PMSCs, supporting their adhesion, proliferation, and replication. PMSCs are able to differentiate into osteogenic, chondrogenic, and adipogenic lineages. They naturally produce collagen-based ECM associated with calcium deposits, promoting bone formation. Their potential for both osteogenic and chondrogenic differentiation supports intramembranous and endochondral ossification processes, respectively. Since achieving absolute stability in a CSBD is challenging and healing often relies on endochondral ossification, this bipotentiality is highly advantageous.

- **Is it possible/better to leverage intrinsic over extrinsic GFs?**

Extrinsic GFs can sometimes have harmful effects, such as causing ectopic ossification or triggering oncogenic processes. Therefore, using intrinsic GFs may be more advantageous. After decellularization, D-HFL retains a higher concentration of BMPs than D-HP, endowing it with inherent potential for chondrogenic and osteogenic differentiation. Although D-HFL and D-HP cannot induce spontaneous differentiation on their own, they may act as catalysers for seeded PMSCs, maintaining them in an undifferentiated state during rest phases and supporting differentiation when required.

- **Is it possible/better to implant differentiated or undifferentiated cells?**

For bone formation, an osteoinductive signal is essential to trigger PMSCs differentiation into osteogenic or chondrogenic lineages. D-HFL alone cannot initiate this switch but contact with an MBA can. Seeding undifferentiated PMSCs on the superficial layer of D-HFL, which can be reversed to face the bone, allows the cells to retain their proliferation and replication rates while enabling differentiation upon contact with the MBA.

In summary, D-HFL, combined with an MBA, acts as an excellent scaffold for undifferentiated PMSCs, supporting their proliferation and replication and enhancing their potential for chondrogenic and osteogenic differentiation *in vitro*.

– REQUIREMENT SPECIFICATIONS –

Requirement	Specification	Validation
Osteoconductive matrix		
Composition	- Col-1 membrane	V
Morphology	- 2 layers - Thickness (1 thin + 1 thick layers) - Large size - Shapeable	V V V
Biocompatibility	- No immunogenicity - Carrier for cells - No cytotoxicity	V V V
Osteoinductive mediators		
Bioactivity	- Osteogenic GF - Osteogenic differentiation - Chondrogenic differentiation	V V V
Osteogenic cells		
Osteogenicity	- Cell adhesion, proliferation, replication - Osseous ECM production	V V
Mechanical stability		
Membrane properties	- Sheet malleable support - Resistance to handling - Isotropy or anisotropy?	V V ≈
In vivo model	**AND** - Stitchable - Mechanical stability	
Vascularization		
Vascular supply	- Angiogenic properties - Neoangiogenesis **OR** - Intrinsic vascular architecture - Functional vascular network	≈
In vivo transposition		
Clinical needs	- Off-the-shelf availability - One-stage surgery	

CHAPTER IV. *In vivo* transposition – Critical-size bone defect repair

Research questions emerging from the Diamond

Built upon previous chapters and *in vitro* investigations, an *in vivo* large animal model would emphasize previous outcomes and is an essential step before potential clinical translation in human patients. The effectiveness of the new OM is assessed with a model of femoral CSBD in minipig and compared to the standard treatment with a single MBA.

This chapter aims to answer the following questions:

- **How can the preclinical large animal model for CSBD be optimized for use with an OM?**
- **Does the OM promote MBA integration and facilitate creeping substitution?**

Technical considerations

« We are too surprised by what we rarely see and not surprised enough by what we see every day. »

Translated from Madame de Genlis, 1782

A. Model of critical-size bone defect in the porcine femur

In investigations concerning substantial bone defects, the pig model has proven notably advantageous when compared to sheep and goat, particularly in terms of bone mineral density, anatomy, structure, morphology, healing process, and remodelling[59]. Even with its plexiform predominance over dense Haversian structure[59], porcine bone shows the closest resemblance to human samples[59,399,400]. The main issues with the pig model are its ease of handling and its high growth rate[59,400].

A pig femoral non-union model was developed by Thomas Schubert et al., resulting in a CSBD and proving the absence of consolidation after 6 months without additional treatment[398] (Fig. 64). This model is used in our study to reproduce stringent conditions of CSBDs and ensure the added value of the treatment.

B. Mechanical stability & osteosynthesis

B. 1. Mechanical stability, a facet of the Diamond

As already seen, mechanical stability is a paramount facet of the Diamond concept[19,91]. A cryopreserved MBA provides a structural architecture to fill the gap in a CSBD with some immediate mechanical stability. However, its single use is not enough to ensure a stable construct. The association with a fixation by osteosynthesis is primordial. Three types of osteosynthesis might be considered[109].

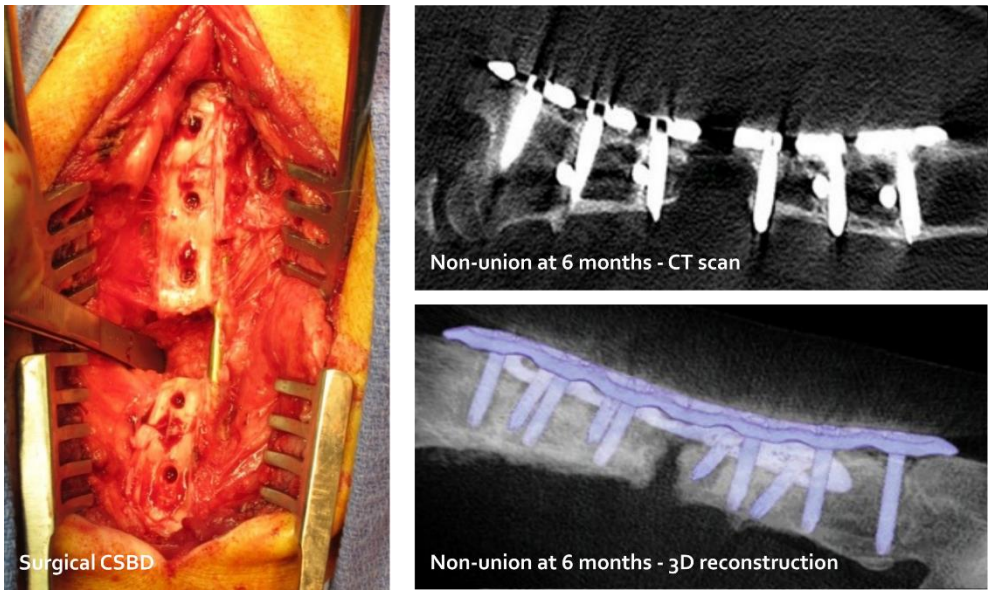

Figure 64. Critical-size bone defect (CSBD) created by Prof. Thomas Schubert in a porcine femur showing non-union after 6 months without additional treatment[398]. Pictures courtesy of Prof. Thomas Schubert.

External fixator = Though an easy-to-use and versatile device[109] offering a real fixation opportunity for a tibia, its application is not suitable for porcine femurs, which are localized at the abdominal level with an imposing soft-tissue mass. The risks of insufficient stability away from the ostectomy site, Schantz screw loosening, or pin track infections[59,109] are too substantial to consider this option in this study.

Plate = Osteosynthesis by plate and screws was the one experimented in our institution to fix similar porcine CSBDs[398]. The stability was achieved by two orthogonal plates on the femoral shaft. The bone allograft usually needs a point of fixation into the plate to avoid implant extrusion. However, periosteal blood flow might be impaired under the plate[109], even with limited contact dynamic compression plate (LC-DCP)[87]. The properties of the new OM or seeded cells might be altered by plate compression (Fig. 65).

Intramedullary nailing (IMN) = This osteosynthesis is now widely considered the standard treatment for lower limb diaphyseal fractures enabling immediate weightbearing, due to its central load-bearing capacity. Precautions should be

taken for potential occurrence of air/fat embolisms and thermal necrosis after reaming[59]. However, axial deviations of an implant are less frequent[59] and the wrapping OM might be constraint-free (Fig. 65).

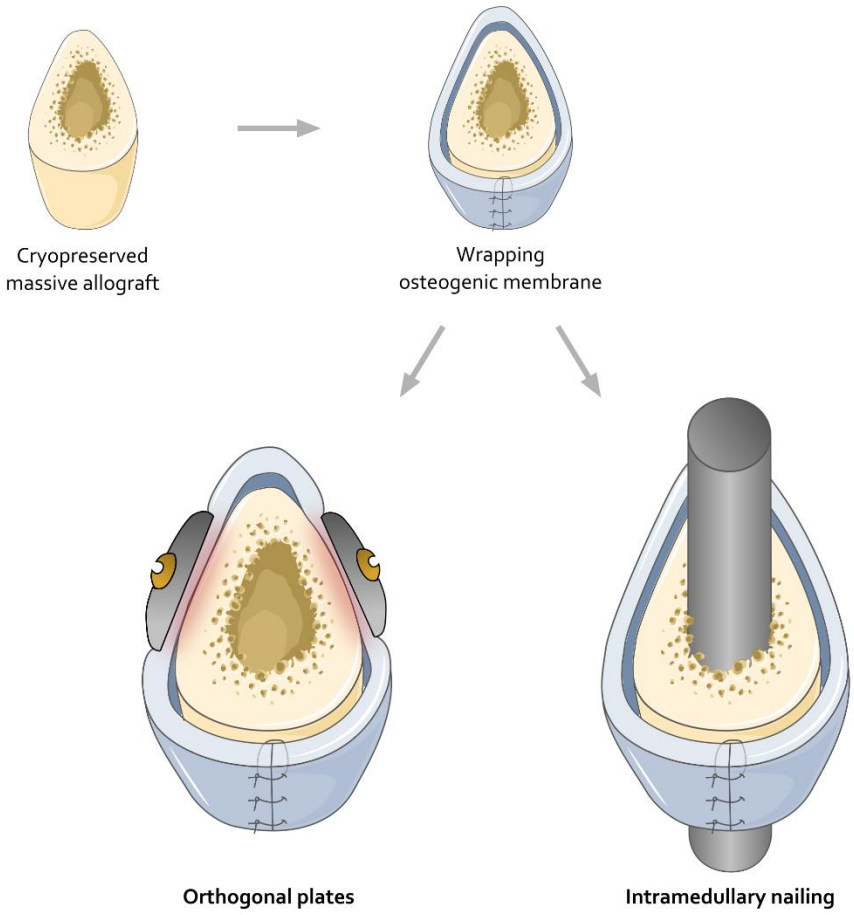

Figure 65. Osteosynthesis choice driven by the compression on the wrapping osteogenic membrane. Two orthogonal plates might compress the membrane, crushing the underlying cells.

B. 2. Intramedullary nailing creation

Considering the aforementioned advantages, the IMN was selected as the preferred osteosynthesis method. However, to the best of our knowledge, a femoral IMN for minipigs does not currently exist. Leveraging recent advancements in metallic 3D-printing technology and the proven compatibility of nickel-titanium materials[401–403], we developed a custom-made IMN, secured with

Angular Stable Locking System (ASLS, © Depuy Synthes, Fig. 66) screws, as detailed in the following paper.

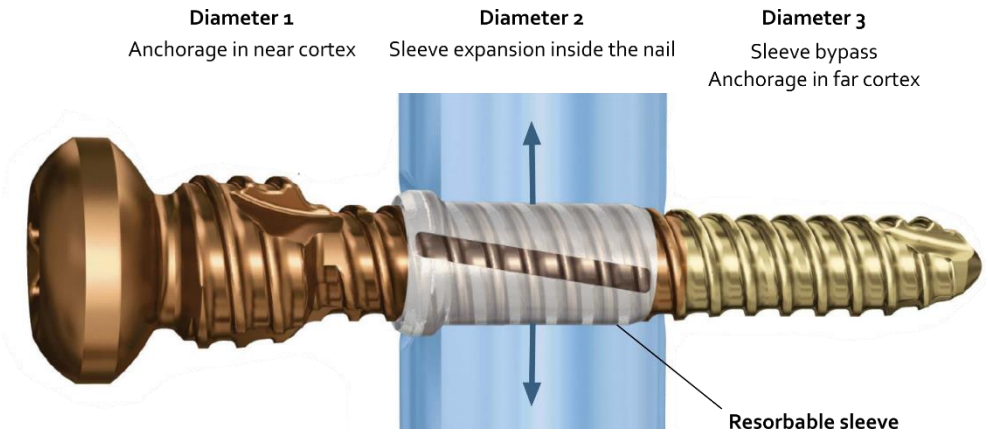

Figure 66. Angular stable locking system (ASLS) screw technology (©Depuy Synthes, Johnson & Johnson) ensures both angular and axial stability. This system incorporates three distinct core diameters in the screw, along with a resorbable plastic sleeve that expands into the nail with the second diameter of the screw. Adapted from the surgical technique guide (©Depuy Synthes Trauma, a division of Synthes GmbH, 2021, SE_831727 AC (DSEM/TRM/0115/0284), EOS: 170541-211019, 10/2021)[404].

C. Surgical table

Another difference from the initially described model is the surgical positioning of the pig. While the minipig was placed in lateral decubitus in the initial technique[398], nailing in ventral decubitus was more convenient. Hence, a custom-made surgical table was engineered to support the minipig upright with its hind limbs free (Fig. 67). This table advantage lies in the ability to operate on both femurs simultaneously during a single surgical session. This eliminates the need to reposition the pig on the table and conduct two separate surgical procedures, thereby potentially reducing the risk of contamination and the surgical time, even and especially because this surgery takes more time than plating. Another crucial advantage of this table is its compatibility with peroperative fluoroscopy, which is essential for the nailing procedure, but impracticable with a standard table.

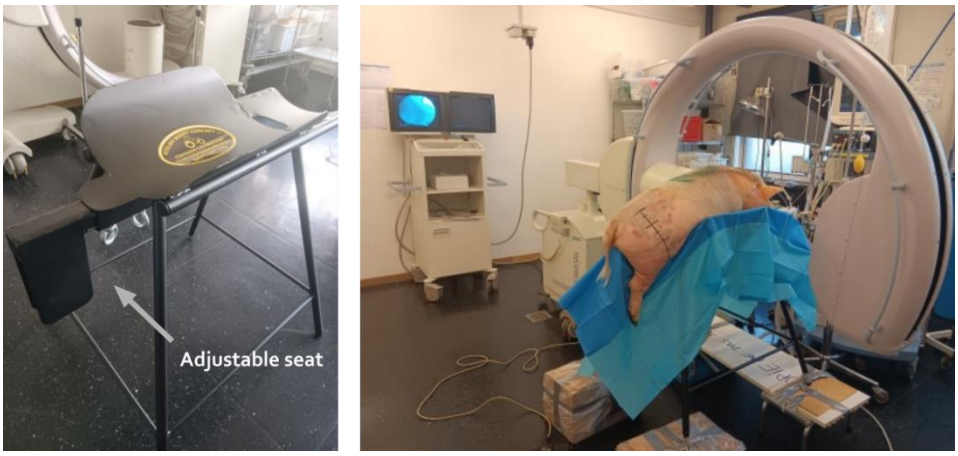

Figure 67. Surgical table allowing both femoral IMN in a single surgical time, as well as fluoroscopy use. Production by Atelier Werry Concept (Clermont-lez-Walcourt, Belgium).

Paper 6 – FixThePig: a custom 3D-printed femoral intramedullary nailing for preclinical research applications

Julie Manon, Alexandre Englebert*, Robin Evrard, Thomas Schubert, Olivier Cornu*

** Share first authorship*

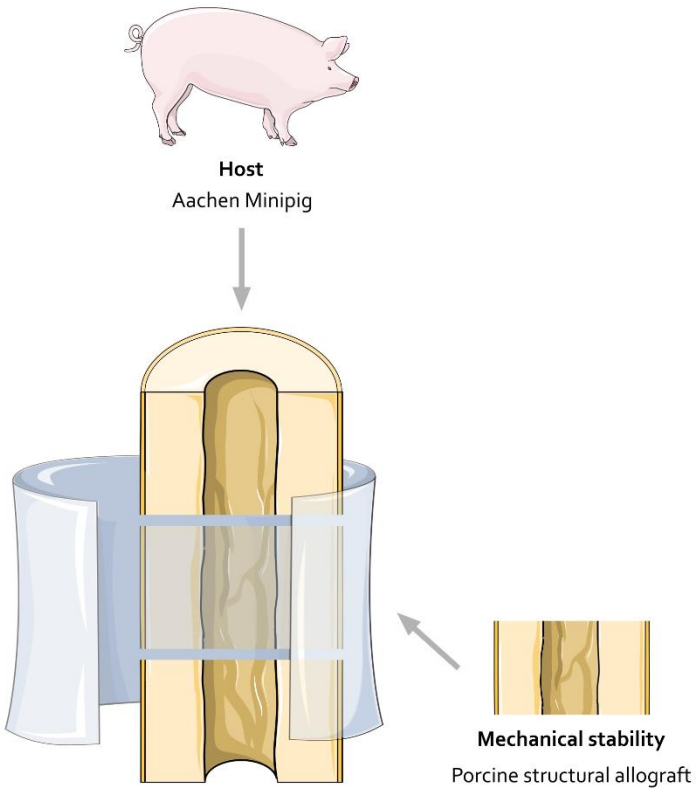

Submitted in

Front. Bioeng. Biotechnol. (IF=6.064)

Abstract

Background: CSBDs pose significant challenges in clinical orthopaedics and traumatology. Developing reliable preclinical models that accurately simulate human conditions is crucial for translational research. This study addresses the need for a reliable preclinical model by evaluating the design and efficacy of a custom-made 3D-printed IMN specifically for CSBDs in minipigs. The study aims to answer the following questions: Can a custom-made 3D-printed IMN be designed for femoral osteosynthesis in minipigs? Does the use of the custom-made IMN result in consistent and reproducible surgical procedures, particularly in the creation and fixation of CSBDs? Can the custom-made IMN effectively treat and promote bone consolidation of CSBDs?

Hypothesis: The custom-made 3D-printed IMN can be designed to effectively create, fix and treat CSBDs in minipigs, resulting in consistent surgical outcomes.

Materials and Methods: The IMN was designed based on CT scans of minipig femurs, considering factors such as femoral curvature, length, and medullary canal diameters. It was 3D-printed in titanium and evaluated through both *in vitro* and *in vivo* testing. Female Aachen minipigs underwent bilateral femoral surgeries to create and fix CSBDs using the custom-made IMN. Post-operative follow-up included X-rays and CT scans every 2 weeks, with manual examination of explanted femurs to assess consolidation and mechanical stability after 3 months.

Results: The custom-made IMN effectively fitted the minipig femoral anatomy and facilitated reproducible surgical outcomes. Symmetric double osteotomies were successfully performed, and allografts showed minimal morphological discrepancies. However, proximal fixation faced challenges, leading to pseudarthrosis in several cases, while most distal osteotomy sites achieved stable consolidation.

Discussion: The custom-made 3D-printed IMN demonstrated potential in modelling and treating CSBDs in minipigs. While the design effectively supported distal bone healing, issues with proximal fixation highlight the need for further refinements. Potential improvements include better screw placement, additional mechanical support, and adaptations such as a reduction clamp or a cephalic screw to enhance stability and distribute forces more effectively.

Full-length article in Appendix.

– TAKEAWAYS –

Paper 6 – FixThePig: a custom 3D-printed femoral intramedullary nailing for preclinical research applications

- *<u>Large animal model</u> = Aachen minipigs*
  Femoral IMN
  Cutting guide clipped on the ancillary
  3D-printing

⇨ *An improved preclinical model for CSBD healing using a wrapping OM.*

Paper 7 – An osteogenic membrane to enhance massive bone allograft integration: *In vivo* pilot study in a minipig model

Authors to be determined

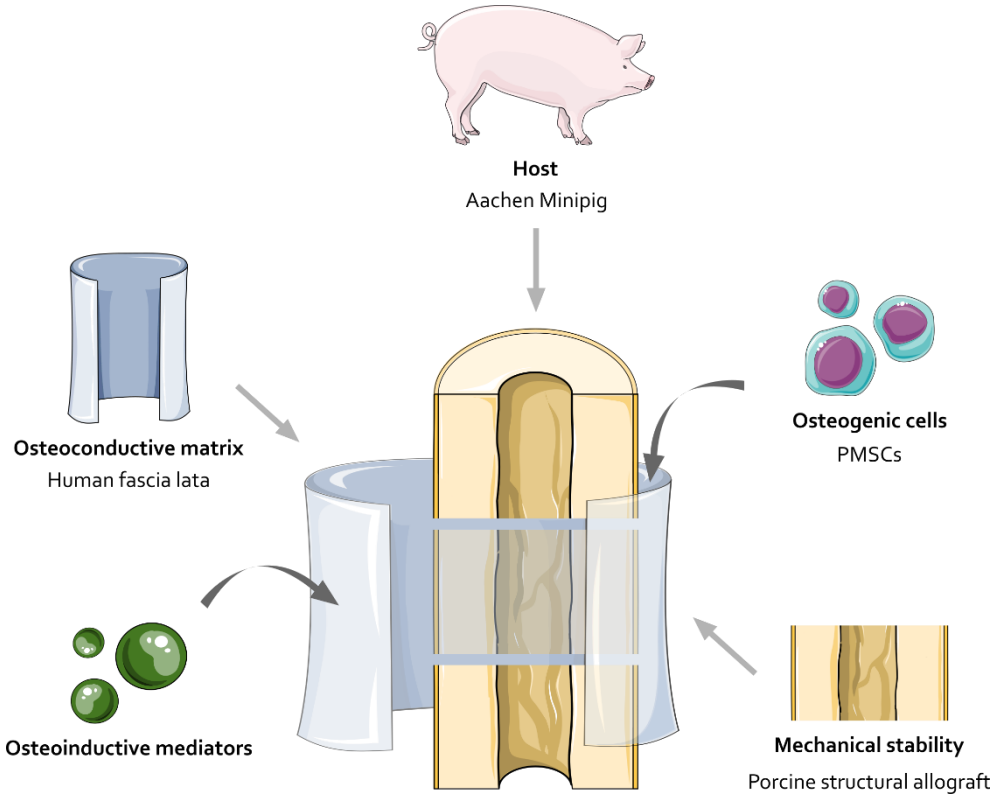

Work in progress

Abstract

CSBDs pose significant challenges in orthopaedic surgery, necessitating innovative approaches for effective reconstruction. This study explores the integration of MBA with or without an OM, derived from decellularized HFL and recellularized with PMSCs, in the minipig femur.

Female Aachen minipigs (N=4) were used as a large animal model for CSBD healing. The first animal was the primary allograft donor and the three others underwent reconstruction. In each pig, the left femur received an MBA alone and the right femur an MBA with the OM. Surgical procedures included standardized CSBD creation by symmetric double osteotomy facilitated by 3D-printed ancillary tools and cutting guides. MBA transplantation with or without OM was fixed using custom-designed 3D-printed IMNs. Post-operative care and follow-up involved radiographic and tomographic imaging, blood tests, and fluorochrome injections to monitor osteogenic activity. After 3 months, femurs were explanted for macroscopic evaluation, histology, IHC, and microCT analyses.

Histological analyses demonstrated new bone formation and evidence of endochondral ossification, accompanied by creeping substitution in the deep centre of MBA. MicroCT analysis will provide 3D morphological insights, with further investigations planned for IHC analyses*.

This study paves the way for optimizing bone regeneration strategies to improve clinical outcomes in orthopaedic surgery.

* These data ought to be available soon.

A. Introduction

Nowadays, CSBD is still a major challenge in orthopaedic reconstruction surgery. Whether the cause is traumatic, tumoral, or septic, the bone architecture, the periosteum, and surrounding soft tissues are destructed and the biological environment around the missing bone is hostile and unfavourable to spontaneous healing. MBA is one of the standards to help healing by providing immediate mechanical support and an osteoconductive scaffold. However, the creeping substitution can not reach the MBA centre. Because of the absence of living cells within the MBA and its lack of osteogenicity[6,157], this treatment is a burden for many complications such as non-union[83,156,158–160], long-term fracture[83,141,156,160], local sepsis[83,141,156,160], or resorption[14,161,162].

Therefore, tissue engineering techniques were used to create very different solutions to increase osteogenesis, viability, and long survival of MBA. Among others, a new OM was developed based on a decellularized HFL, recellularized with PMSCs. HFL was extensively studied in terms of fibre organization[405], optimal decellularization protocol[406], osteogenic and angiogenic characteristics[406], cross-link preservation[351], and showed some similarities with periosteum[290,291], providing an adequate scaffold to support osteogenic cells[291]. As previously explored, this OM might play a role in CSBD healing, at the crossroads between the periosteum, the induced membrane, and the diamond concept. The periosteum is rich in PMSCs and plays a paramount role in callus formation after bone fracture[25,32,69,245,379,380]. The induced membrane, described by Masquelet et al. as a biological reaction against cement spacer, acts as an adjuvant with bone autograft for osseous consolidation[96,98,99,108]. The diamond concept integrates all the facets needed to achieve bone regeneration including osteoconductive scaffold, osteogenic cells, osteoinductive GFs, mechanical stability and vascularization[19,80,91]. All these *in vitro* preliminary results have to be validated in a preclinical *in vivo* model to go further.

When housing facilities are available, the pig bone is a large animal model relatively close to human bone[59,398–400]. A CSBD protocol was previously established with an ostectomy of 2.5cm length in the pig femoral shaft[50,398,407]. In absence of additional treatment, this gap fails to achieve bone union after 6 months and represents a good preclinical model to test the OM. This membrane

will be wrapped around an MBA, in order to assess its potential positive impact on creeping substitution and integration of the MBA compared to the standard treatment, *i.e.* the MBA alone. This design is usually stabilized mechanically by two orthogonal plates; however, a custom-made 3D-printed IMN was recently developed to avoid interfering with the external seeded membrane[407]. This study will use this innovative IMN for CSBD of the femoral shaft.

This research aims to evaluate the efficiency of the OM as an adjunctive treatment with MBA for repairing CSBD in the minipig femur. The outcomes could pave the way to understand how to further advance patient healthcare.

B. Materials & Methods

B. 1. Study design

Figure 68 provides an overview of the methodological approach.

B. 2. Porcine model

Female Aachen minipigs (N=4, 40-55kg, Carfil Quality, Oud-Turnhout, Belgium) were used as a large animal model for CSBD healing[408]. One of them was used to test the whole surgical technique while harvesting the first transplantable bone allografts. The three others were used as long-duration (3 months) experimental models. Potential bias associated with growth was avoided as the animals were already adult (1.5 to 2 years old). This study was approved by the local ethics committee (Ref 2023/UCL/MD/39, approved on the 18th of July 2023). To ensure proper acclimatization, each minipig spent at least 2 weeks in our facilities before undergoing the surgery.

Figure 68. Study design of the experiments. GFP: green fluorescent protein, PMSCs: periosteal mesenchymal stem cells, HFL: human fascia lata, MBA: massive bone allograft, X-rays: radiography, CT scan: computed tomography, Bio: blood and serum samples, OM: osteogenic membrane, MicroCT: microfocus computed tomography, IHC: immunohistochemistry. w-x: time before the surgical event, 0w: time of the surgery, 2w to 12w: time from 2 weeks to 12 weeks after the surgery.

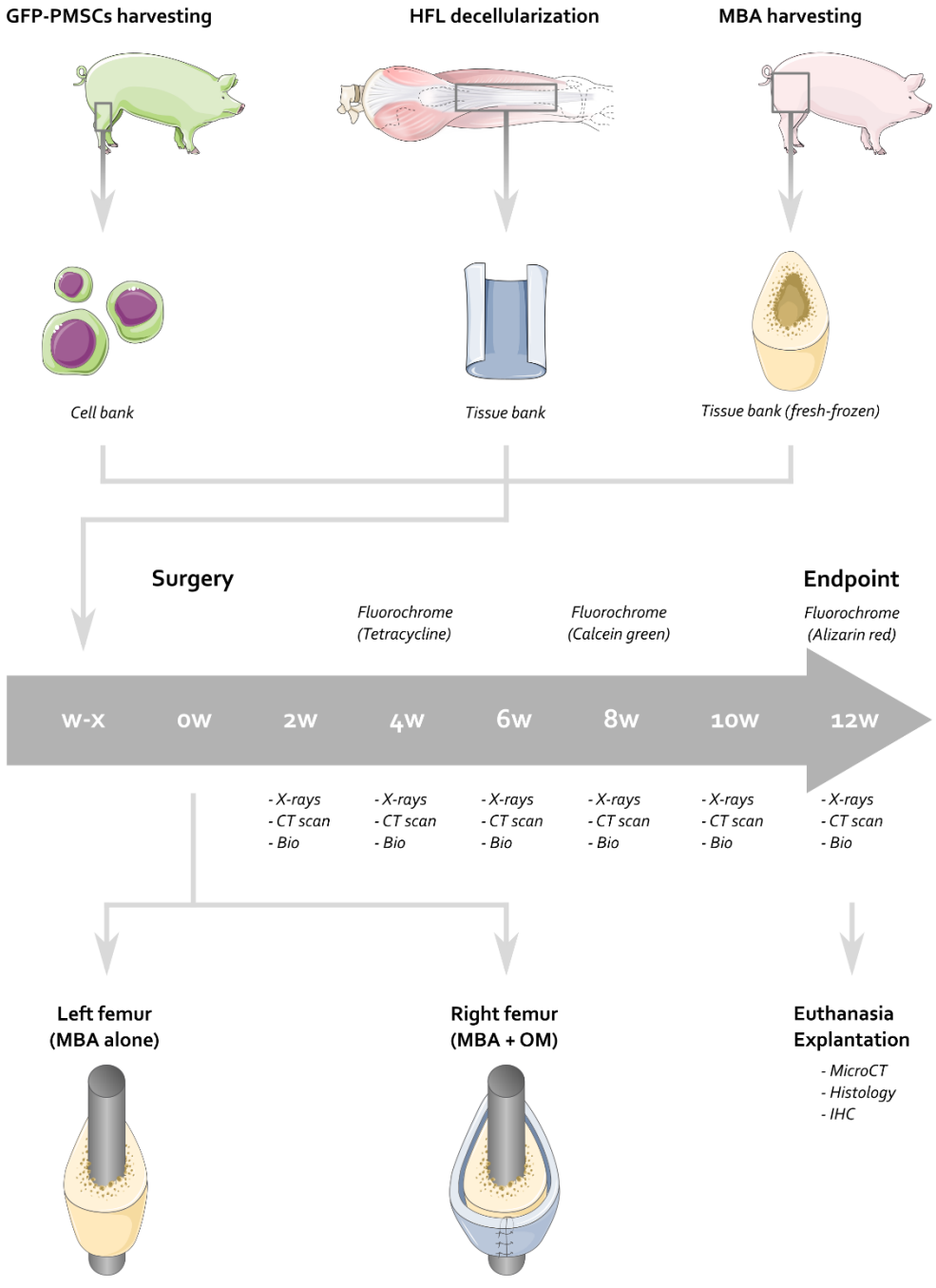
GFP-PMSCs harvesting
HFL decellularization
MBA harvesting
Cell bank
Tissue bank
Tissue bank (fresh-frozen)
Surgery
Endpoint
Fluorochrome (Tetracycline)
Fluorochrome (Calcein green)
Fluorochrome (Alizarin red)
W-X
0W
2W
4W
6W
8W
10W
12W
- X-rays - CT scan - Bio
Left femur (MBA alone)
Right femur (MBA + OM)
Euthanasia Explantation
- MicroCT
- Histology
- IHC

Each animal was operated on both femurs to be its own control. A CSBD was created in each femur following previously described protocols[398,407]. The left femur was reconstructed with fresh frozen MBA alone while the right side was reconstructed with the MBA and a surrounding OM.

B. 3. Osteogenic membrane

OMs were created based on previous protocols[290,291,351]. Briefly, HFLs were harvested from cadavers received at the Anatomy Department of UCLouvain (IRB00008535, Brussels, Belgium), under local ethics committee authorization (Ref 2021-30AOU-356 approved on September 13, 2021). Those membranes were cut into 4x12cm samples (48cm²) and were decellularized with a validated NaOH based-protocol[291,341,406], sterilized by gamma-irradiation (minimal dose of 25kGy, IBA Mediris, Fleurus, Belgium), and stored at -80°C while waiting for recellularization and transplantation.

B. 4. Surgical procedure

Critical-size bone defect creation & Massive bone allograft transplantation

The surgical procedure strictly follows the previously described protocol[407]. Briefly, general anaesthesia was induced by an intramuscular (IM) injection of 6mg/kg Zoletil 100® (Virbac, Carros, France) and 2mg/kg Rompun® (Bayer, Leverkusen, Deutschland), and maintained by endotracheal ventilation with Isoflurane (0-1.5%, Forene®, AbbVie, Wavre, Belgium). Curare, analgesia, and anti-inflammatory drugs were administered through an intrajugular central line. A 2g bolus of Kefzol® (Natrium Cefazoline, Sandoz®, Novartis Company) was injected at induction, with an additional 1g every 3h during surgery. After disinfection, a pure lateral incision centred on the femoral shaft was extended proximally for nail entry at the greater trochanter. The intramedullary canal was reamed until 9mm diameter, and the IMN was inserted under fluoroscopic guidance. Using a fixed cutting guide, a 2.5cm CSBD was created in the mid-shaft of each femur, centred on the nail. Fresh-frozen MBAs were harvested from the preceding minipig for subsequent surgeries, scanned via clinical CT (Somatom Definition AS 128 scanner, Siemens Healthineers) to ensure morphological compatibility with the recipient femurs, and transplanted respecting laterality. The IMN was reinserted through the MBA between the femoral extremities and secured with fixation screws.

Osteogenic membrane wrap

The frozen decellularized membrane was thawed the day before the surgery and rehydrated in large sterile Petri dishes with culture medium DMEM/F-12 (Thermofisher, 11320033, Waltham, MA, USA), supplemented with FBS (10%, Gibco, 10270-106), penicillin-streptomycin (1%, Gibco, 15140-122), and amphotericin B (1%, Gibco, 15290-026)). On the day of the surgery, the rehydrated membrane was recellularized with 75 million PMSCs (1.56 million PMSCs/cm²). These porcine PMSCs expressing green fluorescent protein (GFP) were previously isolated and cultivated until the fourth passage[291]. The seeded membrane was dry incubated at 37°C and 5% CO_2 for 2h to maximize cell adhesion. DMEM/F-12 was then added for cell survival waiting for the transplantation time.

Positive control was analysed by means of H&E staining in histology to assess the quantity and distribution of seeded PMSCs before implantation.

This OM was then placed around the MBA in the right femur of each minipig, with the seeded side confronting the bone. It was sutured on itself with a running stitch and on adjacent soft tissues and periosteum with simple stitches using resorbable suture thread (Polysorb® 4.0).

B. 5. Post-operative care & follow-up

X-rays & CT scans

Immediate post-operative fluoroscopy was performed to confirm the accuracy of the osteosynthesis. Every two weeks, each minipig was subjected to standard X-rays (DigitalDiagnost, Philips, France) and a CT scan (beam collimation 0.6mm, tube voltage 140kV) for 3 months. These imaging modalities were used to monitor for any material protrusion or displacement, as well as to assess bone consolidation and the overall healing kinetics. The consolidation rate was quantified by the mRUS[43,44] and the TUS[41,42]. Briefly, these scoring systems assign a score ranging from 1 (no callus) to 4 (remodelled mature callus) to each visible cortical segment on X-rays (anteroposterior and lateral views) and on paramedian coronal and sagittal reformats for CT scans (2 paramedian reformats per plane). The total score per osteotomy is calculated by summing the individual cortical scores for mRUS and TUS, with the TUS score then halved. A blinded independent

orthopaedic surgeon, unaware of the side of the membrane implantation, performed the scoring of all radiographs and CT scans to ensure unbiased evaluation.

Blood test & serum sampling

Two blood samples were taken each time before the surgery and just after the surgery to estimate the blood loss and checked every 2 weeks until euthanasia at 3 months. They were harvested from the central line if still present or from a sterile jugular puncture. The first blood sample was used to assess classical hemogram. The second one was centrifuged at 3000rpm (1409xg) for 15 minutes, and the resulting serum was isolated and stored at -20°C until ALP quantification. For the latter, 1µL of the serum of each sample was transferred into a 96-well opaque plate with 109µL of Assay Buffer and 20µL of MUP Reaction Mix, following the manufacturer protocol of the Alkaline Phosphatase Assay Kit (Abcam, ab83371). The plate was incubated at 25°C for 30 minutes. Then, 20µL of Stop solution were added to all the samples, and fluorescence was measured three times using a microplate reader (SpectraMax i3x, Molecular Devices; Sunnyvale, CA, USA) at Ex:360/Em:440nm. The mean of the three readings was subsequently averaged across the three pig donors. The activity of the ALP was expressed as the mean enzyme quantity able to hydrolyse 1µmol of MUP Reaction Mix per minute, at pH 10.0 and 25°C.

Fluorochrome injection

Fluorochromes allow to visualize the ossification front at the time they are injected[409]. One different fluorochrome was injected each month just after the blood sampling. Tetracycline (Oxytetracycline dihydrate, 25mg/kg, Cyclosol® 200 Long Acting, Dechra), calcein green (Fluorescein-bis(methyliminodiacetic acid), 10mg/kg, Sigma-Aldrich, C0875), and alizarin complexon (Alizarin-3-methyliminodiacetic acid, 30mg/kg, Sigma Aldrich, A3882) were always injected in bolus at 1 month, 2 months and 3 months, the day just before the euthanasia, respectively. They were all manually slowly injected through a jugular puncture. The next day, coloured urine testified to the good circulation and metabolization of the fluorochrome. The three different agents were visualized on unstained undecalcified slices using a slide scanner Axioscan.z1 (Zeiss, Oberkochen, Germany), highlighting the progressive ossification front respectively in yellow

(Ex. wavelength 653nm, Em. wavelength 668nm), green (Ex. wavelength 493nm, Em. wavelength 517nm) and red (Ex. wavelength 590nm, Em. wavelength 618nm) according to the time.

B. 6. Endpoint & explant analysis

Euthanasia & explantation

One minipig was euthanised immediately post-surgery for the first MBA harvesting, another at 6 weeks, and the other two minipigs after 3 months via IV bolus injection of T61 (0.2mg/kg). For the last three minipigs, both femurs were fully explanted with the IMN intact.

A macroscopic analysis of the entire bone was first performed to give a manual mechanical appraisal of consolidation. The extremities of the allograft were localized using fluoroscopy and the bone was cut 1cm away from each extremity to include the junction between the MBA and the native femur. Non-resorbable threads were used to mark the proximo-lateral side and the proximo-posterior border keeping the orientation of the sample. Then, the samples were fixed in formaldehyde 4% (VWR, 9713.9010) for 10 days, and embedded in resin (Low viscosity Embedding Media Spurr's Kits, Science Services, Munich, Germany) before undecalcified histology and IHC (LLS ROWIAK LaserLabSolutions GmbH, Hannover, Germany). Explanted samples were cut in a cross-section in the middle of the graft to assess creeping substitution and in a longitudinal section to evaluate the primary healing junction (Fig. 69).

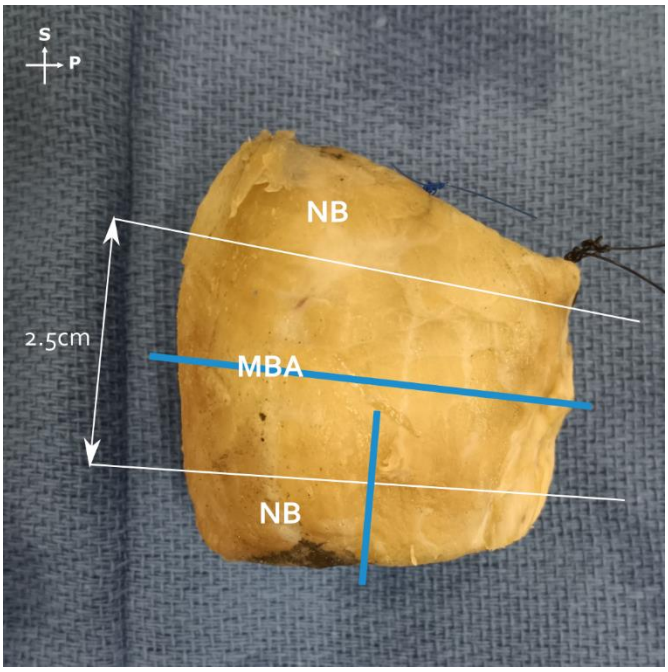

Figure 69. Cut sample of the femoral mid-diaphysis after explantation. Both white lines represent massive bone allograft (MBA) limits and blue lines illustrate the orientation of the slices cut for undecalcified histology and immunohistochemistry. NB: native bone, S: superior, P: posterior.

Histological sections (10µm thick) were stained with H&E, AB, and Von Kossa (VK) for calcium deposit. IHC comprised RunX2 and OC for osteogenic differentiation, alpha smooth muscle actin (α-SMA) to evaluate neoangiogenesis by the smooth muscle of neo-arterioles, and GFP to explore the potential persistence of seeded allogenic PMSCs. Every section was digitalized with the slide scanner Axioscan.z1 (Zeiss, Oberkochen, Germany).

Microfocus computed tomography

Before undecalcified histology and IHC, explants were scanned using a Phoenix NanoTom M (GE Measurement and Control Solutions, Germany), always using the anatomical position thanks to the orientation threads. This technology enabled the evaluation of the explants in 3D[284]. Detailed acquisition and module parameters are resumed in Table 20.

Table 20. MicroCT acquisition and module parameters.

Acquisition parameters	
Voxel size (µm)	15
Source voltage (kV)	150
Tube current (µA)	250
Exposure time (ms)	500
Number of images	5000
*Average**	1
*Skip**	0
Scan time (min)	83

** Information about those parameters was previously given in the literature[288]*

B. 7. Statistics

For descriptive analyses, continuous variables were expressed as mean ± SD, and visually represented by dot plots due to the very small sample size. The normality of distribution was assessed by QQ plot and Shapiro-Wilk test. Since the normal distribution was not respected and the sample size was small, nonparametric tests were used. Friedman and Wilcoxon paired tests were performed. The level of significance was determined at 0.05. All statistics were made using SPSS software (V.27, IBM SPSS, Inc., Chicago, IL, United States).

C. Results

C. 1. Surgeries

After seeding (2h) and a mean of 7h27 (± 1h11) of culture (Fig. 70 – a and b), the OM showed a high cellular density on its surface at the time of implantation (Fig. 70 – c) and was properly implanted. The membrane was wrapped around the MBA (Fig. 70 – d), then stitched (Fig. 70 – e) to entirely recover the allograft (Fig. 70 – f).

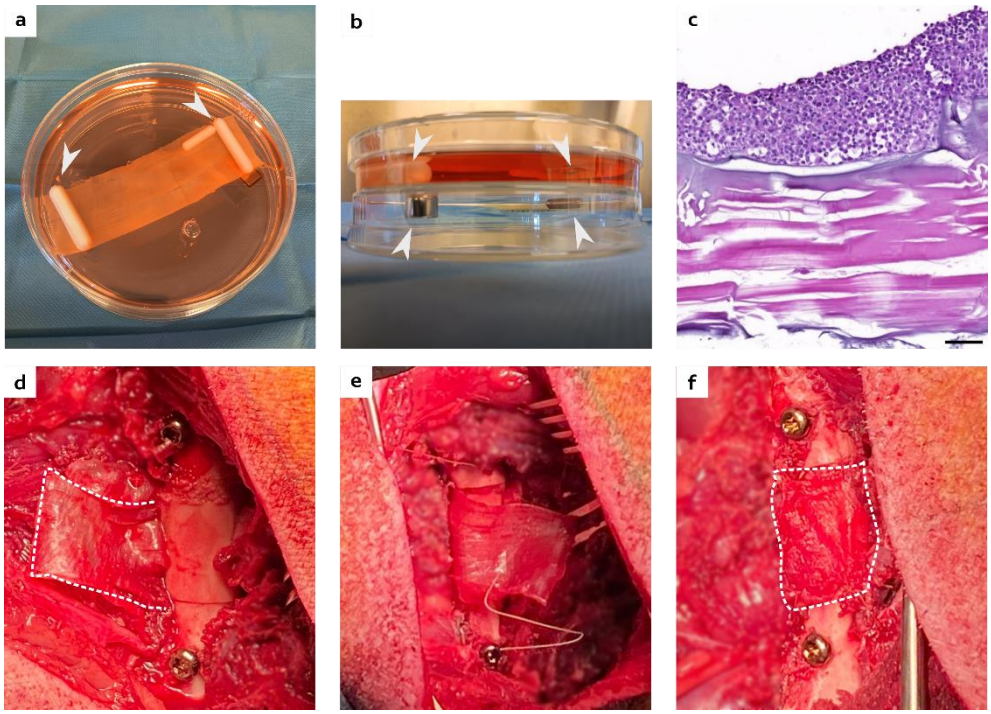

Figure 70. Steps of osteogenic membrane implantation including the rehydration and the seeding (a). The membrane was held in place by sterile magnets (arrowheads) positioned on either side of the Petri dish (b). A dense amount of periosteal mesenchymal stem cells was found on the surface of the membrane at the time of implantation (c). Surgical steps included the wrapping of the membrane (d), the suture (e), and the coverage check (f). Black scale bar=100µm.

Due to the toughness of bilateral physes, the nail of both femurs was not fully inserted and the IMN was locked with only one proximal screw in two minipigs. The third minipig, however, successfully received two proximal screws according to the IMN design.

C. 2. Systemic follow-up

From a systemic point of view, minipigs showed a satisfactory evolution with a decrease in white blood cells (WBC) after 2 weeks, and no significant loss of red blood cells (RBC), haematocrit (HCT), or haemoglobin (Hb) levels (Fig. 71). While they experienced a temporary weight loss immediately after surgery, they regained their initial weight by the 10th week. ALP activity started to increase homogeneously after 2 weeks but with a high SD.

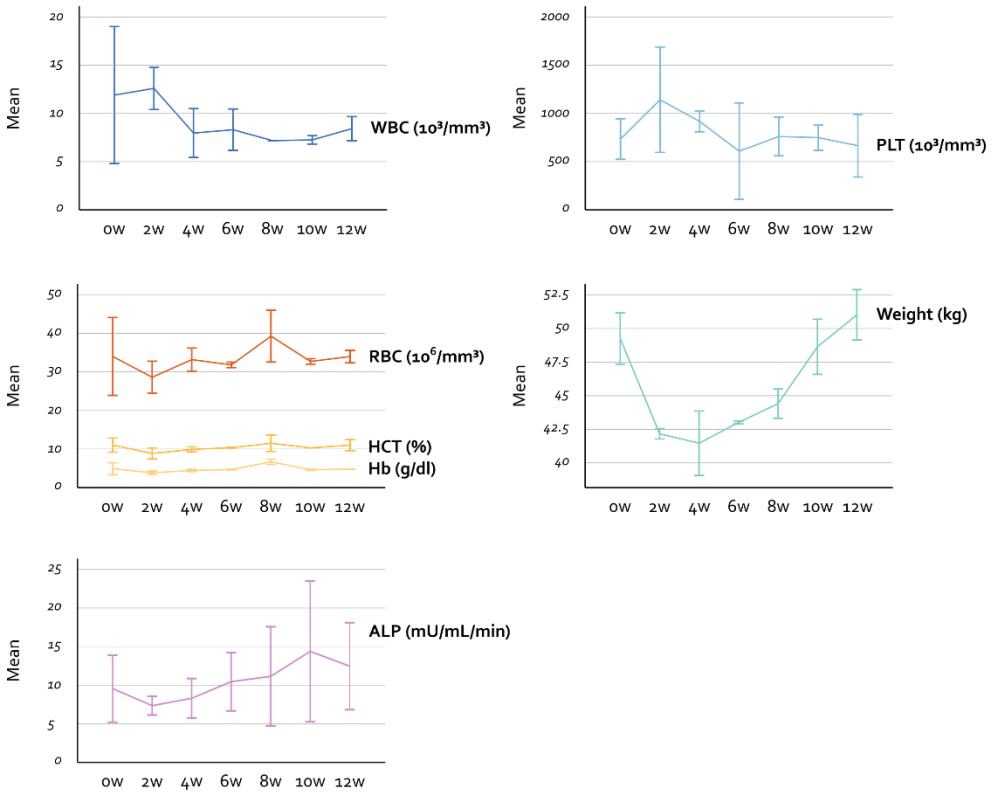

Figure 71. Systemic follow-up of minipigs including biological parameters and weight. WBC: white blood cells, PLT: platelets, RBC: red blood cells, HCT: haematocrit, Hb: haemoglobin, ALP: alkaline phosphatase, w: week, ow: surgery day. Error bars: standard deviation (SD).

C. 3. Imaging follow-up

X-rays and CT scans consistently showed a good reduction of distal osteotomy junctions with a satisfactory healing progression through callus formation (Fig. 72).

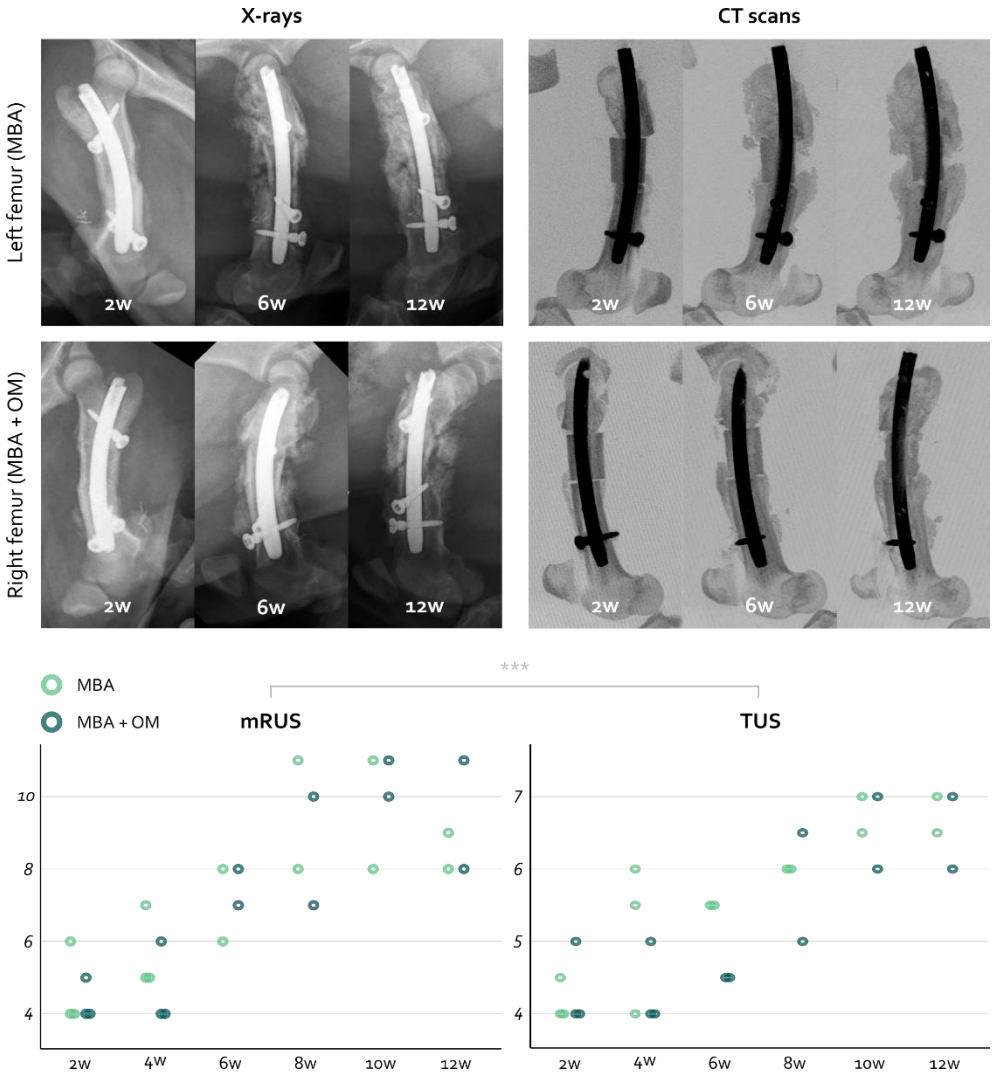

*Figure 72. Radiological follow-up (X-rays and CT scans) at 2, 6, and 12 weeks for both treatments (above). X-rays illustrated the follow-up of the third minipig and CT scans illustrated the follow-up of the second minipig. CT scan pictures are reconstructed with the maximum intensity projections (MIP) on multiplanar reconstruction. Quantitative comparison of healing scores of the distal junction (below) on X-rays (mRUS) and CT scans (TUS) depending on the treatment and the week after the surgery. MBA: massive bone allograft, OM: osteogenic membrane, w: weeks. ***: p<0.001.*

However, proximal junctions were not fully reduced. The minipig that received two proximal screws had to be euthanised at 6 weeks due to proximal femur fractures on both sides. Since this abnormal healing can be attributed to osteosynthesis, only the distal osteotomy junctions were further analysed to compare both treatments.

Concerning quantitative analyses of healing scores, from a global perspective, mRUS were significantly higher than respective TUS ($p<0.001$). However, no difference was observed between the MBA and MBA + OM treatments ($p>0.05$), regardless of the postoperative time. All the scores progressed proportionately but did not exceed 11 at 12 weeks.

C. 4. Femoral explants

Distal osteotomy junction

Microscopic analysis of the junction between the native femoral diaphysis and the MBA showed some similarities and few differences between both treatments. None of the osteotomy lines was bridged by mineralized callus but with soft callus where endochondral ossification was observed (Fig. 73).

On both femurs, new bone formation was predominantly found on both periosteal and endocortical surfaces of the diaphysis but was also visible deep in the cortical bone, both in the MBA and native cortex (Fig. 74 – a). Even if present at both osteotomy sides, more numerous osteoclastic resorption lacunae were visualized on MBA than on native bone (Fig. 74 – b), with sometimes loose bony debris at the periphery (Fig. 74 – c).

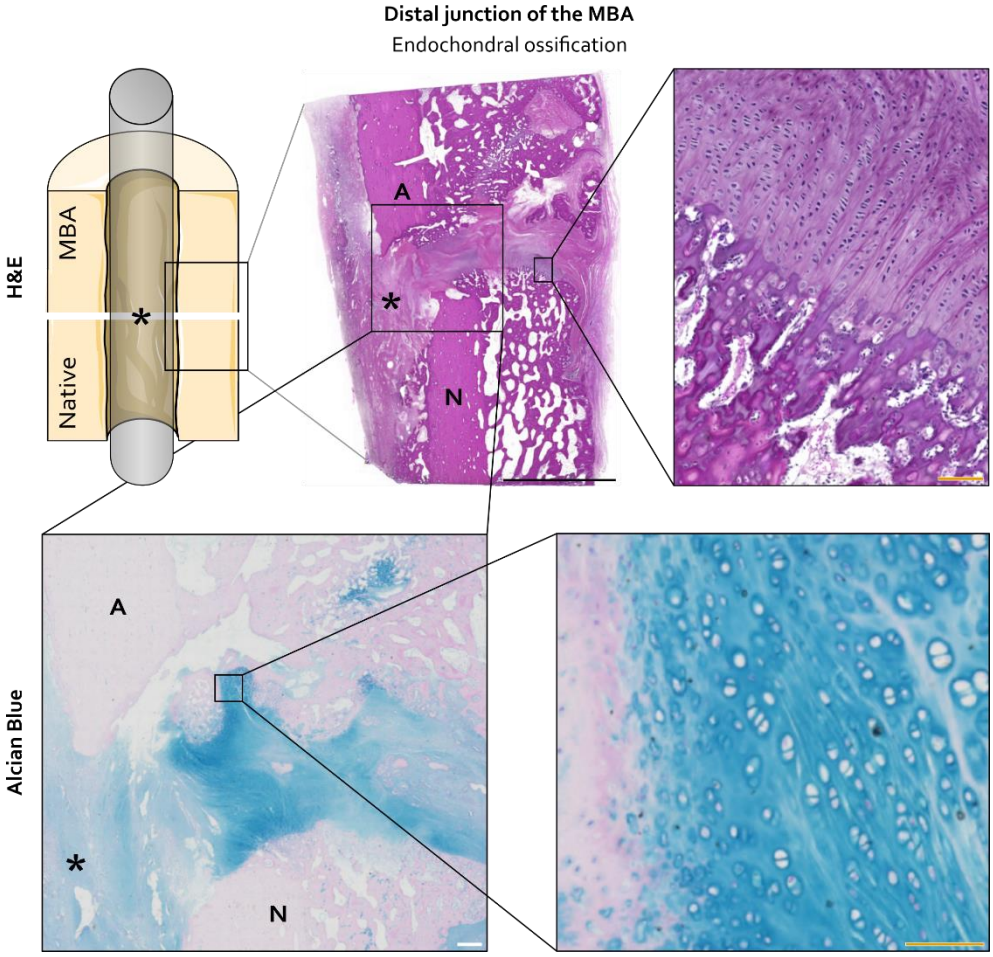

*Figure 73. Longitudinal undecalcified sections through the distal junction between the massive bone allograft (MBA) and the native bone. Endochondral ossification was responsible for the soft callus at the junction. A: allograft, N: native bone, *: medullary cavity, H&E: haematoxylin and eosin. Black scale bars= 5000µm, white scale bars=500µm, yellow scale bars=100µm.*

*Figure 74. Longitudinal undecalcified sections through the distal junction between the massive bone allograft (MBA) and the native bone. New bone formation was seen by the darker pink colour in the periphery and the depth of the allograft (a). Osteoclast activity illustrated remodelling and/or bone resorption (b), with bone debris in the medullary cavity (c). A: allograft, *: medullary cavity, H&E: haematoxylin and eosin. White scale bars=500µm, yellow scale bars=100µm.*

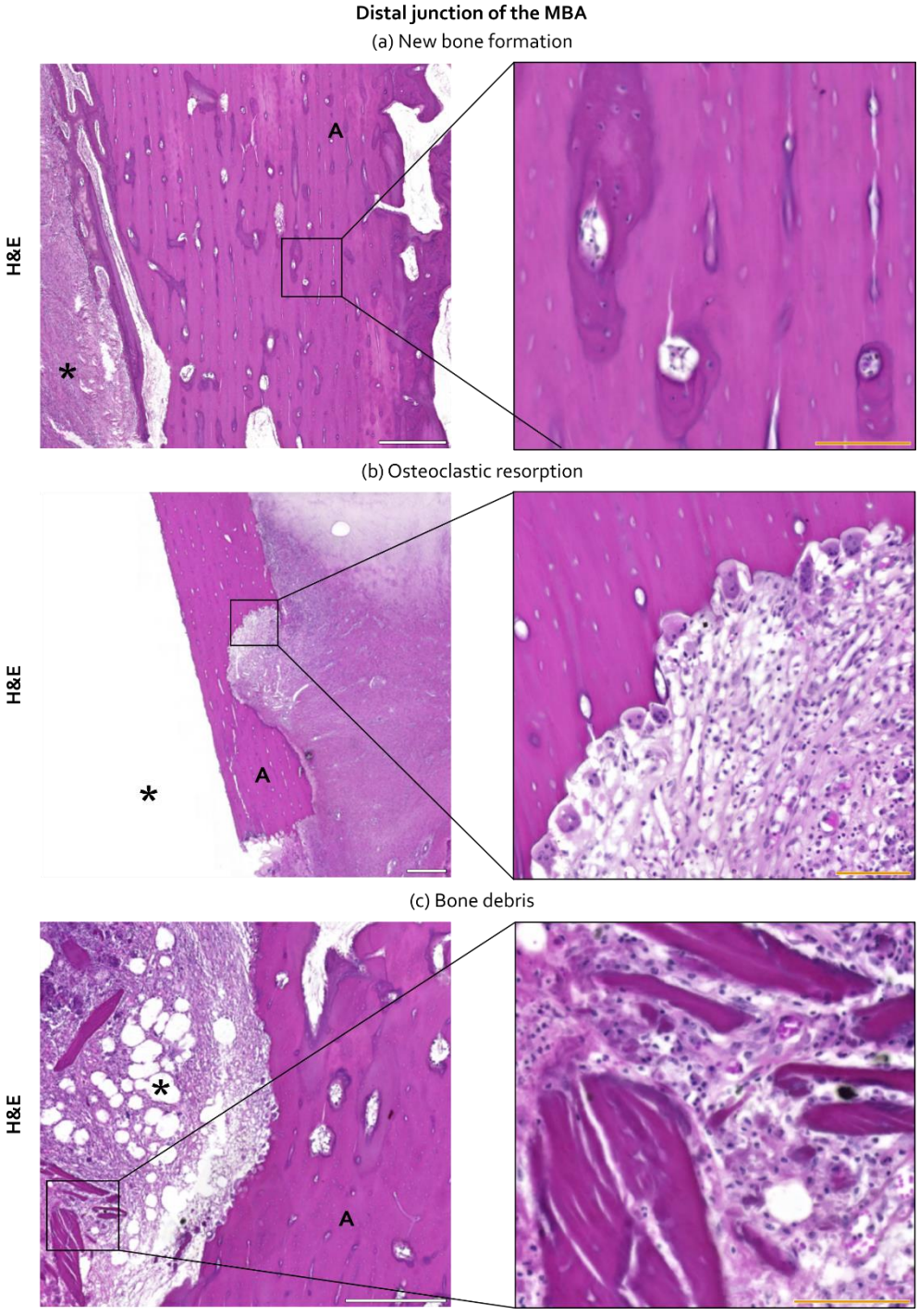
Distal junction of the MBA
(a) New bone formation
H&E
A
*
(b) Osteoclastic resorption
H&E
A
*
(c) Bone debris
H&E
*
A

External mineralized hard callus was more voluminous for the left (MBA alone) than for the right femur (MBA + OM) (Fig. 75) but it was the only remarkable difference. Only one distal junction of the right femur (MBA + OM) was manually not stable after 12 weeks.

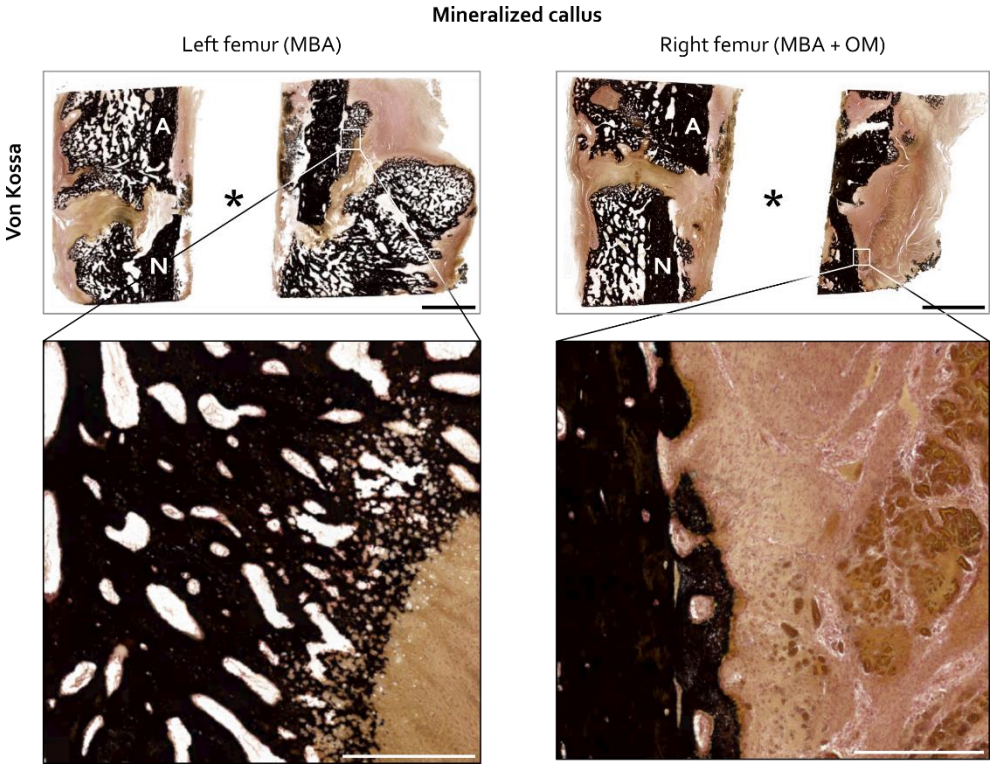

*Figure 75. Longitudinal undecalcified sections through the distal junction between the massive bone allograft (MBA) and the native bone. Mineralized callus was more prominent in the left (MBA alone) than in the right femur (MBA + osteogenic membrane (OM)). A: allograft, N: native bone, *: medullary cavity, Black scale bars= 5000µm, white scale bars=500µm.*

Central part of the massive bone allograft

The central part of the MBA exhibited a more extensive external and internal mineralized callus in the left (MBA alone) than in the right femur (MBA + OM) (Fig. 76 – a). The global aspect of the MBA cortical bone illustrated by the left femoral cortex (Fig. 76 – left b), was similar between both sides. However, the mineralized callus appeared to be still developing in the right femur (MBA + OM) (Fig. 76 – right b). Both MBAs displayed osteoclastic resorption within the cortical bone (Fig. 76 – c), new bone apposition (Fig. 76 – d) with a cutting cone-like structure where osteoclasts were directly followed by osteoblasts around a central growing blood vessel, depositing new bone matrix and entrapping new osteocytes, indicative of creeping substitution (Fig. 76 – e).

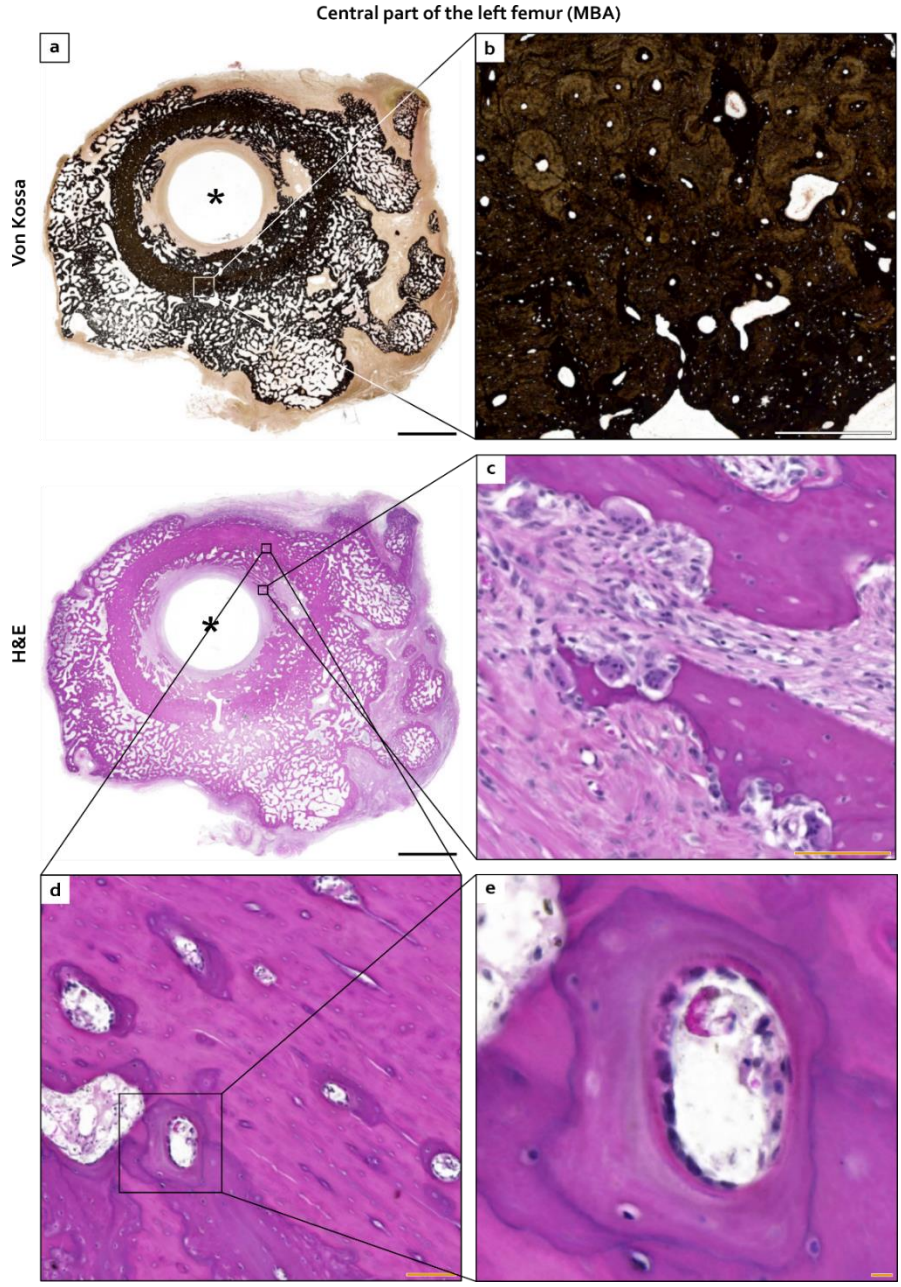

Figure 76. Undecalcified cross-sections through the central part of massive bone allograft (MBA) in left (MBA alone) and right (MBA + osteogenic membrane (OM)) femurs. Overview of the global aspect of the MBA, the external and the internal callus (a). Cortical mineralized bone (left) and progressive mineralization of the callus (right) (b). Caption continued on next page.

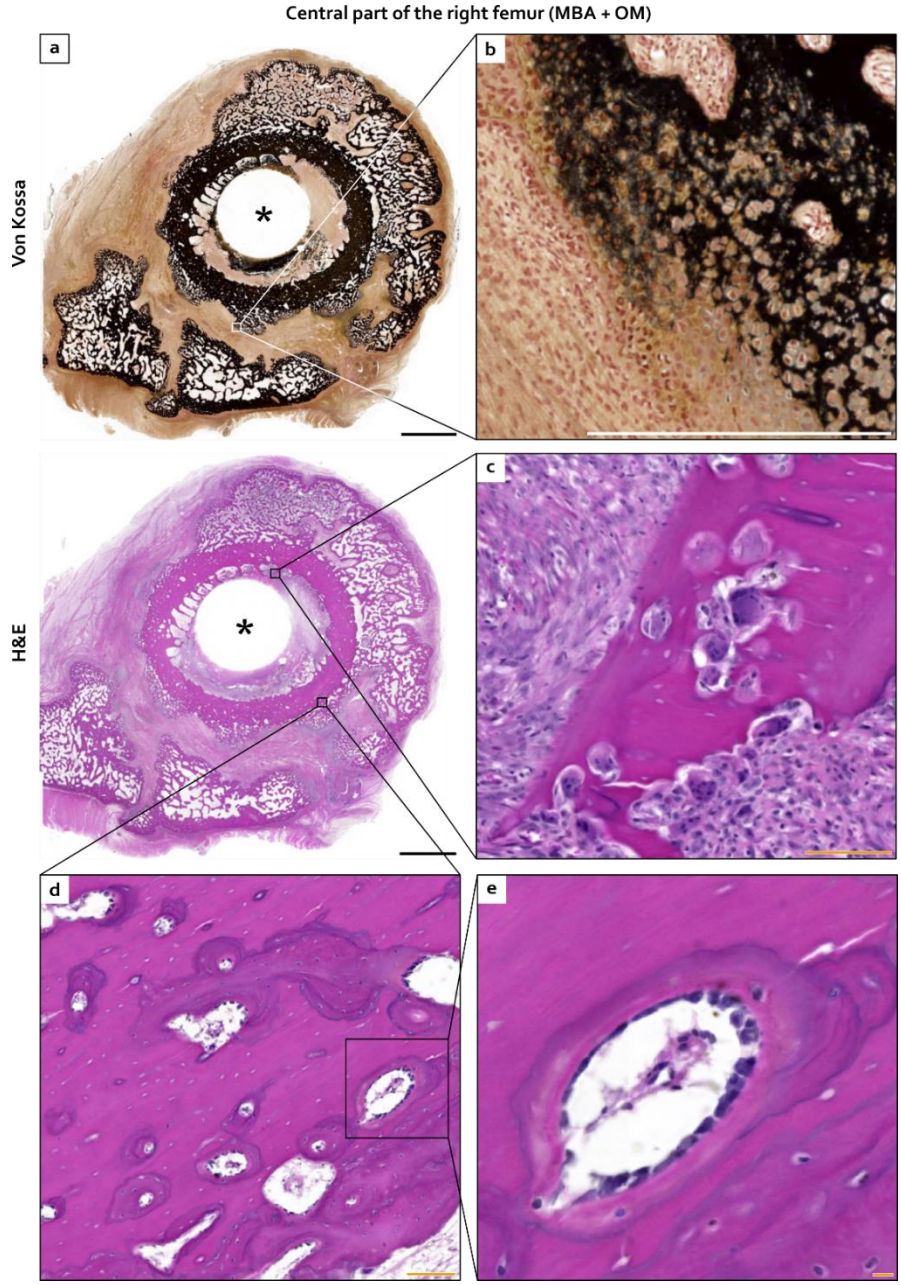

*Caption extension to the Figure 76. Osteoclastic resorption (c). New bone apposition synonym of creeping substitution (d and e). *: medullary cavity after removing the intramedullary nailing. Black scale bars= 5000µm, white scale bars=500µm, yellow scale bars=100µm.*

In the MBA + OM femur, the OM was still present as a dense fibrocollagenic tissue around the MBA and was fully and richly revascularized after 3 months (Fig. 77).

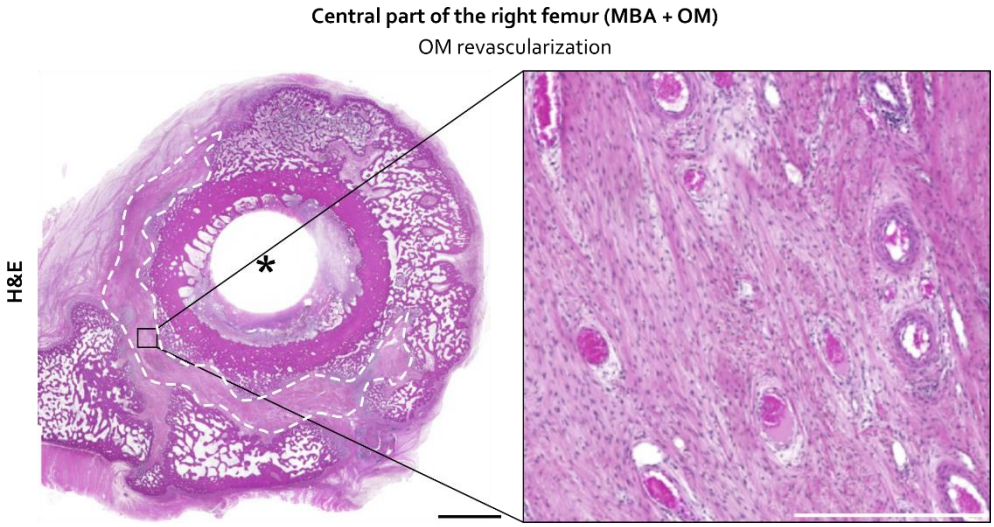

*Figure 77. Undecalcified cross-section through the central part of massive bone allograft (MBA) in right limb (MBA + osteogenic membrane (OM)). OM persistence and revascularization. White dotted line: OM contour, *: medullary cavity after removing the intramedullary nailing. Black scale bars= 5000µm, white scale bars=500µm.*

Endochondral ossification was minimally observed at the periphery of the callus in the left femur (MBA alone) (Fig. 78 – a), in contrast to the right femur, where it was predominant on the seeded side of the membrane in contact with the MBA (Fig. 78 – b), confirming ongoing bone formation activity. While endochondral ossification seemed reduced in the left femur, the interface between the cortical bone and surrounding tissue consisted of a matrix rich in GAGs (Fig. 78 – c).

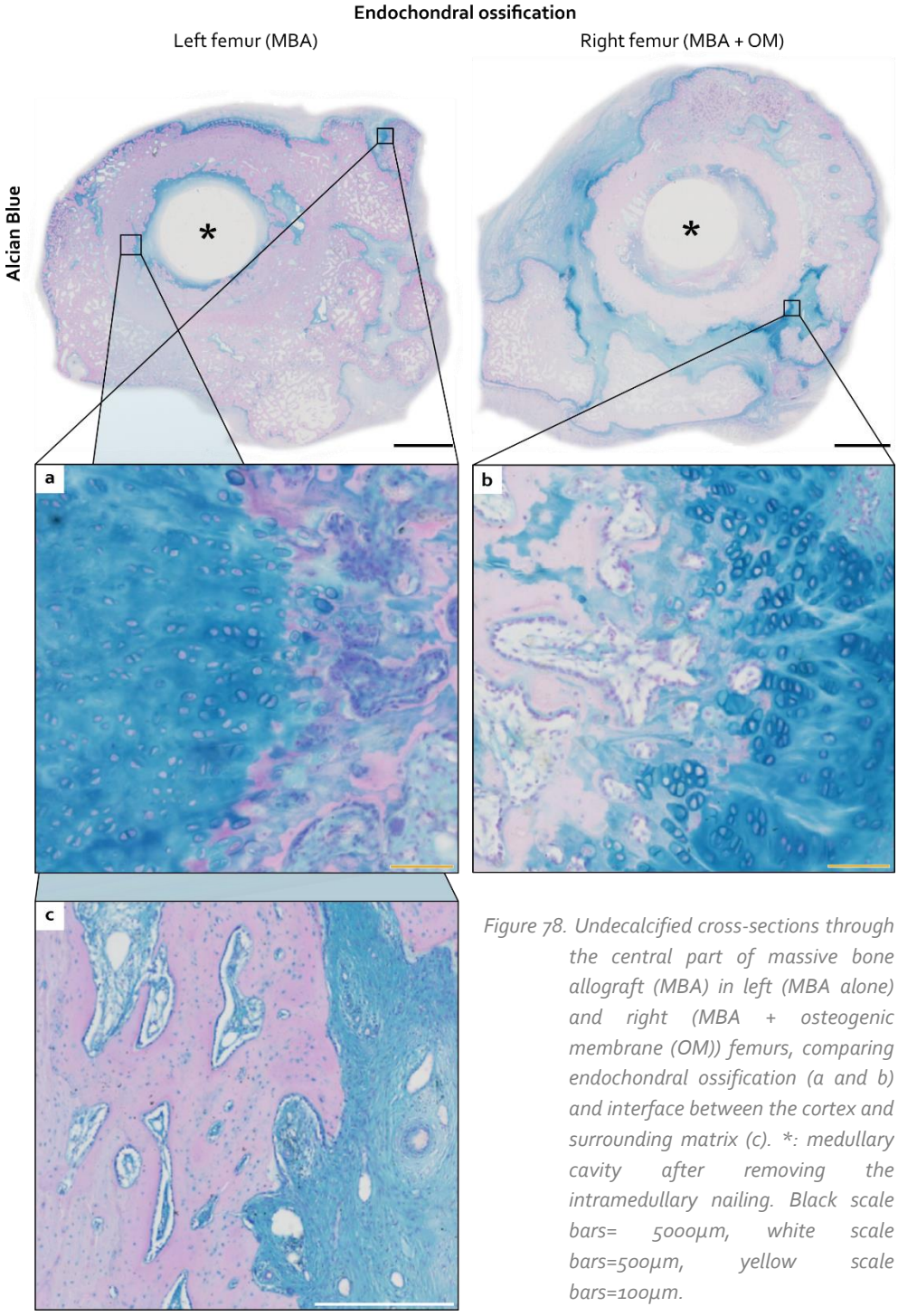

*Figure 78. Undecalcified cross-sections through the central part of massive bone allograft (MBA) in left (MBA alone) and right (MBA + osteogenic membrane (OM)) femurs, comparing endochondral ossification (a and b) and interface between the cortex and surrounding matrix (c). *: medullary cavity after removing the intramedullary nailing. Black scale bars= 5000µm, white scale bars=500µm, yellow scale bars=100µm.*

Ossification front progression

After 6 weeks, when only tetracycline was already injected (one pig), very few scattered labelled surfaces were visible inside the middle of the left MBA (MBA alone) and even less in the right MBA (MBA + AO) (Fig. 79 - above).

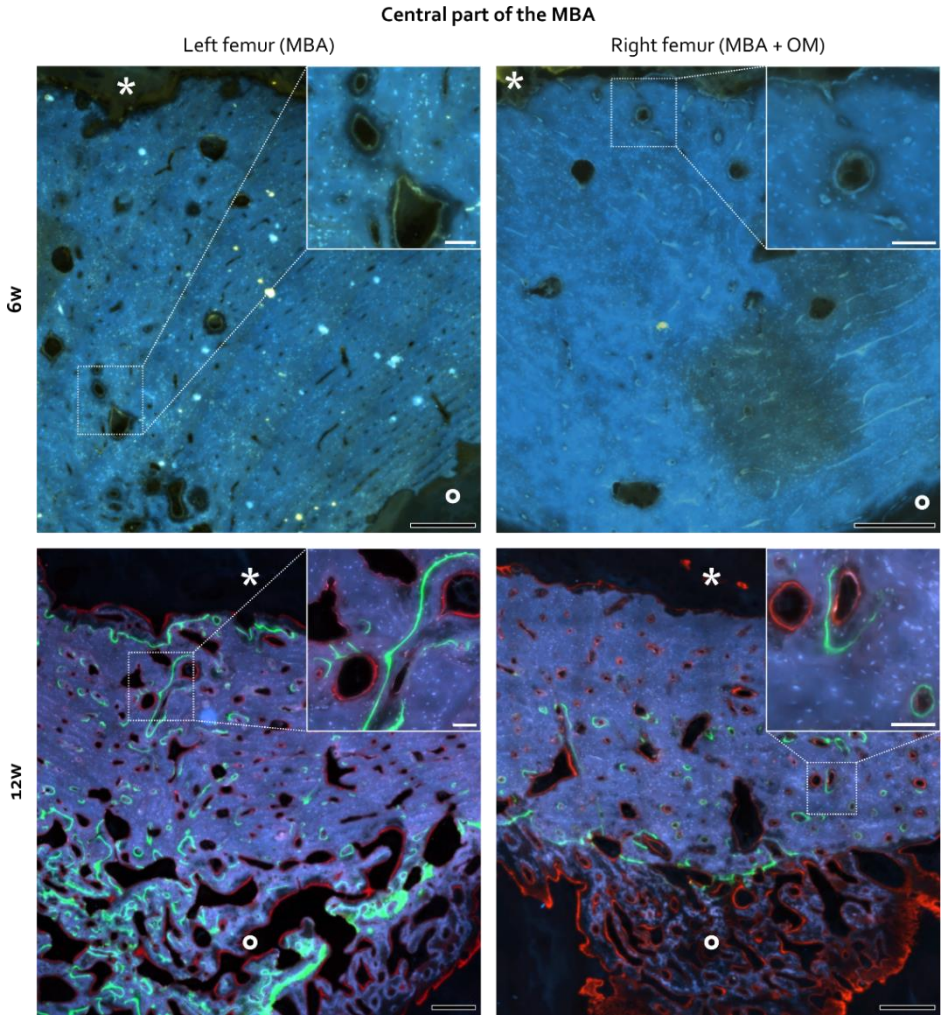

*Figure 79. Undecalcified cross-sections through the central part of the massive bone allograft (MBA) cortex, observed under UV light, illustrate the creeping substitution, and comparison between MBA alone and MBA + osteogenic membrane (OM). Tetracycline (yellow): injected at 4 weeks, calcein green (green): injected at 8 weeks, alizarin red (red): injected at 12 weeks. w: weeks, *: medullary cavity, °: peripheral callus. Black scale bars= 500µm, white scale bars= 100µm.*

After 12 weeks, when the three fluorochromes had been injected, tetracycline and alizarin complexon were not distinguishable since the wavelengths were too close. However, calcein green and alizarin red labelling were visible on all the MBA envelopes (periosteal, endocortical and intracortical) at 8 and 12 weeks, respectively. If the central part of MBA showed a very slight osseous integration at 4 weeks (yellow), the creeping substitution was clearer at 8 (green) and 12 weeks (red) (Fig. 79 – below).

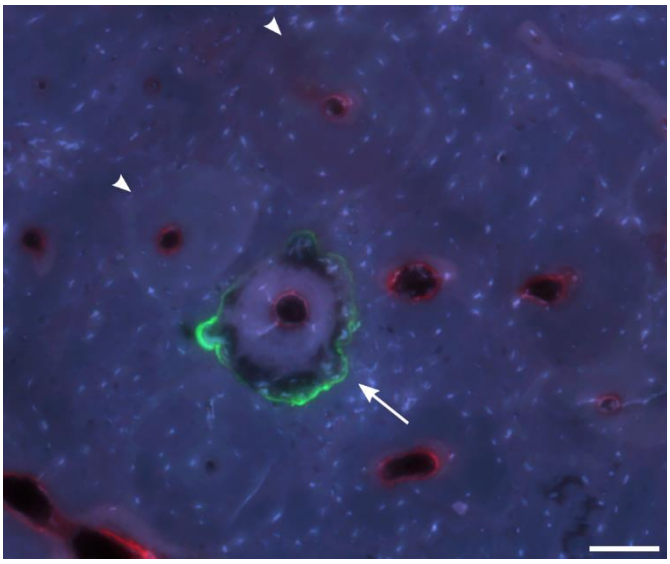

The bone healing also showed creeping substitution with osteon formation (Fig. 80).

Figure 80. Haversian structure in the middle of the massive bone allograft with original osteon from the allograft (arrowheads) and new forming osteon with active ossification fronts at 8 (green) and 12 (red) weeks (arrow). White scale bar= 100µm.

Microfocus computed tomography

While 2D histological analyses indicated the absence of mineralized callus inside the distal junction between the MBA and the native bone, manual mechanical testing mostly indicated stability. To further elucidate this discrepancy that can be explained by periosteal or OM callus, microCT analyses will be determinant in understanding the 3D morphology and microstructure of the mineralized callus (Video 1)[†].

[†] These data ought to be available soon.

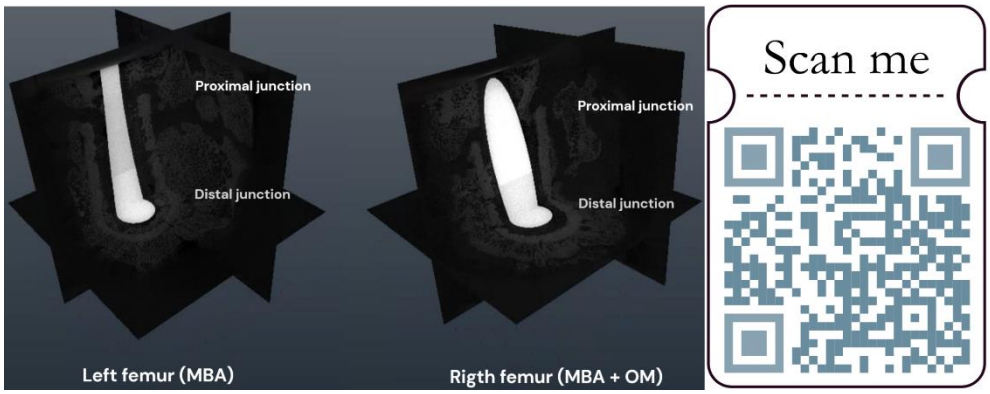

Video 1. MicroCT of both femoral shaft explants of the same pig at 3 months. Both explants with proximal and distal junctions between native bone and the central massive bone allograft, stabilized by the intramedullary nailing.
https://zenodo.org/records/11061046?token=eyJhbGciOiJIUzUxMiJ9.eyJpZCI6IjFhNWM5YWUxLTdkZTctNGY1Zi1hMWQ3LTg1OTM2YzY1NTNmYyIsImRhdGEiOnt9LCJyYW5kb20iOiJjMDQ4ZWU2Mjg2MjRmZmRkNmM4MWVlYjU5NGM4Nzc5ZSJ9.3ZwBzKramEr78Pdny3HsPkPoIOg-lAs82R_lSR8Topy3A9IDzk4esIm32ajNEH1wjpqIpuq8tOgZUMJmt6usTw

D. Discussion

This study explored the role of an OM in MBA integration after CSBD creation in the minipig femur.

Bone healing

The OM demonstrated promising characteristics during *in vitro* development and before implantation, exhibiting high cellular density upon seeding and successful biocompatibility and osteogenicity in contact with MBA[291]. The membrane effectively encapsulated the MBA *in vivo*, suggesting its potential utility in enhancing guided-bone regeneration procedures.

Histological analyses revealed new bone formation originating from the cortical surfaces (periosteal and medullary cavity sides), as well as from the vascular network within the MBA, accompanied by evidence of endochondral ossification. Although osteoclastic resorption was evident, distinguishing its specific role between MBA resorption and bone remodelling proved challenging at this

intermediate-term follow-up of 3 months. Given the pivotal role of osteoclasts in bone formation[410], a longer-term follow-up could clarify this ambivalence. While both treatment groups exhibited a creeping substitution extending into the deep centre of the MBA, discrepancies in external mineralized callus formation were observed, underscoring the potential influence of OM on containing bone healing. The persistence of a highly revascularized OM may facilitate the delivery of essential nutrients and autologous cells for bone regeneration.

All distal junctions were stable upon manual testing, except one. Analysis of distal osteotomy junctions revealed similarities between treatment groups, characterized by predominant new bone formation along cortical borders and the presence of soft callus at osteotomy sites. Variations in mineralized callus formation were identified, suggesting potential differences in treatment efficacy.

Subsequent quantitative analyses of healing scores highlighted significant disparities between radiographic and CT scan-based evaluations, emphasizing the importance of using complementary imaging modalities for precise evaluation of treatment outcomes. The observed statistical difference between mRUS and TUS can be attributed to the degree of refining osseous delineation achieved by CT scan reformats, downgrading radiological cortical score[42]. Although both scores exhibited consistent increases over time, none surpassed a score of 11, indicating incomplete mineralization and remodelling of the callus. However, it is worth noting that the appearance of callus on CT scans varied slightly depending on the slice, and without automated software, the determination of paramedian slices could introduce observer-dependent bias. To mitigate potential bias, a standardized approach was adopted, considering the middle number of slices as the centre of the shaft and the IMN. Paramedian slices were analysed five slices before and after this median line, with the lower score assigned in cases of uncertainty. While the operator remained blinded to the side of membrane transplantation, the visibility of imaging dates could potentially influence scoring outcomes. Given that each minipig served as its own control, systemic parameters did not discriminate between both treatments but enabled global monitoring of the animal.

Considering all aspects, the disparities observed in bone healing and osteotomy consolidation do not warrant definitive conclusions. At this stage, it would be

premature to declare whether the inclusion of the OM is superior or inferior to the standard treatment with MBA alone. However, further investigation is essential to assess the potential advantages of guided-bone regeneration and the establishment of an optimal biological environment, particularly in addressing concerns regarding bone callus containment. These aspects necessitate comprehensive study and validation to ascertain their impact on treatment efficacy.

Surgical Procedure

Given the influence of demographics, comorbidities, and patient-related factors on mechanical stability and complications[52,51,16,411,37], this study sought to mitigate potential confounding variables by conducting paired comparisons on both femurs from the same minipig. One minipig was euthanised at 6 weeks due to technical complications resulting in proximal femoral fractures discussed in an earlier publication. It is also crucial to note the status of the periosteum. While the surgeries conducted in this study involved substantial periosteum stripping, the periosteum itself was not completely excised. The formation of an external callus could be attributed to the resulting periosteal reaction, which might not occur if the periosteum was completely removed. Consequently, this study might be comparing MBA + OM to MBA + periosteum stripping followed by reattachment to the bone surface after soft tissue closure. Caution is warranted in concluding our findings due to this potential bias. The comparison may more accurately reflect the added value of OM in comparison to a reactive, injured periosteum rather than the hostile environment of a CSBD. In such circumstances, OM may play a crucial role in guiding and regulating new bone formation at the local site, potentially preventing the risk of ectopic ossification or hypertrophic callus formation.

Perspectives

First of all, IHC and microCT analyses still have to be made[‡].

[‡] These data ought to be available soon.

The GFP-IHC will inform on the residual presence of GFP-cells. Even if MSCs are known for their immune privilege *in vitro*[7,167,208–212], their immunocompatibility *in vivo* is still debated[412]. The cell fate can also depend on the cell type, differentiation stage, and interaction with biomaterials or GFs[6]. Previous studies graded the persistence of allogenic cells between 1.5% to 71% after 37 days[413,414]. In case of absence in any of the femoral explants, seeded PMSCs would probably be digested by the host immune system. However, A. Caplan, who gave the initial name of « Mesenchymal Stem Cell », recently proposed to change it with the term « Medicinal Signalling Cell »[415]. MSCs might not act as progenitors for tissues but secrete bioactive molecules (cytokines, chemokines, and GF), functioning in a paracrine mode akin to therapeutic drugs within the microenvironment. This *in situ* paracrine signal could support and attract the patient's own tissue-specific resident or circulating stem cells, induce their differentiation, building new tissue[410,415,416].

The 3D microCT analysis will be instrumental in elucidating discrepancies observed between 2D histological assessments and manual mechanical testing results, particularly regarding the presence and morphology of mineralized callus at osteotomy sites. By providing detailed 3D morphological and microstructural insights, microCT analysis will enhance our understanding of bone healing processes and treatment efficacy.

Moreover, quantitative assessment of IHC and fluorochrome label, as well as osteoclast count could aid in elucidating the perceived lack of significant differences between both treatments and provide more robust conclusions. Histology and IHC (cellular content and protein expression), microCT (3D numerical data), and blinded union score are three of the four standards to evaluate bone union[99]. The fourth aspect to consider is mechanical testing, which might be interesting in longer-term follow-up periods once bone healing has been achieved.

This pilot study includes a very small animal number. This could enable to explore some preliminary objectives, but a larger cohort is needed because of the wide inter-animal variations. Alford et al. recommended a sample size of a minimum of eight animals[99].

If tissue engineering methods are used to generate an OM, they can also be applied to directly decellularize MBA through vascular perfusion[353,417]. The underlying hypothesis is centred on the residual presence of immunogenic compounds within MBA, which could potentially limit creeping substitution[157,178,418,419]. Encouraging preliminary *in vivo* findings have been shown[420]. However, it is noteworthy that this model currently lacks osteogenicity and immediate vascularization. Perfusing MSCs through the vascular pathway to partially recellularize the MBA and reendothelialize vessel walls, could address these limitations. Also in this study model, the primary explanation for the lack of observed superiority may stem from the absence of vascularization at the time of implantation. According to Giannoudis et al., achieving the Diamond concept and bone integration requires the presence of five key elements[19,80]. While our surgical model includes an osteoconductive scaffold, osteoinductive factors, and osteogenic cells, the issue of mechanical stability, as discussed earlier, remains a concern, and vascularization is lacking upon implantation. Even if neovascularization was observed, the delay in new vessel formation could account for the delayed integration of the MBA. Therefore, future research could focus on establishing an effective vascular network immediately upon implantation. Recent studies described an intrinsic vascularization of the HFL[421], suggesting its potential use as an autologous HFL flap or the exploration of tissue engineering techniques to restore and enhance its effectiveness.

E. Conclusion

The comprehensive evaluation of this large animal pilot study highlights the multifaceted nature of bone regeneration procedures and the complex interplay between surgical techniques, biomaterials, and host responses. These findings lay the groundwork for further investigation and optimization of bone regeneration strategies, with the ultimate goal of improving clinical outcomes of MBA transplantation in orthopaedic surgery.

– TAKEAWAYS –

Paper 7 – An osteogenic membrane to enhance massive bone allograft integration: In vivo pilot study in a minipig model

- *Osteogenic membrane = Revascularization*
  Endochondral ossification
  Osteoclastic activity
  Guided-bone regeneration
  Creeping substitution

  BUT

⇨ *Lack of immediate vascularization*

Back to the Diamond

- **How can the preclinical large animal model for CSBD be optimized for use with an OM?**

The development of a 3D-printed custom-made IMN addresses the issues associated with two orthogonal plates, which would compress the OM and seeded cells. Stabilizing the MBA and native bones with an intramedullary fixation allows the ready-to-use OM to be wrapped without tension or compression, stitched to itself, and maintain cell viability in contact with the MBA in a single-stage surgery. 3D-printed solid titanium IMNs provide sufficient stability for immediate weightbearing. The cutting guide ensures reproducible CSBDs precisely centred between locking screws. However, the model can still be refined, especially in securing the proximal part of the IMN, which fixes the proximal osteotomy.

- **Does the OM promote MBA integration and facilitate creeping substitution?**

Initial analyses indicate that the OM may be as effective as contralateral stripping HP, as both exhibit similar osteoclastic activity and creeping substitution in the deep centre of the MBA. The OM is also fully revascularized and appears to guide bone regeneration, with allogenic PMSCs providing paracrine signals to trigger and support the host's response. However, quantitative data are still needed to confirm these findings.

A major discussion point is the delay in neoangiogenesis within the OM at 3 months. Immediate vascularization of the OM is a critical aspect that requires further investigation, as this delay is a significant drawback compared to the induced membrane.

– REQUIREMENT SPECIFICATIONS –

Requirement	Specification	Validation
Osteoconductive matrix		
Composition	- Col-1 membrane	V
Morphology	- 2 layers	V
	- Thickness (1 thin + 1 thick layers)	V
	- Large size - Shapeable	V
Biocompatibility	- No immunogenicity	V
	- Carrier for cells	V
	- No cytotoxicity	V
Osteoinductive mediators		
Bioactivity	- Osteogenic GF	V
	- Osteogenic differentiation	V
	- Chondrogenic differentiation	V
Osteogenic cells		
Osteogenicity	- Cell adhesion, proliferation, replication	V
	- Osseous ECM production	V
Mechanical stability		
Membrane properties	- Sheet malleable support	V
	- Resistance to handling	V
	- Isotropy or anisotropy?	≈
	AND	
In vivo model	- Stitchable	V
	- Mechanical stability	V
Vascularization		
Vascular supply	- Angiogenic properties	≈
	- Neoangiogenesis	V
	OR	
	- Intrinsic vascular architecture	
	- Functional vascular network	
In vivo transposition		
Clinical needs	- Off-the-shelf availability	V
	- One-stage surgery	V

CHAPTER V. Vascularization

Relationship between angiogenesis & osteogenesis

« We make a living by what we get, but we make a life by what we give. »

Winston Churchill, mid-20th century

« Bone never forms without vascular interactions »[422].

The interactive function of bone healing and vascularization was introduced as early as the 18th century[26]. Whether for bone growth or repair, angiogenesis was increasingly studied during the 20th century, as a key contributor. Insufficient bone vascularization is associated with poor bone remodelling and regeneration[423]. Vascular diseases (*e.g.* diabetes, aging, radiotherapy) are also associated with fracture non-union and necrosis in 5-10%[14,422]. After a fracture, the haematoma removal altered bone repair and, on the contrary, haematoma transplantation induced bone formation[26,28].

A. Angiogenesis & bone growth/repair

Skeletal development and remodelling happen in close spatial and temporal relationship with angiogenesis[423,424]. In the early stage of skeleton genesis, cartilaginous tissue produce anti-angiogenic factors that avoid local angiogenesis[423]. Nevertheless, neovascularization is acknowledged as a step controlling the rate of mineralization and bone formation[422,425,426]. During bone growth, the penetration of new blood vessels precedes and supports osteogenic differentiation[426] (Fig. 81). During endochondral ossification at growth plates, chondrocytes first proliferate and hypertrophy in a primarily avascular cartilage model[422] followed by cartilage calcification. The vascular invasion and the consequent increase of oxygen level and VEGF at the chondro-osseous junction

induce chondrocyte apoptosis, cartilaginous matrix resorption by chondroclasts, and bone apposition by osteoblasts[425].

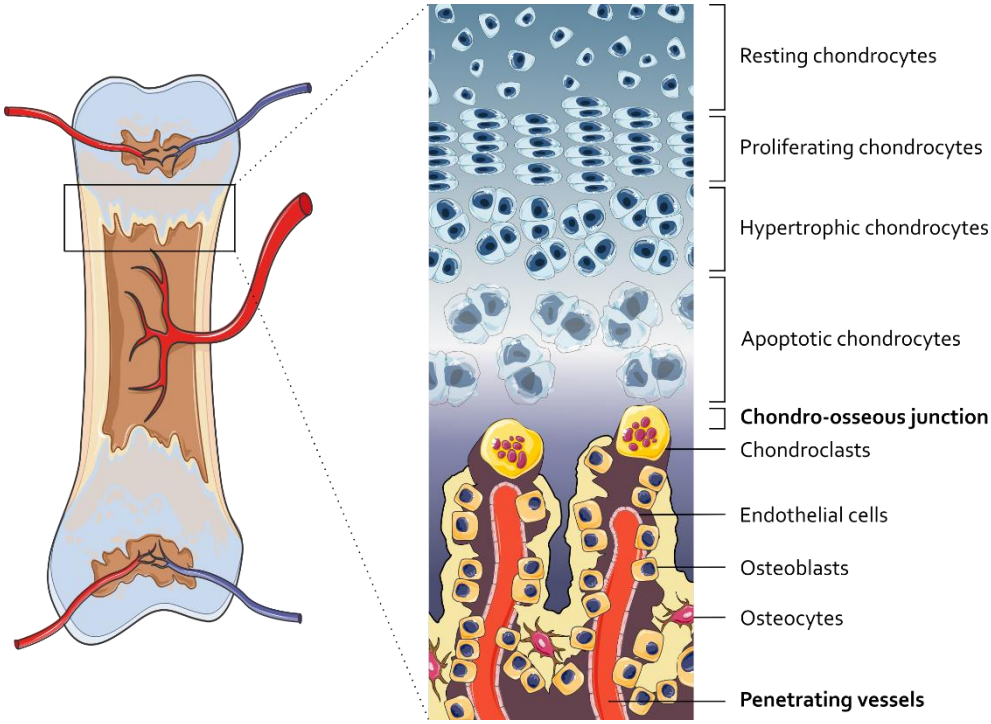

Figure 81. Endochondral ossification at the growth plate, illustrating the role of angiogenesis in the ossification of calcified cartilage. Inspired from Krstic (1978) and Gerber et al. (2000)[425,427].

During fracture healing, the process is similar. Even though a cartilaginous callus forms after a fracture in the absence of blood vessels, the transition from cartilage to mineralized bone only occurs once blood vessels infiltrate the callus[422], and in the immediate proximity of those capillaries[423]. If the vascular ingrowth is artificially blocked, skeletal progenitor cells differentiation can be manipulated towards chondrogenesis, thus limiting nutrient availability and indirectly highlighting its key role in osteogenic induction[428].

Osteoblasts are oxygen-sensing[422] and react in a poor oxygen environment by activating the hypoxia-induced factor (HIF) pathway[422,424] (Fig. 82). HIF-α can boost VEGF secretion for coinvasion of neovessels and osteoblasts precursors[426], leading to a 70% increase of trabecular bone volume[424]. Endothelial cells play a

pivotal role in regulating osteoblast function, and the concept of blood vessels serving as a niche in bone development is an area of ongoing investigation[429–433].

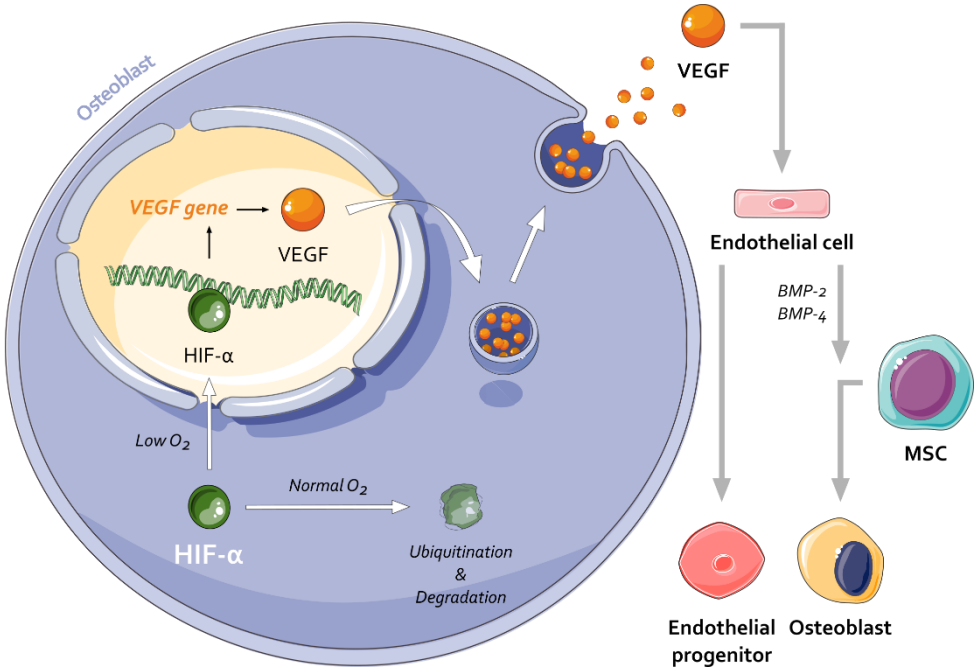

Figure 82. Reaction of osteoblast to normoxia or hypoxia. In case of hypoxia, HIF-α induces VEGF gene expression to synthesize VEGF protein. After exocytosis, VEGF can influence endothelial cells to activate endothelial progenitors for neoangiogenesis and osteoblasts for neoosteogenesis. HIF-α: hypoxia-induced factor alpha, O_2: oxygen, VEGF: vascular endothelial growth factor, BMP: bone morphogenetic protein, MSC: mesenchymal stem cell. Inspired from Towler et al. (2008)[422].

B. Ischemic threshold

Bone vascularization may be compromised due to periosteal stripping following high-energy trauma[14], during septic or oncologic resections, or when surrounding soft tissues are altered[14]. These scenarios can lead to a hypoxic environment, affecting the physiological functions of cells and tissues, which heavily rely on adequate blood supply for viability. Cells and tissues may have distinct oxygen needs. Prolonged reduction or cessation of blood flow can exceed tissue ischemic tolerance, ultimately resulting in tissue necrosis and death[14].

The previous *in vivo* porcine model relied on potential *in situ* neoangiogenesis after implantation. Even if MSCs are highly resistant to hypoxia[211] with a survival after up to 12-24h of ischemia[434–436], osteocytes exhibited an early ischemia after only 3h of afferent arteriole thrombosis while studied for pathogenesis of avascular necrosis[437]. In addition, despite their larger volume and weight compared to other organs, bones receive only 5% of the blood flow rate[14]. The anticipated neoangiogenesis may progress too slowly or might not spread quickly enough to prevent hypoxic complications.

The vascularization of surrounding soft tissue seems to drive revascularization of massive grafts[14]. Therefore, complications might be reduced if the bone allograft could be covered with a pre-vascularized soft tissue flap[438,439], playing the role of vascularized periosteum or induced membrane.

Osteogenic membrane revascularization

« Knowing is not enough ; we must apply.
Willing is not enough; we must do. »

Johann Wolfgang von Goethe, 1795

A. New vascular network creation by tissue engineering

As the size of transplanted tissues increases, a significant challenge lies in vascularizing cells within the core of constructs. Establishing a functional microvascular network is crucial for keeping seeded cells alive and enabling them to play their expected treatment action. Vascularization remains a major, yet extensively explored, challenge in tissue engineering[14,440]. The daunting task of creating a functional vasculature *de novo* persists as a hurdle for tissue engineers[168].

The current strategies already implemented in the preclinical phase include *in vitro* and/or *in vivo* pre-vascularization methods[14,441].

A. 1. In vitro pre-vascularization strategies

The most recognized approach among *in vitro* pre-vascularization techniques is the co-culture of MSCs and endothelial cells (typically, human umbilical vein endothelial cells (HUVECs))[441], forming microvascular structures in 2D and 3D scaffolds or organoids (Fig. 83). Cell sheets stacking or moulded tubular structures can help to build 3D artificial vascular network[441]. The 3D bioprinting is also emerging by printing several distinct cell types in a predetermined 3D scaffold. However, early stage neovessels are immature and instable[442]. All these methods are constrained by thrombotic events and consequent non-functionality upon the graft implantation[440].

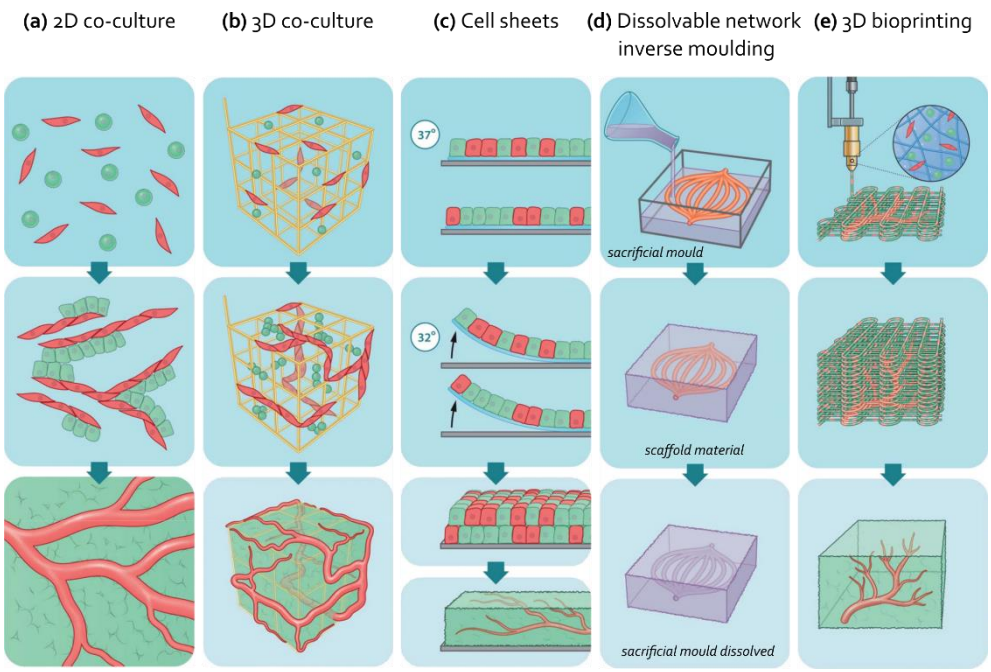

Figure 83. In vitro pre-vascularization strategies in tissue engineering. (a) One of the most straightforward approaches is the co-culture of tissue-specific, progenitor or stem cells (green) alongside endothelial cells (red). (b) Another similar method is the use of a 3D scaffold, aiding in the direction of vascular growth. (c) Cell sheets are a more recent technique aiming to create 3D vascular networks without relying on scaffolds. These cell sheets, made using thermoresponsive materials, are stacked layer by layer to form a 3D structure. An advantage of this system is that the native extracellular matrix is preserved. However, its capacity is restricted by the number of layers, limiting the size of the tissue graft that can be produced. (d) Inverse moulding involves the use of a sacrificial mould. This sacrificial mould is embedded within the scaffold material, and once dissolved, it leaves behind a tubular structure. This structure can then be vascularized and incorporated into a tissue graft. (e) One of the most promising approaches could be the integration of biological and engineering methods, such as 3D bioprinting. This technology allows for the printing of various cell types in a 3D structure to create a graft with existing vessels. Upon implantation, this graft is expected to avoid issues related to hypoxia or nutrient deficiency. Adapted from Rademakers et al. (2019)[441].

A. 2. In vivo pre-vascularization strategies

In vivo pre-vascularization strategies use the body self-regenerative ability as an *in vivo* bioreactor to cultivate elements for tissue regeneration[14,441,443] (Fig. 84).

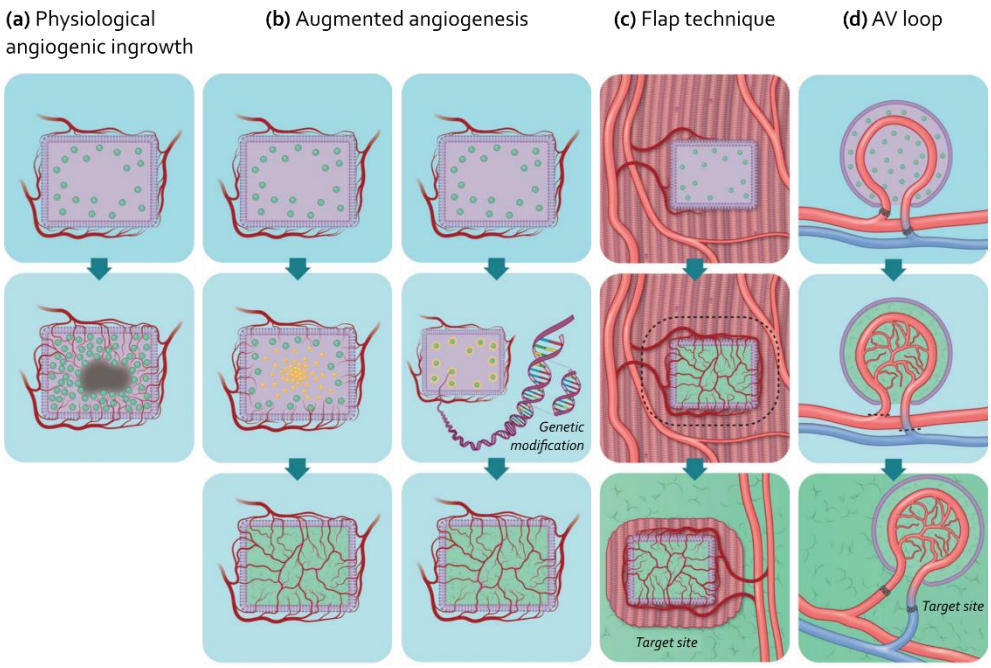

Figure 84. In vivo pre-vascularization strategies in tissue engineering. (a) The primary problem with relying on natural angiogenic growth is insufficient and delayed vascularization, resulting in cell death at the graft core. (b) One strategy to address this issue in vivo is to boost the innate angiogenic response within the graft. This can be achieved by either loading the graft/scaffold with proangiogenic GF (b – left panel) or genetically modifying the graft (b – right panel). (c) Flap technique is an approach involving preimplantation in ectopic (muscle) tissue to establish revascularization of the graft before transplanting into the target site. (d) Arteriovenous (AV) loop method follows a similar principle as the flap technique but can be implemented at any location without damaging the initial donor- site. An encapsulated graft with an AV loop facilitates initial perfusion until further vascularization is established. The revascularized graft can then be transplanted to the intended target site. Similar approaches, like vascular chambers, are also based on the principles of the AV loop/bundle technique. Adapted from Rademakers et al. (2019)[441].

Approaches to *in vivo* pre-vascularization include strategies to augment natural angiogenesis through loading grafts with proangiogenic GF (*e.g.* VEGF, FGF) or genetic modification of grafted cells, with contradictory results[14,441]. A graft can also be implanted in an ectopic site, before the transplantation to the target site when the revascularization is achieved. Another technique involves an encapsulated graft containing an arteriovenous loop/bundle to support initial perfusion until neovascularization is established. Subsequently, the vascularized

graft can be transplanted to the orthotopic location. However, a practical obstacle to this method is the requirement to sacrifice an afferent artery with the vascularized transplant.

While advancements in vascularization engineering are ongoing and awaited, challenges in scaffold vascularization could be addressed by using native tissues to provide an intact vascular network.

B. Native vascular network use

Autologous vascularized periosteal flaps are commonly employed in orthopaedic surgery[32] but their use is limited by the size of available harvest and the finite source, making them unsuitable for CSBDs. However, the HFL potential as a vascularized flap for CSBD treatment remains unexplored. Although the vascularization of the anterolateral thigh (ALT) flap, which overlies the HFL[444], is well-documented in reconstructive surgery[445,446], the intrinsic vascularization within the HFL itself remains unclear and unaddressed in existing literature.

Research questions emerging from the Diamond

If an inherent vascular network exists within the HFL, it could serve as a roadmap for reendothelialization using tissue-engineered techniques or as an autologous flap. However, before exploring strategies to utilize and optimize this vascularization, understanding the presence of an intrinsic vasculature is fundamental. To achieve this, a novel intravascular injection technique was first developed to visualize the vascular network using imaging techniques and during dissection. Subsequently, the vascular potential of a single HFL sheet is thoroughly investigated.

This chapter aims to answer the following questions:

- **How can we reveal or identify the presence of an intrinsic vasculature in the HFL?**
- **Based on the 3D vascular organization, which type of flap can be harvested to obtain a very thin, vascularized collagen membrane for use as a wrapping OM?**

Paper 8 – A single Angiofil-latex injection for both radiological and anatomical assessment of arterial territories in the limbs

Julie Manon, Gaspary Fodjeu, Robin Evrard, Lucien Van den Broeck, Mathieu Jacob, Emmanuel Coche, Olivier Cornu, Catherine Behets†, Benoît Lengelé†

† Share last authorship

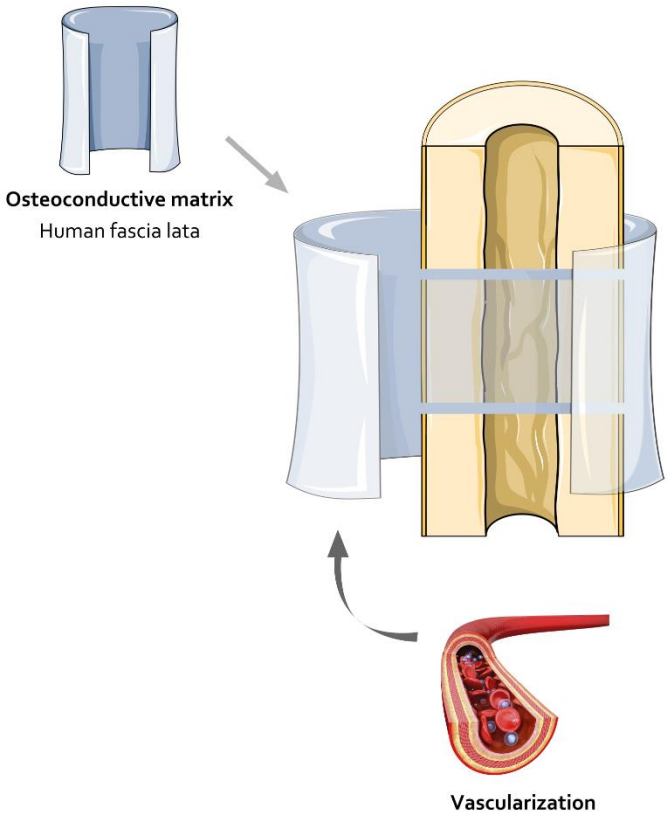

Published in

Annals of Anatomy (IF=2.976)

doi: 10.1016/j.aanat.2024.152312

Abstract

Introduction: Postmortem evaluation of the human vascular system has a long history, with advancements ranging from dissections to modern imaging techniques like CT scans. This study designs a novel combination of Angiofil, a liquid radiopaque polymer, and latex, a flexible cast material, for cadaveric vascular analysis.

Material & methods: The aim was to synergize the advantages of both components, providing accurate radiological images and optimal dissection conditions. Three arterial territories (lateral circumflex femoral artery, profunda brachii artery, and radial artery) were injected and assessed through CT scans and dissections.

Results: The Angiofil-latex mixture allowed successful visualization of the vascular networks, offering a simple, reproducible, and non-toxic approach. Quantitative assessments of the three territories, including diameters (Ø) and lengths, showed comparable results between CT scan and dissection.

Discussion: The technique precision and versatility make it an accessible and valuable tool for anatomical studies, potentially extending its application to MRI analyses. Overall, the Angiofil-latex combination presents a cost-effective solution for researchers, offering enhanced visibility and detailed anatomical insights for various applications, including anatomical variation studies.

Graphical abstract

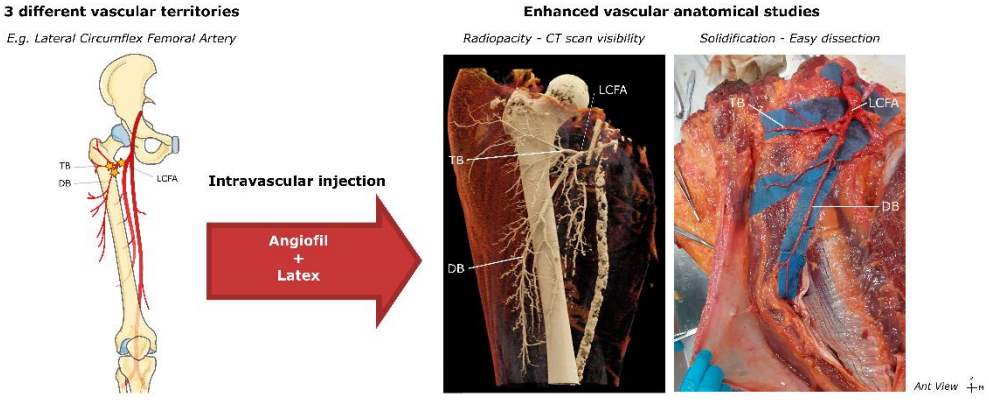

Full-length article in Appendix.

– TAKEAWAYS –

Paper 8 – A single Angiofil-latex injection for both radiological and anatomical assessment of arterial territories in the limbs

- *Single Angiofil-latex injection* =

✓	✗
Artery	*Veins – Capillaries*
X-rays – CT scan	
Dissection	

→ *Fixed outcomes*

⇨ *This injection technique enables the visualization of arteries with a diameter of at least 300µm. MicroCT imaging could enhance precision and provide better visualization of smaller calibres, facilitating the exploration of any potential intrinsic vascularization within the HFL using this method.*

Paper 9 – Beneath the Perforators: Unravelling Fascia Lata Intrinsic Vascular Architecture

Authors to be determined

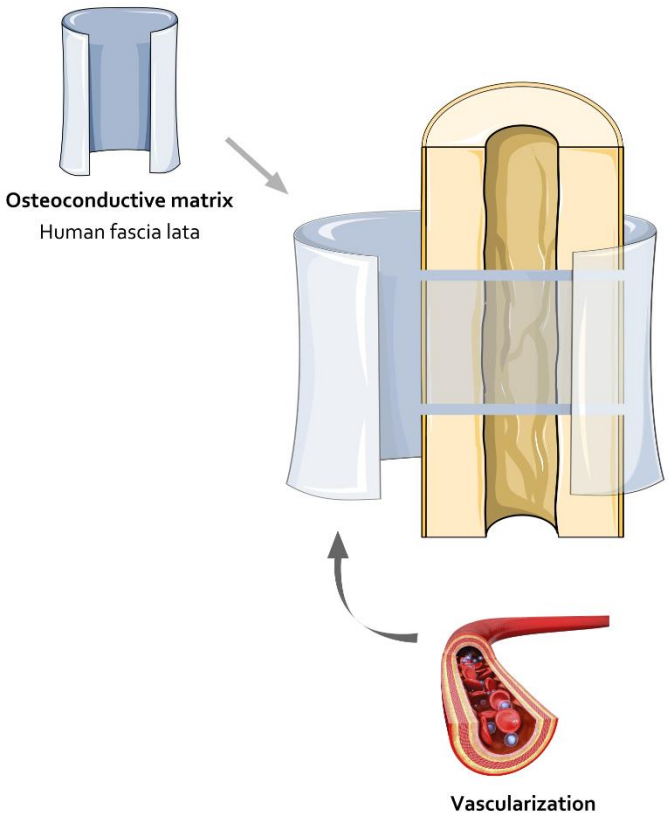

Work in progress

Abstract

The fascia lata (FL), a dense connective tissue enveloping the deep structures of the thigh, has served in reconstructive surgeries for decades, as an avascular scaffold or tissue substitute. However, the demand for vascularized tissue replacements requires a thorough understanding of its intrinsic vascularization. Based on the ALT flap knowledge, this study explores the detailed and quantitative vascular architecture of the FL itself, with the potential of using it as a standalone vascularized flap.

Angiofil-latex was injected in the lateral circumflex femoral artery (LCFA) of 16 lower limbs. High-resolution microCT allowed to study the specific fascial distribution of perforators arising from this artery. Dissection of 11 fresh-frozen lower limbs was performed to identify the main perforating arterioles. The intrinsic vascular network within the FL tissue was then analysed in 5 ALT flaps using microCT.

The study confirmed an average of 2.5 ± 0.5 main perforating trunks giving rise to 5.6 ± 2.9 perforating arterioles per thigh. Notably, microCT revealed a distinct intrinsic vascular network within the FL tissue, with tiny arterioles of 55.39 ± 28.47µm radius and a volumetric density of 33,347,960 ± 23,243,879µm³/mm². This intrinsic vasculature exhibited a high density of bifurcations (branching nodes=1.36 ± 2.26/mm²), demonstrating its potential use as a vascularized flap.

This study unveils the intrinsic vascularization of the FL, supporting its utility as a mega-thin vascularized flap in reconstructive surgery. Based on this vascular carrier, these findings also open new applications for tissue engineering and personalized medicine, toward an improvement of surgical outcomes and patient recovery.

A. Introduction

The FL is a dense connective tissue enveloping the thigh, with a lateral thickening known as the ITT. Composed of collagen fibres[290] with a specific organization, this tissue has been used for several decades in reconstructive surgeries, as a replacement tissue or avascular mesh[447]. Typically decellularized and stored in tissue banks[243,341], the FL is used in various procedures, such as duraplasty[233], colpopexy[236], abdominal wall repair[234,447,448], maxillofacial reconstruction[449,450], or ligamentoplasties[239,241]. However, optimal tissue regeneration in transplantation requires an effective vasculature, crucial for nutrient supply and cell survival. Understanding the FL intricate vascular network is thus pivotal for enhancing its potential in regenerative medicine.

The renowned ALT flap garnered interest due to its significant vascular properties. Described forty years ago[451], it is based on perforating vessels arising from the descending branch (DB) of the LCFA, and offers a reliable long vascular pedicle despite several branching variations. The ALT flap is valued for its ease of raising, adaptable shape and size, large vessel diameter (2.0 to 2.5mm[451,452]), moderate thickness, and ability to incorporate sensitive functions. It also boasts minimal donor-site morbidity with usual primary closure[237,240,444,445,451–456]. Widely used in reconstructive surgery, the ALT flap is usually raised as a thin or ultra-thin skin flap. Including the FL, a composite flap has been also used for patellar or Achilles tendon reconstruction combining a skin paddle with a fascial strip, and mimicking a tendon-like structure[240,457–462].

While previous studies have extensively characterized ALT vascularization, specifically its subdermal and suprafascial vascular plexus[250,451,452], the intrinsic vascularization within the FL itself remains unexplored.

Alongside reviewing the vascular distribution from the LCFA to the thigh integuments, the primary objective is to uncover the intrinsic vascularization within the FL. This microscopic exploration, using advanced injection techniques (Angiofil- latex[421]) and imaging methods (microCT[463]), aims to reveal previously unseen micro-vessels within the FL tissue, shedding light on its vascular intricacies.

B. Materials & methods

B. 1. Fascia lata procurement

Fresh frozen lower limbs (N=16) were provided by the Human Anatomy Department of UCLouvain (IRB00008535, Brussels, Belgium) with approval from the local ethics committee (Ref 2021-30AOU-356, approved on September 13, 2021). The study, divided into macroscopic and microscopic assessments, recorded specimen demographics for each part in Table 21.

Table 21. Demographics of each part of the anatomical study.

	Number of limbs	Number of donors	Sex	Age *(mean ± SD)*	Laterality
Distribution of the LCFA (CT + dissection)	*11*	*8*	*6 ♂ / 2 ♀*	*80.1 ± 15.3*	*5L / 6R*
Intrinsic vascularization of the FL (Dissection + microCT)	*5*	*5*	*3 ♂ / 2 ♀*	*84.7 ± 6.1*	*0L / 5R*
Total	16	13	9 ♂ / 4 ♀	81.9 ± 12.4	5L / 11R

SD: standard deviation, LCFA: lateral circumflex femoral artery, CT: computed tomography, FL: fascia lata, microCT: microfocus computed tomography, ♂: men, ♀: women, L: left, R: right.

B. 2. Angiofil-latex injection

All limbs underwent successful Angiofil-latex intravascular injection according to the previously described technique[421]. Briefly, they were thawed in a hip-down position, then rinsed with pre-heated (56°C) NaCl solution (0.9%) through the common femoral artery (CFA). Injection was performed through the LCFA under continuous manual pressure and involved a latex mixture (Latex «LA», with 0.38% ammonia, 603, Finres, Belgium) supplemented with a 1:5 volume of liposoluble iodine agent (Angiofil, S500.0028, Fumedica AG, Switzerland) (mixture 1:5 contrast agent: solvent, v/v), and red dye droplets (Jesmonite, bright red pigment, 200g, Finres, Belgium). Angiofil allowed vascular opacification for imaging, while

latex facilitated solidification in a cold room (4°C) for 72h. After solidification, outcomes are preserved for subsequent analysis at any time in both imaging and/or dissection.

B. 3. Lateral circumflex femoral artery vascular network distribution and perforators

Computed tomography

The precise artery opacification permitted maximal resolution in clinical CT scans (0.3mm)[421]. This technique was used to evaluate the LCFA vascular network and its perforators[464]. Lower limbs (N=11) were scanned between injection and solidification time, using a Somatom Definition AS 128 scanner (Siemens Healthineers, Erlangen, Germany), in an ultra-high-definition mode (beam collimation=0.3mm, tube voltage=120kV, tube current=200–250mAs). Subsequent reconstructions using both hard and soft kernels (slice thickness=0.4mm) and volume rendering technique[465,466], were performed with the Syngo.Via tool in cinematic rendering mode. CT acquisitions and reconstructions were useful for 3D visualization and dissection planning.

Dissection

Following latex solidification, limbs were dissected according to previously reported protocols[444,446,290,291]. The skin incision followed the standard landmarks between the anterior superior iliac spine (ASIS) and the superolateral border of the patella. The DB of the LCFA was first identified distally between the vastus lateralis and the rectus femoris. The LCFA was dissected in a retrograde way, encompassing the DB and the TB up to the injection catheter. Dissection continued anterogradely through the septum or through the vastus lateralis until reaching the distal perforators. All the perforator pathways were carefully dissected between the LCFA and the FL to reveal the entire LCFA network.

Data collection & analysis

The LCFA vascular network was macroscopically described using a combination of Yu's ABC system and Shieh's vascular classification[445,446]. Yu's classification[445] identified three levels, *i.e.* at the midpoint between the ASIS and the patella (perforator B), and 5cm proximally (perforator A) or distally (perforator C) from this

point. Shieh's classification[446] focused on perforator origin, number, location, and musculo- or septocutaneous characteristics of each pathway. When main perforator trunks gave rise to small perforating branches, they were documented. Qualitative data were expressed as frequency, *i.e.* number of events and percentage.

B. 4. Intrinsic vascularization of the fascia lata

Dissection

Following latex solidification, dissection included a more medial (1cm) skin and fascial incision to flip and lift the entire fasciocutaneous ALT flap (N=5), preserving all perforating vessels[421,444,446]. The incision proceeded vertically through the subcutaneous tissue until passing beneath the FL. The perforators were identified just under the FL and cut on their origin side. The full-thickness flap was harvested, preserving all perforating arterioles (Fig. 85 – a), and was fixed in 4% formaldehyde (VWR, 9713.9010) for 4 days. A thread in the antero-superior corner always provided a precise orientation of the tissue.

Angiofil-latex enhanced microCT

Supposing that FL intrinsic vessels would be thinner than the perforator, an emerging technology was used to investigate deeper details. The microCT allowed a high-resolution 3D study of the specimens until the microscopic level[463], without tissue damage like caused by histology or microstructure changes caused by dissection. Fixed full flaps were first scanned with a Phoenix NanoTom M (GE Measurement and Control Solutions, Germany) at low-resolution (Supplementary data – Table 23) to get an idea of the perforator distribution. The location of the perforating points through the fascia was recorded and classified as being in the ITT, in the anterior fascia, or at the junction between the two.

Angiofil-latex enhanced high-resolution microCT

To further increase the resolution, three flaps (N=3 donors) were trimmed into full-thickness cubes with a surface area of 2x2cm centred on three perforators, meaning 1cm on either side (n=3 cubes x 3 donors=9) (Fig. 85 – b). The four corners of the cube surface were stitched from the fascia to the skin to avoid delamination of tissue components during the high-resolution microCT (15µm).

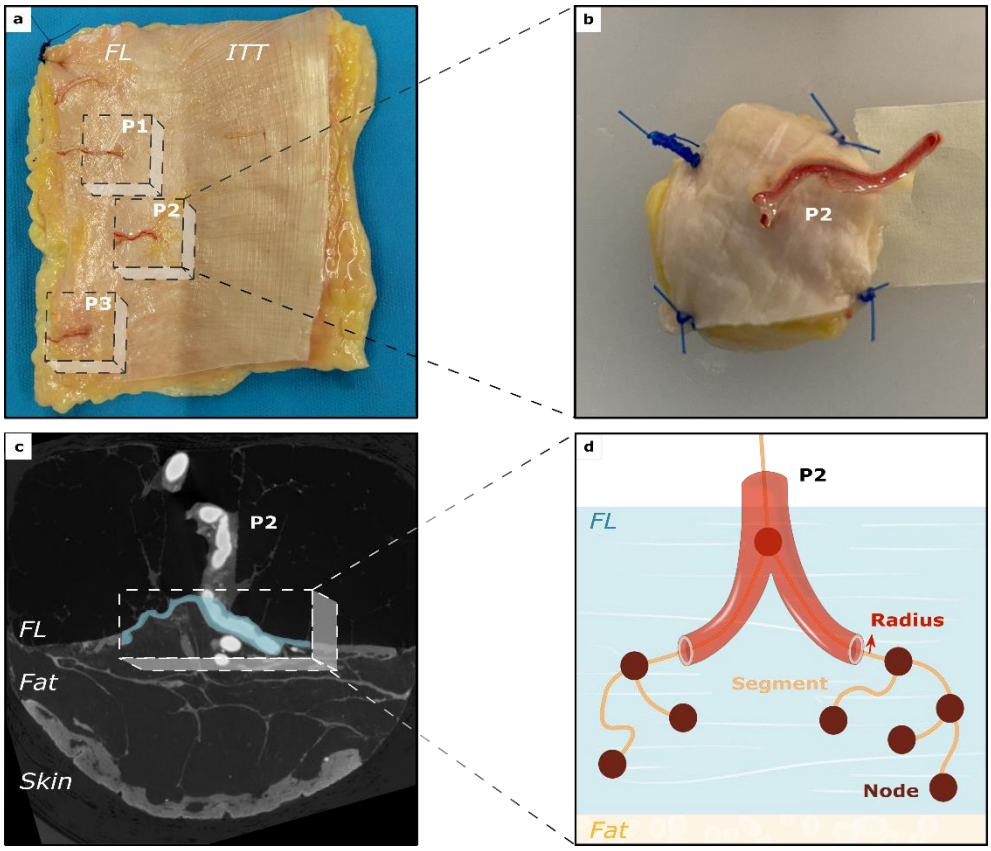

Figure 85. Study design of the experiment. Harvesting of the full-thickness fasciocutaneous anterolateral thigh flap (N=5 donors), seen from its deep surface (a). Cubes of 2x2cm are harvested, centred on the perforating artery (P2) (n=3 cubes x 3 donors=9) (b). Full-thickness cubes were scanned with the microCT and extraction of subvolume containing only the fascia lata (FL) tissue highlighted in light blue (c), which directly permitted the quantification of the vasculature volume inside the FL (d). Autoskeleton module allowed to skeletonize the vascular network into segments and branching nodes that were also quantified.

The cubes were mounted on polystyrene blocks with the perforators within a centred hole, wrapped in parafilm, and scanned with the Phoenix NanoTom M again with higher performance parameters (Supplementary data – Table 23). The Angiofil-latex mixture contrasted the vascular network in white, enabling detailed intrafascial analyses using Avizo software (2022.1, ThermoFisher Scientific, France). Several processing tools were applied successively. First, the FL and the vascular tree were segmented using *semi-manual segmentation tools (brush and magic wand),* and the *Filter Sandbox* module thanks to their grey values. The

sample 3D reconstruction was made using the *volume rendering* tool and allowed a qualitative and visual analysis of the intrinsic FL vascularization.

Data collection & analysis

Subvolumes containing the FL thickness-only were extracted using a combination of *Extract Subvolume* and *Arithmetic* modules (Fig. 85 – c), and quantitative data were obtained. The volume of the vasculature inside the FL was quantified using the *Volume fraction* tool, normalized by the subvolume surface, and expressed as mean ± SD of three samples and three donors. The normalized volume of the main perforating arteriole was calculated based on diameter and fascial thickness, and subtracted from the total normalized vascular volume to estimate the effective FL vascularization volume. A ratio of vascular subvolume to tissular subvolume was computed and expressed as mean percentage ± SD. The number of vascular segments, branching nodes, and arteriole radius were computed from the *Autoskeleton* module (Fig. 85 – d). A vascular segment is defined as a continuous curvilinear segment between two nodes. A node is determined by the vascular ramification into a minimum of two smaller vessels. The variables of segments and branching nodes were normalized by respective subvolume surface, averaged, and expressed as mean ± SD. Full details of acquisitions and module parameters are summarized in Supplementary data – Table 23.

C. Results

C. 1. Distribution of the LCFA vascular network & its perforators

Among 11 dissected thighs, 28 main perforators were identified, averaging 2.5 ± 0.5 main perforator trunks per limb. The DB and the TB yielded 1.1 ± 0.5 and 1.5 ± 0.8 perforators, respectively. The perforator distribution and pattern were described in Table 22, following Yu's classification[445], with the number of limbs that exhibit at least one perforator of each level. Perforators A and B were mostly septocutaneous while perforators C were always musculocutaneous. Each LCFA territory (100%) featured at least one perforator B, the most prevalent (35.7%).

Table 22. Distribution and pattern of perforators according to Yu's ABC classification[445] after dissection.

Yu's ABC classification	*Perforators n (%)*	*Septocutaneous n (%)*	*Musculocutaneous n (%)*	*Limb with one perforator n (%)*
A	*9 (32.1%)*	*6 (66.7%)*	*3 (33.3%)*	*9 (81.8%)*
B	*10 (35.7%)*	*6 (60.0%)*	*4 (40.0%)*	*11 (100%)*
C	*9 (32.1%)*	*0 (0.0%)*	*9 (100%)*	*9 (81.8%)*
Total	28 (100%)	12 (43%)	16 (57%)	11 (100%)

n: number, %: percentage. The percentage of perforators was calculated on the total number of perforators (n=28). The percentages of septo- and musculocutaneous perforators were calculated on the number of perforators of the respective level ABC. The percentage of limbs with one perforator was calculated on the total number of limbs (N=11).

Combining Yu's system with Shieh's classification (Supplementary data – Table 24), no thigh had a single perforator in this study. The most common pattern involved triple perforators from both the DB and the TB (55%).

Additionally, 62 small perforating branches emerged from main perforator trunks to cross the FL, averaging 5.6 ± 2.9 perforating arterioles per limb.

C. 2. Intrinsic vascularization of the fascia lata

Among five entire raised flaps, 28 perforating arterioles were contrasted, *i.e.* 5.6 ± 1.5 perforating arterioles per ALT flap, consistent with the results summarized in Supplementary data – Table 24. The fascial perforating point of arterioles was found twice in the ITT (2/28 – 7.1%), eight times in the junction (8/28 – 28.6%), and most frequently in the anterior thigh fascia (18/28 – 64.3%). The mean diameter of these arterioles was 0.61 ± 0.38mm.

The qualitative exploration of the entire flaps suggested distinct types of perforating arterioles, some of them running along the fascia surface with/without ramifications that could vascularize the FL by diffusion (Fig. 86 – a). However, in most cases, no well-defined intrinsic vascularization was macroscopically apparent (Fig. 86 – b). Further examinations revealed that some perforators sent branches

to the adipose side of the FL (Fig. 86 – c & Video 2), although this vascularization was not easily observable through the FL opacity. Another difficulty is the discrimination to be made between arterioles running within the fascia or just lying down.

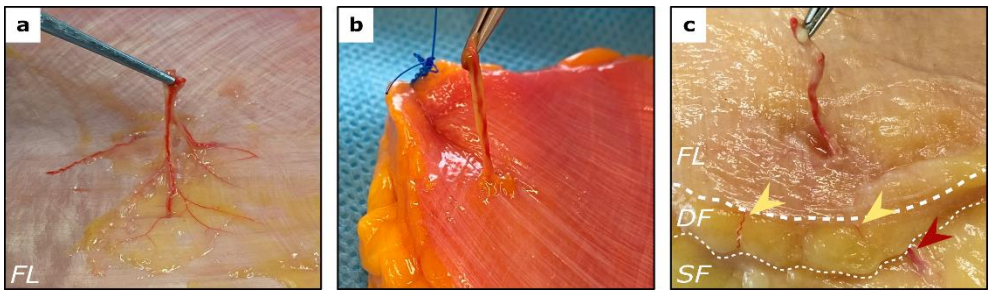

Figure 86. Macroscopic visualization of perforating arterioles: ramified perforator in the subfascial gliding plane (a), isolated perforator (b), and perforating vessel that branches in/after the fascia lata (FL) (c). DF: deep fat, SF: superficial fat. Yellow arrowheads show ramified branches, running along the FL. Red arrowhead marks the continuity of the main perforating arteriole.

MicroCT scans displayed contrasted arterioles within ALT flaps (Fig. 87 – a) but distinguishing fascial intrinsic vessels from extrinsic ones was challenging at this resolution. Further microCT analysis of cubes of 2cm side however revealed small Angiofil-latex enhanced arterioles within the FL itself, emerging from the main perforator and running through the FL, providing its vascularization (Fig. 87 – b). 3D reconstructions confirmed this observation, with the intrinsic fascial vascularization highlighted in yellow (Fig. 87 – c), obviously distinct from extrinsic vessels coloured in red. The 3D view highlighted the arborescence of both intrinsic and extrinsic vasculature, with centrifugal arterioles spreading towards the skin and giving rise to four different networks identified as subfascial, intrafascial, suprafascial, and subdermal plexuses.

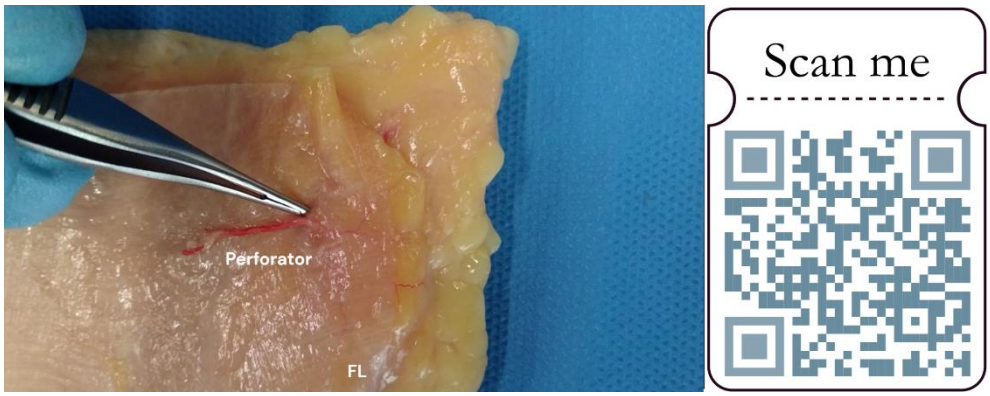

Video 2. Perforating arteriole that ramifies in/after the fascia lata in the intra- and suprafascial plexus, respectively, before sending a connecting artery toward the subdermal area. FL: fascia lata, DF: deep fat, SF: superficial fat.
https://zenodo.org/records/11060858?token=eyJhbGciOiJIUzUxMiJ9.eyJpZCI6ImYyODE1MWE3LTE4MTItNGQ2NC1iYTkyLTRjMDVjYzIwZTEoNSIsImRhdGEiOnt9LCJyYW5kb20iOiIxNjE5OGYoZGU5MWUzZmZmYzU5ODU4NDQyNjJjNGMzZSJ9.Ui2PjWPIklbPMl4ma33-ck1-XZEVTP5QCx4Bf5PUk4bodhMFBYVAksaVPdqkr6apPK3OsB-w4XIyr54TUrLgRw

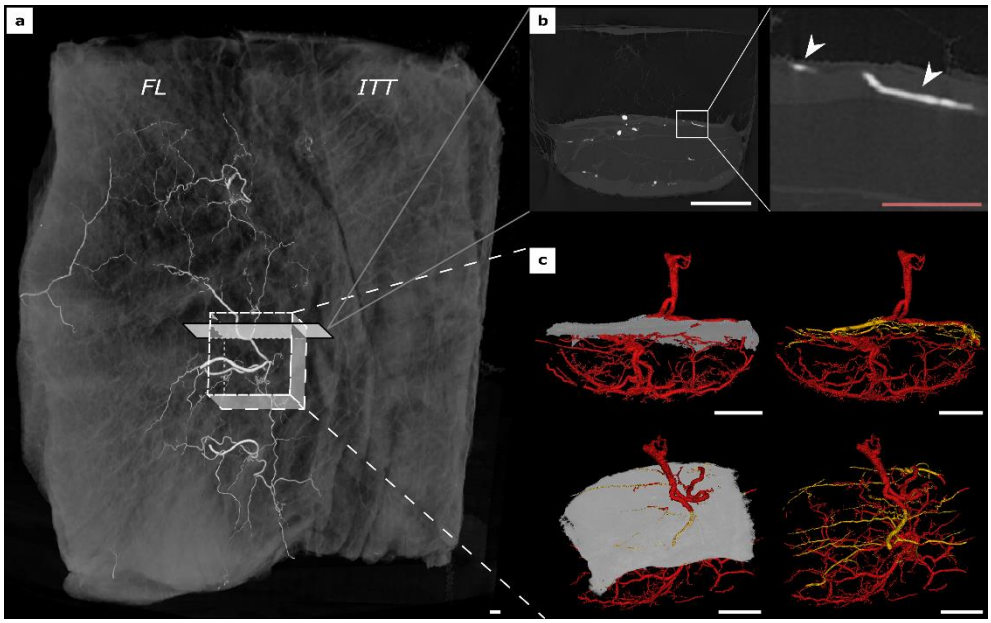

Figure 87. Low-resolution Angiofil-latex enhanced microCT of the whole ALT flap divided into two parts, the fascia lata (FL) and the iliotibial tract (ITT) (a). High-resolution Angiofil-latex enhanced microCT of a full-thickness cube (b) and 3D reconstructions (c) highlighting the extrinsic vascularization (red) and the intrinsic vascularization (yellow) before and after removing the segmented FL in grey. White scale bars: 5mm, pink scale bar: 1mm.

Quantitatively, the total normalized volume of arterioles inside the FL averaged 35,622,356 ± 23,416,866µm³/mm² of FL surface. Considering the volume of the perforating arteriole at 2,274,396 ± 2,020,080µm³/mm², the effective volume of arterioles inherently vascularizing the FL was 33,347,960 ± 23,243,879µm³/mm² of tissue surface. The ratio between vascular subvolume and tissular subvolume was 1.05% ± 0.34. The mean arteriole radius inside the FL was 55.39 ± 28.47µm.

The average number of vascular segments was 2.55 ± 4.16/mm², with 1.36 ± 2.26/mm² branching nodes, indicating the arborescence and ramifications.

D. Discussion

Supported by the advantages of Angiofil-Latex intravascular injection[421] and microCT[463], this study confirmed the macroscopic distribution of LCFA perforators and importantly unveiled the existence of an intrinsic vascular network within the FL.

LCFA vascular network

Like the LCFA origin variability[467], the arborescence of LCFA perforators has been previously studied. Predominant perforators were originally described in a circle of 3cm radius around the midpoint between the ASIS and the patella[444,445,468]. The variable anatomy in route (septocutaneous or musculocutaneous[451–453,468]), origin (DB or TB[445,446]), orientation (horizontal or vertical[445,452]) or level[445,446,454,469] was further confusing[446,452,467,470]. Several classifications followed one another with no strict consensus. In this study, Yu's and Shieh's systems allowed to classify perforators depending on their height and origin and to detail their characteristics comprehensively.

On average 2.5 ± 0.5 main perforating trunks and 5.6 ± 2.9 perforating arterioles per LCFA territory were found, which corresponds to the literature data (1.6 to 3.2 perforators). Cadaver studies always counted more perforators (mean 2.7) than clinical ones (mean 2.1)[250,445,454,455]. Angiofil-latex injection enhanced perforator visualization and dissection, in opposition to surgical observations that concentrate on the main vascular pedicle and may lower consideration for

secondary perforators[453]. The ALT is a confident flap with at least one perforator in 98% of cases[455], but still, clinical studies found no perforator in 5.4% compared to 0% of cases in cadaver studies.

Patterns of perforators observed in this study included at least two perforators, and a predominance of triple perforators from both the TB and DB, differing from other studies[445,446]. Data should be considered with caution given the small sample size. More extensive studies (N>70) and meta-analyses deserve greater confidence when describing a single predominant origin (57 to 100%) from the DB[445,446,454,455].

More than 80% of the limbs exhibited at least one perforator from each level of Yu's classification. The musculocutaneous pattern was common[445,446,452–455,471], with perforator B being the most prevalent (85.6 to 100% in a circle of 5 to 6cm around the midpoint[454]). The most distal level, the most musculocutaneous pathways were found. This simple classification is particularly useful to precisely guide the surgeon's decision. If needed or if perforator B is absent, both other perforators can help. Perforator C is usually thinner and most frequently musculocutaneous while perforator A has a larger diameter but might shorten the pedicle length and increase the fatty thickness[445,446], especially in Western people[445,454]. For all these reasons, even if some authors did not recommend preoperative imaging[444,469], Doppler investigations and angiography, in case of a negative Doppler, can considerably impact surgical planning and reduce the risk of failure[250,445,453,455].

Even though the ALT versatility is tremendous, its bulkiness makes it unsuitable for indications requiring a very-thin vascularized membrane. The groundbreaking advance then lies in the second part of our study which explores the intrinsic FL vascularization.

Intrinsic fascia lata vascularization

Macroscopically, during the dissection, most perforating arterioles (64.3%) were located in the anterior thigh fascia, with an average diameter of 0.61 ± 0.38mm, considered medium calibre[445,455].

Unlike the limitations in the resolution of clinical imaging[421,463], Angiofil-latex enhanced microCT provided microscopic insights into the FL intrinsic

vascularization. A single perforating arteriole gave rise to branches of 55.39 ± 28.47µm radius within the fibrous tissue, equivalent to approximately 0.1mm diameter. Their ramifications really ran inside the FL allowing blood supply for cell and tissue survival.

Quantitative evaluation showed an effective FL vascular volume and a dense network of bifurcations. The dispersion of the volume data was important. Since the methodology was very reproducible based on systematic parameter replication and computerized arithmetic, independent from the operator, this highlights intra- and interpersonal variability of the specimens.

To our knowledge, a detailed exploration of FL intrinsic vascularization for a unique fascial vascularized flap has not been extensively studied. Two previous studies approached this concept differently, with one focusing on TB and ascending branch (AB) vascularization through histological 2D analysis[472]. However, the DB, known to send numerous arterioles to the FL[445,446,454], was not specifically assessed since it was only retrogradely opacified by injection of the profunda femoris artery (PFA) and/or the superior lateral genicular artery, and showed no macroscopic intrinsic opacification. The second study injected methylene blue into the DB to explore FL vascularization macroscopically[250]. However, the adherent adipose tissue was not removed to preserve the perifascial blood supply. Therefore, the discrimination between real intrinsic vascularization and vessels lying down the FL surface was impossible. The authors also mentioned the limited value of methylene blue injection and consequent clinical impact[250], and openly suggested additional exploration with more detailed techniques.

In contrast, our study strongly suggests that the FL has its own supplying network. Additionally, perforating branches of the LCFA give rise to a subfascial and suprafascial network, before spreading their terminal branches in the subdermal plexus.

Limits, perspectives & recommendations

The sample size was small but enough to demonstrate the FL intrinsic vascularization. Future studies on larger cohorts and varied arteriole locations are warranted. Exploring anastomotic networks within the FL could offer insights into potential single-pedicle FL-only flap creation.

This study, conducted on an elderly population with potential involution of FL tissue and its vascularization, suggests that if these findings are significant in older individuals, they could be even more pronounced in younger individuals.

The FL is already processed in tissue banks[291,341] with appropriate decellularization protocol to create an acellular, non-immunogenic biocompatible scaffold while preserving its ECM and skeleton[291,351,406]. However, its avascular nature limits some uses, highlighting the importance of vascular supply. Considering ongoing advancements in tissue engineering, detailed micro-level vascular network studies are essential prerequisites for potential recellularization efforts[456].

Pending improvements in regenerative medicine, this finding support the use of a FL-free flap as an autologous graft acting as a vascular carrier for cells of interest promoting tissue regeneration. Prioritizing examination of the anterior thigh fascia, rich in perforating arterioles, is recommended. The choice of perforators should align with surgical needs, with a preference for a middle perforator when possible due to optimal pedicle calibre, length, intrinsic vascularization, and thinness.

As such, its utilization could cover a huge panel of reconstructive surgery. A mega-thin vascularized FL flap including sub-, intra-, and suprafascial plexuses could benefit various clinical reconstructive conditions such as tympanoplasty[473], several mucosal repairs, head and neck defect covering in the management of osteoradionecrosis[474], or replacement of extensive loss of physiological membranes such as dura mater, pleura or peritoneum[250,472]. However, further clinical applications in reconstructive or regenerative surgery necessitate stronger evidence and a more detailed study of these vascular networks, supplied by the LCFA perforators, which is ongoing in our laboratory.

E. Conclusion

The combination of Angiofil-latex intravascular injection and microCT offers a promising method to unveil the unseen aspects of FL vascularization. This study uniquely details the intrinsic FL vascular network, paving the way for the development of FL-only free flaps.

F. Supplementary data

Supplementary data – Table 23. MicroCT acquisition and module parameters.

Acquisition parameters		Acquisition parameters		Autoskeleton	
Low-resolution scan		*High-resolution scan*			
Voxel size (µm)	66.6	*Voxel size (µm)*	15	*Smoothing coefficient (smooth)*	0.5
Source voltage (kV)	65	*Source voltage (kV)*	65	*Smoothing coefficient (attach to the data)*	0.25
Tube current (µA)	350	*Tube current (µA)*	400	Number of iterations	10
Exposure time (ms)	500	*Exposure time (ms)*	500		
Number of images	2800	*Number of images*	3200		
*Average**	1	*Average**	1		
*Skip**	0	*Skip**	0		
Scan time (min)	23	*Scan time (min)*	26		

** Information about those parameters was previously given in the literature[288]*

Supplementary data – Table 24. Vascular patterns present in this study, out of the 19 patterns described by the combination of Yu's ABC system and Shieh's vascular classification[445,446]. Yu's classification identifies three levels or perforator localization, i.e. at the midpoint between the anterior superior iliac spine and the patella (perforator B), and 5cm proximally (perforator A) or distally (perforator C) from this point. Shieh's classification focused on the perforator origin, number, and location.

		Double perforators		Triple perforators	
Pedicle origin	**A+B**	**B+C**	**A+C**	**A+B+C**	***Total***
DB	9% (n=1) 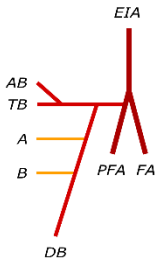	9% (n=1) 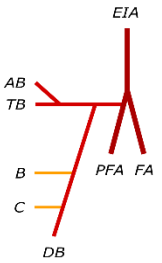	0% (n=0) 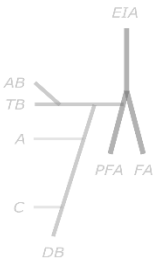	0% (n=0) 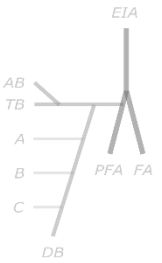	**18%**
TB	9% (n=1) 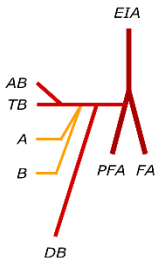	0% (n=0) 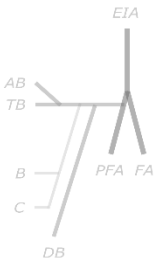	0% (n=0) 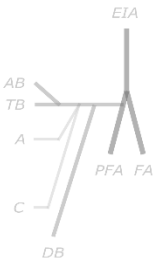	0% (n=0) 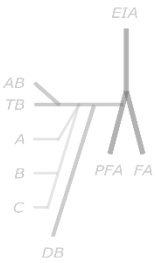	**9%**
DB+TB	0% (n=0) 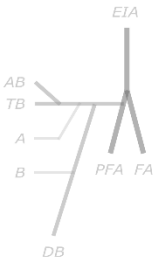	9% (n=1) 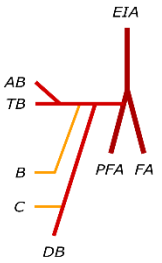	9% (n=1) 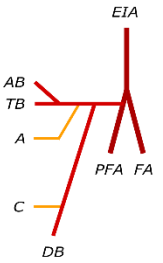	55% (n=6) 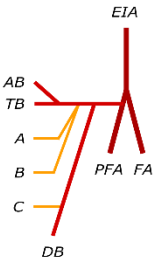	**73%**
Total	**18%**	**18%**	**9%**	**55%**	**100%**

DB: descending branch, TB: transverse branch, AB: ascending branch, EIA: external iliac artery, PFA: profunda femoris artery, FA: femoral artery, n: number.

– TAKEAWAYS –

Paper 9 – Beneath the Perforators: Unravelling Fascia Lata Intrinsic Vascular Architecture

- *Perforator location = Skin landmarks*[444]

  Priority to → *Anterior(-lateral) thigh fascia*

  → *Perforator B*

- *FL intrinsic vascularization unveiled = Perforating arterioles (Ø ± 600µm)*

  Intrinsic arterioles (Ø ± 100µm)

  Survival distance for seeded cell ↵

⇨ *Question: Possibility to raise a unique FL-only vascularized flap?*

⇨ *Answer: Need for investigation of anastomoses and perforasomes*

Paper 10 – Revisiting the variants of the Anterolateral Thigh Flap based on 3D Microscopic Vascular Investigations

Authors to be determined

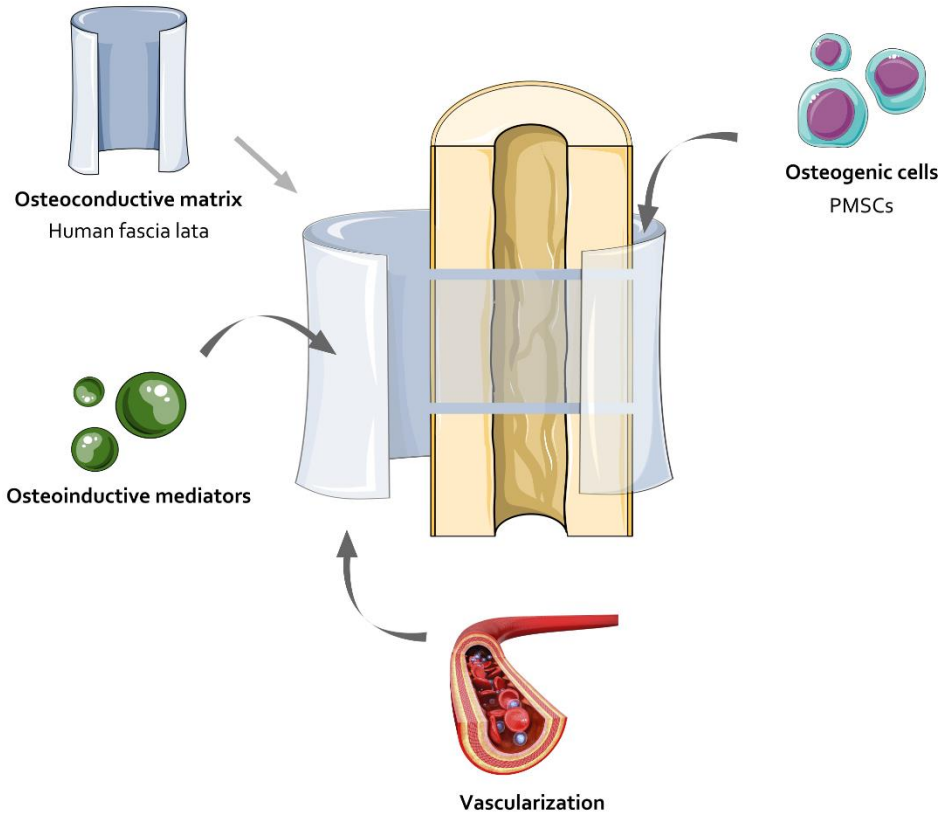

Work in progress

Abstract

Background: The ALT flap is a versatile option in reconstructive surgery, known for its reliable vascular supply and minimal donor-site morbidity. This study aims to provide a comprehensive and quantitative 3D analysis of the ALT flap vascular architecture, focusing on intrinsic FL vasculature and implications for a novel reversed mega-thin flap approach.

Methods: Utilizing new techniques of Angiofil-latex injection and microCT, the microvascularization was assessed in cadaveric specimens (N=11). Perforators from the LCFA and CFA network were discriminated, and a 3D reconstruction was performed to quantify the vascular supply at a microscopic level, for each flap tissular layer.

Results: The study revealed a predominance of LCFA-derived perforators in the anterolateral fascia, with four distinct plexuses vascularizing the subfascial plane, the FL itself, the suprafascial deep fat layer, and the superficial subdermal fat and skin. Quantitative evaluations showed a dense volume of vascularization (67.5%) inside the FL and suprafascial fat. The arborescence and number of microscopic vessels were the most abundant in intrafascial and subdermal plexuses. The fascia superficialis (FS) was localized in the connecting area between the suprafascial and subdermal plexus.

Conclusions: These findings highlight the potential for designing a reversed mega-thin ALT flap, based on a FL-only flap or a FL-to-FS adipofascial flap, offering thinner tissue options with maintained vascularity for further applications in reconstructive or regenerative surgery.

A. Introduction

Described four decades ago[451], the ALT flap is a versatile reconstructive option vascularized by LCFA perforators, notably its DB. Its advantages[451,452,475,445,453,444,454,457,237,455,476,240,456,250] include straightforward surgical techniques, motor and sensory potential, minimal donor-site morbidity, adaptable dimensions, extended vascular pedicle, and sufficient vessel diameter (2.0-2.5mm) for easy surgical anastomoses[451,452]. This flap is essential in reconstructive surgery for maxillofacial, head and neck reconstructions[452,475,445,455,477], defect coverage[445,478], and orthopaedic reconstructions[237,240,453,457–462]. However, its full-thickness version can be bulky for delicate body areas[476,479]. The deep FL has also been used as a thin non-vascularized graft for tissue replacement[233,234,236,239,241,448–450,472]. Research into vascular anatomy intends to reduce flap thickness while retaining the largest surface area. Previous studies identified subdermal and suprafascial plexuses[250,445,451,452,464,480], leading to suprafascial adipocutaneous flap[481,482] or very/ultra-thin ALT raised along the FS and the skin[445,482]. The latter, surviving on the subdermal vascular plexus[480], sometimes requires split-thickness skin graft (STSG) for larger donor-site closures[237,250,446,451]. However, the deep FL could provide a mechanically resistant[290,445,447,476,479], yet thin support for tissue repair without requiring skin tissue.

Recent discoveries in intrinsic vascularization suggest a shift towards a mega-thin flap centred on the deep vascularized FL. Proposals include a sandwich fascial ALT flap[476,479] or a vascularized fascial-only flap[470]. Despite being suggested 30 years ago, limited literature exists on the use of a vascularized FL-only flap, highlighting a lack of anatomical clarity[250,479]. Subsequently, this study aims to explore:

- The vascular microarchitecture from FL-to-skin
- The feasibility of harvesting a free FL-only flap
- The necessity of superficial fat for the blood supply of the FL-only flap
- The possible size of a mega-thin flap on a single pedicle

Using advanced technologies like Angiofil-latex injection[421] and microCT[463], this study seeks to provide static and dynamic 3D assessments of vascular perfusion to inform the design of new flaps[464].

B. Materials & methods

B. 1. Donor demographics

ALT flaps were harvested on fresh frozen limbs (N=11) provided by the Human Anatomy Department of UCLouvain (IRB00008535, Brussels, Belgium). The local ethics committee approved this study (Ref 2021-30AOU-356, approved on September 13, 2021). Different donors and limbs were used to analyse the vascular architecture of the ALT flap and perforasome (Table 25).

Table 25. Demographics of each part of the anatomical study.

	Number of limbs	Number of donors	Sex	Age *(mean ± SD)*	Laterality
Vascular architecture (Dissection + microCT)	*5*	*5*	*3 ♂ / 2 ♀*	*84.7 ± 6.1*	*0L / 5R*
Perforasome (Fluoroscopy + CT)	*6*	*3*	*2 ♂ / 1 ♀*	*95.1 ± 4.1*	*3L / 3R*
Total	11	8	5 ♂ / 3 ♀	88.6 ± 7.4	3L / 8R

SD: standard deviation, microCT: X-ray microfocus computed tomography, CT: computed tomography, ♂: men, ♀: women, L: left, R: right.

B. 2. Angiofil-latex injection

For vascular architecture evaluation, limbs underwent intravascular injection similar to prior investigations[421]. The lower limbs were thawed upside down, and flushed via the CFA with a warmed (56°C) NaCl solution (0.9%). The LCFA was catheterized and injected with a latex mix (Latex «LA», Finres, Belgium) added with a 1:5 volume ratio of liposoluble iodine agent (Angiofil, S500.0028, Fumedica AG, Switzerland), along with red dye droplets (Jesmonite, bright red pigment, Finres, Belgium) under continuous manual pressure. The same mixture but with blue dye droplets (Latex Color Blauw, MIDA Composites, 627-250g, Belgium) was secondarily injected into the CFA after ligating the LCFA origin to differentiate the LCFA perforators in red from the recurrent femoral network in blue. Angiofil

facilitated immediate vascular opacification for imaging, while latex rigidification in a cold room (4°C) for 72h ensured fixation of vascularization for further analysis via imaging or dissection.

B. 3. Anterolateral thigh flap and fascia lata harvesting

Regardless of pre-injection with the Angiofil-latex mixture, all legs underwent uniform dissection procedures. Each ALT flap was harvested following described methods[240,290,291,444,446]. The skin incision was made 1cm medially to the landmark between the ASIS and the superolateral border of the patella to spare perforating vessels[421]. After passing beneath the FL, perforators were dissected retrogradely until the DB of LCFA, situated between the vastus lateralis and rectus femoris muscles. The full-thickness fasciocutaneous flap was harvested along with all their perforators. Perforators were inventoried as originating from the LCFA (red) or the recurrent vascularization from the CFA network, including the FA and PFA (blue). The localization of perforating points was macroscopically described as in the ITT, outside the ITT/within the FL, or at the junction between both.

For perforasome assessment, secondary perforators were clamped with haemostatic metallic clips and cut, while the predominant perforator was meticulously dissected and harvested with the DB pedicle.

B. 4. Angiofil-latex enhanced X-ray microfocus computed tomography

Anterolateral thigh flaps

MicroCT provides a detailed non-destructive 3D exploration at a microscopic scale[463].

Full-thickness ALT flaps were first scanned at the optimal resolution using a Phoenix NanoTom M (GE Measurement and Control Solutions, Germany), and processed using Avizo software (2022.1, ThermoFisher Scientific, France) (scanning parameters resumed in Table 26).

Table 26. MicroCT acquisition and module parameters.

	Acquisition parameters		Module parameters			
	ALT flap	*Perforator zoom*	*Autoskeleton*		*Dilation*	
Voxel size (µm)	66.6	15	*Smoothing coefficient (smooth)*	0.5	*Type*	*Cube*
Source voltage (kV)	65	65	*Smoothing coefficient (attach to the data)*	0.25	*Size (px)*	*20*
Tube current (µA)	350	400	Number of iterations	10		
Exposure time (ms)	500	500				
Number of images	2800	3200				
*Average**	1	1				
*Skip**	0	0				
Scan time (min)	23	26				

** Information about those parameters was extensively explained in the literature[288]*

Semi-manual segmentation tools and the filter sandbox module discriminated Angiofil-latex-opacified arteries from surrounding soft tissues, especially the FL, on 3D reconstructions. Blood supply distribution throughout the entire ALT flap was analysed in terms of organization, plexus formation, linking vessels and anastomoses between perforator complexes. The size of the vascularized area was also measured.

Perforator zoom

To enhance the resolution, microCT was repeated on smaller samples centred on individual perforators. Three full-thickness cubes of 2x2cm surface area per donor, centred on distinct arteries, were fashioned in three different flaps (n=3 cubes x 3 donors=9) (Fig. 88 – a).

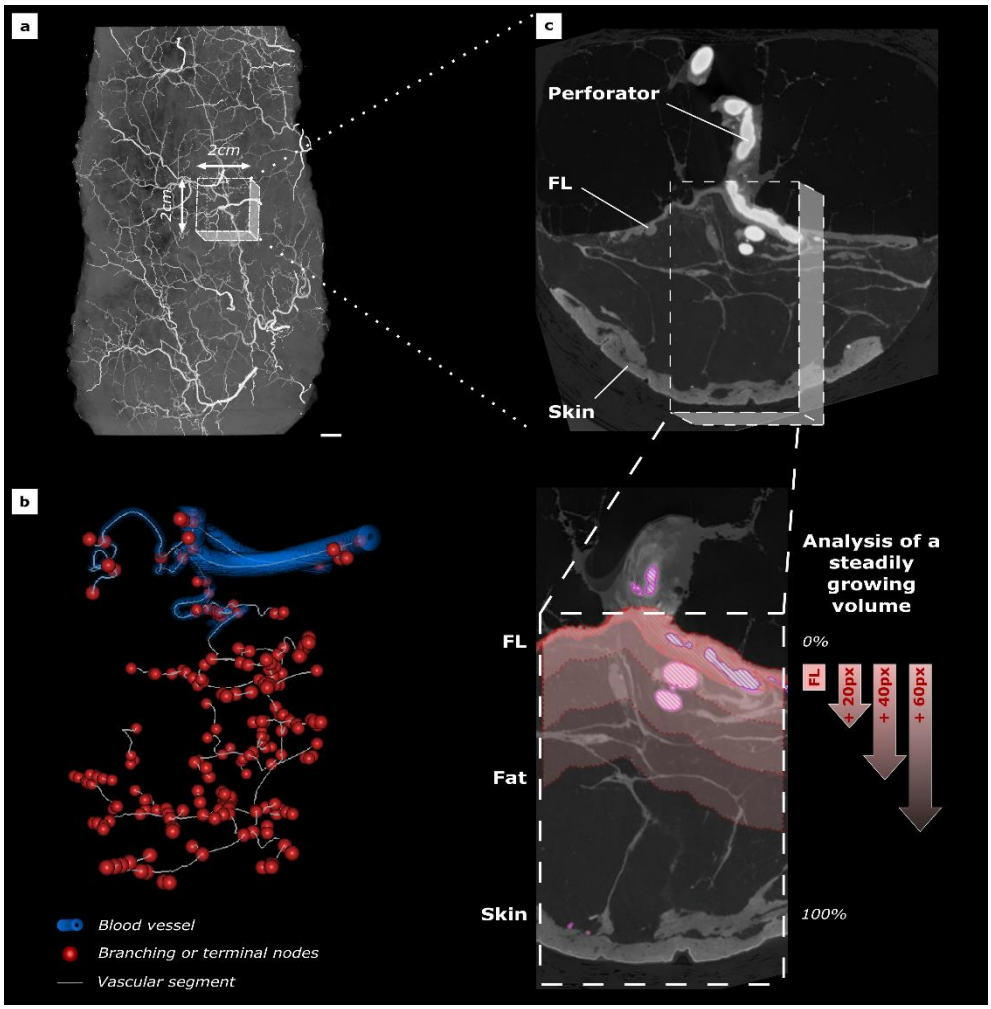

Figure 88. Steps from the ALT flap microCT to the perforator zoom analyses. (a) 3D reconstruction of the whole ALT flap after microCT acquisitions, segmentation of the vasculature and the FL, and 3D rendering. White scale bar: 1cm. (b) Illustration of the Autoskeleton module representing how blood vessels are schematized by segments and nodes. Nodes include the end of a vessel or the point of branching but only branching nodes are quantified in this study. (c) High-resolution microCT acquisition of a full-thickness cube centred on a perforator. Analysis column (dashed lines) of the vascular network organization includes the tissue between the FL (0%) and the skin (100%) that is not crushed and respects the native structure. Schematic representation of successive dilation of 20 pixels (300µm) to measure quantitative variables from the FL intrinsic volume (0%) to the skin final volume (100%). FL: fascia lata, px: pixels.

The corners of each cube were securely stitched from FL-to-skin, maintaining tissue structure integrity. Segmentation and 3D reconstruction were repeated with Avizo software, enabling quantification of vascular architecture. The Autoskeleton module schematized vascular architecture into segments and nodes (Fig. 88 – b). A vascular segment was characterized as an uninterrupted, curved section between two nodes, with each node representing either branching into smaller vessels or the end of a vessel.

Since the samples were dome-shaped, analysis columns were selected in the centre of the dome, where the skin surface is the flattest and the tissue organization is not crushed. Measurements were then taken layer by layer, with a volume dilation progressing from FL-to-skin by incremental volume of 20 pixels (300µm at this resolution) (Fig. 88 – c).

Quantification including the number of segments, the total vascular volume and length, and the number of branching nodes were normalized by analysis column surface and the maximum value of the respective sample to account for anatomical variability, allowing for objective data comparison. This normalized data represented relative evolution from FL (0%) to skin (100%) and was expressed as percentage evolution ± SD. Arteriole radius variable was also quantified and data were expressed as mean raw data ± SD, according to normalized distance.

B. 5. Perforasomes

The perforasome theory[483] described interconnected vascular territories through linking vessels, providing a dynamic vascular dimension[464].

For this analysis, flaps were dissected before vascular injection. Precise haemostasis and cauterization with an electrocautery knife along the ALT borders were crucial to prevent leakage during injection. Only the dominant perforator was isolated and retrogradely dissected until the DB. Other perforators were identified, clipped and cut. Haemostatic metallic clips allowed localization of secondary perforator entry points into the FL under X-ray. The main perforator was catheterized, rinsed and injected with pre-heated (45°C to reduce the viscosity[464,480]) Xenetix (Iobitridol 350mg/mL, Guerbet, the Netherlands) under fluoroscopy Platinum Duet dRF (tube voltage=58-76kV, Apelem-DMS Imaging, France). Flaps were secured between polystyrene plates for vertical acquisitions.

Subsequently, all flaps were scanned with a Somatom Definition AS 128 scanner (Siemens Healthineers, Erlangen, Germany), in an ultra-high-definition mode (beam collimation=0.4mm, tube voltage=140kV, tube current=256–270mAs). The three pairs of flaps were captured in a frontal view (left legs) and a tangential view (right legs) to confirm permeability of previously spotlighted linking vessels for indirect or recurrent blood flow, and how wide/height a flap could be harvested on a single dominant perforator. Measurements were conducted using specific software (Carestream Health, Vue PACS, v. 12.1.5.5151, Philips Medical Systems, the Netherlands) with maximum intensity projections (MIP) on multiplanar reconstruction. Harvested flap size and vascularized flap were measured, expressed as mean ± SD, and compared.

C. Results

C. 1. Qualitative macroscopic perforator origin

Each ALT flap exhibited an average of 9.8 ± 3.0 perforators, with a minimum of 6 per flap. Among analysed flaps, 57.1% (28/49) of perforators emerged from the LCFA, 34.7% (17/49) from the CFA, and 8.2% (4/49) were not filled (Table 27).

Table 27. Origin and zone of entry points of perforators. The LCFA network was injected with a red dye and the CFA network with a blue coloured mixture, enabling their discrimination.

	CFA		LCFA			Not filled		Total
	ITT	FL	ITT	Junction	FL	ITT	FL	
% / territory (n/total of the territory)	47.1% (8/17)	52.9% (9/17)	7.1% (2/28)	28.6% (8/28)	64.3% (18/28)	100% (4/4)	0% (0/4)	-
% / total (n/total)	16.3% (8/49)	18.4% (9/49)	4.1% (2/49)	16.3% (8/49)	36.7% (18/49)	8.2% (4/49)	0% (0/49)	100% (49/49)

CFA: common femoral artery, LCFA: lateral circumflex femoral artery, ITT: iliotibial tract, FL: fascia lata, n: number of occurrence.

Blue perforators were consistently found in the distal third of the flap, while red ones predominated in the middle and proximal thirds. About 28.6% (14/49) of

perforators penetrated the fascia in the ITT zone, 16.3% (8/49) were at the junction, and 55.1% (27/49) entered the anterolateral FL.

C. 2. Qualitative microscopic vascular architecture

Macroscopically, the perforators are evenly distributed across the FL surface (Fig. 89). The superior and middle parts of the ITT do not contain apparent vessels (Fig. 89 – b, black and white asterisks), which do not rhyme with avascular area. The 3D microCT reconstructions usually revealed deep vasculature illustrated by the arborescence of the eighth perforator, even at a low-resolution (66.6µm) (Fig. 89 – c & e, only white residual asterisk). Across the flaps, 96% of the length and 93% of the width were covered by blood vessels, with full-thickness (100%) vascularization consistently observed. Already at low-resolution, inter-perforator anastomoses underscored two main vascular plexuses: the suprafascial and the subdermal plexus, with vertical connections (Fig. 89 – d & e).

*Figure 89. Qualitative evaluation of vascular architecture. (a) To study the perforator origin, the vascular density and architecture, the perforator complex and quantitative data, the whole thigh (N=5) were primary injected with Angiofil-latex before dissection. A red dye was used to opacify the lateral circumflex femoral artery (LCFA) network and a blue dye for the common femoral artery (CFA) network including the profunda femoris artery (PFA) and the femoral artery (FA). (b) ALT flap harvesting and macroscopic assessment of the perforator origin depending on its localization (inside the ITT, or inside the FL). (c) MicroCT and 3D reconstruction of the vasculature of the whole ALT flap. Frontal view of the flap to localize all perforator origins, the limit between ITT and FL and investigate the linking vessels. (d) MicroCT and 3D reconstruction of the vasculature of the whole ALT flap in a profile view to explore connections between the FL and the skin. (e) Schema of the inter-perforator linking vessels and anastomoses according to the suprafascial of the subdermal plexus. FL: fascia lata, ITT: iliotibial tract, 1-8: number of perforators, P: proximal, L: lateral, S: superficial/skin, black and white *: empty zones, white arrows: suprafascial and subdermal plexus on the left and right respectively.*

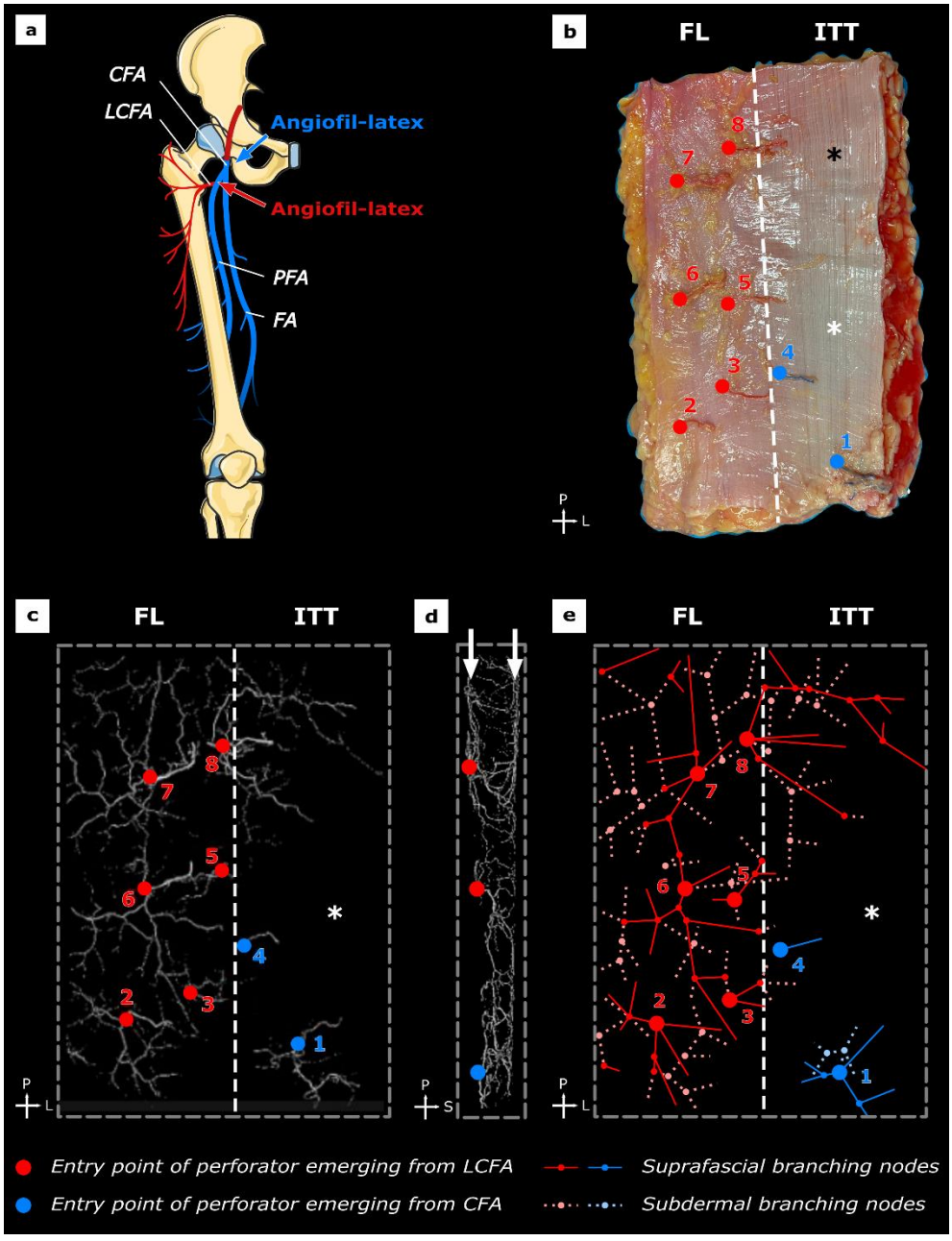
a
CFA
LCFA
Angiofil-latex
Angiofil-latex
PFA
FA
b
FL
ITT
c
FL
ITT
d
e
FL
ITT
Entry point of perforator emerging from LCFA
Entry point of perforator emerging from CFA
Suprafascial branching nodes
Subdermal branching nodes

The perforator zoom revealed not only both plexuses but a low-vascularized zone in the vertical connecting area, and also a rich vascular arborescence within the FL itself covering the majority of its surface area, as well as thin subfascial arterioles (Fig. 90, Video 3).

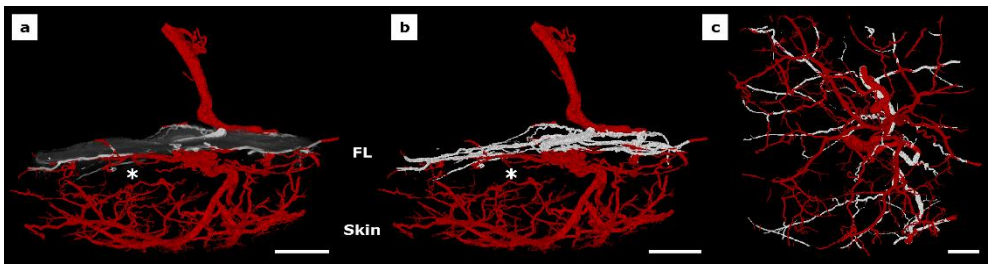

*Figure 90. Perforator zoom (15µm) illustrating the difference of intrinsic vascularization of the FL (white) and extrinsic vascularization in the ALT (red). 3D reconstruction of the perforator complex with (a) or without (b) the FL in grey. (c) Superior view of the perforator complex showing intrafascial plexus (white) covering the whole cube surface area. *: low-vascularized zone, White scale bar: 1cm.*

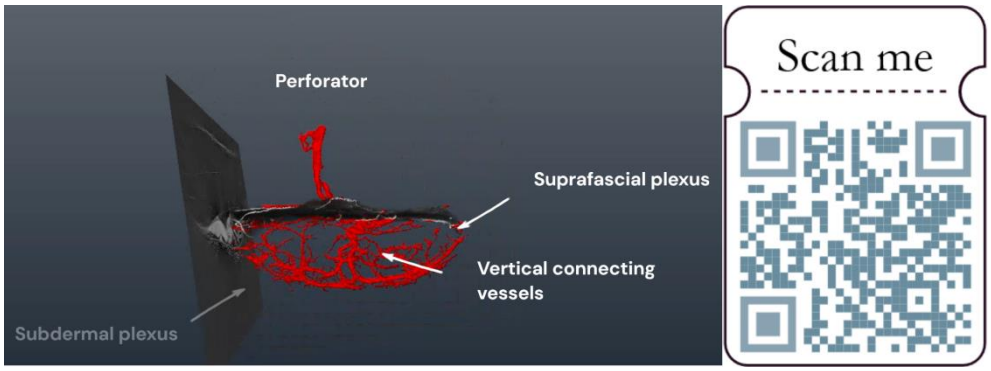

Video 3. 3D vascular organization of the full-thickness cube centred on a perforating arteriole, illustrating the four plexuses with the highlighting of the intrinsic vascularization within the fascia lata (white vessels).
https://zenodo.org/records/11087570?token=eyJhbGciOiJIUzUxMiJ9.eyJpZCI6IjUyMDY4ZjAwLTEzYzAtNGE3Yy1iNDBiLWQ3NzVkMGY1NWJiYyIsImRhdGEiOnt9LCJyYW5kb20iOiIyMzQxMTBjNjMzMTdlNjI2OWFiOTYyMGUzMDgxZTRhZiJ9.NRB-E8GW9mA6EMxTPj7ALRP3aa7W07UfJMXMvqrStH2BT9nIDD9b_lB10KiSrLRt04h7917C7ZIukOrMpDkaYg

C. 3. Quantitative vascular architecture

The perforator complex was quantitatively explored throughout its full-thickness (Fig. 91).

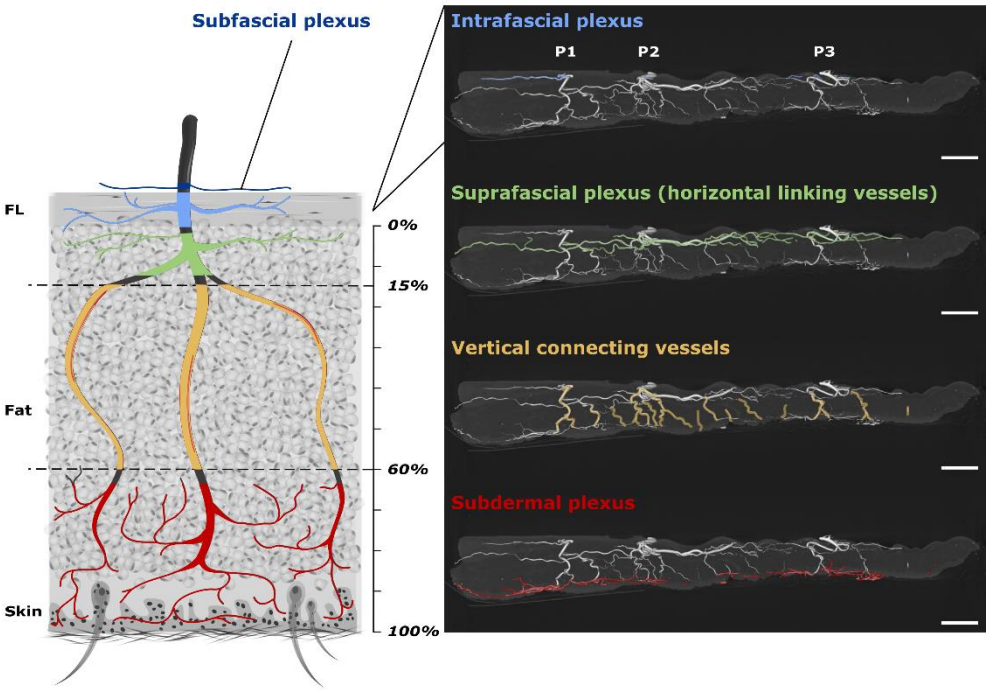

Figure 91. Schematic representation of the perforator complex and its different types of plexuses and connecting vessels. Subfascial plexus lies in the deep surface of the FL, intrafascial plexus stands within the FL, and suprafascial plexus between 0% and 15% of thickness. The connecting vessels link intra- and suprafascial plexuses to subdermal plexus between 15% and 60% of thickness. Above 60% of thickness, subdermal plexus irrigates the superficial tissue and the skin. P1-3: perforator number 1 to 3. White scale bar: 1cm.

Quantitative analysis showed the presence of an intrinsic vascularization within the FL, as indicated by non-zero y-intercepts in Figure 92, unseen at low-resolution microCT.

The cumulative vessel length expressed a proportional increment from the FL (0%) to the skin (100%) (Fig. 92 – a), tracking a linear regression trend (pink dotted line) (R^2=0.931). Vascular volume began at 0.031 ± 0.032mm³/mm² within the FL, representing 34.7 ± 23.8% of the total vascular volume, with a rapid ascent up to 15% above the FL in the suprafascial fat (Fig. 92 – b, green arrow and dashed bar). This region accounted for 67.5 ± 23.2% of the total vascular volume before stabilizing towards the skin, reaching a cumulated ALT vascular volume of 0.126 ± 0.096mm³/mm².

The green threshold at 15% exactly corresponded to the rise of average vessel radius (Fig. 92 – d). The mean radius evolution followed a reverse U-shape, *i.e.* a rapid expansion of the mean radius from the thinnest vessels within the FL (55.4 ± 28.5µm) up to 15% thickness (111.2 ± 39.3µm). The curve achieved a plateau in the suprafascial fat, before undergoing a progressive decrease in opposition with the volume slope (blue arrows). The mean radius of subdermal vessels (73.8 ± 24.1µm) nearly matched that found within the FL.

If the residual gain in vascular volume in the last part of the curve was not explained by vessel enlargement, the quantity of tiny vessels knew a progressive growth from 60% of tissue thickness (Fig. 92 – c and e, orange arrows). The evolution of branching nodes and vascular segments strictly mirrored each other, indicating that 50.4 ± 30.6% of branching vessels were already present within the FL (orange arrows on the Y axis). This arborescence percentage remained stable until 60% of the thickness between the FL-to-skin. The remaining 50% of the vessel division increase took place in the residual 40% of subcutaneous fatty tissue.

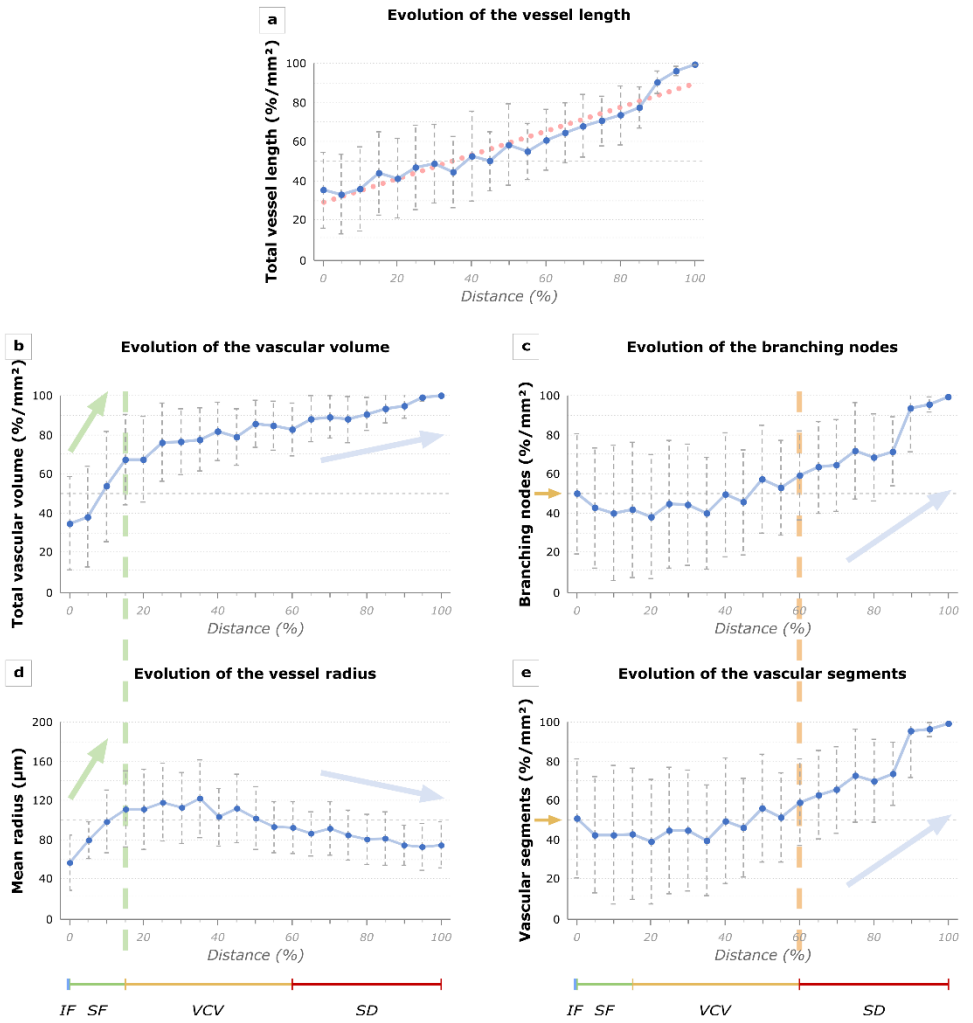

Figure 92. Graphs of the evolution of quantitative variables describing the vascular architecture including the total vessel length (a), the total vascular volume (b), the number of branching nodes (c), the vessel radius (d), and the number of vascular segments (e). IF: intrafascial plexus, SF: suprafascial plexus, VCV: vertical connecting vessels, SD: subdermal plexus. Error bars: SD.

C. 4. Perforasome & flap size

The dominant perforator opacified the entire flap (Fig. 93 – a). The linking vessels authorized recurrent blood flow to connect all metallic clips. Only two flaps showed limited distal connection as previously noted for blue perforators, in remote locations without nearby perforators. The perforator complex

organization was confirmed (Fig. 93 – b). The maximal dimensions of a full-thickness ALT flap harvested on a single main perforator was 20.3cm (± 4.0) height x 13.4cm (± 1.7) wide x 2.0cm (± 0.4) thick.

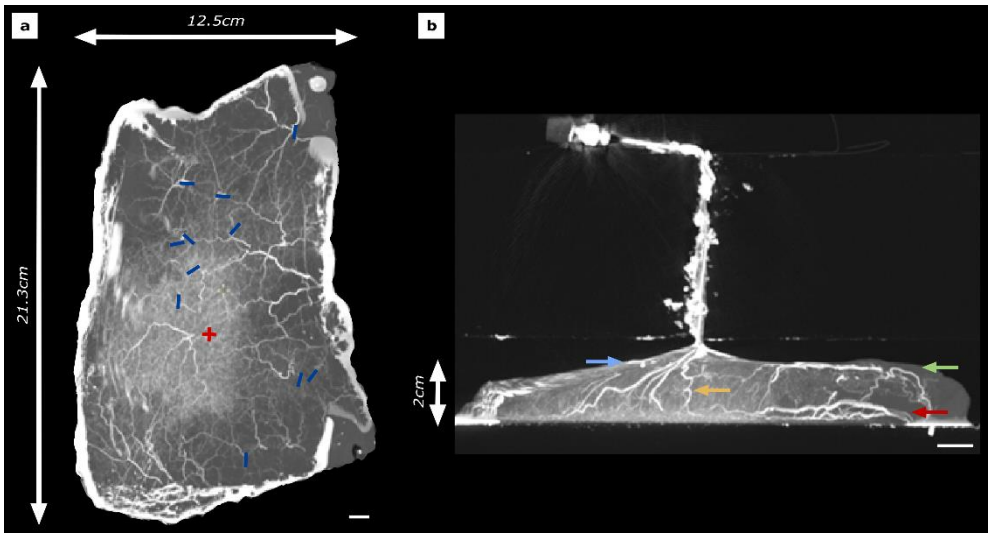

Figure 93. Angioscanner with radiopaque contrast agent opacification of ALT flap to study the perforasome of the dominant perforating arteriole. (a) The injection point on the main perforator is marked by the red cross and all the secondary perforators are recognized by blue metallic clips. (b) A tangential view of the maximum intensity projections (MIP) reconstruction represents the same structure of the perforator complex including intrafascial plexus (blue arrow), suprafascial plexus (green arrow), vertical connecting vessels (yellow arrow), and subdermal plexus (red arrow). White scale bar: 1cm.

C. 5. Reversed mega-thin ALT flap

Considering that 67.5 ± 23.2% of the total vascular volume stands in the FL and 15% of above fat, the possibility of a mega-thin ALT flap harvesting based on deep vasculature was explored. The relative landmarks of 15% and 60% thickness above the FL corresponded to 1.15 ± 0.44mm, and 4.73 ± 1.76mm respectively. However, these values are challenging to reproduce manually in the operating room. To get practical guidance, the FS location was investigated (Fig. 94 – a). Although the FS was often elusive on microCT, two intermediary thinner fasciae were usually found between the FL-to-skin interval, always situated between these two landmarks. A reversed mega-thin ALT flap could be harvested including the most vascularization in-between the FL and the FS (Fig. 94 – b).

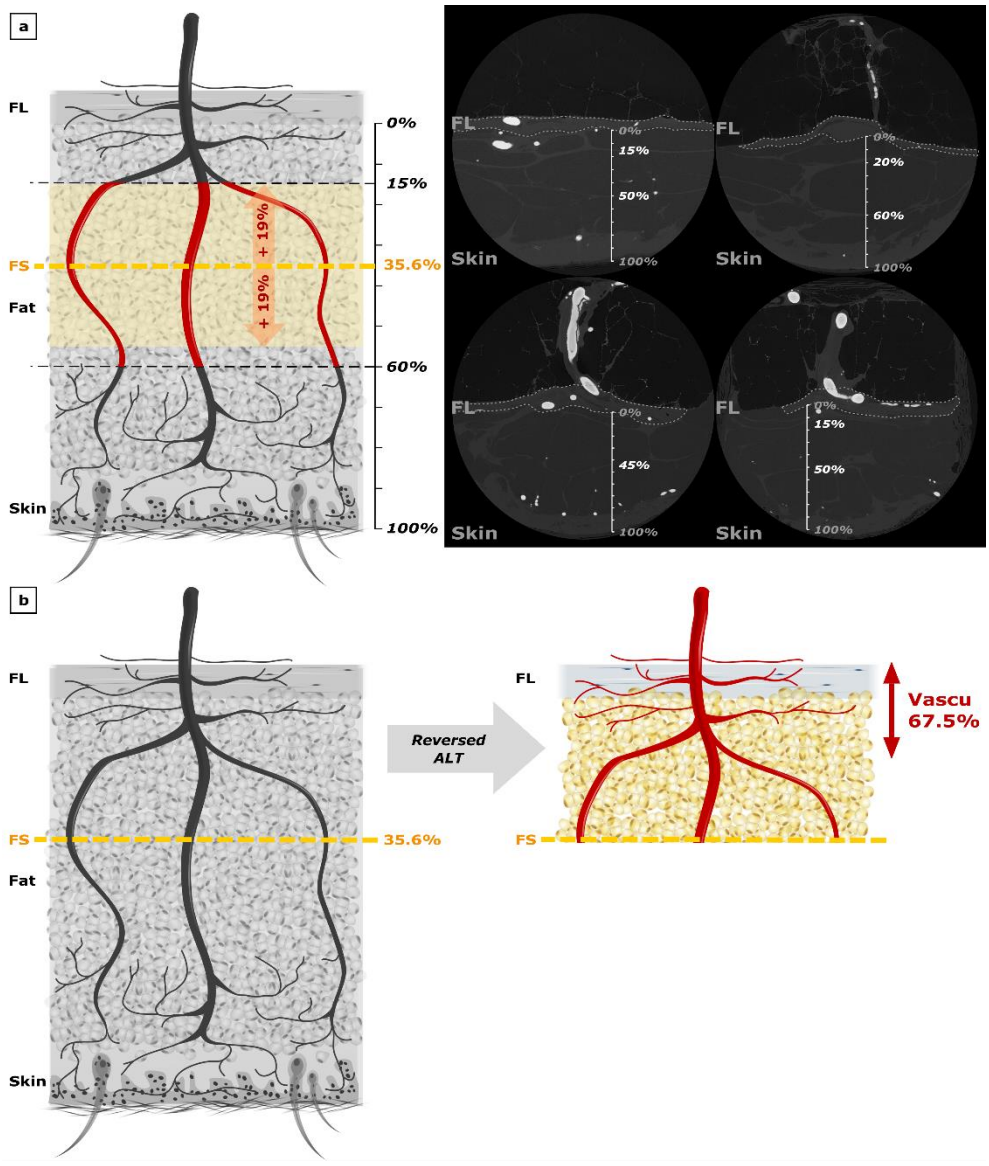

Figure 94. Investigation of the fascia superficialis (FS) localization. (a) The relative FS position compared to previously highlighted landmarks in the full-thickness of an ALT flap, above the fascia lata (FL, grey dotted line). (b) Illustration of the reversed mega-thin ALT flap concept between the FL and the FS, including the most vascularization in-between. ALT: anterolateral thigh.

D. Discussion

This study provides a comprehensive 3D quantitative assessment of vascularization in the ALT flap, emphasizing the LCFA perforators that form four plexuses supplying the FL itself, the sub- and suprafascial zones, and subdermal tissues. This vascular architecture supports the reversed mega-thin ALT flap for specific indications.

Perforator origin

The distinction between LCFA and CFA network perforators was feasible, although the latter encompasses both the PFA and the FA. Recurrent perforators could originate from both territories[472,484] and further studies might separate the injection with three different dyes.

Perforators primarily arise from the LCFA, with most located in the anterolateral FL, especially in the proximal two-thirds. Given the ITT mechanical role in walking, harvesting fascial flaps from these areas[444–446] highly vascularized (71.4% of perforators) is advisable.

Vascular architecture

Intermittent zones with non-opacified vessels were observed, likely due to insufficient injection pressure. Confirming avascular areas is challenging without proper vessel opacification. The differing volumes required for LCFA and CFA injections influence vessel opacification patterns (*e.g.* the fourth perforator in Figure 89 displayed limited arborization, common for blue perforators), requiring higher manual pressure for voluminous vascular reservoirs. The angiosome theory[480] shows how vascular anastomoses fill neighbouring perforator territories within a single angiotome first.

Clinical angiography[464] or low-resolution microCT limited tiny FL vessels visualization. Previous literature outlined two vascular plexuses (suprafascial and subdermal)[250,445,451,452,464]. The suprafascial plexus, previously mistaken for ITT vascularization[456,472], includes morphologically distinct linking vessels between adjacent angiotomes[480]. Peritendon sheets are recognized to be vascularized to improve tenocyte survival and gliding characteristics, which is also an advantage

of this sub- and suprafascial plexus[240,460,479,485]. Recent higher-resolution scans (15µm) discovered an intrafascial plexus, suggesting richer FL vascularization than thought and none of the subvolumes exhibited an avascular zone. Future investigations should focus on subvolumes distant from perforators.

Quantitatively, 67.5% of total vascular volume resided within the FL and 15% of suprafascial fat. With a positive ascending slope similar to the volume, the mean radius doubled from the FL up to 15% thickness indicating the transition into larger connecting vessels. Between 15% and 60% thickness, all the curves reached a transitory steady state. Beyond 60%, the vascular volume increase reflects subcutaneous arborization forming the third subdermal plexus.

Perforasomes

The maximum full-thickness flap size was 20.3 (± 4.0) x 13.4 (± 1.7)cm, surpassing previous reports[250,445,446,453,457,472,479]. Microscopic analysis guarantees vascularization across a larger surface area, invisible to the naked eye. Small secondary perforators, ensuring inter-perforating anastomoses, guide flap size. Maintaining at least one plexus is crucial for flap survival and donor-site health. However, the thinning for very-thin flap might reduce the vascular territory by suprafascial vessel ligation[480]. Detailed study focusing on individualized plexus could reveal linking vessels within the FL and assess risks of skin necrosis post-large FL-only flap harvesting.

Reversed mega-thin flap

Few researchers have investigated the intrinsic vascular microarchitecture for creating a FL-only vascularized flap. Previous 2D histological analysis focused on transversal and ascending branches of LCFA[472] but not on the DB, the major perforator supplier[445,446,454]. Methylene blue injections into the DB, while macroscopically informative, had limitations in discriminating intrafascial and suprafascial plexuses due to adjacent adipose tissue[250], why authors advocated for refined techniques to validate the vascular microarchitecture[250].

Even the discrimination with other connective tissue was not an easy task in the elderly, the FS was predominantly localized in the connecting zone. A pedicled or free reversed mega-thin flap lifted from FL to FS, could maintain the

vascularization of two fascial plexuses with the thinnest thickness, and reproducible anatomical landmarks.

This concept promises reduced donor-site morbidity[237,250,486,487], single straight-line incisions without STSG for even large donor-site closure, and elimination of secondary surgeries for aesthetic revision or debulking fasciocutaneous or muscle flaps[237,250,476,479]. The immediate thinning and its potential vascular complication will no longer be necessary[479]. The fascial surface can re-epithelialization or mucosalize[476,477,488], and revascularize secondarily[489], offering a range of applications in reconstructive surgery, including tympanoplasty or nasal defects[473,487], mucosal repairs[476,477,488], head and neck oncologic reconstruction[452,455,474,476,477], distal extremity repair[479,482,490], and replacement of physiological membranes (dura mater, pleura, scrotum or peritoneum[250,445,472,478]).

Limitations & perspectives

This study included old cadaveric flaps, probably underestimating *in vivo* vascular territories in younger individuals. Emerging preoperative techniques like photoacoustic tomography could provide *in vivo* vascular insights, even if the resolution does not reach the microscopic level[491,492].

The venous system is not as extensively studied as the arterial network. Despite intra- and interpersonal variability, the study reproducible methodology based on systematic parameter reproduction and computer-assisted calculations, could be expanded by investigating venous circulation to understand venous return and avoid blood congestion and consequent ischemia[455,464], crucial for flap survival, whereas the valvules resistance is permeable at the fascia level[464,480].

This microscopic vascular examination of an autologous vascularized flap could benefit tissue engineering aiding bioengineered constructs integration[456]. Non-vascularized FL is commonly processed before being stored in tissue banks[291,341] for mega-thin reconstruction. A specific decellularization method has been devised to produce an acellular, biocompatible and non-immunogenic scaffold[291,351,406] but lacks blood supply, crucial for current tissue engineering techniques[456]. This vascular study could pave the way for reendothelialization or 3D bioprinting of new vascular networks.

E. Conclusion

The reversed mega-thin ALT flap is a promising approach in reconstructive surgery, benefiting from comprehensive 3D vascular anatomical investigations. By combining qualitative macroscopic, microscopic, and quantitative assessments, the intricate vascular network was detailed, highlighting the rich FL vascularization and its potential for standalone grafting. Our findings support this flap potential to offer thinner tissue options while maintaining adequate vascularity. Further research into its clinical applications and surgical optimization will enhance its impact in reconstructive surgery.

– TAKEAWAYS –

Paper 10 – Revisiting the variants of the Anterolateral Thigh Flap based on 3D Microscopic Vascular Investigations

- *4 vascular plexuses* = *Subdermal plexus*

  Suprafascial plexus → *Connecting vessels*

  Intrafascial plexus → *Connecting vessels*

  Subfascial plexus

- *Full-thickness flap size* = ± *20 x 13.5cm*

  Guided by the presence of additional macroscopic perforating vessels

- *Blood reservoir* = *67.5% of total vascular volume between the FL and the 15% suprafascial fatty tissue.*

⇨ *Reversed mega-thin flap between FL and FS*

Back to the Diamond

- **How can we reveal or identify the presence of an intrinsic vasculature in the HFL?**

The new Angiofil-latex intravascular injection can opacify vasculature with diameters down to microns, excluding capillaries. While clinical CT scans cannot reveal capillaries or potential intrinsic FL vessels, microCT can because of its enhanced resolution. This advanced technology unveils the presence of small arteries within the FL itself, vascularizing the membrane. Given the diameter of these small arterioles and the thickness of the fascia, all seeded cells would receive sufficient nutrients to survive.

- **Based on the 3D vascular organization, which type of flap can be harvested to obtain a very thin, vascularized collagen membrane for use as a wrapping OM?**

While anatomical landmarks were verified, perforator locations suggest harvesting the fascia more anteriorly than the ITT. This region contains more perforators and is less critical for functional mechanical stability during walking.

After discovering an intrafascial vascular plexus, the study of the microscopic vascular organization exposes four vascular plexuses. The major blood reservoir lies between the FL and juxtaposed suprafascial fat, connecting to adjacent angiosomes. A large reversed mega-thin flap, pedicled or free, can be harvested between the FL and FS, in the transitional connecting zone. This approach provides anatomical landmarks for the surgeon, promising reduced donor-site morbidity, and single straight-line incisions without the need for STSG for donor-site closure, while eliminating secondary surgeries for flap debulking.

Harvesting a standalone FL flap with its own vascular tree aims to use it directly, leveraging this network for autologous applications or reendothelialization with tissue engineering techniques to create functional vascularization within the OM before implantation.

– REQUIREMENT SPECIFICATIONS –

Requirement	Specification	Validation
Osteoconductive matrix		
Composition	- Col-1 membrane	V
Morphology	- 2 layers	V
	- Thickness (1 thin + 1 thick layers)	V
	- Large size - Shapeable	V
Biocompatibility	- No immunogenicity	V
	- Carrier for cells	V
	- No cytotoxicity	V
Osteoinductive mediators		
Bioactivity	- Osteogenic GF	V
	- Osteogenic differentiation	V
	- Chondrogenic differentiation	V
Osteogenic cells		
Osteogenicity	- Cell adhesion, proliferation, replication	V
	- Osseous ECM production	V
Mechanical stability		
Membrane properties	- Sheet malleable support	V
	- Resistance to handling	V
	- Isotropy or anisotropy?	≈
	AND	
In vivo model	- Stitchable	V
	- Mechanical stability	V
Vascularization		
Vascular supply	- Angiogenic properties	≈
	- Neoangiogenesis	V
	OR	
	- Intrinsic vascular architecture	V
	- Functional vascular network	≈
In vivo transposition		
Clinical needs	- Off-the-shelf availability	V
	- One-stage surgery	V

General discussion & conclusion

Main achievements

« The range of approaches testifies to the complexity of the biological phenomenon, in contrast to the simplicity of the technique. »

Alain-Charles Masquelet, 2020[108]

In the context of CSBD, the quest for the best surgical technique or construct remains open. The body is a wonderful machine capable of regenerating bone segments with only a few inputs[14], but the CSBD pathology overpasses these capacities. An MBA has limited remodelling and minimal vitality even after long-term implantation. This lack of viability contributes to a heightened risk of complications, including non-union and fractures, over time[157].

Tissue engineering principles, the Diamond concept, and Masquelet's theory are clearly articulated as the foundation of the proposed research. By delving into the myriad of bone regeneration concepts, this thesis advances the concept of guided-bone regeneration through the implementation of a wrapping OM around the MBA. Each of the five facets of the Diamond is thoroughly explored.

Osteoconductive matrix = Knowing the ECM role in cell proliferation, differentiation, migration and polarity, decellularized HFL is shown to be an adequate, biocompatible and non immunogenic collagenic membrane, shapeable on demand with similarities to periosteum. The two-layer composition is optimal, featuring a thick deep layer for structural support and a thin superficial for seeding osteogenic cells.

Osteogenic cells = PMSCs are orthotopic osteogenic cells of interest, capable of adhesion, growth, and replication on decellularized HFL. They are primed to produce new bone matrix. In addition, their chondrogenic differentiation potential

also helps in endochondral ossification processes, known to play a role in bone healing, especially in the cases of CSBDs.

Osteoinductive mediators = Decellularized HFL exhibits a signalling role by preserving osteogenic and angiogenic ECM-linked GF, providing a good niche for PMSCs. However, this single matrix is not able to induce osteodifferentiation. The MBA contact is the principal bioactive osteoinductor leading to PMSC self-differentiation toward the osteogenic lineage.

Mechanical stability = The OM demonstrates resistance and ease of handling, being stitchable in the *in vivo* experiment. However, two factors contribute to the mechanical stability of the whole construct, *i.e.* the structural MBA and the osteosynthesis. While MBA possesses intrinsic mechanical characteristics, IMN osteosynthesis is developed to achieve centromedullary stabilization.

Vascularization = Numerous neovessels are observed inside the OM after *in vivo* implantation. However, the delayed onset of neovascularization might slow the healing process. Since an intrinsic vascularization is unveiled within the HFL, with an adequate survival distance for seeded cells, the question of its use is posed.

Limitations

« When you dare, you are often wrong. When you don't, you're always wrong. »

Translated from Romain Rolland, 1915

In addition to every single limitation outlined in each specific paper, some broader limits inherent to the global concept deserve to be acknowledged.

Definitions are a crucial starting point for consideration. The third paper, which delves into the definition of decellularization, highlights the necessary paradigm shift required to include the HLA criterion. However, this is not the only definition in need of revision. Given the recent advancements in fundamental knowledge and cell characterization techniques (*e.g.* lineage tracing and transcriptomic analyses[32]), the minimal criteria given by the Mesenchymal and Tissue Stem Cell Committee of the International Society for Cellular Therapy[200] might be reviewed. The predefined surface markers, once thought to be specific, may not be as precise, particularly in determining tissue origin[32,67]. Various other surface markers and gene expressions have been explored at least for PMSCs (*e.g.* surface markers CD200+, CD146+, CD166+, CD271+, PDPN+ and gene *Prx1*, *α-SMA*, *periostin*)[32,62,67,214,215,493–495]. Yet, no clear consensus has emerged so far.

The OM was extensively compared to both native and decellularized periosteum in this thesis. However, an additional comparison with an *induced membrane* would provide valuable insights. While the induced membrane acts as an OM, it exhibits differences compared to the periosteum. Therefore, juxtaposing these two comparisons could complement each other and offer a more comprehensive understanding (Table 28).

Table 28. Feature comparison between the engineered osteogenic membrane, the periosteum and the induced membrane.

	Periosteum	Osteogenic membrane	Induced membrane
Features			
Thickness (mm)	< 1mm	~ 1mm	> 1mm
Layers (number)	2 - *1 thick longitudinal* - *1 thin transversal*	2 - *1 thick longitudinal* - *1 thin transversal*	2 - *1 thick longitudinal* - *1 thin transversal*
Isotropy	Anisotropic	Anisotropic	Isotropic
MSC content	++	Seed-dependent	+++
Osteogenic GFs (BMP content)	N-HP = induced membrane > D-HFL > D-HP		
Angiogenic GFs (content)	N-HP = induced membrane > D-HFL = D-HP		
Surgery	Native	One-step	Two-step
Immunology	No reaction	Xeno-/Allo-/Autogenic reaction depending on the cell source	Foreign body reaction
Immediate vascularization	+	-	+ *(at the 2nd step)*

MSC: mesenchymal stem cell, GFs: growth factors, BMP: bone morphogenetic protein, N-HP: native human periosteum, D-HP: decellularized periosteum, D-HFL: decellularized fascia lata. Inspired from multiple studies[99,106,111,275].

All three membranes act as natural barriers against soft tissue interposition and ectopic ossification while concentrating pro-regenerative signals within the inner biological chamber. The periosteum functions in normal development,

maintenance, remodelling, and fracture healing, whereas the induced membrane forms as a response to an artificially induced foreign body reaction. The induced membrane has a higher cellular density than N-HP, including lymphocytes and pericytes, which aid in vessel maturation and share traits with MSCs, though with the same number of endothelial cells[111]. The OM offers a good compromise in terms of thickness, mechanical properties, and adaptable cell type and quantity for seeding. While anabolic signals, GFs, and cytokine secretion are predominant in N-HP and the induced membrane, bone healing is closely linked to the inflammatory and immune responses, which require further exploration for the *in vivo* implantation of the OM.

Immunity is therefore the third aspect to consider. Although the decellularization process with HLA removal effectively eliminated xenogenic reactions from the human FL in the final *in vivo* model, the potential for an allogenic response remains and warrants further exploration. Notably, the presence of two distinct sources of allogenicity, *i.e.* allogenic porcine PMSCs and MBA, introduces a potential bias in the *in vivo* model.

On another hand, controlled allogenicity might induce an *inflammatory reaction*. Bone regeneration involves complex interactions between cells from the acute inflammatory stage of fracture healing and bone-forming cells[150,496,497], which are not fully understood. The monocyte-macrophage-osteoclast lineage directly responds to the aggressive stimulus of the fracture, initiating repair through macrophage polarization into the pro-healing M2 phenotype. This process releases cytokines and chemokines, promoting angiogenesis and attracting MSCs and osteoblasts[150,498]. Conversely, osteoblasts can release inflammatory cytokines within 3–7 days of injury[499], which may contribute to self-sustaining bone healing, though less efficient than when mediated by inflammatory cells. Additionally, mesenchymal-derived cells help modulate inflammation and restore normal tissue[150]. The significance of this reciprocal communication is underscored by recommendations to incorporate inflammatory cells as an additional criterion in the Diamond concept, and to explore therapies that modulate inflammation[150].

The fifth paper, focusing on the *in vitro* development of the OM, noted the superior differentiation potential of *decellularized MBA* compared to native MBA. However, throughout the rest of the thesis, the native MBA was consistently used, as the

decellularization of MBA is the primary subject of a concomitant PhD thesis, in which resulting outcomes reaffirmed the interest in using decellularized MBA as an immunocompatible graft for transplantation[353,417,500]. As both lines of research gather further evidence, they may converge to integrate all facets of the Diamond.

The aetiology of bone loss can significantly impact outcomes due to variations in the *initial biological environment*, encompassing both the localized bony environment and the surrounding soft tissue. For instance, the histological characteristics of the induced membrane and subsequent bone formation vary based on their creation site: subcutaneous (thicker), intramuscular (thinner), and osseous (higher bone formation)[501]. Even though the membrane forms more quickly in soft tissue, it appears more active in osseous sites[501], suggesting the need to consider both osseous and soft tissue advantages. Our *in vivo* model may not precisely replicate the clinical scenario of CSBDs, typically characterized by damaged periosteum, extensive fibrous scar tissue, and compromised vascularization, which represents a suboptimal soft tissue environment. To better mimic this challenging environment, one potential approach could involve first creating the CSBD and allowing for a six-month period to simulate non-union before implementing treatments.

The highest barrier now lies in ensuring an immediate and effective *blood supply*. In bone reconstruction, a lot of effort is made to preserve or trigger blood vessel development. Vascularized bone grafts generally have few complications and high success rates. Even avascular grafts can succeed, albeit with lower reliability. Understanding the reasons behind graft failure is essential but remains incompletely figured out. Osteodistraction and Masquelet's technique underscore the critical role of proper blood vessel growth and the repair of nearby soft tissues in successful bone healing. This suggests that while generating bone itself is important, ensuring sufficient blood supply is a primary concern[14].

Future directions & perspectives

« When will I stop? When I cannot go further. »

Sophie Verrier, 2023

Understanding that revascularization represents the bottleneck for all advanced tissue engineering approaches, an exhaustive and meticulous examination of the vascular network at a microscopic scale is unquestionably vital. This initial evaluation serves as a prerequisite before considering potential recellularization via perfusion of a decellularized flap scaffold with endothelial cells. This possibility will be further explored in the ongoing research continuum of this thesis. It will delve into endovascular coating techniques, reendothelialization, and other tissue engineering methods that hold promise for approaching a new competent vascular network.

Until tissue engineering revascularization techniques improve and coming back to the initial reflection in the first paper discussion, the findings of this thesis open doors toward the use of a single mega-thin FL flap as an autologous vascularized graft to serve as an OM. Through meticulous surgical techniques, the vascularized FL might be harvested with its intrinsic vascular plexus and its suprafascial plexus to maximize the vascularization, the thinness, as well as the potential presence of autologous osteogenic AMSC (Fig. 95). This flap could be wrapped around a new bone supply (MBA, cancellous or morselized bone graft, or other) to prevent soft tissue invagination, contain and guide bone regeneration, and prevent ectopic ossifications[107,249,291,456].

If the macroporosity of an MBA is insufficient to support vascular and cellular invasion, a vascularized free-fibula could also serve as the central architectural element within the void, surrounded by autologous cancellous bone graft[108], although mechanical stability might not be sufficient.

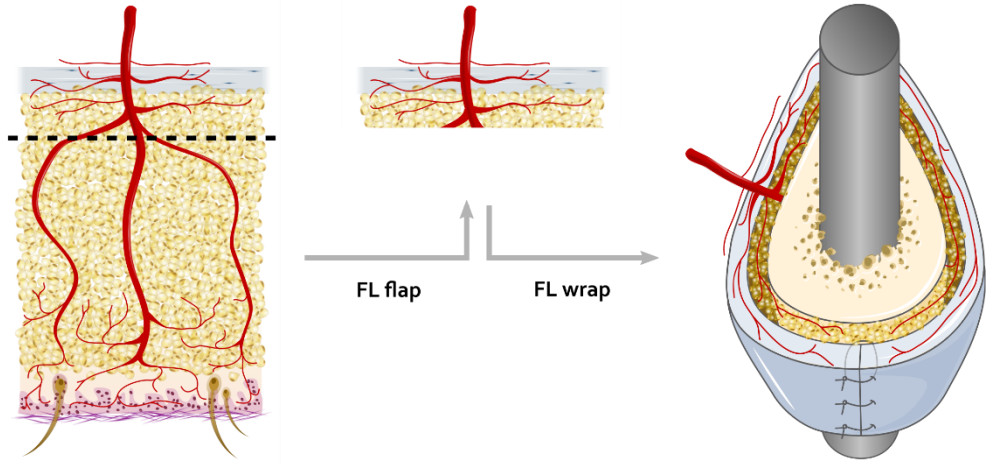

Figure 95. Schematic representation of perspectives on modifying the current ALT flap towards a mega-thin FL flap including its intrinsic and suprafascial vascular plexuses. The association of suprafascial tissue could be beneficial not only for the vascular supply but also for the potential presence of adipose mesenchymal stem cells that could play an osteogenic role. This FL flap could be wrapped around various osseous components to guide bone regeneration.

In this context, this OM could create a biological chamber, allowing the surgeon to fill it with various components tailored to the patient's specific needs. The osteogenicity could rely on the vascular delivery of autologous stem cells or the possibility of locally adding MSCs, GFs, etc. Altogether, these properties could promote osseointegration and accelerate the healing process, exactly like an induced membrane[96,99,108]. Moreover, the FL possesses several advantageous characteristics that make it an ideal candidate for this purpose. Firstly, its rich vascular intrinsic network might ensure blood supply and provide essential nutrients to support graft integration and bone regeneration. Additionally, the FL exhibits remarkable tensile strength and elasticity[290], facilitating its manipulation and conforming to irregular bone surfaces. This innovative approach holds great promise in enhancing outcomes of bone reconstruction surgeries, particularly in cases involving CSBDs or revision procedures. No matter the indication, an only FL vascularized flap can be shapeable on demand towards personalized medicine[291] and could be adapted to every single necessity.

To broaden thinking and horizons, the dream of all surgeons would be to have an off-the-shelf cell-based product devoid of the usual limitations associated with tissue transplants, such as limited availability, donor-site morbidity, necessity for additional surgeries, and risk of disease transmission. This product would be readily deployable for bone regeneration in all patients in one-stage surgery[34]. Concerning tissue engineering approaches and development, numerous questions remain open for future investigations toward clinical efficacy[6,90,91] :

- Should the membrane be semi-permeable or impermeable? Should there be a selective communication? If yes, what level of porosity is required for molecule diffusion?
- Should the membrane and/or the filling bone scaffold be bioresorbable?
- Are biomechanical properties essential for the membrane?
- What tissular microstructure would be ideal?
- Should mono- or polytherapy be employed? Does the membrane require impregnation of GFs or other signalling molecules? If yes, what would be the optimal dosage?
- Is it preferable to implant autologous or allogenic tissues and cells?
- Does the immune system act as a barrier or a helper in the context of bone healing?

Twenty-five years after the first implantation of a cell-seeded biomaterial to repair CSBD in a human patient[502], all these questions about the optimal biomaterial continue to stir debate. *In vivo*, the interplay between cells, structure, and functions is of considerable interest. The cell fate is influenced by various biomaterial-related features, encompassing surface texture (*e.g.* micro- and nano-roughness[6,503,504]), particle size[503,505], dissolution kinetics, and the release of ionic species, each capable of triggering specific biochemical and genetic reactions in cells[7,175]. An ideal bone graft material should possess an interconnecting porosity of at least a size ranging from 15µm to 300µm, facilitating the diffusion of cells, nutrients, and waste products[86,506–508]. Additionally, it should boast a surface conducive to vascular ingrowth, attachment, migration, and proliferation of cells. While hard tissue mechanical strength is essential to withstand loads from surrounding tissues, soft tissue mechanical properties undergo changes as the scaffold is loaded[175], following Danis' law, a corollary of Wolff's law for hard bone tissue.

Delving deeper into the understanding of interactions between cells and various biomaterials to achieve optimal symbiosis will lead to accurate foundations for using 3D bioprinting, merging biological and engineering methods[7,509]. This innovative technique enables the printing of various cell types in a 3D structure, forming a graft with pre-existing ECM and vessels. The interconnected pores[510], surface properties, mechanical properties, and infusion of additives (*e.g.* hormones and GFs[84]) might be controlled. When implanted, this construct is expected to create a graft free from hypoxia or nutrient deficiency issues[441] with all the requisite microstructural and morphological features for the intended function.

De-/recellularization and 3D bioprinting are tissue engineering techniques, but other methods (*e.g.* electrospinning[60]) also explore the same objective. Whether focusing on resorbable spacers, filling scaffolds or biosynthetic membranes, all pave the way to replace an induced membrane in a one-stage surgery.

Ideally, the perfect treatment would integrate all components associated with the lacking function[6]. For instance, in cases requiring endochondral ossification due to a comminuted fracture and periosteal damage, PMSCs would be a suitable choice. In a hypoxic soft callus, collagen or GAGs may be more abundant than in a more mature callus, where calcium would be more appropriate. The third element would involve selecting the right stimulating bioactive molecule for the intended action, such as BMP-2, which has been shown to be crucial for periosteum-driven endochondral ossification[6].

The ideal scaffold ought to possess biocompatibility, bioactivity, suitable porosity and interconnectivity, along with controlled function and biodegradability, while also being cost-effective[91,150]. Currently, 4 to 7 billions of dollars are spent worldwide in the market of fracture repair, bone regeneration, and joint fusion including surgical implants, instrumentation, and orthobiologics[6,167]. Transitioning tissue-engineered products from the bench to the clinical bedside can be as challenging as developing the perfect product. Several steps are impossible to bypass, such as the establishment and understanding of specific regulatory paths, medical device classification depending on the EU (European Medicine Agency (EMA) for drugs and Advanced Therapeutic Medicinal Products (ATMP) for stem cells) or USA (FDA, medical device with drugs – class III) locations, the targeting of specific clinical application, the selection of the most adequate animal model for

pre-clinical studies, the consideration of cost-effectiveness and potential reimbursement by medical care systems depending on the country, and the potential industrialization of the product (manufacturing, sterilization, storage, reproducibility, quality control)[6,169].

Regardless of the technique, biomaterial, or cell type used, the journey toward designing the perfect implant is littered with ideas and prospects awaiting exploration. The ultimate goal is to approach a form of medicine that is adaptable and customizable to each individual patient and unique pathological situation.

Appendices

Paper 4 – Collagen molecular organization preservation in human fascia lata and periosteum after tissue engineering

Julia Vettese, Julie Manon*, Antoine Chretien, Robin Evrard, Lies Fievé, Thomas Schubert, Benoît Lengelé, Catherine Behets†, Olivier Cornu†*

** Share first authorship*
† Share last authorship

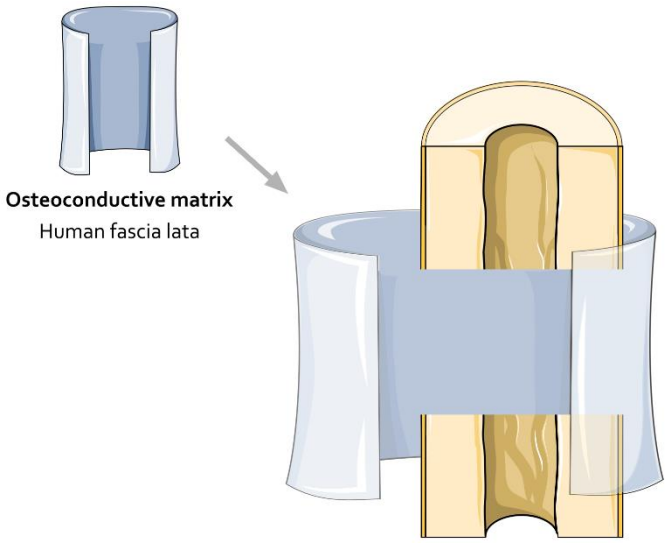

Published in

Front. Bioeng. Biotechnol. 12:1275709. (IF=6.064)

doi: 10.3389/fbioe.2024.1275709

Abstract

Large bone defect regeneration remains a major challenge for orthopaedic surgeons. Tissue engineering approaches are therefore emerging in order to overcome this limitation. However, these processes can alter some of essential native tissue properties such as intermolecular cross-links of collagen triple helices, which are known for their essential role in tissue structure and function.

We assessed the persistence of ECM properties in HFL and HP after tissue engineering processes such as decellularization and sterilization. Harvested from cadaveric donors (N=3), samples from each HFL and HP were decellularized following five different chemical protocols with and without detergents (D1-D4 and D5, respectively). D1 to D4 consisted of different combinations of Triton, SDS and DNAse, while D5 is routinely used in the institutional tissue bank. Decellularized HFL tissues were further gamma-irradiated (minimum 25kGy) in order to study the impact of sterilization on the ECM. PLM was used to estimate the thickness and density of collagen fibres. Tissue hydration and content of hydroxyproline, enzymatic cross-links, and non-enzymatic cross-links (pentosidine) were semi-quantified with Raman spectroscopy. ELISA was also used to analyse the maintenance of the DCN, an important small leucine-rich proteoglycan (SLRP) for fibrillogenesis.

Among the decellularization protocols, detergent-free treatments tended to further disorganize HFL samples, as more thin fibres (+53.7%) and less thick ones (−32.6%) were recorded, as well as less collagen enzymatic cross-links (−25.2%, p=0.19) and a significant decrease of DCN (p=0.036). GAG content was significantly reduced in both tissue types after all decellularization protocols. On the other hand, HP samples were more sensitive to the D1 detergent-based treatments, with more disrupted collagen organization and greater, though not significant loss of enzymatic cross-links (−37.4%, p=0.137). Irradiation of D5 HFL samples led to a further and significant loss in the content of enzymatic cross-links (−29.4%, p=0.037) than what was observed with the decellularization process.

Overall, the results suggest that the decellularization processes did not significantly alter the matrix. However, the addition of gamma-irradiation is deleterious to the collagen structural integrity of the tissue.

A. Introduction

Bone regeneration is a well-regulated process requiring the recruitment of skeletal stem/progenitor cells (SSPCs) from adjacent tissues. Among them periosteum is a connective tissue that surrounds the external surface of bones and has been widely described as physiologically essential for bone development and healing[32,66,511]. This membrane consists of a fibrous outer layer composed of type I collagen and a highly cellular inner layer composed of fibroblasts, osteoprogenitor cells and MSCs[25,512]. However, in case of CSBD after a massive trauma, a tumoral resection or an osteomyelitis, the surrounding soft tissues, such as periosteum, are usually damaged and the normal physiological healing capacity is insufficient[513].

Current strategies for the reconstruction of large bone defects exploit surgical approaches such as Ilizarov's[514] or Masquelet's induced-membrane[96] techniques. However, these methods require lengthy and tedious processing. Bone repair therefore remains a major concern for orthopaedic surgeons[14,156,245] which has led to the emergence of a series of alternative tissue engineering approaches in recent decades[246,291,515]. Among these, Manon et al. recently showed the suitability of using HFL matrices as a periosteal-like scaffold for bone regeneration, mainly through their collagen type I composition and appropriate mechanical properties[290,291]. The HFL is a dense connective tissue made up of three layers of collagen fibre bundles with little cellularity[257,516].

Along with bone marrow and muscle, the periosteum is an important source of SSPCs with a high potential for bone regeneration[67,517]. These progenitors reside in a rich environment formed by the periosteal ECM, where cellular and molecular crosstalk is crucial to achieve bone regeneration[66]. This 3D scaffold therefore not only provides a structural and mechanical support[518–520] but is also a modulator of tissue homeostasis[367]. Consequently, any alteration of this structure can lead to the disruption of tissue function[367]. Collagen constitutes the major ECM component[365,366] and plays a key role in maintaining biological and architectural integrity of tissues as well as providing physical support[343,521] further emphasized this point by revealing that cell-free collagen scaffold of decellularized periosteum alone efficiently promotes orthotopic remodelling of skeletal defects *in vivo*[343].

Fibril forming collagen type I, the most prevalent one, provides tensile strength to tissues[367] through its complex hierarchical structure. Encoded by the COL1A1 and

COL1A2 genes, collagen precursors undergo series of post-translational modifications (PTMs) to form mature molecules[522,523], which are stabilized by two main types of intermolecular cross-links important for their assembly and for collagen functions[366]. First, enzymatic cross-links, considered a PTM of lysine residues, are mediated by the lysyl hydroxylases and lysyl oxidases through a highly controlled mechanism. Initially formed as immature divalent cross-linking (*e.g.*, dehydrodihydroxylysinonorleucine), some are converted into mature trivalent cross-links (*e.g.*, pyridinoline)[366,369,524,525]. Secondly, non-enzymatic cross-links result from a glycation process forming AGEs, among which pentosidine is the most frequently characterized[373,526]. All AGEs are formed by a Lysine-Arginine or Lysine-Lysine interaction and predominantly accumulate in collagen because of its low turnover. Their emergence leads to an increase in connective tissue rigidity and insolubility[374,526]. Finally, interfibrillar bridges also result from the interactions of non-collagenous components between GAG-DCN complexes of adjacent fibrils[377,518,524]. DCN is a member of class 1 SLRPs essential for the regulation of various tissular processes[375,376] but most notably studied for its involvement in collagen fibrillogenesis and matrix stability. This protein also acts as a reservoir of GFs and cytokines[375,378].

In the present study harvested HP and HFL samples were treated with several protocols of decellularization[291] as well as by irradiation. Whereas the general microstructure, composition, and biosafety of the ECM-derived scaffold had received considerable attention, a special analysis of collagen *per se* is required as the main component contributing to matrix-cell crosstalk and, hence, to the global integrity of the periosteum. Therefore, since decellularization and sterilization processes can have a negative impact on the ECM, the aim of the present study was to characterize the collagen scaffold obtained after these engineering processes. Here, we hypothesized and sought to confirm the global persistence of important ECM components of HP and HFL samples after chemical decellularization and sterilization, and therefore a persistence of their functional and structural properties. The ultimate goal of this study is to confirm the maintenance of HFL matrices properties in order to consider their future use as periosteal scaffold substitutes to promote bone regeneration.

B. Materials & methods

B. 1. Sample collection & processing

HFL and HP were harvested from deceased donors (3 donors of average 86.81 ± 3.7 years) of the Human Anatomy Department of UCLouvain (Body donation service, IRB0000853S, Brussels, Belgium) following the same procedure as previously described[290] and were subjected to five chemical decellularization (D) protocols (Table 29) performed under continuous agitation (N=3 donors x 2 tissues x 5 protocols=30 analyses).

Table 29. Decellularization protocols (D), from D1 to D5.

	Decellularization protocols
D1	12h SDS – 4h Triton – 12h DNAse
D2	12h Triton – 4h SDS – 12h DNAse
D3	24h SDS – 4h Triton – 12h DNAse
D4	24h Triton – 4h SDS – 12h DNAse
D5	24h Acetone – 15.5h Ether – 8h Ethanol – 1h NaCl/NaOH – 8h H_2O_2

SDS: sodium dodecyl sulfate, DNAse: deoxyribonuclease, NaCl: sodium chloride, NaOH: sodium hydroxide.

The soap-based detergent protocols, D1 to D4, consisted of different combinations of Triton, SDS and DNAse. Triton is a non-ionic detergent that disturbs the lipid-lipid and protein-DNA interactions. SDS is an ionic detergent that denatures protein structure and solubilizes nuclear and cellular membranes. DNAse treatment is employed to cleave internucleotide bonds and eliminate undesirable cellular waste. In protocol D1, tissues were maintained for 12h in SDS, followed by 4h in Triton. The sequence was reversed for D2, with 12h in Triton and by 4h in SDS. For protocols D3 and D4, the sequence was the same as for D1 and D2, respectively, with an increase in the duration of the first treatment step maintained for 24h instead of 12h (SDS and Triton, respectively). Each protocol ended with a 12h DNAse treatment. D5 protocol is the one routinely used in the institutional tissue bank[291,341]. In brief, it includes sequential immersion in pure acetone to degrease, ether to neutralize the previous compounds and 70° ethanol to further degrease. Following a washing step, sample are immersed in a hypertonic solution of NaCl (7%) and NaOH to finally been placed in H_2O_2 (7.5%). Quality controls were performed to confirm the full decellularization and to

measure the pH and traces of H_2O_2 and acetone. To assess the efficacy of decellularization protocols, microscopic analyses were performed on DAPI and H&E stained slices first. Then, 3 random samples of 25mg were harvested from native and decellularized tissues of all protocols, and freeze-dried. The DNA content was measured using the Quant-iT PicoGreen DNA assay kit (ThermoFisher, Waltham, MA, USA) just after being extracted using the DNeasy® Blood & Tissue kit (Qiagen, Hilden, Germany). The very precise steps are previously described[290,291]. Samples were then stored at -80°C.

Samples of decellularized HFL (D1-D5) were then frozen and sterilized by gamma(γ)-irradiation (HFLi, HFL irradiated) under dry ice using a minimal exposure dose of 25kGy (IBA Mediris, Fleurus, Belgium), the recommended standard sterilization method for clinical applications[527–529].

To perform the various analyses, samples were randomly taken from the entire decellularized scaffold to consider the whole tissue heterogeneity.

B. 2. Polarized light microscopy

After paraffin histology processing, SR staining, an acidic hydrophilic stain, was used to highlight and evaluate qualitative modification in collagen organization ($n_{(HFL)}$=4 samples/protocol, $n_{(HP)}$=3 samples /protocol, with 3 sections per native samples and one per decellularization protocol). Deparaffinized and rehydrated sections were immersed in 1% Phosphomolybdic acid and then in 0.1% SR solution for 2h. Sections were then incubated in HCl before washing and mounting steps, then imaged under polarized light. Parallelly bound to collagen fibrils, this dye intensifies the birefringence of the samples which is manifested by shades of colour under polarized light, each associated with properties of fibres organization. Thin fibres (Ø ≤ 0.8µm) with a more scattered histoarchitecture are characterized by a weak birefringence and are detected in green/yellow while thick (Ø between 1.6-2.4µm) organized ones appeared as shades of red and orange[530]. These parameters are quantified in order to highlight a possible alteration in collagen organization.

SR-stained sections were first imaged using the Axioplan microscope (ZEISS) with a 10-fold magnification. Linear polarization of light was obtained by using two filters that allow light to pass only in one direction of vibration: the polarizer and

the analyser, placed perpendicularly[531]. All slides were examined at the same time to ensure consistency of the experiment and were digitalized using the Nikon Digital sight DS SMC camera with NIS-Element BR 3.0 software. The average of five different acquisitions was assessed for each HFL sections to cover the whole tissue surface, and three for HP, the surface of the sections being smaller. Collagen organization was then estimated with ImageJ software[532] as a surface percentage of each colour with a constructed macro (IREC imaging platform, 2IP). The analysis displayed green, yellow, orange, and red polarization colours.

To further validate our findings, whole slide images were then acquired with the ZEISS Axio Scan.Z1 Slide scanner under polarized light in order to approximate the proportion of each fibre type. These acquisitions were analysed with QuPath[252] calibrated to detect the different shades of colours. With this approach, unlike with the previous one, only green, orange, and red colours are detected.

B. 3. Raman spectroscopy

Spectra acquisition

Molecular composition of fresh frozen and processed HFL, HFLi and HP samples (n=3/protocol for each type of samples) was investigated using Raman spectroscopy (Renishaw confocal Raman inVia Quontor). Spectra of each sample were obtained as the average of three consecutive spectra randomly distributed over the sample surface. Each spectrum was collected using a 785nm monochromatic laser beam with a power of 50mW, a 50-fold magnification and the Renishaw Centrus 21KP95 detector. Two types of spectra ranges were recorded.

Acquisitions were first performed with a static mode in a wavelength range of 700-1800cm^{-1} with an integration time of 10 seconds and 15 accumulations. The presence of non-enzymatic cross-links (pentosidine, 1345cm^{-1}) and hydroxyproline (872cm^{-1}) was normalized to the amount of tissue using the proline peak (920cm^{-1}). Enzymatic cross-link level is assessed by the ratio of mature to immature cross-links (pyridinoline/dehydrodihydroxylysinonorleucine, 1670/1690cm^{-1}). A 1657cm^{-1} supplementary band was added for the Amide-I peak-fit model of HP. This lipid vibration band was used to correct its potential interference on the measure of enzymatic cross-links[533].

To estimate the collagen-bound water content, a second wavelength range of 2700-3800cm^{-1} was recorded with extended mode, 10 seconds integration time, and 6 accumulations. Three parameters were considered: organic matrix-related water (3243cm^{-1}), amine (NH) groups beside organic matrix-related water (3333cm^{-1}) and hydroxide (OH) groups of hydroxyproline beside collagen-related water (3457cm^{-1}). Each of these parameters was normalized to the amount of organic matrix (mainly collagen) assessed at a wavelength of 2940cm^{-1} [534].

Spectra processing

Raman spectra were processed using two different softwares: the Windows®-based Raman Environment (WiRE 3.5, Renishaw) and MATLAB PLS toolbox (PLS_Toolbox 9.0 (23592) Eigenvector Research, Inc., Manson, WA USA 98831). WiRE software was used for peak deconvolution, applying a baseline correction. The latter was used to deconvolve the Amide I subpeaks (1605, 1635, (1657), 1666, 1686cm^{-1}) and those present in the 2700-3800cm^{-1} spectra (2943, 3220, 3333, 3457cm^{-1}). Models were built by measuring the average centres (intensity wavelength), width and Gaussian percentage of each subpeak derived from the deconvolution. The PLS toolbox automates the measurement of height and area of each peak of interest with a local baseline correction, after the manual creation of a model, according to the mean values of the peaks of interest from all spectra.

B. 4. Protein extraction & Enzyme-linked immunosorbent assay

DCN content was evaluated using ELISA. For this purpose, the protein extraction was performed as previously described[290]. Samples of each HFL and HP were weighted, cut and lysed with the buffer solution containing the RIPA (ThermoFisher Scientific, 89900), the protease inhibitor cocktail (Sigma-Aldrich, P8340-1ML), and phosphatase inhibitors (PhosSTOP™, Roche, Basel, Switzerland). The samples were subjected to four cycles in the Precellys homogenizer (Bertin Technologies SAS, France) at 7200rpm (8114xg). The protein concentration in the supernatant was determined with the Pierce™ BCA Protein assay kit (ThermoFisher Scientific, 23227) and normalized to the sample weight.

Subsequently, DCN content was evaluated using the RayBio® Human Decorin ELISA kit (RayBiotech, ELH-Decorin-1,13485) following an adaptation of the manufacturer's instructions. Briefly, since the protein concentration was low,

larger volumes were used to achieve the required concentration per well. Therefore, 145µl of tissue homogenates and standards were incubated in the pre-coated 96 well microplate at RT for 2.5h. Following the washing steps, biotinylated antibody was added for 1h. The subsequent washing step removed unbound antibodies before the addition of streptavidin conjugated HRP solution. 5'-tetramethylbenzidine (TMB) substrate was added after four washes and incubated protected from light. After 30 minutes, the reaction was stopped (Stop solution of 0.2M sulfuric acid) and the plate was red at 450nm. Standard curve was obtained using Sigmaplot 13 software (version 20, SPSS, Inc., Chicago, IL, USA) and results were expressed as pg of DCN per mg of total protein (pg/mg).

B. 5. GAG quantification

The content of sulfated GAGs was quantified in native and decellularized HP and HFL samples (n=3) using the Blyscan Sulfated GAG Assay (Biocolor LTD., Carrickfergus, Northern Ireland) and following the manufacturer's protocol. Sulfated GAGs include chondroitin sulfate, dermatan sulfate, heparan sulfate and keratan sulfate. Three samples of 25mg of each tissue were harvested. Samples were then first freeze-dried and dry-weighted. Before the quantitative measurement, each sample was placed in a Papain reagent (50ml Na_2HPO_4/NaH_2PO_4 0.2M pH 6.4, 400mg sodium acetate, 200mg EDTA and 40mg cysteine HCL, 250µl papain) overnight at 65°C for GAG extraction. Following centrifugation (10min, 10 000rpm, 9.6xg), 100µl of each sample were taken and 1ml of Dye Reagent was added for 30 minutes. The Eppendorfs were centrifuged again at 12 000rpm (13.8xg) for 10 minutes and the supernatant discarded. Dissociation reagent (500µl) was added for 10 minutes and, after a final centrifugation (5min, 12 000rpm, 13.8xg), 200µl of each sample were transferred to a 96-well plate. Standards were also prepared according to the manufacturer's protocol. The plate was read at 630nm three times and the average of the three readings was used for final quantification. The concentration of GAGs was expressed in µg/mg dry weight.

B. 6. Statistics

Statistical analyses were carried out using GraphPad Prism (Version 8.4.0, Inc., San Diego, CA, USA) and SPSS software (Version 27, IBM SPSS, Inc., Chicago, IL, USA). Data were expressed as the mean ± SEM and compared with the non-parametric

Mann-Whitney or Kruskal-Wallis test because of the small dataset and the subsequent non-respect of normality (tested by Shapiro-Wilk test). Pairwise comparisons were performed using the Dunn's test. All tests were two-tailed. The significance level was considered at a p-value < 0.05.

C. Results

All the decellularization protocols successfully achieved the Crapo's criteria[178]. These standards include an absence of nuclei visible by histological analysis (DAPI, H&E staining), a DNA quantity of less than 50ng/mg dry weight and a length of less than 200bp for persistent DNA fragments after treatment. In all the samples, DNA concentration felt below the critical threshold of 50ng/mg of dry weight and no cellular traces were visible on microscopic analyses.

C. 1. Weak alteration of collagen structure

HFL samples appeared to be more disorganized after protocol D5 treatment than the other subgroups, as highlighted by a decrease, although not significant, of thick (1.6-2.4µm) red hue fibres (ImageJ: - 29%; QuPath: - 32.6%) and an increase in thin (≤ 0.8µm) green ones (ImageJ: + 87.9%; QuPath: + 53.7%) (Fig. 96). HP samples seemed to be more affected by protocol D1. Although not significant, the D1-treated tissues presented the lowest proportion of red fibres (ImageJ: - 33.8 %; QuPath: - 68.3%) and the highest of green ones (ImageJ: + 300%, QuPath: + 189%) compared to natives. No significant differences in the amount of intermediate fibres (yellow/orange) were recorded.

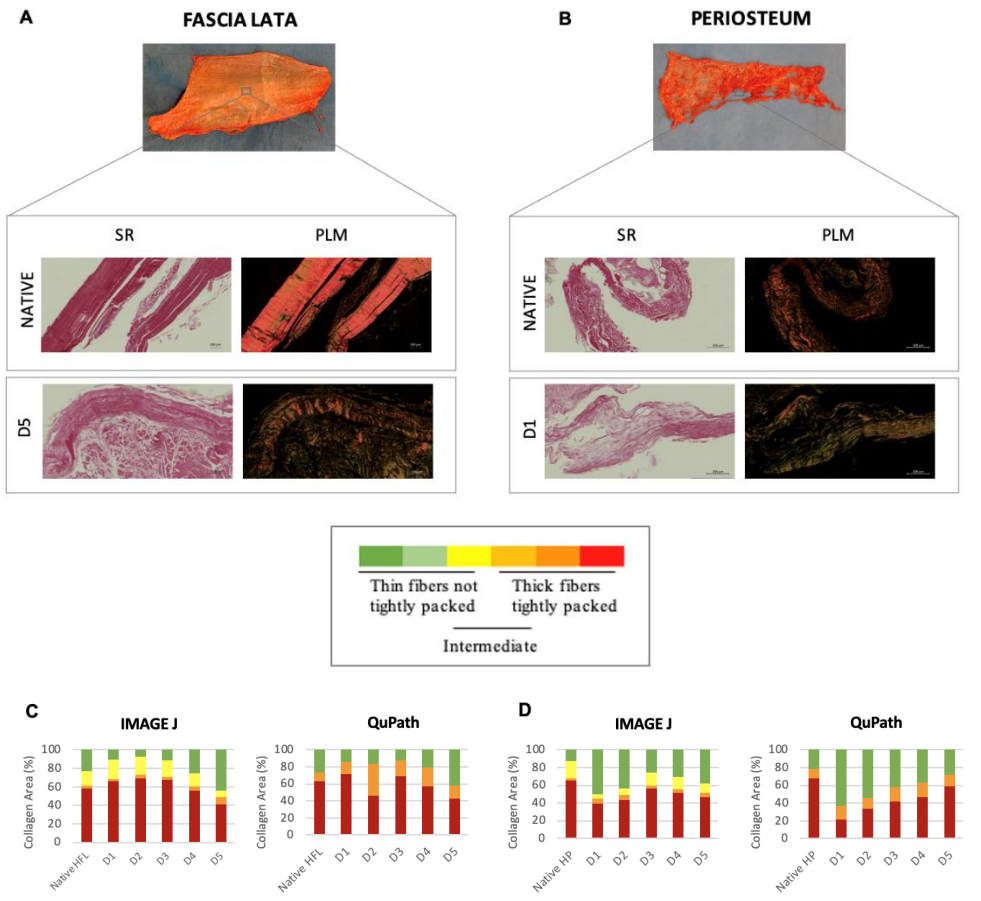

Figure 96. Qualitative (A and B) and quantitative (C and D) evaluations of the collagen organization of sections through native (n=12) and decellularized HFL (n=4) (A and C) and HP (n=3) (B and D). (A and B) Sirius Red staining under bright field (SR, left) and polarized light (PL, right) obtained with ZEISS Axio Scan.Z1 Slide. Same analyses were carried out with polarized light microscope but are not shown. Variation in the polarization of collagen fibres under polarized light reflects differences in fibre thickness, density and packing: from green (thin, ≤0.8µm, and loosely packed) to red (thick, 1.6–2.4µm, and tightly packed)[530]. (C and D) Quantitative analyses were performed using ImageJ for the microscopic images and Qupath for scanner images. The quantitative analysis confirmed the qualitative assumptions: D5 and D1 protocols affected the most the HFL (C) and HP (D) samples respectively, with a higher average of thin fibres and lower of thick ones assessed by both ImageJ (microscope) and QuPath (scanner), despite remaining not significant.

C. 2. Weak difference in the matrix molecular composition in native tissues

Raman spectroscopy revealed no statistical differences between the molecular composition of native HFL and HP. Both tissues presented similar amounts of hydroxyproline and collagen-bound water, although HFL samples showed a slightly higher proportion of enzymatic cross-links (+ 13.6%, $p>0.05$) and a slightly lower amount of non-enzymatic cross-links (- 55.8%, $p>0.05$) than native HP.

C. 3. Weak alteration of the matrix molecular composition in decellularized tissues

Human Fascia lata

Increase in tissue hydration was the most marked modification after HFL decellularization (Table 30), at the limit of significance for all three biomarkers of collagen-related water for all D-protocols: the hydroxyproline OH groups besides water bound to collagen (IR 3457/2943, $p=0.054$), the NH groups beside organic matrix related water (IR 3333/2943, $p=0.052$) and the organic matrix related water parameter (IR 3220/2943, $p=0.061$). These increases were then confirmed, by a pairwise Dunn's comparison, for the three biomarkers in protocols D3 (IR 3220/2943, $p=0.030$; IR 3333/2943 $p=0.047$ and IR 3457/2943, $p=0.037$) and D5 ($p=0.030$, $p=0.023$ and $p=0.037$ respectively) when compared to native tissues. An average loss of 25.2% ($p=0.195$) in the amount of enzymatic cross-links was also observed after the D5 treatment, which was the largest, though not significant, loss among all protocols. Hydroxyproline and pentosidine content were not significantly affected by the chemical treatments as well.

Human periosteum

HP samples hydration also increased with all decellularization protocols (Table 31) but in a less important way than HFL. D1-HP presented the lowest average of enzymatic cross-links (-37.4%, $p=0.137$) and pentosidine (-46.7%, $p=0.332$) among the different decellularization protocols. Once again, the content of hydroxyproline did not significantly vary according to the treatment.

Table 30. Raman spectroscopy data of Human Fascia Lata matrices after decellularization with five different protocols (D1-D5) (n=3/protocol and native). AGEs: Advanced Glycated End Products, NH: amine group, OH: hydroxide. Results are expressed as Mean ± SEM (Kruskal-Wallis).

								Kruskal-Wallis
		Native	***D1***	***D2***	***D3***	***D4***	***D5***	***p-value***
700 -1800 cm^{-1}	Hydroxyproline *875/920*	0.601 ± 0.031	0.600 ± 0.031	0.610 ± 0.045	0.530 ± 0.035	0.637 ± 0.092	0.589 ± 0.080	0.861
	Pentosidine (AGEs) *1342/920*	0.391 ± 0.068	0.365 ± 0.005	0.378 ± 0.039	0.384 ± 0.024	0.322 ± 0.033	0.338 ± 0.015	0.560
	Enzymatic Cross-links *1666/1686*	4.191 ± 0.430	3.435 ± 0.299	3.183 ± 0.142	3.210 ± 0.118	4.490 ± 0.737	3.136 ± 0.172	0.121
2700 - 3800 cm^{-1}	Organic matrix related water 3220*/2943*	0.062 ± 0.016	0.285 ± 0.020	0.252 ± 0.085	0.446 ± 0.083	0.270 ± 0.052	0.377 ± 0.041	0.061
	NH groups beside organic matrix related water *3333/2943*	0.078 ± 0.005	0.141 ± 0.007	0.155 ± 0.027	0.194 ± 0.027	0.131 ± 0.028	0.196 ± 0.016	0.052
	OH groups of hydroxyproline next to collagen-related water *3457/2943*	0.005 ± 0.001	0.054 ± 0.004	0.039 ± 0.020	0.086 ± 0.017	0.055 ± 0.011	0.078 ± 0.008	0.054

Table 31. Raman spectroscopy data of Human Periosteum matrices after decellularization with five different protocols (D1-D5) (n=3/protocol and native). AGEs: Advanced Glycated End Products, NH: amine group, OH: hydroxide. Results are expressed as Mean ± SEM (Kruskal-Wallis).

								Kruskal-Wallis
		Native	***D1***	***D2***	***D3***	***D4***	***D5***	***p-value***
700 -1800 cm^{-1}	Hydroxyproline 875/920	0.922 ± 0.140	0.632 ± 0.043	0.599 ± 0.093	0.663 ± 0.038	0.626 ± 0.058	0.634 ± 0.042	0.544
	Pentosidine (AGEs) 1342/920	0,610 ± 0.111	0,325 ± 0.101	0,381 ± 0.055	0,417 ± 0 .115	0,399 ± 0.071	0,375 ± 0.016	0.460
	Enzymatic Cross-links 1666/1686	3.621 ± 0.099	2.269 ± 0.201	2.465 ± 0.220	2.328 ± 0.250	2.545 ± 0.061	2.346 ± 0.109	0.250
2700 - 3800 cm^{-1}	Organic matrix related water 3220*/2943*	0.152 ± 0.094	0.414 ± 0.065	0.456 ± 0.217	0.927 ± 0.355	0.455 ± 0.179	0.463 ± 0.102	0.267
	NH groups beside organic matrix related water *3333/2943*	0.171 ± 0.050	0.234 ± 0.034	0.176 ± 0.058	0.370 ± 0.150	0.185 ± 0.059	0.223 ± 0.041	0.698
	OH groups of hydroxyproline next to collagen-related water *3457/2943*	0.006 ± 0.004	0.072 ± 0.020	0.084 ± 0.041	0.163 ± 0.054	0.087 ± 0.036	0.093 ± 0.021	0.100

Irradiated human fascia lata

By multiple comparison analyses, we highlighted a further loss in the proportion of enzymatic cross-links in D5i sterilized samples, leading to a significant difference with natives (-29.4%, p=0.037) (Fig. 97). However, hydroxyproline and pentosidine levels were similar to that of native tissues (Table 32). Moreover, while hydration increased after decellularization (D1 to D5) of both tissues (HFL and HP), this proportion decreased after sterilization processes for HFL (D1i to D5i), without returning to basal levels of natives; the data obtained with protocol D5i remained the most different.

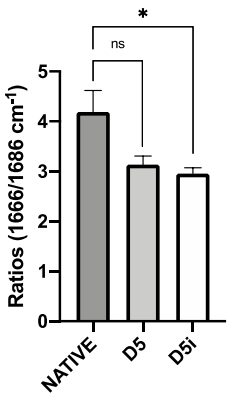

Figure 97. Measurement of enzymatic cross-links by Raman spectroscopy in samples of native HFL and HFL decellularized according to the fifth protocol, followed (D5i) or not (D5) by gamma irradiation. The decellularization chemical treatment impaired the amount of enzymatic cross-links but without significance (–25.2%, p=0.195). However, after sterilization, the amount of enzymatic cross-link was further reduced and this reduction became significant (–29.4%, p=0.037) compared to native.

C. 4. Interfibrillar bridges of decorin

ELISA analyses of protein extracts from HP and HFL samples provide a deeper insight into the effect of chemical treatments on interfibrillar bridges (Fig. 98). The DCN levels in HFL were approximately 6.40 ng/ml (± 0.23) for all subgroups except D5-tissues, which averaged 2.3ng/ml (± 0.33) (p=0.036). HP samples of all D-protocols presented a homogenous alteration of DCN levels compared with the native subgroup, with a mean of 2.2ng/ml (± 0.15) versus 6.2ng/ml (± 0.04) for natives. DCN levels in protocol D2 were the lowest, exhibiting a significant decrease compared to natives (p<0.001), followed by protocol D4 (p=0.010).

Table 32. Raman spectroscopy data of Human Fascia Lata matrix after decellularization with five different protocols followed by irradiation (D1i-D5i) (n=3/protocol and native). AGEs: Advanced Glycated End Products, NH: amine group, OH: hydroxide. Results are expressed as Mean ± SEM (Kruskal-Wallis).

								Kruskal-Wallis
		Native	***D1i***	***D2i***	***D3i***	***D4i***	***D5i***	**p-value**
700 -1800 cm^{-1}	Hydroxyproline 875/920	0.601 ± 0.031	0.670 ± 0.086	0.586 ± 0.018	0.598 ± 0.036	0.607 ± 0.037	0.581 ± 0.077	0.942
	Pentosidine (AGEs) 1342/920	0.391 ± 0.068	0.384 ± 0.036	0.326 ± 0.015	0.320 ± 0.013	0.356 ± 0.024	0.345 ± 0.013	0.666
	Enzymatic Cross-links 1666/1686	4.191 ± 0.430	3.136 ± 0.162	3.134 ± 0.120	3.062 ± 0.090	3.273 ± 0.264	2.957 ± 0.116	0.161
2700 - 3800 cm^{-1}	Organic matrix related water *3220/2943*	0.062 ± 0.016	0.115 ± 0.006	0.102 ± 0.005	0.185 ± 0.065	0.119 ± 0.017	0.279 ± 0.037	0.058
	NH groups beside organic matrix related water *3333/2943*	0.078 ± 0.005	0.084 ± 0.004	0.086 ± 0.003	0.104 ± 0.022	0.086 ± 0.004	0.151 ± 0.023	0.145
	OH groups of hydroxyproline next to collagen-related water *3457/2943*	0.005 ± 0.001	0.020 ± 0.003	0.014 ± 0.0004	0.030 ± 0.013	0.020 ± 0.0006	0.048 ± 0.006	***0.034***

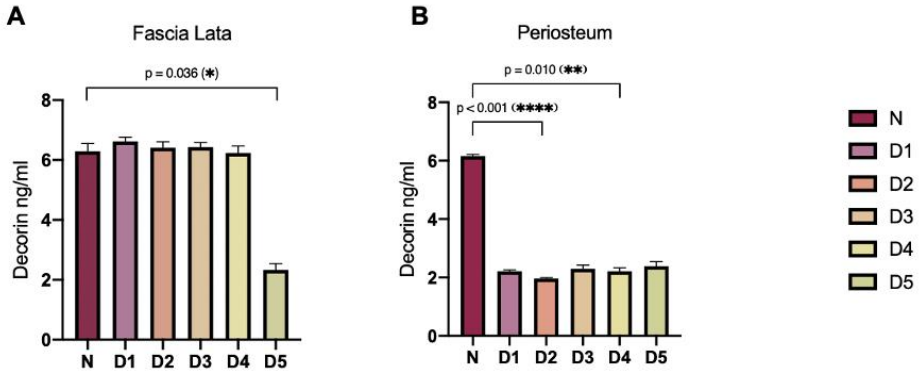

Figure 98. Decorin (DCN) levels (ng/ml) assessed by ELISA in HFL (A) and HP (B) protein extracts according to sample treatments (D1-D5). DCN in HFLs was significantly disrupted by tissue engineering processes in D5-treated tissue (p=0.036). Concerning HP, DCN level was reduced with all decellularization protocols, but most importantly in D2 (p<0.001) and D4 (p=0.010)-treated tissues. Error bars represent the SEM. D: Decellularization protocol: N: native.

Since interfibrillar bridges are formed by an association between DCN and sulfated GAG, we wanted to identify a relationship in their persistence within the tissue-

engineered samples. In both tissue types, total sulfated GAG levels were similarly and significantly decreased after all D-protocols (Fig. 99 – A). HFL decellularized samples contained average levels of 0.24µg of GAGs per mg of dry weight (± 0.20), while native sample levels averaged 3.32µg/mg (± 0.38). For HP samples, a similar ratio was found, with an average of 0.66µg/mg (± 0.19) for decellularized tissues and 3.06µg/mg (± 0.79) for native tissues. No correlation was observed between GAG and DCN levels for both HFL (R^2=0.022) and HP (R^2=0.784) samples (Fig. 99 – B). Changes in DCN and GAG level, resulting from chemical treatments were not related.

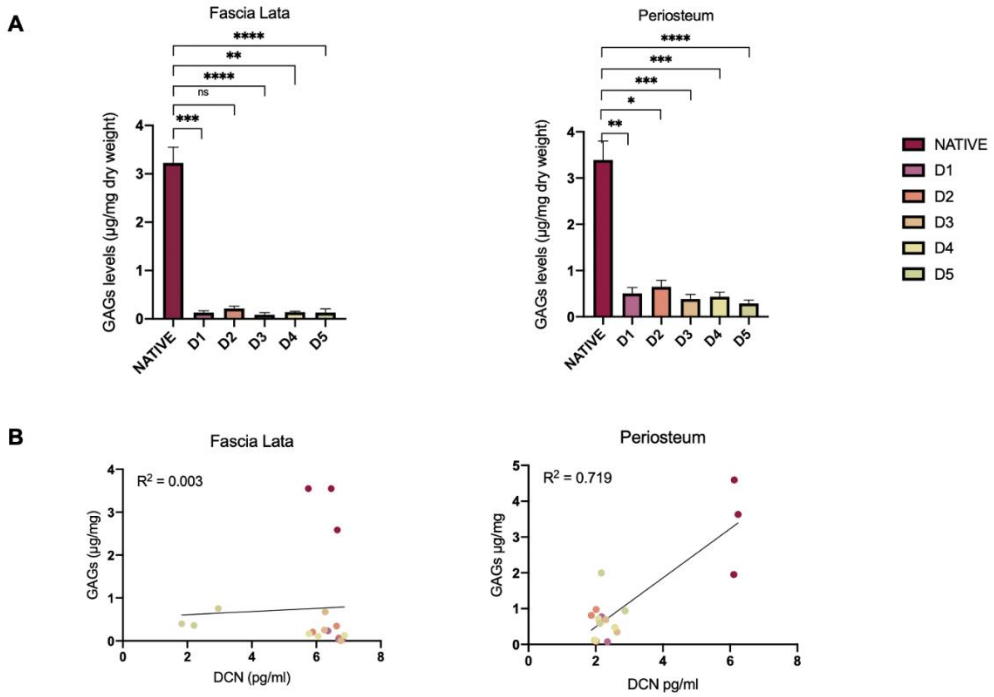

Figure 99. Impact of decellularization approaches on GAGs and DCN. (A) Quantitative analyses of GAG content in HFL and HP samples. The levels significantly decreased after all chemical treatments for both HFL (D1 (p=0.0004), D2 (p=0.024), D3 (p<0.0001), D4 (p=0.012), D5 (p<0.0001)) and HP (D1 (p=0.0002), D2 (p=0.007), D3 (p<0.0001), D4 (p<0.0001), D5 (p=0.007)) samples. (B) Variation of DCN and GAGs resulting from the chemical treatments are not related for both HFL (R^2=0.022) and HP (R^2=0.784). However, all decellularized samples present similar profiles clearly distinguishable from native tissues. Error bars represent the standard error of the mean (SEM). GAGs: Glycosaminoglycans, D: Decellularization protocol.

D. Discussion

None of the five decellularization protocols (D1 to D5, Table 29) significantly altered collagen arrangement. Detergent-free treatment (D5) disorganized HFL samples to a greater extent, significantly reducing DCNs and GAGs, and non-significantly reducing collagen cross-links. HP samples, treated with detergent-based treatment D1, showed collagen disorganization, and a reduction in enzymatic cross-links. Overall, decellularization had minimal impact on the matrix, while the addition of gamma irradiation impact leads to a significant negative effect on the integrity of collagen cross-links.

Structural modifications were therefore most pronounced in HFL when treated with the D5 protocol and in HP with the D1 protocol. This was first observed with the assessment of collagen bundles birefringence using PLM to understand the impact of the engineered treatments on the architectural arrangement[530,531,535]. The robustness of the results is confirmed by the convergence of birefringence measurements between various analysis tools. Interestingly, each of these subgroups, HFL-D5 and HP-D1, also showed the lowest levels of enzymatic cross-links as measured by Raman spectroscopy. In the literature, optical density measures under polarized light were already used as indicator of cross-linked collagen organization[536,537].

Previous studies confirmed collagen persistence in decellularized scaffolds[291,340]. Being the major ECM component, collagen biological and architectural functions have already been well characterized[372,521]. Ensuring the persistence of enzymatic cross-links in decellularized collagen scaffolds is therefore crucial for maintaining the functional properties of native matrices, contributing to fibrils stability and improving tissue biomechanical competence. Therefore, physical and chemical methods are nowadays used to achieve intermolecular collagen cross-linking in engineered scaffolds[521].

In addition to collagen enzymatic cross-links, its overall molecular composition has an impact on its structure and biomechanical properties. Indeed, AGEs are known to alter the mechanical strength of tissues[368]. In addition, as Unal and Akkus (2015) have shown, the hydration level of bones also plays a role in their mechanical properties[534]. Moreover, it is also known that physical training has an impact on collagen crimps, which can be analysed by measuring birefringence[538]. Therefore,

by taking all collagen parameters into account, we could in future investigate a relationship between the structural data of our scaffolds and their mechanical properties.

It is important to note, however, that the samples were taken from old subjects, which may also have an impact on the results. Since the rate of cross-links is age-related, the slight decrease in enzymatic cross-links after the engineering protocols could be explained by an age-related decrease, itself associated with a decrease in the mechanical capacity of the tissue. These decreases could therefore possibly be significant in tissues from younger subjects, which should be verified in the future. Moreover, it should be noted that these analyses were carried out on a small number of samples randomly taken from the entire decellularized scaffold, allowing potential tissue heterogeneity to be taken into account.

Raman spectra of the HFL samples differed slightly from those of the periosteal ones, particularly in the amide I region (1670/1690cm^{-1}). We suspected interference from tissues other than periosteum, adding some background in the spectra. The samples were harvested from old subjects and, despite efforts to remove muscle and fat, some residues remained due to the thinness of the HP. Indeed, anomalies in the spectra were observed for all protocols, including native tissue, with the exception of protocol D5, the only one to include a degreasing step. Therefore, in line with the literature, an additional peak (1657cm^{-1}) was added for deconvolution of this amide region, known to correct for potential interference from lipid vibrations[533]. In addition, we observed increased hydration in samples after decellularization, probably because decellularization disrupts the natural barriers regulating hydration. This leads to increased water uptake during abundant rinsing steps. Irradiation, however, leads to a partial loss of this increased hydration, without returning to baseline levels.

Since these decellularized tissues are intended to regenerate *in vivo* damaged structures, sterilization processes are required to prevent pathogen transmission[527–529]. Although gamma irradiation is commonly used in bone banks for sterilization it causes radiolysis of water molecules, releasing free radicals[161] that damage collagen[528,529]. Previous studies on bones showed a negative synergic effect on mechanical resistance when irradiation was added to freeze-dried samples[189,539], attributed to a significant reduction in enzymatic cross-links

density[540]. This is consistent with our results revealing a more pronounced alteration of cross-links post-irradiation. Future studies should explore decellularization procedures under totally sterile conditions to avoid the detrimental effects of subsequent irradiation on tissue properties.

We did not investigate irradiated periosteum since the priority, for the creation of the new regenerative membrane, was the use of irradiated decellularized HFL[291].

DCN-GAG complexes are essential for the ECM organization, especially in collagen fibrillogenesis, as evidenced by the alteration of the latter in DCN-deficient mice[375,378]. This PG is also involved in stress transfer between collagen fibrils[524] and in the bioavailability of GFs such as TGF-β[375,378]. Alteration in DCN content varies according to the tissue type, with HFL samples globally maintaining their DCN concentration after decellularization, except for D5, while HP samples show a decrease in all D-protocols.

Furthermore, it has already been demonstrated that detergent-based decellularization affects the GAG composition of ECM[340,389,541], as confirmed by our quantitative measurements, with potential dysfunction of persistent GAGs[389]. However, the maintenance of functional GAGs is necessary. Abundantly distributed on cell surface and in the ECM, they modulate various physiological processes. They provide biochemical and mechanical support in the ECM and influence cell behaviour (adhesion, proliferation, differentiation)[542,543].

Despite the lower proportions of DCN and GAGs in decellularized samples compared to native ones, no correlation could be demonstrated in their alteration after chemical treatments. Since GAGs are ubiquitous on the cell surface, their removal by the decellularization protocol is expected. Therefore, proportionally, the loss of GAGs could be greater than that of DCN.

The present study confronts different decellularization approaches. Protocols D1 to D4 are based on the use of Triton, SDS and DNAse and ensure cell membrane lysis, protein solubilization and residual DNA elimination. Triton and SDS are known for their efficiency in decellularization, but also for altering the structure of the ECM[178]. Protocol D5 consists of a succession of solvent- and detergent-based baths, which has also already demonstrated its decellularization potential[291], including the monitoring of Crapo's criteria[178]. In this protocol, solvents such as

ethanol and acetone are used for cell lysis and lipids removing but are both also known as altering the ECM ultrastructure. The additional advantage of this protocol is that it also neutralizes prions, which the other protocols do not allow.

As qualitatively shown in the Figure 96 on the SR stained sections, more undulating collagen structure are observed in decellularized tissues than in native tissues. The cross-links alteration could modify the fibres alignment. In the future, analysis of the collagen distribution could support the observations made in this study. Approaches such as transmission electron microscopy[544], histology and contrast-enhanced microCT[288] could be used and be gathered in order to precisely cartograph the entire HFL structure.

In conclusion, a relationship was observed between the ECM structure and its molecular composition. The decellularization approaches demonstrated not significant alteration of the matrices, which justifies, along with the analysis of other parameters, the future clinical use of these processed matrices for bone regeneration. However, the combination of D5 treatment with subsequent irradiation appears the most deleterious for tissue properties. In the future, an analysis of the entire sample surface would provide more accurate information about potential sample heterogeneity, and precise quantitative analyses of the cross-links content could further validate our results. It would also be interesting to correlate all the observations of this study with the mechanical properties of the tissues.

Paper 6 – FixThePig: a custom 3D-printed femoral intramedullary nailing for preclinical research applications

Julie Manon, Alexandre Englebert*, Robin Evrard, Thomas Schubert, Olivier Cornu*

** Share first authorship*

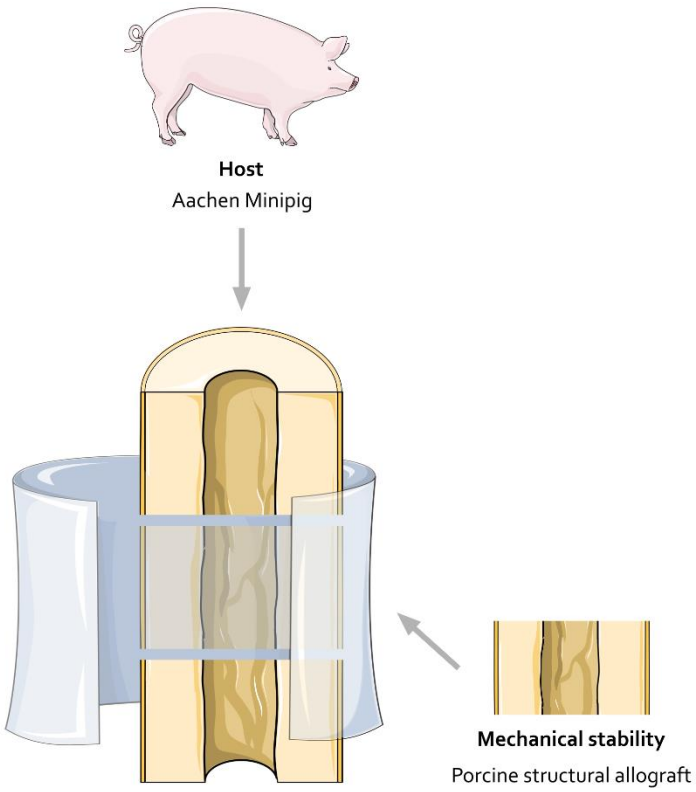

Submitted in

Front. Bioeng. Biotechnol. (IF=6.064)

Abstract

Background: CSBDs pose significant challenges in clinical orthopaedics and traumatology. Developing reliable preclinical models that accurately simulate human conditions is crucial for translational research. This study addresses the need for a reliable preclinical model by evaluating the design and efficacy of a custom-made 3D-printed IMN specifically for CSBDs in minipigs. The study aims to answer the following questions: Can a custom-made 3D-printed IMN be designed for femoral osteosynthesis in minipigs? Does the use of the custom-made IMN result in consistent and reproducible surgical procedures, particularly in the creation and fixation of CSBDs? Can the custom-made IMN effectively treat and promote bone consolidation of CSBDs?

Hypothesis: The custom-made 3D-printed IMN can be designed to effectively create, fix and treat CSBDs in minipigs, resulting in consistent surgical outcomes.

Materials and Methods: The IMN was designed based on CT scans of minipig femurs, considering factors such as femoral curvature, length, and medullary canal diameters. It was 3D-printed in titanium and evaluated through both *in vitro* and *in vivo* testing. Female Aachen minipigs underwent bilateral femoral surgeries to create and fix CSBDs using the custom-made IMN. Post-operative follow-up included X-rays and CT scans every 2 weeks, with manual examination of explanted femurs to assess consolidation and mechanical stability after 3 months.

Results: The custom-made IMN effectively fitted the minipig femoral anatomy and facilitated reproducible surgical outcomes. Symmetric double osteotomies were successfully performed, and allografts showed minimal morphological discrepancies. However, proximal fixation faced challenges, leading to non-union in several cases, while most distal osteotomy sites achieved stable consolidation.

Discussion: The custom-made 3D-printed IMN demonstrated potential in modelling and treating CSBDs in minipigs. While the design effectively supported distal bone healing, issues with proximal fixation highlight the need for further refinements. Potential improvements include better screw placement, additional mechanical support, and adaptations such as a reduction clamp or a cephalic screw to enhance stability and distribute forces more effectively.

A. Introduction

CSBDs, defined as osseous gaps exceeding the spkrontaneous healing capacities within the lifespan of an organism[14], present significant challenges in clinical orthopaedics and traumatology. These defects often result from severe trauma, infection, tumor resection, or congenital abnormalities, and they necessitate innovative treatment strategies to restore structural integrity and function. In clinical practice, the management of these defects commonly involves many surgical treatments (*e.g.* induced membrane technique[96,99,108], bone transport[14,50,140,141], bone grafts[83,121,122]). However, all these interventions often face limitations[149]. Research to improve these treatments and reduce their complications is of prime interest. However, the translation between *in vitro* and *in vivo* studies on small animals, which are the most widespread, toward humans is not as obvious. Accurate preclinical models are indispensable for translational research. It is therefore necessary to develop models, particularly those involving large animals, as close as possible to the clinical conditions. Large animal models offer several advantages, including anatomical and biomechanical similarities to human bones[59,399,400], which are crucial for evaluating the clinical relevance and performance of orthopaedic interventions.

As the Diamond concept highlights, mechanical stability is a key criterion of bone healing[19,80,91]. Most preclinical models usually involved plates or external fixators as osteosynthesis. Osteosynthesis by plate and screws was the one previously experimented to fix similar porcine CSBDs[398]. The stability was achieved by two orthogonal plates on the femoral shaft. All the studies on OMs such as the Masquelet's technique[96,109,545] or artificial/biological off-the-shelf membranes[116,117,290,291] may be biased when the plate fixation compresses the (a-)cellular membrane and could benefit from another fixation to keep free the additional surrounded scaffold[109]. Though an easy-to-use device offering a real fixation opportunity for a tibia, external fixator application is not suitable for large animal femurs, which are localized at belly height with an imposing soft-tissue mass. The risks of insufficient stability away from the CSBD, Schantz screw loosening, or pin track infections[59,109] are too substantial to consider this option in some cases. IMN has been a cornerstone in the treatment of human long bone fractures due to its minimally invasive nature, mechanical stability, central biomechanical transmission, load-bearing capacity, and ability to promote early

mobilization and weightbearing[546–551]. Potential complications might also be controlled by several patient or surgery-dependent factors[16,17,548]. Despite its recognized potential, the implementation of IMN in the context of CSBDs in large animal models remains underexplored.

In recent years, there has been a notable advancement in the field of additive manufacturing for orthopaedic applications. Specifically, the use of 3D-printing in the production of metallic implants has expanded significantly. This includes applications ranging from pre-contoured plates[552], to direct 3D-printing of implants such as osteosynthesis plates[553], arthroplasty[554], nails[401], truss cages[555], or a variety of other implants[402]. 3D-printed Nickel-Titanium implants have shown sufficient biocompatibility in pigs to be used in bone implants[403].

This study aims to address the need for a reliable preclinical model by proposing the development of a custom-made 3D-printed IMN specifically designed for CSBDs in large animal models, specifically minipigs. The study aims to answer the following questions:

- Can a custom-made 3D-printed IMN be designed for femoral osteosynthesis in minipigs?
- Does the use of the custom-made IMN result in consistent and reproducible surgical procedures, particularly in the creation and fixation of CSBDs?
- Can the custom-made IMN effectively treat and promote bone consolidation of CSBDs?

B. Materials & methods

This tailored IMN was designed based on CT scans of minipig femurs, involving several steps from CT scan analyses and template printing to rigorous *ex vivo* testing, culminating in subsequent *in vivo* experiments.

B. 1. Femoral anatomy

CT scans allowed the study of the anatomy of porcine femurs. Both femurs of Aachen minipigs (N=14, from 7 minipigs) were explanted after another study and scanned using a clinical computed tomography (CT scan, Somatom Definition AS

128 scanner, Siemens Healthineers, Erlangen, Germany). These animals were covered by the local ethics committee (Ref 2020/UCL/MD/027 and A1/ UCL/2021-A1). Different measures were reviewed around the proximal and distal metaphyses (medullary dimensions, minimal and maximal cortical thicknesses), as well as the diaphysis (outer and inner diameters, smallest intramedullary diameter, minimal and maximal cortical thicknesses). The femoral bending was also assessed in two orthogonal planes (anteroposterior and mediolateral planes), as well as the femoral length and the distance between the IMN entry point at the greater trochanter and the end of the proximal physis.

B. 2. Device featuring

The custom-made IMN was engineered with respect to multiple aspects including:

- The physiological curvature of the femur
- The length of the diaphysis
- The diameter of the medullary canal
- The screw type
- The screw number
- The screw divergence
- The precise positioning of screws along the length of the nail

B. 3. 3D design

The femoral IMN was custom-designed using Autodesk Fusion360 CAD software. 3D-printed templates were successively improved by *in vitro* testing on synthetic bones (Fig. 100). Those bones were 3D-printed based on CT scans and allowed to adjust and achieve the final nail design.

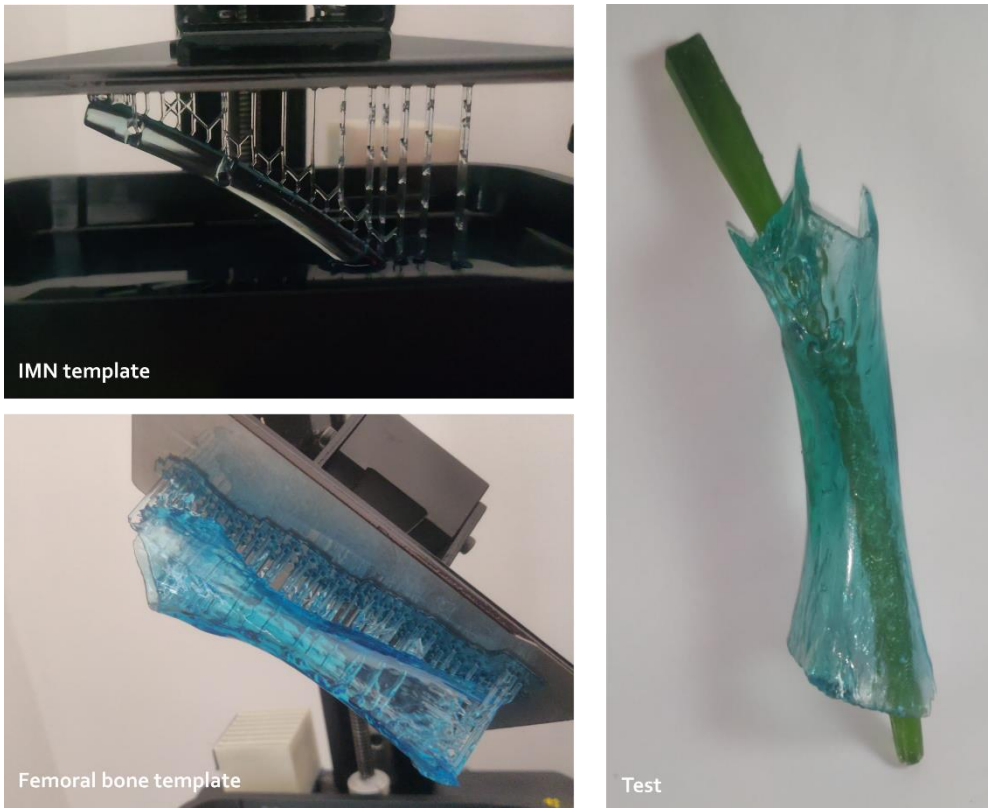

Figure 100. Preliminary tests to study the conceptualization of custom-made intramedullary nailing (IMN) including resin template printing and trials (3DMaterials SuperPP resin and Anycubic resin for the nail and femoral templates, respectively).

Overall design

The general design of the centromedullary nail consists of a curved cylinder with a tapered and rounded distal end to facilitate insertion. The curvature and diameter of the nail are determined based on anatomical studies. A solid design was chosen, which does not allow for the passage of a guide wire in the centre of the nail. While this prevents the use of a guide wire, it enables the nail to be more resistant[556]. Effectively, a smaller diameter than those typically used in humans, associated with a central tunnel for the guide would increase the risk of weakening the final device. The position, number, and type of locking screws are also determined based on anatomical studies and the literature discussing the benefit of a higher number of static locking screws[557–560].

Associated tools

A variety of instrumentation, including guide instruments, have been developed for use with the IMN. Figure 101 shows the various elements presented in this section.

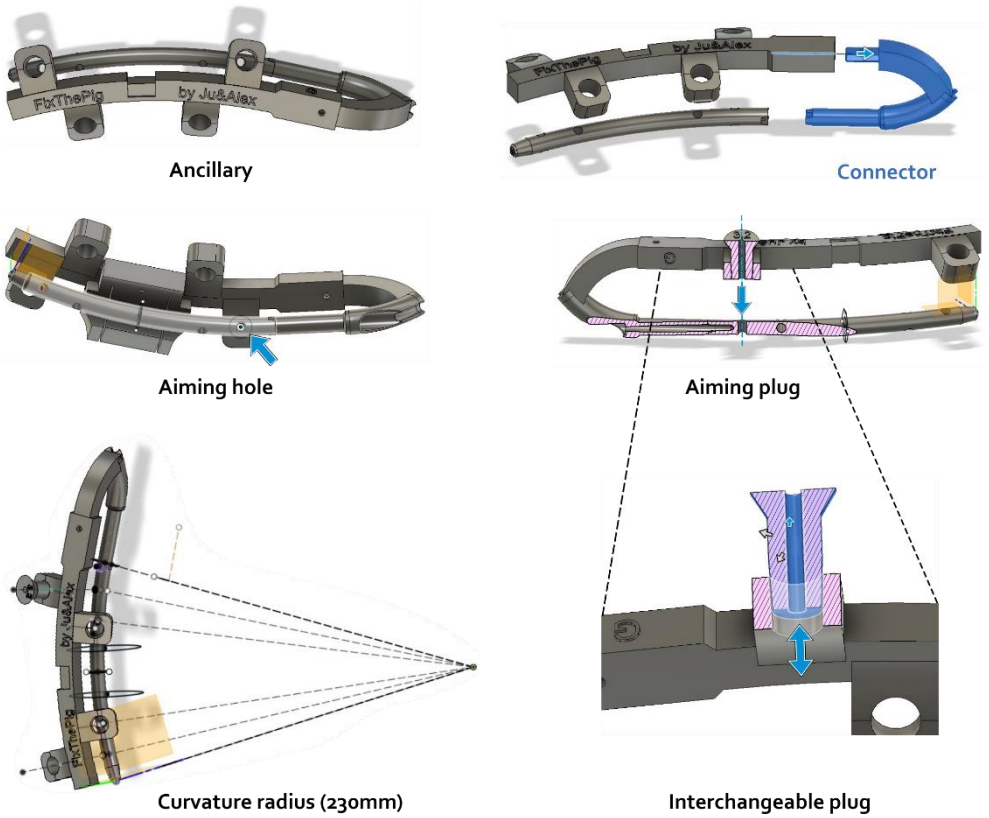

Figure 101. Ancillary modulization using Autodesk Fusion360 CAD software including distinct tools (ancillary, connector, plug) and their aiming function. Actions of aiming hole, aiming plug and interchangeable plug are illustrated by blue arrows. Pink hatched area: frontal section.

The first component, designed to be printed in metal and attached to the nail, consists of a connector that screws onto the nail. This connector has a hook-like shape that allows for a good grip of the nail during insertion into the femur and provides an anchorage point for the accessory. To facilitate attachment to the nail, a blind hole has been incorporated proximally on the nail. The diameter of this hole

is designed to accommodate an M4 screw after tapping. A locking system was also implemented to prevent rotational movement between the connector and the nail once they are screwed together. The portion of the connector that attaches to the nail has the same diameter as the nail, allowing it to enter the bone through the same opening, thereby allowing the nail to be inserted without protruding. The other end of the connector is designed to fit into the ancillary device described below. Fixation is achieved with an M3 screw that is placed perpendicular to and through the connector.

The ancillary device is designed to be 3D-printed in polyamide, resulting in a thicker structure. It has a series of appendages aligned with the axes of the locking screws of the centromedullary nail. These appendages feature slightly tapered holes, to accommodate interchangeable plugs that match the diameters of the various surgical drill bits required during the procedure.

The plugs are also designed to be 3D-printed in polyamide and have a conical shape that complements the holes in the ancillary device's appendages. This design enables the plugs to fit securely while maintaining their axis.

To facilitate a standardized creation of CSBDs for research purposes, a symmetric double osteotomy can be achieved using a custom-designed cutting guide component. This component is engineered to clip into a notch on the ancillary device, ensuring precise and symmetric osteotomies between the screw fixations, thereby enabling reproducible CSBDs.

To enable bone cutting once the guide is positioned relative to the nail via the ancillary, the nail must be temporarily removed. To achieve this, holes in this cutting guide are strategically positioned to allow the placement of K-wires onto the bone, securing the cutting guide to the bone and permitting the temporary removal of the ancillary and nail to perform the osteotomy.

B. 4. Production & post-processing

The IMN was 3D-printed in titanium by Materialise NV (Leuven, Belgium) using Direct Metal Laser Sintering (DMLS) technology. The connector was fabricated in stainless steel via DMLS 3D-printing. All aiming tool components were produced in polyamide material using Selective Laser Sintering technology from Materialise NV (Leuven, Belgium). After the printing, post-processing steps included tapping

the proximal end of the nail to fix the connecting screw between the nail and the connector, and removing the excess material for the plug holes and screw holes in the nail in order to achieve a good fitting of the various elements, without excessive friction.

B. 5. Experimental study

Porcine model

Female Aachen minipigs (N=4, 40-55kg, Carfil Quality, Oud-Turnhout, Belgium) were used as a large animal model for CSBD creation and fixation[408]. This study was approved by the local ethics committee (Ref 2023/UCL/MD/39, approved on the 18th of July 2023). Each minipig was housed in our facilities for a minimum of 2 weeks before the surgery for acclimatization. Each animal was operated on both femurs.

Surgical procedure

The minipig was installed in ventral decubitus on a specific table to allow bilateral one-step surgery, under general anaesthesia (induction with an IM injection of 6mg/kg Zoletil 100® (Virbac, Carros, France) and 2mg/kg Rompun® (Bayer, Leverkusen, Deutschland), followed by endotracheal ventilation with Isoflurane (0-1.5\%, Forene®, AbbVie, Wavre, Belgium)). An intrajugular central line was set up to administer curare, appropriate analgesia, and anti-inflammatory drugs, and provide post-operative analgesia. A 2g bolus of Kefzol® (Natrium Cefazoline, Sandoz® Sol Inj, Novartis Company) was also administered at induction, followed by 1g Kefzol every 3 hours during surgery.

The hindquarter was washed with isobetadine soap, gently shaved, and disinfected with hydroalcoholic isobetadine. Classical surgical drapes allowed a sterile procedure. The surgical approach used a pure lateral incision centred on the femoral diaphysis, proximally extended for the proximal entry point of the nail in the greater trochanter. The intramedullary canal was reamed until a diameter of 9mm. The nail, connected with the ancillary, was inserted and its position was verified with fluoroscopy. The fixed cutting guide allowed the creation of a CSBD of 2.5cm long in the mid-shaft of each femur, centred to the nail. To ensure the reproducibility of the defect, all MBAs were scanned to detect morphological

discrepancies between the donor and host femurs. They were transplanted successively to the following minipig respecting the laterality.

Then, the nail was inserted again through the MBA in between both autologous femoral extremities and locked by fixation screws thanks to the ancillary and aiming plugs.

Post-operative follow-up

A post-operative fluoroscopy was performed immediately after the surgery to validate the osteosynthesis. Every 2 weeks, each minipig underwent standard X-rays (DigitalDiagnost, Philips, France) and a CT scan (beam collimation 0.6mm, tube voltage 140kV) until 3 months of follow-up. These imaging techniques allowed to verify potential material protrusion, displacement or breakage, consolidation, and healing kinetics.

Explant analysis

One minipig was euthanized just after the surgery to harvest MBA, another after 6 weeks, and the last two minipigs were euthanized after 3 months (IV bolus injection of T61, 0.2mg/kg). Both femurs of the last three minipigs were fully explanted with the IMN in place to assess the callus formation and to give a manual mechanical appraisal of consolidation.

C. Results

C. 1. Design of the 3D-printed IMN

IMN featuring depending on anatomical study

Every IMN feature is illustrated in Figure 102.

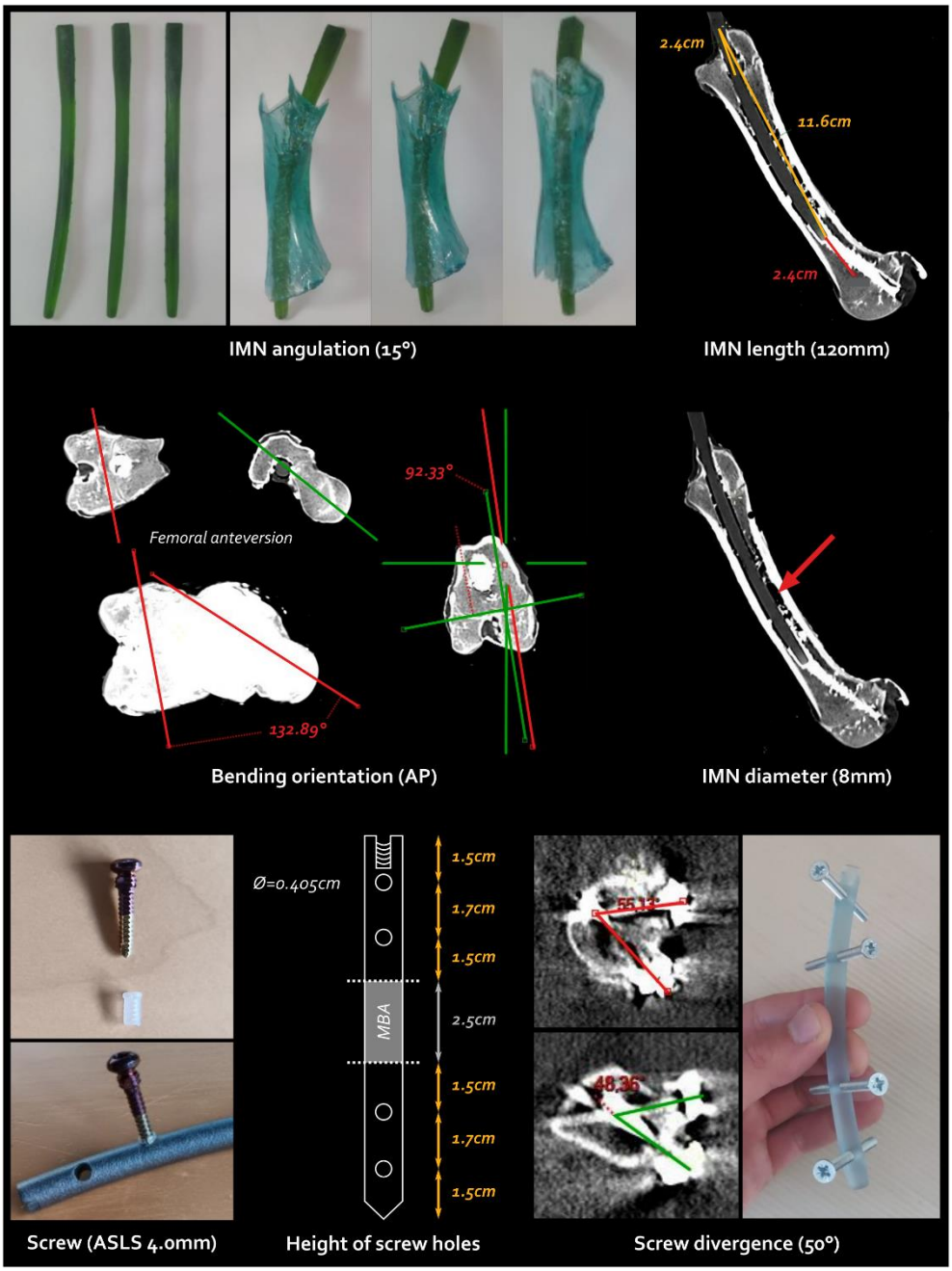

Figure 102. Every single step and feature of the intramedullary nailing (IMN) conception. The screw type is the ASLS screws illustrated at the bottom left, the cross-headed screws shown at the bottom right are pre-test screws. AP: anteroposterior, ASLS: angular stable locking system, Ø: diameter.

IMN bending and orientation = First, a femoral bending of 15° was calculated on CT scans. The IMN then featured a radius of curvature of 230mm. The insertion of the IMN test into an *in vitro* femur, through the intended entry point at the tip of the greater trochanter, led us to ascertain the spontaneous orientation of the IMN. Naturally, the IMN positioned itself with its curvature along the sagittal axis, with the concave curve oriented towards the posterior aspect. This alignment was corroborated by the CT scans, which matched the femoral anteversion (± 130°). This orientation further helped to create the ancillary in an orthogonal plane (90°) compared to the bending axis.

IMN length and diameter = Including this bending, the total IMN length and diameter were determined as 120mm and 8mm, respectively to fit at best the intramedullary canal.

Screw type = Angular Stable Locking System (ASLS, ©Depuy Synthes, Johnson & Johnson) screws were selected to ensure both angular and axial stability within the metaphysis due to the hourglass-shaped diaphysis while reducing the total number of screws[557,561–563]. This system incorporates three distinct core diameters in the screw, along with a resorbable plastic sleeve that expands into the nail with the second diameter of the screw, enhancing angular stability.

Number and height of screw holes = Another benefit of the bending orientation lies in the placement of lateral locking screws, in agreement with the direct lateral surgical approach. The increased stability offered by ASLS screws allowed for the use of only two bicortical screws on each side of the CSBD. Four holes strategically placed along the nail allowed for screw fixation via a lateral approach. Careful attention was paid to the symmetric positioning of the hole heights to prevent any weak points, ensuring the ostectomy was precisely centred within the fixation.

Screw divergence = A maximal divergence angle of 50° was applied, considering the space available within the surgical approach, to further enhance mechanical stability.

Final design of 3D-printed IMN, aiming tools & cutting guide

All the 3D-printed components including the IMN, the stainless steel connector, the ancillary, various plugs, as well as the cutting guide fixed on the ancillary are shown in Figure 103.

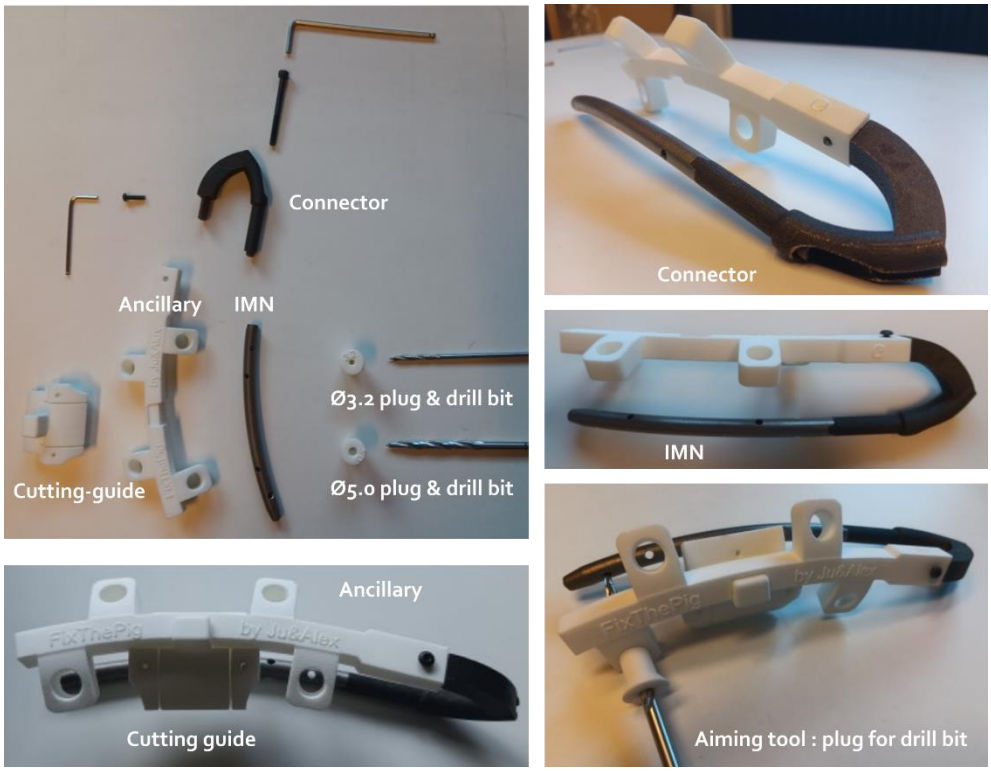

Figure 103. Different components of the intramedullary nailing (IMN) osteosynthesis. The IMN is connected with the ancillary through the connector. The ancillary unit holds the plugs of different diameters (Ø) to guide respective drill bits to the hole of the IMN. A cutting guide is designed to ensure the centralization of both osteotomies and can be clipped on the ancillary.

C. 2. In vivo implantation

During the surgeries, the ancillary and the cutting guide successfully allowed a symmetric double osteotomy. The ostectomy was easily performed and allografts were very reproducible without major morphology discrepancy based on subsequent CT scans analyses (Fig. 104).

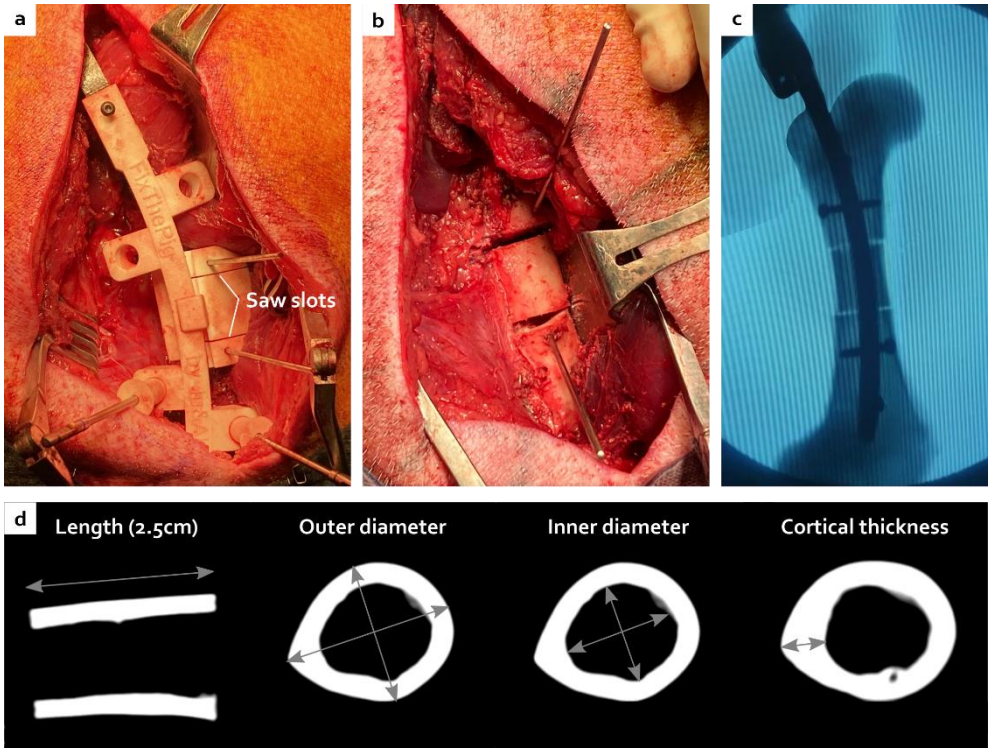

Figure 104. Creation of the critical-size bone defect with the ancillary and the cutting guide (a) leading to a centred ostectomy with reproducible morphology visible during the surgery (b), under fluoroscopy (c) and after CT scan analyses (d).

The proximal and distal metaphyses were very hard areas to go through. The proximal metaphysis was successfully permeabilized using a straight square awl to a depth of 5cm (Fig. 105 – a). However, no surgical instrument was able to penetrate the distal epiphysis (Fig. 105 – b). Therefore, of the three minipigs included in the follow-up, two received only one proximal screw as the nail was not fully inserted (Fig. 105 – c). The third one received two proximal screws as planned (Fig. 105 – d).

C. 3. Bone healing & consolidation with the custom-made IMN

X-rays and CT scans showed that the distal osteotomy was always perfectly reduced and fixed (Fig. 106).

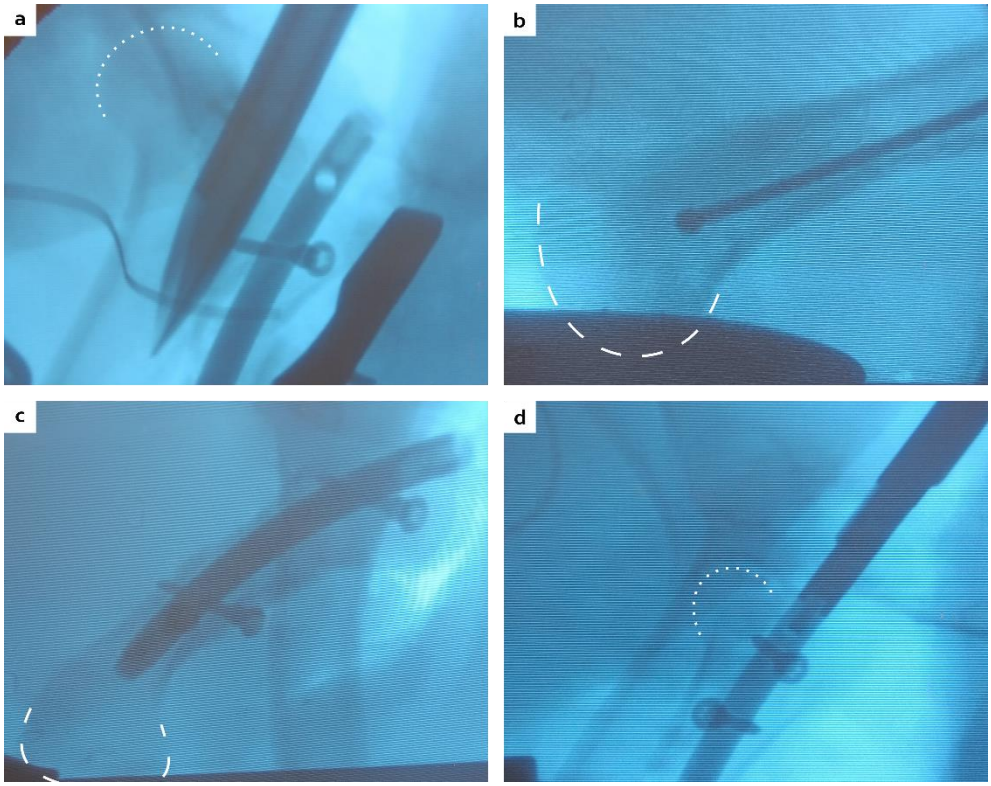

Figure 105. Peroperative fluoroscopies showing the physis passage with a straight square awl (a), the maximal distance reached by the ball-tipped guide wire (b), the final construct with the nail, two distal locking screws and only one proximal locking screw (c), or the double proximal locking screws (d). White dotted lines: femoral head contour, white dashed lines: condyle contour.

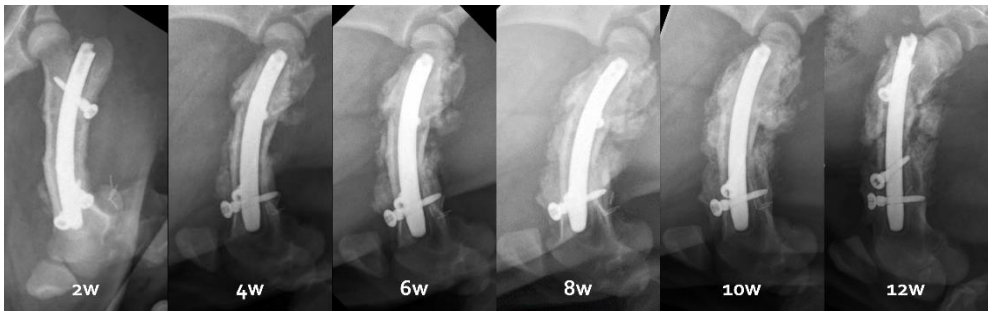

Figure 106. Radiological follow-up from 2 to 12 weeks illustrated by the right femur evolution of the third minipig.

However, for all 6 femurs, the proximal fragment was displaced in a flexed position and external rotation due to the action of the iliopsoas muscle (Fig. 107).

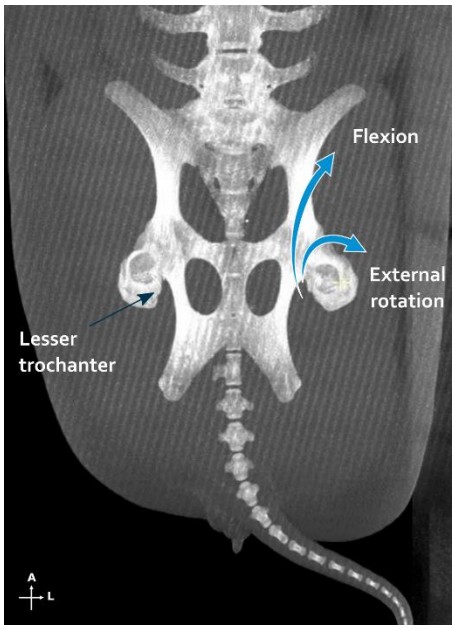

Figure 107. Iliopsoas muscle action illustrated by a maximum intensity projections on the multiplanar reconstruction of both femurs and pelvis. On the left side, the tendon insertion point is shown on the lesser trochanter, while on the right side, the action of the muscle is schematized. A: anterior, L: lateral.

This proximal fixation with only one screw led to hypertrophic callus suggesting pseudarthrosis in 3 of the 6 femurs. The one minipig receiving two proximal screws had to be euthanized at 6 weeks because of both sides proximal femur fracture.

C. 4. Explantation

Manual examination of femoral explants first confirmed pseudarthrosis on half of the proximal osteotomy junctions. Concerning the distal junction, only one right femur was manually not stable after 12 weeks. Every other distal junction was manually stable after 6 or 12 weeks (Video 4).

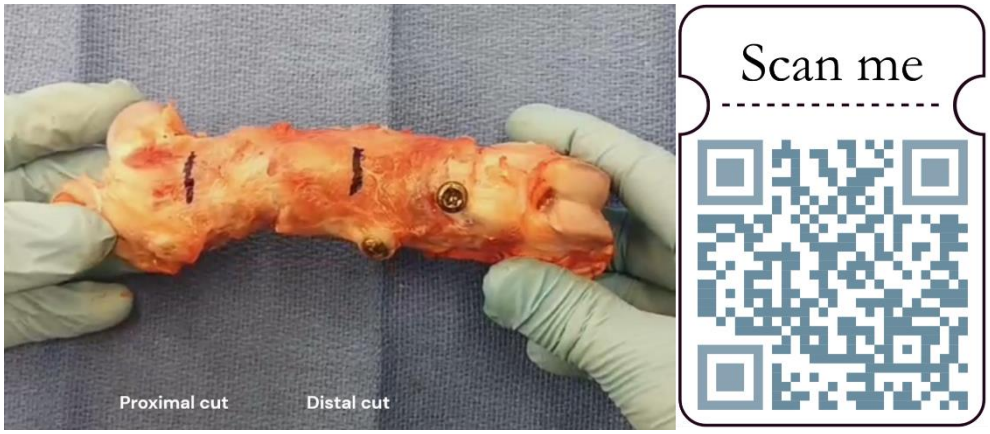

Video 4. Manual stability testing of a femur explant. Black marks located the further cut (1cm proximally and distally from both osteotomy junctions). https://zenodo.org/records/11061177.

D. Discussion

This study proposed a new concept of 3D-printed IMN for preclinical large animal models such as minipigs. The utilization of ancillary tools and cutting guides facilitated the achievement of a symmetric double osteotomy during surgeries. Moreover, the ostectomy process was executed smoothly, resulting in allografts with highly reproducible morphology. These findings underscore the efficacy of the surgical approach and the reliability of the instruments used.

However, the 3D design could still be slightly improved. Notably, during the surgical procedure, the ancillary was found to be susceptible to deformation by surrounding muscles. This can be linked to the deliberate placement of the ancillary in close proximity to the bone, which was intended to enhance stability of the overall assembly and improve the precision of the osteotomy. This placement should be revised to increase the distance between the ancillary and the bone, in addition to making the ancillary more rigid. Concerning the implants, manual examination of femoral explants confirmed the occurrence of pseudarthrosis in some instances at proximal osteotomy junctions. Nevertheless, all distal junctions appeared consolidated upon manual testing, except one.

Certain outcomes may hinge on technical refinements, particularly concerning enhancing mechanical stability. Macroscopic evaluations via X-rays and CT scans revealed perfect reduction and fixation at distal osteotomy sites, juxtaposed with challenges encountered in maintaining consistent reduction at proximal fragments. This imperfect alignment often resulted in hypertrophic callus formation, as evidenced by cases receiving only one proximal screw. In a severe case, proximal femoral fractures necessitated the euthanasia of the pig receiving two proximal screws. As with human femoral nails, the entry point is crucial for the successful placement of the nail[564–566]. In this study, human anatomical landmarks were adapted for use in the porcine femur through radiological anatomical studies. The nail must be initially inserted before creating the osteotomy, allowing for optimal positioning relative to the intact femoral anatomy. This approach minimizes the risk of poor reduction that can result from an improperly located initial entry point, as often seen in femoral fracture reductions. Mechanically, a single proximal screw may permit excessive mobility at the osteotomy site, while two screws might render the construct overly rigid and misaligned with forces transmitted during weightbearing, thereby increasing the risk of fracture. Potential adaptations could involve employing a reduction clamp to stabilize the reduction prior to fixation, shortening the IMN length to accommodate two screws below or at the level of the femoral neck, or designing the upper screw as a cephalic screw to better distribute weightbearing forces, akin to practices in human femoral IMNs. Furthermore, in this study, the loss of bone substance created by the saw blade is not replaced as a graft is transplanted from one pig to another successively. This millimetre loss of height could slightly shorten the femoral length and accentuate the proximal protrusion of the nail. The addition of a mechanical compression system on the nail or the ancillary could prove advantageous in enhancing interfragmentary contact and compression, especially considering the challenges of manual compression during these procedures. Using a sigmoid or step cut technique on at least one side of the MBA could help minimize rotational instability and increase the surface area of bone contact[567,568].

Furthermore, although potentially less rigid[556], titanium alloy hardware in IMN procedures minimized artifacts, thereby enhancing the accuracy of imaging analyses compared to plates or external fixation methods, or other alloys[569].

In investigations concerning substantial bone defects, the pig model has proven notably advantageous when compared to sheep and goats or rabbits[59,109,400,570], particularly in terms of bone mineral density, anatomy, structure, morphology, healing process, and remodelling[59]. Even with its plexiform predominance over dense Haversian structure[59], porcine bone shows the closest resemblance to human samples[59,399,400]. The main issues with the pig model are its ease of handling and its high growth rates[59,400], why minipig was proposed. Since the IMN production was based on a 3D-printed titanium scaffold, the design could be easily adapted to all different bones or animal species according to a preliminary anatomical analysis.

Additionally, the IMN design allows for precise and reproducible CSBD creation and treatment keeping surrounding soft tissues intact. Studies focusing on OM wrapping a CSBD could benefit from an accurate placement of the membranes, ensuring uniform coverage and interaction with the filling bone graft, without being compressed by plates. By facilitating a controlled environment, the IMN system enables a more accurate assessment of the membrane efficacy in enhancing bone regeneration and provides a reliable tool for future investigations into optimizing guided bone regeneration techniques.

In conclusion, this study demonstrated the feasibility of 3D designing an IMN osteosynthesis for preclinical large animal models, like Aachen minipigs, and the ability to multiply surgical techniques and tools according to the specific needs of rigorous and demanding research, such as the implantation of an MBA and a surrounding OM.

Paper 8 – A single Angiofil-latex injection for both radiological and anatomical assessment of arterial territories in the limbs

Julie Manon, Gaspary Fodjeu, Robin Evrard, Lucien Van den Broeck, Mathieu Jacob, Emmanuel Coche, Olivier Cornu, Catherine Behets†, Benoît Lengelé†

† Share last authorship

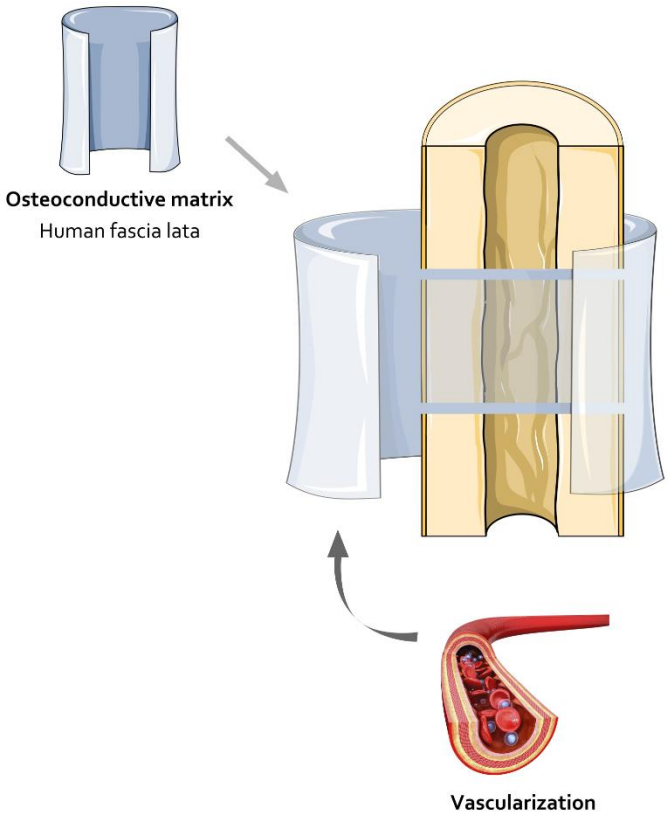

Published in

Annals of Anatomy (IF=2.976)

doi: 10.1016/j.aanat.2024.152312

Abstract

Introduction: Postmortem evaluation of the human vascular system has a long history, with advancements ranging from dissections to modern imaging techniques like CT scans. This study designs a novel combination of Angiofil, a liquid radiopaque polymer, and latex, a flexible cast material, for cadaveric vascular analysis.

Material & methods: The aim was to synergize the advantages of both components, providing accurate radiological images and optimal dissection conditions. Three arterial territories (lateral circumflex femoral artery, profunda brachii artery, and radial artery) were injected and assessed through CT scans and dissections.

Results: The Angiofil-latex mixture allowed successful visualization of the vascular networks, offering a simple, reproducible, and non-toxic approach. Quantitative assessments of the three territories, including diameters and lengths, showed comparable results between CT scan and dissection.

Discussion: The technique precision and versatility make it an accessible and valuable tool for anatomical studies, potentially extending its application to MRI analyses. Overall, the Angiofil-latex combination presents a cost-effective solution for researchers, offering enhanced visibility and detailed anatomical insights for various applications, including anatomical variation studies.

Graphical abstract

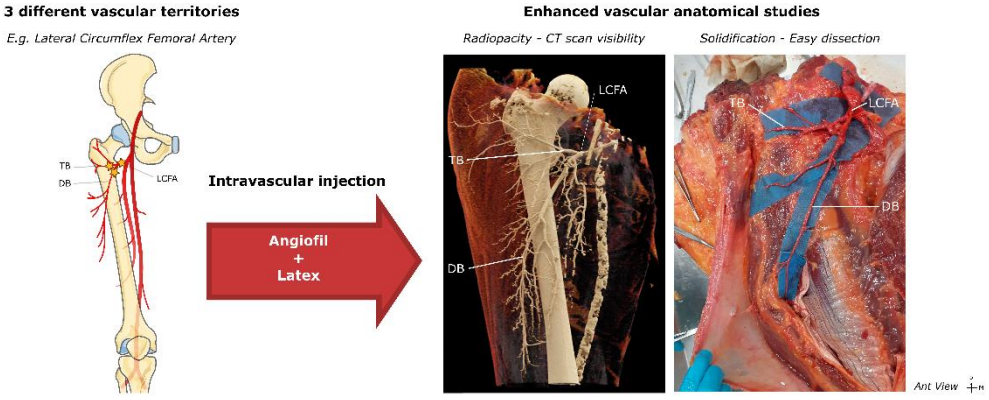

A. Introduction

The human vascular system has been studied postmortem for centuries. The precise description of its anatomy, including its variations, is crucial for further use in education, pathology, forensic medicine, or surgical planning, such as in vascularized flap reconstructions[571,572]. During the 16th century, Andreas Vesalius and Leonardo da Vinci laid the foundation for human vascular anatomy through extensive dissections of cadavers[573–575,571,576,572]. Over the years, numerous intravascular injection techniques have been reported, varying from different liquid-coloured dyes to wax casts (fluid that solidifies intravascularly) and increasing the visibility of blood vessels during dissection[575,571,577,500]. The development of X-rays and CT scans allowed to study human vascular system more extensively in a less invasive way thanks to the injection of radiopaque contrast agents, such as barium, lead oxide, or iodine[572,575,578], even if dissection, direct visualization, and conventional autopsy remained the gold standards[579].

Nowadays, contrast agents and vascular cast materials remain commonly used in postmortem evaluation of vascular anatomy, but separately. Both techniques have advantages and limitations. Studies using contrast agents are typically non-invasive. Most of them are used efficiently *in vivo*, in the diagnosis of vascular diseases or preoperative planning[572]. The main limitations are the agent penetration, the machine resolution, and the allergic reaction risk[580–582]. On the other hand, postmortem injection of coloured casting material provides a detailed 3D view of the vascular tree, including anatomical variations and relationship to other soft tissues or solid organs that are not visible under X-ray. However, this technique is invasive and restricted to cadavers, limiting its use to research, forensic medicine, and educational purposes. Its resolution depends on the degree of penetration and the dissection precision.

Nevertheless, a good mixture for cadaveric vascular studies might combine a suitable radiologic contrast, a coloured macroscopic appearance facilitating the identification of vessels, and a proper solidification over time giving sufficient elasticity for vascular dissections and measurements[572]. Among the various substances available, Angiofil and latex have garnered attention for their unique properties and applications.

Angiofil is a radiopaque liquid polymer based on lipophilic iodine that offers excellent radiological visibility due to its adjustable viscosity and the absence of sedimentation[583]. As an oily contrast agent[579], it has the advantage of its intravascular retention for days after injection without any extravasation[571,572,583,584]. Moreover, histological analyses are not influenced by its injection[585].

Latex is a flexible and resilient cast material that visually guides the gross dissection while preserving vessel integrity thanks to its elasticity[572,575,586]. When injected into blood vessels, latex hardens, creating a 3D replica of the vascular system. With the addition of a few drops of dye, it provides an excellent macroscopic visibility greatly facilitating meticulous dissection[586]. Its manipulation is easy and leads to reproducible results[572]. Delayed analyses are possible thanks to the rigid intravascular moulding. Since pre-vulcanized stabilized with ammonia, the latex might also be used as a suspending medium for lipophilic radiopaque agents[575]. To our knowledge, both these compounds have not yet been associated in a single intravascular injection.

The aim of this study was to develop a simple, cheap, reproducible, and non-toxic mixture of Angiofil and latex for cadaveric anatomic analysis of arteries of the upper and lower limbs. To synergize the advantages of Angiofil and latex in a single vascular injection could lead to a robust methodology that goes beyond the limitations of individual techniques. This research evaluates if this combination could provide both accurate radiological images and optimal dissection under facilitated conditions, from a qualitative and a quantitative point of view.

B. Materials & Methods

B. 1. Human specimens and arterial territories

Human cadaveric donors were received from the Human Anatomy Department of UCLouvain (IRB00008535, Brussels, Belgium). Distinct limbs were harvested for each vascular territory, following local ethics committee authorization (Ref 2021-30AOU-356, approved on the 13th of September 2021). Respective limbs were cut and immediately fresh-frozen within 24-36 hours of death. Three vascular

territories were assessed, namely the LCFA, the profunda brachii artery (PBA), and the radial artery (RA). Demographics of each specimen set are collected in Table 33.

Table 33. Demographics of each set of five samples for each vascular territory.

	Number of limbs	Number of donors	Sex	Age *(mean ± SD)*	Laterality
LCFA	5	4	3 ♂ / 1 ♀	73.3 +/- 19.1	4 L / 1 R
PBA	5	4	2 ♂ / 2 ♀	73.2 +/- 9.3	4 L / 1 R
RA	5	4	2 ♂ / 2 ♀	82.1 +/- 13.5	2 L / 3 R

SD: standard deviation, LCFA: lateral circumflex femoral artery, PBA: profunda brachii artery, RA: radial artery, ♂: men, ♀: women, L: left, R: right.

The limbs were thawed upside down to bleed out at RT for at least 24 hours. The upper limbs were hung by the fifth finger and the lower limbs by the hallux. The blood leaving the vascular system was collected including blood liquid and clots to approximate the fluid volume to be injected next. The physical integrity of the limbs was also inspected (skin aspect, existence of possible lesions, bruises, scars, or other variants of normality).

B. 2. Rinse

All the following steps were performed with the limb lying on a dissection table. Each specimen was rinsed through a main artery upstream of the artery of interest in order to keep the latter as intact as possible and prevent the leakage of rinse or injection. A minimal dissection was made from the proximal extremity of lower and upper limbs to identify the arterial bifurcation between the femoral artery (FA) and the PFA, and between the brachial artery (BA) and the PBA, respectively. In the limbs reserved for analysis of RA territory, a minimal skin incision was made medially to the biceps brachialis tendon in order to locate and dissect the BA.

Each main artery (FA and BA) was cut to insert a metal rinsing cannula, which was clamped to ensure an airtight connection. The cannula was connected with a purged plastic tube to a glass jar filled with 0.9% NaCl solution preheated to 56°C. Subsequently, a pump permitted to circulate (max speed: 30rpm) 400mL, 1L, and 2L of physiological fluid through the arterial network to fully rinse it, for the RA, PBA, and LCFA territories, respectively. The clearing of the venous outflow

attested the efficacy of the rinse. Attention was paid to possible swelling of soft tissues.

B. 3. Angiofil-latex injection

Preliminary tests were conducted on extra specimens (details not reported in this study) to adjust the Angiofil concentration in the mixture and identify potential pitfalls during the establishment of the technique. The preliminary results, which were used to establish the systematic approach of the technique, were not considered in this study.

The injection was performed into the arteries of interest, namely the LCFA, the PBA, and the RA. Their dissection was carried out carefully in order to avoid cutting small collaterals, as well as leakage and accumulation of mixture outside the vascular tree for cleaner radiological and anatomical images.

The LCFA and the PBA were dissected anterogradely. For the RA, a second cutaneous incision was made in the forearm, following a volar Henry's approach[587,588]. The incision started at the distal forearm, between the styloid process of the radius and the flexor carpi radialis tendon. It was extended proximally in the distal third of the forearm, towards the trochlea of the humerus.

After locating and dissecting the artery of interest, a catheter (14-22G, depending on the diameter of the artery, Terumo, Versatus-W) was inserted and fixed with surgical thread (Surgilon™ 2.0). A mixture of latex (Latex "LA", with 0.38% ammoniac, 603, Finres) added with a 20% volume of liposoluble iodine-based agent (Angiofil, S500.0028, Fumedica AG, Switzerland) (1:5 mixture Angiofil: latex, v/v), and a few drops of red dye (Jesmonite, bright red pigment, 200g, Finres) was prepared and shaken by hand at RT until a homogeneous appearance. The mixture was injected into the artery under continuous manual pressure on the syringe. Several limbs were injected under fluoroscopy to visualize the contrast agent progression, to correlate the manual pressure perceived and arterial filling, and to make sure the vascular system was completely filled. The injection volume was estimated on the venous drainage volume. After the volume was injected, the artery was clamped over the catheter to maintain the fluid pressure, ensuring the dissemination to smaller vessels and avoiding any reflux.

B. 4. Angioscanner

The injected limbs were positioned in a fully extended position in the CT scan. The various acquisitions were performed on a Somatom Definition AS 128 scanner (Siemens Healthineers, Erlangen, Germany). The acquisitions were conducted in ultra-high-definition mode (beam collimation 0.3mm, tube voltage 120kV, tube current 200-250mAs). Subsequently, they were reformed using both hard and soft kernels with a slice thickness of 0.4mm. Volume rendering, a post-processing technique[465,466], allowed reconstructions and complex anatomical analyses, using the Syngo.Via tool in cinematic rendering mode. This step was performed the same day as the vascular injection or the next one, as the Angiofil-latex mixture does not need to be solidified to visualize its route. However, for the next step (dissection), it was primordial to place the limb in a cold room (4°C) for 72 hours to permit rigidification.

B. 5. Dissections

All collateral and terminal branches of the artery of interest were identified. The dissection of the LCFA followed previously established protocols[444,446,290,291]. The skin incision was made 1cm medially to the standard landmark between the ASIS and the lateral border of the patella (Fig. 108 – a) in order to preserve the perforator vessels which were further dissected. The DB of the LCFA was always found distally through the intermuscular fascia between the vastus lateralis and the rectus femoris. The LCFA was retrogradely dissected including the DB and the transverse branch (TB) until the PFA proximally, and anterogradely through the vastus lateralis muscle or its fascia until the perforators distally.

The PBA was dissected using a posterior approach of the arm, followed by an anterior approach of the elbow (Fig. 108 – b). The skin was incised following a line between the olecranon and the humerus surgical neck. The lateral and long heads of the triceps brachialis muscle were discarded in order to enter into the radial groove. The radial nerve and the PBA were identified and dissected. The proximal humeral insertion of the lateral head of the triceps brachialis was cut to highlight all collateral branches of the PBA, *i.e.* the radial collateral artery (RCA) and the medial collateral artery (MCA).

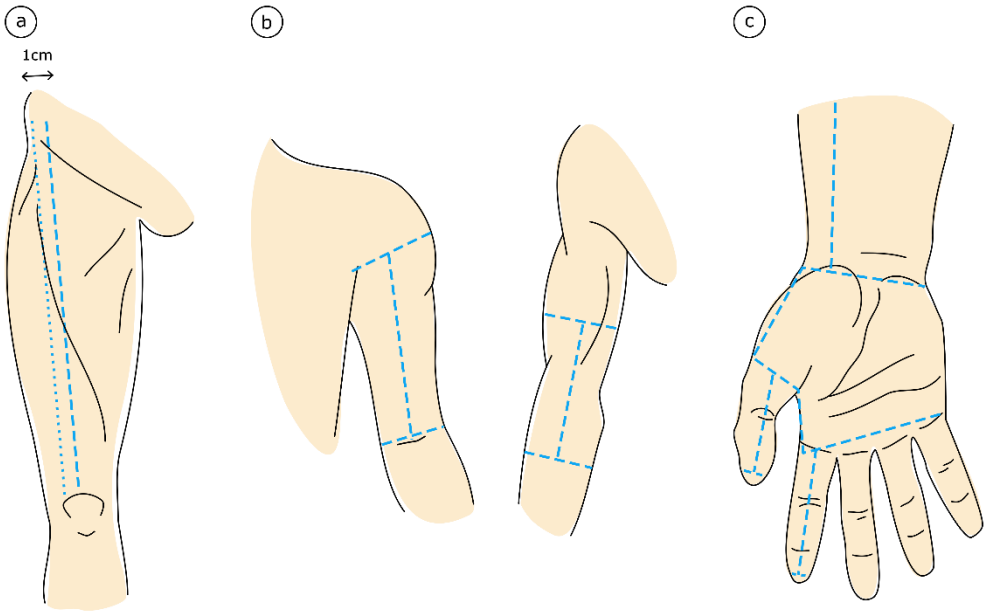

Figure 108. Landmarks for skin incisions (blue dashed lines) in the corresponding anatomical region, for the lateral circumflex femoral artery (LCFA) territory (a), the profunda brachii artery (PBA) territory (b), and the radial artery (RA) territory dissections (c). The blue dotted line (a) represents the theoretical skin incision to perform an anterolateral thigh flap.

To allow a better global view of the ramifications of the PBA, the palmar region of the arm and the elbow was also exposed through a mid-line anterior incision. On the medial side, the superior ulnar collateral artery (SUCA) and inferior ulnar collateral artery (IUCA) were dissected anterogradely from the BA. The bifurcation of the BA into radial and ulnar arteries was identified. Their respective radial recurrent artery (RRA) and ulnar recurrent artery (URA) joined the RCA, MCA, and ulnar collaterals in the articular network of the elbow.

For the RA territory, the dissection began by extending the radial incision distally around the palm until the base of the little finger (Fig. 108 – c). The first and second fingers were also incised to their tip. The superficial palmar aponeurosis was removed to expose and dissect the superficial palmar branch (SPB) of the RA, the superficial palmar arch (SPA) and its branches, with a specific focus on the ulnar palmar digital artery of the index (UPDAI). Subsequently, the SPA as well as flexor tendons were transected at the level of the carpal tunnel and retracted upward. The carpometacarpal joint of the thumb (trapezometacarpal joint) was

disarticulated to provide clear visibility of the entire course of the RA. Furthermore, the deep palmar arch (DPA) and the palmar arteries of the thumb, namely the radial palmar digital artery of the thumb (RPDAT) and the ulnar palmar digital artery of the thumb (UPDAT), known to rise from the princeps pollicis artery, were dissected. The first common palmar digital artery (CPDAI), the radialis indicis artery (RIA, synonym of the radial palmar digital artery of the index), the first (M1), second (M2), and third (M3) palmar metacarpal arteries were also explored.

B. 6. Quantitative analyses

In addition to usual qualitative assessment, diameters and lengths of three arterial territories in limbs were quantified and compared. During the dissection, a digital calliper (resolution=0.01mm ± 0.03mm) and a metal ruler were respectively used to measure artery diameters (Ø) at different specific levels (Fig. 109), and the length from their origin to their termination. Globally, the ØLCFA was taken at its origin, such as for the ØDB and the ØTB. The ØPBA and collaterals were taken at their origin and their end, assuming to be at the thinnest zone of the anastomosis of respective recurrent arteries. The ØRA was measured at the top of the radial styloid process. The diameter of digital arteries was measured at three locations: the metacarpophalangeal joint (MCP), the proximal interphalangeal joint (PIP), and the distal interphalangeal joint (DIP), or interphalangeal joint (IP) for the thumb.

As for the length of the LCFA vascular tree, the length of perforators was taken. The perforators were classified following the Yu's classification[445]. This classification is based on three localizations, *i.e.* A being the most proximal perforators of the thigh, B the middle ones, and C the most distal ones. Two lengths were measured for each perforator, *i.e.* the total length and the perforator length. The total length started from the bifurcation between the PFA and the FA until the location of the perforation of the fascia lata. The perforator length started from the origin of the perforator on its corresponding branch (TB or DB) until the location of the perforation. The RA length was measured from the radial styloid process to the origin of the deep palmar artery (DPA). The length of all the other arteries was measured from their origin to their end.

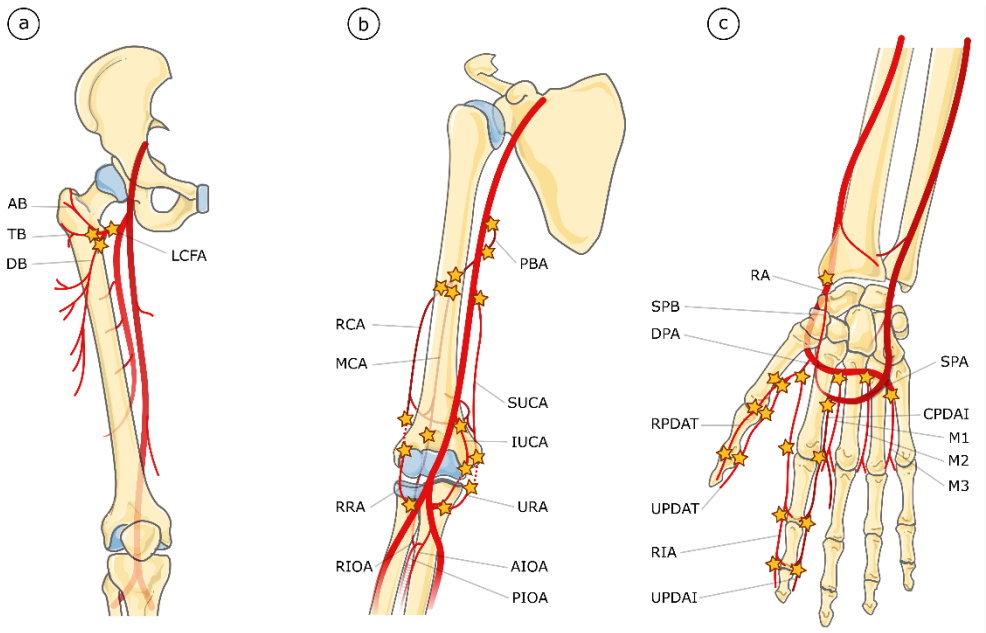

Figure 109. Location of diameter measurements (yellow stars) in the LCFA territory (a), the PBA territory (b), and the RA territory (c). LCFA: lateral circumflex femoral artery, AB: ascending branch, TB: transverse branch, DB: descending branch, PBA: profunda brachii artery, RCA: radial collateral artery, MCA: medial collateral artery, SUCA: superior ulnar collateral artery, IUCA: inferior ulnar collateral artery, RRA: radial recurrent artery, URA: ulnar recurrent artery, RIOA: recurrent interosseous artery, AIOA: anterior interosseous artery, PIOA: posterior interosseous artery, RA: radial artery, SPB: superficial palmar branch of the RA, DPA: deep palmar arch, RPDAT: radial palmar digital artery of the thumb, UPDAT: ulnar palmar digital artery of the thumb, RIA: radialis indicis artery, UPDAI: ulnar palmar digital artery of the index, SPA: superficial palmar arch, CPDAI: common palmar digital artery of the index, M1: 1st palmar metacarpal artery, M2: 2nd palmar metacarpal artery, M3: 3rd palmar metacarpal artery.

Concerning CT scans, all the measurements were taken on a dedicated software (Carestream Health, Vue PACS, v. 12.1.5.5151, Philips Medical Systems, the Netherlands), using the MIP on multiplanar reconstruction. Diameters and lengths were measured at exactly the same locations as those performed during dissection.

B. 7. Statistics

Descriptive analyses first characterized the independent quantitative values. Data were expressed as the mean +/- SD, and/or by boxplots and histograms. Their

distribution was assessed by QQ plots and Shapiro-Wilk tests. Since not every distribution was normal and due to the small sample size, nonparametric Wilcoxon paired tests were performed. The level of significance was determined at 0.05. The agreement between measurements obtained from dissection and CT scan was assessed using the Intraclass Correlation Coefficient (ICC). ICC was calculated using a two-way mixed model with absolute agreement, where each measurement was considered a single observation among a larger dataset. All statistics were made using SPSS software (V.27, IBM SPSS, Inc., Chicago, IL, United States).

C. Results

The injected volume of Angiofil-latex ranged from 9mL to 10mL (average 9.6 +/- 0.9mL) for the LCFA, 7mL to 20mL (average 13.1 +/- 5.2mL) for the PBA, 5.5mL to 10mL (average 7.5 +/- 1.7mL) for the RA to fill in the vascular tree. The death-to-perfusion time was 971.4 +/- 1494.8 days.

C. 1. Preliminary results

During the establishment of the technique, the main pitfalls were pre-studied and revealed blood clots, leakage, and air bubbles as technique failure (Fig. 110). Blood clots are crenelated in the opposite of air bubbles that are rounded thanks to their surface tension. Blood clots were seen after an insufficient rinse and air bubbles after air injection within the mixture. Leakages usually occurred after a not enough meticulous dissection disrupting small collaterals.

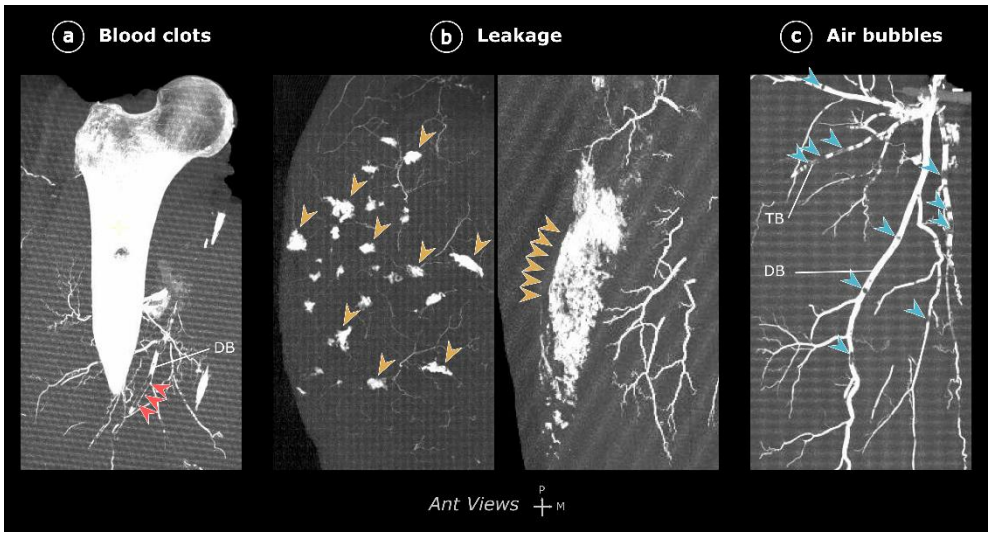

Figure 110. Injection flaws illustrated by maximum intensity projections (MIP) on the multiplanar reconstruction of the LCFA territory. Defects in injection include residual blood clots (a), contrast agent leakage (b), and injection of air bubbles (c). Leakage can be seen in different planes including in the subcutaneous layer (b – left), or the subfascial compartment (b – right). DB: descending branch, TB: transverse branch, Ant: anterior, P: proximal, M: medial.

C. 2. Qualitative observations

The vascular network of the three arteries of interest was visualized on the CT scan (Fig. 111 – above). For the LCFA territory, both the TB and DB were opacified as well as their ramifications. The FA was not opacified but exhibited many calcifications which have the same density as the Angiofil. The PBA territory also showed a complete filling with a retrograde opacification of the BA territory, including the RA, the ulnar artery (UA), and the recurrent arteries of the elbow (RRA and URA respectively). For the RA territory, the opacification went until the small subcutaneous arteries of fingers. The latex was solidified in all specimens and allowed a rigorous dissection thanks to a macroscopic enhancement of the artery visualization (Fig. 111 – below). The protocol also allowed to highlight anastomoses. For example, despite a single injection into the RA, the distal vascular network of the UA was systematically observed and filled with the Angiofil-latex mixture (Fig. 111 – c).

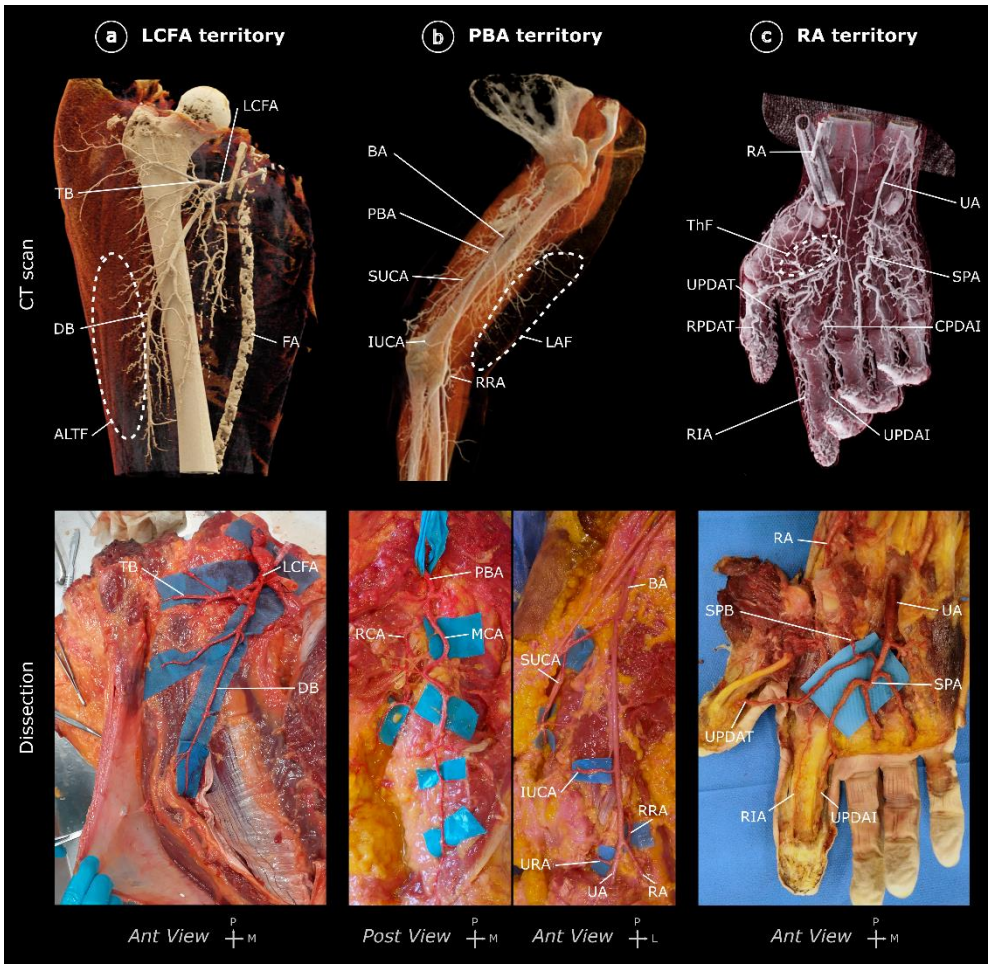

Figure 111. Visualization of the LCFA territory (a), the PBA territory (b), and the RA territory (c), after 3D reconstructions post-CT scan (above), and after dissection (below). Each sample originated from distinct donors. LCFA: lateral circumflex femoral artery, TB: transverse branch, DB: descending branch, ALTF: anterolateral thigh flap, FA: femoral artery, BA: brachial artery, PBA: profunda brachii artery, RCA: radial collateral artery, MCA: medial collateral artery, SUCA: superior ulnar collateral artery, IUCA: inferior ulnar collateral artery, LAF: lateral arm flap, RRA: radial recurrent artery, URA: ulnar recurrent artery, RA: radial artery, UA: ulnar artery, ThF: thenar flap, UPDAT: ulnar palmar digital artery of the thumb, RPDAT: radial palmar digital artery of the thumb, RIA: radialis indicis artery, UPDAI: ulnar palmar digital artery of the index, CPDAI: common palmar digital artery of the index, SPA: superficial palmar arch, SPB: superficial palmar branch of the RA, Ant: anterior, Post: posterior, P: proximal, L: lateral, M: medial.

Furthermore, the combination of Angiofil-latex injection with 3D angioscanner reconstructions also allowed to emphasize, with an increased definition, the numerous perforator vessels supplying the skin territory of the antero-lateral thigh flap (Fig. 111 – a), on the PBA, the cutaneous area of the lateral arm flap (Fig. 111 – b), and on the SPB, the skin paddle of the thenar flap (Fig. 111 – c).

The small subcutaneous vessels were properly filled with Angiofil-latex and were visible during fluoroscopy, CT scan, and dissection (Fig. 112). The smallest visualized artery reached the maximal precision permitted by the CT scan resolution (0.3mm). This resolution however allowed to precisely observe the numerous tiny cutaneous side branches of the palmar digital arteries supporting the blood supply of the Littler's latero-digital flap, as well as the pulpar arterial network supplying the Atazoy's pulpar advancement flap.

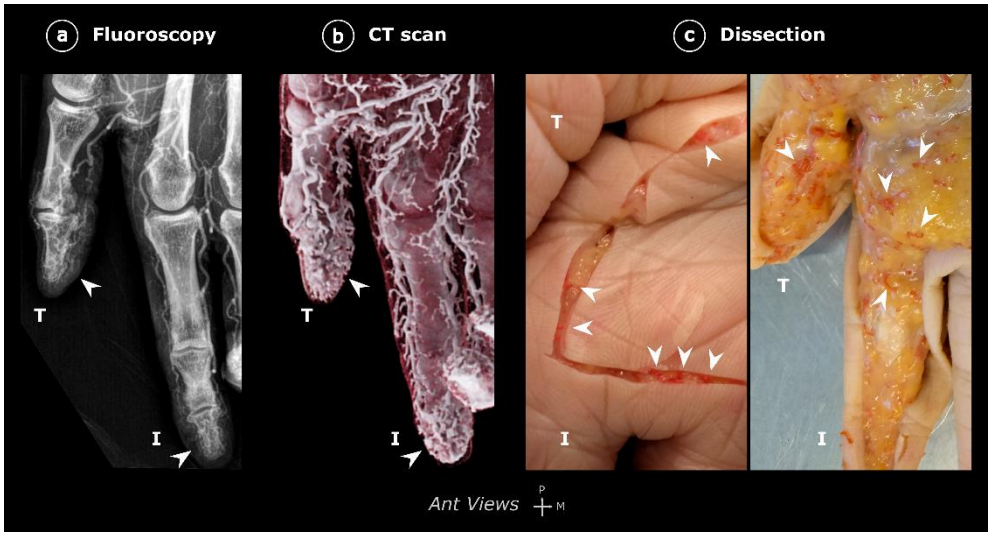

Figure 112. Visualization of the small subcutaneous arteries (white arrowheads) of the thumb and the index, filled with Angiofil-latex on fluoroscopy (a), CT scan (b), and dissection (c). T: thumb, I: index, Ant: anterior, P: proximal, M: medial.

However, one of the five upper limbs presented a leakage of Angiofil-Latex mixture out of the origin of the PBA. This vascular territory was not correctly opacified and the quantitative analyses were not possible.

This protocol allowed to precisely study individual anatomical variations. As an example, the vascularization of the thumb is classically described as primarily

dependent on the princeps pollicis artery[589,590]. This artery would come from the RA after it crosses the first intermetacarpal space, then move towards the thumb and divide into two palmar digital arteries (UPDAT and RPDAT). In our study, those two branches were identified in each hand. However, out of the five dissected hands, only one exhibited a princeps pollicis artery. In the remaining four hands, UPDAT and RPDAT had different origins from the conventional pattern (Table 34).

Table 34. Origin of the two palmar digital arteries of the thumb.

Subjects	Origin of UPDAT	Origin of RPDAT
1	Deep palmar arch	Radial artery (palmar superficial branch)
2	Superficial palmar arch	Radial artery
3	Superficial palmar arch	Radial artery
4	Deep palmar arch	Radial artery (palmar superficial branch)
5	Princeps pollicis artery	

UPDAT: ulnar palmar digital artery of the thumb, RPDAT: radial palmar digital artery of the thumb.

C. 3. Diameters of arteries

Angiofil-latex injection enabled to fill arteries of many different diameters from the larger one in the LCFA (ØLCFA=6.40 +/- 1.66mm) to the smallest ones in the RPDAT at the IP joint (ØRPDAT=0.53 +/- 0.06mm) or the RIA at the DIP joint (ØRIA=0.53 +/- 0.11mm). The diameter consistently decreased as the artery progressed distally (*e.g.* $ØRPDAT_{origin}$=1.13 +/- 0.20mm, $ØRPDAT_{IP}$=0.53 +/- 0.06mm), or from a proximal artery to a more distal one (*e.g.* ØLCFA=6.40 +/- 1.66mm, ØDB=4.27 +/- 0.92mm). This observation was similar even after dissection as on the CT scan (Fig. 113). On the contrary, arteries of the same level have the same diameters (*e.g.* ØMCA=1.40 +/- 0.29mm, ØRCA=1.45 +/- 0.29mm). However, even if the central tendencies (means and medians) seem often higher on the CT scan than on dissection (*e.g.* mean $ØM1_{CT\ scan}$=1.09 +/- 0.23mm and mean $ØM1_{dissection}$=0.92 +/- 0.27mm respectively), statistical difference was not often observed between both techniques (Supplementary data – Table 35). The variabilities of the data were also similar between CT scan and dissection measures. This point is illustrated by the height of the boxplot in Figure 113 (and the SD in Supplementary data – Table 35). This suggests that the dispersion of the measured values remains consistent between the two groups. The ICC was 0.978 (IC95% 0.964 – 0.986), which indicates highly consistent and reliable methods.

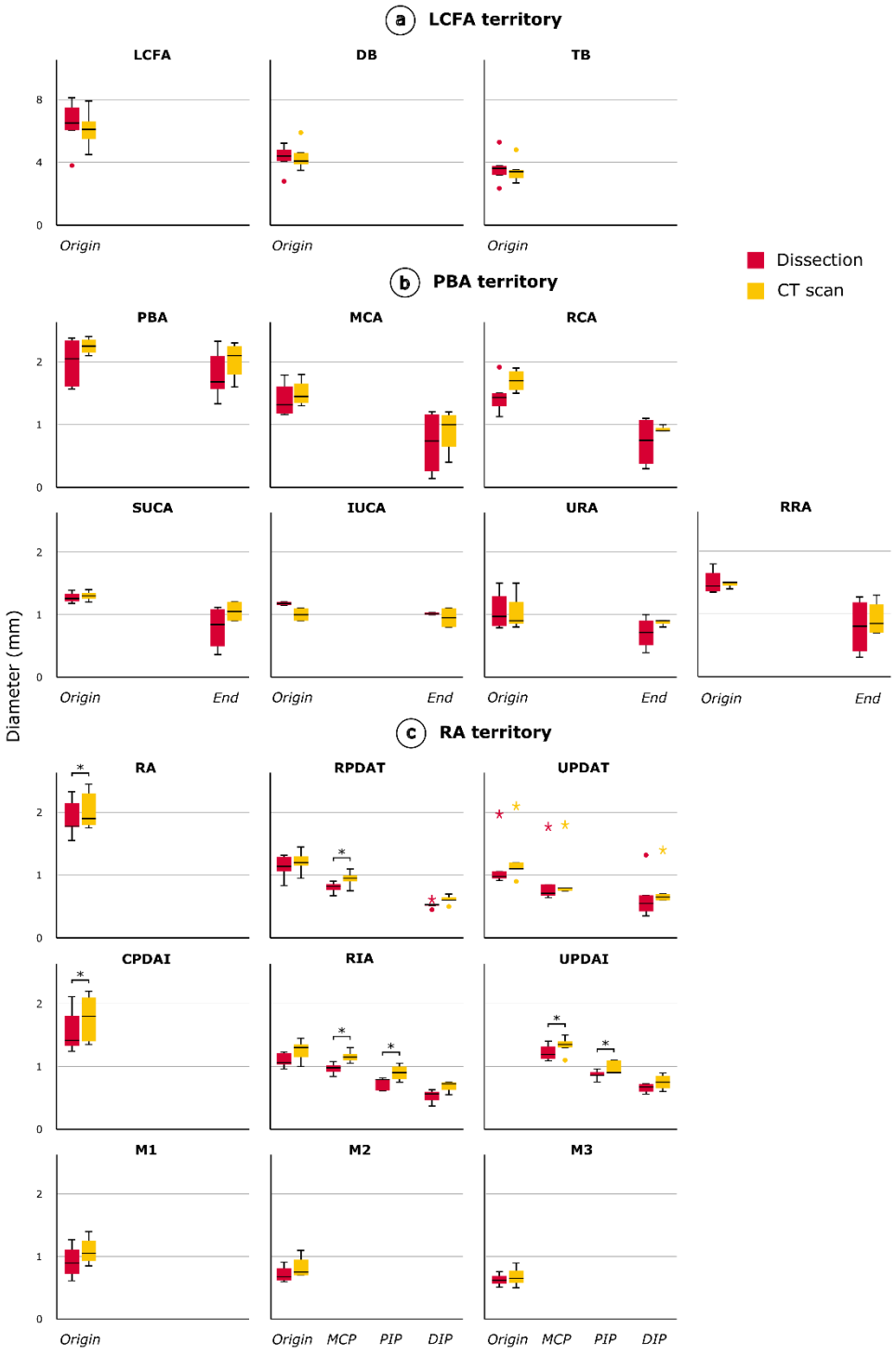
a LCFA territory
LCFA
DB
TB
b PBA territory
PBA
MCA
RCA
SUCA
IUCA
URA
RRA
c RA territory
RA
RPDAT
UPDAT
CPDAI
RIA
UPDAI
M1
M2
M3
Dissection
CT scan
Diameter (mm)
Origin
End
MCP
PIP
DIP

*Figure 113. Boxplots of artery diameter of the LCFA territory (a), the PBA territory (b), and the RA territory (c), and their comparison between dissection and CT scan measurements. LCFA: lateral circumflex femoral artery, DB: descending branch, TB: transverse branch, PBA: profunda brachii artery, MCA: medial collateral artery, RCA: radial collateral artery, RRA: radial recurrent artery, SUCA: superior ulnar collateral artery, IUCA: inferior ulnar collateral artery, URA: ulnar recurrent artery, RA: radial artery, RPDAT: radial palmar digital artery of the thumb, UPDAT: ulnar palmar digital artery of the thumb, CPDAI: common palmar digital artery of the index, RIA: radialis indicis artery, UPDAI: ulnar palmar digital artery of the index, M1: 1st metacarpal artery, M2: 2nd metacarpal artery, M3: 3rd metacarpal artery, MCP: metacarpophalangeal joint, PIP: proximal interphalangeal joint, DIP: distal interphalangeal joint. For the thumb arteries (RPDAT and UPDAT), the DIP joint localization corresponds to the interphalangeal (IP) joint. Yellow and red dots: outliers, yellow and red stars: extreme outliers, black *: p<0.05.*

C. 4. Length of arteries

Most of the data were not significantly different between both techniques (Fig. 114). Only the total length of B perforators (dissection=18.4 +/- 4.1cm, CT scan=16.3 +/- 3.8cm), RA (dissection=6.24 +/- 0.21cm, CT scan=6.56 +/- 0.25cm), UPDAT (dissection=9.60 +/- 2.29cm, CT scan=10.33 +/- 2.90cm), and RIA (dissection=12.64 +/- 0.84cm, CT scan=13.56 +/- 1.17cm) were significantly different when measured on dissection or CT scan ($p<0.05$).

The same observation was made for the length as for the diameter concerning the variabilities of the data. Once again, the similarity was influenced more by the artery itself than the technique used. This point is illustrated by the error bars in Figure 114 (and the SD in Supplementary data – Table 36).

The overall ICC between both methods was 0.952 (IC95% 0.934 – 0.965), which indicates highly consistent and reliable methods, as for the diameter.

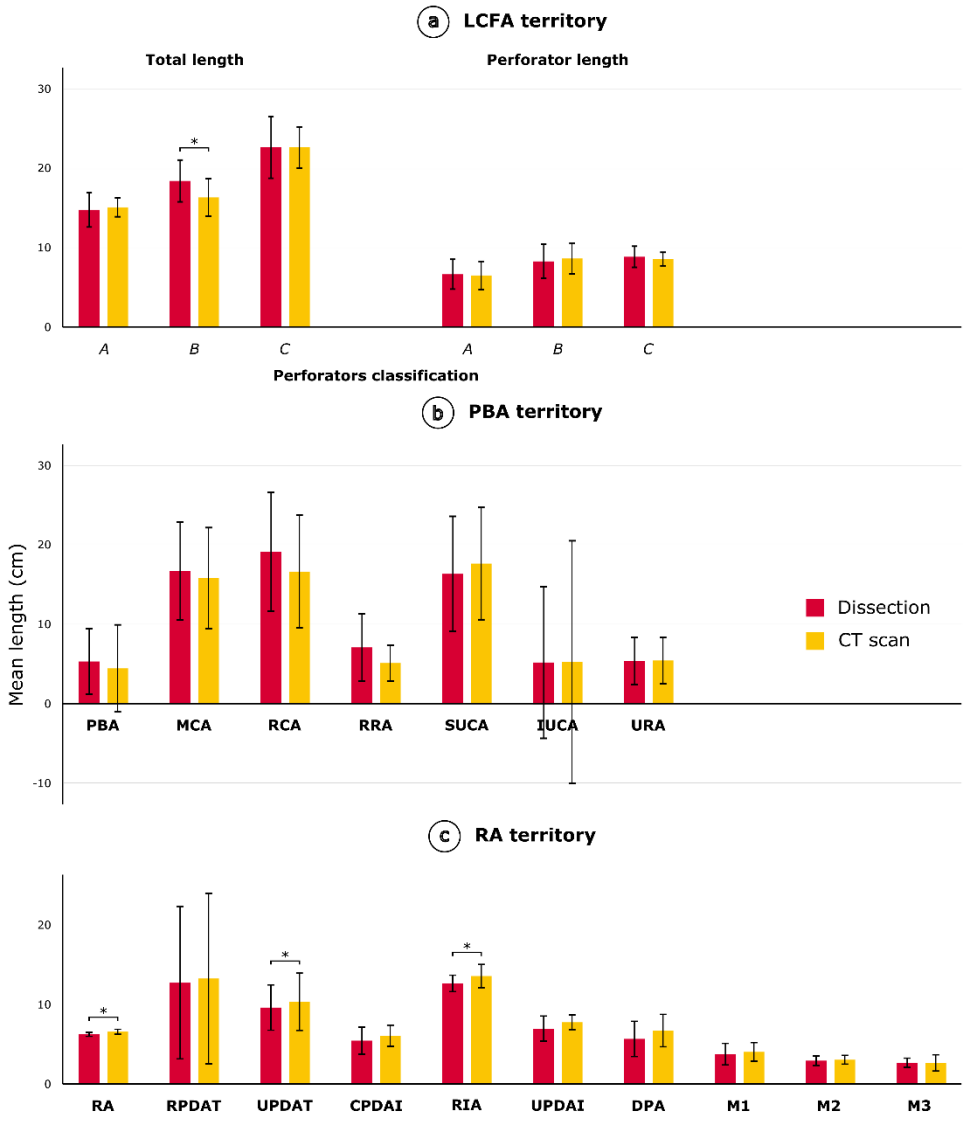

*Figure 114. Histograms of artery length of the LCFA territory (a), the PBA territory (b), and the RA territory (c), and their comparison between dissection and CT scan measurements. LCFA: lateral circumflex femoral artery, DB: descending branch, TB: transverse branch, PBA: profunda brachii artery, MCA: medial collateral artery, RCA: radial collateral artery, SUCA: superior ulnar collateral artery, RRA: radial recurrent artery, IUCA: inferior ulnar collateral artery, URA: ulnar recurrent artery, RA: radial artery, RPDAT: radial palmar digital artery of the thumb, UPDAT: ulnar palmar digital artery of the thumb, CPDAI: common palmar digital artery of the index, RIA: radialis indicis artery, UPDAI: ulnar palmar digital artery of the index, M1-2-3: 1st–2nd–3rd metacarpal arteries. Error bars: 95% CI, *: p<0.05.*

D. Discussion

Qualitatively, the single Angiofil-latex injection allowed to clearly visualize the vascular network of the injected arteries in both CT scan and dissection. CT scan images and 3D reconstructions demonstrated remarkable precision in visualizing the vascular anatomy of small arteries, reaching the maximal precision of the machine (0.3mm). The three vascular territories included arteries of different diameters and lengths revealing a homogeneous success of the technique. The larger trunks were full and expanded, the anastomoses were filled, and the tiny subcutaneous arterioles of the finger were visualized.

Diameter and length comparison

Dissection and CT scan measurements of the diameter and the length were comparable for most of the arteries, with excellent consistency and reliability.

Concerning the diameter, when a significant difference existed, the CT scan diameter was always larger than in dissection. The use of Angiofil may cause an exaggeration of diameters owing to its high concentration and potential overexposure. The adjustment of brightness and contrast of the CT scan needs to be used carefully in order not to create bias in measurements. On the opposite, the use of cast material can sometimes create shrinkage after solidification[571], which can be counterbalanced by the good elasticity of the latex. The use of a calliper during dissections might also slightly compress the vessels, according to the latex elasticity, artificially reducing diameters. However, most of the measurements were not affected by the measurement modality, even for very small arteries, indicating a high level of precision of the injection. The comparison between the diameters in our study and the literature showed good similarities. For example, the ØRCA of 1.5mm (range 1 – 3mm, localization of measurement not specified)[591] was comparable to our $ØRCA_{origin}$ of 1.45 +/- 0.29mm, or ØPBA of 2.05 +/- 0.16mm[592], similar to our $ØPBA_{origin}$ of 1.99 +/- 0.39mm.

A difference of length between dissection and CT scan might come from artery tortuosity. Dissection permits the extension of the artery and a precise measure of its entire length. However, a CT scan is a more favourable approach for 3D visualization of arterial natural paths and waviness quantification. The tortuosity of structures like fibres was previously quantified with microCT[288,405,593]. This

quantification method could be implemented on vessels benefiting from the Angiofil-latex enlightenment on microCT or classical CT scans. While the software in this study did not permit unrolling of the vessels, specific software capable of this could be also considered for future work.

Even if an anatomical variation is not rare, and that small sample size is more sensitive to inter-individual anatomical variations, caution should be paid when comparing results with other studies. Some meaningful variations were found in the literature. For example, a length of 4.97 +/- 1.96cm was described for the MCA[594] whereas we obtained a MCA length of 16.7 +/- 3.9cm. This difference came from the various landmarks. These authors measured the length from the MCA origin to its penetration into the lateral head of the triceps. On the contrary, the artery was measured from its origin until its end, so as until the first anastomosis with recurrent corresponding arteries. Another book chapter describing the lateral arm flap mentioned a RCA length of 6cm (range 4 – 8cm)[591] instead of our RCA length of 19.1 +/- 6.0cm. In this case, the authors only considered the posterior branch of the RCA, not the whole RCA until its final anastomosis.

Therefore, variability and dispersion between CT scan and dissection measures, particularly the length, resulted from anatomical variations rather than the modality of measurement itself.

Angiofil and latex combination

Alone, the Angiofil can opacify capillaries of 15µm[583,584]. Compared to the Microfil (MV-122, Flow-Tech Inc.), a coloured silicone rubber cast agent[571,583], that allows the visualization of vessels below 20µm in diameter[595], the Angiofil was proven to reach the same performance[583]. However, the combination with latex changes the fluidity of the solution. The viscosity is directly related to the calibre of vessels that can be filled[571,583]. Compared to other cast materials, the fluidity of the latex facilitates penetration in the deep vasculature, allowing an excellent distribution in peripheral arteries[572,596]. The hardening time of several days also enables the progressive pressure dispersion to tinier arterioles. However, it does not go through capillaries. The microcirculation or the venous network can not be penetrated like many other cast materials such as gelatin[571]. One cast agent containing barium sulfate, called the Micropaque, could penetrate capillaries when dissolved into water but also leads to extravasation[571,572]. The adjustable viscosity

of the Angiofil depending on the solvent choice and concentration[583] permitted to achieve as small arteries as 0.3mm in diameter, even with a death-to-perfusion time extensively increased. This technique could still be used on fresh-frozen limbs, keeping this precision, without considering the storage duration. The interval between the death and the injection could then be extended without altering outcomes. The absence of extravasation thanks to the hydrophobic characteristic, and the fixation of Angiofil by latex solidification might allow a durable signal visualization[597]. In addition, the CT scan signal of Angiofil was a bit lowered by the adjunction of latex, justifying to increase its concentration in the mixture compared to the literature[583]. The final resolution was only limited by the maximal resolution of the CT scan. The same injected tissues imaged by microCT could allow to precise the minimal vessel diameter this mixture can penetrate[597,598]. This imaging technique combined with the Angiofil injection could enable automated segmentation of the peripheral vascular network, at the level of perforators and the extraction of quantitative data such as length and caliber[583,584,597]. Otherwise, a venous retrograde injection could be imagined to opacify the venous vasculature with the Angiofil-latex mixture, depending on valvular tightness.

The Angiofil-latex technique presents numerous advantages previously mentioned, particularly in terms of accessibility. To our knowledge, only one commercialized product gathers all the same advantages, the µAngiofil[597], which includes an Angiofil contrast agent and cast material based on a polyurethane resin. However, it is twenty times more expensive than the Angiofil for the same volume. Our proposed technique appears much cheaper and more accessible for every researcher while providing the same benefits, and without additional difficulties.

Despite being visible on the CT scan, the Angiofil is also apparent on MRI by expressing a high fatty signal in T1-weighted sequence[572,599]. The study could then be extended to MRI analyses to confirm that this technique might be used for three modalities in the same injection, *i.e.* the CT scan, the MRI, and the dissection.

In this study, the addition of Angiofil did not alter the inherent qualities of latex and despite a little contrast attenuation by the latex, increasing Angiofil concentration solved this potential issue. Finally, it provides a homogeneous mixture reaching very small arteries, which reaffirms the suitability of this

combination as a valuable material for anatomical studies, especially those focused on the design of skin flaps which require precise data about perforators location and distribution, about pedicle calibre and length, and about distal anastomosing networks allowing the elevation of reversed flow flaps.

Those advantages also improve the identification of anatomical variations or anomalies in the vascular network, such as for the origin of UPDAT and RPDAT, supporting the debate in the literature about deleting the term of princeps pollicis artery[589,600]. The anatomical nomenclature tends sometimes to differ between the different studies. This new technique could permit to clarify the standardization of anatomical nomenclature, routes, origins, and variations during further research with a larger sample size, in both modalities.

Pitfalls to avoid and recommendations

The quality of our observations using the single Angiofil-latex injection is based on three essential technical points of attention: rinsing, dissection and system tightness.

First, a good rinse must remove all the blood clots, residue and debris[571,575], ensuring the Angiofil-latex mixture flows smoothly and uniformly. Even if the CT scan has a high sensitivity to detect vascular lesions[579], artery occlusion could be mistakenly interpreted as lesions (Fig. 110 – a). The best way to proceed is to rinse the upstream artery to carefully preserve and ensure complete washing of the downstream network. Cleaning the vascular network with preheated 0.9% NaCl solution reduces fluid viscosity, making vessel walls more pliable and minimizing mechanical resistance.

Secondly, all small collaterals must be carefully dissected and clamped. A coarse dissection before the rinse or the injection will inevitably lead to the rupture of small arterioles that are difficult to see with the naked eye. Any little gap in the vascular wall will further lead to an extravasation of the liquid decreasing the efficacy of the technique and compromising quantitative analyses (Fig. 110 – b). Therefore, a minimal invasive approach and a dissection *a minima* are strongly recommended during these two steps in order to preserve the vascular network, avoid leakage, and achieve optimal results. To avoid other sources of arterial damage, an appropriate size of catheter is required to proceed with a safe

introduction, and a delicate continuous pressure will protect from the rupture risk due to potential overpressure. If an entire part of a limb or a single organ needs to be contrasted, another tip to estimate the injection volume and avoid overflows is to thaw the limb in a head-down position to bleed out and quantify the extracted blood.

Finally, the third pitfall to avoid is the intravascular air injection. Air bubbles can negatively impact the quality of the radiological outcomes, leading to artifacts, opacification skips (Fig. 110 – c) or obstruction and potentially to suboptimal results. Therefore, an airtight system is crucial during all the steps. A good preliminary rinse also helps to eliminate air bubbles, preventing artifacts and incomplete filling[571]. Thus, this step is crucial for preparing vessels and achieving optimal vascular imaging and anatomical analysis.

E. Conclusion

This new combination of Angiofil-latex injection offers a simple, cheap, reliable, and non-toxic possibility to opacify, visualize, and enhance analyses of vascular networks. This association of a contrast agent and a vascular cast material in conjunction with an optimal rinse and injection, allows for clear and detailed visualization of not only large and small arteries vascularizing the deep muscular compartments of the limbs, but also the thin and very thin vessels supplying the overlying integuments.

The enhanced visibility of the vascular network in the CT scan can play a significant role in the preliminary planning of dissections, particularly because the radiological images offer different views and post-processing 3D reconstructions. This information helps in determining the most appropriate approach, guiding the dissection. The dissection is also improved by the rigidification and the colour of the latex. The arteries can be identified by touch, like a solid cord, as well as by sight of the specific colour used. The outcomes are fixed through latex solidification and can be stored in a freezer, enabling multiple reuses for iterative analyses. Taking advantage of this new method could lead to potential major impact on medical research, pathology or nomenclature description, forensic medicine, and education.

F. Supplementary data

Supplementary data – Table 35. Comparison of artery diameters analysed by CT scan or dissection.

Artery	Localization	Dissection (mm) *(mean +/- SD)*	CT scan (mm) *(mean +/- SD)*	P-value
LCFA territory				
LCFA	*Origin*	6.40 +/- 1.66	6.12 +/- 1.27	.345
	DB	4.27 +/- 0.92	4.40 +/- 0.93	.684
	TB	3.64 +/- 1.07	3.48 +/- 0.80	.500
PBA territory				
PBA	*Origin*	1.99 +/- 0.39	2.25 +/- 0.13	.273
	End	1.80 +/- 0.40	2.03 +/- 0.31	.715
MCA	*Origin*	1.40 +/- 0.29	1.50 +/- 0.22	.068
	End	0.71 +/- 0.53	0.90 +/- 0.36	.465
RCA	*Origin*	1.45 +/- 0.29	1.70 +/- 0.18	.465
	End	0.73 +/- 0.41	0.93 +/- 0.05	.465
SUCA	*Origin*	1.27 +/- 0.09	1.30 +/- 0.08	.465
	End	0.79 +/- 0.36	1.05 +/- 0.17	.068
RRA	*Origin*	1.51 +/- 0.20	1.48 +/- 0.05	1.000
	End	0.80 +/- 0.46	0.93 +/- 0.28	.273
IUCA	*Origin*	1.18 +/- 0.04	1.00 +/- 0.14	.180
	End	1.02 +/- 0.04	0.95 +/- 0.21	.655
URA	*Origin*	1.06 +/- 0.32	1.03 +/- 0.32	.465
	End	0.71 +/- 0.26	0.88 +/- 0.05	.197
RA territory				
RA	*Origin*	1.92 +/- 0.32	2.04 +/- 0.32	.043
RPDAT	*Origin*	1.13 +/- 0.20	1.21 +/- 0.19	.345
	MCP	0.80 +/- 0.09	0.94 +/- 0.13	.043
	IP	0.53 +/- 0.06	0.61 +/- 0.07	.080
UPDAT	*Origin*	1.18 +/- 0.45	1.28 +/- 0.47	.080
	MCP	0.93 +/- 0.48	0.98 +/- 0.46	.138
	IP	0.66 +/- 0.39	0.79 +/- 0.34	.104
CPDAI	*Origin*	1.58 +/- 0.37	1.77 +/- 0.39	.043
RIA	*Origin*	1.10 +/- 0.12	1.25 +/- 0.18	.080
	MCP	0.97 +/- 0.09	1.16 +/- 0.10	.043
	PIP	0.73 +/- 0.10	0.90 +/- 0.13	.043
	DIP	0.53 +/- 0.11	0.69 +/- 0.09	.068
UPDAI	*MCP*	1.23 +/- 0.13	1.33 +/- 0.15	.043
	PIP	0.87 +/- 0.08	0.98 +/- 0.11	.043

	DIP	0.66 +/- 0.08	0.75 +/- 0.13	.144
M1	*Origin*	0.92 +/- 0.27	1.09 +/- 0.23	.068
M2	*Origin*	0.71 +/- 0.14	0.83 +/- 0.19	.144
M3	*Origin*	0.63 +/- 0.13	0.68 +/- 0.20	.276

SD: standard deviation, LCFA: lateral circumflex femoral artery, DB: descending branch, TB: transverse branch, PBA: profunda brachii artery, MCA: medial collateral artery, RCA: radial collateral artery, SUCA: superior ulnar collateral artery, RRA: radial recurrent artery, IUCA: inferior ulnar collateral artery, URA: ulnar recurrent artery, RA: radial artery, MCP: metacarpophalangeal joint, IP: interphalangeal joint, PIP: proximal interphalangeal joint, DIP: distal interphalangeal joint, RPDAT: radial palmar digital artery of the thumb, UPDAT: ulnar palmar digital artery of the thumb, CPDAI: common palmar digital artery of the index, RIA: radialis indicis artery, UPDAI: ulnar palmar digital artery of the index, M1-2-3: 1st–2nd–3rd metacarpal arteries.

Supplementary data – Table 36. Comparison of artery lengths analysed by CT scan or dissection.

Length	Artery	Dissection (cm) *(mean +/- SD)*	CT scan (cm) *(mean +/- SD)*	P-value
LCFA territory				
Total	*A*	14.8 +/- 3.6	15.1 +/- 2.0	.196
	B	18.4 +/- 4.1	16.3 +/- 3.8	**.010**
	C	22.6 +/- 5.8	22.6 +/- 3.8	.722
Perforator	*A*	6.6 +/- 3.1	6.5 +/- 2.9	.780
	B	8.3 +/- 3.4	8.6 +/- 3.1	.212
	C	8.8 +/- 2.0	8.6 +/- 1.3	.754
PBA territory				
Total	*PBA*	5.3 +/- 3.3	4.5 +/- 3.4	.144
	MCA	16.7 +/- 3.9	15.8 +/- 4.0	.068
	RCA	19.1 +/- 6.0	16.6 +/- 4.5	.197
	RRA	7.1 +/- 2.7	5.1 +/- 1.4	.068
	SUCA	16.3 +/- 4.6	17.6 +/- 4.4	.068
	IUCA	5.3 +/- 1.1	5.2 +/- 1.7	.655
	URA	5.4 +/- 1.9	5.4 +/- 1.8	.715
RA territory				
Total	*RA*	6.2 +/- 0.2	6.6 +/ 0.2	**.042**
	RPDAT	12.7 +/- 7.7	13.3 +/- 8.6	.233
	UPDAT	9.6 +/- 2.3	10.3 +/- 2.9	**.043**
	CPDAI	5.4 +/- 1.4	6.1 +/- 1.1	.080
	RIA	12.6 +/- 0.8	13.6 +/- 1.2	**.043**
	UPDAI	7.0 +/- 1.3	7.8 +/- 0.7	.068
	DPA	5.7 +/- 1.4	6.7 +/- 1.3	.068
	M1	3.8 +/- 0.9	4.0 +/- 0.7	.068
	M2	2.9 +/- 0.4	3.0 +/- 0.3	.144
	M3	2.7 +/- 0.2	2.6 +/- 0.4	1.000

SD: standard deviation, LCFA: lateral circumflex femoral artery, A, B and C: Perforation classification according to Yu et al.[445], PBA: profunda brachii artery, MCA: medial collateral artery, RCA: radial collateral artery, RRA: radial recurrent artery, SUCA: superior ulnar collateral artery, IUCA: inferior ulnar collateral artery, URA: ulnar recurrent artery, RA: radial artery, RPDAT: radial palmar digital artery of the thumb, UPDAT: ulnar palmar digital artery of the thumb, CPDAI: common palmar digital artery of the index, RIA: radialis indicis artery, UPDAI: ulnar palmar digital artery of the index, DPA: deep palmar arch, M1-2-3: 1st–2nd–3rd metacarpal arteries.

List of abbreviations

α-SMA	*Alpha smooth muscle actin*
Ø	*Diameter*
2D	*Bidimensional*
3D	*Three-dimensional*

A

AB	*Alcian blue*
AB	*Ascending branch*
AGE(s)	*Advanced glycation end product(s)*
AF	*AlexaFluor*
AI	*Antero-inferior*
AIOA	*Anterior interosseous artery*
ALP	*Alkaline phosphatase*
ALT flap	*Anterolateral thigh flap*
AM	*Antero-middle*
AMSC(s)	*Adipose mesenchymal stem cell(s)*
Angio-GFs	*Angiogenic growth factors*
ANOVA	*Analysis of variance*
APC	*Allograft prosthesis composite*
AR	*Alizarin red*
Arg	*Arginine*
AS	*Antero-superior*
ASC(s)	*Adipose-derived stem cell(s)*
ASIS	*Anterior superior iliac spine*
ASLS	*Angular stable locking system*
ATMP	*Advanced therapeutic medicinal products*
AV loop	*Arteriovenous loop*

B

BA	*Brachial artery*
BMI	*Body mass index*
BMP(s)	*Bone morphogenetic protein(s)*

BMSC(s)	*Bone-marrow mesenchymal stem cell(s)*
BSA	*Bovine serum albumin*

C

C-	*Negative control*
C+	*Positive control*
Ca^{++}	*Calcium*
$Ca_{10}(PO_4)_6(OH)_2$)	*Hydroxyapatite*
CCL	*C-C motif ligand*
CD	*Cluster of differentiation*
CDMP	*Cartilage-derived morphogenetic protein*
CECT	*Contrast-enhanced microcomputed tomography*
CESA(s)	*Contrast-enhancing staining agent(s)*
CFA	*Common femoral artery*
CI	*Confidence interval*
CO_2	*Carbon dioxide*
Col-1	*Type I collagen*
CPD	*Critical point drying technique*
CPDAI	*Common palmar digital artery of the index*
Cryo-CECT	*Cryogenic contrast-enhanced microcomputed tomography*
CSBD(s)	*Critical-size bone defect(s)*
CT scan(s)	*Computed tomography(ies)*
CTX	*C-terminal telopeptide of type I collagen*

D

D-HFL	*Decellularized human fascia lata*
D-HP	*Decellularized human periosteum*
D-PBA	*Decellularized porcine bone allograft*
d0, d1, d3, d5, d7, dx	*Day zero, 1st day, 3rd day, 5th day, 7th day, xth day*
D1 to D5	*Decellularization protocol 1 to protocol 5*
D1i to D5i	*Decellularization protocol 1 to 5 + gamma-irradiation*
DAB	*3,3'-diaminobenzidine*
DAMPs	*Damage-associated molecular patterns*
DAPI	*4',6-diamidino-2-phenylindole*
DB	*Descending branch*

DBM	*Demineralized bone matrix*
DCN	*Decorin*
DIP	*Distal interphalangeal joint*
DNA	*Deoxyribonucleic acid*
DNAse	*Deoxyribonuclease*
DM	*Differentiation medium*
DMEM	*Dulbecco's modified eagle medium*
DMEM-F12	*Dulbecco's modified eagle medium/nutrient mixture F-12*
DMLS	*Direct metal laser sintering*
DPA	*Deep palmar arch/artery*
dsDNA	*Double-stranded DNA*
DVR	*Decapentaplegic Vg-related proteins*

E

ECM	*Extracellular matrix*
EDTA	*Ethylenediaminetetraacetic acid*
EGF	*Epidermal growth factor*
EGTA	*Ethyleneglycoldiaminetetraacetic acid*
EIA	*External iliac artery*
ELISA	*Enzyme-linked immunosorbent assay*
EMA	*European medicine agency*
ENA-78	*Epithelial neutrophil-activating peptide-78*

F

FA	*Femoral artery*
FBS	*Fetal bovine serum*
FDA	*Food and drug administration (U.S.)*
(β-)FGF	*(Beta-)Fibroblast growth factor*
FL	*Fascia lata*
FS	*Fascia superficialis*

G

GAG(s)	*Glycosaminoglycan(s)*
GDF	*Growth differentiation factor*
GF(s)	*Growth factor(s)*

GFP	*Green fluorescent protein*
GRO a/b/g	*Growth-regulated oncogene a/b/g*

H

H&E	*Haematoxylin and eosin*
H_2O_2	*Hydrogen peroxide*
Hb	*Haemoglobin*
HBSS	*Hanks' balanced salt solution*
HBV	*Hepatitis B virus*
HCl	*Hydrochloric acid*
HCT	*Haematocrit*
HCV	*Hepatitis C virus*
Hf-WD POM	*Hafnium(IV)-substituted Wells-Dawson polyoxometalate*
HFL	*Human fascia lata*
HFLi	*Decellularized and gamma-irradiated human fascia lata*
HLA	*Human leucocyte antigen*
HIF	*Hypoxia induced factor*
HIV	*Human immunodeficiency virus*
HP	*Human periosteum*
HRP	*Horseradish peroxidase*
HUVEC(s)	*Human umbilical vein endothelial cell(s)*

I

ICC	*Intraclass correlation coefficient / Interobserver agreement*
IFN-γ	*Gamma interferon*
IGF	*Insulin-like growth factor*
IgG	*Immunoglobulin G*
IHC	*Immunohistochemistry*
IL	*Interleukin*
IM	*Intramuscular*
IMN(s)	*Intramedullary nailing(s)*
IP	*Interphalangeal joint of the thumb*
ITT	*Iliotibial tract*
IUCA	*Inferior ulnar collateral artery*

J/K

L

LC-DCP	*Limited contact dynamic compression plate*
LCFA	*Lateral circumflex femoral artery*
LIF	*Leukaemia inhibitory factor*
LIPUS	*Low-intensity pulsed ultrasound*
Lys	*Lysine*

M

M_1-M_2-M_3	*Palmar metacarpal arteries*
MAPK	*Mitogen-activated protein kinase*
MBA(s)	*Massive bone allograft(s)*
MCA	*Medial collateral artery*
MCP	*Metacarpophalangeal joint*
MCP-1	*Monocyte chemoattractant protein 1*
MCSF	*Macrophage colony-stimulating factor*
MHC	*Major histocompatibility complex*
MHC-1	*Major histocompatibility complex class I*
MI	*Medio-inferior*
MicroCT	*Microfocus computed tomography*
mIF-IHC	*Multiplex immunofluorescence IHC*
MIP	*Maximum intensity projections*
MM	*Medio-middle*
MMP	*Matrix metalloproteinases*
MRI	*Magnetic resonance imaging*
mRUS	*Modified radiographic union score*
MS	*Medio-superior*
MSC(s)	*Mesenchymal stem cell(s)*
MT	*Masson's trichrome*
mTLD	*Mammalian tolloid*

N

N	*Native tissue/bone*
N-HFL	*Native human fascia lata*

N-HP	*Native human periosteum*
N-PBA	*Native porcine bone allograft*
N-PP	*Native porcine periosteum*
NaCl	*Sodium chloride*
NaOH	*Sodium hydroxide*
NB	*Native bone*
NISSSA	*Nerve injury, ischemia, soft tissue injury, skeletal injury, shock, and age of patient score*
NUSS	*Non-union scoring system*

O

OC	*Osteocalcin*
OM	*Osteogenic membrane*
OP	*Osteogenic protein*
OPG	*Osteoprotegerin*
ORIF	*Open reduction and internal fixation*
ORO	*Oil red O*
Osx	*Osterix gene*

P

P_4	*Cells at passage 4*
PBA	*Profunda brachii artery*
PBA(s)	*Porcine bone allograft(s)*
PBMC(s)	*Peripheral blood mononuclear cell(s)*
PBS	*Phosphate buffered saline*
PDGF	*Platelet-derived growth factor*
PDPN	*Podoplanin*
PDSC(s)	*Periosteal-derived stem cell(s)*
PFA	*Profunda femoris artery*
PGA	*Polyglycolic acid*
PI	*Postero-inferior*
PI_3-K	*Phosphoinositide-3-kinase*
PINP	*N-terminal propeptide of type I collagen*
PIOA	*Posterior interosseous artery*
PIP	*Proximal interphalangeal joint*

PJI	*Prosthetic joint infection*
PlGF	*Placental growth factor*
PLA	*Polylactic acid*
PLM	*Polarized light microscopy*
PLT	*Platelets*
PM	*Proliferation medium*
PM	*Postero-middle*
PMMA	*Polymethyl methacrylate*
PMSC(s)	*Periosteal mesenchymal stem cell(s)*
PPAR-γ	*Peroxisome proliferator-activated receptor gamma*
PRP	*Platelet-rich plasma*
PS	*Postero-superior*
PSR	*Picrosirius red*
PTH	*Parathyroid hormone*
PTM(s)	*Post-translational modification(s)*

Q/R

RA	*Radial artery*
RANK	*Receptor activator of nuclear factor kappa-B*
RANKL	*Receptor activator of nuclear factor kappa-B ligand*
RANTES	*Regulated upon activation normal T cell expressed & secreted*
RBC	*Red blood cells*
RCA	*Radial collateral artery*
RIA	*Radialis indicis artery*
RIA technique	*Reamer/irrigator/aspirator technique*
RIOA	*Recurrent interosseous artery*
RIPA	*Radioimmunoprecipitation assay*
RPDAT	*Radial palmar digital artery of the thumb*
RRA	*Radial recurrent artery*
RT	*Room temperature*
RunX2	*Runt-related transcription factor 2*

S

SCMPMD	*Scientific committee on medical products & medical devices*
SD(s)	*Standard deviation(s)*

SDS	*Sodium dodecyl sulfate*
SEM	*Scanning electron microscopy*
SEM	*Standard error of the mean*
SLRP(s)	*Small leucine-rich proteoglycan(s)*
SPA	*Superficial palmar arch*
SPB	*Superficial palmar branch*
SR	*Sirius red*
SSPC(s)	*Skeletal stem/progenitor cell(s)*
STSG	*Split-thickness skin graft*
SUCA	*Superior ulnar collateral artery*

T

TB	*Transverse branch*
TBS	*Tris-buffered saline*
TCP	*Tricalcium phosphate*
TGF-β	*Transforming growth factor beta*
TIMP	*Tissue inhibitor of metalloproteinase*
TMB	*5'-tetramethylbenzidine*
TNF-α	*Tumor necrosis factor alpha*
TPO	*Thrombopoietin*
TSA	*Tyramide signal amplification*
TUS	*Tomographic union score*

U

UA	*Ulnar artery*
UPDAI	*Ulnar palmar digital artery of the index*
UPDAT	*Ulnar palmar digital artery of the thumb*
URA	*Ulnar recurrent artery*
US	*Ultrasonography*

V

VEGF	*Vascular endothelial growth factor*
VK	*Von Kossa*

W

WBC	*White blood cells*
Wnt	*Wingless-related integration site proteins*

X

X-rays	*X-rays radiography*

Y/Z

Definitions of useful terms

Allograft	*Tissue transplanted between individuals of the same species, but with different genetic composition.*
Angiosome	*Comprehensive unit of a 3D block of tissue that includes not only the arterial supply but also the venous drainage. Angiosomes are clinically relevant in reconstructive surgery and wound healing because they help surgeons predict tissue viability and plan surgical interventions based on the vascular anatomy.*
Angiotome	*Specific territory of the body that is supplied by a single arterial branch or a group of arterial branches. It focuses on the arterial supply alone and typically includes all tissues irrigated by a particular artery or group of arteries.*
Autograft	*Tissue transplanted from one part of an individual's body to another within the same individual.*
Biocompatibility	*Ability of a material or substance to integrate and function in harmony with living host tissue without eliciting an immune response.*
Biomaterial	*Any biocompatible substance, natural or synthetic, that is engineered to interact with biological systems for a medical purpose, such as treating, augmenting, or replacing any tissue, organ, or function of the body.*
Creeping substitution	*Gradual replacement of old/necrotic bone or a temporary scaffold with natural bone tissue through the combined activity of osteoclastic resorption, osteoblastic formation and neoangiogenesis.*
Cytotoxicity	*Characteristic of a component to be toxic for living cells, usually leading to their death.*
Multipotency	*Ability of a cell to differentiate into discrete cell types (e.g. hematopoietic stem cells, mesenchymal stem cells).*

Niche	*Subset of tissue cells and extracellular matrix favouring the stemness maintenance of the cell.*
Orthobiologics	*Tissue engineering field including bioactive molecules, scaffolds and stem cells in the specific goal of bone repair.*
Ostectomy	*Exeresis/excision of a segmental intercalary bone.*
Osteoconduction	*Passive property of a scaffold allowing cell migration and ingrowth of new bone formation.*
Osteogenesis	*Active cell-related capacity to form new bone.*
Osteoinduction	*Active property of a biomaterial allowing recruitment, stimulation and differentiation of MSCs into bone-forming cells or osteoprogenitors.*
Pluripotency	*Ability of a cell to differentiate into any of the three germ layers but not extra-embryonic tissues (e.g. embryonic stem cells).*
Sterilization	*Process intended to remove, deactivate, or destroy all forms of viable microorganisms, including bacterial spores, from a surface, fluid, or compound.*
Totipotency	*Greatest differentiation potential of a cell, which is able to create every three germ layers (ectoderm, mesoderm, endoderm), as well as germ cells lines.*
Unipotency	*Ability of a cell to differentiate into one specific cell type only.*
Xenograft	*Tissue transplanted from one species to another.*

References

1. Lengele B. L'anatomie au chevet de l'Histoire. *Morphologie*. 2023;107(359, Supplement):100612. doi:10.1016/j.morpho.2023.100612
2. Accueil | Belgian Cancer Registry. Accessed April 3, 2024. https://kankerregister.org/fr/node
3. Gorasso V, Silversmit G, Arbyn M, et al. The non-fatal burden of cancer in Belgium, 2004–2019: a nationwide registry-based study. *BMC Cancer*. 2022;22(1):58. doi:10.1186/s12885-021-09109-4
4. admin-sciensano. Cancer. Vers une Belgique en bonne santé. February 14, 2023. Accessed April 3, 2024. https://www.belgiqueenbonnesante.be/fr/etat-de-sante/maladies-non-transmissibles/cancer
5. Premkumar A, Kolin DA, Farley KX, et al. Projected Economic Burden of Periprosthetic Joint Infection of the Hip and Knee in the United States. *The Journal of Arthroplasty*. 2021;36(5):1484-1489.e3. doi:10.1016/j.arth.2020.12.005
6. Ho-Shui-Ling A, Bolander J, Rustom LE, Johnson AW, Luyten FP, Picart C. Bone regeneration strategies: engineered scaffolds, bioactive molecules and stem cells Current stage and future perspectives. *Biomaterials*. 2018;180:143-162. doi:10.1016/j.biomaterials.2018.07.017
7. Kargozar S, Mozafari M, Hamzehlou S, Brouki Milan P, Kim HW, Baino F. Bone Tissue Engineering Using Human Cells: A Comprehensive Review on Recent Trends, Current Prospects, and Recommendations. *Applied Sciences*. 2019;9(1):174. doi:10.3390/app9010174
8. Ham AW, Harris WR. Repair and transplantation of bone. In: *The Biochemistry and Physiology of Bone*. Elsevier; 1956:475-505.
9. Lacroix. *The Organization of Bones*. J. & A. Churchill. J. & A. Churchill; 1951.
10. Enlow DH. *Principles of Bone Remodeling: An Account of Post-Natal Growth and Remodeling Processes in Long Bones and the Mandible*. Charles C. Thomas.; 1963.
11. Meyer U, Wiesmann HP. *Bone and Cartilage Engineering*. Heidelberg. Springer-Verlag; 2006. doi:10.1007/3-540-33606-0
12. Frost HM. *Bone Remodelling Dynamics*. Charles C. Thomas.; 1963.
13. Vaughan JM. The physiology of bone. Published online 1975.
14. Dalisson B, Charbonnier B, Aoude A, et al. Skeletal regeneration for segmental bone loss: Vascularised grafts, analogues and surrogates. *Acta Biomaterialia*. 2021;136:37-55. doi:10.1016/j.actbio.2021.09.053
15. Buckley RE, Moran CG, Apivatthakakul T. *AO Principles of Fracture Management*. Third Edition. Thieme ; AO Pub; 2017.
16. Manon J, Detrembleur C, Van de Veyver S, Tribak K, Cornu O, Putineanu D. Predictors of mechanical complications after intramedullary nailing of tibial fractures. *Orthopaedics & Traumatology: Surgery & Research*. 2019;105(3):523-527. doi:10.1016/j.otsr.2019.01.015
17. Manon J, Detrembleur C, Van De Veyver S, Tribak K, Cornu O, Putineanu D. Can infection be predicted after intramedullary nailing of tibial shaft fractures? *Acta Orthop Belg*. 2020;86(2):313-319.
18. Dimitriou R, Jones E, McGonagle D, Giannoudis PV. Bone regeneration: current concepts and future directions. *BMC Med*. 2011;9:66. doi:10.1186/1741-7015-9-66
19. Andrzejowski P, Giannoudis PV. The "diamond concept" for long bone non-union management. *J Orthop Traumatol*. 2019;20(1):21. doi:10.1186/s10195-019-0528-0
20. Perren SM. Evolution of the internal fixation of long bone fractures. The scientific basis of biological internal fixation: choosing a new balance between stability and biology. *The Journal*

of Bone & Joint Surgery British Volume. 2002;84-B(8):1093-1110. doi:10.1302/0301-620X.84B8.0841093

21. Sheen JR, Mabrouk A, Garla VV. Fracture Healing Overview. In: *StatPearls*. StatPearls Publishing; 2024. Accessed March 16, 2024. http://www.ncbi.nlm.nih.gov/books/NBK551678/
22. Foster AL, Moriarty TF, Zalavras C, et al. The influence of biomechanical stability on bone healing and fracture-related infection: *the legacy of Stephan Perren. Injury*. 2021;52(1):43-52. doi:10.1016/j.injury.2020.06.044
23. Coutelier L. *Recherches Sur La Guérison Des Fractures*. UCL-Université Catholique de Louvain; 1969.
24. Willenegger H, Perren SM, Schenk R. [Primary and secondary healing of bone fractures]. *Chirurg*. 1971;42(6):241-252.
25. Dwek JR. The periosteum: what is it, where is it, and what mimics it in its absence? *Skeletal Radiol*. 2010;39(4):319-323. doi:10.1007/s00256-009-0849-9
26. Carano RAD, Filvaroff EH. Angiogenesis and bone repair. *Drug Discovery Today*. 2003;8(21):980-989. doi:10.1016/S1359-6446(03)02866-6
27. Lu F, Verleg SMNE, Groven RVM, Poeze M, van Griensven M, Blokhuis TJ. Is there a role for N1-N2 neutrophil phenotypes in bone regeneration? A systematic review. *Bone*. 2024;181:117021. doi:10.1016/j.bone.2024.117021
28. Street J, Winter D, Wang JH, Wakai A, McGuinness A, Redmond HP. Is human fracture hematoma inherently angiogenic? *Clin Orthop Relat Res*. 2000;(378):224-237. doi:10.1097/00003086-200009000-00033
29. Wolff J. *The Law of Bone Remodelling*. Springer; 1986. doi:10.1007/978-3-642-71031-5
30. Frost HM. Wolff's Law and bone's structural adaptations to mechanical usage: an overview for clinicians. *Angle Orthod*. 1994;64(3):175-188. doi:10.1043/0003-3219(1994)064<0175:WLABSA>2.0.CO;2
31. Frost HM. *The Laws of Bone Structure. Springfield Il*. Charles C. Thomas.; 1964.
32. Perrin S, Colnot C. Periosteal Skeletal Stem and Progenitor Cells in Bone Regeneration. *Curr Osteoporos Rep*. 2022;20(5):334-343. doi:10.1007/s11914-022-00737-8
33. Wang RN, Green J, Wang Z, et al. Bone Morphogenetic Protein (BMP) signaling in development and human diseases. *Genes & Diseases*. 2014;1(1):87-105. doi:10.1016/j.gendis.2014.07.005
34. Campana V, Milano G, Pagano E, et al. Bone substitutes in orthopaedic surgery: from basic science to clinical practice. *J Mater Sci Mater Med*. 2014;25(10):2445-2461. doi:10.1007/s10856-014-5240-2
35. Pountos I, Georgouli T, Pneumaticos S, Giannoudis PV. Fracture non-union: Can biomarkers predict outcome? *Injury*. 2013;44(12):1725-1732. doi:10.1016/j.injury.2013.09.009
36. Greenblatt MB, Tsai JN, Wein MN. Bone Turnover Markers in the Diagnosis and Monitoring of Metabolic Bone Disease. *Clin Chem*. 2017;63(2):464-474. doi:10.1373/clinchem.2016.259085
37. Cunningham BP, Brazina S, Morshed S, Miclau T. Fracture healing: A review of clinical, imaging and laboratory diagnostic options. *Injury*. 2017;48:S69-S75. doi:10.1016/j.injury.2017.04.020
38. Fisher JS, Kazam JJ, Fufa D, Bartolotta RJ. Radiologic evaluation of fracture healing. *Skeletal Radiol*. 2019;48(3):349-361. doi:10.1007/s00256-018-3051-0
39. Whelan DB, Bhandari M, McKee MD, et al. Interobserver and intraobserver variation in the assessment of the healing of tibial fractures after intramedullary fixation. *J Bone Joint Surg Br*. 2002;84(1):15-18. doi:10.1302/0301-620x.84b1.11347
40. Whelan DB, Bhandari M, Stephen D, et al. Development of the radiographic union score for tibial fractures for the assessment of tibial fracture healing after intramedullary fixation. *J Trauma*. 2010;68(3):629-632. doi:10.1097/TA.0b013e3181a7c16d

41. Perlepe V, Michoux N, Heynen G, Vande Berg B. Semi-quantitative CT assessment of fracture healing: How many and which CT reformats should be analyzed? *European Journal of Radiology*. 2019;118:181-186. doi:10.1016/j.ejrad.2019.07.026
42. Perlepe V, Michoux N, Kirchgesner T, Lecouvet F, Vande Berg B. Semi-quantitative CT scoring of nailed shaft fractures during normal healing and in non-unions: comparison with radiographic scoring. *Eur J Radiol*. 2021;138:109618. doi:10.1016/j.ejrad.2021.109618
43. Litrenta J, Tornetta P, Mehta S, et al. Determination of Radiographic Healing: An Assessment of Consistency Using RUST and Modified RUST in Metadiaphyseal Fractures. *J Orthop Trauma*. 2015;29(11):516-520. doi:10.1097/BOT.0000000000000390
44. Perlepe V, Cerato A, Putineanu D, et al. Value of a radiographic score for the assessment of healing of nailed femoral and tibial shaft fractures: A retrospective preliminary study. *European Journal of Radiology*. 2018;98:36-40. doi:10.1016/j.ejrad.2017.10.020
45. Calori GM, Colombo M, Mazza EL, et al. Validation of the Non-Union Scoring System in 300 long bone non-unions. *Injury*. 2014;45 Suppl 6:S93-97. doi:10.1016/j.injury.2014.10.030
46. Schmal H, Brix M, Bue M, et al. Nonunion - consensus from the 4th annual meeting of the Danish Orthopaedic Trauma Society. *EFORT Open Rev*. 2020;5(1):46-57. doi:10.1302/2058-5241.5.190037
47. Tzioupis C, Giannoudis PV. Prevalence of long-bone non-unions. *Injury*. 2007;38:S3-S9. doi:10.1016/S0020-1383(07)80003-9
48. Mills LA, Aitken SA, Simpson AHRW. The risk of non-union per fracture: current myths and revised figures from a population of over 4 million adults. *Acta Orthop*. 2017;88(4):434-439. doi:10.1080/17453674.2017.1321351
49. Antonova E, Le TK, Burge R, Mershon J. Tibia shaft fractures: costly burden of nonunions. *BMC musculoskeletal disorders*. 2013;14:1-10.
50. Nauth A, Schemitsch E, Norris B, Nollin Z, Watson JT. Critical-Size Bone Defects: Is There a Consensus for Diagnosis and Treatment? *J Orthop Trauma*. 2018;32 Suppl 1:S7-S11. doi:10.1097/BOT.0000000000001115
51. Santolini E, West R, Giannoudis PV. Risk factors for long bone fracture non-union: a stratification approach based on the level of the existing scientific evidence. *Injury*. 2015;46 Suppl 8:S8-S19. doi:10.1016/S0020-1383(15)30049-8
52. Ebraheim NA, Martin A, Sochacki KR, Liu J. Nonunion of distal femoral fractures: a systematic review. *Orthop Surg*. 2013;5(1):46-50. doi:10.1111/os.12017
53. Cierny GI, Mader JT, Penninck JJ. The Classic: A Clinical Staging System for Adult Osteomyelitis. *Clinical Orthopaedics and Related Research®*. 2003;414:7. doi:10.1097/01.blo.0000088564.81746.62
54. Weber BG, Čech O. *Pseudarthrosis: Pathophysiology, Biomechanics, Therapy, Results*. Hans Huber Publishers; 1976.
55. Reed A a. C, Joyner CJ, Brownlow HC, Simpson AHRW. Human atrophic fracture non-unions are not avascular. *J Orthop Res*. 2002;20(3):593-599. doi:10.1016/S0736-0266(01)00142-5
56. Sanders DW, Bhandari M, Guyatt G, et al. Critical-sized defect in the tibia: is it critical? Results from the SPRINT trial. *J Orthop Trauma*. 2014;28(11):632-635. doi:10.1097/BOT.0000000000000194
57. Haines NM, Lack WD, Seymour RB, Bosse MJ. Defining the Lower Limit of a "Critical Bone Defect" in Open Diaphyseal Tibial Fractures. *J Orthop Trauma*. 2016;30(5):e158-163. doi:10.1097/BOT.0000000000000531
58. Fayaz HC, Giannoudis PV, Vrahas MS, et al. The role of stem cells in fracture healing and nonunion. *Int Orthop*. 2011;35(11):1587-1597. doi:10.1007/s00264-011-1338-z
59. Reichert JC, Saifzadeh S, Wullschleger ME, et al. The challenge of establishing preclinical models for segmental bone defect research. *Biomaterials*. 2009;30(12):2149-2163. doi:10.1016/j.biomaterials.2008.12.050

60. Ahmed H, Shakshak M, Trompeter A. A review of the Masquelet technique in the treatment of lower limb critical-size bone defects. *Ann R Coll Surg Engl*. Published online June 27, 2023. doi:10.1308/rcsann.2023.0022
61. Zhang W, Wang N, Yang M, et al. Periosteum and development of the tissue-engineered periosteum for guided bone regeneration. *J Orthop Translat*. 2022;33:41-54. doi:10.1016/j.jot.2022.01.002
62. Roberts SJ, van Gastel N, Carmeliet G, Luyten FP. Uncovering the periosteum for skeletal regeneration: the stem cell that lies beneath. *Bone*. 2015;70:10-18. doi:10.1016/j.bone.2014.08.007
63. Viel C. Duhamel du Monceau, naturaliste, physicien et chimiste. *Revue d'histoire des sciences*. 1985;38(1):55-71. doi:10.3406/rhs.1985.3993
64. Henri Duhamel du Monceau, Dadonville. Tourisme Loiret. Accessed March 21, 2024. https://www.tourismeloiret.com/fr/diffusio/illustres/henri-duhamel-du-monceau-dadonville_TFOILLCEN045V509S0L
65. Redelinghuys K. Anatomy of a tree. Trees SA. April 23, 2018. Accessed March 21, 2024. https://www.trees-sa.co.za/anatomy-of-a-tree/
66. Julien A, Perrin S, Martínez-Sarrà E, et al. Skeletal Stem/Progenitor Cells in Periosteum and Skeletal Muscle Share a Common Molecular Response to Bone Injury. *J of Bone & Mineral Res*. 2022;37(8):1545-1561. doi:10.1002/jbmr.4616
67. Duchamp de Lageneste O, Julien A, Abou-Khalil R, et al. Periosteum contains skeletal stem cells with high bone regenerative potential controlled by Periostin. *Nat Commun*. 2018;9(1):773. doi:10.1038/s41467-018-03124-z
68. Maia Ferreira Alencar CH, Sampaio Silveira CR, Cavalcante MM, et al. Periosteum: An imaging review. *Eur J Radiol Open*. 2020;7:100249. doi:10.1016/j.ejro.2020.100249
69. Orwoll ES. Toward an Expanded Understanding of the Role of the Periosteum in Skeletal Health. *J Bone Miner Res*. 2003;18(6):949-954. doi:10.1359/jbmr.2003.18.6.949
70. O'Driscoll SWM, Saris DBF, Ito Y, Fitzimmons JS. The chondrogenic potential of periosteum decreases with age. *Journal of Orthopaedic Research*. 2001;19(1):95-103. doi:10.1016/S0736-0266(00)00014-0
71. Frost HM. *Bone Remodeling and Its Relationship to Metabolic Bone Diseases*. Vol III. Charles C. Thomas. Springfield; 1973.
72. Wenaden AET, Szyszko TA, Saifuddin A. Imaging of periosteal reactions associated with focal lesions of bone. *Clin Radiol*. 2005;60(4):439-456. doi:10.1016/j.crad.2004.08.017
73. Moore ER, Zhu YX, Ryu HS, Jacobs CR. Periosteal progenitors contribute to load-induced bone formation in adult mice and require primary cilia to sense mechanical stimulation. *Stem Cell Res Ther*. 2018;9(1):190. doi:10.1186/s13287-018-0930-1
74. Zannit HM, Silva MJ. Proliferation and Activation of Osterix-Lineage Cells Contribute to Loading-Induced Periosteal Bone Formation in Mice. *JBMR Plus*. 2019;3(11):e10227. doi:10.1002/jbm4.10227
75. Chanavaz M. Anatomy and histophysiology of the periosteum: quantification of the periosteal blood supply to the adjacent bone with 85Sr and gamma spectrometry. *The Journal of oral implantology*. 1995;21(3):214-219.
76. Ott SM. Cortical or Trabecular Bone: What's the Difference? *American Journal of Nephrology*. 2018;47(6):373-375. doi:10.1159/000489672
77. Grüneboom A, Hawwari I, Weidner D, et al. A network of trans-cortical capillaries as mainstay for blood circulation in long bones. *Nat Metab*. 2019;1(2):236-250. doi:10.1038/s42255-018-0016-5
78. Asghar A, Narayan RK, Kumar A, Naaz S. The transcortical vessel is replacement of cortical capillary or a separate identity in diaphyseal vascularity. *Anat Cell Biol*. 2020;53(1):107-110. doi:10.5115/acb.19.171

79. Liao P, Chen L, Zhou H, et al. Osteocyte mitochondria regulate angiogenesis of transcortical vessels. *Nat Commun*. 2024;15(1):2529. doi:10.1038/s41467-024-46095-0
80. Giannoudis PV, Einhorn TA, Marsh D. Fracture healing: the diamond concept. *Injury*. 2007;38 Suppl 4:S3-6. doi:10.1016/s0020-1383(08)70003-2
81. Professor Peter Giannoudis – British Trauma Society. Accessed March 24, 2024. https://www.britishtrauma.com/executive-member/professor-peter-giannoudis/
82. Health F of M&. Professor Peter Giannoudis | School of Medicine | University of Leeds. Accessed March 24, 2024. https://medicinehealth.leeds.ac.uk/medicine/staff/1785/professor-peter-giannoudis
83. Delloye C, Cornu O, Druez V, Barbier O. Bone allografts: What they can offer and what they cannot. *J Bone Joint Surg Br*. 2007;89(5):574-579. doi:10.1302/0301-620X.89B5.19039
84. Wickramasinghe ML, Dias GJ, Premadasa KMGP. A novel classification of bone graft materials. *J Biomed Mater Res B Appl Biomater*. 2022;110(7):1724-1749. doi:10.1002/jbm.b.35029
85. Roberts TT, Rosenbaum AJ. Bone grafts, bone substitutes and orthobiologics: The bridge between basic science and clinical advancements in fracture healing. *Organogenesis*. 2012;8(4):114. doi:10.4161/org.23306
86. Docquier PL, Schubert T. Techniques et indications des greffes osseuses et ostéocartilagineuses. *EMC-Techniques chirurgicales-Orthopédie-Traumatologie*. 2020;(0):1-26.
87. Perren SM, Allgower M, Brunner H, Burch H, Cordey J, Ganz R. The concept of biological plating using the limited contact — dynamic compression plate (LC-DCP). *Injury*. 1991;22:1-41. doi:10.1016/0020-1383(91)90123-V
88. Perren SM. Fracture healing: fracture healing understood as the result of a fascinating cascade of physical and biological interactions. Part I. *Acta Chir Orthop Traumatol Cech*. 2014;81(6):355-364.
89. Perren SM. Fracture healing: Fracture Healing Understood as the Result of a Fascinating Cascade of Physical and Biological Interactions. Part II. *ACHOT*. 2015;82(1):13-21. doi:10.55095/achot2015/002
90. Calori GM, Giannoudis PV. Enhancement of fracture healing with the diamond concept: the role of the biological chamber. *Injury*. 2011;42(11):1191-1193. doi:10.1016/j.injury.2011.04.016
91. Giannoudis PV, Einhorn TA, Schmidmaier G, Marsh D. The diamond concept--open questions. *Injury*. 2008;39 Suppl 2:S5-8. doi:10.1016/S0020-1383(08)70010-X
92. Jagodzinski M, Krettek C. Effect of mechanical stability on fracture healing--an update. *Injury*. 2007;38 Suppl 1:S3-10. doi:10.1016/j.injury.2007.02.005
93. Rubin J, Rubin C, Jacobs CR. Molecular pathways mediating mechanical signaling in bone. *Gene*. 2006;367:1-16. doi:10.1016/j.gene.2005.10.028
94. Wang X, Friis T, Glatt V, Crawford R, Xiao Y. Structural properties of fracture haematoma: current status and future clinical implications. *J Tissue Eng Regen Med*. 2017;11(10):2864-2875. doi:10.1002/term.2190
95. Lu F, Groven RVM, van Griensven M, et al. Polytherapy versus monotherapy in the treatment of tibial non-unions: a retrospective study. *J Orthop Traumatol*. 2024;25(1):21. doi:10.1186/s10195-024-00763-5
96. Masquelet AC, Begue T. The Concept of Induced Membrane for Reconstruction of Long Bone Defects. *Orthopedic Clinics of North America*. 2010;41(1):27-37. doi:10.1016/j.ocl.2009.07.011
97. The Meyer Award - Innovation in Orthopaedics. The Meyer Award. Accessed March 22, 2024. https://meyeraward.org/
98. Mathieu L, Durand M, Collombet JM, de Rousiers A, de l'Escalopier N, Masquelet AC. Induced membrane technique: a critical literature analysis and proposal for a failure classification scheme. *Eur J Trauma Emerg Surg*. 2021;47(5):1373-1380. doi:10.1007/s00068-020-01540-9

99. Alford AI, Nicolaou D, Hake M, McBride-Gagyi S. Masquelet's induced membrane technique: Review of current concepts and future directions. *J Orthop Res*. 2021;39(4):707-718. doi:10.1002/jor.24978
100. Masquelet AC. Induced Membrane Technique: Pearls and Pitfalls. *J Orthop Trauma*. 2017;31 Suppl 5:S36-S38. doi:10.1097/BOT.0000000000000979
101. Mauffrey C, Hake ME, Chadayammuri V, Masquelet AC. Reconstruction of Long Bone Infections Using the Induced Membrane Technique: Tips and Tricks. *J Orthop Trauma*. 2016;30(6):e188-193. doi:10.1097/BOT.0000000000000500
102. Gessmann J, Rosteius T, Baecker H, et al. Is the bioactivity of induced membranes time dependent? *Eur J Trauma Emerg Surg*. 2022;48(4):3051-3061. doi:10.1007/s00068-021-01844-4
103. Masquelet AC. La technique de la membrane induite dans les reconstructions osseuses segmentaires: développement et perspectives. *Bulletin de l'Académie Nationale de Médecine*. 2017;201(1):439-453. doi:10.1016/S0001-4079(19)30514-X
104. Masquelet AC, Kishi T, Benko PE. Very long-term results of post-traumatic bone defect reconstruction by the induced membrane technique. *Orthopaedics & Traumatology: Surgery & Research*. 2019;105(1):159-166. doi:10.1016/j.otsr.2018.11.012
105. Mi M, Papakostidis C, Wu X, Giannoudis PV. Mixed results with the Masquelet technique: A fact or a myth? *Injury*. 2020;51(2):132-135. doi:10.1016/j.injury.2019.12.032
106. Durand M, Collombet JM. Physiologie de la membrane induite: Ce que l'on sait et ce que l'on ignore. État de la recherche et orientations futures. In: A.C M, ed. *La Technique de La Membrane Induite. Principes, Pratiques et Perspectives*. Sauramps Médical; 2020:127-139. Accessed July 31, 2024. https://hal.science/hal-04006525
107. Taylor BC, French BG, Fowler TT, Russell J, Poka A. Induced Membrane Technique for Reconstruction To Manage Bone Loss: *Journal of the American Academy of Orthopaedic Surgeons*. 2012;20(3):142-150. doi:10.5435/JAAOS-20-03-142
108. Masquelet AC. The induced membrane technique. *Orthopaedics & Traumatology: Surgery & Research*. 2020;106(5):785-787. doi:10.1016/j.otsr.2020.06.001
109. Klein C, Monet M, Barbier V, et al. The Masquelet technique: Current concepts, animal models, and perspectives. *J Tissue Eng Regen Med*. 2020;14(9):1349-1359. doi:10.1002/term.3097
110. Nau C, Seebach C, Trumm A, et al. Alteration of Masquelet's induced membrane characteristics by different kinds of antibiotic enriched bone cement in a critical size defect model in the rat's femur. *Injury*. 2016;47(2):325-334. doi:10.1016/j.injury.2015.10.079
111. Cuthbert RJ, Churchman SM, Tan HB, McGonagle D, Jones E, Giannoudis PV. Induced periosteum a complex cellular scaffold for the treatment of large bone defects. *Bone*. 2013;57(2):484-492. doi:10.1016/j.bone.2013.08.009
112. Masquelet AC. The Evolution of the Induced Membrane Technique: Current Status and Future Directions. *Techniques in Orthopaedics*. 2016;31(1):3. doi:10.1097/BTO.0000000000000160
113. Gouron R, Petit L, Boudot C, et al. Osteoclasts and their precursors are present in the induced-membrane during bone reconstruction using the Masquelet technique. *J Tissue Eng Regen Med*. 2014;11(2):382-389. doi:10.1002/term.1921
114. Pelissier P, Masquelet AC, Bareille R, Pelissier SM, Amedee J. Induced membranes secrete growth factors including vascular and osteoinductive factors and could stimulate bone regeneration. *J Orthop Res*. 2004;22(1):73-79. doi:10.1016/S0736-0266(03)00165-7
115. Morelli I, Drago L, George DA, Gallazzi E, Scarponi S, Romanò CL. Masquelet technique: myth or reality? A systematic review and meta-analysis. *Injury*. 2016;47 Suppl 6:S68-S76. doi:10.1016/S0020-1383(16)30842-7
116. Lu Y, Lai CY, Lai PJ, Yu YH. Induced Membrane Technique for the Management of Segmental Femoral Defects: A Systematic Review and Meta-Analysis of Individual Participant Data. *Orthop Surg*. 2023;15(1):28-37. doi:10.1111/os.13604

117. Hsu CA, Chen SH, Chan SY, Yu YH. The Induced Membrane Technique for the Management of Segmental Tibial Defect or Nonunion: A Systematic Review and Meta-Analysis. *BioMed Research International*. 2020;2020:e5893642. doi:10.1155/2020/5893642
118. Morwood MP, Streufert BD, Bauer A, et al. Intramedullary Nails Yield Superior Results Compared With Plate Fixation When Using the Masquelet Technique in the Femur and Tibia. *J Orthop Trauma*. 2019;33(11):547-552. doi:10.1097/BOT.0000000000001579
119. Durand M, Barbier L, Mathieu L, et al. Towards understanding therapeutic failures in Masquelet surgery: First evidences that defective induced membrane properties are associated with clinical failures. *Bone Reports*. 2020;13:100365. doi:10.1016/j.bonr.2020.100365
120. Longo UG, Trovato U, Loppini M, et al. Tissue engineered strategies for pseudoarthrosis. *Open Orthop J*. 2012;6:564-570. doi:10.2174/1874325001206010564
121. Giannoudis PV, Dinopoulos H, Tsiridis E. Bone substitutes: an update. *Injury*. 2005;36 Suppl 3:S20-27. doi:10.1016/j.injury.2005.07.029
122. Albert A, Leemrijse T, Druez V, Delloye C, Cornu O. Are bone autografts still necessary in 2006? A three-year retrospective study of bone grafting. *Acta Orthop Belg*. 2006;72(6):734-740.
123. Flierl MA, Smith WR, Mauffrey C, et al. Outcomes and complication rates of different bone grafting modalities in long bone fracture nonunions: a retrospective cohort study in 182 patients. *J Orthop Surg Res*. 2013;8:33. doi:10.1186/1749-799X-8-33
124. Hu M, Zeng W, Zhang J, et al. Fixators dynamization for delayed union and non-union of femur and tibial fractures: a review of techniques, timing and influence factors. *J Orthop Surg Res*. 2023;18(1):577. doi:10.1186/s13018-023-04054-3
125. Ramoutar DN, Rodrigues J, Quah C, Boulton C, Moran CG. Judet decortication and compression plate fixation of long bone non-union: Is bone graft necessary? *Injury*. 2011;42(12):1430-1434. doi:10.1016/j.injury.2011.03.045
126. Judet PR, Patel A. Muscle pedicle bone grafting of long bones by osteoperiosteal decortication. *Clin Orthop Relat Res*. 1972;87:74-80.
127. Pieske O, Wittmann A, Zaspel J, et al. Autologous bone graft versus demineralized bone matrix in internal fixation of ununited long bones. *J Trauma Manag Outcomes*. 2009;3:11. doi:10.1186/1752-2897-3-11
128. Govender S, Csimma C, Genant HK, et al. Recombinant human bone morphogenetic protein-2 for treatment of open tibial fractures: a prospective, controlled, randomized study of four hundred and fifty patients. *J Bone Joint Surg Am*. 2002;84(12):2123-2134. doi:10.2106/00004623-200212000-00001
129. Delloye C, Suratwala SJ, Cornu O, Lee FY. Treatment of allograft nonunions with recombinant human bone morphogenetic proteins (rhBMP). *Acta Orthop Belg*. 2004;70(6):591-597.
130. Calori GM, Tagliabue L, Gala L, d'Imporzano M, Peretti G, Albisetti W. Application of rhBMP-7 and platelet-rich plasma in the treatment of long bone non-unions: a prospective randomised clinical study on 120 patients. *Injury*. 2008;39(12):1391-1402. doi:10.1016/j.injury.2008.08.011
131. Marx RE, Carlson ER, Eichstaedt RM, Schimmele SR, Strauss JE, Georgeff KR. Platelet-rich plasma: Growth factor enhancement for bone grafts. *Oral Surg Oral Med Oral Pathol Oral Radiol Endod*. 1998;85(6):638-646. doi:10.1016/s1079-2104(98)90029-4
132. Hsu WK, Mishra A, Rodeo SR, et al. Platelet-rich plasma in orthopaedic applications: evidence-based recommendations for treatment. *J Am Acad Orthop Surg*. 2013;21(12):739-748. doi:10.5435/JAAOS-21-12-739
133. Cadossi R, Massari L, Racine-Avila J, Aaron RK. Pulsed Electromagnetic Field Stimulation of Bone Healing and Joint Preservation: Cellular Mechanisms of Skeletal Response. *J Am Acad Orthop Surg Glob Res Rev*. 2020;4(5):e1900155. doi:10.5435/JAAOSGlobal-D-19-00155

134. Zhang B, Xie Y, Ni Z, Chen L. Effects and Mechanisms of Exogenous Electromagnetic Field on Bone Cells: A Review. *Bioelectromagnetics*. 2020;41(4):263-278. doi:10.1002/bem.22258
135. Gebauer D, Mayr E, Orthner E, Ryaby JP. Low-intensity pulsed ultrasound: effects on nonunions. *Ultrasound Med Biol*. 2005;31(10):1391-1402. doi:10.1016/j.ultrasmedbio.2005.06.002
136. Jiang X, Savchenko O, Li Y, et al. A Review of Low-Intensity Pulsed Ultrasound for Therapeutic Applications. *IEEE Trans Biomed Eng*. 2019;66(10):2704-2718. doi:10.1109/TBME.2018.2889669
137. Harrison A, Alt V. Low-intensity pulsed ultrasound (LIPUS) for stimulation of bone healing - A narrative review. *Injury*. 2021;52 Suppl 2:S91-S96. doi:10.1016/j.injury.2021.05.002
138. Sen MK, Miclau T. Autologous iliac crest bone graft: should it still be the gold standard for treating nonunions? *Injury*. 2007;38 Suppl 1:S75-80. doi:10.1016/j.injury.2007.02.012
139. Hernigou P, Poignard A, Beaujean F, Rouard H. Percutaneous autologous bone-marrow grafting for nonunions. Influence of the number and concentration of progenitor cells. *J Bone Joint Surg Am*. 2005;87(7):1430-1437. doi:10.2106/JBJS.D.02215
140. Napora JK, Weinberg DS, Eagle BA, Kaufman BR, Sontich JK. Hexapod Stacked Transport for Tibial Infected Nonunions With Bone Loss: Long-Term Functional Outcomes. *J Orthop Trauma*. 2018;32(1):e12-e18. doi:10.1097/BOT.0000000000001005
141. Zekry KM, Yamamoto N, Hayashi K, et al. Reconstruction of intercalary bone defect after resection of malignant bone tumor. *J Orthop Surg (Hong Kong)*. 2019;27(1):2309499019832970. doi:10.1177/2309499019832970
142. Beris AE, Lykissas MG, Korompilias AV, et al. Vascularized fibula transfer for lower limb reconstruction. *Microsurgery*. 2011;31(3):205-211. doi:10.1002/micr.20841
143. Taylor GI, Miller GD, Ham FJ. The free vascularized bone graft. A clinical extension of microvascular techniques. *Plast Reconstr Surg*. 1975;55(5):533-544. doi:10.1097/00006534-197505000-00002
144. Calori GM, Colombo M, Malagoli E, Mazzola S, Bucci M, Mazza E. Megaprosthesis in post-traumatic and periprosthetic large bone defects: Issues to consider. *Injury*. 2014;45 Suppl 6:S105-110. doi:10.1016/j.injury.2014.10.032
145. Delloye C, Cnockaert N, Cornu O. Bone substitutes in 2003: an overview. *Acta Orthop Belg*. 2003;69(1):1-8.
146. Panagiotopoulou VC, Santolini E, Jones E, Jha A, Giannoudis PV. Adhesives for treatment of bone fractures: A review of the state-of-the art. *Injury*. 2022;53:S20-S25. doi:10.1016/j.injury.2021.02.019
147. Abumunaser LA, Al-Sayyad MJ. Evaluation of the calori et Al nonunion scoring system in a retrospective case series. *Orthopedics*. 2011;34(5):359. doi:10.3928/01477447-20110317-31
148. Calori GM, Phillips M, Jeetle S, Tagliabue L, Giannoudis PV. Classification of non-union: need for a new scoring system? *Injury*. 2008;39 Suppl 2:S59-63. doi:10.1016/S0020-1383(08)70016-0
149. Vincken L, van der Broeck L, Geurts J, Qiu Shao SS, Poeze M, Blokhuis TJ. The effect of post-traumatic long bone non-unions on health-related quality of life. *Injury*. 2023;54 Suppl 5:110929. doi:10.1016/j.injury.2023.110929
150. Loi F, Córdova LA, Pajarinen J, Lin T hua, Yao Z, Goodman SB. Inflammation, Fracture and Bone Repair. *Bone*. 2016;86:119-130. doi:10.1016/j.bone.2016.02.020
151. Younger EM, Chapman MW. Morbidity at bone graft donor sites. *J Orthop Trauma*. 1989;3(3):192-195. doi:10.1097/00005131-198909000-00002
152. Delloye C, De Halleux J, Cornu O, Wegmann E, Buccafusca GC, Gigi J. Organizational and investigational aspects of bone banking in Belgium. *Acta Orthop Belg*. 1991;57 Suppl 2:27-34.
153. Delloye C, Bannister GC, eds. *Impaction Bone Grafting in Revision Arthroplasty*. CRC Press; 2004. doi:10.4324/9780203913680

154. Pirnay JP, Baudoux E, Cornu O, et al. Access to human tissues for research and product development. *EMBO Rep*. 2015;16(5):557-562. doi:10.15252/embr.201540070
155. Bracey DN, Jinnah AH, Willey JS, et al. Investigating the Osteoinductive Potential of a Decellularized Xenograft Bone Substitute. *Cells Tissues Organs*. 2019;207(2):97-113. doi:10.1159/000503280
156. Delloye C, Van Cauter M, Dufrane D, Francq BG, Docquier PL, Cornu O. Local complications of massive bone allografts : an appraisal of their prevalence in 128 patients. *Acta Orthop Belg*. 2014;80(2):196-204. doi:PMID: 25090792
157. Delloye C. How to improve the incorporation of massive allografts? *Chir Organi Mov*. 2003;88(4):335-343.
158. Vander Griend RA. The effect of internal fixation on the healing of large allografts. *J Bone Joint Surg Am*. 1994;76(5):657-663. doi:10.2106/00004623-199405000-00005
159. Hornicek FJ, Gebhardt MC, Tomford WW, et al. Factors affecting nonunion of the allograft-host junction. *Clin Orthop Relat Res*. 2001;(382):87-98. doi:10.1097/00003086-200101000-00014
160. Bus MPA, Dijkstra PDS, van de Sande M a. J, et al. Intercalary allograft reconstructions following resection of primary bone tumors: a nationwide multicenter study. *J Bone Joint Surg Am*. 2014;96(4):e26. doi:10.2106/JBJS.M.00655
161. Nguyen H, Morgan DAF, Forwood MR. Sterilization of allograft bone: effects of gamma irradiation on allograft biology and biomechanics. *Cell Tissue Bank*. 2007;8(2):93-105. doi:10.1007/s10561-006-9020-1
162. Enneking WF, Burchardt H, Puhl JJ, Piotrowski G. Physical and biological aspects of repair in dog cortical-bone transplants. *J Bone Joint Surg Am*. 1975;57(2):237-252.
163. Hill C, Purtill D. Learning from the bone allograft tuberculosis outbreak in the USA. *Lancet Infect Dis*. 2022;22(11):1522-1523. doi:10.1016/S1473-3099(22)00432-7
164. Ortiz-Cruz E, Gebhardt MC, Jennings LC, Springfield DS, Mankin HJ. The results of transplantation of intercalary allografts after resection of tumors. A long-term follow-up study. *J Bone Joint Surg Am*. 1997;79(1):97-106. doi:10.2106/00004623-199701000-00010
165. Mankin HJ, Gebhardt MC, Jennings LC, Springfield DS, Tomford WW. Long-term results of allograft replacement in the management of bone tumors. *Clin Orthop Relat Res*. 1996;(324):86-97. doi:10.1097/00003086-199603000-00011
166. Langer R, Vacanti JP. Tissue Engineering. *Science*. 1993;260(5110):920-926. doi:10.1126/science.8493529
167. Salgado AJ, Coutinho OP, Reis RL. Bone tissue engineering: state of the art and future trends. *Macromol Biosci*. 2004;4(8):743-765. doi:10.1002/mabi.200400026
168. Rustad KC, Sorkin M, Levi B, Longaker MT, Gurtner GC. Strategies for organ level tissue engineering. *Organogenesis*. 2010;6(3):151-157.
169. Poh PSP, Chhaya MP, Wunner FM, et al. Polylactides in additive biomanufacturing. *Advanced Drug Delivery Reviews*. 2016;107:228-246. doi:10.1016/j.addr.2016.07.006
170. O'Brien FJ. Biomaterials & scaffolds for tissue engineering. *Materials Today*. 2011;14(3):88-95. doi:10.1016/S1369-7021(11)70058-X
171. Reddy MSB, Ponnamma D, Choudhary R, Sadasivuni KK. A Comparative Review of Natural and Synthetic Biopolymer Composite Scaffolds. *Polymers*. 2021;13(7):1105. doi:10.3390/polym13071105
172. Alaribe F, Manoto S, Motaung S. Scaffolds from biomaterials: Advantages and limitations in bone and tissue engineering. *Biologia*. 2016;71. doi:10.1515/biolog-2016-0056
173. Ye B, Wu B, Su Y, Sun T, Guo X. Recent Advances in the Application of Natural and Synthetic Polymer-Based Scaffolds in Musculoskeletal Regeneration. *Polymers (Basel)*. 2022;14(21):4566. doi:10.3390/polym14214566

174. Keane TJ, Swinehart IT, Badylak SF. Methods of tissue decellularization used for preparation of biologic scaffolds and in vivo relevance. *Methods*. 2015;84:25-34. doi:10.1016/j.ymeth.2015.03.005
175. Badylak S, Freytes D, Gilbert T. Extracellular matrix as a biological scaffold material: Structure and function. *Acta Biomaterialia*. 2009;5(1):1-13. doi:10.1016/j.actbio.2008.09.013
176. Hulshof FFB, Papenburg B, Vasilevich A, et al. Mining for osteogenic surface topographies: In silico design to *in vivo* osseo-integration. *Biomaterials*. 2017;137:49-60. doi:10.1016/j.biomaterials.2017.05.020
177. Van Bael S, Chai YC, Truscello S, et al. The effect of pore geometry on the in vitro biological behavior of human periosteum-derived cells seeded on selective laser-melted Ti6Al4V bone scaffolds. *Acta Biomaterialia*. 2012;8(7):2824-2834. doi:10.1016/j.actbio.2012.04.001
178. Crapo PM, Gilbert TW, Badylak SF. An overview of tissue and whole organ decellularization processes. *Biomaterials*. 2011;32(12):3233-3243. doi:10.1016/j.biomaterials.2011.01.057
179. Hoshiba T, Chen G, Endo C, et al. Decellularized Extracellular Matrix as an *In Vitro* Model to Study the Comprehensive Roles of the ECM in Stem Cell Differentiation. *Stem Cells International*. 2016;2016:1-10. doi:10.1155/2016/6397820
180. Nagata S, Hanayama R, Kawane K. Autoimmunity and the clearance of dead cells. *Cell*. 2010;140(5):619-630. doi:10.1016/j.cell.2010.02.014
181. Sterilization of health care products-Radiation-Part 3: Guidance on dosimetric aspects of development, validation and routine control. *ANSI/AAMI/ISO 11137-3:2017/(R)2023; Sterilization of health care products?Radiation?Part 3: Guidance on dosimetric aspects of development, validation and routine control*. Published online May 17, 2022. doi:10.2345/9781570206900.ch1
182. Sterilization of health care products-Microbiological methods-Guidance on conducting bioburden determinations and tests of sterility for biologics and tissue-based products. *AAMI/ISO TIR22456:2022; Sterilization of health care products?Microbiological methods?Guidance on conducting bioburden determinations and tests of sterility for biologics and tissue-based products*. Published online March 24, 2023. doi:10.2345/9781570208652.ch1
183. Anastasescou M, Cornu O, Delloye C, Gigi J. Contamination rate and logarithmic reduction of bacteria by processing of freeze-dried cancellous bone. In: *3d Congress of the European Federation of National Associations of Orthopaedics and Traumatology (EFORT), 6th Annual Meeting of EAMST*. ; 1997.
184. Pruss A, Kao M, Gohs U, Koscielny J, von Versen R, Pauli G. Effect of gamma irradiation on human cortical bone transplants contaminated with enveloped and non-enveloped viruses. *Biologicals*. 2002;30(2):125-133. doi:10.1006/biol.2002.0326
185. Conrad EU, Gretch DR, Obermeyer KR, et al. Transmission of the hepatitis-C virus by tissue transplantation. *J Bone Joint Surg Am*. 1995;77(2):214-224. doi:10.2106/00004623-199502000-00007
186. Smith RA, Ingels J, Lochemes JJ, Dutkowsky JP, Pifer LL. Gamma irradiation of HIV-1. *J Orthop Res*. 2001;19(5):815-819. doi:10.1016/S0736-0266(01)00018-3
187. Miekka SI, Forng RY, Rohwer RG, et al. Inactivation of viral and prion pathogens by gamma-irradiation under conditions that maintain the integrity of human albumin. *Vox Sang*. 2003;84(1):36-44. doi:10.1046/j.1423-0410.2003.00256.x
188. Sun WQ, Leung P. Calorimetric study of extracellular tissue matrix degradation and instability after gamma irradiation. *Acta Biomater*. 2008;4(4):817-826. doi:10.1016/j.actbio.2008.02.006
189. Cornu O, Banse X, Docquier PL, Luyckx S, Delloye C. Effect of freeze-drying and gamma irradiation on the mechanical properties of human cancellous bone. *J Orthop Res*. 2000;18(3):426-431. doi:10.1002/jor.1100180314
190. Gouk SS, Lim TM, Teoh SH, Sun WQ. Alterations of human acellular tissue matrix by gamma irradiation: histology, biomechanical property, stability, in vitro cell repopulation, and

remodeling. *J Biomed Mater Res B Appl Biomater*. 2008;84(1):205-217. doi:10.1002/jbm.b.30862
191. Anderson MJ, Keyak JH, Skinner HB. Compressive mechanical properties of human cancellous bone after gamma irradiation. *J Bone Joint Surg Am*. 1992;74(5):747-752.
192. Moreau MF, Gallois Y, Baslé MF, Chappard D. Gamma irradiation of human bone allografts alters medullary lipids and releases toxic compounds for osteoblast-like cells. *Biomaterials*. 2000;21(4):369-376. doi:10.1016/S0142-9612(99)00193-3
193. Meirelles L da S, Nardi NB. Methodology, biology and clinical applications of mesenchymal stem cells. *Front Biosci (Landmark Ed)*. 2009;14(11):4281-4298. doi:10.2741/3528
194. Pountos I, Giannoudis PV. Biology of mesenchymal stem cells. *Injury*. 2005;36(3, Supplement):S8-S12. doi:10.1016/j.injury.2005.07.028
195. Takahashi K, Yamanaka S. Induction of pluripotent stem cells from mouse embryonic and adult fibroblast cultures by defined factors. *Cell*. 2006;126(4):663-676. doi:10.1016/j.cell.2006.07.024
196. Takahashi K, Tanabe K, Ohnuki M, et al. Induction of pluripotent stem cells from adult human fibroblasts by defined factors. *Cell*. 2007;131(5):861-872. doi:10.1016/j.cell.2007.11.019
197. Friedenstein AJ, Piatetzky-Shapiro II, Petrakova KV. Osteogenesis in transplants of bone marrow cells. *J Embryol Exp Morphol*. 1966;16(3):381-390.
198. Caplan AI. Mesenchymal stem cells. *J Orthop Res*. 1991;9(5):641-650. doi:10.1002/jor.1100090504
199. Kolf CM, Cho E, Tuan RS. Biology of adult mesenchymal stem cells: regulation of niche, self-renewal and differentiation. *Arthritis Res Ther*. 2007;9(1):204. doi:10.1186/ar2116
200. Dominici M, Le Blanc K, Mueller I, et al. Minimal criteria for defining multipotent mesenchymal stromal cells. The International Society for Cellular Therapy position statement. *Cytotherapy*. 2006;8(4):315-317. doi:10.1080/14653240600855905
201. Zhang Y, Khan D, Delling J, Tobiasch E. Mechanisms Underlying the Osteo- and Adipo-Differentiation of Human Mesenchymal Stem Cells. *ScientificWorldJournal*. 2012;2012:793823. doi:10.1100/2012/793823
202. Wabitsch M, Hauner H, Heinze E, Teller WM. The role of growth hormone/insulin-like growth factors in adipocyte differentiation. *Metabolism*. 1995;44:45-49. doi:10.1016/0026-0495(95)90220-1
203. Chang HR, Kim HJ, Xu X, Ferrante AW. Macrophage and adipocyte IGF1 maintain adipose tissue homeostasis during metabolic stresses. *Obesity (Silver Spring)*. 2016;24(1):172-183. doi:10.1002/oby.21354
204. Jeyaraman M, Muthu S, Gangadaran P, et al. Osteogenic and Chondrogenic Potential of Periosteum-Derived Mesenchymal Stromal Cells: Do They Hold the Key to the Future? *Pharmaceuticals*. 2021;14(11):1133. doi:10.3390/ph14111133
205. Maya Fakhry EH, Buchet DM. Molecular mechanisms of mesenchymal stem cell differentiation towards osteoblasts. *World Journal of Stem Cells*. 2013;5(4):136-148. doi:10.4252/wjsc.v5.i4.136
206. Aubin JE. Chapter 4 - Mesenchymal Stem Cells and Osteoblast Differentiation. In: Bilezikian JP, Raisz LG, Martin TJ, eds. *Principles of Bone Biology (Third Edition)*. Academic Press; 2008:85-107. doi:10.1016/B978-0-12-373884-4.00026-4
207. Crane NJ. A nondestructive method for monitoring in vitro stem cell osteogenic differentiation with Raman spectroscopic mapping. *Spectroscopy*. 2009;24(3):9.
208. Ryan JM, Barry FP, Murphy JM, Mahon BP. Mesenchymal stem cells avoid allogeneic rejection. *J Inflamm (Lond)*. 2005;2:8. doi:10.1186/1476-9255-2-8
209. Nauta AJ, Fibbe WE. Immunomodulatory properties of mesenchymal stromal cells. *Blood*. 2007;110(10):3499-3506. doi:10.1182/blood-2007-02-069716

210. Ghannam S, Bouffi C, Djouad F, Jorgensen C, Noël D. Immunosuppression by mesenchymal stem cells: mechanisms and clinical applications. *Stem Cell Res Ther*. 2010;1(1):2. doi:10.1186/scrt2
211. Schubert T, Xhema D, Veriter S, et al. The enhanced performance of bone allografts using osteogenic-differentiated adipose-derived mesenchymal stem cells. *Biomaterials*. 2011;32(34):8880-8891. doi:10.1016/j.biomaterials.2011.08.009
212. Camassola M, de Macedo Braga LMG, Chagastelles PC, Nardi NB. Methodology, biology and clinical applications of human mesenchymal stem cells. *Methods Mol Biol*. 2012;879:491-504. doi:10.1007/978-1-61779-815-3_30
213. Ferretti C, Mattioli-Belmonte M. Periosteum derived stem cells for regenerative medicine proposals: Boosting current knowledge. *World J Stem Cells*. 2014;6(3):266-277. doi:10.4252/wjsc.v6.i3.266
214. Cao Y, Buckels EJ, Matthews BG. Markers for Identification of Postnatal Skeletal Stem Cells In Vivo. *Curr Osteoporos Rep*. 2020;18(6):655-665. doi:10.1007/s11914-020-00622-2
215. Owston HE, Ganguly P, Tronci G, Russell SJ, Giannoudis PV, Jones EA. Colony Formation, Migratory, and Differentiation Characteristics of Multipotential Stromal Cells (MSCs) from "Clinically Accessible" Human Periosteum Compared to Donor-Matched Bone Marrow MSCs. *Stem Cells International*. 2019;2019:1-14. doi:10.1155/2019/6074245
216. Colnot C. Skeletal cell fate decisions within periosteum and bone marrow during bone regeneration. *J Bone Miner Res*. 2009;24(2):274-282. doi:10.1359/jbmr.081003
217. Lee CS, Burnsed OA, Raghuram V, Kalisvaart J, Boyan BD, Schwartz Z. Adipose stem cells can secrete angiogenic factors that inhibit hyaline cartilage regeneration. *Stem Cell Res Ther*. 2012;3(4):35. doi:10.1186/scrt126
218. Hayashi O, Katsube Y, Hirose M, Ohgushi H, Ito H. Comparison of Osteogenic Ability of Rat Mesenchymal Stem Cells from Bone Marrow, Periosteum, and Adipose Tissue. *Calcif Tissue Int*. 2008;82(3):238-247. doi:10.1007/s00223-008-9112-y
219. Augello A, Kurth TB, De Bari C. Mesenchymal stem cells: a perspective from in vitro cultures to in vivo migration and niches. *Eur Cell Mater*. 2010;20:121-133. doi:10.22203/ecm.v020a11
220. Bilkay U, Tokat C, Helvaci E, et al. Osteogenic capacities of tibial and cranial periosteum: a biochemical and histologic study. *J Craniofac Surg*. 2008;19(2):453-458. doi:10.1097/SCS.0b013e318052fe3d
221. De Bari C, Dell'Accio F, Vanlauwe J, et al. Mesenchymal multipotency of adult human periosteal cells demonstrated by single-cell lineage analysis. *Arthritis Rheum*. 2006;54(4):1209-1221. doi:10.1002/art.21753
222. Khaund R, Flynn SH. Iliotibial Band Syndrome: A Common Source of Knee Pain. *afp*. 2005;71(8):1545-1550.
223. Benjamin M. The fascia of the limbs and back – a review. *Journal of Anatomy*. 2009;214(1):1-18. doi:10.1111/j.1469-7580.2008.01011.x
224. Huang BK, Campos JC, Michael Peschka PG, et al. Injury of the gluteal aponeurotic fascia and proximal iliotibial band: anatomy, pathologic conditions, and MR imaging. *Radiographics*. 2013;33(5):1437-1452.
225. Otsuka S, Yakura T, Ohmichi Y, et al. Site specificity of mechanical and structural properties of human fascia lata and their gender differences: A cadaveric study. *J Biomech*. 2018;77:69-75. doi:10.1016/j.jbiomech.2018.06.018
226. Fede C, Gaudreault N, Fan C, Macchi V, De Caro R, Stecco C. Morphometric and dynamic measurements of muscular fascia in healthy individuals using ultrasound imaging: a summary of the discrepancies and gaps in the current literature. *Surg Radiol Anat*. 2018;40(12):1329-1341. doi:10.1007/s00276-018-2086-1

227. Pirri C, Fede C, Petrelli L, et al. An anatomical comparison of the fasciae of the thigh: A macroscopic, microscopic and ultrasound imaging study. *Journal of Anatomy*. 2021;238(4):999-1009. doi:10.1111/joa.13360
228. Kumka M, Bonar J. Fascia: a morphological description and classification system based on a literature review. *J Can Chiropr Assoc*. 2012;56(3):179-191.
229. Flato R, Passanante GJ, Skalski MR, Patel DB, White EA, Matcuk GR. The iliotibial tract: imaging, anatomy, injuries, and other pathology. *Skeletal radiology*. 2017;46:605-622.
230. Manaster BJ, Andrews CL, Crim J. *Diagnostic and Surgical Imaging Anatomy: Musculoskeletal*. Amirsys; 2007.
231. Stecco C, Porzionato A, Lancerotto L, et al. Histological study of the deep fasciae of the limbs. *Journal of Bodywork and Movement Therapies*. 2008;12(3):225-230. doi:10.1016/j.jbmt.2008.04.041
232. Evans P. The postural function of the iliotibial tract. *Annals of the Royal college of Surgeons of England*. 1979;61(4):271.
233. Finn MA, Faulkner ND, Hetzel SJ, Anderson PA. Spinal duraplasty materials and hydrostasis: a biomechanical study: Laboratory investigation. *SPI*. 2011;15(4):422-427. doi:10.3171/2011.5.SPINE10851
234. Song Z, Yang D, Yang J, et al. Abdominal wall reconstruction following resection of large abdominal aggressive neoplasms using tensor fascia lata flap with or without mesh reinforcement. *Hernia*. 2018;22(2):333-341. doi:10.1007/s10029-018-1738-8
235. Molnar TF, Rendeki S, Lukacs L, Horvath OP. Improvement of air tightness of stapled lung parenchyma using fascia lata. *Interact Cardiovasc Thorac Surg*. 2003;2(4):503-505. doi:10.1016/S1569-9293(03)00126-9
236. Bock ME, Nagle R, Soyster M, et al. Robotic Sacral Colpopexy Using Autologous Fascia Lata Compared with Mesh. *Journal of Endourology*. 2021;35(6):801-807. doi:10.1089/end.2020.0537
237. Fox P, Endress R, Sen S, Chang J. Fascia-only anterolateral thigh flap for extremity reconstruction. *Ann Plast Surg*. 2014;72 Suppl 1:S9-13. doi:10.1097/SAP.0000000000000146
238. Philippon MJ, Briggs KK, Hay CJ, Kuppersmith DA, Dewing CB, Huang MJ. Arthroscopic labral reconstruction in the hip using iliotibial band autograft: technique and early outcomes. *Arthroscopy: The Journal of Arthroscopic & Related Surgery*. 2010;26(6):750-756.
239. Matthewson G, Coady CM, Wong IHB. Rotator Cuff Reconstruction Using Fascia Lata Patch Autograft for the Nonrepairable Rotator Cuff Tear. *Arthroscopy Techniques*. 2020;9(1):e123-e130. doi:10.1016/j.eats.2019.09.006
240. Sapino G, Zaugg P, Cherix S, et al. ALT flap with vascularized fascia lata for one-stage functional patellar tendon reconstruction. *Journal of Plastic, Reconstructive & Aesthetic Surgery*. 2019;72(3):467-476. doi:10.1016/j.bjps.2018.11.002
241. Ferretti A, Monaco E, Fabbri M, Mazza D, De Carli A. The Fascia Lata Anterolateral Tenodesis Technique. *Arthroscopy Techniques*. 2017;6(1):e81-e86. doi:10.1016/j.eats.2016.09.005
242. de Wouters S, Tran Duy K, Docquier PL. Patient-specific instruments for surgical resection of painful tarsal coalition in adolescents. *Orthop Traumatol Surg Res*. 2014;100(4):423-427. doi:10.1016/j.otsr.2014.02.009
243. Fawzi-Grancher S, Goebbels RM, Bigare E, et al. Human tissue allograft processing: impact on in vitro and in vivo biocompatibility. *J Mater Sci Mater Med*. 2009;20(8):1709-1720. doi:10.1007/s10856-009-3726-0
244. Chen X, Yu B, Wang Z, Li Q, Dai C, Wei J. Progress of Periosteal Osteogenesis: The Prospect of In Vivo Bioreactor. *Orthopaedic Surgery*. Published online July 6, 2022:os.13325. doi:10.1111/os.13325
245. Evans SF, Chang H, Knothe Tate ML. Elucidating multiscale periosteal mechanobiology: a key to unlocking the smart properties and regenerative capacity of the periosteum? *Tissue Engineering Part B: Reviews*. 2013;19(2):147-159.

246. Chen K, Lin X, Zhang Q, et al. Decellularized periosteum as a potential biologic scaffold for bone tissue engineering. *Acta Biomater*. 2015;19:46-55. doi:10.1016/j.actbio.2015.02.020
247. Moore SR, Heu C, Yu NY, et al. Translating Periosteum's Regenerative Power: Insights From Quantitative Analysis of Tissue Genesis With a Periosteum Substitute Implant. *Stem Cells Transl Med*. 2016;5(12):1739-1749. doi:10.5966/sctm.2016-0004
248. Yu Y, Wang Y, Zhang W, et al. Biomimetic periosteum-bone substitute composed of preosteoblast-derived matrix and hydrogel for large segmental bone defect repair. *Acta Biomaterialia*. 2020;113:317-327. doi:10.1016/j.actbio.2020.06.030
249. Yu Z, Geng J, Gao H, Zhao X, Chen J. Evaluations of guided bone regeneration in canine radius segmental defects using autologous periosteum combined with fascia lata under stable external fixation. Published online 2015:8.
250. Janik S, Hirtler L, Traxler H, Weninger WJ, Seemann R, Erovic BM. The vascularized fascia lata free flap: an anatomical study and clinical considerations. *Eur Arch Otorhinolaryngol*. 2020;277(6):1733-1739. doi:10.1007/s00405-020-05861-8
251. Watson TS, Panicco J, Parekh A. Allograft Tendon Interposition Arthroplasty of the Hallux Metatarsophalangeal Joint: A Technique Guide and Literature Review. *Foot Ankle Int*. 2019;40(1):113-119. doi:10.1177/1071100718807738
252. Bankhead P, Loughrey MB, Fernández JA, et al. QuPath: Open source software for digital pathology image analysis. *Sci Rep*. 2017;7(1):16878. doi:10.1038/s41598-017-17204-5
253. Horwitz EM, Le Blanc K, Dominici M, et al. Clarification of the nomenclature for MSC: The International Society for Cellular Therapy position statement. *Cytotherapy*. 2005;7(5):393-395. doi:10.1080/14653240500319234
254. Di Meglio F, Nurzynska D, Romano V, et al. Optimization of Human Myocardium Decellularization Method for the Construction of Implantable Patches. *Tissue Engineering Part C: Methods*. 2017;23(9):525-539. doi:10.1089/ten.tec.2017.0267
255. Zhang J, Zhang Q, Chen J, et al. Preparation and Evaluation of Tibia- and Calvarium-Derived Decellularized Periosteum Scaffolds. *ACS Biomater Sci Eng*. 2017;3(12):3503-3514. doi:10.1021/acsbiomaterials.7b00548
256. Hsiao HY, Yang CY, Liu JW, Brey EM, Cheng MH. Periosteal Osteogenic Capacity Depends on Tissue Source. *Tissue Engineering Part A*. 2018;24(23-24):1733-1741. doi:10.1089/ten.tea.2018.0009
257. Pancheri FQ, Eng CM, Lieberman DE, Biewener AA, Dorfmann L. A constitutive description of the anisotropic response of the fascia lata. *Journal of the Mechanical Behavior of Biomedical Materials*. 2014;30:306-323. doi:10.1016/j.jmbbm.2013.12.002
258. Schwarz, Gögele, Ondruschka, Hammer, Kohl, Schulze-Tanzil. Migrating Myofibroblastic Iliotibial Band-Derived Fibroblasts Represent a Promising Cell Source for Ligament Reconstruction. *IJMS*. 2019;20(8):1972. doi:10.3390/ijms20081972
259. White AP, Vaccaro AR, Hall JA, Whang PG, Friel BC, McKee MD. Clinical applications of BMP-7/OP-1 in fractures, nonunions and spinal fusion. *International Orthopaedics (SICO*. 2007;31(6):735-741. doi:10.1007/s00264-007-0422-x
260. Even J, Eskander M, Kang J. Bone Morphogenetic Protein in Spine Surgery: Current and Future Uses. *Journal of the American Academy of Orthopaedic Surgeons*. 2012;20(9):6.
261. Ong KL, Villarraga ML, Lau E, Carreon LY, Kurtz SM, Glassman SD. Off-Label Use of Bone Morphogenetic Proteins in the United States Using Administrative Data: *Spine*. 2010;35(19):1794-1800. doi:10.1097/BRS.0b013e3181ecf6e4
262. De La Vega RE, van Griensven M, Zhang W, et al. Efficient healing of large osseous segmental defects using optimized chemically modified messenger RNA encoding BMP-2. *Sci Adv*. 2022;8(7):eabl6242. doi:10.1126/sciadv.abl6242
263. Ji W, Kerckhofs G, Geeroms C, Marechal M, Geris L, Luyten FP. Deciphering the combined effect of bone morphogenetic protein 6 and calcium phosphate on bone formation capacity

of periosteum derived cell-based tissue engineering constructs. *Acta Biomaterialia*. 2018;80:97-107. doi:10.1016/j.actbio.2018.09.046

264. Maruyama M, Rhee C, Utsunomiya T, et al. Modulation of the Inflammatory Response and Bone Healing. *Front Endocrinol*. 2020;11:386. doi:10.3389/fendo.2020.00386
265. Schlundt C, Fischer H, Bucher CH, Rendenbach C, Duda GN, Schmidt-Bleek K. The multifaceted roles of macrophages in bone regeneration: A story of polarization, activation and time. *Acta Biomaterialia*. 2021;133:46-57. doi:10.1016/j.actbio.2021.04.052
266. Butler DL, Grood ES, Noyes FR, Zernicke RF, Brackett K. Effects of structure and strain measurement technique on the material properties of young human tendons and fascia. *Journal of Biomechanics*. 1984;17(8):579-596. doi:10.1016/0021-9290(84)90090-3
267. Hinton R, Jinnah RH, Johnson C, Warden K, Clarke HJ. A biomechanical analysis of solvent-dehydrated and freeze-dried human fascia lata allografts: A preliminary report. *Am J Sports Med*. 1992;20(5):607-612. doi:10.1177/036354659202000521
268. Bertram JEA, Polevoy Y, Cullinane DM. Mechanics of Avian Fibrous Periosteum: Tensile and Adhesion Properties During Growth. *Bone*. 1998;22(6):669-675. doi:10.1016/S8756-3282(98)00035-0
269. Debelmas A, Picard A, Kadlub N, Boisson J. Contribution of the periosteum to mandibular distraction. Garcia Aznar JM, ed. *PLoS ONE*. 2018;13(6):e0199116. doi:10.1371/journal.pone.0199116
270. Erivan R, Aubret S, Villatte G, et al. Irradiation at 11 kGy conserves the biomechanical properties of fascia lata better than irradiation at 25 kGy. *Clinical Biomechanics*. 2018;60:100-107. doi:10.1016/j.clinbiomech.2018.10.016
271. Pukšec M, Semenski D, Ježek D, et al. Biomechanical Comparison of the Temporalis Muscle Fascia, the Fascia Lata, and the Dura Mater. *J Neurol Surg B*. 2019;80(01):023-030. doi:10.1055/s-0038-1661349
272. McBride SH, Evans SF, Knothe Tate ML. Anisotropic mechanical properties of ovine femoral periosteum and the effects of cryopreservation. *J Biomech*. 2011;44(10):1954-1959. doi:10.1016/j.jbiomech.2011.04.036
273. Li N, Song J, Zhu G, et al. Periosteum tissue engineering—a review. *Biomater Sci*. 2016;4(11):1554-1561. doi:10.1039/C6BM00481D
274. Pirri C, Fede C, Petrelli L, et al. Elastic Fibres in the subcutaneous tissue: Is there a difference between superficial and muscular fascia? A cadaver study. *Skin Research and Technology*. 2022;28(1):21-27. doi:10.1111/srt.13084
275. Stecco C, Macchi V, Porzionato A, Duparc F, De Caro R. The Fascia : the Forgotten Structure. *IJAE : Italian Journal of Anatomy and Embryology : 116, 3, 2011*. Published online 2011:127-138. doi:10.1400/207563
276. Schleip R, Hedley G, Yucesoy CA. Fascial nomenclature: Update on related consensus process. *Clinical Anatomy*. 2019;32(7):929-933. doi:10.1002/ca.23423
277. Stecco C, Delmas V, Richard A. *Atlas fonctionnel du système fascial humain*. Illustrated édition. Tita Editions; 2020.
278. Sher I, Umans H, Downie SA, Tobin K, Arora R, Olson TR. Proximal iliotibial band syndrome: what is it and where is it? *Skeletal radiology*. 2011;40:1553-1556.
279. Khoury AN, Brooke K, Helal A, et al. Proximal iliotibial band thickness as a cause for recalcitrant greater trochanteric pain syndrome. *Journal of Hip Preservation Surgery*. 2018;5(3):296-300. doi:10.1093/jhps/hny025
280. Ucpinar BA, Bankaoglu M, Eren OT, Erturk SM. Measurement of iliotibial band diameter in iliotibial band friction syndrome and comparison with an asymptomatic population. *Acta Radiologica*. Published online September 16, 2020. doi:10.1177/0284185120958407

281. Joseph MF, Taft K, Moskwa M, Denegar CR. Deep friction massage to treat tendinopathy: a systematic review of a classic treatment in the face of a new paradigm of understanding. *J Sport Rehabil*. 2012;21(4):343-353. doi:10.1123/jsr.21.4.343
282. Stecco C, Pavan P, Pachera P, De Caro R, Natali A. Investigation of the mechanical properties of the human crural fascia and their possible clinical implications. *Surg Radiol Anat*. 2014;36(1):25-32. doi:10.1007/s00276-013-1152-y
283. Kerckhofs G, Stegen S, van Gastel N, et al. Simultaneous three-dimensional visualization of mineralized and soft skeletal tissues by a novel microCT contrast agent with polyoxometalate structure. *Biomaterials*. 2018;159:1-12. doi:10.1016/j.biomaterials.2017.12.016
284. de Bournonville S, Vangrunderbeeck S, Kerckhofs G. Contrast-Enhanced MicroCT for Virtual 3D Anatomical Pathology of Biological Tissues: A Literature Review. *Contrast Media Mol Imaging*. 2019;2019:8617406. doi:10.1155/2019/8617406
285. Shearer T, Rawson S, Castro SJ, et al. X-ray computed tomography of the anterior cruciate ligament and patellar tendon. *Muscles Ligaments Tendons J*. 2014;4(2):238-244.
286. Balint R, Lowe T, Shearer T. Optimal Contrast Agent Staining of Ligaments and Tendons for X-Ray Computed Tomography. *PLOS ONE*. 2016;11(4):e0153552. doi:10.1371/journal.pone.0153552
287. Sartori J, Köhring S, Witte H, Fischer MS, Löffler M. Three-dimensional imaging of the fibrous microstructure of Achilles tendon entheses in Mus musculus. *J Anat*. 2018;233(3):370-380. doi:10.1111/joa.12837
288. Maes A, Pestiaux C, Marino A, et al. Cryogenic contrast-enhanced microCT enables nondestructive 3D quantitative histopathology of soft biological tissues. *Nat Commun*. 2022;13(1):6207. doi:10.1038/s41467-022-34048-4
289. Sieck GC. Physiology in Perspective: Structure and Function—Anatomy and Physiology Are Integral. *Physiology*. 2017;32(4):264-265. doi:10.1152/physiol.00014.2017
290. Manon J, Evrard R, Maistriaux L, et al. Periosteum and fascia lata: Are they so different? *Front Bioeng Biotechnol*. 2022;10:944828. doi:10.3389/fbioe.2022.944828
291. Manon J, Evrard R, Fievé L, et al. A New Osteogenic Membrane to Enhance Bone Healing: At the Crossroads between the Periosteum, the Induced Membrane, and the Diamond Concept. *Bioengineering*. 2023;10(2):143. doi:10.3390/bioengineering10020143
292. Blanc R, Westenberger P. Comparison of fiber orientation analysis methods in Avizo. *e-Journal of Nondestructive Testing*. 2017;22(03). Accessed January 16, 2024. https://www.ndt.net/search/docs.php3?id=20865&msgID=0&rootID=0
293. Stecco C, Hammer W, Vleeming A, De Caro R. 8 - Fasciae of the Lower Limb. In: Stecco C, Hammer W, Vleeming A, De Caro R, eds. *Functional Atlas of the Human Fascial System*. Churchill Livingstone; 2015:289-366. doi:10.1016/B978-0-7020-4430-4.00008-7
294. Goh LA, Chhem RK, Wang S chang, Chee T. Iliotibial band thickness: Sonographic measurements in asymptomatic volunteers. *Journal of Clinical Ultrasound*. 2003;31(5):239-244. doi:10.1002/jcu.10168
295. Gyaran IA, Spiezia F, Hudson Z, Maffulli N. Sonographic measurement of iliotibial band thickness: an observational study in healthy adult volunteers. *Knee Surg Sports Traumatol Arthrosc*. 2011;19(3):458-461. doi:10.1007/s00167-010-1269-z
296. Kim H sook, Yoon T lim. Comparison of Relative Thickness of the Iliotibial Band Following Four Self-Stretching Exercises. 2012;19(4):24-31.
297. Wang HK, Ting-Fang Shih T, Lin KH, Wang TG. Real-time morphologic changes of the iliotibial band during therapeutic stretching; an ultrasonographic study. *Manual Therapy*. 2008;13(4):334-340. doi:10.1016/j.math.2007.03.002
298. Bonaldi L, Berardo A, Pirri C, Stecco C, Carniel EL, Fontanella CG. Mechanical Characterization of Human Fascia Lata: Uniaxial Tensile Tests from Fresh-Frozen Cadaver Samples and Constitutive Modelling. *Bioengineering*. 2023;10(2):226. doi:10.3390/bioengineering10020226

299. Benetazzo L, Bizzego A, De Caro R, Frigo G, Guidolin D, Stecco C. 3D reconstruction of the crural and thoracolumbar fasciae. *Surg Radiol Anat*. 2011;33(10):855-862. doi:10.1007/s00276-010-0757-7
300. Kaplan EB. Surgical approach to the lateral (peroneal) side of the knee joint. *Surg Gynecol Obstet*. 1957;104(3):346-356.
301. Merican AM, Amis AA. Anatomy of the lateral retinaculum of the knee. *J Bone Joint Surg Br*. 2008;90(4):527-534. doi:10.1302/0301-620X.90B4.20085
302. Ottani V, Raspanti M, Ruggeri A. Collagen structure and functional implications. *Micron*. 2001;32(3):251-260. doi:10.1016/s0968-4328(00)00042-1
303. Stecco C, Fede C, Macchi V, et al. The fasciacytes: A new cell devoted to fascial gliding regulation. *Clinical Anatomy*. 2018;31(5):667-676. doi:10.1002/ca.23072
304. Yagi M, Taniguchi M, Tateuchi H, et al. Properties of the iliotibial band and their relationships with gait parameters among patients with knee osteoarthritis. *Journal of Orthopaedic Research*. 2023;41(6):1177-1185. doi:10.1002/jor.25466
305. Inoue H, Hara K, Arai Y, et al. Outcome of Low-Invasive Local Split-Thickness Lengthening for Iliotibial Band Friction Syndrome. *Int J Sports Med*. 2018;39(03):232-236. doi:10.1055/s-0043-122152
306. Tateuchi H, Shiratori S, Ichihashi N. The effect of three-dimensional postural change on shear elastic modulus of the iliotibial band. *J Electromyogr Kinesiol*. 2016;28:137-142. doi:10.1016/j.jelekin.2016.04.006
307. Albuquerque CE de, Bibin F, Bussarolo JM, Dalmolin EB, Bertolini GRF, Nuñez SC. The influence of iliotibial tract thickness on clinical outcomes in women with patellofemoral pain. *The Knee*. 2022;39:319-324. doi:10.1016/j.knee.2022.10.007
308. Dejea H, Bonnin A, Cook AC, Garcia-Canadilla P. Cardiac multi-scale investigation of the right and left ventricle ex vivo: a review. *Cardiovasc Diagn Ther*. 2020;10(5):1701-1717. doi:10.21037/cdt-20-269
309. Charras G, Yap AS. Tensile Forces and Mechanotransduction at Cell-Cell Junctions. *Curr Biol*. 2018;28(8):R445-R457. doi:10.1016/j.cub.2018.02.003
310. Saraswathibhatla A, Indana D, Chaudhuri O. Cell-extracellular matrix mechanotransduction in 3D. *Nat Rev Mol Cell Biol*. 2023;24(7):495-516. doi:10.1038/s41580-023-00583-1
311. Kao TW, Liu YS, Yang CY, Lee OKS. Mechanotransduction of mesenchymal stem cells and hemodynamic implications. *Chin J Physiol*. 2023;66(2):55-64. doi:10.4103/cjop.CJOP-D-22-00144
312. Pierson RN. Antibody-mediated xenograft injury: Mechanisms and protective strategies. *Transplant Immunology*. 2009;21(2):65-69. doi:10.1016/j.trim.2009.03.008
313. Afzali B, Lechler RI, Hernandez-Fuentes MP. Allorecognition and the alloresponse: clinical implications. *Tissue Antigens*. 2007;69(6):545-556. doi:10.1111/j.1399-0039.2007.00834.x
314. Sheldon S, Poulton K. HLA Typing and Its Influence on Organ Transplantation. In: *Transplantation Immunology*. Vol 333. Humana Press; 2006:157-174. doi:10.1385/1-59745-049-9:157
315. Ayala García MA, González Yebra B, López Flores AL, Guaní Guerra E. The Major Histocompatibility Complex in Transplantation. *Journal of Transplantation*. 2012;2012:1-7. doi:10.1155/2012/842141
316. Badylak SF, Gilbert TW. Immune response to biologic scaffold materials. *Seminars in Immunology*. 2008;20(2):109-116. doi:10.1016/j.smim.2007.11.003
317. Hillebrandt K, Polenz D, Butter A, et al. Procedure for Decellularization of Rat Livers in an Oscillating-pressure Perfusion Device. *JoVE*. 2015;(102):53029. doi:10.3791/53029
318. Al-Akkad W, Acedo P, Vilia MG, et al. Tissue-Specific Human Extracellular Matrix Scaffolds Promote Pancreatic Tumour Progression and Chemotherapy Resistance. *Cells*. 2022;11(22):3652. doi:10.3390/cells11223652

319. Berger C, Bjørlykke Y, Hahn L, et al. Matrix decoded – A pancreatic extracellular matrix with organ specific cues guiding human iPSC differentiation. *Biomaterials*. 2020;244:119766. doi:10.1016/j.biomaterials.2020.119766
320. Jank BJ, Goverman J, Guyette JP, et al. Creation of a Bioengineered Skin Flap Scaffold with a Perfusable Vascular Pedicle. *Tissue Engineering Part A*. 2017;23(13-14):696-707. doi:10.1089/ten.tea.2016.0487
321. Gerli MFM, Guyette JP, Evangelista-Leite D, Ghoshhajra BB, Ott HC. Perfusion decellularization of a human limb: A novel platform for composite tissue engineering and reconstructive surgery. Soncini M, ed. *PLoS ONE*. 2018;13(1):e0191497. doi:10.1371/journal.pone.0191497
322. Simões IN, Vale P, Soker S, et al. Acellular Urethra Bioscaffold: Decellularization of Whole Urethras for Tissue Engineering Applications. *Sci Rep*. 2017;7(1):41934. doi:10.1038/srep41934
323. Brown BN, Valentin JE, Stewart-Akers AM, McCabe GP, Badylak SF. Macrophage phenotype and remodeling outcomes in response to biologic scaffolds with and without a cellular component. *Biomaterials*. 2009;30(8):1482-1491. doi:10.1016/j.biomaterials.2008.11.040
324. Keane TJ, Londono R, Turner NJ, Badylak SF. Consequences of ineffective decellularization of biologic scaffolds on the host response. *Biomaterials*. 2012;33(6):1771-1781. doi:10.1016/j.biomaterials.2011.10.054
325. Xu H, Wan H, Sandor M, et al. Host Response to Human Acellular Dermal Matrix Transplantation in a Primate Model of Abdominal Wall Repair. *Tissue Engineering Part A*. 2008;14(12):2009-2019. doi:10.1089/ten.tea.2007.0316
326. Keane TJ, Badylak SF. The host response to allogeneic and xenogeneic biological scaffold materials: Host response to biological scaffoldsc. *J Tissue Eng Regen Med*. 2015;9(5):504-511. doi:10.1002/term.1874
327. Londono R, Dziki JL, Haljasmaa E, Turner NJ, Leifer CA, Badylak SF. The effect of cell debris within biologic scaffolds upon the macrophage response: Effect of cell debris within ECM bioscaffolds. *J Biomed Mater Res*. 2017;105(8):2109-2118. doi:10.1002/jbm.a.36055
328. Söhling N, Leiblein M, Schaible A, et al. First Human Leucocyte Antigen (HLA) Response and Safety Evaluation of Fibrous Demineralized Bone Matrix in a Critical Size Femoral Defect Model of the Sprague-Dawley Rat. *Materials*. 2020;13(14):3120. doi:10.3390/ma13143120
329. He J, Li Z, Yu T, et al. *In vitro* and *in vivo* biocompatibility study on acellular sheep periosteum for guided bone regeneration. *Biomed Mater*. 2020;15(1):015013. doi:10.1088/1748-605X/ab597f
330. Mahdi BM. A glow of HLA typing in organ transplantation. *Clinical and Translational Medicine*. 2013;2(1). doi:10.1186/2001-1326-2-6
331. Mallis P, Michalopoulos E, Dinou A, et al. Development of HLA-matched vascular grafts utilizing decellularized human umbilical artery. *Human Immunology*. 2018;79(12):855-860. doi:10.1016/j.humimm.2018.09.001
332. Gallon LG, Leventhal JR, Kaufman DB. Pretransplant Evaluation of Renal Transplant Candidates. *Seminars in Nephrology*. 2002;22(6):515-525. doi:10.1053/snep.2002.35966
333. Lemieux W, Mohammadhassanzadeh H, Klement W, Daniel C, Sapir-Pichhadze R. Matchmaker, matchmaker make me a match: Opportunities and challenges in optimizing compatibility of HLA eplets in transplantation. *Int J Immunogenet*. 2021;48(2):135-144. doi:10.1111/iji.12525
334. Lux M, Haller R, Giere B, et al. Advantages and challenges in processing and quality control of decellularized heart valves. *Cell Tissue Bank*. Published online May 3, 2023. doi:10.1007/s10561-023-10092-2
335. Baskett RJF, Nanton MA, Warren AE, Ross DB. Human leukocyte antigen-DR and ABO mismatch are associated with accelerated homograft valve failure in children: implications for

therapeutic interventions. *The Journal of Thoracic and Cardiovascular Surgery*. 2003;126(1):232-238. doi:10.1016/S0022-5223(03)00210-1

336. Coti I, Wenda S, Andreeva A, et al. Donor-specific HLA antibodies after fresh decellularized vs cryopreserved native allograft implantation. *HLA*. 2020;96(5):580-588. doi:10.1111/tan.14077
337. Affonsodacosta F, Dohmen P, Duarte D, et al. Immunological and echocardiographic evaluation of decellularized versus cryopreserved allografts during the Ross operation. *European Journal of Cardio-Thoracic Surgery*. 2005;27(4):572-578. doi:10.1016/j.ejcts.2004.12.057
338. Kneib C, Von Glehn CQC, Costa FDA, Costa MTBA, Susin MF. Evaluation of humoral immune response to donor HLA after implantation of cellularized versus decellularized human heart valve allografts. *Tissue Antigens*. 2012;80(2):165-174. doi:10.1111/j.1399-0039.2012.01885.x
339. Fretwurst T, Gad LM, Steinberg T, et al. Detection of major histocompatibility complex molecules in processed allogeneic bone blocks for use in alveolar ridge reconstruction. *Oral Surgery, Oral Medicine, Oral Pathology and Oral Radiology*. 2018;126(1):16-21. doi:10.1016/j.0000.2018.01.018
340. Duisit J, Maistriaux L, Taddeo A, et al. Bioengineering a Human Face Graft: The Matrix of Identity. *Annals of Surgery*. 2017;266(5):754-764. doi:10.1097/SLA.0000000000002396
341. van Steenberghe M, Schubert T, Guiot Y, Bouzin C, Bollen X, Gianello P. Enhanced vascular biocompatibility of decellularized xeno-/allogeneic matrices in a rodent model. *Cell Tissue Bank*. 2017;18(2):249-262. doi:10.1007/s10561-017-9610-0
342. Duisit J, Amiel H, Wüthrich T, et al. Perfusion-decellularization of human ear grafts enables ECM-based scaffolds for auricular vascularized composite tissue engineering. *Acta Biomaterialia*. 2018;73:339-354. doi:10.1016/j.actbio.2018.04.009
343. Lin X, Zhao C, Zhu P, et al. Periosteum Extracellular-Matrix-Mediated Acellular Mineralization during Bone Formation. *Adv Healthc Mater*. 2018;7(4). doi:10.1002/adhm.201700660
344. Inci I, Norouz Dizaji A, Ozel C, Morali U, Dogan Guzel F, Avci H. Decellularized inner body membranes for tissue engineering: A review. *J Biomater Sci Polym Ed*. 2020;31(10):1287-1368. doi:10.1080/09205063.2020.1751523
345. van Steenberghe M, Schubert T, Xhema D, et al. Enhanced vascular regeneration with chemically/physically treated bovine/human pericardium in rodents. *J Surg Res*. 2018;222:167-179. doi:10.1016/j.jss.2017.09.043
346. Anastasescou M, Cornu O, Banse X, König J, Hassoun A, Delloye C. Ethanol treatment of tendon allografts: a potential HIV inactivating procedure. *Int Orthop*. 1998;22(4):252-254. doi:10.1007/s002640050253
347. Fages J, Poirier B, Barbier Y, et al. Viral inactivation of human bone tissue using supercritical fluid extraction. *ASAIO J*. 1998;44(4):289-293. doi:10.1097/00002480-199807000-00009
348. Pruss A, Baumann B, Seibold M, et al. Validation of the sterilization procedure of allogeneic avital bone transplants using peracetic acid-ethanol. *Biologicals*. 2001;29(2):59-66. doi:10.1006/biol.2001.0286
349. Marée R, Rollus L, Stévens B, et al. Collaborative analysis of multi-gigapixel imaging data using Cytomine. *Bioinformatics*. 2016;32(9):1395-1401. doi:10.1093/bioinformatics/btw013
350. Mendoza-Novelo B, Avila EE, Cauich-Rodríguez JV, et al. Decellularization of pericardial tissue and its impact on tensile viscoelasticity and glycosaminoglycan content. *Acta Biomaterialia*. 2011;7(3):1241-1248. doi:10.1016/j.actbio.2010.11.017
351. Vettese J, Manon J, Chretien A, et al. Collagen molecular organization preservation in human fascia lata and periosteum after tissue engineering. *Front Bioeng Biotechnol*. 2024;12. doi:10.3389/fbioe.2024.1275709
352. Fung YC. *Biomechanics: Mechanical Properties of Living Tissues*. Springer Science & Business Media; 2013.

353. Rougier G, Maistriaux L, Fievé L, et al. Decellularized vascularized bone grafts: A preliminary in vitro porcine model for bioengineered transplantable bone shafts. *Front Bioeng Biotechnol*. Published online 2022. doi:10.3389/fbioe.2022.1003861
354. Maistriaux L, Foulon V, Fievé L, et al. Reconstruction of the human nipple–areolar complex: a tissue engineering approach. *Front Bioeng Biotechnol*. 2024;11:1295075. doi:10.3389/fbioe.2023.1295075
355. Zhang Q, Raoof M, Chen Y, et al. Circulating mitochondrial DAMPs cause inflammatory responses to injury. *Nature*. 2010;464(7285):104-107. doi:10.1038/nature08780
356. Guo S, DiPietro LA. Factors Affecting Wound Healing. *J Dent Res*. 2010;89(3):219-229. doi:10.1177/0022034509359125
357. Angaswamy N, Tiriveedhi V, Sarma NJ, et al. Interplay between immune responses to HLA and non-HLA self-antigens in allograft rejection. *Human Immunology*. 2013;74(11):1478-1485. doi:10.1016/j.humimm.2013.07.002
358. Ansaloni L, Cambrini P, Catena F, et al. Immune Response to Small Intestinal Submucosa (Surgisis) Implant in Humans: Preliminary Observations. *Journal of Investigative Surgery*. 2007;20(4):237-241. doi:10.1080/08941930701481296
359. Allman AJ, McPherson TB, Badylak SF, et al. Xenogeneic extracellular matrix grafts elicit a TH2-restricted immune response: *Transplantation*. 2001;71(11):1631-1640. doi:10.1097/00007890-200106150-00024
360. Wang L, Johnson JA, Chang DW, Zhang Q. Decellularized musculofascial extracellular matrix for tissue engineering. *Biomaterials*. 2013;34(11):2641-2654. doi:10.1016/j.biomaterials.2012.12.048
361. Levy RJ, Vyavahare N, Ogle M, Ashworth P, Bianco R, Schoen FJ. Inhibition of cusp and aortic wall calcification in ethanol- and aluminum-treated bioprosthetic heart valves in sheep: background, mechanisms, and synergism. *J Heart Valve Dis*. 2003;12(2):209-216; discussion 216.
362. Jorge-Herrero E, Fernández P, De La Tone N, et al. Inhibition of the calcification of porcine valve tissue by selective lipid removal. *Biomaterials*. 1994;15(10):815-820. doi:10.1016/0142-9612(94)90036-1
363. Padula SL, Pensato R, Pizza C, et al. Face Transplant: Indications, Outcomes, and Ethical Issues—Where Do We Stand? *Journal of Clinical Medicine*. 2022;11(19). doi:10.3390/jcm11195750
364. Longo B, Pomahac B, Giacalone M, Cardillo M, Cervelli V. 18 years of face transplantation: Adverse outcomes and challenges. *J Plast Reconstr Aesthet Surg*. 2023;87:187-199. doi:10.1016/j.bjps.2023.09.043
365. Shoulders MD, Raines RT. Collagen structure and stability. *Annu Rev Biochem*. 2009;78:929-958. doi:10.1146/annurev.biochem.77.032207.120833
366. Yamauchi M, Sricholpech M. Lysine post-translational modifications of collagen. *Essays Biochem*. 2012;52:113-133. doi:10.1042/bse0520113
367. Theocharis AD, Skandalis SS, Gialeli C, Karamanos NK. Extracellular matrix structure. *Adv Drug Deliv Rev*. 2016;97:4-27. doi:10.1016/j.addr.2015.11.001
368. Saito M, Marumo K. Collagen cross-links as a determinant of bone quality: a possible explanation for bone fragility in aging, osteoporosis, and diabetes mellitus. *Osteoporos Int*. 2010;21(2):195-214. doi:10.1007/s00198-009-1066-z
369. Saito M, Marumo K. Effects of Collagen Crosslinking on Bone Material Properties in Health and Disease. *Calcif Tissue Int*. 2015;97(3):242-261. doi:10.1007/s00223-015-9985-5
370. Gaar J, Naffa R, Brimble M. Enzymatic and non-enzymatic crosslinks found in collagen and elastin and their chemical synthesis. *Org Chem Front*. 2020;7(18):2789-2814. doi:10.1039/D0QO00624F

371. Depalle B, Qin Z, Shefelbine SJ, Buehler MJ. Influence of cross-link structure, density and mechanical properties in the mesoscale deformation mechanisms of collagen fibrils. *J Mech Behav Biomed Mater*. 2015;52:1-13. doi:10.1016/j.jmbbm.2014.07.008
372. Snedeker JG, Gautieri A. The role of collagen crosslinks in ageing and diabetes - the good, the bad, and the ugly. *Muscles Ligaments Tendons J*. 2014;4(3):303-308.
373. Pritchard JM, Willett TL. Pentosidine as a Biomarker for Poor Bone Quality and Elevated Fracture Risk. In: Patel VB, Preedy VR, eds. *Biomarkers in Bone Disease*. Springer Netherlands; 2017:355-392. doi:10.1007/978-94-007-7693-7_32
374. Gautieri A, Redaelli A, Buehler MJ, Vesentini S. Age- and diabetes-related nonenzymatic crosslinks in collagen fibrils: Candidate amino acids involved in Advanced Glycation End-products. *Matrix Biology*. 2014;34:89-95. doi:10.1016/j.matbio.2013.09.004
375. Gubbiotti MA, Vallet SD, Ricard-Blum S, Iozzo RV. Decorin interacting network: A comprehensive analysis of decorin-binding partners and their versatile functions. *Matrix Biol*. 2016;55:7-21. doi:10.1016/j.matbio.2016.09.009
376. Halper J. Proteoglycans and diseases of soft tissues. *Adv Exp Med Biol*. 2014;802:49-58. doi:10.1007/978-94-007-7893-1_4
377. Scott JE. Elasticity in extracellular matrix 'shape modules' of tendon, cartilage, etc. A sliding proteoglycan-filament model. *J Physiol*. 2003;553(Pt 2):335-343. doi:10.1113/jphysiol.2003.050179
378. Zhang W, Ge Y, Cheng Q, Zhang Q, Fang L, Zheng J. Decorin is a pivotal effector in the extracellular matrix and tumour microenvironment. *Oncotarget*. 2018;9(4):5480-5491. doi:10.18632/oncotarget.23869
379. Coutelier L, Delloye C. [The induction of chondrogenesis after fracture repair]. *Int Orthop*. 1983;7(2):121-132. doi:10.1007/bf00266461
380. Bragdon BC, Bahney CS. Origin of Reparative Stem Cells in Fracture Healing. *Curr Osteoporos Rep*. 2018;16(4):490-503. doi:10.1007/s11914-018-0458-4
381. Debnath S, Yallowitz AR, McCormick J, et al. Discovery of a periosteal stem cell mediating intramembranous bone formation. *Nature*. 2018;562(7725):133-139. doi:10.1038/s41586-018-0554-8
382. Aboubakar Nana F, Hoton D, Ambroise J, et al. Increased Expression and Activation of FAK in Small-Cell Lung Cancer Compared to Non-Small-Cell Lung Cancer. *Cancers*. 2019;11(10):1526. doi:10.3390/cancers11101526
383. Nauth A, Ristevski B, Li R, Schemitsch EH. Growth factors and bone regeneration: How much bone can we expect? *Injury*. 2011;42(6):574-579. doi:10.1016/j.injury.2011.03.034
384. Ahlmann E, Patzakis M, Roidis N, Shepherd L, Holtom P. Comparison of anterior and posterior iliac crest bone grafts in terms of harvest-site morbidity and functional outcomes. *The Journal of Bone and Joint Surgery-American Volume*. 2002;84(5):716-720. doi:10.2106/00004623-200205000-00003
385. Steffen T, Downer P, Steiner B, Hehli M, Aebi M. Minimally invasive bone harvesting tools. *E Spine J*. 2000;9(S1):S114-S118. doi:10.1007/PL00008316
386. Phieffer LS, Goulet JA. Delayed unions of the tibia: *The Journal of Bone and Joint Surgery-American Volume*. 2006;88(1):205-216. doi:10.2106/00004623-200601000-00026
387. Kang SH, Park JB, Kim I, Lee W, Kim H. Assessment of stem cell viability in the initial healing period in rabbits with a cranial bone defect according to the type and form of scaffold. *J Periodontal Implant Sci*. 2019;49(4):258-267. doi:10.5051/jpis.2019.49.4.258
388. Reing JE, Brown BN, Daly KA, et al. The effects of processing methods upon mechanical and biologic properties of porcine dermal extracellular matrix scaffolds. *Biomaterials*. 2010;31(33):8626-8633. doi:10.1016/j.biomaterials.2010.07.083
389. Uhl FE, Zhang F, Pouliot RA, et al. Functional role of glycosaminoglycans in decellularized lung extracellular matrix. *Acta Biomaterialia*. 2020;102:231-246. doi:10.1016/j.actbio.2019.11.029

390. Salbach-Hirsch J, Rauner M, Hofbauer C, Hofbauer LC. New insights into the role of glycosaminoglycans in the endosteal bone microenvironment. *Biological Chemistry*. 2021;402(11):1415-1425. doi:10.1515/hsz-2021-0174
391. Zhao G, Monier-Faugere MC, Langub MC, et al. Targeted Overexpression of Insulin-Like Growth Factor I to Osteoblasts of Transgenic Mice: Increased Trabecular Bone Volume without Increased Osteoblast Proliferation [1]. *Endocrinology*. 2000;141(7):2674-2682. doi:10.1210/endo.141.7.7585
392. Manolagas SC. Birth and Death of Bone Cells: Basic Regulatory Mechanisms and Implications for the Pathogenesis and Treatment of Osteoporosis*. *Endocrine Reviews*. 2000;21(2):115-137. doi:10.1210/edrv.21.2.0395
393. Marie PJ. Fibroblast growth factor signaling controlling osteoblast differentiation. *Gene*. 2003;316:23-32. doi:10.1016/S0378-1119(03)00748-0
394. Zhang X, Xing H, Qi F, Liu H, Gao L, Wang X. Local delivery of insulin/IGF-1 for bone regeneration: carriers, strategies, and effects. *Nanotheranostics*. 2020;4(4):242-255. doi:10.7150/ntno.46408
395. Dicarlo M, Bianchi N, Ferretti C, Orciani M, Di Primio R, Mattioli-Belmonte M. Evidence Supporting a Paracrine Effect of IGF-1/VEGF on Human Mesenchymal Stromal Cell Commitment. *Cells Tissues Organs*. 2016;201(5):333-341. doi:10.1159/000445346
396. Mauney JR, Jaquiéry C, Volloch V, Heberer M, Martin I, Kaplan DL. In vitro and in vivo evaluation of differentially demineralized cancellous bone scaffolds combined with human bone marrow stromal cells for tissue engineering. *Biomaterials*. 2005;26(16):3173-3185. doi:10.1016/j.biomaterials.2004.08.020
397. Vogelin E, Jones NF, Huang JI, Brekke JH, Lieberman JR. Healing of a critical-sized defect in the rat femur with use of a vascularized periosteal flap, a biodegradable matrix, and bone morphogenetic protein. *J Bone Joint Surg Am*. 2005;87(6):1323-1331. doi:10.2106/JBJS.C.00913
398. Schubert T, Lafont S, Beaurin G, et al. Critical size bone defect reconstruction by an autologous 3D osteogenic-like tissue derived from differentiated adipose MSCs. *Biomaterials*. 2013;34(18):4428-4438. doi:10.1016/j.biomaterials.2013.02.053
399. Aerssens J, Boonen S, Lowet G, Dequeker J. Interspecies differences in bone composition, density, and quality: potential implications for in vivo bone research. *Endocrinology*. 1998;139(2):663-670. doi:10.1210/endo.139.2.5751
400. Pearce AI, Richards RG, Milz S, Schneider E, Pearce SG. Animal models for implant biomaterial research in bone: a review. *Eur Cell Mater*. 2007;13:1-10. doi:10.22203/ecm.v013a01
401. Honda S, Fujibayashi S, Shimizu T, et al. Strontium-loaded 3D intramedullary nail titanium implant for critical-sized femoral defect in rabbits. *J Biomed Mater Res B Appl Biomater*. 2024;112(3):e35393. doi:10.1002/jbm.b.35393
402. Popov VV, Muller-Kamskii G, Kovalevsky A, et al. Design and 3D-printing of titanium bone implants: brief review of approach and clinical cases. *Biomed Eng Lett*. 2018;8(4):337-344. doi:10.1007/s13534-018-0080-5
403. Naujokat H, Gökkaya AI, Açil Y, et al. In vivo biocompatibility evaluation of 3D-printed nickel-titanium fabricated by selective laser melting. *J Mater Sci Mater Med*. 2022;33(2):13. doi:10.1007/s10856-022-06641-y
404. Angular Stable Locking System | DePuy Synthes. J&J MedTech. Accessed April 4, 2024. https://www.jnjmedtech.com/en-US/product/angular-stable-locking-system
405. Manon J, Gallant L, Gérard P, et al. 2D and 3D microstructural analysis of the iliotibial tract. *Journal of Anatomy*. 2024;00:1-15. doi:10.1111/joa.14125
406. Manon J, Evrard R, Maistriaux L, et al. HLA Awareness in Tissue Decellularization: A Paradigm Shift for Enhanced Biocompatibility, studied on the Model of the Human Fascia Lata Graft. *Biomaterials*. Published online August 2, 2024:122741. doi:10.1016/j.biomaterials.2024.122741

407. Manon J, Englebert A, Evrard R, Schubert T, Cornu O. FixThePig: a custom 3D-printed femoral intramedullary nailing for preclinical research applications. *Front Bioeng Biotechnol*. 2024;Submitted.
408. Pawlowsky K, Ernst L, Steitz J, et al. The Aachen Minipig: Phenotype, Genotype, Hematological and Biochemical Characterization, and Comparison to the Göttingen Minipig. *Eur Surg Res*. 2017;58(5-6):193-203. doi:10.1159/000471483
409. van Gaalen SM, Kruyt MC, Geuze RE, de Bruijn JD, Alblas J, Dhert WJA. Use of Fluorochrome Labels in In Vivo Bone Tissue Engineering Research. *Tissue Engineering Part B: Reviews*. 2010;16(2):209-217. doi:10.1089/ten.teb.2009.0503
410. Gamblin AL, Brennan MA, Renaud A, et al. Bone tissue formation with human mesenchymal stem cells and biphasic calcium phosphate ceramics: the local implication of osteoclasts and macrophages. *Biomaterials*. 2014;35(36):9660-9667. doi:10.1016/j.biomaterials.2014.08.018
411. Manon J, Detrembleur C, Van de Veyver S, Tribak K, Cornu O, Putineanu D. Quels sont les facteurs prédictifs d'une complication mécanique après enclouage centromédullaire d'une fracture diaphysaire du tibia? *Revue de Chirurgie Orthopédique et Traumatologique*. 2019;105(3):353-357.
412. Poncelet AJ, Vercruysse J, Saliez A, Gianello P. Although Pig Allogeneic Mesenchymal Stem Cells Are Not Immunogenic In Vitro, Intracardiac Injection Elicits an Immune Response In Vivo: *Transplantation*. 2007;83(6):783-790. doi:10.1097/01.tp.0000258649.23081.a3
413. Brennan MÁ, Renaud A, Amiaud J, et al. Pre-clinical studies of bone regeneration with human bone marrow stromal cells and biphasic calcium phosphate. *Stem Cell Res Ther*. 2014;5(5):114. doi:10.1186/scrt504
414. Eyckmans J, Roberts SJ, Schrooten J, Luyten FP. A clinically relevant model of osteoinduction: a process requiring calcium phosphate and BMP/Wnt signalling. *J Cell Mol Med*. 2010;14(6b):1845-1856. doi:10.1111/j.1582-4934.2009.00807.x
415. Caplan AI. Mesenchymal Stem Cells: Time to Change the Name! *Stem Cells Transl Med*. 2017;6(6):1445-1451. doi:10.1002/sctm.17-0051
416. Colnot C, Huang S, Helms J. Analyzing the cellular contribution of bone marrow to fracture healing using bone marrow transplantation in mice. *Biochem Biophys Res Commun*. 2006;350(3):557-561. doi:10.1016/j.bbrc.2006.09.079
417. Evrard R, Manon J, Maistriaux L, et al. Decellularization of Massive Bone Allografts By Perfusion: A New Protocol for Tissue Engineering. *Tissue Eng Part A*. 2024;30(1-2):31-44. doi:10.1089/ten.TEA.2023.0182
418. Blaudez F, Ivanovski S, Hamlet S, Vaquette C. An overview of decellularisation techniques of native tissues and tissue engineered products for bone, ligament and tendon regeneration. *Methods*. 2020;171:28-40. doi:10.1016/j.ymeth.2019.08.002
419. Taylor B, Indano S, Yankannah Y, Patel P, Perez XI, Freeman J. Decellularized Cortical Bone Scaffold Promotes Organized Neovascularization In Vivo. *Tissue Eng Part A*. 2019;25(13-14):964-977. doi:10.1089/ten.tea.2018.0225
420. Evrard R, Manon J, Maistriaux L, et al. Enhancing the biological integration of massive bone allografts: A porcine preclinical in vivo pilot-study. *Bone*. 2024;187:117213. doi:10.1016/j.bone.2024.117213
421. Manon J, Fodjeu G, Evrard R, et al. A single Angiofil-latex injection for both radiological and anatomical assessment of arterial territories in the limbs. *Annals of Anatomy - Anatomischer Anzeiger*. 2024;256:152312. doi:10.1016/j.aanat.2024.152312
422. Towler DA. The osteogenic-angiogenic interface: novel insights into the biology of bone formation and fracture repair. *Curr Osteoporos Rep*. 2008;6(2):67-71. doi:10.1007/s11914-008-0012-x
423. Brandi ML, Collin-Osdoby P. Vascular biology and the skeleton. *J Bone Miner Res*. 2006;21(2):183-192. doi:10.1359/JBMR.050917

424. Wang Y, Wan C, Deng L, et al. The hypoxia-inducible factor alpha pathway couples angiogenesis to osteogenesis during skeletal development. *J Clin Invest*. 2007;117(6):1616-1626. doi:10.1172/JCI31581
425. Gerber HP, Ferrara N. Angiogenesis and Bone Growth. *Trends in Cardiovascular Medicine*. 2000;10(5):223-228. doi:10.1016/S1050-1738(00)00074-8
426. Maes C, Kobayashi T, Selig MK, et al. Osteoblast precursors, but not mature osteoblasts, move into developing and fractured bones along with invading blood vessels. *Dev Cell*. 2010;19(2):329-344. doi:10.1016/j.devcel.2010.07.010
427. Krstic RV. Ultrastruktur der Säugetierzelle: Ein Atlas zum Studium für Mediziner und Biologen. 1975. Accessed August 2, 2024. https://www.abebooks.com/9783540075066/Ultrastruktur-S%C3%A4ugetierzelle-Atlas-Studium-Mediziner-3540075062/plp
428. van Gastel N, Stegen S, Eelen G, et al. Lipid availability determines fate of skeletal progenitor cells via SOX9. *Nature*. 2020;579(7797):111-117. doi:10.1038/s41586-020-2050-1
429. Owen-Woods C, Kusumbe A. Fundamentals of bone vasculature: Specialization, interactions and functions. *Seminars in Cell & Developmental Biology*. 2022;123:36-47. doi:10.1016/j.semcdb.2021.06.025
430. Hendriks M, Ramasamy SK. Blood Vessels and Vascular Niches in Bone Development and Physiological Remodeling. *Front Cell Dev Biol*. 2020;8. doi:10.3389/fcell.2020.602278
431. Watson EC, Adams RH. Biology of Bone: The Vasculature of the Skeletal System. *Cold Spring Harb Perspect Med*. 2018;8(7):a031559. doi:10.1101/cshperspect.a031559
432. Stegen S, Carmeliet G. The skeletal vascular system - Breathing life into bone tissue. *Bone*. 2018;115:50-58. doi:10.1016/j.bone.2017.08.022
433. Lafage-Proust MH, Roche B, Langer M, et al. Assessment of bone vascularization and its role in bone remodeling. *Bonekey Rep*. 2015;4:662. doi:10.1038/bonekey.2015.29
434. Deschepper M, Oudina K, David B, et al. Survival and function of mesenchymal stem cells (MSCs) depend on glucose to overcome exposure to long-term, severe and continuous hypoxia. *J Cell Mol Med*. 2011;15(7):1505-1514. doi:10.1111/j.1582-4934.2010.01138.x
435. Lau F, Dalisson B, Zhang YL, Zhao J, Eliopoulos N, Barralet JE. Effects of Oxygen and Glucose on Bone Marrow Mesenchymal Stem Cell Culture. *Adv Biosyst*. 2020;4(11):e2000094. doi:10.1002/adbi.202000094
436. Moya A, Paquet J, Deschepper M, et al. Human Mesenchymal Stem Cell Failure to Adapt to Glucose Shortage and Rapidly Use Intracellular Energy Reserves Through Glycolysis Explains Poor Cell Survival After Implantation. *Stem Cells*. 2018;36(3):363-376. doi:10.1002/stem.2763
437. Yuan H, Jiang W, Chen Y, Kim BYS. Study of Osteocyte Behavior by High-Resolution Intravital Imaging Following Photo-Induced Ischemia. *Molecules*. 2018;23(11):2874. doi:10.3390/molecules23112874
438. Mastorakos DP, Disa JJ, Athanasian E, Boland P, Healey JH, Cordeiro PG. Soft-tissue flap coverage maximizes limb salvage after allograft bone extremity reconstruction. *Plast Reconstr Surg*. 2002;109(5):1567-1573. doi:10.1097/00006534-200204150-00012
439. Struckmann V, Schmidmaier G, Ferbert T, Kneser U, Kremer T. Reconstruction of Extended Bone Defects Using Massive Allografts Combined with Surgical Angiogenesis: A Case Report. *JBJS Case Connect*. 2017;7(1):e10. doi:10.2106/JBJS.CC.16.00098
440. Ben-Shaul S, Landau S, Merdler U, Levenberg S. Mature vessel networks in engineered tissue promote graft-host anastomosis and prevent graft thrombosis. *Proc Natl Acad Sci U S A*. 2019;116(8):2955-2960. doi:10.1073/pnas.1814238116
441. Rademakers T, Horvath JM, van Blitterswijk CA, LaPointe VLS. Oxygen and nutrient delivery in tissue engineering: Approaches to graft vascularization. *J Tissue Eng Regen Med*. 2019;13(10):1815-1829. doi:10.1002/term.2932
442. Watson EC, Grant ZL, Coultas L. Endothelial cell apoptosis in angiogenesis and vessel regression. *Cell Mol Life Sci*. 2017;74(24):4387-4403. doi:10.1007/s00018-017-2577-y

443. Huang RL, Kobayashi E, Liu K, Li Q. Bone Graft Prefabrication Following the In Vivo Bioreactor Principle. *EBioMedicine*. 2016;12:43-54. doi:10.1016/j.ebiom.2016.09.016
444. Saint-Cyr M, Oni G, Lee M, Yi C, Colohon SM. Simple Approach to Harvest of the Anterolateral Thigh Flap: *Plastic and Reconstructive Surgery*. 2012;129(1):207-211. doi:10.1097/PRS.0b013e318233ef4a
445. Yu P. Characteristics of the anterolateral thigh flap in a Western population and its application in head and neck reconstruction. *Head & Neck*. 2004;26(9):759-769. doi:10.1002/hed.20050
446. Lee YC, Chen WC, Chou TM, Shieh SJ. Anatomical Variability of the Anterolateral Thigh Flap Perforators: Vascular Anatomy and Its Clinical Implications. *Plastic and Reconstructive Surgery*. 2015;135(4):1097-1107. doi:10.1097/PRS.0000000000001103
447. Stecco C, Tiengo C, Stecco A, et al. Fascia redefined: anatomical features and technical relevance in fascial flap surgery. *Surg Radiol Anat*. 2013;35(5):369-376. doi:10.1007/s00276-012-1058-0
448. Disa JJ, Goldberg NH, Carlton JM, Robertson BC, Slezak S. Restoring abdominal wall integrity in contaminated tissue-deficient wounds using autologous fascia grafts. *Plast Reconstr Surg*. 1998;101(4):979-986. doi:10.1097/00006534-199804040-00014
449. Alemán RM, Martínez MG. Lateral thigh fascia lata as interpositional graft for temporomandibular joint ankylosis. *J Maxillofac Oral Surg*. 2012;11(3):354-357. doi:10.1007/s12663-011-0304-z
450. Karaaltin MV, Batioglu-Karaaltin A, Orhan KS, Demirel T, Guldiken Y. Autologous fascia lata graft for contour restoration and camouflage in tertiary rhinoplasty. *J Craniofac Surg*. 2012;23(3):719-723. doi:10.1097/SCS.0b013e31824dbb92
451. Song YG, Chen GZ, Song YL. The free thigh flap: a new free flap concept based on the septocutaneous artery. *Br J Plast Surg*. 1984;37(2):149-159. doi:10.1016/0007-1226(84)90002-x
452. Shieh SJ, Chiu HY, Yu JC, Pan SC, Tsai ST, Shen CL. Free anterolateral thigh flap for reconstruction of head and neck defects following cancer ablation. *Plast Reconstr Surg*. 2000;105(7):2349-2357; discussion 2358-2360. doi:10.1097/00006534-200006000-00006
453. Sananpanich K, Tu YK, Kraisarin J, Chalidapong P. Flow-through anterolateral thigh flap for simultaneous soft tissue and long vascular gap reconstruction in extremity injuries: anatomical study and case report. *Injury*. 2008;39 Suppl 4:47-54. doi:10.1016/j.injury.2008.08.031
454. Lakhiani C, Lee MR, Saint-Cyr M. Vascular anatomy of the anterolateral thigh flap: a systematic review. *Plast Reconstr Surg*. 2012;130(6):1254-1268. doi:10.1097/PRS.0b013e31826d1662
455. Smith RK, Wykes J, Martin DT, Niles N. Perforator variability in the anterolateral thigh free flap: a systematic review. *Surg Radiol Anat*. 2017;39(7):779-789. doi:10.1007/s00276-016-1802-y
456. Buergin J, Werth L, Largo R, Scherberich A, Schaefer DJ, Kaempfen A. Cross-sectional Vascularization Pattern of the Adipofascial Anterolateral Thigh Flap for Application in Tissue-engineered Bone Grafts. *Plast Reconstr Surg Glob Open*. 2022;10(2):e4136. doi:10.1097/GOX.0000000000004136
457. Song SH, Choi S, Kim YM, Lee SR, Choi YW, Oh SH. The composite anterolateral thigh flap for knee extensor and skin reconstruction. *Arch Orthop Trauma Surg*. 2013;133(11):1517-1520. doi:10.1007/s00402-013-1833-3
458. Kuo YR, An PC, Kuo MH, Kueh NS, Yao SF, Jeng SF. Reconstruction of knee joint soft tissue and patellar tendon defects using a composite anterolateral thigh flap with vascularized fascia lata. *J Plast Reconstr Aesthet Surg*. 2008;61(2):195-199. doi:10.1016/j.bjps.2006.06.012
459. Youn SK, Kim SW, Kim YH, Hwang KT. The composite anterolateral thigh flap for achilles tendon and soft tissue defect reconstruction with tendon repair by fascia with double or triple folding technique. *Microsurgery*. 2015;35(8):615-621. doi:10.1002/micr.22490

460. Ehrl D, Heidekrueger PI, Schmitt A, et al. The Anterolateral Thigh Flap for Achilles Tendon Reconstruction: Functional Outcomes. *Plast Reconstr Surg*. 2019;143(6):1772-1783. doi:10.1097/PRS.0000000000005652
461. Imaizumi A, Toyota Y. One-stage reconstruction of the complex defects of the Achilles tendon and the adjoining calcaneus using the chimeric superolateral thigh flap: A case report. *Microsurgery*. 2022;42(6):611-616. doi:10.1002/micr.30937
462. Liang Yii RS, Chai SC, Zainal HM, Basiron N. Single-stage reconstruction of a traumatic tendocutaneous defect of the Achilles using free composite anterolateral thigh flap with vascularized fascia lata. *Jt Dis Relat Surg*. 2022;33(3):673-679. doi:10.52312/jdrs.2022.843
463. Leyssens L, Pestiaux C, Kerckhofs G. A Review of Ex Vivo X-ray Microfocus Computed Tomography-Based Characterization of the Cardiovascular System. *Int J Mol Sci*. 2021;22(6):3263. doi:10.3390/ijms22063263
464. Saint-Cyr M, Schaverien M, Arbique G, Hatef D, Brown SA, Rohrich RJ. Three- and four-dimensional computed tomographic angiography and venography for the investigation of the vascular anatomy and perfusion of perforator flaps. *Plast Reconstr Surg*. 2008;121(3):772-780. doi:10.1097/01.prs.0000299338.97612.90
465. Dappa E, Higashigaito K, Fornaro J, Leschka S, Wildermuth S, Alkadhi H. Cinematic rendering – an alternative to volume rendering for 3D computed tomography imaging. *Insights Imaging*. 2016;7(6):849-856. doi:10.1007/s13244-016-0518-1
466. de Spiegeleire X, Vanhaebost J, Coche E. Post-mortem CT angiography of mesenteric vessels using cinematic rendering vision. *Diagnostic and Interventional Imaging*. 2019;100(9):533-534. doi:10.1016/j.diii.2019.05.005
467. Tomaszewski KA, Vikse J, Henry BM, et al. The variable origin of the lateral circumflex femoral artery: a meta-analysis and proposal for a new classification system. *Folia Morphol (Warsz)*. 2017;76(2):157-167. doi:10.5603/FM.a2016.0056
468. Xu DC, Zhong SZ, Kong JM, et al. Applied anatomy of the anterolateral femoral flap. *Plast Reconstr Surg*. 1988;82(2):305-310.
469. Lin SJ, Rabie A, Yu P. Designing the anterolateral thigh flap without preoperative Doppler or imaging. *J Reconstr Microsurg*. 2010;26(1):67-72. doi:10.1055/s-0029-1234023
470. Koshima I, Fukuda H, Utunomiya R, Soeda S. The anterolateral thigh flap; variations in its vascular pedicle. *Br J Plast Surg*. 1989;42(3):260-262. doi:10.1016/0007-1226(89)90142-2
471. Kimata Y, Uchiyama K, Ebihara S, Nakatsuka T, Harii K. Anatomic variations and technical problems of the anterolateral thigh flap: a report of 74 cases. *Plast Reconstr Surg*. 1998;102(5):1517-1523. doi:10.1097/00006534-199810000-00026
472. Tokumoto H, Akita S, Mitsukawa N, et al. An anatomical and histological study of the vascularized iliotibial tract graft. *Microsurgery*. 2016;36(4):325-329. doi:10.1002/micr.30006
473. May JG, Kerr J, May JA, Tassone P, Rivera AL. The use of a simultaneous fascia lata-free flap with cochlear implantation after radical Mastoidectomy. *Clinical Case Reports*. 2022;10(8):e6159. doi:10.1002/ccr3.6159
474. Sreenath SB, Grafmiller KT, Tang DM, et al. Free Tissue Transfer for Skull Base Osteoradionecrosis: A Novel Approach in the Endoscopic Era. *Laryngoscope*. 2023;133(3):562-568. doi:10.1002/lary.30315
475. Wei F chan, Jain V, Celik N, Chen H chi, Chuang DCC, Lin C hung. Have we found an ideal soft-tissue flap? An experience with 672 anterolateral thigh flaps. *Plast Reconstr Surg*. 2002;109(7):2219-2226; discussion 2227-2230. doi:10.1097/00006534-200206000-00007
476. Cherubino M, Berli J, Turri-Zanoni M, et al. Sandwich Fascial Anterolateral Thigh Flap in Head and Neck Reconstruction: Evolution or Revolution? *Plast Reconstr Surg Glob Open*. 2017;5(1):e1197. doi:10.1097/GOX.0000000000001197

477. Cherubino M, Turri-Zanoni M, Battaglia P, et al. Chimeric anterolateral thigh free flap for reconstruction of complex cranio-orbito-facial defects after skull base cancers resection. *J Craniomaxillofac Surg*. 2017;45(1):87-92. doi:10.1016/j.jcms.2016.10.017
478. Yu P, Sanger JR, Matloub HS, Gosain A, Larson D. Anterolateral thigh fasciocutaneous island flaps in perineoscrotal reconstruction. *Plast Reconstr Surg*. 2002;109(2):610-616; discussion 617-618. doi:10.1097/00006534-200202000-00030
479. Cherubino M, Stocco C, Ronga M, et al. Comparisons of fascio-cutaneous anterolateral thigh and sandwich fascial ALT free flap in the distal extremity reconstruction. *Microsurgery*. 2020;40(4):452-459. doi:10.1002/micr.30515
480. Schaverien M, Saint-Cyr M, Arbique G, Hatef D, Brown SA, Rohrich RJ. Three- and four-dimensional computed tomographic angiography and venography of the anterolateral thigh perforator flap. *Plast Reconstr Surg*. 2008;121(5):1685-1696. doi:10.1097/PRS.0b013e31816b4587
481. Chen YC, Scaglioni MF, Carrillo Jimenez LE, Yang JCS, Huang EY, Lin TS. Suprafascial Anterolateral Thigh Flap Harvest: A Better Way to Minimize Donor-Site Morbidity in Head and Neck Reconstruction. *Plast Reconstr Surg*. 2016;138(3):689-698. doi:10.1097/PRS.0000000000002496
482. Seth AK, Iorio ML. Super-Thin and Suprafascial Anterolateral Thigh Perforator Flaps for Extremity Reconstruction. *J Reconstr Microsurg*. 2017;33(7):466-473. doi:10.1055/s-0037-1601422
483. Saint-Cyr M, Wong C, Schaverien M, Mojallal A, Rohrich RJ. The perforasome theory: vascular anatomy and clinical implications. *Plast Reconstr Surg*. 2009;124(5):1529-1544. doi:10.1097/PRS.0b013e3181b98a6c
484. Gosain AK, Yan JG, Aydin MA, Das DK, Sanger JR. The vascular supply of the extended tensor fasciae latae flap: how far can the skin paddle extend? *Plast Reconstr Surg*. 2002;110(7):1655-1661; discussion 1662-1663. doi:10.1097/01.PRS.0000033023.09635.B4
485. Chen CH, Cao Y, Wu YF, Bais AJ, Gao JS, Tang JB. Tendon healing in vivo: gene expression and production of multiple growth factors in early tendon healing period. *J Hand Surg Am*. 2008;33(10):1834-1842. doi:10.1016/j.jhsa.2008.07.003
486. Collins J, Ayeni O, Thoma A. A systematic review of anterolateral thigh flap donor site morbidity. *Can J Plast Surg*. 2012;20(1):17-23. doi:10.1177/229255031202000103
487. Seth R, Revenaugh PC, Scharpf J, Shipchandler TZ, Fritz MA. Free anterolateral thigh fascia lata flap for complex nasal lining defects. *JAMA Facial Plast Surg*. 2013;15(1):21-28. doi:10.1001/2013.jamafacial.5
488. Kerr RP, Hanick A, Fritz MA. Fascia Lata Free Flap Reconstruction of Limited Hard Palate Defects. *Cureus*. 10(3):e2356. doi:10.7759/cureus.2356
489. Liao YT, Li HS, Li Y, Tang KL, Li J, Zhou BH. Revascularization character of autologous fascia lata graft following shoulder superior capsule reconstruction by enhanced magnetic resonance imaging. *J Orthop Surg Res*. 2022;17(1):485. doi:10.1186/s13018-022-03375-z
490. Bhadkamkar MA, Wolfswinkel EM, Hatef DA, et al. The ultra-thin, fascia-only anterolateral thigh flap. *Journal of reconstructive microsurgery*. 2014;30(9):599-605. doi:10.1055/s-0033-1361843
491. Tsuge I, Saito S, Sekiguchi H, et al. Photoacoustic Tomography Shows the Branching Pattern of Anterolateral Thigh Perforators In Vivo. *Plast Reconstr Surg*. 2018;141(5):1288-1292. doi:10.1097/PRS.0000000000004328
492. Tsuge I, Saito S, Yamamoto G, et al. Preoperative vascular mapping for anterolateral thigh flap surgeries: A clinical trial of photoacoustic tomography imaging. *Microsurgery*. 2020;40(3):324-330. doi:10.1002/micr.30531
493. Grcevic D, Pejda S, Matthews BG, et al. In vivo fate mapping identifies mesenchymal progenitor cells. *Stem Cells*. 2012;30(2):187-196. doi:10.1002/stem.780

494. Kawanami A, Matsushita T, Chan YY, Murakami S. Mice expressing GFP and CreER in osteochondro progenitor cells in the periosteum. *Biochem Biophys Res Commun*. 2009;386(3):477-482. doi:10.1016/j.bbrc.2009.06.059
495. Chan CKF, Gulati GS, Sinha R, et al. Identification of the Human Skeletal Stem Cell. *Cell*. 2018;175(1):43-56.e21. doi:10.1016/j.cell.2018.07.029
496. Mountziaris PM, Spicer PP, Kasper FK, Mikos AG. Harnessing and modulating inflammation in strategies for bone regeneration. *Tissue Eng Part B Rev*. 2011;17(6):393-402. doi:10.1089/ten.TEB.2011.0182
497. Kolar P, Schmidt-Bleek K, Schell H, et al. The early fracture hematoma and its potential role in fracture healing. *Tissue Eng Part B Rev*. 2010;16(4):427-434. doi:10.1089/ten.TEB.2009.0687
498. Mantovani A, Biswas SK, Galdiero MR, Sica A, Locati M. Macrophage plasticity and polarization in tissue repair and remodelling. *J Pathol*. 2013;229(2):176-185. doi:10.1002/path.4133
499. Kon T, Cho TJ, Aizawa T, et al. Expression of osteoprotegerin, receptor activator of NF-kappaB ligand (osteoprotegerin ligand) and related proinflammatory cytokines during fracture healing. *J Bone Miner Res*. 2001;16(6):1004-1014. doi:10.1359/jbmr.2001.16.6.1004
500. Evrard R, Manon J, Rafferty C, et al. Vascular study of decellularized porcine long bones: Characterization of a tissue engineering model. *Bone*. 2024;182:117073. doi:10.1016/j.bone.2024.117073
501. Liu H, Hu G, Shang P, et al. Histological characteristics of induced membranes in subcutaneous, intramuscular sites and bone defect. *Orthopaedics & Traumatology: Surgery & Research*. 2013;99(8):959-964. doi:10.1016/j.otsr.2013.08.009
502. Quarto R, Mastrogiacomo M, Cancedda R, et al. Repair of large bone defects with the use of autologous bone marrow stromal cells. *N Engl J Med*. 2001;344(5):385-386. doi:10.1056/NEJM200102013440516
503. Anselme K, Davidson P, Popa AM, Giazzon M, Liley M, Ploux L. The interaction of cells and bacteria with surfaces structured at the nanometre scale. *Acta Biomaterialia*. 2010;6(10):3824-3846. doi:10.1016/j.actbio.2010.04.001
504. Kargozar S, Mozafari M. Nanotechnology and Nanomedicine: Start small, think big. *Materials Today: Proceedings*. 2018;5(7, Part 3):15492-15500. doi:10.1016/j.matpr.2018.04.155
505. Kargozar S, Lotfibakhshaiesh N, Ai J, et al. Strontium- and cobalt-substituted bioactive glasses seeded with human umbilical cord perivascular cells to promote bone regeneration via enhanced osteogenic and angiogenic activities. *Acta Biomater*. 2017;58:502-514. doi:10.1016/j.actbio.2017.06.021
506. Bignon A, Chouteau J, Chevalier J, et al. Effect of micro- and macroporosity of bone substitutes on their mechanical properties and cellular response. *J Mater Sci Mater Med*. 2003;14(12):1089-1097. doi:10.1023/b:jmsm.0000004006.90399.b4
507. Karageorgiou V, Kaplan D. Porosity of 3D biomaterial scaffolds and osteogenesis. *Biomaterials*. 2005;26(27):5474-5491. doi:10.1016/j.biomaterials.2005.02.002
508. Abbasi N, Hamlet S, Love RM, Nguyen NT. Porous scaffolds for bone regeneration. *Journal of Science: Advanced Materials and Devices*. 2020;5(1):1-9. doi:10.1016/j.jsamd.2020.01.007
509. Ganguly P, Jones E, Panagiotopoulou V, et al. Electrospun and 3D printed polymeric materials for one-stage critical-size long bone defect regeneration inspired by the Masquelet technique: Recent Advances. *Injury*. 2022;53:S2-S12. doi:10.1016/j.injury.2022.02.036
510. Garot C, Bettega G, Picart C. Additive Manufacturing of Material Scaffolds for Bone Regeneration: Toward Application in the Clinics. *Adv Funct Mater*. 2021;31(5):2006967. doi:10.1002/adfm.202006967
511. de lageneste OD, Colnot C. Periostin in Bone Regeneration. *Periostin*. 2019;1132:49-61.
512. Squier CA, Ghoneim S, Kremenak CR. Ultrastructure of the periosteum from membrane bone. *J Anat*. 1990;171:233-239.

513. Vidal L, Kampleitner C, Brennan MÁ, Hoornaert A, Layrolle P. Reconstruction of Large Skeletal Defects: Current Clinical Therapeutic Strategies and Future Directions Using 3D Printing. *Front Bioeng Biotechnol*. 2020;8. doi:10.3389/fbioe.2020.00061
514. Aktuglu K, Erol K, Vahabi A. Ilizarov bone transport and treatment of critical-sized tibial bone defects: a narrative review. *Journal of Orthopaedics and Traumatology*. 2019;20(1):22. doi:10.1186/s10195-019-0527-1
515. Lou Y, Wang H, Ye G, et al. Periosteal tissue engineering: current developments and perspectives. *Advanced Healthcare Materials*. 2021;10(12):2100215.
516. Blottner D, Huang Y, Trautmann G, Sun L. The fascia: Continuum linking bone and myofascial bag for global and local body movement control on Earth and in Space. A scoping review. *Reach*. 2019;14:100030.
517. Zhang X, Xie C, Lin AS, et al. Periosteal Progenitor Cell Fate in Segmental Cortical Bone Graft Transplantations: Implications for Functional Tissue Engineering. *J Bone Miner Res*. 2005;20(12):2124-2137. doi:10.1359/JBMR.050806
518. Costa-Almeida R, Gonçalves AI, Gershovich P, Rodrigues MT, Reis RL, Gomes ME. Tendon stem cell niche. *Tissue-specific stem cell niche*. Published online 2015:221-244.
519. Hussey GS, Dziki JL, Badylak SF. Extracellular matrix-based materials for regenerative medicine. *Nat Rev Mater*. 2018;3(7):159-173. doi:10.1038/s41578-018-0023-x
520. Sainio A, Järveläinen H. Extracellular matrix-cell interactions: Focus on therapeutic applications. *Cell Signal*. 2020;66:109487. doi:10.1016/j.cellsig.2019.109487
521. Dong C, Lv Y. Application of collagen scaffold in tissue engineering: recent advances and new perspectives. *Polymers*. 2016;8(2):42.
522. Gjaltema RA, Bank RA. Molecular insights into prolyl and lysyl hydroxylation of fibrillar collagens in health and disease. *Critical reviews in biochemistry and molecular biology*. 2017;52(1):74-95.
523. Rappu P, Salo AM, Myllyharju J, Heino J. Role of prolyl hydroxylation in the molecular interactions of collagens. *Essays Biochem*. 2019;63(3):325-335. doi:10.1042/EBC20180053
524. Thorpe C. Extracellular matrix synthesis and degradation in functionally distinct tendons. Published online October 28, 2010.
525. Kamml J, Ke CY, Acevedo C, Kammer DS. The influence of AGEs and enzymatic cross-links on the mechanical properties of collagen fibrils. *journal of the mechanical behavior of biomedical materials*. 2023;143:105870.
526. Paul RG, Bailey AJ. Glycation of collagen: the basis of its central role in the late complications of ageing and diabetes. *Int J Biochem Cell Biol*. 1996;28(12):1297-1310. doi:10.1016/s1357-2725(96)00079-9
527. Dziedzic-Goclawska A, Kaminski A, Uhrynowska-Tyszkiewicz I, Stachowicz W. Irradiation as a safety procedure in tissue banking. *Cell and tissue banking*. 2005;6:201-219.
528. Seto A, Gatt CJ, Dunn MG. Radioprotection of tendon tissue via crosslinking and free radical scavenging. *Clin Orthop Relat Res*. 2008;466(8):1788-1795. doi:10.1007/s11999-008-0301-9
529. Harrell CR, Djonov V, Fellabaum C, Volarevic V. Risks of using sterilization by gamma radiation: the other side of the coin. *International journal of medical sciences*. 2018;15(3):274.
530. Dayan D, Hiss Y, Hirshberg A, Bubis JJ, Wolman M. Are the polarization colors of picrosirius red-stained collagen determined only by the diameter of the fibers? *Histochemistry*. 1989;93:27-29.
531. Rittié L. Method for Picrosirius Red-Polarization Detection of Collagen Fibers in Tissue Sections. *Methods Mol Biol*. 2017;1627:395-407. doi:10.1007/978-1-4939-7113-8_26
532. Schneider CA, Rasband WS, Eliceiri KW. NIH Image to ImageJ: 25 years of image analysis. *Nat Methods*. 2012;9(7):671-675. doi:10.1038/nmeth.2089
533. Mandair GS, Oest ME, Mann KA, Morris MD, Damron TA, Kohn DH. Radiation-induced changes to bone composition extend beyond periosteal bone. *Bone Reports*. 2020;12:100262.

534. Unal M, Akkus O. Raman spectral classification of mineral- and collagen-bound water's associations to elastic and post-yield mechanical properties of cortical bone. *Bone*. 2015;81:315-326. doi:10.1016/j.bone.2015.07.024
535. Ribeiro JF, Anjos EHM dos, Mello MLS, Vidal B de C. Skin Collagen Fiber Molecular Order: A Pattern of Distributional Fiber Orientation as Assessed by Optical Anisotropy and Image Analysis. *PLOS ONE*. 2013;8(1):e54724. doi:10.1371/journal.pone.0054724
536. Kirby MA, Heuerman AC, Yellon SM. Utility of optical density of picrosirius red birefringence for analysis of cross-linked collagen in remodeling of the peripartum cervix for parturition. *Integrative gynecology and obstetrics journal*. 2018;1(2).
537. Lien CH, Chen ZH, Phan QH. Birefringence effect studies of collagen formed by nonenzymatic glycation using dual-retarder Mueller polarimetry. *Journal of Biomedical Optics*. 2022;27(8):087001-087001.
538. Mazon J, de Aro AA, Simões PW, Pimentel ER. Effect of different resistance-training protocols on the extracellular matrix of the calcaneal tendon of rats. *Annals of Anatomy-Anatomischer Anzeiger*. 2018;216:75-81.
539. Cornu O, Boquet J, Nonclercq O, et al. Synergetic effect of freeze-drying and gamma irradiation on the mechanical properties of human cancellous bone. *Cell and tissue banking*. 2011;12:281-288.
540. Cornu O. Influence of freeze-drying and irradiation on mechanical properties of human cancellous bone: application to impaction bone grafting. *Zorzi A Bone Grafting Croatia: InTech*. Published online 2012:41-58.
541. Liguori GR, Liguori TTA, de Moraes SR, et al. Molecular and biomechanical clues from cardiac tissue decellularized extracellular matrix drive stromal cell plasticity. *Frontiers in bioengineering and biotechnology*. 2020;8:520.
542. Salbach J, Rachner TD, Rauner M, et al. Regenerative potential of glycosaminoglycans for skin and bone. *J Mol Med (Berl)*. 2012;90(6):625-635. doi:10.1007/s00109-011-0843-2
543. Menezes R, Vincent R, Osorno L, Hu P, Arinzeh TL. Biomaterials and tissue engineering approaches using glycosaminoglycans for tissue repair: Lessons learned from the native extracellular matrix. *Acta Biomaterialia*. 2023;163:210-227. doi:10.1016/j.actbio.2022.09.064
544. Adeoye AO, Mukasheva F, Smatov S, et al. A biomimetic synthetic nanofiber-based model for anterior cruciate ligament regeneration. *Front Bioeng Biotechnol*. 2022;10. doi:10.3389/fbioe.2022.969282
545. Masquelet AC, Fitoussi F, Begue T, Muller GP. [Reconstruction of the long bones by the induced membrane and spongy autograft]. *Ann Chir Plast Esthet*. 2000;45(3):346-353.
546. Kuntscher G. Di Marknagelung von Knockenbruchen. *Langenbeck's Archiv far Klinische Chirurgie vereinigt mit Deutsche Zeitschrift fur Chirurgie*. 1940;200:443-449.
547. Soeur R. Intramedullary pinning of diaphyseal fractures. *JBJS*. 1946;28(2):309-331.
548. Watson-Jones R, Adams JC, Bonnin JG, et al. Medullary nailing of fractures after fifty years. *The Journal of Bone & Joint Surgery British Volume*. 1950;32(4):694-729.
549. Bong MR, Koval KJ, Egol KA. The history of intramedullary nailing. *Bull NYU Hosp Jt Dis*. 2006;64(3-4):94-97.
550. Bong MR, Kummer FJ, Koval KJ, Egol KA. Intramedullary nailing of the lower extremity: biomechanics and biology. *J Am Acad Orthop Surg*. 2007;15(2):97-106. doi:10.5435/00124635-200702000-00004
551. Ricci WM, Gallagher B, Haidukewych GJ. Intramedullary nailing of femoral shaft fractures: current concepts. *J Am Acad Orthop Surg*. 2009;17(5):296-305. doi:10.5435/00124635-200905000-00004
552. Maini L, Sharma A, Jha S, Sharma A, Tiwari A. Three-dimensional printing and patient-specific pre-contoured plate: future of acetabulum fracture fixation? *Eur J Trauma Emerg Surg*. 2018;44(2):215-224. doi:10.1007/s00068-016-0738-6

553. Shuang F, Hu W, Shao Y, Li H, Zou H. Treatment of Intercondylar Humeral Fractures With 3D-Printed Osteosynthesis Plates. *Medicine (Baltimore)*. 2016;95(3):e2461. doi:10.1097/MD.0000000000002461
554. Arabnejad S, Johnston B, Tanzer M, Pasini D. Fully porous 3D printed titanium femoral stem to reduce stress-shielding following total hip arthroplasty. *J Orthop Res*. 2017;35(8):1774-1783. doi:10.1002/jor.23445
555. Tetsworth K, Block S, Glatt V. Putting 3D modelling and 3D printing into practice: virtual surgery and preoperative planning to reconstruct complex post-traumatic skeletal deformities and defects. *SICOT J*. 2017;3:16. doi:10.1051/sicotj/2016043
556. Gkouvas G, Agathangelidis F, Nakas C, David C, Sagris D, Petsatodis G. Biomechanical comparison of six intramedullary nails, for the treatment of ex-tra-articular, proximal tibial fractures. *Hippokratia*. 2019;23(2):58-63.
557. Horn J, Linke B, Höntzsch D, Gueorguiev B, Schwieger K. Angle stable interlocking screws improve construct stability of intramedullary nailing of distal tibia fractures: a biomechanical study. *Injury*. 2009;40(7):767-771. doi:10.1016/j.injury.2009.01.117
558. Freeman AL, Craig MR, Schmidt AH. Biomechanical comparison of tibial nail stability in a proximal third fracture: do screw quantity and locked, interlocking screws make a difference? *J Orthop Trauma*. 2011;25(6):333-339. doi:10.1097/BOT.0b013e3181f982e5
559. Li YH, Yu T, Shao W, Liu Y, Zhu D, Tan L. Distal locked versus unlocked intramedullary nailing for stable intertrochanteric fractures, a systematic review and meta-analysis. *BMC Musculoskelet Disord*. 2020;21(1):461. doi:10.1186/s12891-020-03444-6
560. Martínez-Aznar C, Mateo J, Ibarz E, Gracia L, Rosell J, Puértolas S. Biomechanical Behavior of Dynamic vs. Static Distal Locking Intramedullary Nails in Subtrochanteric Femur Fractures. *Bioengineering*. 2023;10(10):1179. doi:10.3390/bioengineering10101179
561. Wähnert D, Stolarczyk Y, Hoffmeier KL, Raschke MJ, Hofmann GO, Mückley T. The primary stability of angle-stable versus conventional locked intramedullary nails. *Int Orthop*. 2012;36(5):1059-1064. doi:10.1007/s00264-011-1420-6
562. Wähnert D, Stolarczyk Y, Hoffmeier KL, Raschke MJ, Hofmann GO, Mückley T. Long-term stability of angle-stable versus conventional locked intramedullary nails in distal tibia fractures. *BMC Musculoskeletal Disorders*. 2013;14(1):66. doi:10.1186/1471-2474-14-66
563. Lenz M, Gueorguiev B, Richards RG, et al. Fatigue performance of angle-stable tibial nail interlocking screws. *Int Orthop*. 2013;37(1):113-118. doi:10.1007/s00264-012-1633-3
564. Charopoulos I, Giannoudis PV. Ideal entry point in antegrade femoral nailing: Controversies and innovations. *Injury*. 2009;40(8):791-794. doi:10.1016/j.injury.2009.06.002
565. Robles AS, Najdawi JJ, Wang J, et al. Optimizing the Entry Point for Reconstruction Nailing of the Femur. *J Am Acad Orthop Surg*. 2023;31(18):e721-e726. doi:10.5435/JAAOS-D-22-00778
566. Alzahrani MM, Aljamaan Y, Alsayigh J, Alghamdi S, Alqahtani SM, Papp SR. Optimal entry point for antegrade and retrograde femoral intramedullary nails. *Chin J Traumatol*. 2023;26(5):249-255. doi:10.1016/j.cjtee.2023.03.006
567. Cascio BM, Thomas KA, Wilson SC. A mechanical comparison and review of transverse, step-cut, and sigmoid osteotomies. *Clin Orthop Relat Res*. 2003;(411):296-304. doi:10.1097/01.blo.0000069895.31220.e8
568. Gundavda MK, Lazarides AL, Burke ZDC, Tsoi K, Ferguson PC, Wunder JS. Reconstructive Allograft Preparation for Long Bone Intercalary Segments After Tumor Resections: Toronto Sarcoma Protocol. *JBJS Essent Surg Tech*. 2023;13(2):e22.00011. doi:10.2106/JBJS.ST.22.00011
569. Buckwalter KA, Lin C, Ford JM. Managing Postoperative Artifacts on Computed Tomography and Magnetic Resonance Imaging. *Semin Musculoskelet Radiol*. 2011;15(04):309-319. doi:10.1055/s-0031-1286013

570. Viateau V, Guillemin G, Calando Y, et al. Induction of a barrier membrane to facilitate reconstruction of massive segmental diaphyseal bone defects: an ovine model. *Vet Surg*. 2006;35(5):445-452. doi:10.1111/j.1532-950X.2006.00173.x
571. Grabherr S, Djonov V, Yen K, Thali MJ, Dirnhofer R. Postmortem angiography: review of former and current methods. *AJR Am J Roentgenol*. 2007;188(3):832-838. doi:10.2214/AJR.06.0787
572. Renard Y, Hossu G, Chen B, Krebs M, Labrousse M, Perez M. A guide for effective anatomical vascularization studies: useful ex vivo methods for both CT and MRI imaging before dissection. *J Anat*. 2018;232(1):15-25. doi:10.1111/joa.12718
573. Salmon M. Artères de la peau. In: *Arteres de La Peau*. ; 1936:246-246.
574. Taylor IG, Pan WR. Angiosomes of the Leg: Anatomic Study and Clinical Implications. *Plastic and Reconstructive Surgery*. 1998;102(3):599.
575. Bergeron L, Tang M, Morris SF. A review of vascular injection techniques for the study of perforator flaps. *Plast Reconstr Surg*. 2006;117(6):2050-2057. doi:10.1097/01.prs.0000218321.36450.9b
576. Taylor GI, Corlett RJ, Ashton MW. The Functional Angiosome: Clinical Implications of the Anatomical Concept. *Plast Reconstr Surg*. 2017;140(4):721-733. doi:10.1097/PRS.0000000000003694
577. Jackowski C, Persson A, Thali MJ. Whole body postmortem angiography with a high viscosity contrast agent solution using poly ethylene glycol as contrast agent dissolver. *J Forensic Sci*. 2008;53(2):465-468. doi:10.1111/j.1556-4029.2008.00673.x
578. Grabherr S, Grimm J, Dominguez A, Vanhaebost J, Mangin P. Advances in post-mortem CT-angiography. *The British Journal of Radiology*. 2014;87(1036). doi:10.1259/bjr.20130488
579. Chevallier C, Doenz F, Vaucher P, et al. Postmortem computed tomography angiography vs. conventional autopsy: advantages and inconveniences of each method. *Int J Legal Med*. 2013;127(5):981-989. doi:10.1007/s00414-012-0814-3
580. Boyd B, Zamora CA, Castillo M. Managing Adverse Reactions to Contrast Agents. *Magn Reson Imaging Clin N Am*. 2017;25(4):737-742. doi:10.1016/j.mric.2017.06.008
581. Bruen R, Stirling A, Ryan M, Sheehan M, MacMahon P. Shelling the myth: allergies to Iodine containing substances and risk of reaction to Iodinated contrast media. *Emerg Radiol*. 2022;29(1):67-73. doi:10.1007/s10140-021-01989-0
582. Rosado Ingelmo A, Doña Diaz I, Cabañas Moreno R, et al. Clinical Practice Guidelines for Diagnosis and Management of Hypersensitivity Reactions to Contrast Media. *J Investig Allergol Clin Immunol*. 2016;26(3):144-155; quiz 2 p following 155. doi:10.18176/jiaci.0058
583. Grabherr S, Dominietto M, Yu L, Djonov V, Müller B, Friess S. Angiofil: a novel radio-contrast agent for post-mortem micro-angiography. In: Stock SR, ed. ; 2008:70781O. doi:10.1117/12.792077
584. Grabherr S, Hess A, Karolczak M, et al. Angiofil-mediated visualization of the vascular system by microcomputed tomography: a feasibility study. *Microsc Res Tech*. 2008;71(7):551-556. doi:10.1002/jemt.20585
585. Stumm CJP, Wittig H, Kalberer NM, Scheurer E. Histomorphological assessment of isolated abdominal organs after targeted perfusion with the contrast agent Angiofil® in postmortem computed tomography angiography. *Forensic Science International*. 2020;315:110427-110427. doi:10.1016/j.forsciint.2020.110427
586. Fonkoue L, Behets C, Steyaert A, Kouassi JK, Detrembleur C, Cornu O. Anatomical study of the descending genicular artery and implications for IMAGE-GUIDED interventions for knee pain. *Clinical Anatomy*. 2021;34(4):634-643. doi:10.1002/ca.23680
587. Catalano LW, Zlotolow DA, Hitchcock PB, Shah SN, Barron OA. Surgical exposures of the radius and ulna. *J Am Acad Orthop Surg*. 2011;19(7):430-438. doi:10.5435/00124635-201107000-00006

588. Protopsaltis TS, Ruch DS. Volar approach to distal radius fractures. *J Hand Surg Am*. 2008;33(6):958-965. doi:10.1016/j.jhsa.2008.04.018
589. Miletin J, Sukop A, Baca V, Kachlik D. Arterial supply of the thumb: Systemic review. *Clin Anat*. 2017;30(7):963-973. doi:10.1002/ca.22973
590. Park H, Kim DJ, Hwang J. Reconstruction of a Mangled Hand with a Thoracodorsal Artery Perforator Free Flap: A Report of Two Cases. *Archives of Hand and Microsurgery*. 2021;26. doi:10.12790/ahm.20.0072
591. Ninkovic M, Dornseifer U. Lateral arm flap. In: *Flaps and Reconstructive Surgery*. Elsevier; 2009:305-319. doi:10.1016/B978-0-7216-0519-7.00024-1
592. Przybycień W, Bonczar M, Ostrowski P, et al. The deep brachial artery—A meta-analysis of its origin and diameter with a review of the literature. *Clinical Anatomy*. 2022;35(7):838-846. doi:10.1002/ca.23853
593. Leyssens L, Balcaen T, Pétré M, et al. Non-destructive 3D characterization of the blood vessel wall microstructure in different species and blood vessel types using contrast-enhanced microCT and comparison with synthetic vascular grafts. *Acta Biomaterialia*. 2023;164:303-316. doi:10.1016/j.actbio.2023.04.013
594. Souza FI de, Saito M, Torres LR, Wei TH, Mattar Junior R, Zumiotti AV. Anatomic study of lateral arm flap with retrograde flow. *Acta ortop bras*. 2010;18:39-43. doi:10.1590/S1413-78522010000100008
595. Marxen M, Thornton MM, Chiarot CB, et al. MicroCT scanner performance and considerations for vascular specimen imaging. *Medical Physics*. 2004;31(2):305-313. doi:10.1118/1.1637971
596. Alvernia JE, Pradilla G, Mertens P, Lanzino G, Tamargo RJ. Latex injection of cadaver heads: technical note. *Neurosurgery*. 2010;67(2 Suppl Operative):362-367. doi:10.1227/NEU.0b013e3181f8c247
597. Hlushchuk R, Haberthür D, Djonov V. Ex vivo microangioCT: Advances in microvascular imaging. *Vascular Pharmacology*. 2019;112:2-7. doi:10.1016/j.vph.2018.09.003
598. Bernard F, Mercier P, Chappard D. Microvascularization of the human central and peripheral nervous system: A new microcomputed tomography method. *Morphologie*. 2020;104(347):247-253. doi:10.1016/j.morpho.2020.05.004
599. Bruguier C, Egger C, Vallée JP, et al. Postmortem magnetic resonance imaging of the heart ex situ: development of technical protocols. *Int J Legal Med*. 2015;129(3):559-567. doi:10.1007/s00414-014-1058-1
600. Gnanasekaran D, Veeramani R, Karuppusamy A. Reappraisal of arterial anatomy of thumb. *Anat Cell Biol*. 2022;55(4):414-422. doi:10.5115/acb.22.052

Grants & awards related to this thesis

Grants

F.R.S. – FNRS (Fonds National de la Recherche Scientifique), Research fellow (Aspirant)
Belgium

F.S.R. Fund (Fonds Spécial pour la Recherche), Aspirant
Université Catholique de Louvain, Belgium

Saint-Luc Foundation grant
Cliniques universitaires Saint-Luc, Belgium

International mobility grant
Fédération Wallonie – Bruxelles (FWB), Belgium

Scientific meeting abroad grant
F.R.S. – FNRS, Belgium

Awards

Scientific Research Price (2021)
1st Rencontres Internationales de Chirurgie Française (RICF), Académie Nationale de Chirurgie (ANC), Paris, France

ESTES Congress Grants Awards (2023)
Sponsored by Deutsche Gesellschaft für Unfallchirurgie (DGU, Germany) in Ljubljana, Slovenia

All the surgical instruments used in the experimental pig models were purchased from Stryker and DePuy Synthes, for which I would like to thank Mrs Maggy Gosset, Daphné Paternostre and Mr Amaury L'Olivier, respectively.

Some figures were partly generated using templates provided by Servier Medical Art (http://smart.servier.com/, downloaded on the 14 July 2022), licensed under a Creative Commons Attribution 3.0 unported license (https://creativecommons.org/licenses/by/3.0/, accessed on the 14 July 2022).

Videos were realized with the Microsoft Clipchamp software.

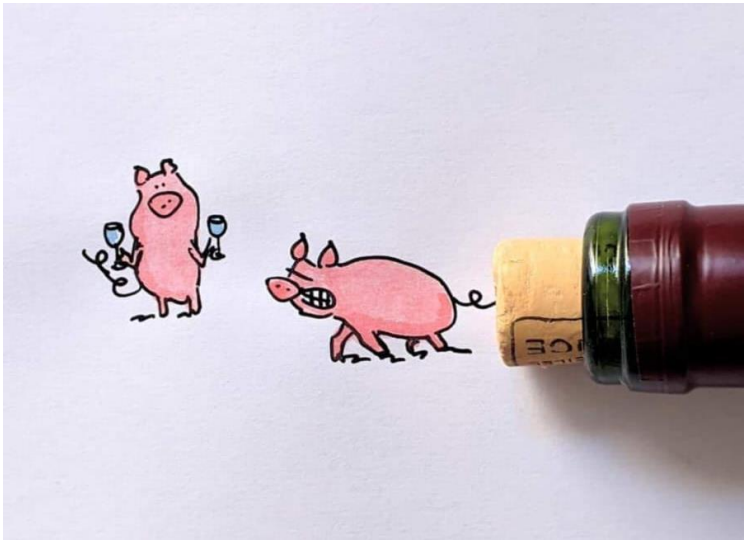

Courtesy of Romain Joly, https://romainjolyillustration.com/

Thesis annexe

Tharsis mission – A Martian Simulation

Related scientific publications

1. Manon J, Saint-Guillain M, Pletser V, et al. Adequacy of in-mission training to treat tibial shaft fractures in mars analogue testing. Scientific reports. 2023;13(1):18072.

2. Manon J, Pletser V, Saint-Guillain M, et al. An Easy-To-Use External Fixator for All Hostile Environments, from Space to War Medicine: Is It Meant for Everyone's Hands? JCM. 2023;12(14):4764. doi:10.3390/jcm12144764.

3. Manon J, Vanderdonckt J, Saint-Guillain M, et al. A Multi-session Evaluation of a Haptic Device in Normal and Critical Conditions : a Mars analogue Mission. Under review in International Journal of Interactive Multimedia and Artificial Intelligence (IJIMAI).

4. Saint-Guillain M, Vanderdonckt J, Burny N, et al. Enabling astronaut self-scheduling using a robust advanced modelling and scheduling system: An assessment during a Mars analogue mission. Advances in Space Research. Published online April 5, 2023. doi:10.1016/j.asr.2023.03.045



Courtesy of Romain Joly, https://romainjolyillustration.com/

Summary

Everyone knows someone who has suffered from a major trauma, cancer or infection. These pathologies also affect bones, leading to critical-size bone defects (CSBDs) – a huge challenge in orthopaedic and reconstructive surgery.

This thesis explores innovative strategies for bone regeneration after CSBDs based on tissue engineering principles. The importance of guided-bone regeneration is emphasized by a wrapping bioactive membrane derived from decellularized fascia lata (FL) recellularized with periosteal mesenchymal stem cells. Through extensive *in vitro* explorations, the osteogenic membrane was designed and tested on an *in vivo* preclinical model. Despite advancements, challenges remain in defining tissue engineering parameters, addressing immune responses, and translating products to clinical practice. Future directions can build on the discovery of an intrinsic vascularization within the FL to optimize tissue engineering approaches and to personalize bone regeneration therapies.

Chacun d'entre nous connaît quelqu'un qui a subi un traumatisme majeur, un cancer ou une infection. Les os sont également touchés par ces pathologies, entraînant des pertes de substance osseuse critiques (PSOCs) - un énorme défi en chirurgie orthopédique et reconstructrice.

Cette thèse explore des stratégies innovantes pour la régénération osseuse après PSOCs, basées sur les principes de l'ingénierie tissulaire. L'importance de la régénération osseuse guidée est soulignée à l'aide d'une membrane bioactive dérivée du fascia lata (FL), décellularisée et recellularisée avec des cellules souches mésenchymateuses périostées. Grâce à des analyses *in vitro* approfondies, la membrane ostéogénique a été conçue et testée sur un modèle préclinique *in vivo*. Malgré les progrès réalisés, des défis restent à relever quant aux définitions émanant de l'ingénierie tissulaire, la gestion des réponses immunitaires et la transposition vers la pratique clinique. Les travaux futurs pourront s'appuyer sur la découverte d'une vascularisation intrinsèque au sein du FL pour optimiser les approches d'ingénierie tissulaire et personnaliser les thérapies de régénération osseuse.

UCLouvain
Secteur des sciences de la santé

Institut de recherche expérimentale et clinique (IREC)

Promoteurs : Professeur Olivier Cornu et Professeur Catherine Behets

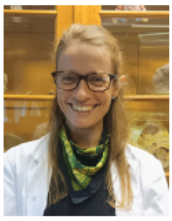

Julie Manon, diplômée en kinésithérapie (2013) et en médecine (2018) à l'UCLouvain, se passionne pour la reconstruction osseuse. Après deux ans de spécialisation en chirurgie orthopédique et traumatologique, elle entreprend un doctorat visant à revitaliser des allogreffes osseuses massives. Parallèlement, elle explore les possibilités de guérison des fractures en milieu spatial hostile, alliant ainsi sa passion pour l'espace à ses recherches médicales, en vue d'améliorer le devenir des patients.

Chacun d'entre nous connaît quelqu'un qui a subi un traumatisme majeur, un cancer ou une infection. Les os sont également touchés par ces pathologies, entraînant des pertes de substance osseuse critiques (PSOCs) - un énorme défi en chirurgie orthopédique et reconstructrice.
Cette thèse explore des stratégies innovantes pour la régénération osseuse après PSOCs, basées sur les principes de l'ingénierie tissulaire. L'importance de la régénération osseuse guidée est soulignée à l'aide d'une membrane bioactive dérivée du fascia lata (FL), décellularisée et recellularisée avec des cellules souches mésenchymateuses périostées. Grâce à des analyses *in vitro* approfondies, la membrane ostéogénique a été conçue et testée sur un modèle préclinique *in vivo*. Malgré les progrès réalisés, des défis restent à relever quant aux définitions émanant de l'ingénierie tissulaire, la gestion des réponses immunitaires et la transposition vers la pratique clinique. Les travaux futurs pourront s'appuyer sur la découverte d'une vascularisation intrinsèque au sein du FL pour optimiser les approches d'ingénierie tissulaire et personnaliser les thérapies de régénération osseuse.

Everyone knows someone who has suffered from a major trauma, cancer or infection. These pathologies also affect bones, leading to critical-size bone defects (CSBDs) – a huge challenge in orthopaedic and reconstructive surgery.
This thesis explores innovative strategies for bone regeneration after CSBDs based on tissue engineering principles. The importance of guided-bone regeneration is emphasized by a wrapping bioactive membrane derived from decellularized fascia lata (FL) recellularized with periosteal mesenchymal stem cells. Through extensive in vitro explorations, the osteogenic membrane was designed and tested on an in vivo preclinical model. Despite advancements, challenges remain in defining tissue engineering parameters, addressing immune responses, and translating products to clinical practice. Future directions can build on the discovery of an intrinsic vascularization within the FL to optimize tissue engineering approaches and to personalize bone regeneration therapies.